



Raveendiraraj, Arunasalam (2009) *Coupling of mechanical behaviour and water retention behaviour in unsaturated soils*. PhD thesis.

<http://theses.gla.ac.uk/717/>

Copyright and moral rights for this thesis are retained by the author

A copy can be downloaded for personal non-commercial research or study, without prior permission or charge

This thesis cannot be reproduced or quoted extensively from without first obtaining permission in writing from the Author

The content must not be changed in any way or sold commercially in any format or medium without the formal permission of the Author

When referring to this work, full bibliographic details including the author, title, awarding institution and date of the thesis must be given

**COUPLING OF MECHANICAL BEHAVIOUR AND
WATER RETENTION BEHAVIOUR IN
UNSATURATED SOILS**

by

Arunasalam Raveendiraraj

A thesis submitted in fulfilment of the
requirements for the degree of

Doctor of Philosophy



**UNIVERSITY
of
GLASGOW**

Department of Civil Engineering

April 2009

© Arunasalam Raveendiraraj, April 2009

*To those who dedicated their lives to the
pursuit of social justice and human
rights in Sri Lanka*

DECLARATION

I declare that this thesis is a record of the original work carried out by myself under the supervision of Prof. S. J. Wheeler in the Department of Civil Engineering at the University of Glasgow, United Kingdom, during the period of May 2005 to April 2009. The copyright of this thesis therefore belongs to the author under the terms of the United Kingdom Copyright acts. Due acknowledgement must always be made of the use of any material contained in, or derived from, this thesis. The thesis has not been presented elsewhere in consideration for a higher degree.

TABLE OF CONTENTS

| | |
|---|------|
| Declaration | i |
| Table of Contents | i |
| List of symbols/abbreviations..... | viii |
| Acknowledgments | xiii |
| Abstract | xiv |
| CHAPTER 1: INTRODUCTION | 1 |
| 1.1 Unsaturated soils | 1 |
| 1.2 Mechanical behaviour of unsaturated soils | 3 |
| 1.3 Water retention behaviour..... | 5 |
| 1.4 Coupling of mechanical behaviour and water retention behaviour | 7 |
| 1.5 Problem statement and research objectives..... | 8 |
| 1.6 Research methodology..... | 9 |
| 1.7 Thesis layout..... | 10 |
| CHAPTER 2: BEHAVIOUR, CONSTITUTIVE MODELLING AND EXPERIMENTAL TESTING OF UNSATURATED SOILS | 12 |
| 2.1 Occurrence of unsaturated soils..... | 12 |
| 2.1.1 Evapo-transpiration from the ground surface | 12 |
| 2.1.2 Gassy soils..... | 14 |
| 2.1.3 Compacted soils | 14 |
| 2.2 Suction in unsaturated soils | 17 |
| 2.2.1 Total suction..... | 17 |
| 2.2.2 Osmotic suction | 18 |
| 2.2.3 Matric suction | 18 |
| 2.3 Importance of meniscus water rings..... | 20 |
| 2.4 Stress state variables | 24 |

| | | |
|-------|--|----|
| 2.5 | Mechanical behaviour | 26 |
| 2.5.1 | Volume change | 26 |
| 2.5.2 | Shear strength..... | 29 |
| 2.6 | Constitutive modelling of mechanical behaviour | 31 |
| 2.6.1 | Barcelona Basic Model (BBM)..... | 31 |
| 2.6.2 | Alternative elasto-plastic models | 35 |
| 2.7 | Water retention behaviour..... | 39 |
| 2.7.1 | Features of typical water retention curves..... | 40 |
| 2.7.2 | Modelling water retention behaviour | 43 |
| 2.8 | Methods of suction control and measurement..... | 47 |
| 2.8.1 | Axis translation technique | 47 |
| 2.8.2 | Osmotic control of matric suction | 49 |
| 2.8.3 | Control of relative humidity by saturated salt solutions | 51 |
| 2.8.4 | Measurement of suction with tensiometers..... | 52 |
| 2.8.5 | Alternative methods of suction measurement..... | 54 |
| 2.9 | Methods of measuring sample volume change | 54 |
| 2.9.1 | Indirect measurement of sample volume change..... | 55 |
| 2.9.2 | Direct measurement of sample volume change | 60 |
| 2.9.3 | Measurement of pore air and pore water volume changes | 60 |

CHAPTER 3: COUPLING OF MECHANICAL BEHAVIOUR AND WATER

| | | |
|-------|--|----|
| | RETENTION BEHAVIOUR IN UNSATURATED SOILS..... | 62 |
| 3.1 | Hydro-mechanical coupling in saturated and unsaturated soils | 62 |
| 3.1.1 | Saturated soil..... | 62 |
| 3.1.2 | Unsaturated soil..... | 63 |
| 3.2 | Influence of degree of saturation on mechanical behaviour | 65 |
| 3.2.1 | Influence of degree of saturation on mechanical behaviour during isotropic loading | 66 |
| 3.2.2 | Mechanical behaviour during cycles of wetting and drying..... | 67 |
| 3.3 | Influence of void ratio on water retention behaviour..... | 69 |
| 3.4 | Coupling of mechanical behaviour and water retention behaviour | 71 |
| 3.5 | Models incorporating coupling of mechanical and water retention behaviour..... | 72 |
| 3.6 | Wheeler et al. (2003) framework..... | 76 |
| 3.6.1 | Modelling concepts..... | 76 |
| 3.6.2 | Illustrative model for isotropic stress states | 80 |
| 3.6.3 | Extension of Wheeler et al. (2003) model to triaxial stress states..... | 84 |

CHAPTER 4: NEW BOUNDING SURFACE PLASTICITY MODELS FOR

| | |
|---|-----|
| UNSATURATED SOILS | 91 |
| 4.1 Limitations of classical elasto-plasticity..... | 91 |
| 4.1.1 Mechanical behaviour..... | 92 |
| 4.1.2 Water retention behaviour | 94 |
| 4.2 Bounding surface plasticity..... | 95 |
| 4.2.1 Introduction..... | 95 |
| 4.2.2 Drawbacks of basic bounding surface plasticity models..... | 98 |
| 4.3 Development of bounding surface water retention models | 101 |
| 4.3.1 Previous research | 101 |
| 4.3.2 Development of a new bounding surface plasticity model for rigid soils | 102 |
| 4.3.3 Extension of the model to deformable soils..... | 111 |
| 4.4 A fully coupled mechanical-water retention model..... | 114 |
| 4.4.1 Uncoupled mechanical behaviour | 114 |
| 4.4.2 Formulation of coupled bounding surface plasticity model | 116 |
| 4.4.3 Qualitative model simulations..... | 121 |
| 4.5 Summary | 127 |
| CHAPTER 5: EXPERIMENTAL APPARATUS AND CALIBRATION..... | 128 |
| 5.1 System A – controlled-suction isotropic cell | 128 |
| 5.1.1 Isotropic cell..... | 129 |
| 5.1.2 Pedestal arrangement | 130 |
| 5.1.3 Top cap arrangement | 131 |
| 5.1.4 Overall system layout | 132 |
| 5.1.5 Measurement devices..... | 134 |
| 5.1.6 Diffused air flushing system..... | 135 |
| 5.2 System B- controlled-suction triaxial cell..... | 137 |
| 5.2.1 Triaxial cell | 137 |
| 5.2.2 Overall system layout | 139 |
| 5.3 System C- triaxial cell for testing saturated soils..... | 140 |
| 5.4 Logging and control system..... | 142 |
| 5.5 Calibration of transducers | 143 |
| 5.5.1 Calibration of pressure transducers | 144 |
| 5.5.2 Calibration of volume gauges..... | 145 |
| 5.5.3 Calibration of load cells..... | 146 |
| 5.5.4 Calibration of axial displacement transducers | 146 |

| | | |
|---|--|------------|
| 5.6 | Calibration of controlled-suction cells for apparent volume change..... | 146 |
| 5.6.1 | Time-dependent effects | 147 |
| 5.6.2 | Calibration for temperature fluctuation..... | 149 |
| 5.6.3 | Calibration of apparent cell volume change with pressure..... | 151 |
| 5.7 | Calibration for volume change of pore water line | 155 |
| CHAPTER 6: SAMPLE PREPARATION AND TESTING PROCEDURES | | 157 |
| 6.1 | Material selection | 157 |
| 6.2 | Sample preparation..... | 158 |
| 6.2.1 | Preparation of kaolin aggregates | 159 |
| 6.2.2 | Preparation of sample | 159 |
| 6.3 | Setting-up procedure | 160 |
| 6.3.1 | Saturation of high air entry filter | 160 |
| 6.3.2 | De-airing procedure | 161 |
| 6.3.3 | Setting up procedure for System A | 162 |
| 6.3.4 | Setting up procedure for System B..... | 164 |
| 6.3.5 | Setting up procedure for System C..... | 164 |
| 6.4 | Control strategies..... | 165 |
| 6.5 | Stress path stages..... | 167 |
| 6.5.1 | Initial equalisation..... | 167 |
| 6.5.2 | Equalisation stages..... | 167 |
| 6.5.3 | Isotropic loading and unloading | 167 |
| 6.5.4 | Wetting and drying | 168 |
| 6.5.5 | Shearing..... | 168 |
| 6.5.6 | Constant volume wetting and drying | 168 |
| 6.5.7 | Constant degree of saturation wetting and drying | 169 |
| 6.5.8 | Stress path with constant deviator stress | 169 |
| 6.6 | Data processing | 169 |
| CHAPTER 7: INITIAL TEST RESULTS AND CALIBRATION OF MODELS..... | | 171 |
| 7.1 | Initial conditions of samples | 171 |
| 7.2 | Initial Equalisation | 175 |
| 7.3 | Determination of bbm parameter values | 181 |
| 7.3.1 | Parameters related to elastic behaviour of BBM model | 182 |
| 7.3.2 | Parameters related to isotropic normal compression lines and LC yield curve | 183 |
| 7.3.3 | Parameters related to shear strength..... | 189 |
| 7.4 | Determination of Wheeler et al. (2003) model parameter values..... | 191 |

| | | |
|-------|---|-----|
| 7.4.1 | Parameters of mechanical behaviour for isotropic stress states (κ and λ) | 192 |
| 7.4.2 | Parameters related to water retention behaviour (κ_s and λ_s) | 193 |
| 7.4.3 | Coupling parameters k_1 and k_2 | 195 |
| 7.4.4 | Initial states | 199 |
| 7.4.5 | Parameters related to shearing G and M | 200 |
| 7.5 | Determination of parameter values for bounding surface plasticity version of Wheeler et al. (2003) model | 201 |

CHAPTER 8: ISOTROPIC TEST RESULTS, SIMULATIONS AND

| | | |
|-------|---|-----|
| | DISCUSSION..... | 203 |
| 8.1 | Tests to investigate the performance of the Wheeler et al. (2003) model | 203 |
| 8.1.1 | Elastic stress-strain relationships (Test A1) | 204 |
| 8.1.2 | Relationship for coupled inward movement of LC yield curve (Test A3)..... | 212 |
| 8.1.3 | Relationship for coupled upward movement of SD yield curve (Test A4)..... | 219 |
| 8.1.4 | Investigation of SI and SD yield curves (Test A5)..... | 226 |
| 8.1.5 | Suction cycles under constant volume condition (Test A6)..... | 232 |
| 8.1.6 | Suction cycles under constant S_r condition (Tests A7 and A8)..... | 239 |
| 8.2 | Other tests investigating the coupling of mechanical behaviour and water retention behaviour | 249 |
| 8.2.1 | Test A9 | 249 |
| 8.2.2 | Test A10 | 255 |
| 8.2.3 | Test A11 | 262 |
| 8.2.4 | Test A12 | 269 |

CHAPTER 9: TRIAXIAL TEST RESULTS, SIMULATIONS AND

| | | |
|-------|---|-----|
| | DISCUSSION..... | 277 |
| 9.1 | Preliminary test (Test B1)..... | 277 |
| 9.2 | Influence of a wetting and drying cycle on the shear behaviour of unsaturated soil | 279 |
| 9.2.1 | Shearing at 200 kPa suction (Tests B2 and B3)..... | 279 |
| 9.2.2 | Shearing at 300 kPa suction (Tests B4, B5, B8 and B9)..... | 286 |
| 9.3 | Other tests | 295 |
| 9.3.1 | Test B6 | 295 |

| | | |
|---|---|-----|
| 9.3.2 | Test B7 | 302 |
| 9.3.3 | Test B10 | 310 |
| 9.3.4 | Tests C1, C2 and C3 | 316 |
| CHAPTER 10: DISCUSSION OF WHEELER ET AL. (2003) MODEL | | 319 |
| 10.1 | Stress state variables | 319 |
| 10.2 | Shape of LC yield curve and flow rule..... | 321 |
| 10.3 | SD and SI yield curves..... | 323 |
| 10.4 | Prediction of behaviour during isotropic loading..... | 325 |
| 10.5 | A problem of inconsistency identified in the illustrative model of Wheeler et al. (2003) | 327 |
| 10.6 | Overall comparison of performance of the WM and WM (BS) against that of the BBM | 333 |
| CHAPTER 11: CONCLUSIONS AND RECOMMENDATIONS..... | | 336 |
| 11.1 | Constitutive model development | 336 |
| 11.2 | Experimental equipment and procedures | 337 |
| 11.2.1 | Suction-controlled isotropic and triaxial cells | 337 |
| 11.2.2 | Sample preparation technique | 337 |
| 11.2.3 | Experimental techniques | 338 |
| 11.3 | Experimental results (basic behaviour) | 338 |
| 11.3.1 | Equalisation..... | 338 |
| 11.3.2 | Isotropic loading and unloading | 339 |
| 11.3.3 | Wetting and drying | 339 |
| 11.3.4 | Shearing | 340 |
| 11.3.5 | Calibration of models | 340 |
| 11.4 | Coupling of mechanical behaviour and water retention behaviour: experimental results and model predictions | 341 |
| 11.4.1 | Influence of wetting and drying on isotropic loading..... | 341 |
| 11.4.2 | Wetting and drying | 341 |
| 11.4.3 | Shearing | 342 |
| 11.5 | Overall performance of WM and WM(BS) | 343 |
| 11.5.1 | Elastic behaviour..... | 343 |
| 11.5.2 | Yield curves and flow rules..... | 344 |
| 11.5.3 | Revised choice of some model parameter values | 344 |

| | | |
|------------|--|-----|
| 11.5.4 | Inconsistency in the WM model..... | 345 |
| 11.6 | Recommendations for future work..... | 345 |
| 11.6.1 | Experimental technique..... | 345 |
| 11.6.2 | Experimental results..... | 346 |
| 11.6.3 | Constitutive modelling..... | 347 |
| REFERENCES | | 350 |
| APPENDIX | | 370 |
| A.1 | Calculation of incremental quantities for the simulations..... | 370 |
| A.1.1 | The WM..... | 370 |
| A.1.2 | The WM (BS)..... | 372 |
| A.1.3 | The BBM..... | 374 |
| A.2 | Calculation procedures..... | 375 |
| A.2.1 | The WM..... | 375 |
| A.2.2 | The WM(BS)..... | 381 |
| A.2.3 | The BBM..... | 384 |

LIST OF SYMBOLS/ABBREVIATIONS

| | |
|------------------|--|
| a | Parameter related to air-entry value of soil (in Brooks & Corey 1964, Van Genuchten 1980 and Fredlund & Xing 1994) |
| b | Parameter related to pore size distribution of the soil (in Brooks & Corey 1964) |
| BBM | Barcelona Basic Model |
| c' | Effective cohesion |
| CF | Capillary fringe |
| CRSP | Constant Rate of Strain Pump |
| CSL | Critical State Line |
| dp_0^* | Incremental movement of LC yield curve (in the WM) |
| DPT | Differential Pressure Transducer |
| ds_D^* | Incremental movement of SD yield curve (in the WM) |
| ds_I^* | Incremental movement of SI yield curve (in the WM) |
| dS_r | Increment of degree of saturation |
| dS_r^e | Elastic increment of degree of saturation |
| dS_r^p | Plastic increment of degree of saturation |
| $d\epsilon_{ij}$ | Strain increment tensor |
| $d\epsilon_s$ | Increment of shear strain |
| $d\epsilon_s^e$ | Increment of elastic shear strain |
| $d\epsilon_s^p$ | Increment of plastic shear strain |
| $d\epsilon_v$ | Increment of volumetric strain |
| $d\epsilon_v^e$ | Increment of elastic volumetric strain |
| $d\epsilon_v^p$ | Increment of plastic volumetric strain |
| e | Void ratio |
| F | Deviator force |
| f, g | Exponents (in the WM(BS)) |
| G | Elastic shear modulus |
| G_s | Specific gravity of soil particles |

| | |
|----------------|--|
| h | Hydraulic head |
| H_0 | Height of the sample at the start of the stage |
| IC | Imperial College |
| k | Material constant giving linear shift of the critical state line with suction in the $q : \bar{p}$ plane (in the BBM) |
| K_0 | Earth pressure coefficient at rest |
| k_1, k_2 | Coupling parameters (in the WM) |
| LC | Loading Collapse |
| LVDT | Linear Variable Displacement Transducer |
| M | Gradient of the Critical State Line in the $q : \bar{p}$ plane |
| m | Parameter related to asymmetric shape of retention curve (in Van Genuchten 1980 and Fredlund & Xing 1994) |
| M^* | Gradient of the Critical State Line in the $q : p^*$ plane |
| M_0 | Mass of the sample at the start of the test |
| MCC | Modified Cam Clay |
| M_s | Mass of solids within the sample |
| M_w | Molar mass of water vapour |
| n | Porosity/Parameter related to rate of change slope of the retention curve (in Van Genuchten 1980 and Fredlund & Xing 1994) |
| $N(s)$ | Specific volume of soil on the normal compression line for suction s at reference pressure p^c (in BBM) |
| \bar{p} | Mean net stress |
| p^* | Mean Bishop's stress |
| \bar{p}_0 | Net stress on the LC yield curve (in the BBM) |
| p_{atm} | Atmospheric pressure |
| p^c | Reference pressure (in the BBM) |
| PEG | Polyethylene glycol |
| PM | Pressure multiplier |
| p_0^* | Position of LC yield curve at isotropic stress states (in the WM) |
| $\bar{p}_0(0)$ | Value of \bar{p}_0 at zero suction (in the BBM) |
| p_p | Partial water vapour pressure |
| p_s | Saturated water vapour pressure |

| | |
|-------------------|---|
| PT | Pressure transducer |
| q | Deviator stress |
| q_{mem} | Membrane correction for 1% axial strain |
| R | Universal gas constant/ Radius of spherical particles |
| r | Parameter related to the minimum value of $\lambda(s)$ (in the BBM) |
| r_1, r_2 | Principal radii of curvature of the air-water interface |
| R_p | Scaling function for mechanical behaviour (in the WM(BS)) |
| R_s | Scaling function for water retention behaviour (in the WM(BS)) |
| s | Matric suction |
| s^* | Modified suction |
| SD | Suction Decrease |
| s_D^* | Position of SD yield surface (in the WM) |
| SI | Suction Increase |
| s_I^* | Position of SI yield surface (in the WM) |
| SM | Stepper motor |
| S_N | Saturated zone with negative pore water pressure |
| S_p | Saturated zone with positive pore water pressure |
| S_r | Degree of saturation |
| T | Absolute temperature |
| TC | Thermocouple |
| T_s | Surface tension |
| U | Unsaturated zone |
| u | Pore pressure |
| u_a | Pore air pressure |
| u_w | Pore water pressure |
| v | Specific volume |
| V_0 | Sample volume at the start of the stage |
| V_1, V_2, \dots | Valves |
| VC | Volume change device |
| v_w | Specific water volume |

| | |
|---------------|--|
| w | Gravimetric water content |
| WM | Wheeler et al. (2003) model |
| WM(BS) | Bounding surface plasticity version of Wheeler et al. (2003) model |
| z | Elevation relative to some reference datum |
| α | Parameter in non-associated flow rule |
| β | Parameter giving the rate of change of compressibility with suction (in the BBM) |
| γ_w | Unit weight of water |
| δ | Distance between the current stress point and the image stress point |
| δ_0 | Distance between the point of projection and the image stress point |
| Δc | Difference in the concentration between two solutions |
| ΔH | Axial displacement of the sample since the start of the stage |
| δ_{ij} | Kroneker's delta |
| ΔN | Additional inter-particle normal force |
| ΔV | Reduction of the sample volume since the start of the stage |
| ΔV_w | Reduction of pore water volume since the start of the test |
| η^* | Stress ratio (in the WM) |
| θ | Volumetric water content |
| κ | Gradient of elastic swelling lines in the $v : \ln p^*$ plane (in the WM) or in the $v : \ln \bar{p}$ plane in the BBM |
| κ_s | Gradient of elastic scanning lines in the $S_r : \ln s^*$ plane (in the WM) or elastic shrinkage lines in the $v : \ln s$ plane in the BBM |
| λ | Conventional gradient of the saturated normal compression line |
| $\lambda(0)$ | Value of $\lambda(s)$ at zero suction (in the BBM) |
| $\lambda(s)$ | Slope of normal compression line in the $v : \ln \bar{p}$ plane (for the BBM) |
| λ_s | Elasto-plastic gradient of the main drying or main wetting curves in the $S_r : \ln s^*$ plane (in the WM) |
| π | Osmotic suction |
| ρ_w | Density of water |
| σ | Total stress |
| σ^* | Average inter-granular stress or Bishop's stress |
| σ' | Effective stress |

| | |
|--------------------------------|--|
| $\sigma_1, \sigma_2, \sigma_3$ | Principal stresses |
| σ_a | Axial stress |
| σ_{ij} | Total stress tensor |
| τ | Shear strength |
| φ^* | Soil constant (in Gallipoli et al., (2003a)) |
| φ' | Friction angle associated with effective stress/net stress |
| φ^b | Friction angle associated with changes in suction |
| χ | Parameter related to degree of saturation |
| ψ | Total suction |
| ψ^* | Soil constant (in Gallipoli et al., (2003a)) |

ACKNOWLEDGMENTS

This project was supported by an EU-funded Marie Curie Research Training Network on Mechanics of Unsaturated Soils for Engineering (MUSE). The financial support from ORSAS is also gratefully acknowledged. The experimental programme was carried out in the Department of Civil Engineering at the University of Glasgow.

I am grateful to my supervisor, Professor S.J. Wheeler, for his valuable supervision and critical suggestion throughout the research period. His expertise in constitutive modelling and experimental testing in unsaturated soils improved my research skills and understanding of soil mechanics in general. I would also like to acknowledge many researchers related (directly and indirectly) to the MUSE Network for the useful discussions which helped me, particularly in the experimental programme.

I am indebted to the staff members of the Civil Engineering Department, particularly Mr. Tim Montgomery, Mr. Stuart McLean and Mr. Alan Yuill, for their help regarding the technical aspects of experimental programme, and Mrs. Eileen Davies, Ms. Barbara Grant and Miss. Amanda Smith, for their help regarding administrative issues, and Mr. Kenneth McColl, for his help regarding computing. Also acknowledged is Mr. Steven Ackerley, Research Officer at Imperial College, for his help with volume change devices. I would like to thank also Mark Buisson, who developed the experimental systems used in the research. His internal report on the experimental systems helped me to understand the operation of the systems relatively quickly.

My special appreciation goes to my fellow research students and research fellows particularly Douglas Bertram, Laurent Glasson, Tomaz Koziara, Joseph Zhou, Konard Kukla, Patsani Kumambala, Miguel Piedra, Anne Ockelford, Elisa Vignaga, Francesca D'Onza, Muhamad Hezmi, Stephen Woodcock, Muayad Al-Sharrad, Osama Katwan, Le Minh Hue and Sung Oh, and my other friends especially Suthakar, Rajeev, Sanjeevan and Sivasithamparam for their encouragement and useful discussions. Last but not least, I would like to thank my parents (Arunasalam and Saraswathy), brother (Surendraraj) and sister (shupothini) for their constant support and love, without which I would not have been able to carry out my research successfully.

ABSTRACT

Previous research has shown coupling of mechanical behaviour and water retention behaviour in unsaturated soils at a constitutive level, with degree of saturation (in addition to suction) influencing mechanical behaviour and volumetric strains influencing water retention behaviour. An innovative elasto-plastic modelling framework incorporating coupling of mechanical behaviour and water retention behaviour has been proposed by Wheeler, Sharma and Buisson (2003) for isotropic stress states. These authors presented a single constitutive model for both mechanical behaviour and water retention behaviour. They did not, however, fully validate the model against experimental results.

The objectives of the current research included undertaking an experimental programme specifically designed to investigate the coupling between mechanical behaviour and water retention behaviour, and using experimental results to investigate the validity of the Wheeler et al. (2003) model. Developments and refinement of the model were also to be explored

An experimental programme of suction-controlled testing was carried out on one-dimensionally compacted samples of speswhite kaolin in a single steel-walled triaxial cell and an isotropic cell. In addition to standard stress paths, such as isotropic loading, unloading, wetting, drying and shearing, many non-standard stress path tests were also performed. These produced a unique data set, providing evidence of aspects of behaviour never previously studied.

In terms of constitutive model development, the Wheeler et al. (2003) model was extended to triaxial stress states, to include the role of deviator stress. In addition, bounding surface plasticity concepts were used to develop simple realistic water retention models for rigid or deformable unsaturated soils, and a new bounding surface plasticity version of the Wheeler et al. (2003) model was developed. However, a problem of theoretical inconsistency in the Wheeler et al. (2003) model was identified, which occurs if plastic volumetric strains are predicted while the soil is fully saturated.

A simple, but rather unsatisfactory, solution to this inconsistency was identified, and further research is required to identify a more satisfactory solution.

Codes were developed for stress point simulations with the original version of the Wheeler et al. (2003) model, the new bounding surface plasticity version of the model and the conventional Barcelona Basic Model. Simulations were performed of all the experimental tests performed in the current research, to explore the performance of the different models.

Comparison of model simulations with experimental results showed that the Wheeler et al. (2003) model was able to represent basic concepts of the mechanical behaviour of unsaturated soils, but sometimes not with the same level of accuracy or flexibility as the Barcelona Basic Model. The Wheeler et al. (2003) model was however able to capture features of mechanical and water retention behaviour that could not be represented by the Barcelona Basic Model or by other conventional models for mechanical or water retention behaviour. The bounding surface plasticity version of the Wheeler et al. (2003) model sometimes produced improved predictions. There remained, however, specific aspects of behaviour that were not well matched by either versions of the Wheeler et al. (2003) model. Some of these may be solved in the future by refinement of specific constitutive equations within the Wheeler et al. (2003) model, but others appear more likely to be insoluble without a major change to the proposed modelling framework.

CHAPTER 1

INTRODUCTION

1.1 UNSATURATED SOILS

In unsaturated soils, the pores are filled with two or more fluids, most commonly air and water. However, it should be noted that in some special cases, unsaturated soils can contain more than two fluid media. For example, oil, water and gas can occur as pore fluids in hydrocarbon-bearing soils. In addition, partly frozen soils, which contain a mixture of liquid water and ice in the pores, can be analysed using many concepts from unsaturated soil mechanics.

Unsaturated soils with gas (typically air) and liquid water as pore fluids can occur either as natural soils or where soil is placed as a fill material. Unsaturated natural soils occur above the water table. The thickness of the unsaturated zone can vary from a few centimetres (some locations in cool temperate regions) to many metres (in arid, semi-arid or tropical regions). Generation of natural gases (e.g. methane) within a soil stratum can also cause unsaturated conditions. Placement and compaction of soil as a fill material (e.g. in embankments, beneath foundations or behind retaining structures) generally results in unsaturated conditions. The evaporation that occurs due to a heating element could also desaturate the soil lying within a certain range from it (e.g. the region around a buried canister which contains nuclear waste).

Although unsaturated soils occur widely throughout the world, unsaturated soil concepts are rarely applied in geotechnical engineering practice due to the following issues:

- In cool temperate regions (such as Northern Europe and North East USA, where much of the pioneering development of Soil Mechanics and Geotechnical Engineering occurred) natural soils are typically unsaturated to only very shallow depth and the majority of foundation construction and other geotechnical activity will take place beneath the unsaturated zone.

- Understanding the mechanical behaviour of soils under unsaturated conditions has proved far more difficult than under saturated conditions.
- Laboratory testing of unsaturated soils has proven to be costly, time-consuming (as the permeability of soil is lower under unsaturated conditions than under saturated conditions) and less reliable (due to the difficulties involved with measuring negative pore water pressure and volume change of unsaturated soil samples).
- Constitutive modelling of the behaviour of unsaturated soils has been found to be very complex, even at the basic level of prediction, partly because of the interaction between mechanical, water retention, thermal and chemical behaviour. In addition, the role of soil fabric produced by either natural or manmade processes may be particularly important under unsaturated conditions.
- Numerical modelling of problems involving unsaturated soil has proved to be highly complex because of coupling between mechanical, hydraulic, thermal and chemical processes and because of complex constitutive models with many parameters which are difficult to determine reliably.

The facts listed above mean that most practicing geotechnical engineers have employed classical (saturated) soil mechanics to analyse geotechnical engineering problems even if unsaturated conditions are involved. This is wrong, because some of the fundamental features of unsaturated soil behaviour, such as volumetric compression during wetting (often called “collapse compression”) can not be properly represented without an understanding based on unsaturated soil mechanics. In reality, field applications such as analysis of slope instabilities, landslides, underground disposal of radioactive waste, earth dams, embankments and highways all require proper understanding of the behaviour of unsaturated soils, as do foundations and all other geotechnical activities in regions where the natural soil is unsaturated to considerable depth.

Within the last four decades, considerable improvement in the understanding of the behaviour of unsaturated soils has been achieved with developments in experimental, constitutive modelling, numerical and analytical techniques. However, there is still more work to be done to develop a comprehensive understanding of unsaturated soil

behaviour, especially in the area of constitutive modelling, where different modelling approaches have been proposed without being able to capture all significant features of the behaviour of unsaturated soils.

1.2 MECHANICAL BEHAVIOUR OF UNSATURATED SOILS

The mechanical behaviour of soils relates stresses and strains, and includes volume change and shear strength. Mechanical behaviour can be represented mathematically by a mechanical constitutive model, consisting of a set of constitutive equations. A mechanical constitutive model is typically proposed based on the physical principles involved and then supported or modified by the results of experimental tests.

Understanding the volume change behaviour of unsaturated soils has proved more difficult than is the case for saturated soils, because of the role of two different pore pressures and the geometric arrangement of the two pore fluids. To be precise, the ability of the water to occur not only as “bulk water” (like in saturated soils) but also as “meniscus water” (formed around particle contacts) has a profound impact on mechanical properties and causes the complex nature of the volume change behaviour. Changes of pressure in bulk water produce both tangential and normal forces at inter-particle contacts whereas meniscus water exerts only normal forces at inter-particle contacts, providing additional stability to the contacts. During a wetting process, increase of pore water pressure within bulk water causes swelling of the soil, while the possible loss of meniscus water rings can trigger inter-particle slippage, resulting in volumetric compression. The magnitudes of these two opposite forms of behaviour depend upon the confining stress, the previous stress history and the physico-chemical properties of the soil (e.g. Matyas & Radhakrishna, 1968, Jennings & Burland, 1962). Several early proposals were made to explain the volume change behaviour using constitutive equations (e.g. Fredlund & Morgenstern, 1976 and Lloret & Alonso, 1985). However, these equations are not able to describe features of volume change behaviour in a comprehensive manner.

Shear strength of unsaturated soils may be uniquely related to certain stress state variables, such as mean net stress \bar{p} (total stress in excess of pore air pressure) and matric suction s (pore air pressure in excess of pore water pressure), because the

critical state may not likely to depend on the initial conditions or previous stress history. Early experimental programmes conducted on unsaturated soils led to suggestions that the shear strength increased linearly with increasing matric suction (Fredlund et al., 1978, Escario, 1980). However, later experimental evidence and physical explanations indicated that a linear relationship will not hold for all types of soils and for a wide range of suction (e.g. Gan & Fredlund, 1988 and Escario & Saez, 1986). Several constitutive equations have been put forward to predict the shear strength of unsaturated soils mostly based on net stress and suction or water retention curves (e.g. Fredlund et al., 1978 and Vanapalli et al., 1996)

Treating volume change behaviour and shear strength separately is not an entirely successful approach to understand the mechanical behaviour of unsaturated soils, as these two aspects of behaviour are related to each other. A constitutive model for unsaturated soils based on critical state concepts is helpful to describe significant features of both volume change and shear strength behaviour accurately. Initial attention focused on proposing a stress state variable equivalent to “effective stress” in saturated soils, so that all significant features of mechanical behaviour of unsaturated soils could be explained by this variable. One of the famous examples is the stress variable proposed by Bishop (1959) incorporating total stress, pore air pressure and pore water pressure. However, significant experimental evidence and theoretical discrepancies have been put forward against a single stress state variable approach. It has therefore been proved that two independent stress state variables should be used in order to correctly predict the mechanical behaviour of unsaturated soils (Matyas & Radhakrishna, 1968 and Fredlund & Morgenstern, 1976).

Most of the recent mechanical constitutive models are formulated in terms of net stress and matric suction. Alonso et al. (1987) were among the first researchers to present a qualitative description for an elasto-plastic constitutive model in terms of net stress and suction for unsaturated soils, based on critical state concepts. This idea was then developed to a complete elasto-plastic model with mathematical formulation by Alonso et al., (1990). This model is now known as the Barcelona Basic Model (BBM). This framework has been able to describe many of the important mechanical features of unsaturated soils. A key feature is the inclusion of a Loading Collapse (LC) yield curve, named by its ability to explain plastic volumetric compression occurring either

during isotropic loading or during wetting as the same process (i.e. yielding on the LC yield curve). Wheeler and Sivakumar (1995) presented comprehensive experimental test results supporting the qualitative ideas proposed by Alonso et al., (1987). They also have proposed an elasto-plastic model which was intended to be more flexible and realistic than the BBM in modelling the mechanical behaviour of unsaturated soils.

1.3 WATER RETENTION BEHAVIOUR

Water retention behaviour of a soil can be defined as the relationship between water content (or degree of saturation) and appropriate stress state variables (most generally suction). The amount of water in the voids of a soil can be expressed as gravimetric water content (w), volumetric water content (θ) or degree of saturation (S_r).

Figure 1-1 shows typical water retention behaviour expressed in terms of S_r and suction. It can be seen from the figure that during each wetting and drying process, water retention curves follow different paths. This phenomenon, called 'hydraulic hysteresis', means that no unique relationship between water content and suction can be established. Due to hydraulic hysteresis, a soil which does not exhibit any volume change during wetting and drying path would tend to have the following features of water retention behaviour (Croney, 1952 and Vachaud et al., 1971): (1) a main drying curve (followed during drying from a saturated state); (2) a main wetting curve (followed during wetting from an infinite (or very high) value of suction); (3) scanning curves (these are drying and wetting curves commencing at intermediate value of suction). In addition to the irreversibility shown in Figure 1-1, the complexity of the water retention behaviour is increased by the fact that changes in size of pore voids and of passageways between voids modifies the suction necessary to flood or empty the voids, hence shifting the main wetting and drying curves (Wheeler et al., 2003).

Many researchers have attempted to correlate some other hydraulic or mechanical properties of unsaturated soils with the water retention behaviour (Fredlund & Rahardjo, 1993). For example, the variation of water permeability of an unsaturated soil had often been expressed in terms of the water retention function and the saturated permeability of the soil (e.g. Fredlund et al., 1994 and Leong & Rahardjo, 1997). Several proposals have also been made to derive the variation of shear strength with

suction from water retention behaviour and the saturated shear strength relationship (Fredlund et al., 1995 and Vanapalli et al., 1996).

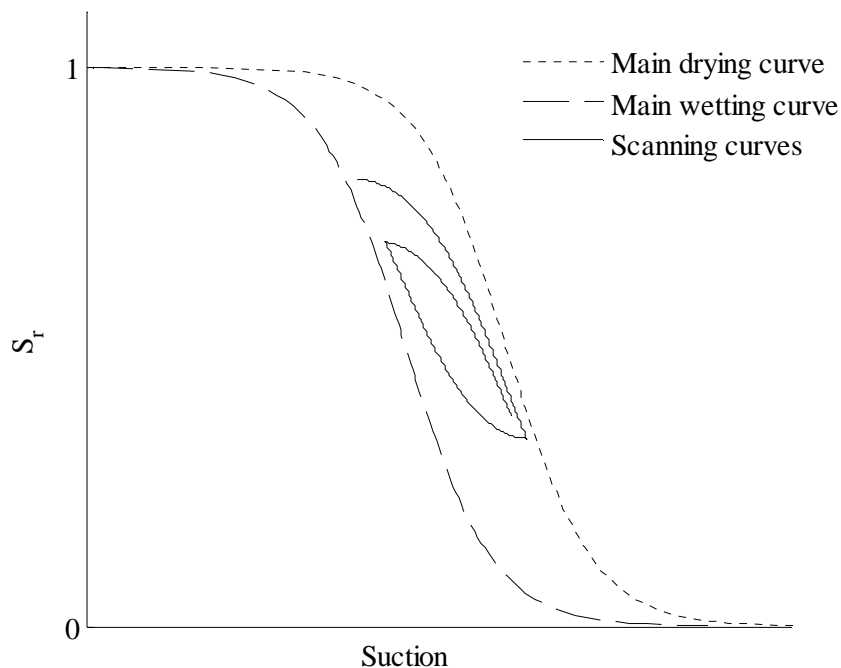


Figure 1-1 Typical water retention behaviour for non-deformable soils

Correlation between permeability or shear strength and the water retention behaviour may be feasible because of the close relationship between the water retention curve and the pore size distribution of the soil. For example, as the permeability depends on the pore size distribution, knowing the water retention curve may provide some information on the variation of permeability with suction. However, it should be noted that the water retention curve is significantly influenced by the void ratio of unsaturated soils (Gallipoli et al., 2003a), meaning that shear strength functions based on the water retention curve unrealistically predict different values of shear strength for different initial void ratio. It is therefore unrealistic to expect that a complete picture of shear strength variation, or of some other aspect of mechanical behaviour, can be derived simply from knowledge of a water retention curve.

1.4 COUPLING OF MECHANICAL BEHAVIOUR AND WATER RETENTION BEHAVIOUR

As mentioned in Section 1.3, changes in the size of voids (i.e. change in void ratio arising from volumetric straining) modify the water retention curves. This shows the influence of mechanical behaviour on water retention behaviour (Gallipoli et al., 2003a, Vanapalli et al., 1999, Romero & Vaunat, 2000). With decreasing void ratio water retention curves in the $S_r : s$ plane are shifted to higher suction range, because the values of suction necessary to flood or empty the voids are inversely related to the void dimensions.

Two soil samples, equivalent in terms of net stress, suction and specific volume but, with different degree of saturation, will have different numbers of voids filled with bulk water and influenced by meniscus water. As a consequence, mechanical behaviour of the two samples would differ significantly, due to the differences in the inter-particle contact forces in the two cases. This means that changes of degree of saturation (arising from the water retention behaviour) affect the mechanical behaviour of unsaturated soils, in addition to the role of suction (Jommi, 2000; Gallipoli et al., 2003b, Wheeler et al. 2003 and Tamagnini, 2004)

From the above arguments, it can be concluded that water retention behaviour and mechanical behaviour are coupled together, in both directions, at a constitutive level (Wheeler et al., 2003). This means that any model, which ignores the coupling phenomenon, will not be able to fully explain either mechanical behaviour or water retention behaviour.

Most of the elasto-plastic models for mechanical behaviour proposed to date are expressed in terms of net stresses and suction. The use of these stress state variables means that it is difficult to incorporate the influence of water retention behaviour because degree of saturation is not included through stress state variables. Due to this reason, several other models (e.g. Jommi, 2000 and Gallipoli et al., 2003b) have been proposed in terms of alternative stress state variables, in which at least one of the stress variables contains degree of saturation. Several elasto-plastic models have also been proposed for water retention behaviour taking into account the influence of void ratio

(Gallipoli et al., 2003a, Romero & Vaunat, 2000). However, these models for mechanical behaviour or water retention behaviour do not couple both behaviours mutually at a constitutive level. Wheeler et al. (2003) put forward an innovative and comprehensive elasto-plastic framework in terms of alternative stress state variables, in order to describe both mechanical and water retention behaviour in a single constitutive model, incorporating coupling in both directions at constitutive level. A detailed discussion of this model can be found in Chapter 3.

1.5 PROBLEM STATEMENT AND RESEARCH OBJECTIVES

Even though significant improvements in understanding and modelling the behaviour of unsaturated soils have been made in the last two decades and a considerable amount of data has been generated, some complex areas of the behaviour of unsaturated soils have not yet been addressed properly. One of the important aspects to be addressed is the coupling of mechanical behaviour and water retention behaviour, which occurs at a constitutive level in unsaturated soils. Any model which ignores this phenomenon will not be able to model the soil behaviour properly because of the interdependency between mechanical and water retention behaviour. A few mechanical modelling frameworks, such as Gallipoli et al. (2003b) and Tamagnini (2004) are able to partially address the problem. However, these models for mechanical behaviour need a separate water retention model or experimental results of water retention behaviour if they are to be used for simulations even for problems where the variation of suction is fully defined. Wheeler et al. (2003) proposed a single model for mechanical and water retention behaviour, where both aspects of behaviour are coupled at constitutive level. However, this model had not yet been properly validated against experimental results.

In this research, an attempt is made to increase the knowledge and understanding of the interaction between mechanical behaviour and water retention behaviour of unsaturated soils, in order to facilitate more comprehensive modelling of unsaturated soil behaviour. In order to accomplish this goal, experimental testing under a wide variety of stress paths was required. Suction-controlled isotropic and triaxial stress path tests were carried out on statically compacted kaolin samples. The experimental data arising from the project, together with other data from the literature, were used to investigate the validity of the Wheeler et al. (2003) model. The intention was that this

would lead to validation of the model or to modification of the model or, if necessary, to the proposal of an entirely new model.

The specific objectives of this research were as follows:

- to undertake a programme of experimental testing specifically designed to investigate the coupling (at constitutive level) between mechanical behaviour and water retention behaviour;
- to use experimental testing to investigate the validity of both the underlying conceptual ideas of the Wheeler et al. (2003) modelling framework and the specific forms of the constitutive equations proposed in the Wheeler et al. (2003) model;
- to revise the modelling framework and the specific form of the constitutive equations (if necessary) in the light of experimental results;
- to extend the model to non-isotropic stress states and investigate against experimental test results;
- to address some unrealistic features of the model (e.g. water retention behaviour) with appropriate modelling technique such as bounding surface plasticity, without compromising the simplicity of the model;
- to propose an alternative new framework, if the experimental results indicate that there are fundamental weaknesses in the Wheeler et al. (2003) framework.

1.6 RESEARCH METHODOLOGY

An experimental programme was carried out for both isotropic and triaxial stress states employing the axis translation technique to investigate the inter-dependency of mechanical and water retention behaviour and the capabilities of the Wheeler et al. (2003) constitutive model. Samples of speswhite kaolin were prepared by one-dimensional static compaction. In addition to the experimental programme, bounding surface plasticity concepts were introduced into the Wheeler et al. (2003) modelling framework in order to improve the model performance.

1.7 THESIS LAYOUT

Chapter 2 of the thesis provides a general background review in two major sections. The first section describes the occurrence, mechanical behaviour, water retention behaviour and various modelling frameworks for unsaturated soils. Particular attention is given to the Barcelona Basic Model. The second section covers experimental testing of unsaturated soils and summarises techniques available for control or measurement of suction and for measurement of sample volume change in triaxial testing of unsaturated soil samples.

Chapter 3 explains the coupling of mechanical behaviour and water retention behaviour in unsaturated soils, and summarises the combined mechanical and water retention model proposed by Wheeler et al. (2003). Included within this chapter is extension of the model of Wheeler et al. (2003) to include the role of deviator stress (Wheeler et al., 2003 limited their proposal to isotropic stress states).

Chapter 4 presents the development of improved models incorporating bounding surface plasticity concepts. First, a bounding surface plasticity water retention model is presented for rigid and deformable soils. Then this concept is extended to mechanical behaviour to formulate a bounding surface plasticity version of the combined mechanical and water retention model of Wheeler et al. (2003).

Chapter 5 describes the experimental equipment used in the research project along with the measurement and calibration techniques.

Chapter 6 describes the experimental procedures used for sample preparation, setting up of the samples, suction-controlled testing and data processing.

Chapter 7 presents some initial test results in order to determine model parameter values. Parameter value determination was performed for the BBM, the Wheeler et al. (2003) model and the bounding surface plasticity version of the Wheeler et al. (2003) model.

Chapter 8 presents experimental results for isotropic stress states, including complex sequences of variation of net stress and suction. Simulations with the BBM and the

Wheeler et al. (2003) models (elasto-plastic and bounding surface plasticity versions) are presented along with the experimental results in order to examine the performance of the models.

Chapter 9 presents triaxial test results along with corresponding simulations from both the BBM and the Wheeler et al. (2003) model.

Chapter 10 discusses the Wheeler et al. (2003) model in the light of the experimental results. A problem of inconsistency in the Wheeler et al. (2003) model is also detailed.

Chapter 11 presents the conclusions from the research and makes recommendations for further research.

CHAPTER 2

BEHAVIOUR, CONSTITUTIVE MODELLING AND EXPERIMENTAL TESTING OF UNSATURATED SOILS

This chapter describes the history of development of unsaturated soil mechanics, paying attention to the evolution of constitutive modelling of mechanical behaviour and water retention behaviour and to the advancement of experimental techniques.

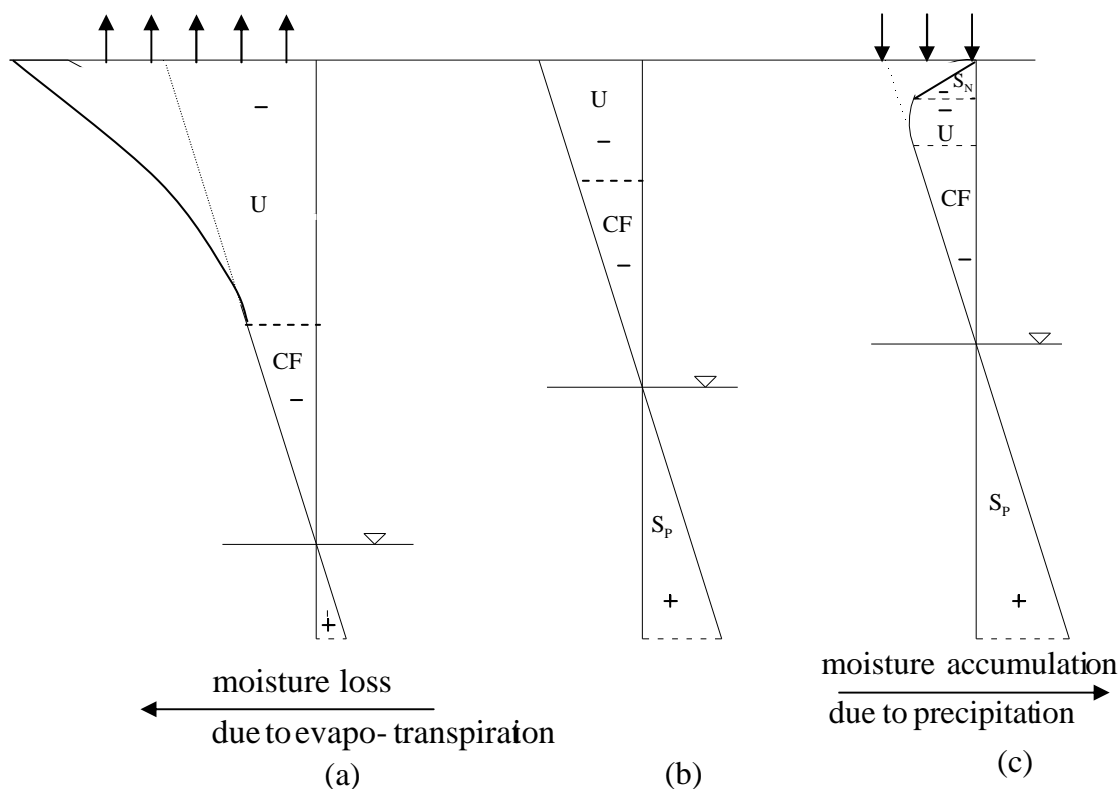
2.1 OCCURRENCE OF UNSATURATED SOILS

The occurrence of unsaturated soils is very common, as a consequence of either natural processes of desaturation or practices adopted in geotechnical engineering such as placement and compaction of fills. Based on the different formation processes involved, unsaturated soils can be categorised into three different types as set out in the following sections.

2.1.1 Evapo-transpiration from the ground surface

The surface deposits are typically unsaturated in all regions. The depth of the unsaturated zone can vary from a few centimetres to several metres depending on the weather condition and type of soil. Figure 2-1 shows three different pore water pressure profiles for varying weather conditions in a simplified and qualitative manner. In reality, the pore water pressure distribution would take different shapes. For example, if the water flow affects the saturated layers below unsaturated zone the pore water pressure distribution in this saturated zone will have different gradient to that of hydrostatic pressure distribution, with magnitude depending upon the flow velocity. The soil below the water table is generally saturated and the pore water pressures are positive. Immediately above the water table is the capillary fringe, a zone of saturated soil with negative values of pore water pressure relative to atmospheric pressure (see Figure 2-1b). The effective stress principle can be applied within both these saturated zones, irrespective of whether the pore water pressure is positive or negative. The thickness of the layer of saturated capillary fringe depends mainly on the pore size

distribution of the soil. Above the capillary fringe there will generally be an unsaturated zone, with the pore air at atmospheric pressure and the pore water at negative pressure. Consider the pore water distribution shown in Figure 2-1b, which corresponds to a hydrostatic distribution, as a starting point. During dry weather conditions, moisture from the surface layer of soil will be lost due to evapo-transpiration, the depth of the unsaturated zone increases and the pore water pressures within it become more negative (see Figure 2-1a). On the other hand, during wet weather conditions, pore water pressure in the surface layer of soil will be increased (due to precipitation) to reach atmospheric pressure (see Figure 2-1c). This may result in a surface layer of saturated soil (at positive or negative pore water pressure) above the unsaturated zone and capillary fringe. In extreme wet conditions the unsaturated zone and capillary fringe may disappear entirely, as the water table rises to ground surface.



U - Unsaturated zone, S_N - Saturated zone with negative pore water pressure, CF - Capillary fringe, S_p - Saturated zone with positive pore water pressure

Figure 2-1 Typical pore water pressure distribution in natural soil deposit

2.1.2 Gassy soils

Gassy soils occur where natural gases are released within the soil or migrate into it from a source at depth. Sources of the gas include decomposition of organic materials, bacterial activity, gas flows from deeper hydrocarbon reservoirs or melting of gas hydrates. Offshore and estuarial environments, organic deposits and marshy land, such as swamps, are some of the places where this type of soil can generally be observed. The gas produced by the biological or other activities generally occurs as discrete bubbles. The size of these discrete bubbles can be either significantly smaller or bigger than the average particle sizes. In the former case, gas bubbles can be accommodated within the water-filled voids without affecting the soil skeleton, leading to the applicability of effective stress principle with a modification for the additional compressibility of the pore fluid arising from the compression of occluded gas bubbles. Similarly, a constitutive model for unsaturated soil can be modified to incorporate the additional compressibility due to small gas bubbles within the pore water void. Vanoudheusden et al. (2003) proposed a model to explain the mechanical features of gassy soils based on elasto-plastic unsaturated expansive soil model proposed by Alonso et al. (1994).

In the latter case of large gas bubbles, each bubble is surrounded by many particles meaning that effective stress approach is no longer applicable. Hence, the gas bubbles and surrounding saturated soil matrix should be treated as two different phases being coupled to each other. In addition, several mechanisms of water and gas flow between these two phases (e.g. flooding of gas bubble with water) should be considered for the better representation of soil behaviour (see Wheeler, 1988a). These bubbles can significantly influence the mechanical behaviour of the soils such as compressibility and shear strength (Sills & Nageswaran, 1984, Wheeler, 1988b and Sills et al., 1991).

2.1.3 Compacted soils

Compaction is defined as a method of mechanically increasing the density of the soil by reducing the volume of air voids and arranging the soil particles to a lower void ratio. Compaction is utilized in almost every civil engineering construction project, such as placement of fills behind retaining walls or beneath foundations and construction of embankments and earth dams. Compaction will not exclude all air

voids, so soils will almost inevitably be in an unsaturated state immediately after compaction.

A compaction process often leads to a distinct type of fabric in unsaturated fine-grained soils. Following the work by Proctor (1933) on compaction properties of soils, a considerable amount of research has been carried out on the influence of the compaction process on soil fabric and the consequent effects on mechanical and water retention behaviour of unsaturated soils. With the introduction of Mercury Intrusion Porosimetry (MIP) and Scanning Electron Microscopy (SEM) methods, pore size distribution and fabric can be either quantitatively measured or directly observed (e.g. Barden & Sides, 1970, Diamond, 1970 and Prapaharan et al., 1991). These techniques have provided a realistic picture of the fabric of compacted soils.

The MIP method involves progressive intrusion of a non-wetting fluid (mercury) into the evacuated pores of a soil sample by applying an external pressure. The pressure required to force mercury into a given pore is related to contact angle, pore size and shape and surface tension of the fluid (Diamond, 1970). By assuming that the pores are cylindrical in shape, it is possible to relate the applied pressure with an equivalent pore diameter.

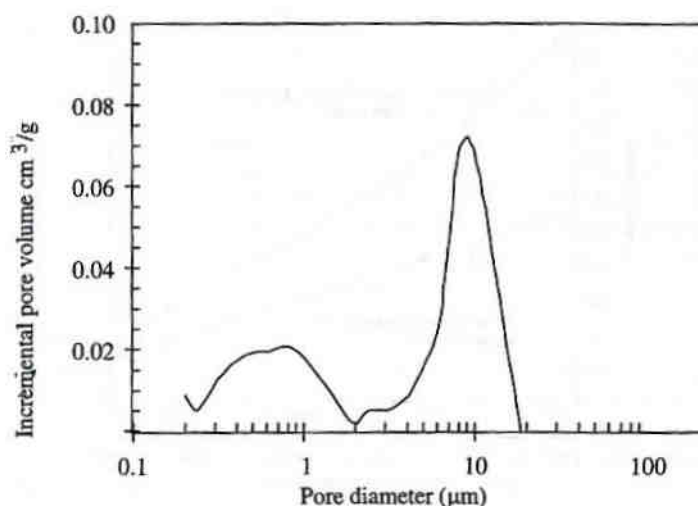


Figure 2-2 Pore size distribution of a sample of aggregated kaolin after compaction (Thom et al., 2006)

Figure 2-2 shows the measured pore size distribution for a sample of aggregated kaolin compacted dry of optimum. Two distinct peaks can be observed in the figure, suggesting the existence of two different pore populations within the sample. This bi-modal pore size distribution can be explained (Alonso et al., 1995 and Wan et al., 1995) by the existence of large pores between aggregates (inter-aggregate pores) and small pores between clay particles inside the aggregates (intra-aggregate pores).

Figure 2-3 shows a typical compacted clay fabric showing two different pore populations. The intra-aggregate pore water is mainly affected by the particle surface forces, such as physico-chemical clay-water interaction, and these pores tend to be saturated unless the suction is extremely high, whereas inter-aggregate pore water is influenced by the capillary forces and generally the pores are unsaturated (Alonso et al., 1990). For samples compacted wet of optimum, a different fabric is observed, involving a uni-modal pore size distribution with a single peak (Juang and Holtz, 1986).

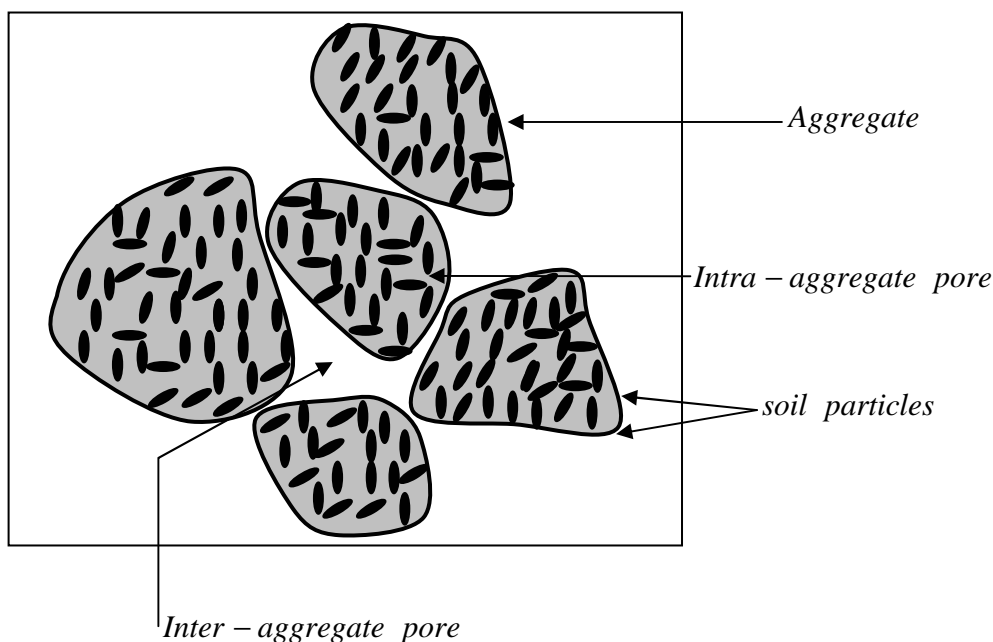


Figure 2-3 Idealised fabric of a fine-grained compacted soil (dry of optimum)

The different fabrics (i.e. uni-modal and bi-modal pore size distributions) produced during compaction wet or dry of optimum can significantly influence the mechanical behaviour of soils. Gens et al. (1995) conducted a series of tests in a suction-controlled oedometer apparatus to investigate the effect of soil fabric on the volume change

behaviour during wetting. Samples were prepared by compaction either wet or dry of optimum water content. In order to eliminate the effects of initial void ratio, water content and suction, samples compacted wet of optimum were taken through a specific stress path prior to final wetting, so that the void ratio, water content and suction for soil compacted wet of optimum and dry of optimum would be the same. The results showed that the initial compaction fabric had significant influence on the volumetric strain during wetting. Sivakumar & Wheeler (2000) investigated the effect of compaction pressure, compaction water content and method of compaction on the subsequent behaviour of compacted speswhite kaolin under isotropic stress states. They concluded that compaction water content (i.e. soil fabric) radically influences the behaviour (compared to other factors) by not only affecting the initial state of soils but also the positions of normal compression lines for different values of suction. This finding was further confirmed by Wheeler & Sivakumar (2000) for triaxial stress states, where the locations of critical state lines for different values of suction were found to be influenced by the change in compaction water content.

2.2 SUCTION IN UNSATURATED SOILS

The conceptual idea of suction has been used by soil physicists from the early 1900s (e.g. Buckingham, 1907). Aitchison (1965) provided general definitions of soil suction and suction components from a thermodynamics point of view.

2.2.1 Total suction

Total suction (ψ) is defined as the total free energy of the soil water per unit volume. Total suction can be mathematically defined using Kelvin's law as follows:

$$\psi = -\frac{RT}{M_w} \ln\left(\frac{p_p}{p_s}\right) \quad (2-1)$$

where R , T , M_w , p_p and p_s are respectively universal gas constant (8.314 J/mol K), absolute temperature, molar mass of water vapour, partial pressure of water vapour in equilibrium with the pore water in the soil and saturated water vapour pressure in equilibrium with pure water with a flat surface at the same temperature. (p_p/p_s) is the relative humidity of air in equilibrium with the pore water.

Total suction is important for flow of liquid water through unsaturated soils, because flow of liquid water is driven by the gradient of total hydraulic head h , which is defined by:

$$h = z + \frac{u_a}{\gamma_w} - \frac{\psi}{\gamma_w} \quad (2-2)$$

where z is the elevation relative to some reference datum, u_a is the pore air pressure and Equation 2-2 ignores the kinetic energy of the pore water (which is typically negligible). Hence, if the pore air pressure is constant throughout the soil and after accounting for elevation differences, it is the gradient of total suction that produces flow of liquid water through soil given that the soil presents some degree of osmotic efficiency i.e. the soil should act, at least partially, as an osmotic membrane.

As the name implies, the total suction is an addition of components, namely: matric suction (s) and osmotic suction (π).

$$\psi = \pi + s \quad (2-3)$$

2.2.2 Osmotic suction

Osmotic suction arises from differences in the salt concentration within the pore water from that of pure water. For example, when a pool of pure water is placed in contact with a salt solution through a membrane, which allows only the water to flow through, an osmotic potential will develop due to the difference in the concentration of salt solution and water will flow through membrane. Van't Hoff (1887) derived an equation for the osmotic suction as shown below:

$$\pi = RT\Delta c \quad (2-4)$$

where, T and Δc are absolute temperature and difference in the concentration between two solutions.

2.2.3 Matric suction

Matric suction s is defined as the pore air pressure (u_a) in excess of the pore water pressure (u_w) in unsaturated soils and is written as:

$$s = u_a - u_w \quad (2-5)$$

Matric suction is related to surface tension at a curved air-water interface giving rise to a capillary phenomenon.

Figure 2-4 shows an infinitesimally small element of air-water interface in equilibrium state with forces exerted by air pressure, water pressure and surface tension. Considering the equilibrium of the element, an equation can be derived for matric suction as follows (Fisher, 1926):

$$u_a - u_w = T_s \left(\frac{1}{r_1} + \frac{1}{r_2} \right) \quad (2-6)$$

where T_s is surface tension and r_1 and r_2 are the principal radii of curvature of the air-water interface, considered to be positive when measured on the air side and negative when measured on the water side. Within the pore spaces of a soil, geometrical constraints and the need to satisfy the appropriate contact angle, where the air-water interface comes into contact with a soil particle, means that the content of the bracket in Equation 2-6 is invariably positive. As a consequence pore air pressure u_a is always greater than pore water pressure u_w .

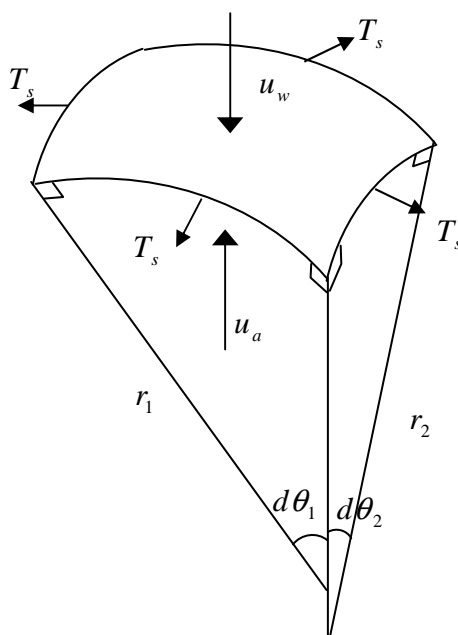


Figure 2-4 Forces acting on a infinitesimally small element of air-water interface

Under field conditions, u_a is typically equal to atmospheric pressure, given that the air voids are inter-connected and connected to the atmosphere at the ground surface. This means that, in the field, pore water pressure u_w in unsaturated soils is negative compared to atmospheric pressure.

For non-expansive soils, the variation in matric suction is much more important than the variation of osmotic suction in controlling the mechanical behaviour of unsaturated soils (Alonso et al., 1987 and Tang et al., 2002). However, for expansive soils, high salt content or chemically active contents in the pore water (i.e. pore fluid chemistry) can have significant influence on the mechanical behaviour of the soil (Iwata et al., 1995). This influence is often interpreted as due to osmotic suction, so that these effects can be conveniently explained through pressures. The mathematical definition of osmotic suction takes account of only pore fluid chemistry (see for example Equation 2-4), even though the interaction between active minerals within the soil particles and pore fluid chemistries is, in fact, what contributes to the mechanical behaviour of expansive unsaturated soils. It is therefore possible for two different fine-grained soils with the same pore fluid chemistry (i.e. the same osmotic value of suction) and the same matric suction to show differences in the mechanical behaviour. This means that osmotic suction cannot simply be added to matric suction to explain the mechanical behaviour of unsaturated soils i.e. the effects on the mechanical behaviour of different unsaturated soils for 1 kPa change of matric suction would not be same as the effects of a 1 kPa change in osmotic suction.

This research is primarily concerned about the behaviour of non-expansive soils, and therefore the term suction will be often used to refer to matric suction.

2.3 IMPORTANCE OF MENISCUS WATER RINGS

Pore water and pore air are the most common fluids contained in unsaturated soils. As stated in Section 1.2, pore water can exist in two different forms, namely bulk water and meniscus water, as shown in Figure 2-5. Bulk water occupies water-filled voids, as in saturated soils, whereas meniscus water forms around the particle contacts where there are air-filled voids. The influence of meniscus water on forces transmitted at particle contacts is radically different from that of bulk water. Changes of pore water

pressure in bulk water produce changes of both tangential and normal forces transmitted at particle-contacts, just like in saturated soils, whereas the presence of a meniscus water ring produces only an additional normal force at inter-particle contacts (Fisher 1926).

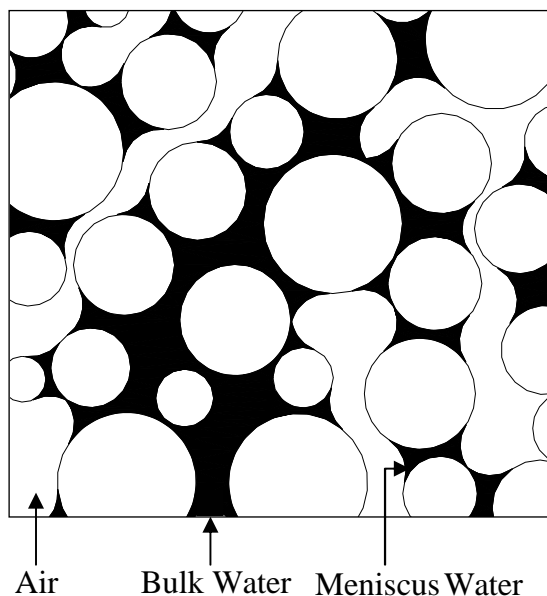


Figure 2-5 Idealized structure of unsaturated soils (after Wheeler et al. 2003)

Figure 2-6 shows two idealized spherical particles of radius R in contact, showing the additional inter-particle force ΔN produced by the meniscus water ring. Making the simplifying assumption that the cross-sectional profile of meniscus water rings is circular of radius r_1 , then simple application of Pythagoras' theorem produces the following relationship between the two principal radii of curvature of the air-water interface r_1 and r_2 (where r_2 is measured on the water side of the interface, see Figure 2-6):

$$r_1 = \frac{r_2^2}{2(R - r_2)} \quad (2-7)$$

Equation 2-7 can be combined with Equation 2-6 (remembering to apply a negative sign to r_2 in Equation 2-6) to give the following expression for matric suction in terms of the dimensionless ratio r_2/R , as given by (Sharma 1998):

$$u_a - u_w = \frac{T_s}{R} \left(\frac{2 - 3\left(\frac{r_2}{R}\right)}{\left(\frac{r_2}{R}\right)^2} \right) \quad (2-8)$$

It can be noted from Equation 2-8 that when $r_2/R = 2/3$ suction is zero (because $r_1 = r_2$) and as r_2/R approaches zero suction tends to infinity.

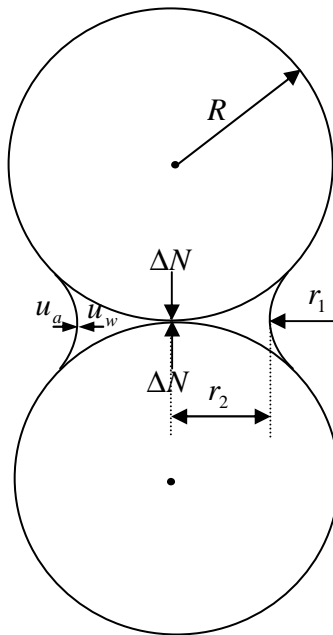


Figure 2-6 Additional inter-particle force at contact point for idealized spherical soil particles

Considering the equilibrium of forces at the inter-particle contact and making use of Equations 2-6 and 2-7 an equation for the additional inter-particle force ΔN produced by a meniscus water ring can be derived as follows (Fisher, 1926):

$$\Delta N = \pi T_s R \left(2 - \frac{r_2}{R} \right) \quad (2-9)$$

Equations 2-8 and 2-9 can be used to calculate how the additional inter-particle normal force ΔN varies with matric suction $u_a - u_w$. For a soil with particles of radius R , suction can be calculated for any given value of r_2/R from Equation 2-8 and the corresponding value of ΔN can be calculated using Equation 2-9. From Equations 2-7 and 2-8 it can be seen that under zero suction, the radius of curvature of meniscus

water rings on air side (r_1) is equal to the radius of curvature on the water side (r_2). This condition is geometrically possible for the two idealized spherical particles in contact (see Figure 2-6) meaning that there can be an inter-particle force even under zero suction (see Equation 2-9). Figure 2-7 shows the resulting variation of ΔN with $(u_a - u_w)$, presented in non-dimensional form, as $\Delta N/T_s R$ plotted against $(u_a - u_w)R/T_s$. The figure clearly shows that an increase in suction will raise inter-particle contact forces providing additional stability at contacts. However, ΔN reaches a limiting value as suction tends to infinity. The increase in additional inter-particle normal force when suction varies from 0 to ∞ is only 50 % of the value at zero suction (see Figure 2-7). This influence of suction on the additional stability at particle contacts, and its role on the yielding of the soil, is taken into account implicitly or explicitly in some constitutive models in which the influence on water retention behaviour on the mechanical behaviour is incorporated (e.g. Gallipoli et al., 2003b). In contrast, Wheeler et al. (2003) argued that the variation of additional inter-particle contact forces with suction can be ignored, because the formation of a meniscus water ring around a particle contact or the disappearance of the meniscus water ring occurs at intermediate values of suction (see Wheeler et al., (2003)). Further discussion on this aspect with experimental evidence will be given in Chapter 8.

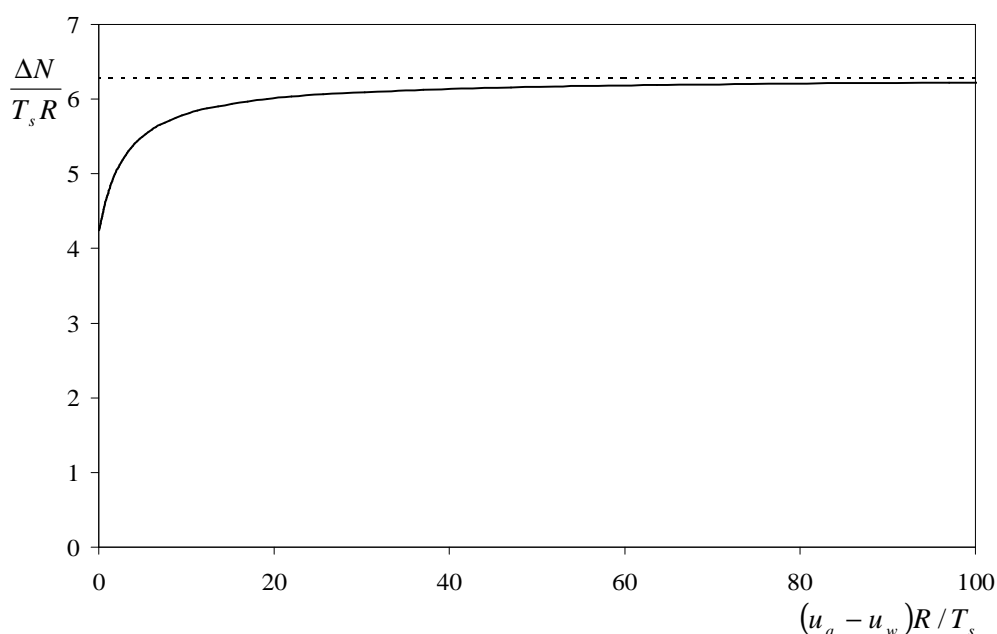


Figure 2-7 Variation of additional inter-particle force ΔN with suction in non-dimensional form

2.4 STRESS STATE VARIABLES

The mechanical behaviour of soil is expressed in terms of stress state variables and appropriate strain variables through specified constitutive relations. For saturated soil, Terzaghi (1936) put forward a tensorial stress state variable, called “effective stress”, to express the mechanical behaviour of saturated soils. He stated;

“the stresses at any point of a section through a mass of soil can be computed from the total principal stresses $\sigma_1, \sigma_2, \sigma_3$ which act at this point. If the voids of the soil are filled with water under stress u , the total principal stresses consist of two parts. One part, u acts in the water and in the solid in every direction with equal intensity. It is called the neutral stress (or pore water pressure). The balance $\sigma'_1 = \sigma_1 - u$, $\sigma'_2 = \sigma_2 - u$ and $\sigma'_3 = \sigma_3 - u$ represents an excess over the neutral stress u and it has its seat exclusively in the solid phase of the soil. This fraction of the total principal stresses will be called the effective principle stresses....”

All the measurable effects of stress changes, including volume change and shear strength, can be expressed in terms of effective stresses in saturated soils. Several attempts have been made to find an equivalent effective stress variable in unsaturated soils. One of the most well known proposals of equivalent effective stress for unsaturated soil was suggested by Bishop (1959), who put forward the following relationship:

$$\sigma' = \sigma - \chi u_w - (1 - \chi)u_a \quad (2-10)$$

where σ' is effective stress, σ is total stress, u_a is pore air pressure, u_w is pore water pressure and χ is a material parameter which mainly depends on degree of saturation and varies from 1 (at saturated state) to 0 (at dry state). If the proposed relationship holds for unsaturated soils, it should be possible to express all stress-strain behaviour, including change in volume and shear strength, exclusively in terms of this effective stress tensor and the behaviour of an unsaturated soil sample should be identical to that of a saturated sample of the same soil which experiences the same variation of effective stress as the unsaturated soil sample (Jennings and Burland 1962). This

implies that every expression for saturated soil behaviour could also be used for unsaturated soil behaviour by simply using Bishop's definition of effective stress. For example, as stated by Bishop et al. (1960), the shear strength would be given by;

$$\tau = c' + (\sigma - \chi u_w - (1 - \chi)u_a) \tan \phi' \quad (2-11)$$

where cohesion c' and friction angle ϕ' are independent of degree of saturation.

Unfortunately, at a very early stage, the effective stress proposal of Bishop (1959) was found to be unsuccessful. When an unsaturated soil sample is wetted (decrease of suction) under low normal / isotropic load, the sample will swell. In contrast, when the sample is wetted at higher normal/ isotropic load the sample will reduce in volume (collapse compression). These two different aspects of mechanical behaviour under wetting cannot be explained by the single effective stress approach. In contrast, the effective stress approach would always predict swelling on wetting, despite the fact that collapse may actually occur at higher magnitudes of normal/isotropic load as reported by Jennings and Burland (1962). These experimental observations clearly proved that a single stress state approach is unable to capture the yielding behaviour of unsaturated soils in a comprehensive manner. The inability of the single stress state approach to capture the yielding behaviour of unsaturated soils leads to unrealistic prediction of volume change behaviour. This was explained by the occurrence of meniscus water rings between soil particles which apply the stress only through the contact points, whereas isotropic applied pressure would produce a uniform soil skeleton stress throughout the sample. This probably makes it impossible to relate the volume change with applied stress by using a single unique stress function as pointed out by Burland (1965).

Consider a situation where suction is increased. This will result in elastic deformation of the soil particles under the increased normal and tangential inter-particle forces, resulting in elastic compression of the soils. This would be interpreted as an increase in effective stress, as in saturated soil. On the other hand, the same increase of suction will decrease the possibility of slippage (plastic strain) at inter-particle contacts, by increasing the normal force exerted by the meniscus water rings. This reduction in the possibility of plastic straining would be interpreted as a decrease in effective stress in a

saturated soil. These two apparently opposite effects on the effective stress during a change of suction prove that a single effective stress approach can not satisfy the fundamental mechanisms behind the mechanical behaviour of unsaturated soils. Based on the experimental evidence and theoretical discrepancy of an effective stress approach, researchers (e.g. Matyas & Radhakrishna 1968, Fredlund & Morgenstern 1976) realised that mechanical behaviour should be presented through two independent stress state variables.

Fredlund and Morgenstern (1976) stated that the mechanical behaviour of unsaturated soils can be well explained by two independent stress variables selected from $(\sigma - u_a)$, $(\sigma - u_w)$ and $(u_a - u_w)$. The two normally selected are “net stress” $(\sigma - u_a)$ and suction $(u_a - u_w)$. Null tests conducted by Fredlund and Morgenstern (1977), by keeping net stress and suction constant while changing pore air pressure, pore water pressure and total pressure, produced no volume change of the soil. This provided further support to the applicability of two independent stress state variables to unsaturated soil.

Many researchers (e.g.: Bolzon et al., 1996, Jommi & Di Prisco, 1994, Kohgo et al., 1993a, Kohgo et al., 1993b, Khalili & Khabbaz, 1998 and Lloret & Khalili, 2000) have made attempts to describe the behaviour of unsaturated soil through alternative pairs of stress variables. In some of these proposals, one stress variable was called “effective stress”. The effect of a second stress state variable (typically suction) is however implicitly or explicitly introduced, often as a hardening parameter in an elasto-plastic model. However, it is now widely accepted by the research community that the terminology “effective stress” should not be used in unsaturated soil unless the proposed stress variable can be used to describe every aspect of mechanical behaviour by itself. Reviews of alternative pairs of stress state variables for unsaturated soils are presented by Wheeler & Karube (1995) and Gens (1995).

2.5 MECHANICAL BEHAVIOUR

2.5.1 Volume change

Many efforts have been made, particularly from the early 1950s, in order to understand the volume change behaviour of unsaturated soils. Even though some features of

behaviour, such as collapse compression during wetting, were reported by researchers like Bishop and Blight (1963), a comprehensive understanding was only possible from the 1980s with the improvement of experimental techniques to measure and control the relevant pressures and volumes accurately. Consequently, a better representation of the volume change behaviour of unsaturated soil has been proposed in a comprehensive manner (e.g. Alonso et al., 1987). In this section, the current understanding and modelling concepts of the features of volume change behaviour of unsaturated soils are listed.

- During isotropic loading stages at different values of suction, the yield stress increases with increasing suction, known as suction hardening as reported by many researchers like Wheeler & Sivakumar (1995) (see Figure 2-8).
- The slope $\lambda(s)$ and the position of 1-D or isotropic constant suction normal compression lines in the $v : \ln(\bar{p} \text{ or } \sigma_a)$ plane for different values of suction depends on suction level. Many researchers reported an increase in the slope with increasing suction to reach a peak value and then reduce slightly (e.g. Wheeler & Sivakumar, 1995 and Sivakumar, 2007). There are also some suggestions that the slope of constant suction normal compression lines would increase with suction to reach a constant value (e.g. Estabragh and Javadi, 2008). The equation of a normal compression line can be written as below:

$$v = N(s) - \lambda(s) \ln \bar{p} \quad (2-12)$$

In fact, one would expect that the normal compression lines at non-zero suction progressively converge towards the saturated line during isotropic or 1-D loading. This means that a constant gradient for a normal compression line may not be appropriate. An example of non-linear behaviour of a constant suction normal compression line will be presented in Section 8.1.5.

- During an isotropic or 1-D unloading stage, swelling of the soil occurs. This can be characterised as elastic behaviour. Many researchers such as Sivakumar (1993) reported that the gradient of swelling lines is almost independent of suction.

- During a wetting stage swelling occurs at low values of net stress and collapse compression is observed at high values of net stress (e.g. Matyas and Radhakrishna, 1968). This can be explained by investigating the constant suction compression curves for different suction levels. Figure 2-9 shows the compression lines for saturated and unsaturated soil crossing at a net stress of \bar{p}_i . If wetting was performed at a net stress less than \bar{p}_i , swelling would be observed. However, if wetting was performed at a net stress larger than \bar{p}_i , then it would result in collapse compression.
- During a drying path, shrinkage is observed, often with an apparent yield point (e.g. Alonso et al., 1995). This aspect of yielding during drying will be discussed in detail in the context of coupling of mechanical behaviour and water retention behaviour in Section 3.2.2.

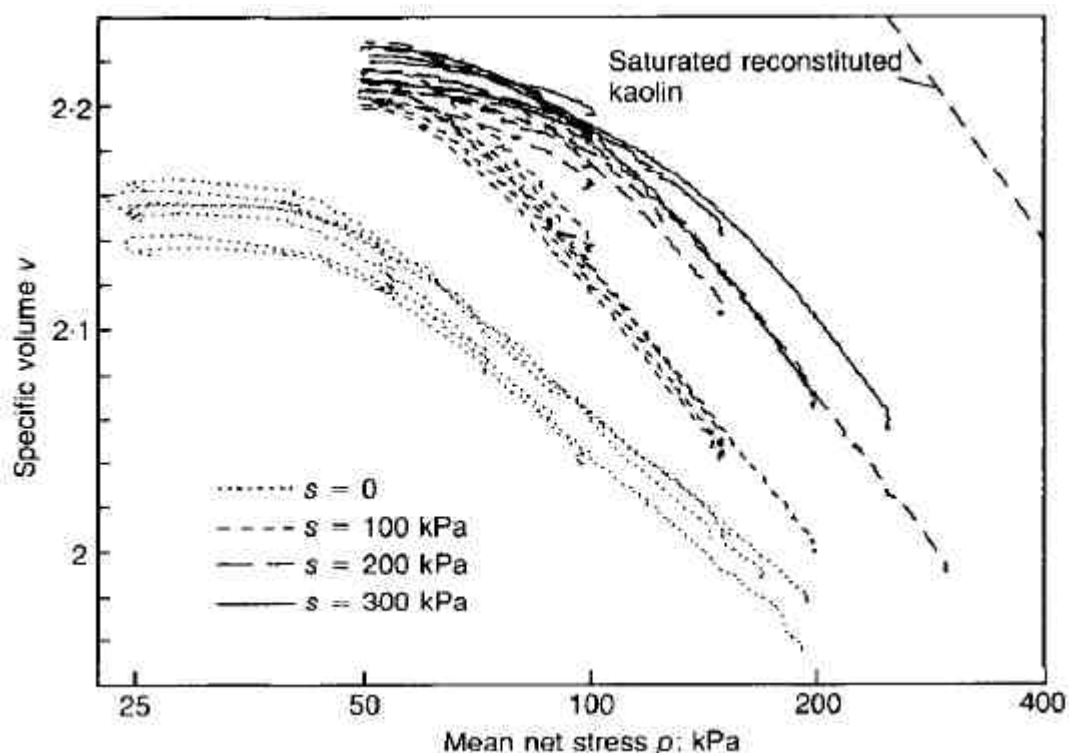


Figure 2-8 Variation of specific volume during isotropic loading (Wheeler & Sivakumar, 1995)

Many of the aspects of behaviour listed above are inconsistent with the early proposals for representing volume change in unsaturated soils, such as the state surface approach (Bishop & Blight, 1963 and Matyas and Radhakrishna, 1968), where a unique (i.e.

elastic) “state surface” was proposed relating void ratio e to net stress $(\sigma - u_a)$ and suction $(u_a - u_w)$. A second unique state surface was proposed relating degree of saturation S_r to $(\sigma - u_a)$ and $(u_a - u_w)$.

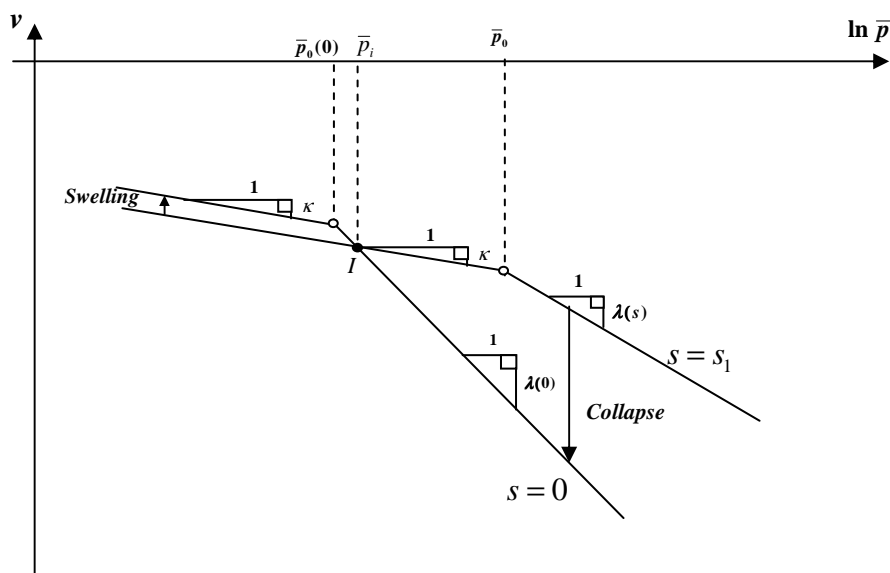


Figure 2-9 compression curves for saturated and unsaturated soil in $v : \ln \bar{p}$ plane (after Alonso, Gens and Josa, 1990)

Based on the fact that aspects of mechanical behaviour listed above are inter-related (see Figure 2-9), Alonso, Gens and Hight (1987) proposed a yield curve in the $s : \bar{p}$ plane, called the Loading Collapse (LC) yield curve, which enables the model to treat collapse compression under wetting and elasto-plastic compression during isotropic loading of net stress as the same phenomenon (i.e. yielding on the LC yield curve). A mathematical form for the LC yield curve was later proposed by Alonso Gens and Josa (1990). (see Section 2.6.1 for more detail)

2.5.2 Shear strength

Much experimental evidence shows that the shear strength of a soil in an unsaturated condition is higher than that of the same soil in saturated conditions at the same net stress (e.g. Fredlund et al., 1978). Several expressions have been proposed by researchers to represent the shear strength variation of unsaturated soils. Most of them have been able to predict the shear strength τ with reasonable accuracy. One of the most widely known expressions was proposed by Fredlund et al. (1978) using two independent stress variables as follows:

$$\tau = c' + (\sigma - u_a) \tan \phi' + (u_a - u_w) \tan \phi^b \quad (2-13)$$

where ϕ' is the friction angle associated with changes in net stress and ϕ^b is a friction angle associated with changes in suction. Fredlund et al. (1978) treated ϕ^b as constant for a particular soil. However, it subsequently became apparent that ϕ^b can not be a constant, because when suction increases to very high values (infinity in theory) the soil can not have infinite value of shear strength, which means that ϕ^b should decrease with increasing suction (Escario & Saez, 1986; Fredlund et al., 1987; and Gan & Fredlund, 1988). In fact, the value of ϕ^b would be equal to ϕ' until suction reaches the air entry value of the soil, which is sufficient for pore air to start entering the soil. After this transition from saturated to unsaturated state, the tangent value of ϕ^b would keep on decreasing to a value much lower than that of ϕ' as the suction increases. This phenomenon is supported by many sets of experimental results, including Escario and Juca (1989). Physically this can be explained by the following argument. As the suction increases from zero, more and more water-filled voids become air-filled voids, leading to additional stability at particle contacts (see Section 2.3). However, once most of the voids become air-filled (i.e. very few voids are still filled with bulk water) additional stability at inter particle contacts primarily depends on suction but, as shown in Figure 2-7, additional inter-particle forces reaches a limiting value, meaning that any increase in shear strength after a certain value of suction would be insignificant.

Some researchers (e.g. Vanapalli et al., 1996) have suggested that knowledge of the water retention curve can be used to calculate the variation of shear strength of an unsaturated soil with suction. However, as mentioned in Section 1.3, it is unrealistic to expect a unique shear strength function relating shear strength to water retention, as the water retention behaviour is more complex than the shear strength behaviour.

Many other researchers, such as Bolzon, Schrefler & Zienkiewicz (1996), Kohgo et al. (1993a), Khalili & Khabbaz (1998), proposed alternative stress state variables for their constitutive models, in such a way that one stress state variable can exclusively represent the variation of shear strength.

2.6 CONSTITUTIVE MODELLING OF MECHANICAL BEHAVIOUR

2.6.1 Barcelona Basic Model (BBM)

The irreversible nature of unsaturated soil behaviour and the need to predict volume changes and shear strength behaviour through a single framework motivated researchers to propose an elasto-plastic critical state model for unsaturated soils (equivalent to models such as Modified Cam Clay for saturated soils). Alonso, Gens and Hight (1987) presented a qualitative description of an elasto-plastic constitutive model for unsaturated soils. As a continuation of that, Alonso Gens and Josa (1990) proposed the mathematical formulation of an unsaturated elasto-plastic critical state model which could merge to the Modified Cam Clay (MCC) model as suction reached zero. This model was intended to model low plasticity and moderate plasticity fine-grained soils. The model is now widely known as the Barcelona Basic Model (BBM).

In the formulation of the BBM, isotropic normal compression lines for different values of suction s were assumed to have different gradients and intercepts. The expression for specific volume on these isotropic normal compression lines was given by:

$$v = N(s) - \lambda(s) \ln\left(\frac{\bar{p}}{p^c}\right) \quad (2-14)$$

where \bar{p} is the mean net stress ($\bar{p} = p - u_a$). $N(s)$ is the value of specific volume v on the normal compression line when \bar{p} is equal to a reference value p^c (p^c is an additional soil constant) and $\lambda(s)$ is the gradient of the normal compression line, which was assumed to decrease monotonically with increasing suction. The variation of $\lambda(s)$ with suction was assumed to be as follows:

$$\lambda(s) = \lambda(0)[(1 - r)\exp(-\beta s) + r] \quad (2-15)$$

Where $\lambda(0)$ is the saturated value of $\lambda(s)$ (at zero suction), r is a parameter related to the minimum value of $\lambda(s)$ ($\lambda(s)$ tends to a minimum value of $r\lambda(0)$ as suction tends to infinity) and β is a parameter giving the rate of change of compressibility with suction. Assuming a value of r between zero and 1, Equation 2-15 predicts decreasing compressibility of the soil with increasing suction.

Elastic changes of specific volume v are given by:

$$dv^e = -\kappa \frac{d\bar{p}}{\bar{p}} - \kappa_s \frac{ds}{(s + p_{atm})} \quad (2-16)$$

The soil constant κ is related to elastic compressibility of the soil with respect to changes of \bar{p} and the soil constant κ_s is related to the elastic compressibility of the soil with respect to changes in suction. Atmospheric pressure p_{atm} was arbitrarily introduced to avoid prediction of infinite elastic volumetric strains as suction tends to zero.

Figure 2-10a shows the predicted variation of specific volume with net stress for two different constant suction values ($s = 0$ and $s = s$) during isotropic loading and subsequent unloading and reloading. The corresponding LC yield curve is shown in Figure 2-10b.

Having defined the variation of $\lambda(s)$ with suction together with form of elastic behaviour, Alonso et al. (1990) showed, by considering a stress path 1-2-3 in Figure 2-10, that the LC yield curve expression is given by:

$$\left(\frac{\bar{p}_0}{p^c} \right) = \left(\frac{\bar{p}_0(0)}{p^c} \right)^{[\lambda(0)-\kappa]/[\lambda(s)-\kappa]} \quad (2-17)$$

Here \bar{p}_0 is the net stress on the LC yield curve (under isotropic stress states with deviator stress $q = 0$) at a given suction s and $\bar{p}_0(0)$ is the value of \bar{p}_0 at zero suction (the intercept of the yield curve with the \bar{p} axis).

The above derivation involves one additional assumption, that the LC yield curve is a straight vertical line when at the reference pressure p^c . However, there is no experimental evidence for this particular feature of the modelling and this assumption has introduced some unrealistic features into the model (see Wheeler, Gallipoli and Karstunen (2002) for more information).

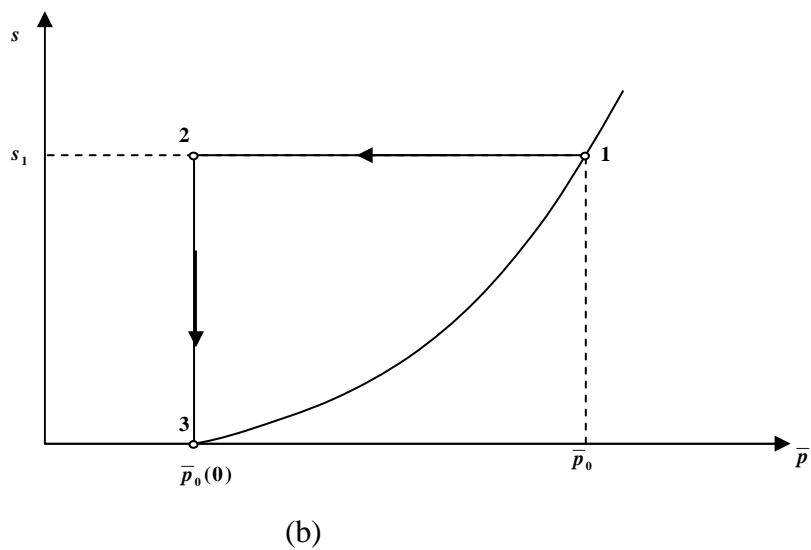
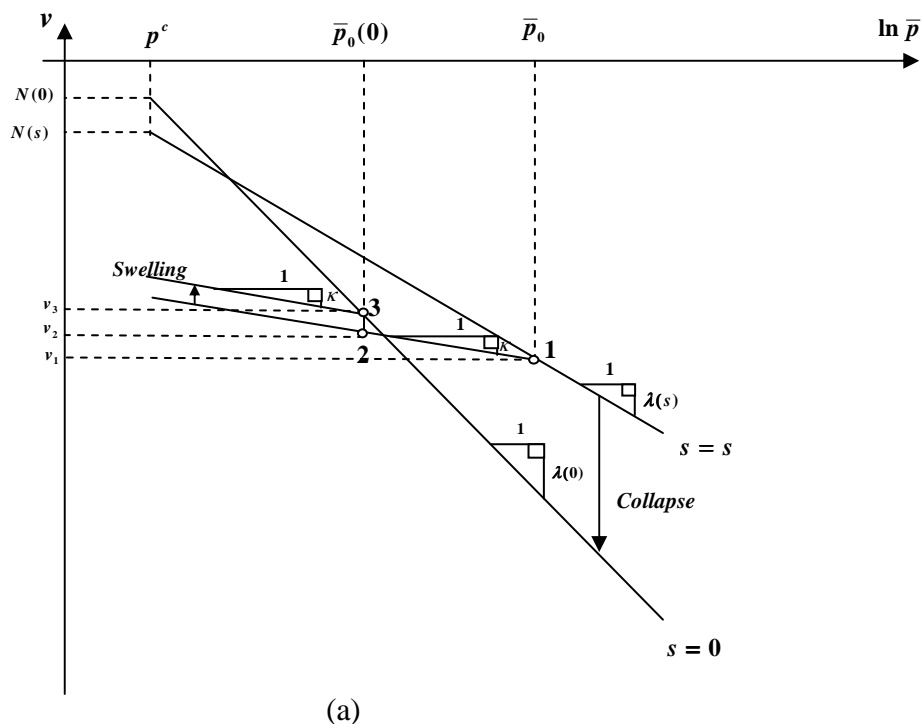


Figure 2-10 Relationship between preconsolidation stresses \bar{p}_0 and $\bar{p}_0(0)$: (a) compression curves for saturated and unsaturated soil; (b) stress path and yield curve in (\bar{p}, s) stress plane (after Alonso, Gens and Josa, 1990)

Cross-sections of the yield surface at constant suction are assumed to be elliptical in shape in the $q : \bar{p}$ plane (see Figure 2-11a) and given by:

$$q^2 - M^2(\bar{p} + ks)(\bar{p}_0 - \bar{p}) = 0 \tag{2-18}$$

Where k is a material constant giving an assumed linear shift of the critical state line with suction in the $q : \bar{p}$ plane (see Figure 2-11a). The critical state line is then given by:

$$q = M\bar{p} + Mks \tag{2-19}$$

where M is the gradient of the Critical State Line in the $q : \bar{p}$ plane (see Figure 2-11a).

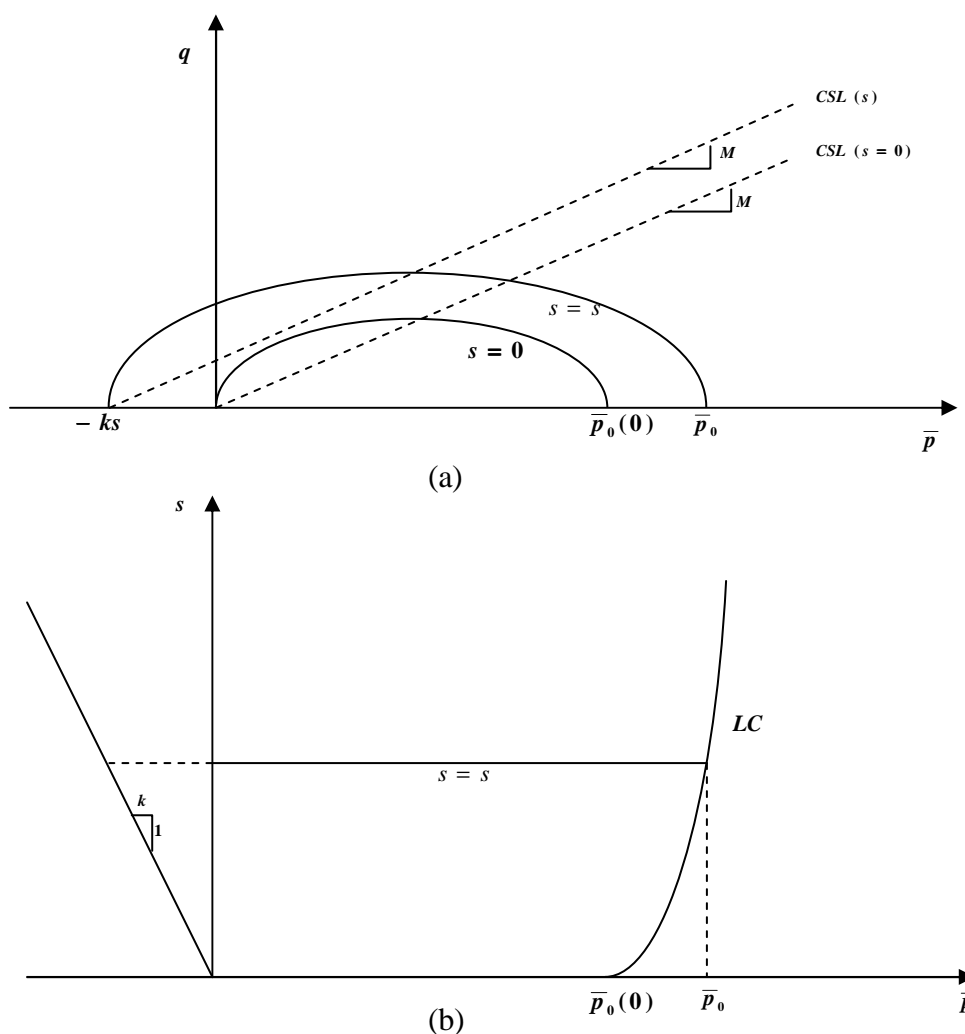


Figure 2-11 LC yield surface: (a) constant suction yield curves (b) isotropic stress states (after Alonso, Gens and Josa, 1990)

As clearly shown by Equation 2-19, the shift of the critical state line with suction (i.e. the increase of shear strength with suction) was assumed to vary linearly with suction and M was assumed to be independent of suction. These assumptions were introduced

for simplicity, but they reduce the flexibility of the model. In particular, the assumption of a linear variation of shear strength with suction, which is equivalent to the proposal by Fredlund et al., 1978 (see Section 2.5.2), is contrary to the experimental observations (e.g. Escario and Juca, 1989). A non-associated flow rule was assumed on the yield surface by Alonso Gens and Josa (1990).

The Barcelona Basic Model was the first milestone in the development of elasto-plastic constitutive models for unsaturated soils, being able to describe many of the complex mechanical features within a single framework. However, the model has its own limitations due to some assumptions made to simplify the model in order to make life easy for numerical modelling and application in the field. Wheeler, Gallipoli and Karstunen (2002) discussed some of the limitations of the Barcelona Basic Model proposed by Alonso et al. (1990) which arise from the possible combination of p^c and r values.

2.6.2 Alternative elasto-plastic models

2.6.2.a Wheeler and Sivakumar (1995) model

Wheeler and Sivakumar (1995) proposed a similar model to Alonso et al. (1990). Fewer simplifications were made in the model in order to keep the model more flexible and realistic. Unlike the BBM, normal compression lines were fitted through experimental data for different values of suction. The shifting of the critical state line with suction in the $q : \bar{p}$ plane was related to a function of suction rather than directly proportional to the suction value as assumed in the BBM. An associated flow rule was assumed on the yield surface.

2.6.2.b Models for anisotropic soils

Although the BBM and the model of Wheeler and Sivakumar (1995) assume isotropic behaviour, many unsaturated soils display anisotropic behaviour (just like saturated soils). Cui & Delage (1996) carried out several tests under isotropic and triaxial stress states on one-dimensionally compacted Jossigny silt samples. For the volumetric behaviour for isotropic stress states, BBM was found to be adequate to explain the features of behaviour. However, constant suction cross-sections of the yield surface were found to be inclined in the $q : \bar{p}$ plane, having the K_0 line as an axis. Figure 2-12

shows the inclined elliptical constant suction cross-sections of the yield surface proposed by Cui & Delage (1996) compared with their corresponding experimental yield points in the $q : \bar{p}$ plane. Due to a few simplifications, the model was unable to provide a good fit for all suctions.

Stropeit et al. (2008) proposed an anisotropic elasto-plastic model by incorporating the features of the S-CLAY1 model (a model proposed by Wheeler et al., (2003b) for saturated soft clay with anisotropy) into the conventional BBM to model unsaturated soil. Simulations with the new anisotropic model and the conventional BBM were carried out of the experimental tests of Cui & Delage (1996). It was shown that the anisotropic version of the model was able to better fit the experimental results, including the shape and size of yield surfaces and the volumetric strain during constant suction shearing, than the original BBM.

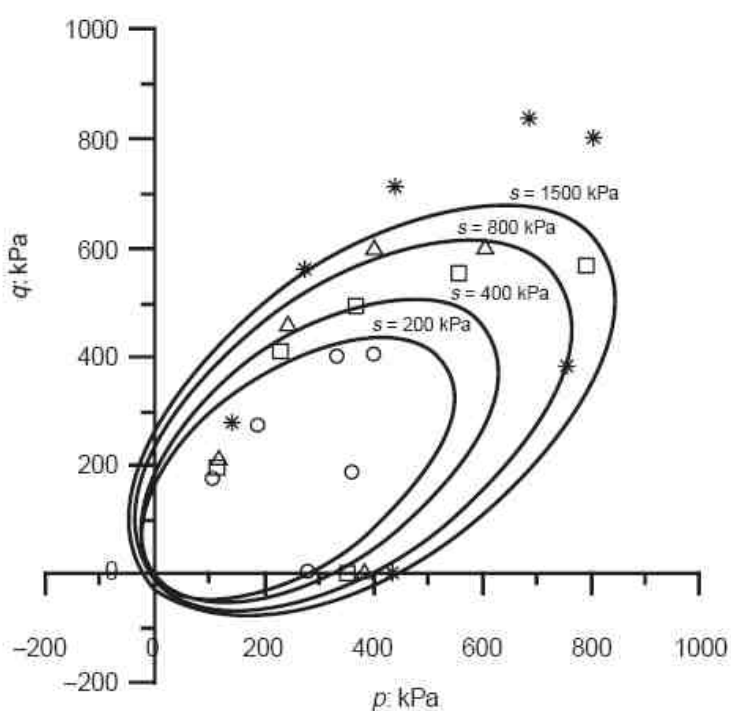


Figure 2-12 Model yield curves and experimental yield points in the $q : \bar{p}$ plane (Cui & Delage, 1996)

2.6.2.c Models for expansive soils

Unsaturated soils containing highly expansive clay minerals, such as montmorillonite, show significantly different behaviour compared to slightly or moderately expansive

soils, particularly during a first wetting process, where a substantial irreversible component of swelling can be observed. Chu & Mou (1973) carried out wetting and drying cycles on highly expansive clay. A major irreversible swelling was observed during the first wetting as shown in Figure 2-13. This type of behaviour could not be captured by models like the BBM. Gens & Alonso (1992), Alonso et al. (1994) and later Alonso, Vaunat & Gens (1999) proposed a modified version of BBM to account for irreversible volume change during wetting and drying cycles in highly expansive soils. The irreversible volume change was explained by analysing the unsaturated soil at macro- and micro-structural levels. As stated in Section 2.1.3, compacted unsaturated soils are commonly found to include two levels of pore size: micro-pores and macro-pores (double porosity).

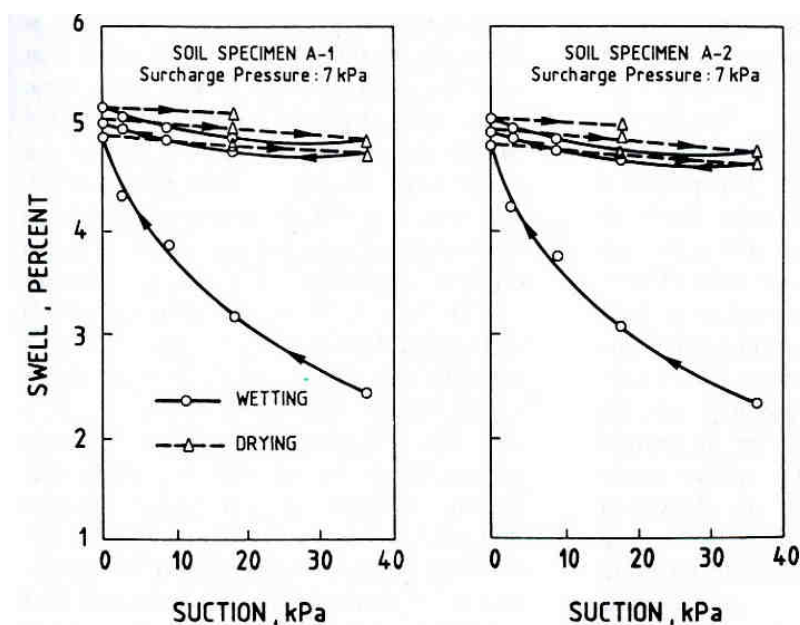


Figure 2-13 Wetting and drying cycles on highly expansive clay (Chu & Mou, 1973)

The irreversible volume change was explained by Gens and Alonso (1992) by the elastic expansion or compression of saturated micro-pores with clay packets exceeding a threshold limit of the macro-structure, and hence introducing plastic volume change of the macro-voids. This was represented by two additional yield curves (SI and SD yield curves) as shown in Figure 2-14. Upon yielding on SI or SD yield curve, cyclic wetting and drying of an unsaturated soil may produce a net irreversible swelling or shrinkage depending on the 'coupling functions' applying for yielding on the SD and SI curves. These coupling functions give the ratio of the plastic volumetric strain of the

macro-structure to the elastic volumetric strain of the micro-structure as a function of the confining and yield stresses.

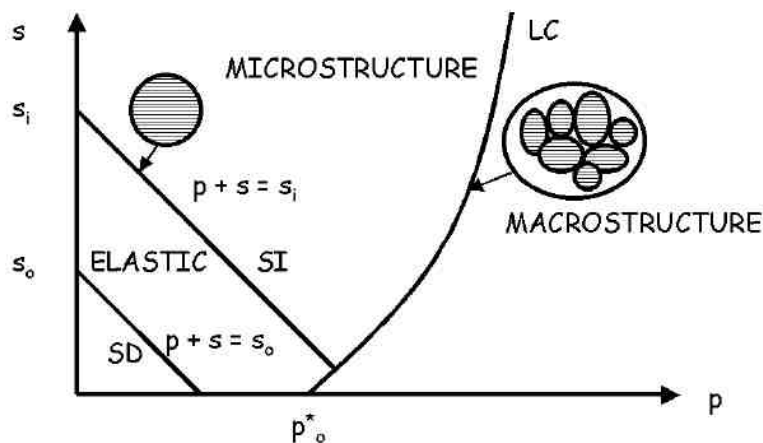


Figure 2-14 Yield loci for an elasto-plastic double structure model (Alonso, 1998)

2.6.2.d Models based on alternative stress state variables

The commonest stress state variables used in the development of constitutive models for unsaturated soils are the net stresses and the suction. However, a substantial number of researchers (e.g. Kohgo et al., 1993a, Kohgo et al., 1993b, Jommi & Di Prisco 1994, Modaressi & Abou-Bekr, 1994, Pakzad, 1995, Bolzon, Schrefler & Zienkiewicz 1996 and Khalili & Khabbaz, 1998) have proposed elasto-plastic models employing different stress state variables. In many cases, one of the variables is selected in such a way that the shear strength can be related solely to this stress variable.

Many of these alternative stress state variable models explicitly or implicitly include degree of saturation in one of the stress state variables. For example, several of them use, as one of two stress state variables, a tensorial stress parameter referred to as either the “average inter-granular stress” or the “Bishop’s stress”, defined as follows:

$$\sigma^* = \sigma - S_r u_w - (1 - S_r) u_a \quad (2-20)$$

where σ is total stress. Typically suction s or some function of suction is employed as the second stress variable. In order to use such models to predict the mechanical behaviour of an unsaturated soil, even at a stress point level, the mechanical model

must be solved simultaneously with a water retention relationship or model (which provides the variation of degree of saturation S_r for use in the Bishop's stress variable defined by Equation 2-20). In this sense the water retention behaviour influences the mechanical behaviour at a constitutive level. However, such models are generally not capable of modelling some of the key features resulting from the full coupling of mechanical behaviour and water retention behaviour at a constitutive level, which are discussed more thoroughly in Chapter 3.

One model which had the potential to be developed to fully represent the coupling of mechanical behaviour and water retention behaviour at constitutive level was the one presented by Jommi & Di Prisco (1994). This mechanical model is expressed in terms of the "Bishop's stress" tensor, but with the yield stresses also dependent on the degree of saturation S_r (in order to represent the stabilizing effect of meniscus water rings). Jommi & Di Prisco (1994) went on to use a unique water retention relationship between degree of saturation S_r and suction s , which effectively meant that their mechanical model reduced to one that could be expressed in terms of Bishop's stress and suction. If, however, they had assumed a water retention model incorporating features such as hydraulic hysteresis (see Section 2.7), their mechanical model would have had the capability of capturing some of the crucial features resulting from the coupling of mechanical behaviour and water retention behaviour. This issue of coupling of mechanical behaviour and water retention behaviour at a constitutive level is discussed more fully in Chapter 3.

2.7 WATER RETENTION BEHAVIOUR

A water retention curve from its name means the variation of amount of water retained within a soil with the stress state variables. The amount of water retained in soil pores at a particular suction depends on the shapes and size distribution of the pores, mineralogy and surface activity of the solid particles and the chemical composition of the soil water. For example, at a given suction a clay soil can typically retain significantly more pore water than an equivalent sand (i.e. with the same void ratio).

The water retention curve is generally expressed as a relationship between either water content w or degree of saturation S_r and the suction s . Suction can be either matric

suction or total suction depending on the significance of the role played by the interaction between pore water chemistry and particle mineralogy, which is often not well represented by the definition of osmotic suction. In general, at higher suction levels, matric suction and total suction can be considered to be equivalent (Fredlund & Xing, 1994). However, like in mechanical behaviour (see Section 2.2.1), the same changes in osmotic suction and matric suction would not produce equal changes in water content or degree of saturation, meaning that matric suction and osmotic suction cannot always be added together.

2.7.1 Features of typical water retention curves

Figure 2-15 illustrates typical water retention curves for a soil at constant volume, showing some of the important features. If a soil sample with constant volume is dried from a saturated state, the water retention behaviour follows a unique curve of variation of degree of saturation (or water content) with suction, known as the ‘main drying curve’. As the suction is increased to about 1,000,000 kPa, water content or degree of saturation is observed to reach zero value (Croney & Coleman 1961) regardless of soil type or pore size distribution, and this observation was also supported by thermodynamic considerations (Richards 1965). During wetting of the sample from a dry state the behaviour traces a different unique curve, namely the ‘main wetting curve’ (see Figure 2-15). While following a main wetting or main drying curve, if suction variation is reversed then the water retention state of the soil traces a different curve called a ‘scanning curve’. Infinite numbers of scanning curves can be observed, gradually re-joining the main wetting curve or the main drying curve if the suction is monotonically increased or decreased. The existence of different curves during wetting and drying is described as hydraulic hysteresis, which can be caused by following the reasons (as described by authors such as Klausner 1991):

- the cross-sectional areas of void passageways are generally irregular in shape, meaning that advancing and receding air-water interfaces along a passageway would correspond to different suction levels, a phenomenon known as the “ink-bottle effect” (Haines 1930);
- the contact angle on the water side of an advancing air-water interface is always greater than that of a receding air-water interface;

- air trapped in the voids may have different volumes during wetting and drying; several researchers have reported significant volumes of trapped air (being unable to achieve full saturation) during a wetting process, whereas a first drying path may start from a saturated state (e.g. Liu & Muraleetharan 2006).

Change of void ratio of the soil has a significant influence on the positions of the main wetting and main drying curves. This is because the void ratio change implies alteration of the pore size distribution, which influences the water retention behaviour. For example, reduction in void ratio would shift the water retention curves to higher suction range, because the size of the voids is reduced, hence requiring higher suction to empty or fill the voids with water. Gallipoli et al. (2003a) plotted S_r against suction for different values of specific volume v for the experimental data of Sivakumar (1993) on compacted Speswhite Kaolin, as shown in Figure 2-16. A clear shift in the water retention curve can be observed due to the modification of v (all curves shown in the figure effectively correspond to wetting curves)

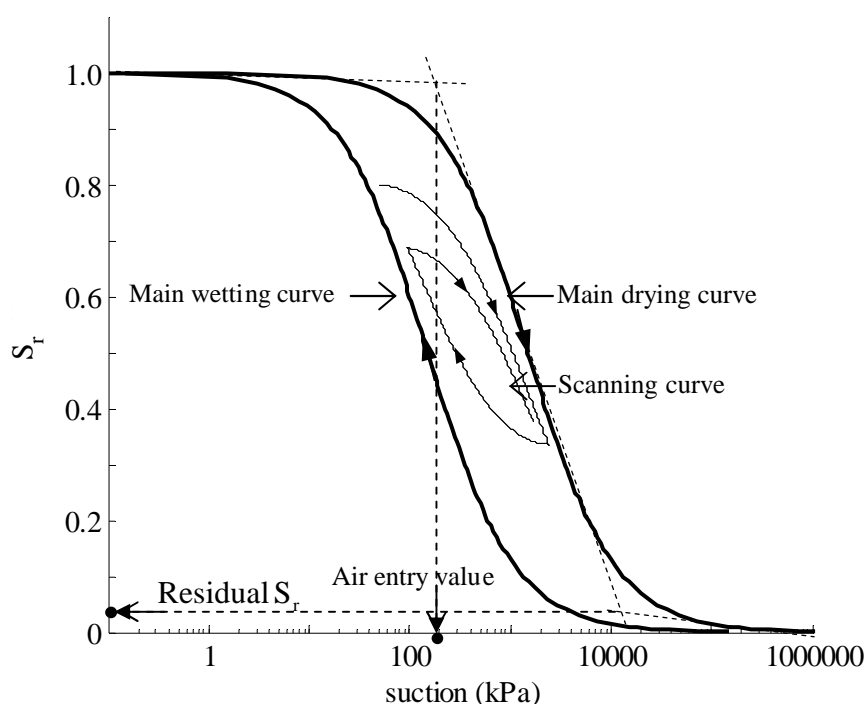


Figure 2-15 Typical water retention curves for fine-grained soils

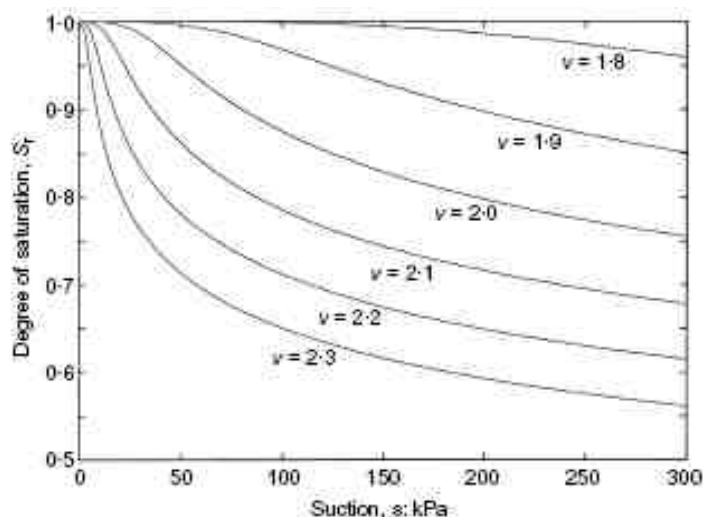


Figure 2-16 Water retention curves at different value of ν fitted to experimental data of Sivakumar (1993) (Gallipoli et al. 2003a)

The main drying curve and the main wetting curve usually take a shape similar to a sigmoidal function curve having an inflection point, when plotted on a semi-logarithmic scale. However, water retention curves can also have more complex shapes, mainly because of the pore size distribution. For example, for a soil with a strong bi-modal pore size distribution, the drying curve and wetting curve may exhibit two inflection points (Al-Mukhtar et al., 2006).

The “air entry value” is the suction required for air to enter the largest pores during a main drying curve. At suctions less than the air entry value, the soil can be assumed to be saturated, and mechanical behaviour can be explained by the conventional saturated ‘effective stress’ proposed by Terzaghi (1936). If the suction is increased beyond the air entry value, a significant decrease in S_r can be observed. In this situation, understanding of unsaturated soil mechanics is necessary to explain the mechanical behaviour of soils.

A residual state in water retention behaviour can be defined as a state where the water phase is discontinuous and occurring only as meniscus water rings at inter-particle contacts or as thin film (contractile skin) surrounding the soil particles (Luckner et al., 1989 and Sillers, 1997). In this state, water can only be transferred through the soil as water vapour. The residual water content or degree of saturation has been defined from the shape of the water retention curve in many ways in the literature, based on

empirical rules (Brooks & Corey 1964, Van Genuchten 1980), physical arguments (Sillers 1997) or graphical construction (Van Genuchten et al. 1991).

2.7.2 Modelling water retention behaviour

2.7.2.a Equations for main wetting and drying curves

Several proposals have been made in the last four decades to model water retention behaviour. Most of the proposals are empirical in nature, and based on the shape of main wetting or drying curves (Gardner 1956, Brooks & Corey 1964, Brutsaert 1966, McKee & Bumb 1987). The pore size distribution function and capillary theory (statistical or micro mechanical approach) have also been utilized to derive water retention models (e.g. Van Genuchten, 1980, Kosugi, 1994 and Fredlund & Xing, 1994). Among the most widely used equations are Brooks & Corey (1964), Van Genuchten (1980) and Fredlund & Xing (1994).

The constitutive equation proposed by Brooks & Corey (1964) is given by:

$$S_r = 1 \quad s < a$$

$$S_r = \left(\frac{s}{a}\right)^{-b} \quad s > a \quad (2-21)$$

where a is the air-entry value of soil and b is a parameter related to the pore size distribution of the soil. It can be seen that the Brooks & Corey (1964) equation assumes $S_r = 1$ for suction less than the air entry value and a power law decrease in S_r as suction increases from the air entry value. The model is simple in terms of the number of parameters needed and the form of the equation. However, it is less flexible than many of the alternatives and the discontinuity of the equation at the air entry value can give rise to numerical instability.

Van Genuchten (1980) proposed a closed form equation for the entire range of suction, given by:

$$S_r = \frac{1}{\left(1 + \left(\frac{s}{a}\right)^n\right)^m} \quad (2-22)$$

where a , n and m are parameters related to air entry value, rate of change slope of curve and asymmetric shape of the curve respectively. The Van Genuchten (1980) equation generally provides better fitting than the Brooks & Corey (1964) equation as it is more flexible and it describes a continuous function. The parameters a , n and m can be related to physical properties of the soil to some extent.

Fredlund & Xing, (1994) proposed an equation somewhat similar to Van Genuchten (1980) for main wetting and drying curve as given below;

$$S_r = \frac{1}{\left(\ln \left(e + \left(\frac{s}{a} \right)^n \right) \right)^m} \quad (2-23)$$

where a , n and m are parameters related to air entry value, rate of change slope of curve and asymmetric shape of the curve respectively (and e is the base of natural logarithms). Even though Van Genuchten (1980) and Fredlund & Xing, (1994) equations show great similarity, it has been observed that Fredlund & Xing, (1994) equation requires fewer iterations to determine the parameter values in order to fit experimental data (Sillers, 1997).

A detailed review of the water retention equations mentioned above can be found in papers by Leong & Rahardjo (1997b) and Sillescu et al. (2001), paying attention to advantages and disadvantages of the different equations.

2.7.2.b Water retention models incorporating scanning curves

The water retention curve equations, mentioned in the last section are able to describe the main wetting and drying curves. However, even a water retention model for rigid soils will only be complete if the ability to represent the scanning curves is accommodated into the model. Several proposals have been made for this purpose, based on either physical arguments (or domain models) or simply as empirical equations with parameter values determined by curve fitting.

Numerous researchers (such as Néel (1942, 1943), Pouloussis 1962, Philip 1964, and Mualem 1974) used the domain concept to describe hydraulic hysteresis and hence

the form of scanning curves. Most of the domain models assume that two different suction values can be assigned to a pore, one corresponding to filling with water and the other corresponding to emptying of water. A group of pores, called the domain, corresponds to narrow suction ranges within which the pores can either fill or empty of water. Several domains can combine together to form a porous system (e.g. a soil). If the behaviour of a particular domain is assumed to be unaffected by neighbouring domains, then it will be called an independent domain system, leading to an independent domain model. On the other hand, a dependent domain model takes into account possible influence between domains, such as blockage of water or air entry from adjacent domains. The domain model theory has been widely used in soil physics and several improvements have been made in the last few decades.

Several proposals have also been made based on experimental observations to model hydraulic hysteresis by empirical equations. Some of these models describe scanning curves purely based on fitting the curve against experimental data (e.g. Kawai et al. 2000, Feng & Fredlund 1999) while others were proposed relating scanning curves to main wetting and drying curves (e.g. Dane & Wierenga, 1975; Hanks et al. 1969 and Hayashida 2003,). In the latter case, a few models were proposed based on elasto-plasticity (e.g. Dangla et al., 1997 and Wheeler et al., 2003) whereas a few others were based on bounding surface plasticity (e.g. Li, 2005 and Liu & Muraleetharan, 2006). The empirical approach to describe scanning curves has proved to be useful and provides reasonably good predictions of experimental results.

2.7.2.c Water retention model incorporating change of void ratio

As discussed in Section 2.7.1, water retention behaviour is significantly affected by changes of void ratio. In geotechnical engineering practice, soils often have to be treated as deformable materials, as the mechanical behaviour is the centre of interest in analysing geotechnical based applications. This means that a water retention model which does not include the influence of changing void ratio (i.e. the impact of mechanical behaviour on water retention behaviour) will not only be able to correctly represent real water retention behaviour but also the mechanical behaviour itself due to the coupling between mechanical behaviour and water retention behaviour (see Chapter 3).

Kawai et al. (2000) proposed a water retention model based on the Brooks & Corey (1964) equation. The parameters a and b in Equation. 2-21 were modified to incorporate the influence of void ratio.

Romero & Vaunat (2000) modified the Van Genuchten equation (Equation 2-22) in order to take into account only the water retention curves in inter-aggregate region (see Section 3.3). The influences of void ratio on the parameters a , n and m were determined by curve fitting against varying void ratio.

Gallipoli et al. (2003a) proposed modification of the Van Genuchten (1980) equation (Equation 2-22) in order to incorporate the influence of changing void ratio on the water retention behaviour. Parameter a in Equation 2-22, which is closely linked to the air entry value of a soil was replaced with a function of void ratio e as given below:

$$a = \phi^* e^{\psi^*} \quad (2-24)$$

where, ϕ^* and ψ^* are soil constants. The model have been validated against experimental test data from Sivakumar (1993) and Zakaria (1995), including isotropic loading and unloading at constant suction, shearing at constant suction and shearing at constant water content.

Wheeler et al. (2003) proposed a water retention model based on elasto-plasticity, which includes both hydraulic hysteresis and dependency on changes of void ratio. Main wetting and drying curves are represented by straight lines of the same slope in the $S_r : \ln s^*$ plane (s^* is suction multiplied by porosity of the soil, see Section 3.6). These curves will be shifted horizontally to higher suctions if plastic volumetric strain occurs during a stress path. Movement along the main wetting or main drying curve is assumed to involve both elastic and plastic components of change of degree of saturation. Scanning curves are represented by elastic behaviour, also with straight lines in the $S_r : \ln s^*$ plot. More detail of this model will be discussed in Chapter 3.

Sun et al. (2006) analysed the effect of soil density (i.e. void ratio) on the water retention curves by carrying out several triaxial tests on samples compacted with different compaction energy but the same water content. They also proposed a water

retention model which is linear in the $S_r : \ln s$ plot. Unlike the Wheeler et al. (2003) model, Sun et al. (2006) assumed main wetting and drying curves to have different slopes.

2.8 METHODS OF SUCTION CONTROL AND MEASUREMENT

For unsaturated soils, suction is an additional (compared to saturated soil) and important stress state variable. Hence, it is necessary to measure or control suction in laboratory or field testing in order to understand and model the behaviour of unsaturated soils. Unfortunately, suction has been found to be very difficult to measure or control reliably for various reasons. For example, as mentioned in Section 2.2.3, pore water pressure in unsaturated soil in the field is typically negative with respect to atmospheric pressure. If the same situation is to be reproduced in the laboratory, then cavitation (a dynamic process of nucleation and rapid growth) can occur in the pore water pressure line, leading to bubble formation and problems with correct pressure application or measurement as well as problems with incorrect measurement of the volume of water flowing into or out of the soil sample. In the last five decades, several methods have been developed and improvements have been made in the experimental techniques to reliably measure or control suction.

2.8.1 Axis translation technique

Hilf (1956) was the first researcher to propose the axis translation technique, which involves increasing total pressure σ , pore air pressure u_a and pore water pressure u_w by equal amounts so that u_w can be raised to a positive pressure with respect to atmospheric pressure in order to avoid cavitation. Many laboratory experiments have been successfully carried out using this technique, with equipment including oedometers (Alonso et al. 1995), direct shear apparatus (Escario & Saez 1986) and triaxial apparatus (Matyas & Radhakrishna 1968 and Wheeler & Sivakumar 1995).

Pore water pressure is applied to a soil sample through a high air entry porous filter (generally a ceramic disc) in order to prevent air from the soil sample at pressure u_a flowing into the pore water line which is at a lower pressure u_w . Figure 2-17 shows such an arrangement with an idealized porous filter (the pores are represented by cylindrical tubes), where the air-water interfaces on the top surface of filter are

concave on the air side, because $u_a > u_w$. The radius of curvature of the air-water interfaces is inversely proportional to the suction as stated in Equation 2-6. If suction $u_a - u_w$ is increased gradually, the radius of the interfaces will reduce until it reaches a critical radius corresponding to the radius of the (largest) pores in the high air entry porous filter. Any further increase in $u_a - u_w$ could not be sustained by the air-water interfaces, and would cause air to flow into the pore water line. The suction corresponding to the critical radius is called the air entry value of the porous disc. Even with suction less than the air entry value, small amounts of dissolved air can diffuse through the ceramic disc, causing problems in correctly measuring pressure and volume if the dissolved air subsequently comes out of solution after passing through the ceramic disc. This problem will be further discussed in Section 5.1.6.

The axis translation technique is widely used because it is relatively easy to convert existing equipment for saturated soil testing by simply adding a high air entry filter and an air pressure source. In addition to that, all pressures, including suction can be varied in a continuous fashion so that the detailed response of a soil sample can be obtained.

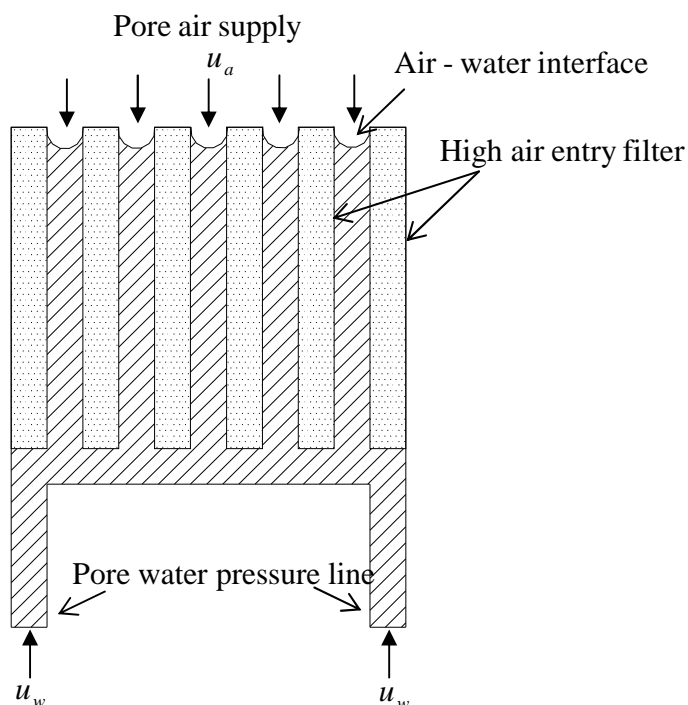


Figure 2-17 Schematic picture showing the principle behind high air-entry value filter

One of the disadvantages of the axis translation is that field conditions, such as possible cavitation within the soil due to negative pore water pressure, cannot be reproduced. This means that any consequence of cavitation can not be represented by this technique. For example, during de-saturation of a sample from a saturated state using the axis translation technique, each water-filled void becomes air-filled only if the suction reaches the air entry value corresponding to the pore size. However, under field conditions, a water-filled void can become air-filled even before the corresponding air entry suction is reached if cavitation occurs.

Another limitation of the axis translation technique pertains to the maximum values of cell pressure and suction that can be achieved in experimental testing. The maximum air entry value of filters that are available commercially is 1500 kPa, meaning that suctions more than this value can not be applied. Also, as suction is increased, the cell pressure must also be raised, requiring a high pressure capacity cell if high suctions are to be investigated.

Axis translation requires the air and water phases to be continuous in order to characterize actual suction within the soil sample. However, at higher degree of saturation, pore air often occurs as occluded bubble (Tarantino & Mongiovi, 2000). In this scenario, the response time of the sample to reach equilibrium conditions after changes of applied net stress or suction would be very slow, because equilibration of u_a between the occluded air bubbles within the soil and the value applied at the boundary of the sample would only be possible by the diffusion of dissolved air.

2.8.2 Osmotic control of matric suction

In the osmotic technique for controlling matric suction, a soil sample is placed in contact with a semi-permeable membrane while an aqueous solution of large size molecules of polyethylene glycol (PEG) at atmospheric pressure is circulated on the other side of membrane. The semi-permeable membrane allows only smaller size molecules, such as water to pass, but not large PEG molecules. Due to the concentration difference of ions in the soil water and in the PEG solution, water will flow from the soil sample through the semi-permeable membrane to the PEG solution. This withdrawal of water from the sample will reduce the pore water pressure within the soil (an increase of matric suction), generating a pressure difference between the

PEG solution and the pore water. This pressure difference induces a corresponding tendency for water flow into the soil sample from the PEG solution. Equilibrium is reached when the matric suction within the soil sample is sufficient to generate a tendency for inward flow of water which exactly compensates the tendency for outward flow of water caused by the concentration difference across the semi-permeable membrane. Hence, by changing the concentration of the PEG solution, different values of matric suction can be attained within the soil. The important point is that this can be achieved without having negative values of pressure within the (PEG-filled) external tubing, thus removing the risk of cavitation within the tubing.

The osmotic technique was first used in biology (Lagerwerff et al. 1961) and then in soil science (Zur, 1966 and Waldron & Manbeian 1970). Subsequently, the technique was introduced in geotechnical engineering by Kassiff and Ben Shalom (1971). Delage et al. (1992) carried out testing in an oedometer using the osmotic technique by circulating PEG solution using a peristaltic pump at the bottom of the soil sample (see Figure 2-18). Water exchange was measured using a burette and the PEG solution bottle was placed in a temperature-controlled water bath in order to avoid any influence from temperature fluctuation on burette measurement. Dineen and Burland (1995) resolved the problem regarding temperature fluctuation by measuring the weight of PEG solution (rather than volume) by placing the bottle on an electronic balance. The osmotic technique has also been applied to triaxial testing (e.g. Cui & Delage, 1996).

The main advantage of the osmotic control of matric suction is that real field condition of negative pore water pressure can be replicated (i.e. cavitation within the soil is allowed). In addition, higher suctions can be reached without needing to raise the cell pressure like in the axis translation technique. Suctions as high as 10 MPa can be reached by increasing the PEG concentration to near saturation (Delage et al. 1998).

A disadvantage of the osmotic control technique is that continuous variation of suction is difficult to achieve, as the PEG concentration is typically varied in steps. In addition, pore water exchange during application of a given suction will modify the intended concentration of the PEG solution. This can be partially solved by using a large volume of PEG solution (Delage et al. 1992). Another drawback of this method is that

the cellulosic semi-permeable membrane is fragile to bacterial attack (partially solved by applying penicillin) and excessive stress (Delage & Cui, 2008). Slatter et al. (2000) and Monroy et al. (2007) avoided this problem by using a synthetic sulfonated membrane instead of cellulosic membrane. Several researchers, such as Dineen and Burland (1995), Tarantino & Mongiovi (2000) and Monroy et al. (2007), reported that the calibration curve, between PEG concentration and induced matric suction, is influenced by the type of membrane.

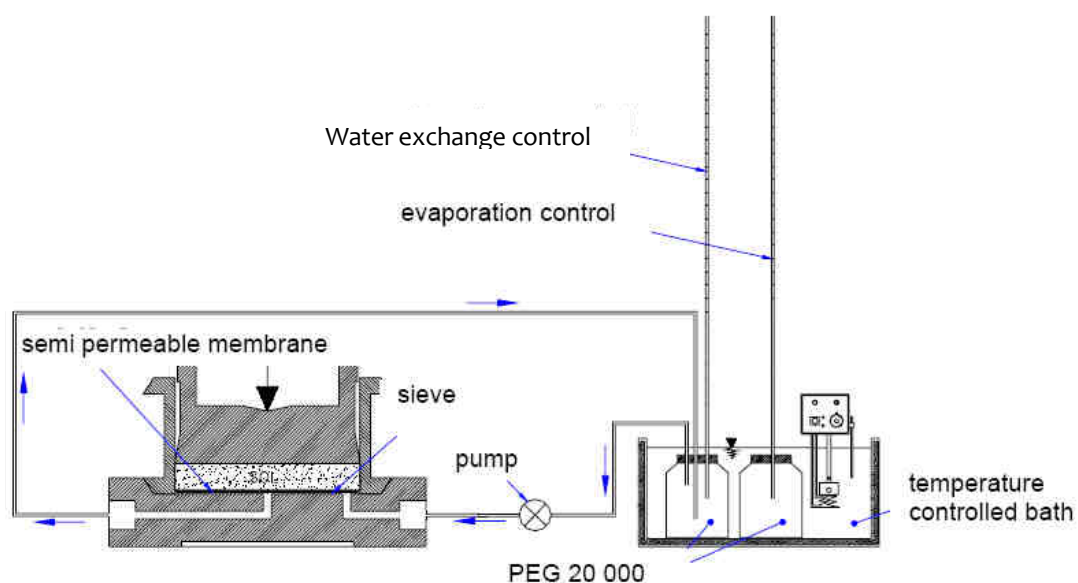


Figure 2-18 Osmotic technique applied to oedometer (Delage & Cui, 2008 –modified after Delage et al. 1992)

2.8.3 Control of relative humidity by saturated salt solutions

As stated in Equation 2-1, under local equilibrium, the relative humidity of the air in contact with pore water can be related to total suction. It is therefore possible to control total suction by controlling the relative humidity of the pore air, which can be achieved by having a sealed volume of air in contact with a saturated solution of a specific salt (see Figure 2-19(a)). Relative humidity can be altered by using different saturated salt solutions or varying the concentration of same salt solution leading to different total suction values.

Advantages related to this technique are similar to those of the osmotic control of suction technique. In addition, very high values of suction (in excess of 1000 MPa) can be applied using this technique.

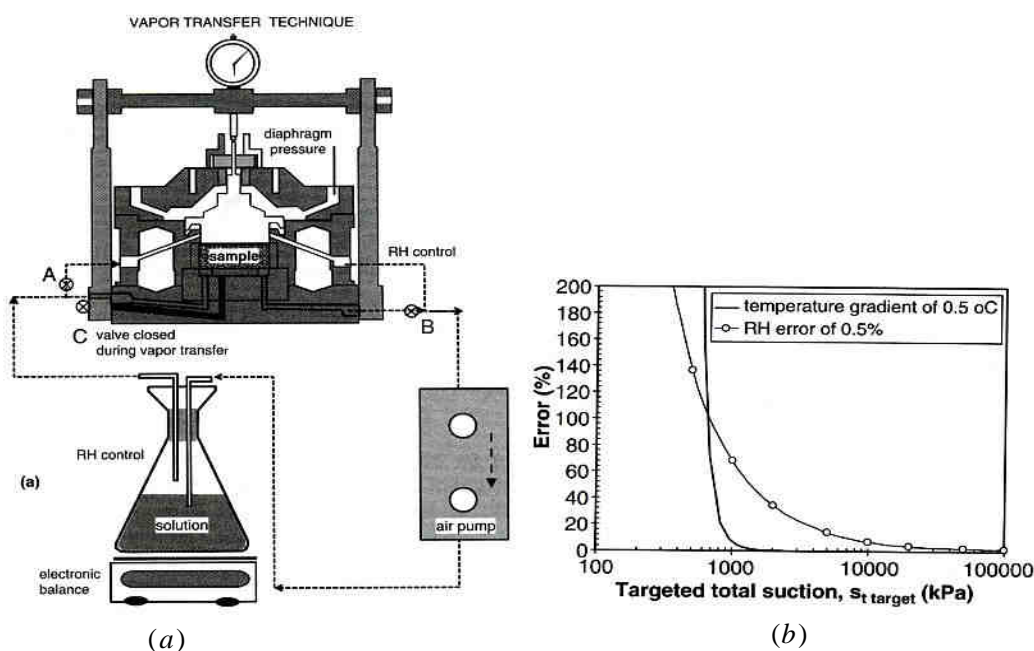


Figure 2-19 (a) Controlling relative humidity with saturated salt solution (Hoffmann et al. 2005) (b) Error in total suction in vapour equilibrium transfer technique (Agus & Schanz 2005)

A disadvantage of this technique is that continuous variation of suction is difficult to achieve, as the concentration of salt solution is typically varied in steps. In addition, as the pore water exchange occurs in vapour form, a very long time is required to achieve the equilibrium suction throughout the soil sample and measurement of the volume of water inflow or outflow to the sample is difficult. Vapour is usually circulated along the surface of the soil sample in order to reduce the equalization period (see Figure 2-19a). This technique is not reliable for total suction values below 10 MPa, because measurement error or fluctuation in relative humidity and temperature can produce large errors in the resulting total suction. Figure 2-19b shows the errors in total suction caused by a temperature difference of only 0.5 °C or an error in relative humidity of only 0.5%.

2.8.4 Measurement of suction with tensiometers

Theoretically, pure water can withstand a negative pressure of 500 MPa (Tabor, 1979) if there are no impurities in the water to form nucleation sites for cavitation. Ridley & Burland (1993) were among the first researchers to use this fact in order to measure negative pore water pressures greater than 1 atmosphere in soil samples by developing a miniature tensiometer. Figure 2-20 illustrates a typical design of such a tensiometer.

A miniature tensiometer essentially consists of a high air entry filter serving as an interface to allow the water flow in or out of a water reservoir from the soil, a small water reservoir and a pressure transducer (typically consisting of a strain-gauged diaphragm). When the high air entry filter is in contact with an unsaturated soil sample with a negative pore water pressure, this pressure will transfer negative pressure to the water reservoir. This negative pressure deflects the diaphragm, which is in contact with the water reservoir, and this diaphragm deflection is detected by the strain gauge. If the deflection of the diaphragm is calibrated against known pressure then it can be used to measure negative pore water pressure within a soil sample. The tensiometer is normally calibrated against positive water pressure after saturation of the ceramic disc and reservoir, and this calibration is then extrapolated into the negative range. Tensiometers can typically measure matric suction up to about 1500 kPa (limited by the air entry value of the ceramic discs that are available commercially).

The problem often encountered while measuring negative water pressure is cavitation at suction as low as 100 kPa. Cavitation is mainly attributed to the fact that undissolved gas nuclei often exist in the interstices on the surface of the water reservoir rather than within the water (Harvey et al. 1944). Full saturation of the filter and water reservoir has been found to be crucial to achieve the full range of suction measurement and stable measurement avoiding cavitation (Ridley & Burland 1993).

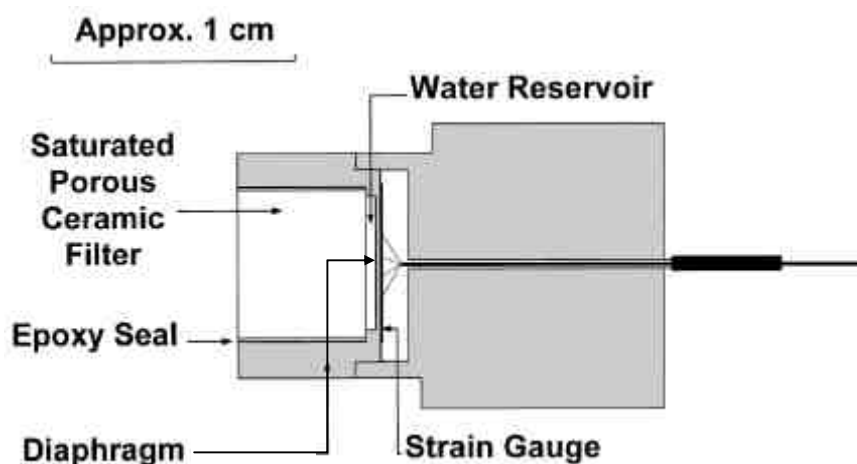


Figure 2-20 Schematic picture of Imperial College tensiometer (Ridley & Burland, 1999)

2.8.5 Alternative methods of suction measurement

Several other methods for measuring suction can be found in the literature. Many of these methods use indirect measurements, such as the water content of a filter paper in direct contact or close proximity with the soil, to measure suction. The calibrations of these devices are generally carried out using one of the techniques for suction application discussed in Sections 2.8.1, 2.8.2, 2.8.3 and 2.8.4. Table 2-1 summarises some of the techniques of suction measurement found in the literature.

| Device | Measurement Mode | Range (kPa) | Approximate Equilibrium time |
|------------------------------------|------------------|------------------------|------------------------------|
| Thermocouple psychrometer | Total suction | 100-7,500 | minutes |
| Thermistor/Transistor psychrometer | Total suction | 100-71,000 | minutes |
| Chilled-mirror psychrometer | Total suction | 500-30,000 (or higher) | 10 minutes |
| Filter paper (no-contact) | Total suction | 400-30,000 | 7-14 days |
| Filter paper (contact) | Matric suction | 30-30,000 | 7 days |
| Thermal conductivity sensor | Matric suction | 1-1500 | Hours to days |
| Electrical conductivity sensor | Matric suction | 50-1500 | 6-50 hours |

Table 2-1 Alternative methods of measuring suction (after Ridley & Wray 1995)

2.9 METHODS OF MEASURING SAMPLE VOLUME CHANGE

The volume change of a saturated soil sample in a triaxial apparatus can be directly related to the volume of water flowing in or out of the sample. In the case of unsaturated soils, volume change measurement in triaxial apparatus is more complex, because total volume change is attributed not only to pore water volume change but also to the volume change of pore air due to compression and exchange. During the last three decades, several methods for measuring the total volume change of unsaturated triaxial test samples have been proposed (Geiser et al., 2000). These methods divide into three basic categories:

- Indirect measurement: measuring the inflow or outflow of the cell fluid surrounding the soil sample, generally with the help of a double-wall cell or some other form of special cell design;
- Direct measurement: measuring sample volume by mounting local lateral and radial displacement gauges on the soil sample or by obtaining deformation profiles using laser or image processing techniques;
- Separate measurement of pore water volume changes and pore air volume changes.

2.9.1 Indirect measurement of sample volume change

In order to correctly measure the sample volume change by an indirect measurement method, a calibration for the apparent volume change of the cell (the inner cell if a double-walled cell is employed) with cell pressure change is necessary. It would therefore be ideal to have any apparent volume change being eliminated or reduced to an acceptable level. In the latter case, it is preferable to have a linear response of apparent volume change with cell pressure and no (or negligible) creep.

Bishop & Donald (1961) developed a triaxial cell by adding an inner cell attached to the base of the existing cell, as shown in Figure 2-21. The lower part of the inner cell was filled with mercury to a level above the top of the soil sample. The upper part of the inner cell and the entire outer cell were filled with water. Overall volume change of the soil sample during a test was measured by monitoring the vertical movement of a stainless steel ball that was floating in the mercury, using a cathetometer. To avoid any volume change caused by expansion/contraction of the inner cell, the pressures in the inner and outer cells were kept equal by having a direct connection at the top of the cell (through a “cut-away” in the inner acrylic cylinder).

The major disadvantages of this technique were that volume changes could not be automatically logged or controlled and the safety issues associated with the use of mercury as a cell fluid. The latter problem was avoided by Cui & Delage (1996) by replacing mercury with coloured water and applying confining pressure with air. Dissolution of air into water and evaporation was minimized by adding a silicon oil layer above the coloured water. Subsequently, the automatic logging of volume change

of the soil sample was achieved by Ng et al. (2002) by measuring the difference between the water level in the inner cell and a reference water level in the outer cell by using a differential pressure transducer as shown in Figure 2-22. Any problem concerning absorption of water by an acrylic material (Wheeler and Sivakumar, 1995) were avoided by Ng et al. (2002) by the use of an inner cell made out of aluminium. However, this prevents visual inspection of the soil sample during a test. Also, evaporation of water may be a problem in case of long duration of testing. It should also be noted that there are safety issues in the designs of Cui & Delage (1996) and Ng et al. (2002), because compressed air is used as a confining fluid.

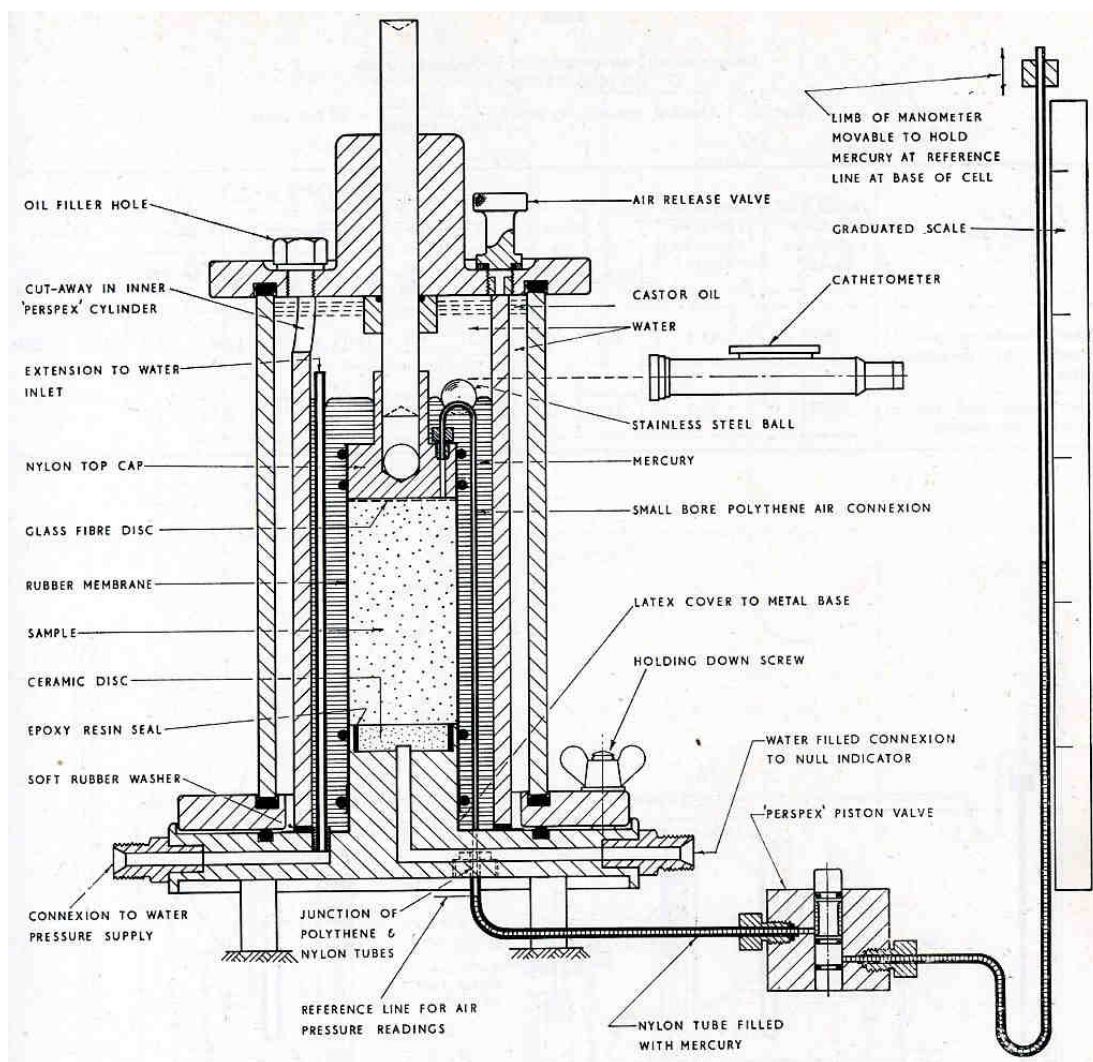


Figure 2-21 Modified apparatus for testing unsaturated soils (Bishop & Donald, 1961)

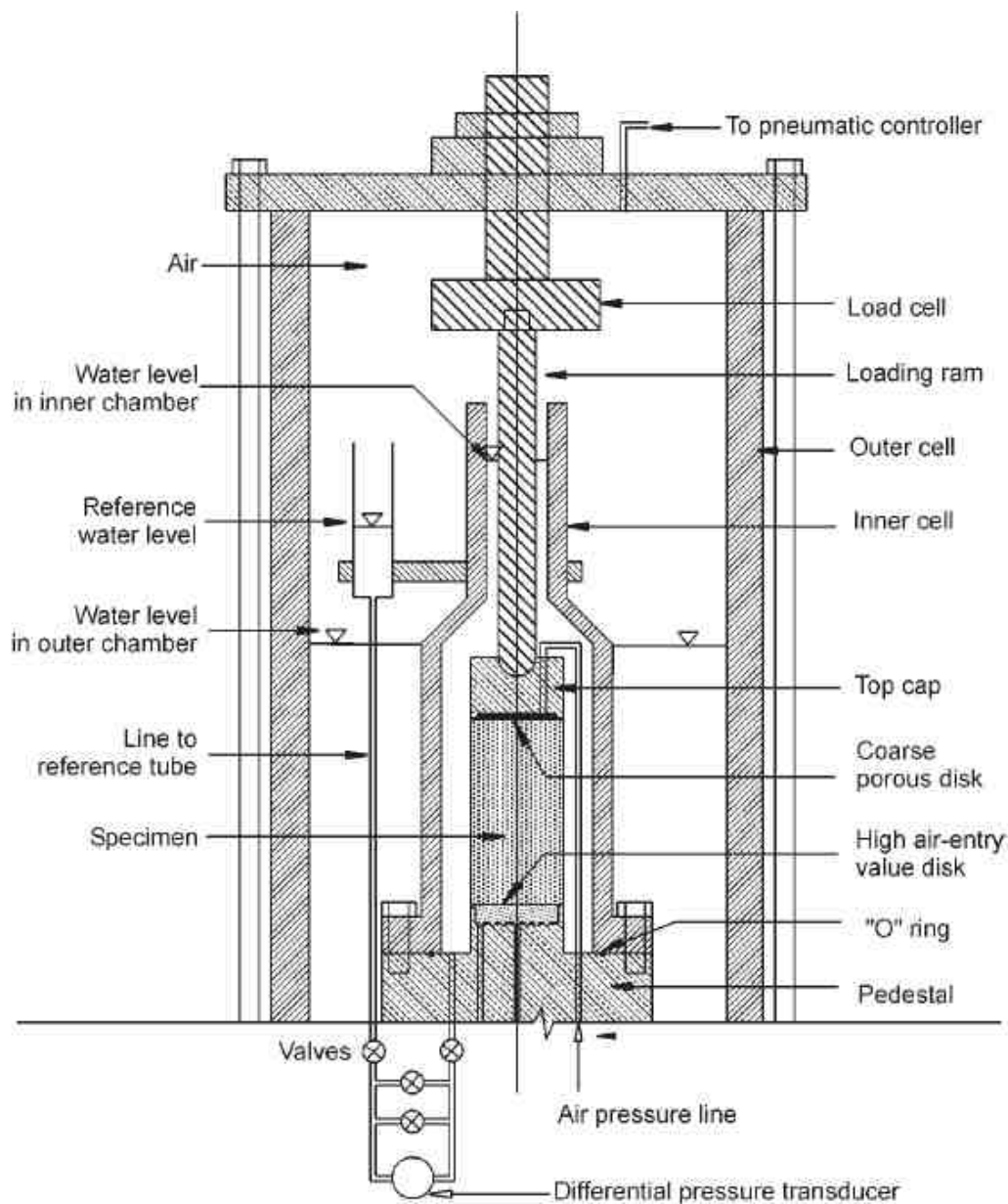


Figure 2-22 Double-walled cell triaxial apparatus (Ng et al., 2002)

Wheeler (1986) took a slightly different approach to measure the volume change of unsaturated soil samples by modifying the Bishop & Donald (1961) technique (see Figure 2-23). Instead of mercury, his inner cell was entirely filled with water, and there was no connection between inner and outer cells at the top of the cell. By applying same pressure to inner and outer cells, it was theoretically possible to avoid apparent volume change of the inner cell and to monitor sample volume change by measuring the flow of water in or out of the inner cell. However, a calibration is still required in order to account for apparent volume change of the inner cell due to flexure of the top plate and bottom pedestal, compression of the water, expansion of the connections and

absorption of water by the acrylic cell. In this approach, the safety issues were resolved and also sample volume change could be logged automatically. This kind of triaxial cell is now widely known as a double-walled triaxial cell. Several researchers such as Wheeler (1986), Sivakumar (1993), Sharma (1998) and Sivakumar (2007) reported reliable measurement of sample volume change using this technique. The original Wheeler (1986) design had a few drawbacks, such as absorption of water by the inner acrylic cell and flexure of the top plate and the bottom plate of the inner cell as the cell pressure was varied, because the top plate of the inner cell was not subjected to equal pressure on top and bottom over the full area (see Figure 2-23). The absorption issue is generally solved by conducting calibration (Wheeler & Sivakumar, 1995).

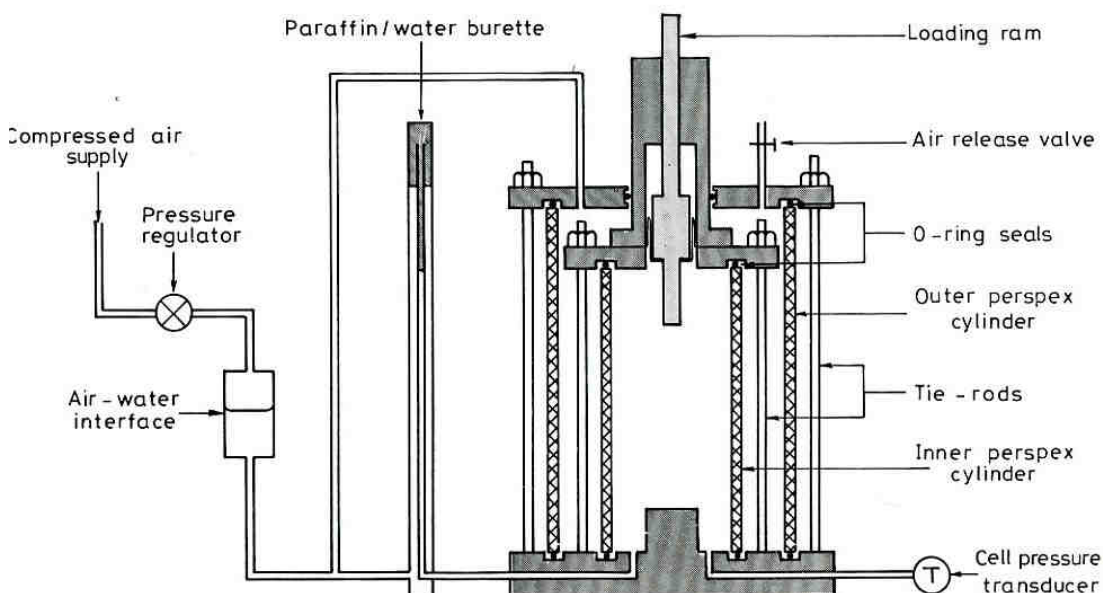


Figure 2-23 Modified apparatus for testing unsaturated soils (Wheeler, 1986)

Sivakumar (2007) modified the original design of Wheeler (1988), as shown in Figure 2-24. In this “twin-cell” arrangement, the inner cell was accommodated entirely inside the outer cell so that expansion of the inner cell during confining pressure changes due to flexure of the inner cell top plate was eliminated.

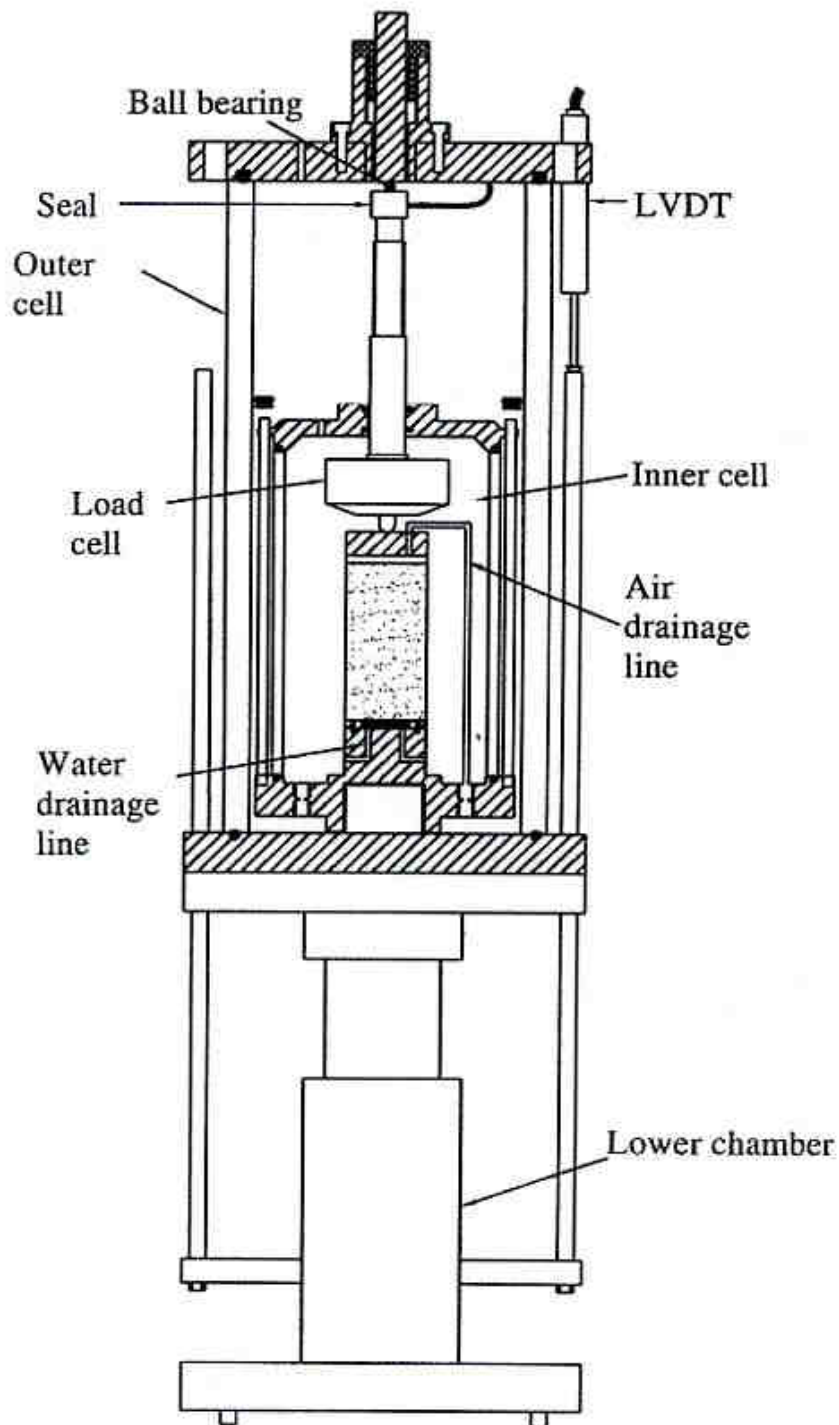


Figure 2-24 Modified apparatus for testing unsaturated soils (Sivakumar, 2007)

The double-wall cell or twin cell is generally employed in order to eliminate the relatively large volume change caused by pressure changes due to the expansion/contraction of the cell. On the other hand, with a suitable calibration, it is possible to measure the volume change utilizing a single cell. The magnitude of

volume change during pressure changes can be minimised if a stiff material (such as steel) is used and if a thick cell wall is used. Buisson (2002) developed single steel wall cells for both isotropic and triaxial testing. Unlike double wall or twin cell designs, setting up of a sample in the single steel wall cells designed by Buisson (2002) is relatively easy. The major disadvantage of this technique is that visual inspection of the soil sample during a test is not possible. A single steel wall isotropic cell and a single steel wall triaxial cell developed by Buisson (2002) were used to conduct the experimental programme on unsaturated soils in the current research (see Chapter 5).

2.9.2 Direct measurement of sample volume change

Sample volume change during unsaturated triaxial testing can also be monitored by measuring the axial and radial strains of the sample (e.g. Matouk et al., 1995 and Zakaria, 1995). This can be achieved by directly mounting local gauges on the soil sample. This technique is advantageous for measurement of small strains and to monitor any anisotropy of soil response (Zakaria 1995). However, at large strains, local strain measurement would provide unrepresentative overall volume change because of non-uniform deformation such as barrelling and local shearing.

Several other methods have also been used to measure the sample volume change such as using a laser to profile the sample boundary (Romero et al., 1997) and image processing (i.e. employing a contouring technique to profile the boundary) using a digital camera (Macari et al., 1997 and Gachet et al., 2007).

2.9.3 Measurement of pore air and pore water volume changes

Overall volume change of an unsaturated triaxial test sample can also be estimated by measuring the pore air and water exchanges independently. Several methods have been proposed to measure the air volume change (e.g. Bishop & Henkel, 1962, Dunlap & Weber, 1971 and Adams et al. 1996). Measurement of air volume change is critical, because air is highly compressible and also the influence of temperature change on air volume is several time higher than that of water. It is almost impossible to get accurate measurement of pore air volume change in this method, due to the following reasons:

- it is very difficult to measure or calculate with sufficient accuracy the quantities of gaseous air and dissolved air leaving or entering the soil sample;

- air tends to diffuse through the tubes and the membrane enclosing the soil sample;
- it is very difficult to prevent air leakage through the connections;
- a small change in pressure or temperature would cause a big change in the air volume as the air is a highly compressible fluid, keeping in mind that a small fluctuation of pressure and temperature is inevitable even within a controlled environment.

CHAPTER 3

COUPLING OF MECHANICAL BEHAVIOUR AND WATER RETENTION BEHAVIOUR IN UNSATURATED SOILS

In this chapter, the coupling of mechanical behaviour and water retention behaviour occurring in unsaturated soils is first explained and demonstrated with experimental evidence. This is followed by discussion on some of the constitutive models which incorporate the coupling, or at least the influence of water retention behaviour on the mechanical behaviour. Finally, the Wheeler et al. (2003) model is presented and an extension of the model to triaxial stress states is proposed.

3.1 HYDRO-MECHANICAL COUPLING IN SATURATED AND UNSATURATED SOILS

3.1.1 Saturated soil

In saturated soils, in order to solve a mechanical boundary value problem under drained conditions (i.e. pore water pressure is known at all points), the following balance and constitutive equations should be solved simultaneously:

- Balance equations:
 - ⇒ Equilibrium of stresses (momentum balance);
 - ⇒ Compatibility of strains.

- Constitutive equations:
 - ⇒ Stress-strain relations (mechanical constitutive model).

However, for a full, time-dependent solution of a boundary value problem, where pore water pressure is unknown and can vary spatially and temporally (e.g. consolidation analysis), one additional balance equation (mass balance of water) and one more

constitutive equation (a hydraulic model e.g. Darcy's law for flow of water) are required. The required equations to solve the boundary value problem are listed below:

- Balance equations:
 - ⇒ Equilibrium of stresses (momentum balance);
 - ⇒ Compatibility of strains;
 - ⇒ Mass balance of water.
- Constitutive equations:
 - ⇒ Stress-strain relations (mechanical constitutive model);
 - ⇒ Darcy's law for flow of water (hydraulic model).

The mechanical and hydraulic components in the balance and constitutive equations means that the problem is coupled and can be termed as a “coupled hydro-mechanical boundary value problem”. The coupling generally is assumed to occur only at the level of the boundary value problem not at constitutive level i.e. a mechanical model can be solved at a stress point level, without requiring a hydraulic model, if stresses and pore pressures at the point are defined. Similarly, a hydraulic model can be solved if the pore pressure variation is known, without requiring a mechanical model. However, in reality, the permeability, which is a parameter in the hydraulic model, depends on the void ratio, which is predicted by the mechanical constitutive model. This means that mechanical behaviour influences the hydraulic behaviour at a “constitutive level”.

3.1.2 Unsaturated soil

If pore water pressure and pore air pressure in an unsaturated soil are known at all points in space in a mechanical boundary value problem (i.e. drained conditions) and no coupling at constitutive level is assumed, the requirements for solution of the boundary value problem are the equations for equilibrium stresses, compatibility of strains and a mechanical constitutive model. This is a similar situation to a mechanical boundary value problem in saturated soil. However, for full time-dependent solutions of boundary value problems in unsaturated soils, where pore water pressure and pore air pressure are unknown and can vary spatially and temporally, the following balance and constitutive equations are required to be solved simultaneously.

- Balance equations:
 - ⇒ Equilibrium of stresses (momentum balance);
 - ⇒ Compatibility of strains;
 - ⇒ Mass balance of water;
 - ⇒ Mass balance of air.

- Constitutive equations:
 - ⇒ Stress-strain relations (mechanical model);
 - ⇒ Water retention relations (water retention model);
 - ⇒ Darcy's law for advective flow of liquid (hydraulic model);
 - ⇒ Darcy's law for advective flow of gas;
 - ⇒ Fick's law for flow of water vapour (hydraulic model);
 - ⇒ Fick's law for flow of dissolved air.

From the above list, it is clear that balance equations, mechanical model, water retention model and hydraulic model are required to be solved for a full time-dependent boundary value problem in unsaturated soils leading to coupling at the level of the boundary value problem.

In reality, one constitutive model may depend on the other constitutive models. For example, the hydraulic model can be influenced by the mechanical model and water retention model, because the liquid permeability depends on both void ratio and degree of saturation. This represents coupling in one direction.

Typically, the mechanical behaviour is assumed to be unaffected by the water retention behaviour or hydraulic behaviour, in models such as BBM, i.e. the mechanical model can be solved at a stress point level if all stresses and pore pressures are known, without knowledge of the water retention model or hydraulic model. However, this is not true in reality. For example, the mechanical behaviour is affected by the degree of saturation (coming from the water retention behaviour) in addition to stresses such as suction and net stress. On the other hand, the water retention behaviour is influenced by changes of void ratio, which comes from the mechanical behaviour. This means that coupling occurs between mechanical behaviour and water retention behaviour, in

both directions, at constitutive level. It is therefore necessary to incorporate this coupling into the constitutive models, if the features of behaviour arising from the coupling are intended to be captured. The following Sections 3.2, 3.3 and 3.4 describes the importance of coupling of mechanical behaviour and water retention behaviour, by providing experimental evidence and theoretical arguments.

3.2 INFLUENCE OF DEGREE OF SATURATION ON MECHANICAL BEHAVIOUR

Wheeler et al. (2003) presented a physical argument for why water retention behaviour should influence mechanical behaviour. Figure 3-1a shows the idealized structure of an unsaturated soil with specified net stresses, suction, void ratio and degree of saturation. Figure 3-1b represents the soil after a wetting and drying cycle, with net stresses and suction at the same values as in Figure 3-1a.

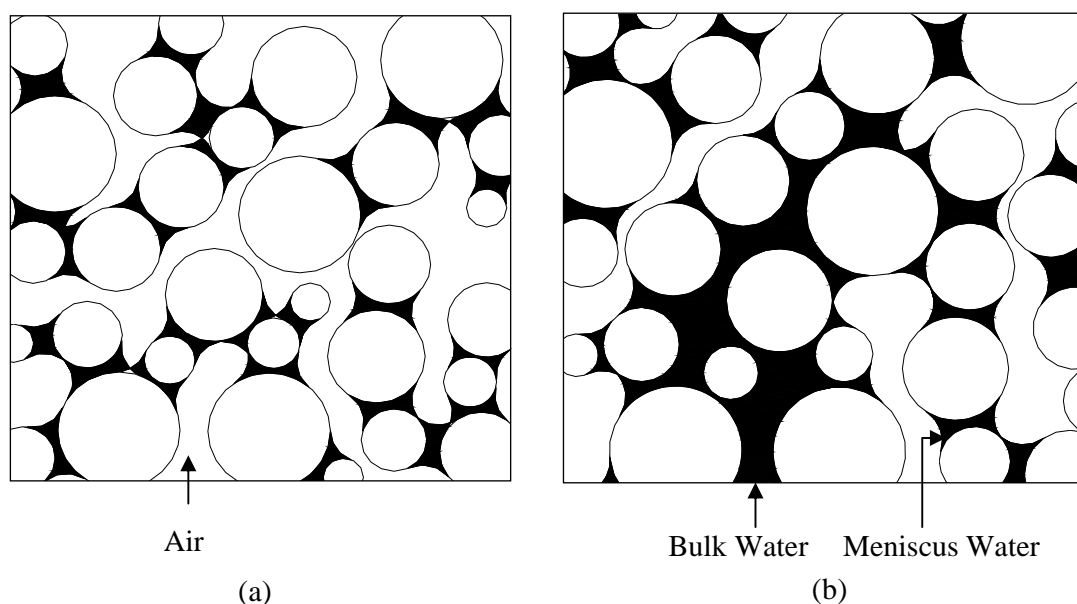


Figure 3-1 (a) Idealized structure of an unsaturated soil at a particular net stress, suction and void ratio; (b) idealized structure of the soil sample with same stress state and void ratio but, after a wetting and drying process.

During the wetting and drying process, no slippage occurred at particle contacts (no plastic strains) meaning that any change in void ratio after wetting and drying is insignificant. However, a significant increase in degree of saturation occurred, because of the influence of hydraulic hysteresis (see Section 2.7). This increase in S_r means that there are a greater number of water-filled voids in Figure 3-1b than in Figure 3-1a

and a smaller number of air-filled voids in Figure 3-1b than in Figure 3-1a. One consequence of this is that there are fewer meniscus water rings at inter-particle contacts (see Section 2.3) in Figure 3-1b than in Figure 3-1a. This implies that the stability of many inter-particle contacts was reduced significantly after the wetting and drying cycle even though suction, net stresses and void ratio were the same before and after the wetting and drying. This means that degree of saturation (in addition to suction) influences mechanical behaviour and therefore that water retention behaviour will influence mechanical behaviour at a constitutive level.

3.2.1 Influence of degree of saturation on mechanical behaviour during isotropic loading

Figure 3-2 and Figure 3-3 show results from two isotropic loading tests on bentonite-kaolin samples performed by Sharma (1998). In the first test (Figure 3-2), the sample was subjected to isotropic loading (a-b) to a mean net stress of 100 kPa, unloading (b-c), isotropic loading (c-d) to a higher mean net stress of 250 kPa and final unloading (d-e), all performed at a constant suction of 200 kPa. During re-loading c-d the sample yielded at a value of mean net stress equal to maximum stress previously applied. This type of behaviour would be predicted by the Barcelona Basic Model (BBM) (see Section 2.6.1).

In the second test (Figure 3-3), an identical sample was subjected to an identical first cycle of loading and unloading (a-b-c) at a suction 200 kPa, but it was then subjected to a wetting-drying cycle (c-d-e), before the final isotropic loading/unloading cycle at a suction of 200 kPa (e-f-g). During the wetting drying cycle c-d-e there was no net change of void ratio (see Figure 3-3), but there was a substantial net increase in the degree of saturation, as a consequence of hydraulic hysteresis. Inspection of Figure 3-3 shows that the sample yielded in the second loading stage e-f at a mean net stress that was lower than the maximum stress previously applied, despite the fact that no irreversible volume change occurred in the wetting and drying process (c-d-e). Wheeler et al. (2003) argued that the lower yield stress was a consequence of the increase of degree of saturation during the wetting-drying cycle, leading to reduced stability of the soil skeleton as a consequence of the reduced number of stabilising meniscus water rings. This feature can not be predicted by conventional constitutive

models like BBM, which do not account for the influence of degree of saturation on mechanical behaviour.

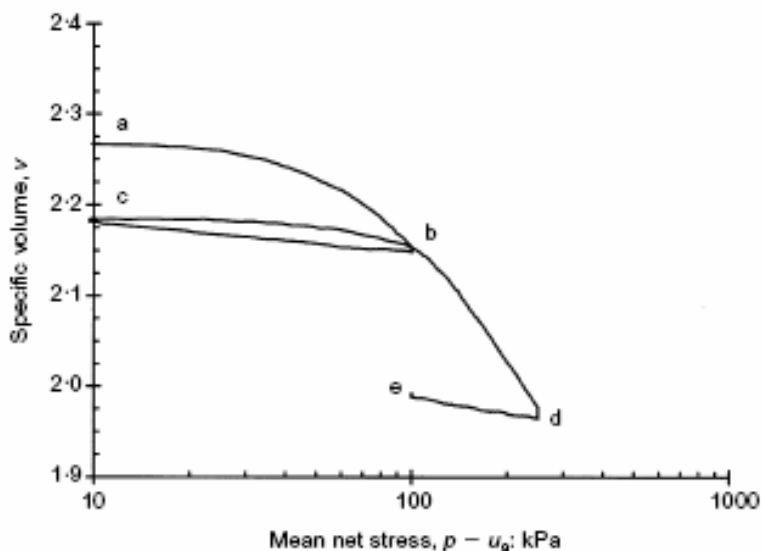


Figure 3-2 Behaviour of bentonite-kaolin during isotropic loading at constant suction (Sharma 1998)

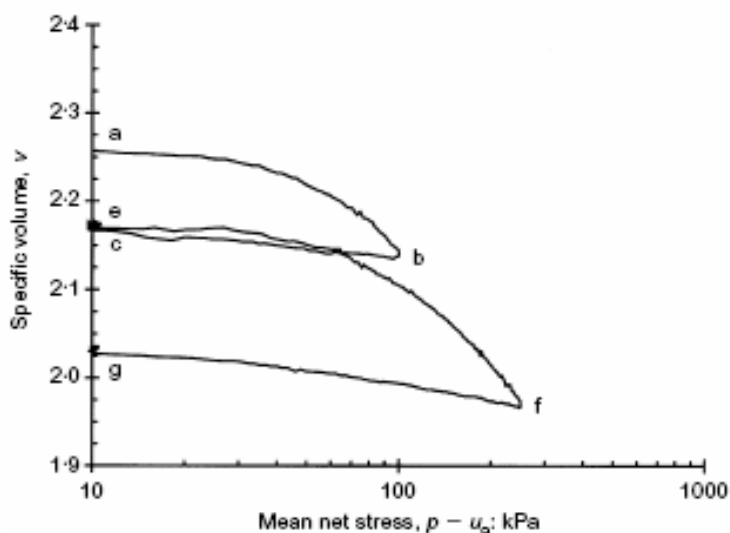


Figure 3-3 Influence of wetting and drying on subsequent behaviour of bentonite-kaolin during isotropic loading (Sharma 1998)

3.2.2 Mechanical behaviour during cycles of wetting and drying

Figure 3-4 shows the results from an oedometer test carried out by Alonso et al. (1995) on compacted Boom clay. The first wetting stage C_1 provided swelling followed by collapse compression. The first drying stage C_2 produced substantial compression,

with the clear suggestion of a yield point during the stage. Similarly, there was the suggestion of a yield point in the second drying stage C_4 and a corresponding subsequent plastic component of compression (although smaller than in the first drying stage C_2). Wetting stages C_3 and C_5 can be represented by elastic swelling. Models like the BBM could capture the occurrence of swelling followed by plastic compression during the first wetting stage C_1 (through yielding on the LC yield curve) but would not predict any occurrence of plastic compression during drying stages C_2 and C_4 .

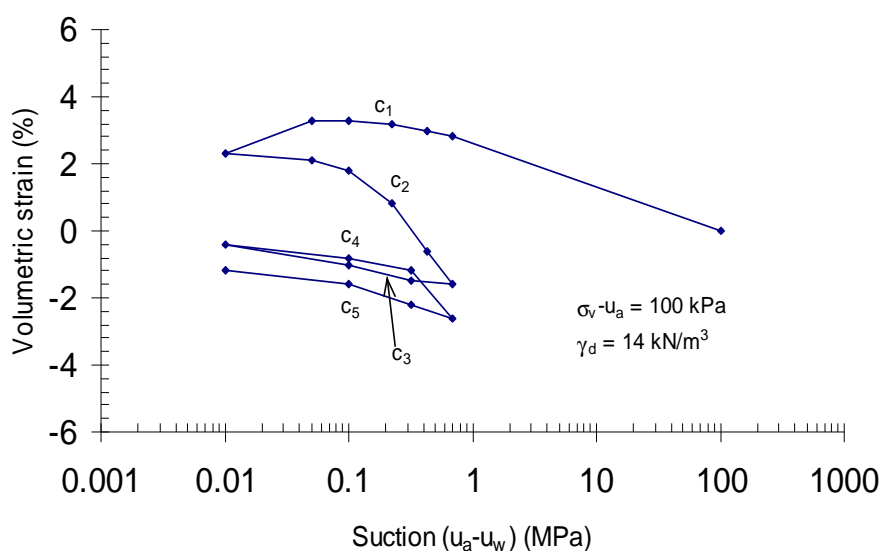


Figure 3-4 Volumetric shrinkage over wetting and drying (Alonso et al. 1995)

Alonso et al. (1995) attributed the irreversible behaviour during drying and wetting cycles C_2 and C_5 in Figure 3-4 to the highly expansive nature of the clay minerals and the role of the double structure (macro and micro), as described in Section 2.6.2. However, Sharma and Wheeler (2000) raised doubts about this explanation in the light of experimental evidence by Sharma (1998), where they showed that the type of behaviour presented in Figure 3-3 and Figure 3-4 occurred in non-expansive unsaturated soils (such as speswhite kaolin) as well as in soils containing highly expansive clay minerals. In addition, it can be shown that yielding in successive drying stages, such as shown in Figure 3-4, can be predicted by the double-structure model of Alonso et al. (1999) only if there is also yielding during each wetting stage (not apparent in Figure 3-4). Also the double-structure model can not predict that a wetting-drying cycle would reduce the yield stress observed during subsequent isotropic

loading (as shown in Figure 3-3) unless the wetting-drying cycle produced some irreversible volume change (not apparent in Figure 3-3). Sharma & Wheeler (2000), Buisson & Wheeler (2000) and Wheeler et al. (2003) argued that all of the features of behaviour shown in Figure 3-3 and Figure 3-4 could be explained by the influence of degree of saturation on mechanical behaviour.

3.3 INFLUENCE OF VOID RATIO ON WATER RETENTION BEHAVIOUR

Any change in void ratio of the soil would modify the water retention behaviour, by shifting the main drying and wetting curves in the $S_r : s$ plane. This can be explained by the fact that changes in air entry value and water entry value for individual voids (the value of suction at which these voids empty or fill with water during drying and wetting respectively) occur if there are changes in the dimensions of the voids and of the connecting passageways between voids (see Section 2.7.2). This implies an influence of mechanical behaviour on water retention behaviour.

Romero & Vaunat (2000) examined the influence of void ratio on main wetting and drying curves. Figure 3-5 shows the variation of degree of saturation with suction for samples of a kaolinitic-illitic soil compacted to three different dry unit weights (i.e. three different void ratios). All samples were statically compacted at a water content dry of optimum and exhibited double porosity from the analysis of mercury intrusion-extrusion porosimetry test results. The water retention results in Figure 3-5 show main drying curves on samples compacted to three widely different void ratios (0.591, 0.932 and 1.459) and main wetting curves on the first two of these samples. It is clear that compaction to a lower void ratio has shifted both main drying curve and main wetting curve to higher suction values, as expected.

Figure 3-6 shows the same experimental data as in Figure 3-5 (for the two samples compacted to $e = 0.591$ and $e = 0.932$), but re-plotted as water content against suction. Inspection shows that the main drying curves for the two samples now coincide in the high suction (low water content) range, and the same is true for the main wetting curves. Romero & Vaunat (2000) argued that this showed that the sizes of the intra-aggregate micro-voids were unaffected by compaction to a lower void

ratio, and that it was the inter-aggregate macro-voids (which control the water retention behaviour at low suctions) that were compressed during compaction. This finding was further confirmed by Tarantino (2007) for the main wetting curves of compacted kaolin samples.

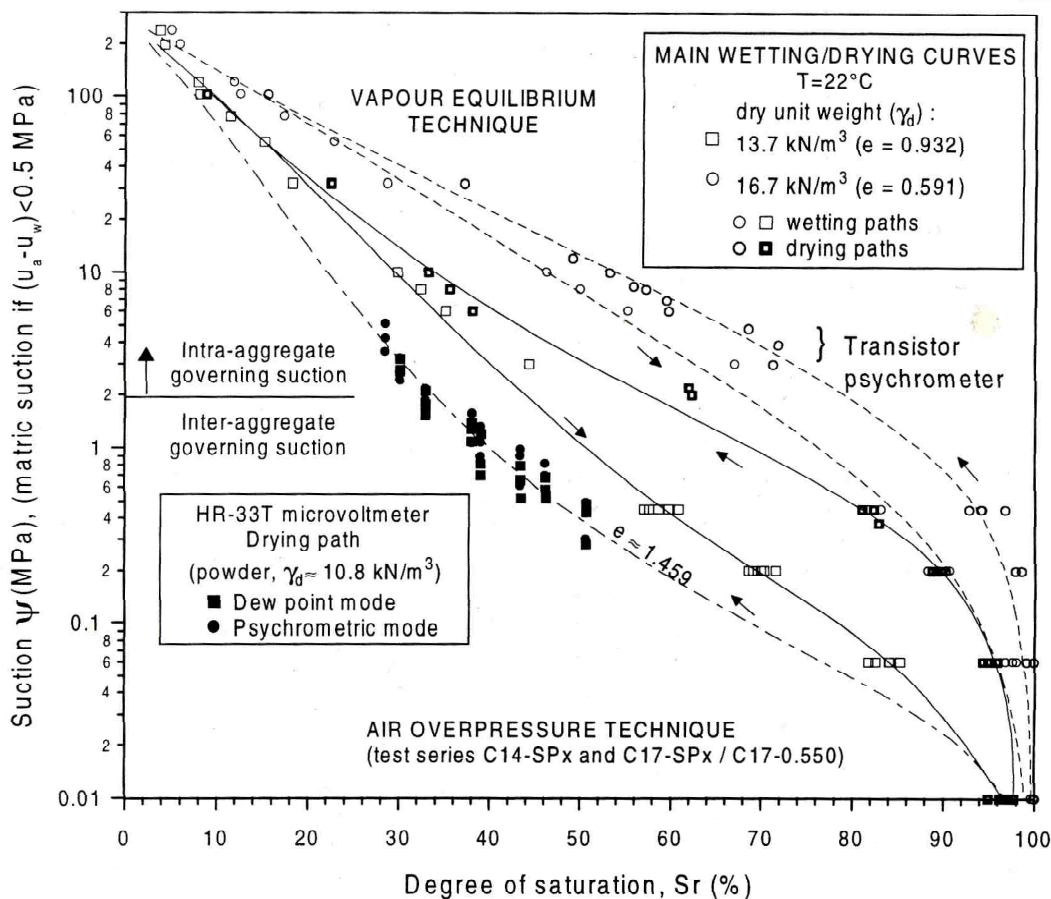


Figure 3-5 Main wetting and drying curves for different void ratios plotted as degree of saturation against suction (Romero, 1999)

One question to emerge from Figure 3-5 and Figure 3-6 is whether it is more useful to plot water retention curves as degree of saturation against suction or as water content against suction. Interpretation and modelling in the low suction range is probably easier in terms of S_r , because all curves approach $S_r = 1.0$ as suction is reduced towards zero (see Figure 3-5). However, interpretation and modelling in the high suction range may be easier in terms of w , because the behaviour may then become independent of void ratio (see Figure 3-6), if intra-aggregate micro-voids experience little change of volume. There is still no general consensus on this issue.

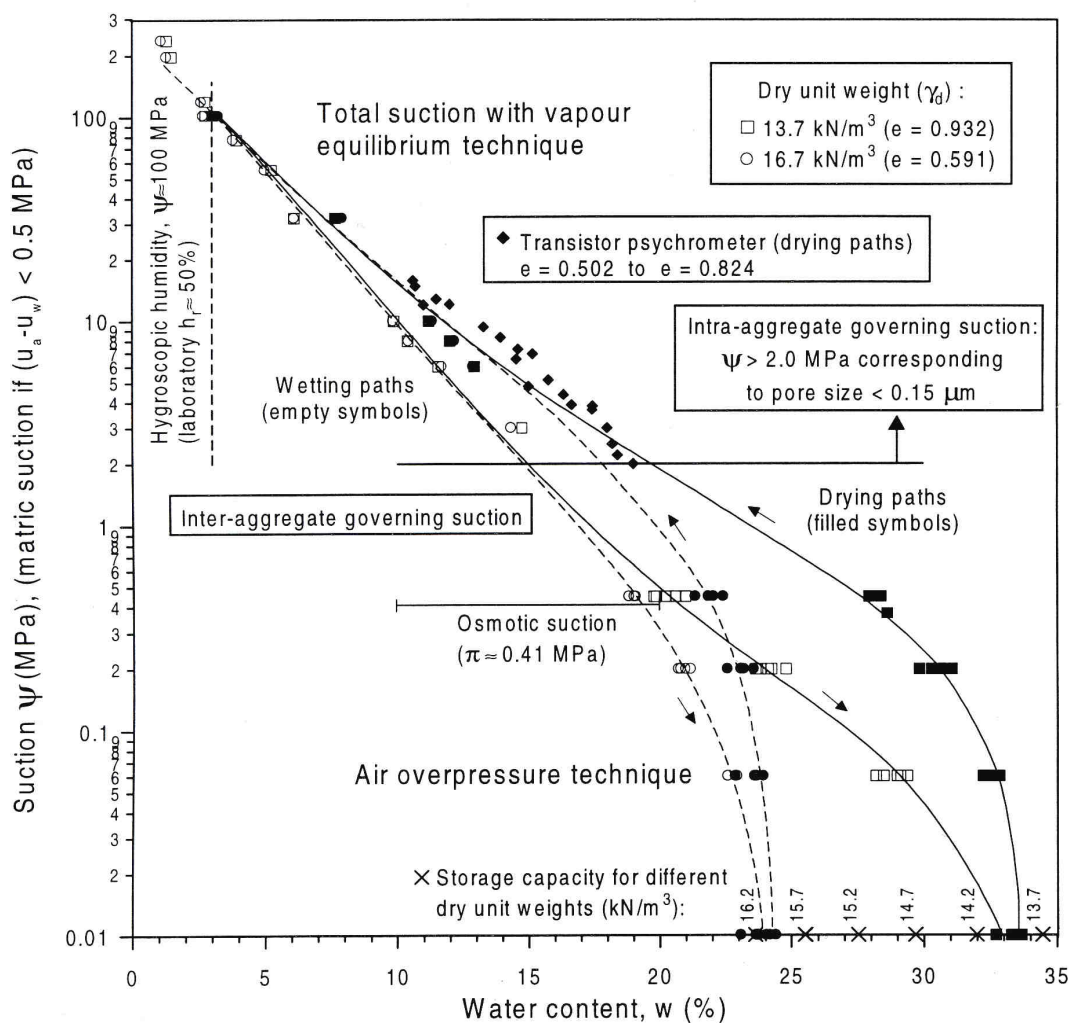


Figure 3-6 Main wetting and drying curves for different void ratios plotted as water content against suction (Romero, 1999).

3.4 COUPLING OF MECHANICAL BEHAVIOUR AND WATER RETENTION BEHAVIOUR

In Sections 3.2 and 3.3, the influence of water retention behaviour on mechanical behaviour and vice versa have been explained with physical arguments and supported by experimental evidence. These two aspects of behaviour interact with each other in both directions at a constitutive level. Hence, it is important to incorporate the coupling phenomena into constitutive models for mechanical behaviour or water retention behaviour in order to represent the real behaviour of unsaturated soils subjected to different stress paths.

In the last few years, several proposals have been made, particularly for mechanical constitutive models incorporating the influence of water retention behaviour. Only a few of these models were expressed in terms of net stresses and suction (e.g. Vaunat et al., 2000 and Buisson & Wheeler, 2000), because these conventional stress state variables do not include variables such as the degree of saturation, making it difficult to easily incorporate some features such as transition between saturated and unsaturated states. Most of the models have been formulated using alternative stress state variables, in which at least one of the stress state variables contains a water retention state variable such as degree of saturation (e.g. Jommi 2000; Wheeler et al., 2003; Gallipoli et al., 2003b and Tamagnini, 2004).

Most of the models developed to capture features of behaviour arising from the coupling phenomena, have either made use of two separate models for mechanical behaviour and water retention behaviour (e.g. Tamagnini, 2004) or relied on experimental data for water retention behaviour (e.g. Jommi, 2000 and Gallipoli et al., 2003b). The disadvantages of this type of approach are the difficulty and complexity arising in terms of constitutive equations, the need to couple two separate models and the large numbers of parameters involved. In contrast, Buisson & Wheeler (2000), Vaunat et al. (2000) and Wheeler et al. (2003) each proposed a single framework in order to explain both mechanical behaviour and water retention behaviour. Of these three models, Buisson & Wheeler (2000) and Wheeler et al., (2003) include coupling in both directions, whereas Vaunat et al. (2000) incorporates only the influence of mechanical behaviour on water retention behaviour (but not vice versa)

3.5 MODELS INCOPORATING COUPLING OF MECHANICAL AND WATER RETENTION BEHAVIOUR

In this section, some fully coupled elasto-plastic models for mechanical behaviour and water retention behaviour and some models for mechanical behaviour incorporating the influence of water retention behaviour are discussed.

Vaunat et al. (2000) proposed an elasto-plastic mechanical-water retention model for unsaturated soils in terms of net stresses and suction. The framework consists of two separate modelling hypotheses for mechanical behaviour and water retention

behaviour. The water retention model developed by Romero & Vaunat (2000) (see Sections 2.7.2 and 3.3) was coupled with the BBM for mechanical behaviour. Three yield curves have been proposed; the Suction Decrease (SD) and Suction Increase (SI) yield curves both representing water retention behaviour and the Loading Collapse (LC) yield curve representing mechanical behaviour (see Figure 3-7). However, the constitutive relations for coupling are complex and 14 model parameters are needed to represent the mechanical and water retention behaviour for isotropic stress states. In addition, the influence of water retention on the mechanical behaviour was not taken into account leading to coupling only in one direction.

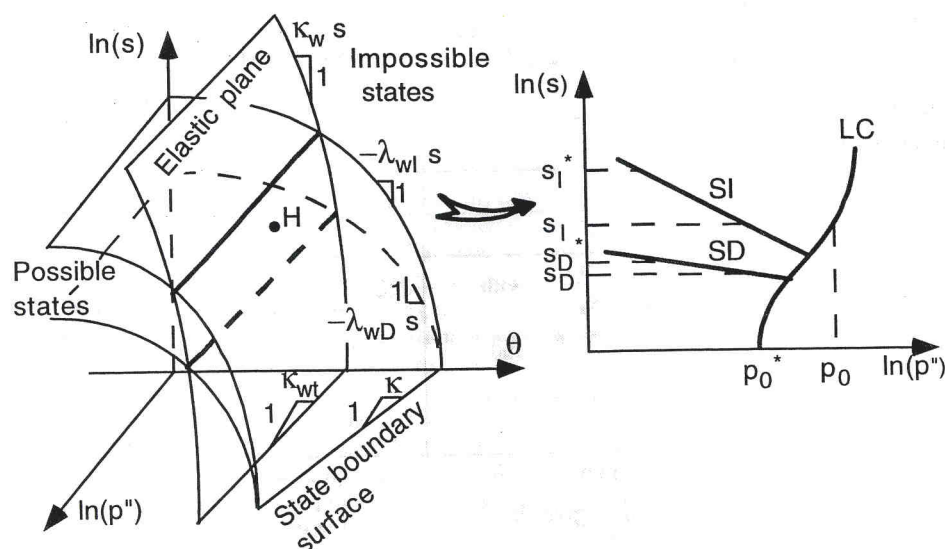


Figure 3-7 Yield curves in suction –net stress plane (Romero & Vaunat, 2000)

Jommi (2000) stated that suction has two different effects on mechanical behaviour at a macroscopic level: (1) modifying the mean stress acting on the soil skeleton; (2) a stabilizing effect at inter-particle contacts through the influence of meniscus water rings. It can be noted that the first effect can be represented by use of “Bishop’s stress” (see Section 2.6.2), but that the second effect can not be modelled by a single stress state variable. Jommi (2000) proposed a mechanical constitutive model for unsaturated soil, based on Modified Cam Clay, but with Bishop’s stress in place of effective stresses and an additional hardening function which depends on degree of saturation in order to represent the influence of meniscus water rings.

Later, Tamagnini (2004) combined the mechanical model of Jommi (2000) with the water retention model of Romero & Vaunat (2000) in order to provide a combination of a mechanical model and a water retention model that incorporated coupling in both directions. The models of Tamagnini (2004) require 12 parameters in order to model the coupled mechanical and water retention behaviour under isotropic stress states. Most of the parameters were required for water retention behaviour (i.e. 8 parameters).

A weakness of the model of Jommi (2000) and Tamagnini (2004) is that plastic volumetric strain during drying is likely to be predicted only on a first drying path. This contrasts with some of the experimental observations, where yield points and subsequent plastic compression can be observed not only on first drying but also on subsequent drying (e.g. Alonso et al. 1995, see Figure 3-4).

Gallipoli et al. (2003b) put forward an elasto-plastic framework for mechanical behaviour of unsaturated soils incorporating the influence of degree of saturation in addition to suction. The model was formulated in terms of Bishop's stress and a scalar constitutive variable, termed the "bonding factor", to represent the stabilising effect of meniscus water rings. The bonding factor was a function of suction and degree of saturation. Gallipoli et al. (2003b) demonstrated that, for isotropic virgin loading and for critical states, the ratio of the void ratio e of an unsaturated soil at a particular value of Bishop's stress to the void ratio e_s of saturated soil at the same value of Bishop's stress was a unique function of the bonding factor, using experimental data from Sivakumar (1993), Sharma (1998) and Toll (1990). Later, further experimental evidence was provided for this relationship by Gallipoli et al. (2008) with experimental data from Cui (1993) and Barrera (2002). With this empirical relationship, the model was able to provide good predictions against experimental results, provided that the degree of saturation was obtained from experimental results. However, it would be possible to couple the mechanical model with a suitable water retention model, such as Gallipoli et al. (2003a), to provide a full predictive model (although this possibility was not tested by Gallipoli et al. 2003b).

Gallipoli et al. (2008) extended the investigation on the relationship between unsaturated critical state shear strength, mean Bishop's stress and the capillary "bonding factor" based on the experimental test results from Cui (1993), Barrera

(2002), Sivakumar (1993) and Wheeler & Sivakumar (1995). The critical stress ratio (the ratio of critical state shear strength of an unsaturated soil at a particular value of Bishop's stress to the critical state shear strength of saturated soil at the same value of Bishop's stress) was plotted against the bonding factor. A decrease in the critical stress ratio with increase in bonding factor was observed for experimental results except Cui (1993), which exhibited no variation of critical stress ratio with bonding factor suggesting that the influence of meniscus water rings on the shear strength behaviour may be negligible.

Several other models (e.g. Buisson & Wheeler, 2000 and Li, 2007a, 2007b) have also been proposed to deal with coupling of mechanical and water retention behaviour at a constitutive level. Buisson & Wheeler (2000) presented a single qualitative framework for modelling both mechanical behaviour and water retention behaviour within a single model, incorporating coupling in both directions. However, subsequent development of the qualitative framework to a full mathematical constitutive model proved impossible. Li (2007a) has proposed a framework for mechanical and water retention behaviour of unsaturated soils based on thermodynamic principles, treating soil as open multi phase system displaying coupling effects among phases and examining work-energy-dissipation relation. In addition to elasto-plastic deformation of soil and hydraulic response, a relationship for state of pore air has also been established. Later, Li (2007b) used the framework to propose a new elasto-plastic model for the response of the soil skeleton (Li, 2007a) and water retention behaviour (Li, 2005). Model simulations for various stress paths, such as wetting, consolidation and shearing, were compared against the experimental results from Sivakumar & Wheeler (2000) and Wheeler & Sivakumar (2000), and were shown to capture some basic features of behaviour of unsaturated soils.

Almost all the models discussed in this section either have been expressed as two separate frameworks (for mechanical and water retention behaviour) coupled together or a single framework with separate yield curves dedicated to mechanical behaviour and to water retention behaviour.

3.6 WHEELER ET AL. (2003) FRAMEWORK

Wheeler et al. (2003) proposed a single fully coupled mechanical-water retention constitutive framework. This framework is considered to have advantages over the various alternatives discussed in the previous section, and it is described in detail in this section. This description includes an introduction to the basic concepts (Section 3.6.1) and description of the illustrative model for isotropic stress states presented by Wheeler et al. (2003) (Section 3.6.2). This is then followed by extension of the model to include the role of deviator stress (Section 3.6.3). This last stage is an original contribution of the author, not included in the paper of Wheeler et al. (2003).

3.6.1 Modelling concepts

The framework has been formulated in terms of alternative stress state variables, rather than the conventional variables of net stresses and suction. The first stress variable is the “Bishop’s stress” tensor or “average skeleton stress” tensor, as described in Section 2.6.2 and given by:

$$\sigma_{ij}^* = \sigma_{ij} - [S_r u_w + (1 - S_r) u_a] \delta_{ij} \quad (3-1)$$

where σ_{ij} is the total stress tensor, S_r is the degree of saturation, u_w is the pore water pressure, u_a is the pore air pressure and δ_{ij} is Kroneker’s delta. Bishop’s stress is selected as a physically significant stress, which is intended to represent the influence of total stresses, pore air pressure (within air-filled voids) and pore water pressure in bulk water (within water-filled voids) on inter-particle or inter-aggregate forces, by using degree of saturation to determine a weighted average of the two pore pressures. Empirical evidence suggests that it may be possible to relate both elastic straining and shear strength exclusively to this stress variable. Not all aspects of mechanical behaviour can, however, be related solely to Bishop’s stress, because this stress variable cannot represent the effect of meniscus water bridges on inter-particle or inter-aggregate forces. These meniscus water bridges have a stabilizing effect on inter-particle or inter-aggregate contacts (reducing the possibility of slippage at the contacts) and therefore have an important influence on yielding (see Section 2.3).

The second stress state variable is a scalar quantity called the “modified suction” and is given by:

$$s^* = n(u_a - u_w) \quad (3-2)$$

where n is porosity. The modified suction stress variable has been selected in combination with the Bishop’s stress tensor by considering the incremental work input for unsaturated soils (see Houlsby, 1997). Strain increment variables conjugate to the Bishop’s stress tensor and the modified suction are the conventional strain increment tensor $d\varepsilon_{ij}$ and the decrement of degree of saturation $-dS_r$, respectively. For isotropic stress states, the stress variables simplify to mean Bishop’s stress p^* and modified suction s^* , with the work-conjugate strain increment variables being the volumetric strain increment $d\varepsilon_v$ and the decrement of degree of saturation $-dS_r$.

Wheeler et al. (2003) proposed two separate physical mechanisms for the occurrence of plastic volumetric strain (mechanical behaviour) and plastic changes of degree of saturation (water retention behaviour), along with couplings between these two aspects of behaviour. Plastic volumetric strain was assumed to be caused by inter-particle or inter-aggregate slippage while plastic changes of degree of saturation were attributed to flooding and emptying of voids by water.

Figure 3-8 illustrates the logic behind elasto-plastic modelling of water retention behaviour. As suction decreases (Figure 3-8a) from a particular value, an air-water interface would move from position 1 to 2. If the suction decreases further the air-water interface would move further towards the air-filled void, as the radius of curvature of the interface increases. A limiting condition is reached when the radius of the air-water interface becomes equal to the radius of the largest sphere that can be accommodated within the air-filled void (see position 3 in Figure 3-8a). Any further decrease in suction would lead to flooding of the air-filled void with water (Fredlund, 1979). During a drying process (Figure 3-8b), air-water interfaces migrate towards the water-filled void from position 4 to 5 as the radius of curvature of the air-water interfaces decreases. As the suction increases further, the radius of curvature of an air-water interface reaches a critical value, which is just enough to bridge the throat

joining the water-filled voids to an adjacent air-filled void. Any further increase in suction would therefore make air break through into the void, displacing the water into adjacent water-filled voids.

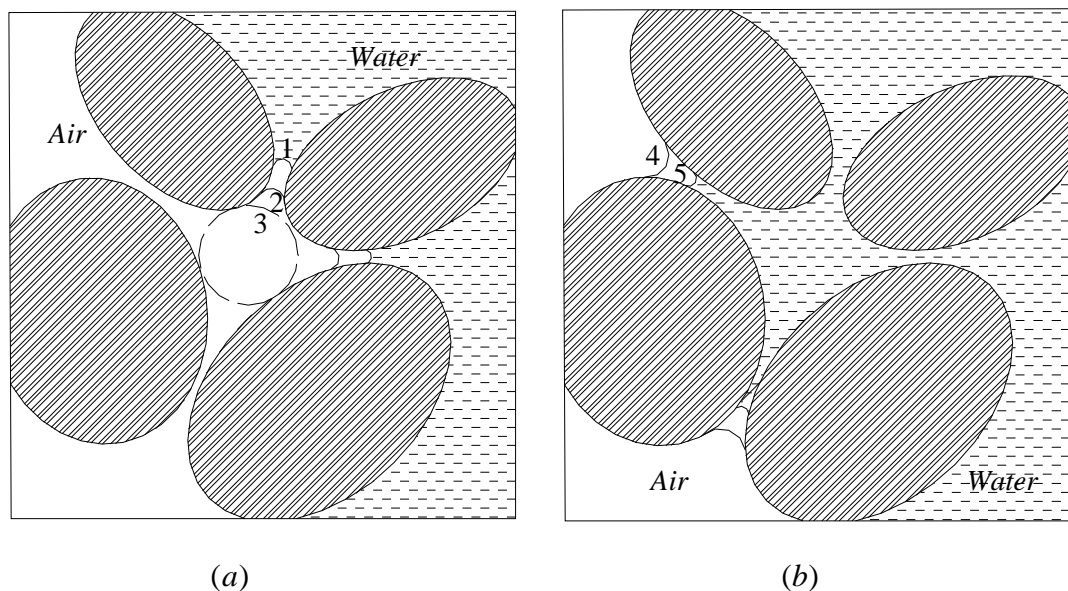


Figure 3-8 Movement of air-water interfaces (a) filling of a void with water during wetting (b) emptying of water void during drying (after Buisson & Wheeler, 2000)

The movement of an air-water interface from position 1 to 2 or position 4 to 5 could be considered as an elastic process, despite small irreversibility due to differences in the contact angle during advance and withdrawal of interfaces. The above mentioned movements of air-water interfaces are therefore associated with elastic changes of degree of saturation. On the other hand, the processes of flooding or emptying of a void with water are irreversible, as the radii of curvature corresponding to position 3 (flooding an air-filled void with water) and position 5 (emptying of a water-filled void) are different. Hence, these processes of flooding or emptying of voids with water are associated with plastic changes of degree of saturation.

Figure 3-9 shows the three yield curves proposed in the Wheeler et al. (2003) model for isotropic stress states, namely the Loading Collapse (LC) yield curve, the Suction Increase (SI) yield curve and the Suction Decrease (SD) yield curve. Yielding on the LC yield curve is associated with inter-particle or inter-packet slippage and would produce plastic volumetric strain (mechanical behaviour) but no plastic change of degree of saturation. Yielding on the SD or SI yield curves is associated with flooding

or emptying of voids with water and would generate plastic change of degree of saturation (water retention behaviour) but no plastic volumetric strain.

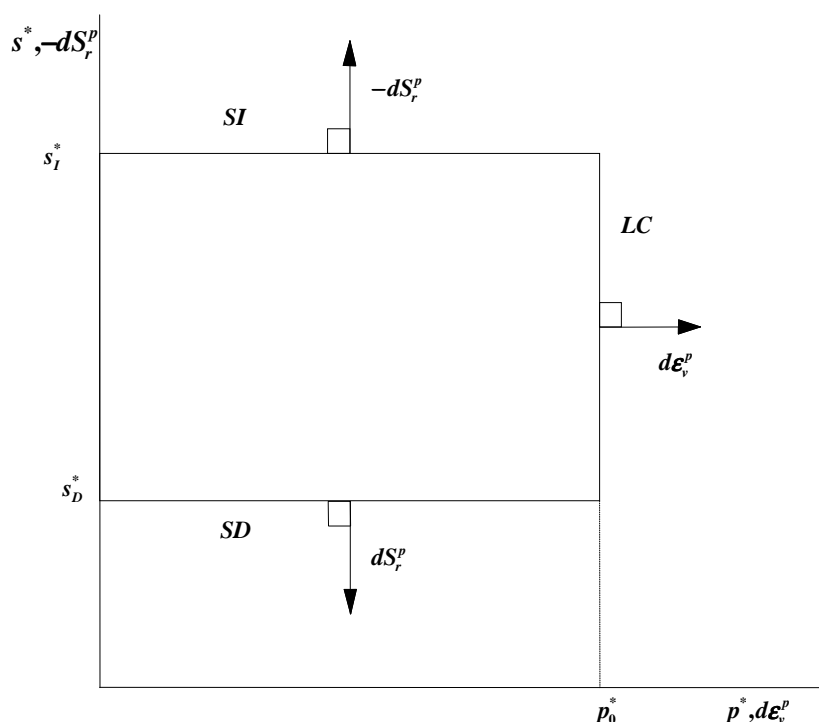


Figure 3-9 Yield curves for isotropic stress states (Wheeler et al., 2003)

For a given configuration of the soil particles, the value of Bishop's stress required to cause inter-particle or inter-aggregate slippage is influenced solely by the stabilizing effect of the meniscus water bridges. It is assumed that this stabilizing effect is dependent only on the number of inter-particle contacts surrounded by meniscus water bridges and is independent of the suction (or modified suction) within these water bridges (see Section 2.3). As a consequence, the LC yield curve takes the form of a straight vertical line in the $s^* : p^*$ plane (no influence of s^* on yielding), but the position of the LC yield curve is affected by the occurrence of any plastic changes of degree of saturation (arising due to yielding on the SI or SD curves), corresponding to emptying or flooding of voids with water (increasing or decreasing the number of meniscus water bridges). As a result, any yielding on SI or SD curves causes a coupled outward or inward movement of the LC yield curve respectively. There is no plastic volumetric strain associated with this coupled outward movement of the LC yield curve (because no inter-particle or inter-aggregate slippage is occurring); only direct yielding on the LC curve causes plastic volumetric strain.

With a particular set of voids filled with water, and the remainder filled with air, it is assumed that the values of modified suction s^* required to cause either emptying of further voids of water (during drying) or filling of further voids with water (during wetting) are dependent solely on the packing arrangement of the soil particles (which determines the dimensions of the voids and of the connecting passageways between voids). It is further assumed that this packing arrangement is unaffected by elastic volumetric strains caused by any changes of mean Bishop's stress p^* , and is influenced solely by plastic volumetric strains (arising from yielding on the LC yield curve). As a consequence, the SI and SD yield curves are straight horizontal lines in the $s^* : p^*$ plane (no influence of p^* and hence elastic volumetric strains on water retention behaviour), but any yielding on the LC curve causes coupled upward movements of the SI and SD yield curves (as the void dimensions reduce during plastic volumetric straining). There are no plastic changes of degree of saturation associated with these coupled movements of the SI and SD yield curves (because no emptying or flooding of voids with water is occurring); only direct yielding on the SI or SD curve causes a plastic change of degree of saturation.

For stress points lying at the corner between the LC and SI yield curves, four possible types of behaviour can occur, depending on the direction of the stress path: elastic unloading; yielding on only the LC curve; yielding on only the SI curve; and simultaneous yielding on both LC and SI curves (with plastic volumetric strains and plastic decreases of degree of saturation both occurring). Similar possibilities exist for stress points lying at the corner between the LC and SD yield curves. For example, the occurrence of collapse compression during a wetting path corresponds to simultaneous yielding on LC and SD curves, with the stress point at the corner between the two curves.

3.6.2 Illustrative model for isotropic stress states

Wheeler et al., (2003) presented a possible mathematical model for isotropic stress states, as an example of how their conceptual framework could be used. Figure 3-10 shows the proposed water retention model. It can be seen that the air entry was assumed to occur in correspondence of the main wetting curve rather than main drying

curve contrasting experimental evidence. However, this particular assumption was made in order to avoid the prediction of irreversible changes S_r in the elastic domain.

Within the proposed model, elastic volumetric strains and elastic changes of degree of saturation are given by:

$$d\varepsilon_v^e = \frac{\kappa dp^*}{\nu p^*} \quad (3-3)$$

$$dS_r^e = -\frac{\kappa_s ds^*}{s^*} \quad (3-4)$$

where κ and κ_s are two elastic constants. The parameter κ_s gives the gradient of elastic scanning curves in the water retention plot of S_r against the natural logarithm of s^* (see Figure 3-10). A key assumption is that elastic volumetric strains depend solely on changes of p^* and elastic changes of degree of saturation depend solely on changes of s^* . This type of elastic uncoupling is not possible in models expressed in terms of net stress and suction (such as the BBM).

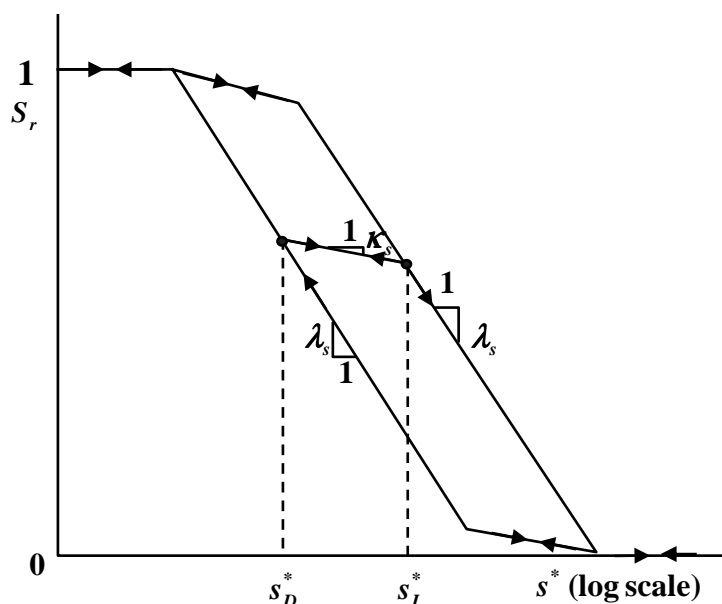


Figure 3-10 Water retention model without any influence of mechanical behaviour (Wheeler, Sharma & Buisson 2003)

Yielding on the LC yield curve alone would produce a plastic increment of volumetric strain as follows:

$$d\varepsilon_v^p = \frac{(\lambda - \kappa)dp_0^*}{vp_0^*} \quad (3-5)$$

where λ the conventional gradient of the saturated normal compression line and p_0^* is mean Bishop's stress on the LC yield curve (see Figure 3-9).

The occurrence of plastic volumetric strain during yielding on the LC yield curve would reduce the dimensions of voids and of connecting passageways between voids and would therefore increase the suctions required for flooding or emptying of voids with water. This is represented by coupled upward movements of the SD and SI yield curves, given by the following equation:

$$\frac{ds_I^*}{s_I^*} = \frac{ds_D^*}{s_D^*} = k_2 \frac{dp_0^*}{p_0^*} \quad (3-6)$$

where k_2 is a coupling parameter. An associated flow rule was assumed on the LC yield curve:

$$\frac{dS_r^p}{d\varepsilon_v^p} = 0 \quad (3-7)$$

Yielding on the SI or SD curve alone will produce a plastic change in degree of saturation as follows:

$$-dS_r^p = \frac{(\lambda_s - \kappa_s)ds_I^*}{s_I^*} = \frac{(\lambda_s - \kappa_s)ds_D^*}{s_D^*} \quad (3-8)$$

λ_s defines the (plastic) gradient of the main drying or main wetting curves in the water retention plot of S_r against $\ln(s^*)$ (see Figure 3-10).

The plastic increment of degree of saturation can be thought of as controlling the change in number of meniscus water rings, which means a change in stability of inter-

particle contacts. This is modelled by coupled outward movement of the LC yield curve during yielding on the SI curve and coupled inward movement of the LC yield curve during yielding on the SD curve. These coupled movements of the LC curve are both given by:

$$\frac{dp_0^*}{p_0^*} = k_1 \frac{ds_I^*}{s_I^*} = k_1 \frac{ds_D^*}{s_D^*} \quad (3-9)$$

where, k_1 is a second coupling parameter. An associated flow rule was assumed on the SD and SI yield curves:

$$\frac{d\epsilon_v^p}{dS_r^p} = 0 \quad (3-10)$$

In general, the overall movement of the LC yield curve therefore includes a direct component of movement (due to any yielding on the curve), given by Equation 3-5, and a coupled component of movement (due to any plastic change of degree of saturation), given by Equations 3-9 and 3-8:

$$\frac{dp_0^*}{p_0^*} = \frac{v}{\lambda - \kappa} d\epsilon_v^p + \frac{k_1}{\lambda_s - \kappa_s} (-dS_r^p) \quad (3-11)$$

Similarly, the overall movements of the SD and SI yield curves include a direct component (due to any yielding on SD or SI yield curve), given by Equation 3-8, and a coupled component of movement (due to any plastic volumetric strain), given by Equations 3-6 and 3-5:

$$\frac{ds_I^*}{s_I^*} = \frac{ds_D^*}{s_D^*} = \frac{-dS_r^p}{\lambda_s - \kappa_s} + \frac{k_2 v}{\lambda - \kappa} d\epsilon_v^p \quad (3-12)$$

The general case presented above (see Equations 3-11 and 3-12) includes the possibility of both plastic volumetric strains and plastic changes of degree of saturation occurring simultaneously. This behaviour corresponds to yielding on SD and LC curves simultaneously or SI and LC curves simultaneously, and plastic volumetric

strain and plastic changes of degree of saturation can then be expressed by the following equations by combining Equations 3-11 and 3-12:

$$d\varepsilon_v^p = \frac{(\lambda - \kappa)}{v(1 - k_1 k_2)} \left(\frac{dp_0^*}{p_0^*} - k_1 \frac{ds_I^*}{s_I^*} \right) = \frac{(\lambda - \kappa)}{v(1 - k_1 k_2)} \left(\frac{dp_0^*}{p_0^*} - k_1 \frac{ds_D^*}{s_D^*} \right) \quad (3-13)$$

$$-dS_r^p = \frac{(\lambda_s - \kappa_s)}{(1 - k_1 k_2)} \left(\frac{ds_I^*}{s_I^*} - k_2 \frac{dp_0^*}{p_0^*} \right) = \frac{(\lambda_s - \kappa_s)}{(1 - k_1 k_2)} \left(\frac{ds_D^*}{s_D^*} - k_2 \frac{dp_0^*}{p_0^*} \right) \quad (3-14)$$

The model of Wheeler et al. (2003) can predict, at a qualitative level, observed features of mechanical behaviour and water retention behaviour which arise from coupling of these two types of behaviour. This includes irreversible volumetric strains during a drying stage (see Figure 3-4) and a decrease in the yield stress during isotropic loading due to a previous wetting and drying cycle (see Figure 3-3)

The model of Wheeler et al. (2003) was an illustrative example, and still requires:

- validation of some of the basic assumptions of the modelling framework (e.g. uncoupled elastic behaviour, simple shapes of the 3 yield curves (Figure 3-9), qualitative forms of coupling relationships and associated flow rules (Equations 3-7 and 3-10));
- enhancement of the water retention model (see Figure 3-10) to better reflect real soil behaviour (e.g. by introducing a bounding surface plasticity formulation);
- validation of the specific forms of elastic relationships (Equations 3-3 and 3-4), hardening laws (Equations 3-5 and 3-8) and coupling relationships (Equations 3-6 and 3-9);
- extension of the model to triaxial stress states.

3.6.3 Extension of Wheeler et al. (2003) model to triaxial stress states

The illustrative constitutive model presented by Wheeler et al. (2003) was limited to isotropic stress states. In this section, a possible form of extension of the model to triaxial stress states is proposed i.e. incorporating the role of deviator stress q , including the shear strength behaviour.

Unlike volume change behaviour, shear strength of unsaturated soils can be exclusively related to a single stress state variable with reasonable accuracy (Bishop & Blight, 1963). Several proposals have been made for such a stress state variable, mostly modifying the Bishop's stress by replacing degree of saturation with suitable material parameters. Khalili & Khabbaz (1998) showed that shear strength of unsaturated soils can be adequately related to a stress variable similar to Bishop's stress, but with a power function in terms of suction and air entry value in place of S_r . Tarantino (2007), on the other hand, suggested that a component of S_r with respect to macro-voids instead of total S_r can be employed in the stress variable used for shear strength behaviour. However, several authors argue that Bishop's stress (without modification) is sufficient to describe the variation of shear strength of some soils (e.g. Nuth & Laloui, 2007 and Gallipoli et al., 2008).

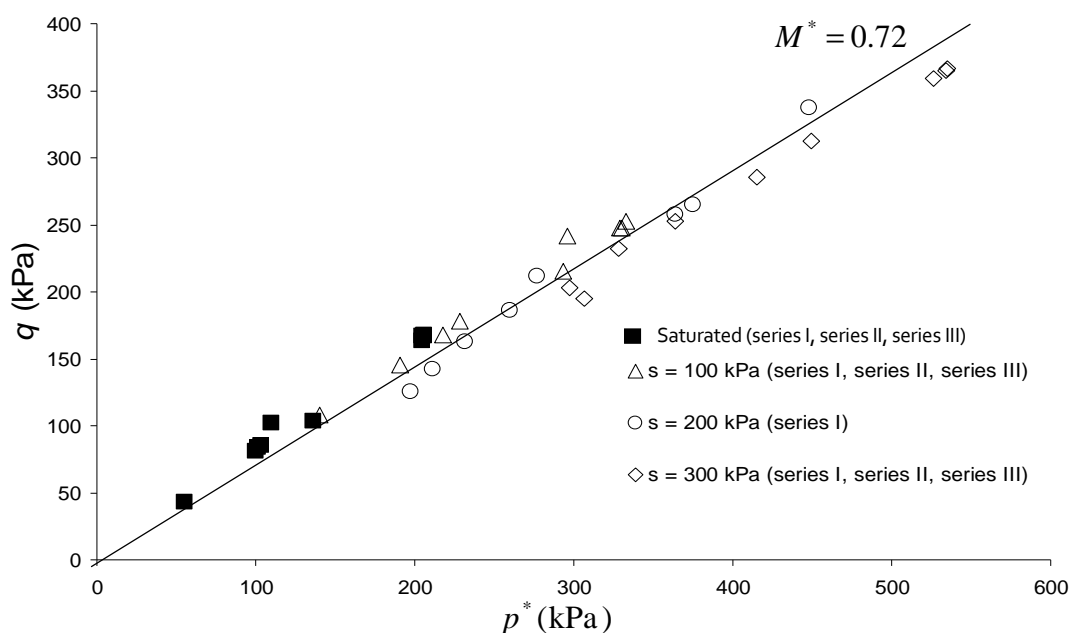


Figure 3-11 Critical state values of q for compacted speswhite kaolin plotted against mean Bishop's stress for Sivakumar (1993) and Wheeler & Sivakumar (2000) experimental test data (Gallipoli et al., 2008)

Figure 3-11 shows critical state values of deviator stress q plotted against mean Bishop's stress p^* for the experimental data on compacted speswhite kaolin of Sivakumar (1993) and Wheeler & Sivakumar (2000) (re-plotted by Gallipoli et al., 2008). The results cover suctions ranging from zero to 300 kPa, and re-plotted in this

way they can be approximated by a unique critical state line of gradient $M = 0.72$. Closer inspection of Figure 3-11, however, suggests that the critical state relationship between q and p^* may not be entirely unique, as there is a small but consistent trend with variation of suction, with the saturated data points lying at the top of the range and the highest suction data points lying at the bottom of the range.

Figure 3-12 shows equivalent critical state data for the compacted Barcelona clayey silt tested by Barrera (2002) (also re-plotted by Gallipoli et al., 2008). Again a unique critical state line between q and p^* seems a reasonable approximation. In contrast with Figure 3-11, the saturated test data in Figure 3-12 appear to lie at the bottom of the range of experimental data. It is, however difficult to conclude whether there is any consistent trend of the influence of suction in Figure 3-12, because of the limited number of data points.

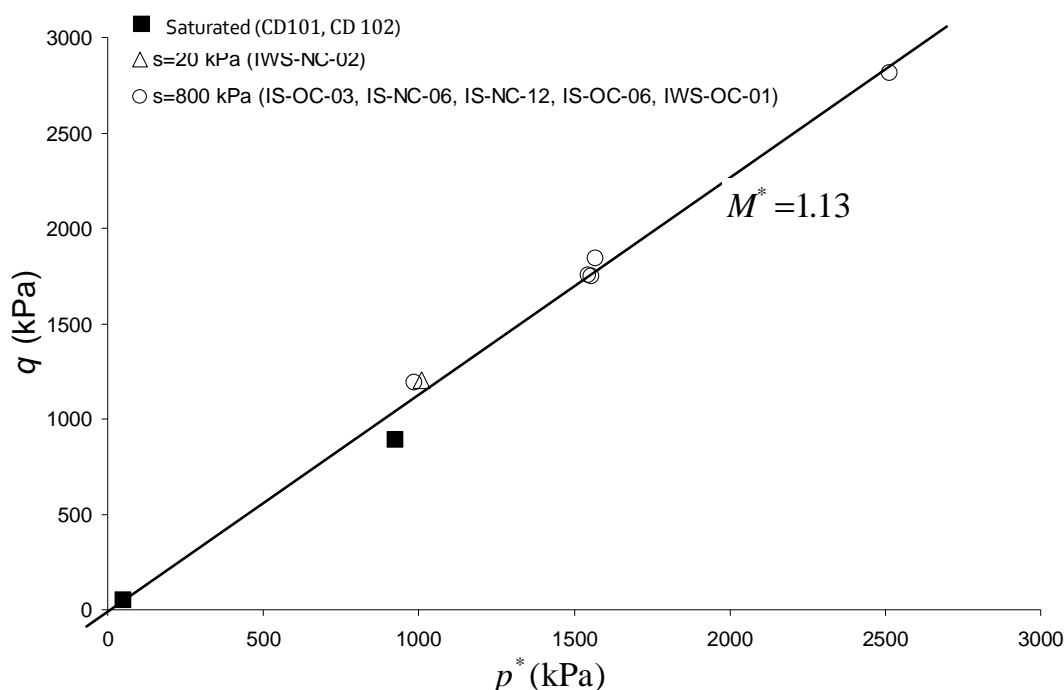


Figure 3-12 Critical state values of q for compacted Barcelona clayey silt plotted against mean Bishop's stress for Barrera (2002) experimental test data (Gallipoli et al., 2008)

With the experimental evidence shown in Figure 3-11 and Figure 3-12, the simplest extension of the LC yield curve of Wheeler et al. (2003) to include the role of deviator stress is to assume that constant s^* cross-sections of the LC yield surface form

elliptical yield curves in the $q : p^*$ plane, as shown in Figure 3-13. The yield curve in the $q : p^*$ plane is identical to the Modified Cam Clay yield curve for saturated soil i.e. an ellipse of aspect ratio M^* passing through the origin and intersecting the p^* axis at the isotropic yield stress p_0^* . The aspect ratio M^* is constant, independent of the value of modified suction s^* , or of the size of the yield curve (i.e. it does not vary with p_0^*). The fact that all elliptical yield curves pass through the origin differs from the suggestion of Wheeler et al. (2003), who presented a diagram showing an elliptical yield curve spanning to negative values of p^* .

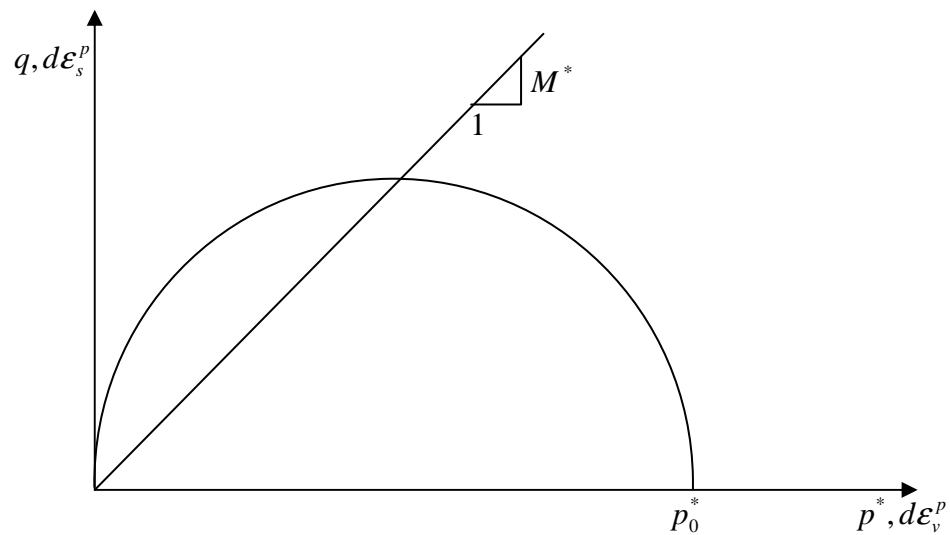


Figure 3-13 proposed constant s^* cross-section of LC yield surface

Three different yield surfaces can now be visualized in $q : p^* : s^*$ space, as shown in Figure 3-14. The equation representing the LC yield surface is given by:

$$q^2 - M^* p^* (p_0^* - p^*) = 0 \quad (3-15)$$

Both SI and SD yield surfaces are assumed to be vertical planes in $q : p^* : s^*$ space, (i.e. the yield values of s^* on the SI and SD yield surfaces are assumed to be independent of deviator stress q as well as p^*), and given respectively by:

$$s^* = s_I^* \quad (3-16)$$

$$s^* = s_D^* \quad (3-17)$$

Inside these yield surfaces (i.e. LC, SD and SI yield surfaces), the behaviour of the soil is assumed to be elastic. The relationships for elastic volumetric strain and elastic changes of degree of saturation have already been defined in Section 3.6.2 (see Equations 3-3 and 3-4). The elastic shear strain can be determined by the following equation:

$$d\varepsilon_s^e = \frac{dq}{3G} \quad (3-18)$$

where G is the elastic shear modulus.

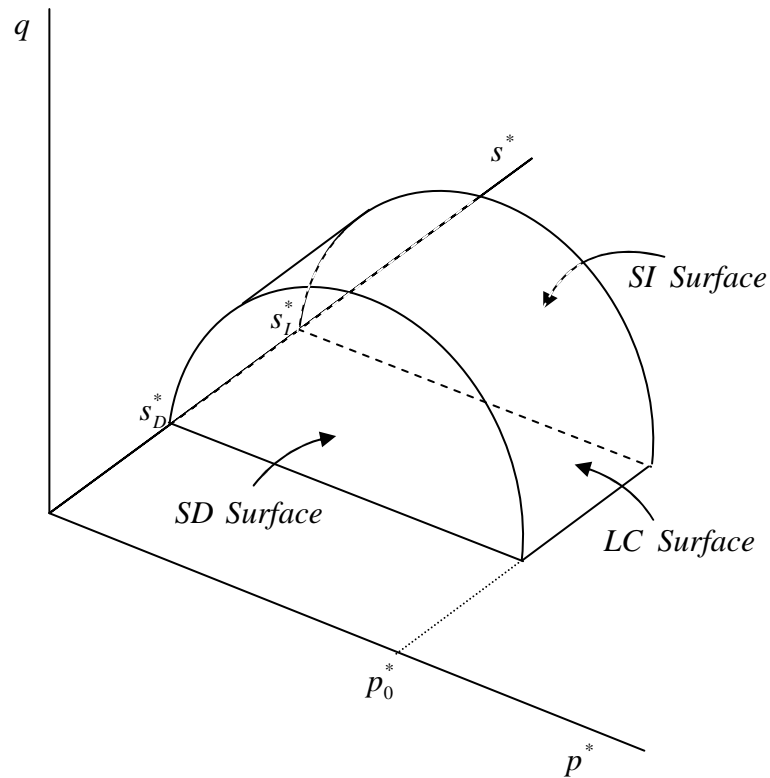


Figure 3-14 Proposed yield surfaces for anisotropic stress states

Two possible forms of flow rule on the LC yield surface are proposed i.e. associated and non-associated flow rules. The associated flow rule is given by:

$$\frac{d\varepsilon_s^p}{d\varepsilon_v^p} = \frac{2\eta^*}{M^{*2} - \eta^{*2}} \quad (3-19)$$

$$dS_r^p = 0 \quad (3-20)$$

where $\eta^* = \frac{q}{p^*}$

The non-associated flow rule is given by:

$$\frac{d\varepsilon_s^p}{d\varepsilon_v^p} = \frac{2\eta^* \alpha}{M^{*2} - \eta^{*2}} \quad (3-21)$$

$$dS_r^p = 0 \quad (3-22)$$

where α is a constant given by Alonso et al., (1990) to match experimental K_0 stress ratio for saturated soils:

$$\alpha = \frac{M^*(M^* - 9)(M^* - 3)}{(6 - M^*)} \left\{ \frac{1}{1 - \kappa/\lambda} \right\} \quad (3-23)$$

Either of these flow rules is associated at the apex of the elliptical yield curve in the $q : p^*$ plane (see Figure 3-13). This corresponds to a critical state point in the $q : p^*$ plane. The critical state line is then given by:

$$q = M^* p^* \quad (3-24)$$

The above critical state line equation is proposed based on the experimental evidence, including experimental data in Figure 3-11 and Figure 3-12. However, the author acknowledges that this proposal may not be appropriate for a wide range of soils.

Flow rules on the SI and SD yield surfaces are still given by Equation 3-10 (i.e. an associated flow rule). The hardening laws and coupling relationships are also unchanged and, given by Equations 3-11 to 3-14.

A simulations code was developed at stress point level for the Wheeler et al. (2003) model, using Matlab software. The simultaneous incremental equations which must be solved for increments of stress, strain and degree of saturation are presented in the

Appendix, together with the algorithms employed in the Matlab coding in order to run simulations for required stress paths.

CHAPTER 4

NEW BOUNDING SURFACE PLASTICITY MODELS FOR UNSATURATED SOILS

This chapter contains two major sections. In first section the limitations of classical elasto-plasticity in representing the mechanical behaviour and water retention behaviour of saturated and unsaturated soils are first discussed, with the help of some experimental evidence from the literature. The idea of bounding surface plasticity and some modelling approaches using this concept are then presented, in order to demonstrate certain advantages of bounding surface plasticity modelling over classical elasto-plasticity. The second section covers the proposal of new bounding surface plasticity models for water retention behaviour and a new bounding surface plasticity version of the Wheeler et al. (2003) model.

4.1 LIMITATIONS OF CLASSICAL ELASTO-PLASTICITY

Incremental responses of internal variable such as volumetric strain and degree of saturation with the changes of stresses are accommodated in a classical elasto-plasticity mechanical model with the following ingredients: (1) elastic response; (2) yield curves; (3) flow rule or plastic potential and (4) hardening rules. Most of the mechanical constitutive models for both saturated and unsaturated soils are based on classical elasto-plasticity, because of its simple concept, efficiency (in terms of number of parameters) and relative accuracy of modelling the behaviour of soils.

The Modified Cam Clay model for saturated clayey soils and the BBM for unsaturated moderate plasticity soils are some examples of mechanical models formulated on the basis of classical elasto-plasticity. Critical states, volumetric strain and shear strain of normally consolidated soils have been shown to be satisfactorily predicted by these classical elasto-plastic models. However, the basic assumption that behaviour inside the yield curve is elastic, leads the models to unrealistically predict some features of mechanical behaviour of soils.

Similarly, a few researchers modelled water retention behaviour in unsaturated soils as an elasto-plastic process (e.g. Wheeler et al., 2003). Unlike mechanical behaviour, the elasto-plastic approach does not provide a reasonable representation of the basic features of water retention behaviour, in particular the forms of scanning curves cannot be well represented. The drawbacks of classical elasto-plastic modelling are discussed here with respect to mechanical behaviour and water retention behaviour.

4.1.1 Mechanical behaviour

In contrast to the assumption made in classical elasto-plasticity, the real stress-strain behaviour of soils exhibits highly complex features during some specific stress paths. These features of behaviour include the gradual onset of plastic strains during yielding, highly non-linear stress-strain behaviour even at small strains, dependence of stiffness on changes of stress path direction and the stress-strain behaviour during cyclic loading. These features are discussed in detail in the following sub-sections.

4.1.1.a Yielding characteristics

A classical elasto-plasticity model predicts sudden onset of plastic strains, with a sharp discontinuity of stiffness at yield points. However, in reality, the onset of plastic strains is generally more gradual, leading to a progressive change in the stiffness. This feature of behaviour (i.e. gradual change in stiffness near the yield stress) can be partially captured by multiple yield surface models (e.g. Prevost, 1977 & 1978 and Mroz et al., 1978). Bounding surface plasticity is however an ideal method to capture this feature of behaviour (e.g. Dafalias and Herrmann, 1982 and Al-Tabbaa, 1987). This will be discussed further in Section 4.2.

4.1.1.b Non-linear stress-strain behaviour

Several researchers, including Jardine et al. (1985) and Burland (1989), reported non-linear stress-strain behaviour of soil during the very early stage of loading. The variation of stiffness with stress or strain can be identified based on the range of strain the soil is subjected to (Atkinson & Sallfors, 1991) or based on stress space by having different zones (e.g. Jardine, 1985 & 1992). The non-linear stress-strain behaviour at small strains cannot be predicted by a classical elasto-plastic model, as linear elastic behaviour (at least for shear straining) is usually assumed within the yield surface.

Non-linear stress-strain behaviour at small strain levels can be tackled, to a degree, by incorporating non-linear elastic behaviour in a classical elasto-plastic model (e.g. Jardine et al., 1986 & 1991). However, in order to reproduce the non-linear stress-strain behaviour for the full range of strain, the concept of multi-yield surface models (e.g. Puzrin & Burland, 1998) or bounding surface plasticity models may be necessary.

4.1.1.c Dependence of stiffness on recent stress history or stress path direction

Several researchers, such as Atkinson et al. (1990) and Clayton & Heymann (2001), reported dependence of stiffness on the recent stress history, particularly at small strain levels (i.e. inside the “yield surface” of classical elasto-plasticity). The highest stiffness is reported after 180° changes in stress path direction in the $q : p'$ plane and the lowest after no change of stress path direction (e.g. Atkinson et al. 1990). This is known as dependency of stiffness on “recent stress history”.

In order to incorporate these features into a constitutive model, a kinematic hardening model (e.g. multiple-yield surface model) is required. A basic bounding surface plasticity model (without kinematic hardening) can also solve this problem partially. However, inner kinematic surfaces are necessary for a comprehensive representation of recent stress history effects, even for a bounding surface plasticity model.

4.1.1.d Behaviour during cyclic stress paths

Cyclic loading on a soil typically produces plastic straining over many cycles and the progressive accumulations of strain. After many cycles the soil may either reach a stable elastic or plastic “shakedown” condition (converging to a fixed elastic or hysteretic loop) or strains may increase at an accelerating rate until shear failure (“ratcheting”) occurs (Collins & Boulbibane, 2000). The latter case can also sometimes be associated with “liquefaction” in undrained condition due to the increase in excess pore pressures.

A classical elasto-plastic model cannot describe the behaviour mentioned above during cyclic loading. Models based on classical elasto-plasticity would always predict reversible behaviour during a loading and unloading cycle as the stress point would be inside the yield surfaces. A bounding surface plasticity model can naturally incorporate most of the features of behaviour during cyclic loading.

4.1.2 Water retention behaviour

Unlike mechanical behaviour, even the basic water retention behaviour in unsaturated soils can not be satisfactorily modelled with classical elasto-plasticity due to the complex variation of water content or degree of saturation with stress state variables (see Figure 2-15). This section describes four main aspects of water retention behaviour that can not be satisfactorily modelled by the classical elasto-plasticity approach. These are the gradual change in the gradient when a scanning curve approaches the main wetting curve or the main drying curve, highly non-linear behaviour for almost the full range of degree of saturation, dependency on the recent stress history or changes of stress path direction and the behaviour during cycles of wetting and drying.

4.1.2.a Re-joining of scanning curves with main wetting/drying curve

During a wetting or a drying stage, the scanning curves gradually re-join the main wetting or main drying curve respectively. A classical elasto-plastic water retention model, such as Wheeler et al. (2003), would predict sharp discontinuities of gradient as the scanning curves re-join main wetting or drying curves, whereas the transition is actually a gradual process (e.g. Liu & Muraleetharan, 2006). A bounding surface plasticity model can naturally incorporate this feature of behaviour.

4.1.2.b Non-linear water retention behaviour

The water retention curves are often observed to be highly non-linear for the full range of degree of saturation or water content. A linear representation of degree of saturation/water content against suction by a classical elasto-plastic model would therefore be rather unrealistic. However, at the expense of some additional complexity, non-linear elasto-plastic models can capture this feature of behaviour. A bounding surface plasticity model on the other hand would generally capture the non-linearity with relatively manageable complexity.

4.1.2.c Dependency on recent stress history or stress path direction

The gradients of scanning curves are actually dependent on suction reversals and recent stress history. It is often observed that upon a suction reversal the scanning curves exhibit a stiffer response (e.g. Liu & Muraleetharan 2006). A classical elasto-

plastic model can not take into account the recent stress history. A kinematic hardening model based on elasto-plasticity or bounding surface plasticity is required to capture this feature of behaviour.

4.1.2.d Behaviour during cycles of wetting and drying

During cyclic wetting and drying (over a fixed suction range) an elasto-plastic model would predict either elastic behaviour or a closed elasto-plastic loop (e.g. Wheeler et al., 2003), whereas in reality, scanning curve development actually shows progressive changes of S_r over many cycles. A bounding surface plasticity model can naturally predict this type of behaviour.

4.2 BOUNDING SURFACE PLASTICITY

As mentioned in Section 4.1, classical elasto-plasticity has proved to be simple and reasonably accurate for modelling the mechanical behaviour of soils. However, in reality, there is no sharp boundary (as assumed in classical elasto-plasticity) to separate elastic behaviour and elasto-plastic behaviour, rather plastic increments of strain variables almost always occur (even though plastic strain components may be very small in some cases) whenever there are changes in stress state variables. Several approaches, including generalized plasticity (Zienkiewicz and Mróz, 1984 and Pastor et al., 1990), multiple-yield surface models (e.g. Mroz et al., 1978 and Puzrin & Burland, 1998) and bounding surface plasticity (e.g. Dafalias & Herrmann, 1982 and Russell and Khalili, 2004) have been proposed to tackle this issue in modelling mechanical behaviour of soils. In particular, these different approaches, such as bounding surface plasticity, are much better at representing behaviour during cyclic loading than a classical elasto-plastic model.

4.2.1 Introduction

The theory of bounding surface plasticity is based on the assumption that a smooth transition occurs between elastic and elasto-plastic behaviour, which can be modelled by a gradual change in plastic modulus when the stress path approaches a bounding surface. A bounding surface plasticity model was first introduced by Dafalias (1975) for mechanical behaviour of metals. It was then extended to the modelling of mechanical behaviour of saturated soils by Dafalias & Hermann (1982). In bounding

surface plasticity models, the conventional yield surface is replaced by a bounding surface. If the stress point is moving towards the bounding surface, plastic strains occur. The plastic strains can be calculated by suitable hardening and flow rules by considering the relationship between the current stress point and a corresponding image stress point on the bounding surface.

As an illustration, Figure 4-1 and Figure 4-2 show two possible bounding surface plasticity versions of the Modified Cam Clay model for saturated soils (difference between them will be discussed in the next paragraph). The current stress point C is indicated in the $q : p'$ plane. The current stress point always lies inside a curve named the “bounding curve” (elliptical curve of continuous line in Figure 4-1 and Figure 4-2), which replaces the yield curve of conventional elasto-plastic models. A “loading curve” (elliptical curve of discontinuous line) can be constructed through the current stress point C , having the same shape as the bounding curve. The loading curve separates stress path directions moving towards the bounding curve (i.e. loading paths involving occurrence of plastic strains) from stress path directions moving away from bounding curve (elastic unloading). An “image stress point” \bar{C} on the bounding curve is defined such that the direction of the outward normal to bounding curve at point \bar{C} is the same as the direction of the outward normal to the loading curve at point C (i.e. the image stress point is a conjugate point on the bounding curve to the current stress point on the loading curve).

In Figure 4-1, the “projection point” is defined as a fixed point (in this case, the origin in $q : p'$ plot) and indicated by letter O . Alternatively, the version of bounding surface plasticity model shown in Figure 4-2 has the projection point defined as a variable point based on last stress reversal. During the initial loading path $O - A$, the projection point is at the origin in the $q : p'$ plot. However, the unloading stage $A - B$ alters the position of the projection point. During a loading stage (e.g. stage $B - C$) from stress point B , the projection point would move along a curve (with same shape as the bounding curve), called the “projection curve” in such a way that the direction of outward normal to the loading curve would be equal to that to the projection curve at point O_c (current projection point). These two different approaches to defining the

projection point have their own advantages and drawbacks. These will be explained in detail in the next section.

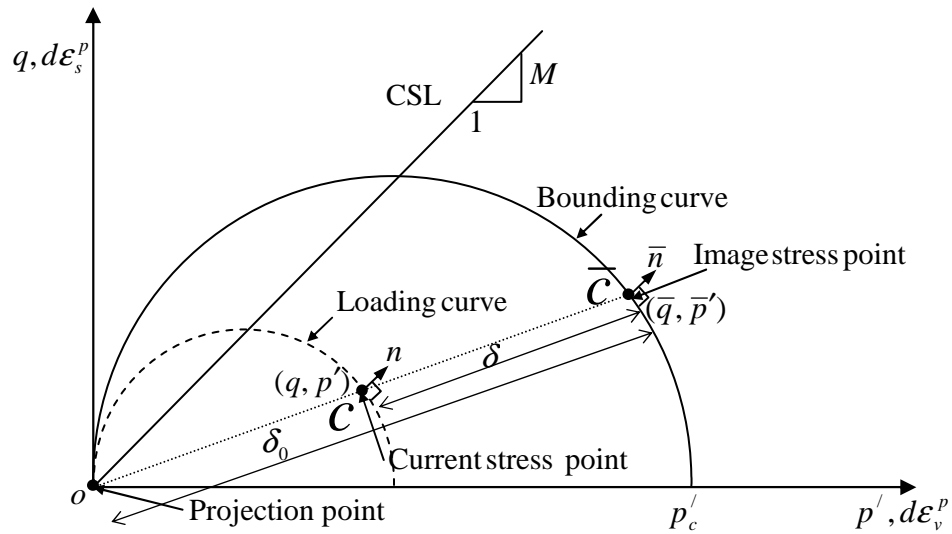


Figure 4-1 A typical bounding surface plasticity version of MCC with projection point fixed at origin

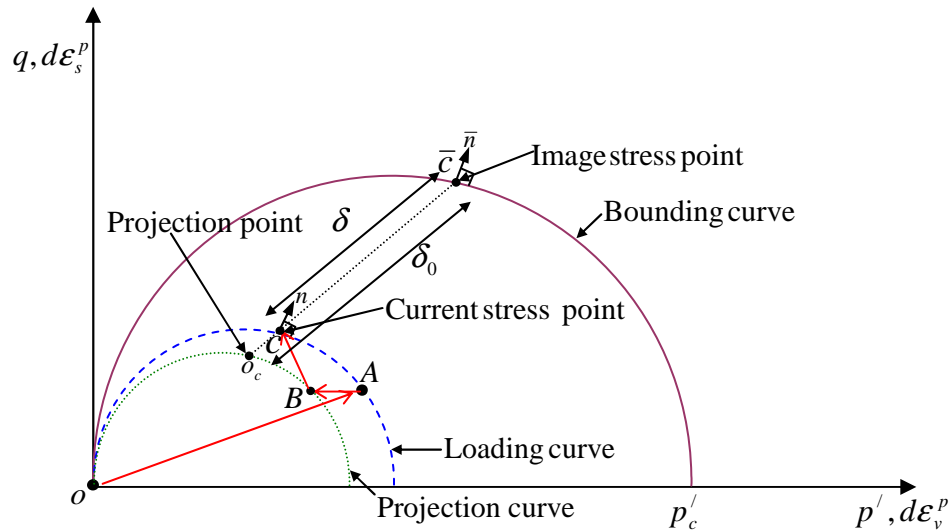


Figure 4-2 A typical bounding surface plasticity version of MCC with projection point based on last stress reversal point

A hardening rule, to calculate the plastic modulus at the current stress point, can be obtained in terms of δ (the distance between the current stress point C and the image stress point \bar{C}), δ_0 (the distance between the projection point O and the image stress point \bar{C}), the plastic modulus on the bounding curve and material parameters, in such a way that plastic modulus decreases smoothly from infinity at the projection point to a

limiting value on the bounding curve at the image stress point. Any occurrence of plastic strain, caused by movement of the current stress point towards the bounding curve, would produce a corresponding movement in the bounding curve. The movement of the current stress point and the image stress point would be such that if yielding were to continue indefinitely both points would coincide. This mechanism ensures a gradual change of plastic modulus as the current stress point approaches the bounding curve.

Several researchers proposed bounding surface plasticity models for the mechanical behaviour of saturated soils (e.g. Dafalias & Hermann, 1982, Bardet 1986, Whittle, 1993, Borja and Amies, 1994, Russell and Khalili, 2004, Khalili et al., 2005). Most of these models were proposed specifically in order to model the behaviour during cyclic loading. Bounding surface plasticity modelling of mechanical behaviour has recently been extended to unsaturated soils by Datcheva et al. (2003), Russell and Khalili (2006) and Yang et al., (2008).

4.2.2 Drawbacks of basic bounding surface plasticity models

Even though bounding surface plasticity is able to incorporate several features of soil behaviour that can not be accommodated by classical elasto-plasticity, it does however have some drawbacks. One of the disadvantages of basic bounding surface plasticity models is that the predictions during unloading-reloading or abrupt change in stress path direction have been found to be rather unrealistic, particularly for models which use a fixed projection point regardless of stress reversal.

For example, consider the behaviour of soil in the $\sigma : \varepsilon$ plane for cycles of unloading-reloading, with the real behaviour of soil shown in Figure 4-3a and prediction by a basic bounding surface plasticity model with a fixed projection point shown in Figure 4-3b. During the stress path $A - B$ the real behaviour of soil shows plastic components of strain. During the subsequent unloading and re-loading cycles $B - C - D - E - F - G - H$ two features of behaviour can be identified in real soil behaviour: (a) elasto-plastic response during unloading stages (though it can be very small); (b) a stiff response immediately following any stress reversals. These two features leads to a hysteresis behaviour shown in Figure 4-3a (a partially closed hysteretic loop). In contrast, a basic bounding surface plasticity model with a fixed

projection point would unrealistically predict an open hysteretic loop as shown in Figure 4-3b. The second of these two features of real soil behaviour can be incorporated into a bounding surface plasticity model either by defining the projection point based on the last stress reversal (see Figure 4-2) or by introducing an elastic bubble within which the behaviour is fully elastic (e.g. Al-Tabbaa & Muir Wood, 1989). On the other hand, the first feature (plastic straining during unloading) cannot be incorporated into a basic bounding surface plasticity model by the choice of projection point; rather the model should be modified to incorporate plastic strains during unloading.

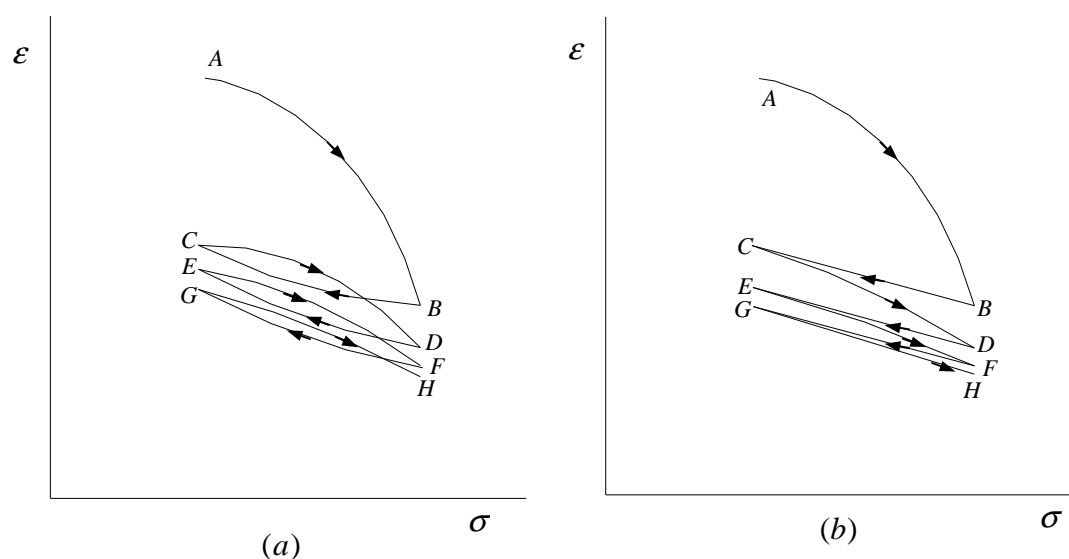


Figure 4-3 Unloading-reloading response (a) real soil behaviour, (b) basic bounding surface model prediction

Forms of models have been proposed by several researchers in order to incorporate the behaviour shown in Figure 4-3a. This includes the approach adopted by Whittle (1993), who combined a perfect hysteretic loop (Hueckel & Nova, 1979) within bounding surface plasticity (see in Figure 4-4). An alternative approach involves the introduction of several kinematic surfaces inside the bounding surface by researchers such as Mroz et al. (1979), Hashiguchi (1985) Al-Tabbaa & Muir Wood (1989) and Stallebrass & Taylor (1997).

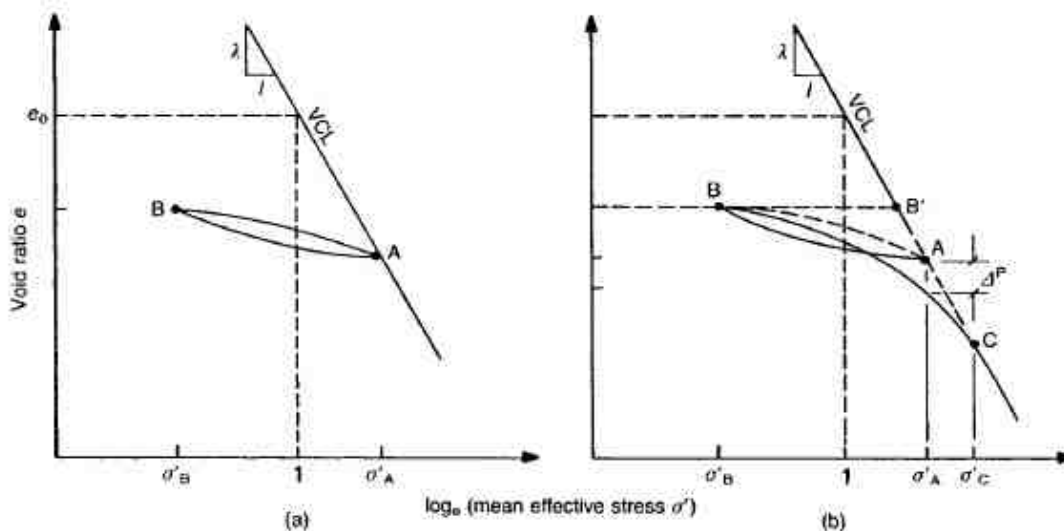


Figure 4-4 Modelling the behaviour of saturated soil for unloading-reloading isotropic stress path in MIT-E3 model: (a) perfect hysteresis; (b) hysteresis and bounding surface plasticity (Whittle, 1993)

The bounding surface plasticity models which characterize last stress reversal as the projection point can also encounter specific problems during small unloading-reloading fluctuations. For example, consider a monotonic loading stress path, which produces plastic straining. If an extremely small stress reversal occurs before continuing the same (previous) stress path, in reality, this small stress reversal will not produce any significant influence on the subsequent behaviour of the soil during re-loading. However, a basic bounding surface plasticity model having a projection point based on last stress reversal can give a different behaviour as the point of projection will be translated to a new position at the end of the last stress reversal. These tiny stress reversals would lead to unrealistic predictions in a finite element program, as there will always be small fluctuations in the stresses in a finite element program because of numerical errors. This issue can be solved again by incorporating internal yield surface(s) (or “bubbles”).

Elastic bubbles within the bounding surface were proposed by several researchers, such as Mroz et al. (1979), Hashiguchi (1985) and Al-Tabbaa & Muir Wood (1989). In this type of framework, the behaviour of soil is assumed to be elastic within the bubble and plastic strain starts to occur as soon as the stress point engages on the boundary of the elastic bubble, which is translated with movement of the stress point towards the bounding surface.

A single bubble kinematic yield surface discussed above is sufficient to describe the “immediate stress history” at small strain level. However, for complex stress paths such as cycles of loading and unloading, an additional kinematic surface is required between the elastic bubble and the bounding surface, to represent the hysteresis produced during past history (e.g. Atkinson & Stallebrass, 1991).

The main disadvantage of the kinematic hardening models is that mathematical formulation is relatively complex, requiring large numbers of hardening parameters, leading to relatively time consuming computation.

In the following sections, models based on basic bounding surface plasticity will be proposed first for water retention behaviour (see Section 4.3) then for fully coupled mechanical-water retention behaviour as an extension of the Wheeler et al. (2003) model (Section 4.4). No attempt will be made to incorporate internal kinematic surfaces within the models for the sake of simplicity.

4.3 DEVELOPMENT OF BOUNDING SURFACE WATER RETENTION MODELS

4.3.1 Previous research

Several authors have modelled water retention behaviour using bounding surface plasticity in the recent past. Li (2005) proposed a water retention model based on bounding surface plasticity in order to capture the hysteretic water retention behaviour of unsaturated soils in the $S_r : s$ plane. Figure 4-5 illustrates the formulation of the model. The model includes two bounding retention curves: a bounding drying curve and a bounding wetting curve. During increase of suction, on a drying path, at point P , the plastic changes of S_r are related to the plastic changes that would take place at an image point I_p on the bounding drying retention curve. This relationship involves the distance between I_p and P and the distance between I_p and the projection point O_p which corresponds to the last suction reversal. Conversely, during decrease of suction on a wetting path at point Q , the image point is on the bounding wetting retention curve at I_q and the projection point is at the last suction reversal O_q . Any suitable forms can be incorporated for the shapes of the bounding retention curves (e.g.

the equation proposed by Fredlund and Xing (1994). Li (2005) also suggested various refinements that could be incorporated within his bounding surface plasticity model (e.g. a threshold distance within which wetting/drying processes are completely reversible).

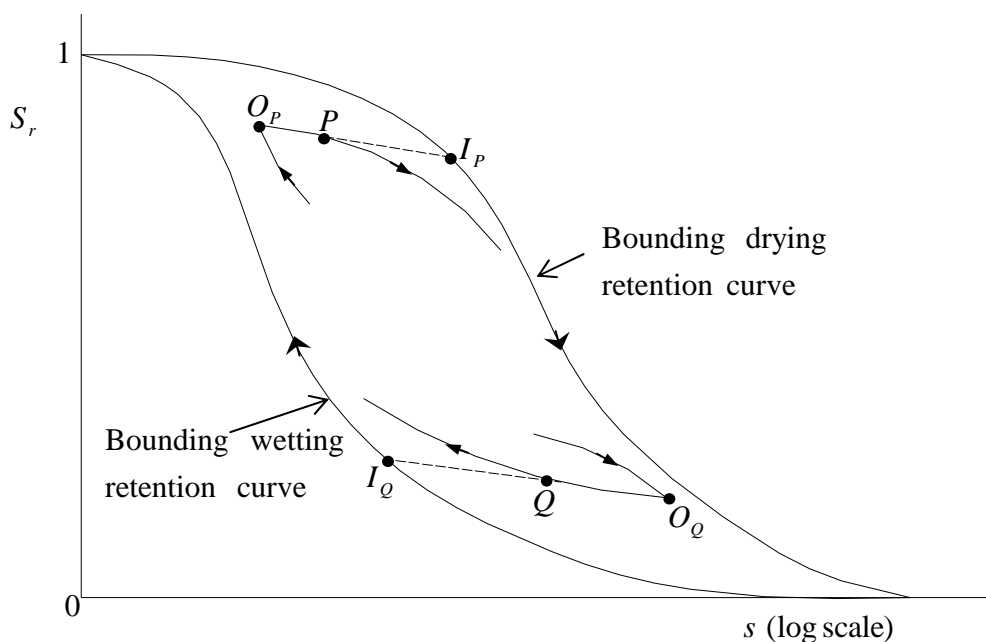


Figure 4-5 Bounding surface water retention model of Li (2005)

Liu and Muraleetharan (2006) proposed an alternative bounding surface plasticity model for water retention behaviour. The model is similar to that proposed by Li (2005) by taking the projection point as the last stress reversal and having a similar hardening rule. However, the model by Liu and Muraleetharan (2006) incorporated elastic behaviour while elastic behaviour was ignored in the Li (2005) model. The model was calibrated and validated against test results from Ottawa sand for several wetting and drying processes, including main wetting and drying curves.

4.3.2 Development of a new bounding surface plasticity model for rigid soils

A new water retention model based on bounding surface plasticity is presented here, initially for rigid soils and then extended to deformable soils. The model is presented here in terms of the modified suction variable s^* (defined in Equation 3-2), rather than suction s . This is so that the model can subsequently be developed to a fully coupled mechanical-water retention model i.e. a bounding surface plasticity version of the Wheeler et al. (2003) model (see Section 4.4). However, if the bounding surface

plasticity water retention models described in Sections 4.3.2 and 4.3.3 are to be used in combination with a conventional mechanical model for unsaturated soils employing net stresses and suction (such as the BBM), then s^* can simply be replaced by s .

Figure 4-6 illustrates the formulation of the new bounding surface plasticity model for water retention behaviour. Suction Increase (SI) and Suction Decrease (SD) yield curves proposed by Wheeler et al. (2003) in the $s^* : p^*$ plane are now replaced by corresponding bounding curves. A straight line traced through the current stress point is termed a wetting/drying line, and separates stress path directions considered as wetting (approaching the SD bounding curve) from stress path directions considered as drying (approaching the SI bounding curve). Plastic changes of degree of saturation occur as soon as current stress point moves towards either of the bounding curves, and if a decrease or increase in suction continues indefinitely the wetting/drying line will asymptotically approach the SD or SI bounding curve, representing a scanning retention curve joining a bounding wetting or drying retention curve.

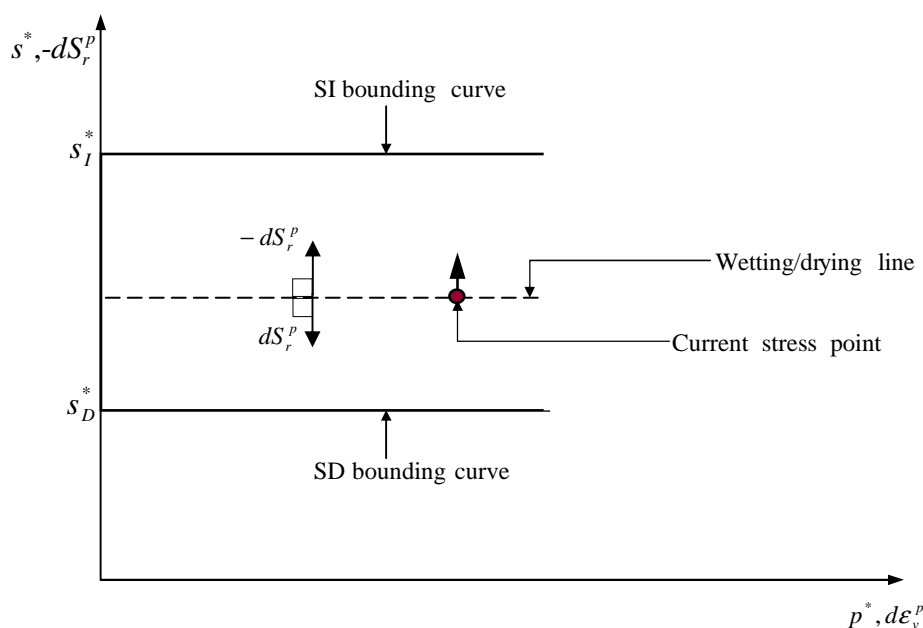


Figure 4-6 SI and SD bounding curves for water retention behaviour

4.3.2.a A simple water retention model (analogous to Wheeler et al., 2003)

Wheeler et al. (2003) proposed a simple water retention model based on elasto-plasticity (see Section 3.6.2) in which a linear variation of S_r was assumed with the

logarithm of modified suction s^* . An analogous water retention model is presented here but with bounding surface plasticity. The equation for elastic changes of degree of saturation is unchanged and given by:

$$-dS_r^e = \kappa_s \frac{ds^*}{s^*} \quad (4-1)$$

where κ_s is the gradient of the elastic part of a water retention curve in the $S_r : \ln s^*$ plot. The plastic changes of degree of saturation on the bounding retention curve can be given by:

$$-dS_r^p = (\lambda_s - \kappa_s) \frac{ds^*}{s^*} \quad (4-2)$$

The changes in degree of saturation, when on one of the two bounding retention curves, can then be given by adding elastic and plastic component of changes of degree of saturation and given by:

$$-dS_r = \lambda_s \frac{ds^*}{s^*} \quad (4-3)$$

where λ_s is the gradient of the wetting/drying bounding retention curves in the $S_r : \ln s^*$ plot. The plastic changes of degree of saturation on a scanning retention curve can be obtained by scaling down the right hand side of Equation 4-2 with a scaling function R_s , and given by:

$$-dS_r^p = R_s (\lambda_s - \kappa_s) \frac{ds^*}{s^*} \quad (4-4)$$

The expressions for the scaling function R_s are given by:

$$R_s = \left(\frac{s^*}{s_I^*} \right)^g \quad \text{for } ds^* > 0 \quad (4-5)$$

$$R_s = \left(\frac{s_D^*}{s^*} \right)^g \quad \text{for } ds^* < 0 \quad (4-6)$$

The exponent g is a material parameter (an additional soil constant) which takes a positive value greater than 1. Equation 4-5 shows that the scaling function R_s takes a positive value less than 1 for drying stress paths moving towards the SI bounding curve ($ds^* > 0$), with R_s approaching 1 as s^*/s_I^* approaches 1 (i.e. plastic decreases of degree of saturation build up as the current stress point approaches the SI bounding curve). Equation 4-6 shows that R_s also takes a positive value less than 1 for wetting stress paths moving towards the SD bounding curve ($ds^* < 0$), with R_s approaching 1 as s_D^*/s^* approaches 1 (i.e. plastic increases of degree of saturation build up as the current stress point approaches the SD bounding curve).

The movements of the SI and SD bounding curves are then given by rearranging Equation 4-2:

$$\frac{ds_I^*}{s_I^*} = \frac{ds_D^*}{s_D^*} = \frac{-dS_r^p}{(\lambda_s - \kappa_s)} \quad (4-7)$$

This equation is necessary in order to update the positions of the bounding curves, so that it is possible to calculate the new value of the scaling function R_s for the next increment of s^* .

Equations 4-5 and 4-6 imply that the projection point is located at $s^* = 0$ during drying paths and at $s^* = \infty$ during wetting paths. The location of project point during wetting path is not straightforward as in the case of drying path. However, from the fact that the value of R_s should be zero when current stress point is located at projection point, the Equation 4-6 implies that the projection point should be located at $s^* = \infty$. In both cases, this corresponds to a fixed projection point, rather than a projection point at the last stress reversal, as employed in the bounding surface plasticity retention model of Li (2005) (see Section 4.3.1). This type of formulation has certain advantages and disadvantages. For example, unlike a bounding surface

plasticity model with the projection point based on last stress reversal, the model described here, with a fixed projection point, does not predict unrealistic behaviour for small fluctuations (reversals) of stress during an essentially monotonic loading stage, as explained in Section 4.2.2. On the other hand, the behaviour predicted by this model with a fixed projection point is independent of recent stress history, which is unrealistic.

Figure 4-7 shows simulations from the model assuming linear bounding retention curves in a semi-logarithmic plot. For the simulations shown in Figure 4-7, elastic changes of S_r have been ignored ($\kappa_s = 0$) and a value of 1 has been assumed for the soil constant g .

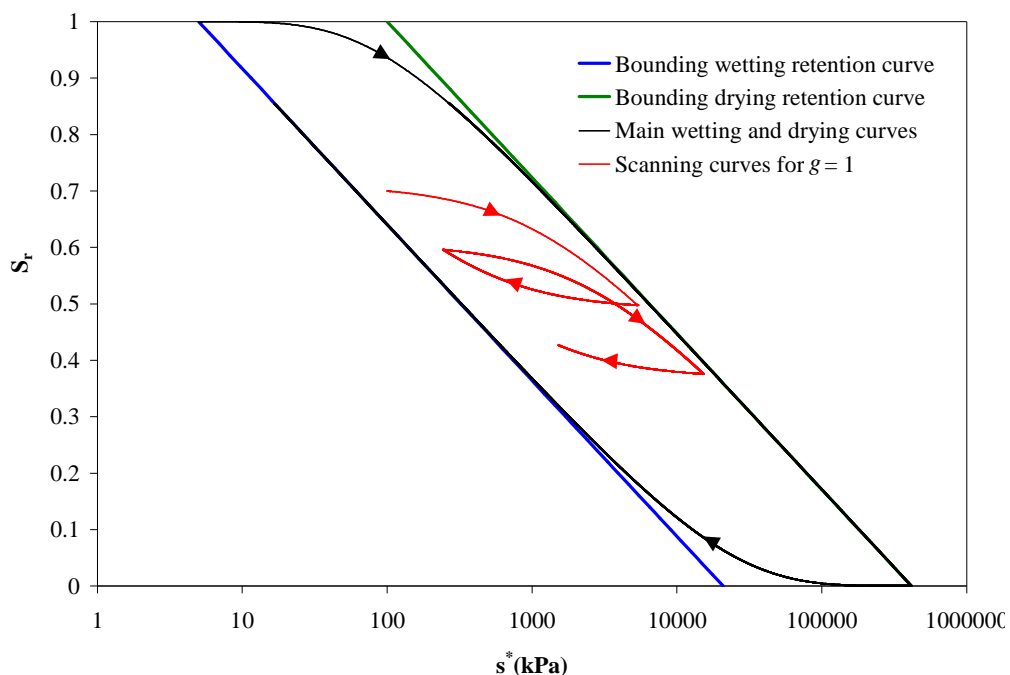


Figure 4-7 Model simulations with linear bounding retention curves on semi-logarithmic plot

One of the main advantages achieved by employing bounding surface plasticity is a more realistic prediction of scanning curves, which are rather unrealistically predicted as an elastic process in the Wheeler et al. (2003) model. In addition, the shape of the main drying curve predicted by the bounding surface plasticity model now shows a gradual change in gradient from a fully saturated state until the curve reaches the bounding drying retention curve i.e. a more realistic main drying curve is predicted, even though a very simple linear relationship (on a semi-logarithmic plot) is still

assumed for the bounding drying retention curve. However, once the main drying curve has reached the bounding drying retention curve, it shows a linear variation of degree of saturation S_r with logarithmic value of s^* . This limitation arises from the fact that a linear relation for bounding retention curves has been proposed in this particular formulation. However, it is possible to replace the linear bounding retention curves with more realistic forms of bounding retention curves, using equations such as those proposed by Brooks & Corey (1964) or Van Genuchten (1980). In the next two sections (Sections 4.3.2.b and 4.3.2.c), the idea of bounding surface plasticity formulation will be extended to more complex forms of bounding retention curves.

4.3.2.b Inclusion of Brooks & Corey (1964) equation

In this section a bounding surface plasticity model is presented, with the Brooks & Corey (1964) equation employed for the bounding retention curves. The Brooks & Corey (1964) equation can be written as:

$$S_r = 1 \quad \text{for } s < a$$

$$S_r = \frac{1}{\left(\frac{s}{a}\right)^b} \quad \text{for } s \geq a \quad (4-8)$$

For $s > a$, differentiating the above equation, the changes of degree of saturation on one of the two bounding retention curves can be given by:

$$\frac{-dS_r}{S_r} = \lambda_s \frac{ds^*}{s^*} \quad (4-9)$$

where $\lambda_s (= b)$ gives the gradient of the water retention curve in a $\ln S_r : \ln s^*$ plot (it also gives the initial gradient (at $S_r = 1$) in the conventional $S_r : \ln s^*$ plot. This equation can be compared with Equation 4-3. By analogy, the changes in degree of saturation on the bounding retention curves can be divided into elastic and plastic parts as given below:

$$\frac{-dS_r^e}{S_r} = \kappa_s \frac{ds^*}{s^*} \quad (4-10)$$

$$\frac{-dS_r^p}{S_r} = (\lambda_s - \kappa_s) \frac{ds^*}{s^*} \quad (4-11)$$

On scanning curves, the elastic part is given by Equation 4-10 and the plastic component is given by:

$$\frac{-dS_r^p}{S_r} = R_s (\lambda_s - \kappa_s) \frac{ds^*}{s^*} \quad (4-12)$$

By re-arranging Equation 4-11 the movement of the SI and SD bounding curves will be given by:

$$\frac{ds_I^*}{s_I^*} = \frac{ds_D^*}{s_D^*} = \frac{-dS_r^p}{(\lambda_s - \kappa_s) S_r} \quad (4-13)$$

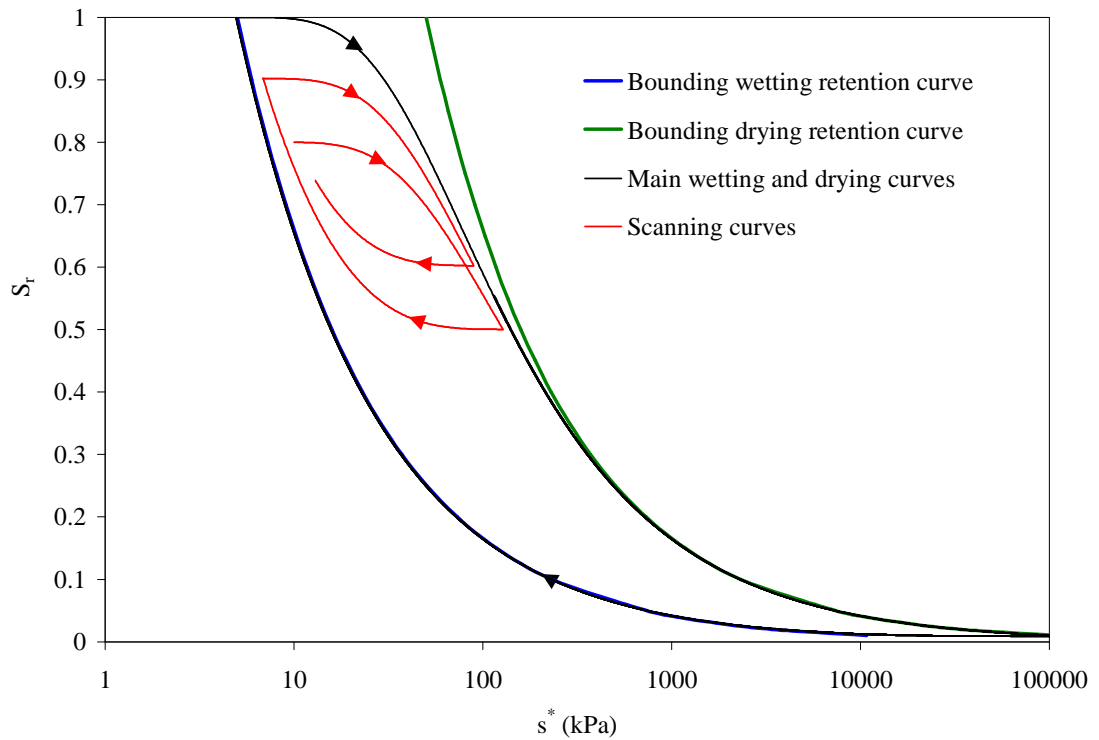


Figure 4-8 Model simulations with Brooks & Corey (1964) bounding retention curves

Figure 4-8 shows simulations from the model incorporating the Brooks & Corey (1964) equation for the bounding retention curves. For the simulations shown in Figure 4-8, elastic changes of S_r have been ignored ($\kappa_s = 0$). When compared to linear

bounding retention curves (in the semi-logarithmic plot), as described in the previous section, a better representation of water retention curves at low degree of saturation is predicted (i.e. the gradient of water retention curves gradually reduces to zero at low degree of saturation). However, during a wetting path, the model predicts a monotonic increase in the gradient of the curve which does not agree with most experimental observations, where the gradient decreases with reducing suction at high degree of saturation (in a semi-logarithmic plot). This particular issue can be resolved by incorporating a more realistic equation for the bounding retention curves, such as Van Genuchten (1980).

4.3.2.c Inclusion of Van Genuchten (1980) Equation

The Van Genuchten (1980) equation for bounding retention curves can be written as:

$$S_r = \frac{1}{\left(1 + \left(\frac{s}{a}\right)^n\right)^m} \quad (4-14)$$

where the parameters a , n and m are related to the air entry value, the gradient of the water retention curve and the asymmetric shape of the curve respectively. By differentiating the above equation the changes of S_r along a bounding retention curve can be given by:

$$\frac{-dS_r}{mS_r \left(1 - S_r^{1/m}\right)} = \lambda_s \frac{ds^*}{s^*} \quad (4-15)$$

where $\lambda_s = n$. This equation can be compared with Equation 4-3. By analogy, the changes in degree of saturation along a bounding retention curve can be divided into elastic and plastic parts as given below:

$$\frac{-dS_r^e}{mS_r \left(1 - S_r^{1/m}\right)} = \kappa_s \frac{ds^*}{s^*} \quad (4-16)$$

$$\frac{-dS_r^p}{mS_r \left(1 - S_r^{1/m}\right)} = (\lambda_s - \kappa_s) \frac{ds^*}{s^*} \quad (4-17)$$

On scanning curves, the elastic part is given by Equation 4-16 and the plastic component is given by:

$$\frac{-dS_r^p}{mS_r(1-S_r^{1/m})} = R_s(\lambda_s - \kappa_s) \frac{ds^*}{s^*} \quad (4-18)$$

By re-arranging Equation 4-17 the movement of SI and SD bounding curve will be given by:

$$\frac{ds_I^*}{s_I^*} = \frac{ds_D^*}{s_D^*} = \frac{-dS_r^p}{m(\lambda_s - \kappa_s)S_r(1-S_r^{1/m})} \quad (4-19)$$

Figure 4-9 shows simulations from the model incorporating the Van Genuchten (1980) equation for bounding retention curves. For the simulations shown in Figure 4-9, elastic changes of S_r have been ignored ($\kappa_s = 0$) and $m = 1$. It can be seen that the main wetting/drying curves are virtually indistinguishable from the bounding wetting/drying retention curves. Main wetting/drying curves and scanning curves are predicted more realistically than in the previous cases which employed linear or Brooks & Corey (1964) equation for the bounding retention curves.

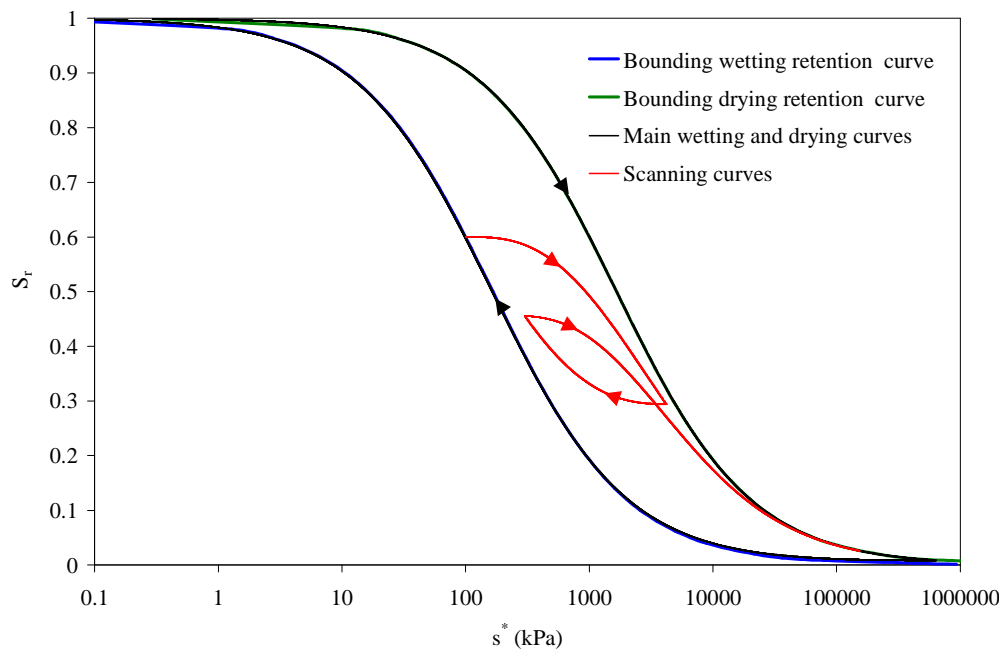


Figure 4-9 Model simulations with Van Genuchten (1980) bounding retention curves

4.3.3 Extension of the model to deformable soils

As discussed in Section 2.7.1, any change in void ratio would influence the water retention behaviour. For example, any compression of the soil would reduce the dimensions of the voids and of the connecting passageways between voids, subsequently increasing the suction values necessary for air to break through into the water-filled voids during drying or for water to flood back into the voids during wetting. This has the effect of shifting the main drying and main wetting retention curves to higher suctions. This phenomenon has been observed or modelled (in quantitative or qualitative fashion) by several researchers, including Gallipoli et al. (2003a), Wheeler et al. (2003), Tarantino & Tombolato (2005) and Sun & Xiang (2007).

Gallipoli et al. (2003a) proposed an equation to describe the water retention behaviour of deformable soil, by modifying the Van Genuchten (1980) equation (see Equation 4-14). Gallipoli et al. (2003a) proposed an equation for the parameter a as a function of specific volume v , to describe the horizontal shifting of the retention curves during volumetric straining as follows:

$$a = \phi^* (v - 1)^{\psi^*} \quad (4-20)$$

where ϕ^* and ψ^* are material parameters. Improved predictions (compared to a state surface approach for predicting degree of saturation (see Section 2.7.2.c)) were observed against experimental data from Sivakumar (1993). These experimental data involved isotropic loading, wetting and shearing, but all involved only wetting from the as-compacted suction i.e. no suction reversals and therefore no influence of hydraulic hysteresis.

The bounding surface plasticity water retention model described in the previous section can be modified to account for the influence of changing void ratio by employing modified Van Genuchten expressions for the bounding retention curves, with a given by Equation 4-20 from Gallipoli et al. (2003a). The elastic changes of S_r will be given by Equation 4-16 and plastic changes of S_r along bounding retention curves and the movement of SI or SD bounding curve is given by:

$$\frac{-dS_r^p}{mS_r(1-S_r^{1/m})} = (\lambda_s - \kappa_s) \left(\frac{ds^*}{s^*} + \psi^* \frac{de}{e} \right) \quad (4-21)$$

where e is void ratio. On a scanning curve, the plastic changes of S_r is given by:

$$\frac{-dS_r^p}{mS_r(1-S_r^{1/m})} = R_s (\lambda_s - \kappa_s) \left(\frac{ds^*}{s^*} + \psi^* \frac{de}{e} \right) \quad (4-22)$$

Different equations for bounding retention curves can be incorporated within this bounding surface plasticity model. For example, if the Brooks and Corey (1964) equation is employed for bounding retention curve then by analogy with Equation 4-21 the plastic changes of S_r on the bounding retention curves can be given by:

$$\frac{-dS_r^p}{S_r} = (\lambda_s - \kappa_s) \left(\frac{ds^*}{s^*} + \psi^* \frac{de}{e} \right) \quad (4-23)$$

The elastic changes of S_r will be given by the Equation 4-10. Similarly, by analogy with Equation 4-22 the plastic changes of S_r on a scanning curve can be given by:

$$\frac{-dS_r^p}{S_r} = R_s (\lambda_s - \kappa_s) \left(\frac{ds^*}{s^*} + \psi^* \frac{de}{e} \right) \quad (4-24)$$

Similarly if a linear bounding retention curve (in a semi-logarithmic plot) is employed, the elastic changes of S_r can be given by Equation 4-1 and the plastic changes of S_r along the bounding retention curves will be written as:

$$-dS_r^p = (\lambda_s - \kappa_s) \left(\frac{ds^*}{s^*} + \psi^* \frac{de}{e} \right) \quad (4-25)$$

Subsequently, the expression for plastic changes of S_r along a scanning curve can be obtained as below:

$$-dS_r^p = R_s (\lambda_s - \kappa_s) \left(\frac{ds^*}{s^*} + \psi^* \frac{de}{e} \right) \quad (4-26)$$

Figure 4-10 shows the prediction of scanning curves during both wetting and drying stages for the bounding surface plasticity model with linear bounding retention curves. During drying process PP' , a volume reduction occurs (shrinkage) and causes a shift of the bounding retention curves to higher suctions (i.e. the bounding drying retention curve moves from position X_0 to X_2), as a consequence of the influence of void ratio on the water retention behaviour. The positions of bounding wetting retention curve are not shown for clarity.

Similarly, during wetting stage QQ' a collapse compression is assumed to occur. Due to this reduction in void ratio, the bounding retention curves are shifted to higher suctions (i.e. the bounding wetting retention curves moves from position Y_0 to Y_2). The scanning curve approaches the instantaneous bounding wetting retention curve during the wetting process. Once again, the bounding drying retention curve is not shown to avoid confusion.

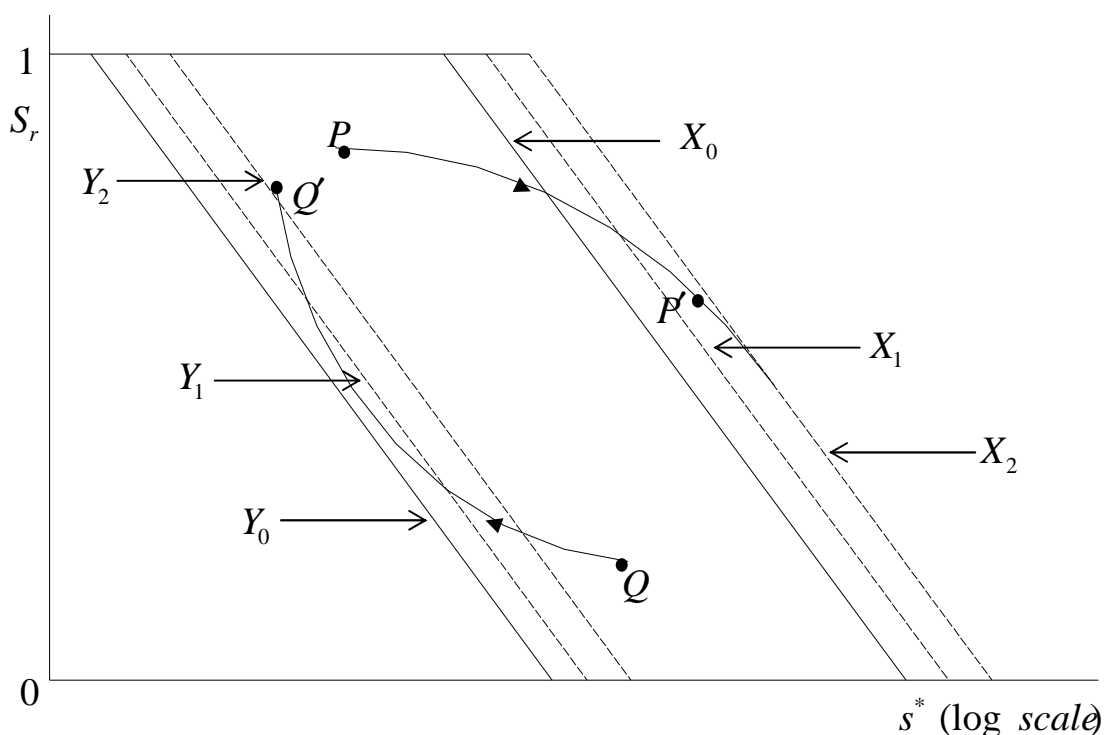


Figure 4-10 Prediction of scanning curves during wetting and drying stages with the occurrence of volumetric strain for bounding surface plasticity model (with linear bounding retention curves)

Using a constitutive model for mechanical behaviour such as the BBM, the proposed water retention model for deformable soil can be utilized to predict the water retention behaviour with the influence of mechanical behaviour. However, a fully coupled analysis which incorporates all the features of coupling can only be achieved with a mechanical model which incorporates the influence of degree of saturation on the mechanical behaviour (e.g. Wheeler et al. 2003, Gallipoli et al. 2003b or Tamagnini 2004). In that case, the proposed constitutive equations for water retention behaviour and any of the above mechanical constitutive model equations should be solved simultaneously.

4.4 A FULLY COUPLED MECHANICAL-WATER RETENTION MODEL

In this section, a possible form of inclusion of bounding surface plasticity into the Wheeler et al. (2003) fully coupled mechanical-water retention model is presented for isotropic stress states. Initially, uncoupled mechanical behaviour (behaviour related to the LC curve) is presented using bounding surface plasticity concepts. Subsequently, this is combined with the bounding surface plasticity model for uncoupled water retention behaviour presented in Section 4.3.2 together with appropriate coupling mechanisms between the bounding curves in order to formulate a fully coupled bounding surface plasticity mechanical-water retention model for unsaturated soils.

4.4.1 Uncoupled mechanical behaviour

In the proposed mechanical model the LC yield curve in the Wheeler et al. (2003) model is replaced by an LC bounding curve (see Figure 4-11). Plastic increments of volumetric strain occur if the stress point is moving towards the LC bounding curve (i.e. an increase in p^*). A decrease in p^* , so that the current stress point is moving away from the LC bounding curve, produces no plastic volumetric strain (elastic unloading).

The relationships between the movement of the LC bounding curve, the plastic volumetric strain and the movement of the current stress point are given by:

$$\frac{dp_0^*}{p_0^*} = \frac{v}{\lambda - \kappa} d\varepsilon_v^p = R_p \frac{dp^*}{p^*} \quad (4-27)$$

where λ is the conventional gradient of the saturated normal compression line in a semi-logarithmic plot of v against mean effective stress. The relationship between the movement of the bounding curve dp_0^* and the plastic volumetric strain given in Equation 4-27 is the same as in the conventional elasto-plastic version of the model (Wheeler et al. 2003). The relationship to the movement of the current stress point dp^* given in Equation 4-27 involves a scaling function R_p , which is defined by:

$$R_p = \left(\frac{p}{p_0^*} \right)^f \quad \text{for } dp^* > 0 \quad (4-28)$$

$$R_p = 0 \quad \text{for } dp^* < 0 \quad (4-29)$$

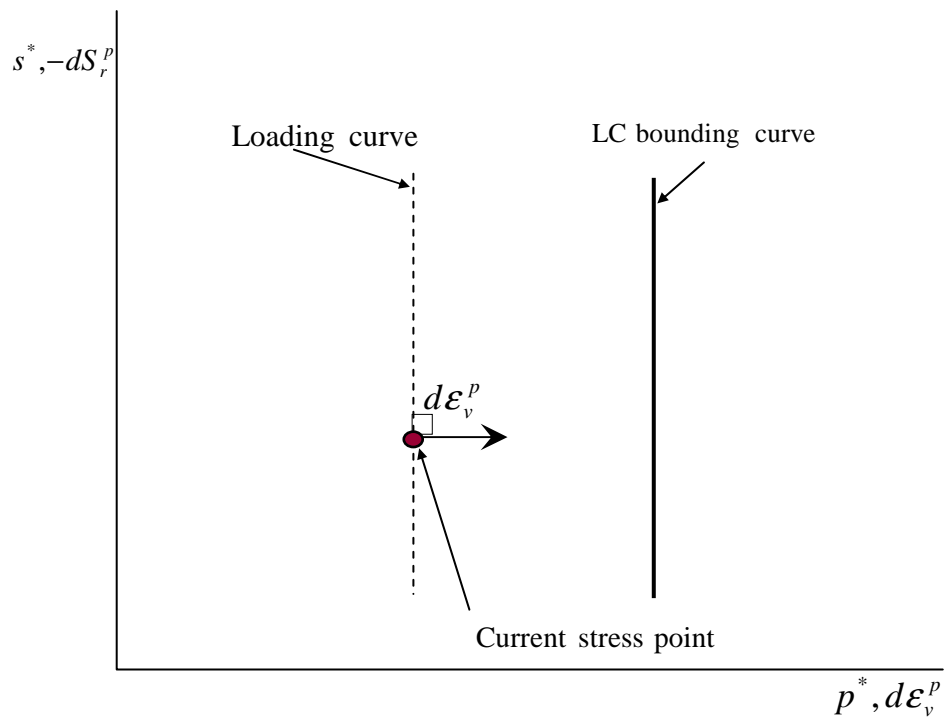


Figure 4-11 LC bounding curve for uncoupled mechanical behaviour

Similarly, elastic volumetric strains are given by:

$$d\epsilon_v^e = \frac{\kappa}{v} \frac{dp^*}{p^*} \quad (4-30)$$

The exponent f in Equation 4-28 is a material parameter (an additional soil constant) which takes a positive value greater than 1. Equation 4-28 shows that the scaling function R_p takes a positive value less than 1 for stress paths moving towards the LC bounding curve ($dp^* > 0$), with R_p approaching 1 as p^*/p_0^* approaches 1 (i.e. plastic volumetric straining builds up as the current stress point approaches the LC bounding curve). Equation 4-29 shows that no plastic volumetric strain, or corresponding movement of the bounding curve, occurs for stress paths moving away from the bounding curve (elastic unloading).

Figure 4-12 shows the variation of specific volume predicted by the model for monotonic isotropic loading and for multiple cycles of isotropic loading and unloading. Unlike conventional elasto-plasticity, plastic components of volumetric strain are predicted not only for the first loading path but also for all subsequent reloading paths. The predicted magnitude of additional plastic volumetric strain decreases with each successive loading cycle.

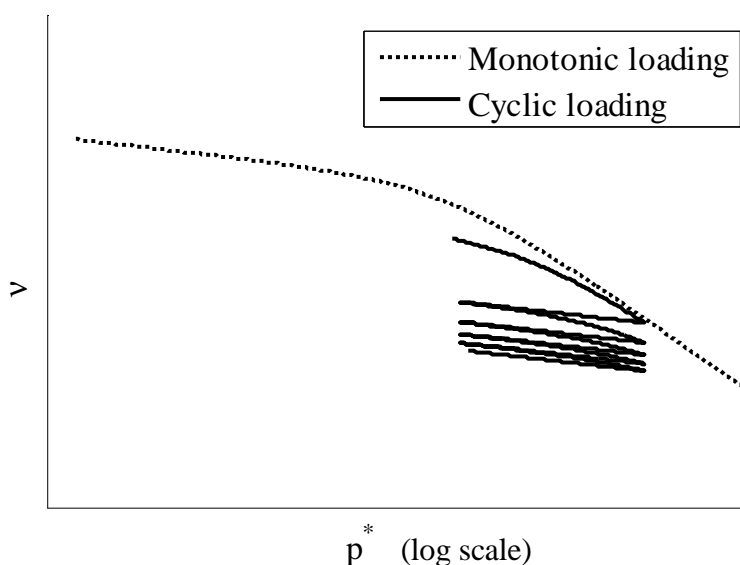


Figure 4-12 Model simulations for cycles of loading and unloading

4.4.2 Formulation of coupled bounding surface plasticity model

Figure 4-13 shows the LC, SI and SD bounding curves for isotropic stress states in the complete fully coupled bounding surface plasticity model for mechanical behaviour

and water retention behaviour. If the current stress point X_1 , at mean Bishop's stress p^* and modified suction s^* , moves to a new position X_2 , plastic volumetric strains will occur if the stress point is moving towards the LC bounding curve and plastic changes of degree of saturation will occur if the stress point is moving towards the SI or SD bounding curve. Plastic volumetric strain is directly associated with a corresponding component of movement of the LC bounding curve (given by Equation 4-27). There is, however, an additional coupled component of movement of the LC bounding curve as a consequence of any plastic change of degree of saturation (representing the influence of a change in the number of stabilizing meniscus water bridges on the mechanical behaviour, as in the conventional elasto-plastic model of Wheeler et al. 2003). Similarly, a plastic change of degree of saturation is directly associated with corresponding components of movement of the SI and SD bounding curves (given by Equation 4-7), but there are additional coupled components of movement of the SI and SD bounding curves as a consequence of any plastic volumetric strain (representing the influence of a change in the void dimensions arising from plastic volumetric strain on the water retention behaviour, as in the original Wheeler et al. (2003) model). When considering whether the stress point is moving towards the LC bounding curve (i.e. whether to treat as a loading path or an unloading path), it is important to allow for any coupled component of movement of the LC bounding curve towards or away from the current stress point. Similarly, when considering whether the stress point is moving towards the SI bounding curve or the SD bounding curve (i.e. whether to treat as a drying path or a wetting path), it is important to allow for any coupled component of movement of the SI and SD bounding curves towards or away from the stress point.

The total movement of the LC bounding curve is given by:

$$\frac{dp_0^*}{p_0^*} = \frac{v}{\lambda - \kappa} d\varepsilon_v^p + \frac{k_1}{\lambda_s - \kappa_s} (-dS_r^p) \quad (4-31)$$

where k_1 is a coupling parameter introduced by Wheeler et al. (2003). The first term on the right hand side of Equation 4-31 is the direct component of movement of the LC bounding curve, associated with the plastic volumetric strain caused by the stress

point moving towards the LC bounding curve. The second term on the right hand side of Equation 4-31 is the coupled component of movement of the LC bounding curve as a consequence of any plastic change of degree of saturation (caused by any movement of the stress point towards the SI or SD bounding curve).

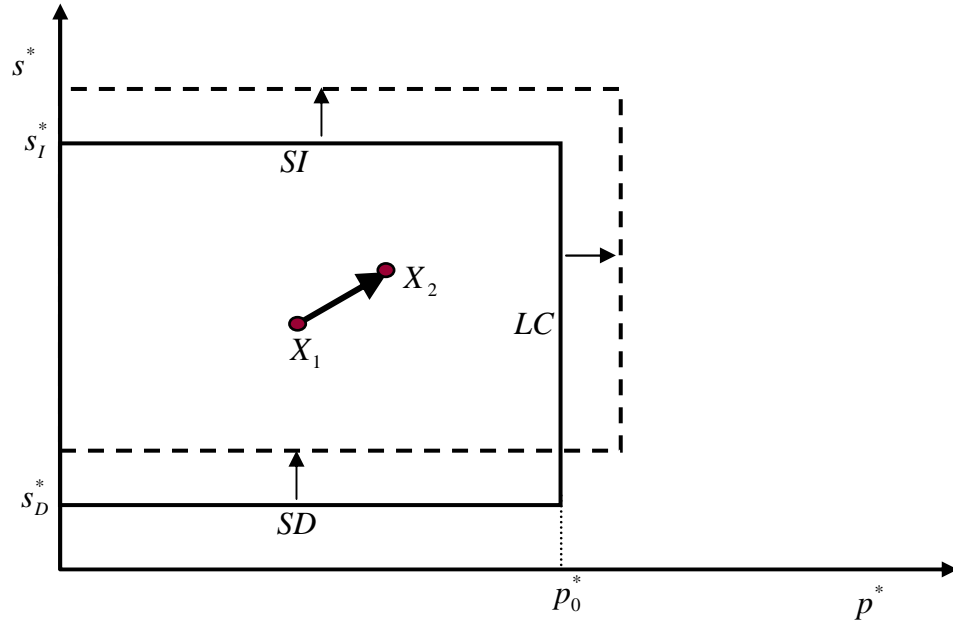


Figure 4-13 LC, SI and SD bounding curves

Similarly, the total movements of the SI and SD bounding curves are given by:

$$\frac{ds_I^*}{s_I^*} = \frac{ds_D^*}{s_D^*} = \frac{-dS_r^p}{\lambda_s - \kappa_s} + \frac{k_2 v}{\lambda - \kappa} d\varepsilon_v^p \quad (4-32)$$

where k_2 is a second coupling parameter introduced by Wheeler et al. (2003). The first term on the right hand side of Equation 4-32 is the direct component of movement of the SI and SD bounding curves, associated with the plastic change of degree of saturation caused by the stress point moving towards the SI bounding curve or the SD bounding curve. The second term on the right hand side of Equation 4-32 is the coupled component of movement of the SI and SD bounding curves as a consequence of any plastic volumetric strain (caused by any movement of the stress point towards the LC bounding curve). Equations 4-31 and 4-32 are identical to the expressions for the movements of the LC yield curve and SI and SD yield curves respectively in the

conventional elasto-plastic version of the model presented by Wheeler et al. (2003) (see Section 3.6.2).

In the bounding surface plasticity version of the model, plastic volumetric strain occurs if the current stress point is moving towards the LC bounding curve, but this consideration of movement of the stress point towards the LC bounding curve must also take account of any coupled movement of the bounding curve towards or away from the stress point. The magnitude of plastic volumetric strain increment is therefore given by:

$$\frac{v}{\lambda - \kappa} d\epsilon_v^p = R_p \left(\frac{dp^*}{p^*} - \frac{k_1}{\lambda_s - \kappa_s} (-dS_r^p) \right) \quad (4-33)$$

The first term inside the main bracket on the right hand side of Equation 4-33 represents the movement of the stress point and the second term represents the coupled component of movement of the LC bounding curve away from the stress point. The scaling function R_p takes the value given in Equation 4-28 if the stress point is getting closer to the LC bounding curve (in a plot with p^* on a logarithmic scale), i.e. if the content of the main bracket on the right hand side of Equation 4-33 is positive, and a value of zero (elastic unloading) if the stress point is getting further away from LC bounding curve.

A plastic decrease of degree of saturation occurs if the current stress point is moving towards the SI bounding curve, whereas a plastic increase of degree of saturation occurs if the stress point is moving towards the SD bounding curve, but again this consideration of movement of the stress point towards the SI or SD bounding curve must take account of any coupled movements of the curves towards or away from the stress point. The magnitude of plastic decrement of degree of saturation is therefore given by:

$$\frac{-dS_r^p}{\lambda_s - \kappa_s} = R_s \left(\frac{ds^*}{s^*} - \frac{k_2 v}{\lambda - \kappa} d\epsilon_v^p \right) \quad (4-34)$$

The first term inside the main bracket on the right hand side of Equation 4-34 represents the movement of the stress point and the second term represents the coupled component of movement of the SI and SD bounding curves. The scaling function R_s takes the value given by Equation 4-5 if the current stress point is getting closer to the SI bounding curve (in a plot with s^* on a logarithmic scale), i.e. if the content of the main bracket on the right hand side of Equation 4-34 is positive. R_s takes the value given in Equation 4-6 if the current stress point is getting closer to the SD bounding curve i.e. if the content of the main bracket on the right hand side of Equation 4-34 is negative. Equations 4-33 and 4-34 can be combined to give expressions for the plastic volumetric strain increment and plastic decrement of degree of saturation in terms of the stress increments dp^* and ds^* :

$$d\varepsilon_v^p = \frac{R_p(\lambda - \kappa)}{v(1 - k_1 k_2 R_p R_s)} \left(\frac{dp^*}{p^*} - k_1 R_s \frac{ds^*}{s^*} \right) \quad (4-35)$$

$$-dS_r^p = \frac{R_s(\lambda_s - \kappa_s)}{(1 - k_1 k_2 R_p R_s)} \left(\frac{ds^*}{s^*} - k_2 R_p \frac{dp^*}{p^*} \right) \quad (4-36)$$

Equations 4-35, 4-36, 4-31 and 4-32 define the plastic aspects of both mechanical behaviour and water retention behaviour. Equations 4-35 and 4-36 give the plastic increments of volumetric strain and degree of saturation caused by the stress increments dp^* and ds^* , and Equations 4-31 and 4-32 give the corresponding movements of the LC bounding curve and the SI and SD bounding curves respectively.

The stress point is moving closer to the LC bounding curve if the contents of the final bracket in Equation 4-35 are positive. Similarly, the stress point is moving closer to the SI bounding curve if the contents of the final bracket of Equation 4-36 are positive, but closer to the SD bounding curve if the contents of this bracket are negative. The expressions for the scaling functions R_p and R_s are therefore as follows:

$$R_p = \left(\frac{p^*}{p_0} \right)^f \quad \text{for} \quad \frac{dp^*}{p^*} > k_1 R_s \frac{ds^*}{s^*} \quad (4-37)$$

$$R_p = 0 \quad \text{for} \quad \frac{dp^*}{p^*} < k_1 R_s \frac{ds^*}{s^*} \quad (4-38)$$

$$R_s = \left(\frac{s^*}{s_I^*} \right)^g \quad \text{for} \quad \frac{ds^*}{s^*} > k_2 R_p \frac{dp^*}{p^*} \quad (4-39)$$

$$R_s = \left(\frac{s_D^*}{s^*} \right)^g \quad \text{for} \quad \frac{ds^*}{s^*} < k_2 R_p \frac{dp^*}{p^*} \quad (4-40)$$

The inequalities in Equations 4-37 and 4-38, which determine which expression should be used for R_p , involve the value of R_s . Conversely, the inequalities in Equations 4-39 and 4-40, which determine which expression should be used for R_s , involve the value of R_p . The process for calculating values for R_p and R_s for the current increment may therefore have to start by assuming that a particular inequality holds true, and if this subsequently leads to inconsistency the procedure must then be repeated with the alternative assumption for the initial inequality.

The bounding surface plasticity version of the fully coupled model requires 8 soil parameters to describe the mechanical and water retention behaviour for isotropic stress states: λ , κ , λ_s , κ_s , k_1 , k_2 , f and g . This is two more parameters (f and g) than the original elasto-plastic version of the model presented by Wheeler et al. (2003). With the introduction of bounding surface plasticity, however, it will often be possible to ignore any elastic changes of degree of saturation ($\kappa_s = 0$) and still achieve realistic modelling of scanning water retention curves. In this case the number of soil parameters is reduced to 7.

In selecting values for the coupling parameters k_1 and k_2 , the following inequality must be observed (as in the original model of Wheeler et al., 2003):

$$k_1 k_2 < 1 \quad (4-41)$$

4.4.3 Qualitative model simulations

Three different stress path simulations are presented here to investigate the capabilities and shortcomings of the model at a qualitative level. All the simulations presented here

are for isotropic stress states. The values of soil parameters used in the simulations were: $\lambda=0.13$, $\kappa=0.025$, $\lambda_s=0.1$, $\kappa_s=0$, $k_1=0.6$, $k_2=0.8$, $f=10$ and $g=2$. In all simulations, the initial state was given by: mean net stress $\bar{p}=10$ kPa, suction $s=300$ kPa, specific volume $v=2.15$ and degree of saturation $S_r=0.55$, leading to $p^*=175$ kPa and $s^*=160.5$ kPa. Initial positions of the bounding curves were given by $p_0^*=250$ kPa, $s_l^*=600$ kPa and $s_d^*=150$ kPa.

The stress paths followed in the different simulations were specified in terms of mean net stress (\bar{p}) and suction s . Increments of p^* and s^* were then calculated from the following relationships:

$$dp^* = d\bar{p} + S_r ds + s dS_r \quad (4-42)$$

$$ds^* = nds - \frac{s}{v} d\varepsilon_v \quad (4-43)$$

Because Equations 18 and 19 involve dS_r and $d\varepsilon_v$ respectively, they had to be solved simultaneously with the constitutive model equations before the stress path could be defined in terms of p^* and s^* (see Wheeler et al., 2003). A simulation code was developed at stress point level for the bounding surface plasticity version of the Wheeler et al. (2003) model using Matlab software. The simultaneous incremental equations which must be solved for increments of stress, strain and degree of saturation are presented in the Appendix, together with the algorithms employed in the Matlab coding in order to run simulations for required stress paths.

4.4.3.a Isotropic loading and unloading at constant suction

In this simulation, the soil was first isotropically loaded from mean net stress $\bar{p}=10$ kPa to $\bar{p}=300$ kPa at constant suction $s=300$ kPa ($A-B$ in Figure 4-14). Mean net stress was then reduced to 10 kPa ($B-C$), followed by re-loading to mean net stress of 800 kPa ($C-D$), with the suction maintained constant throughout at 300 kPa.

Figure 4-14 shows the predicted variation of v and S_r with mean net stress during isotropic loading, unloading and re-loading at constant suction. During isotropic

loading $A - B$, the variation of v shows an apparent “yield point” (see Figure 4-14a) as the stress path approaches the LC bounding curve and plastic volumetric straining increases significantly. This plastic volumetric strain causes a coupled upward component of movement of the SD and SI bounding curves. As a consequence, the SD bounding curve is getting closer to the stress point and this produces plastic increases of degree of saturation (Figure 4-14b).

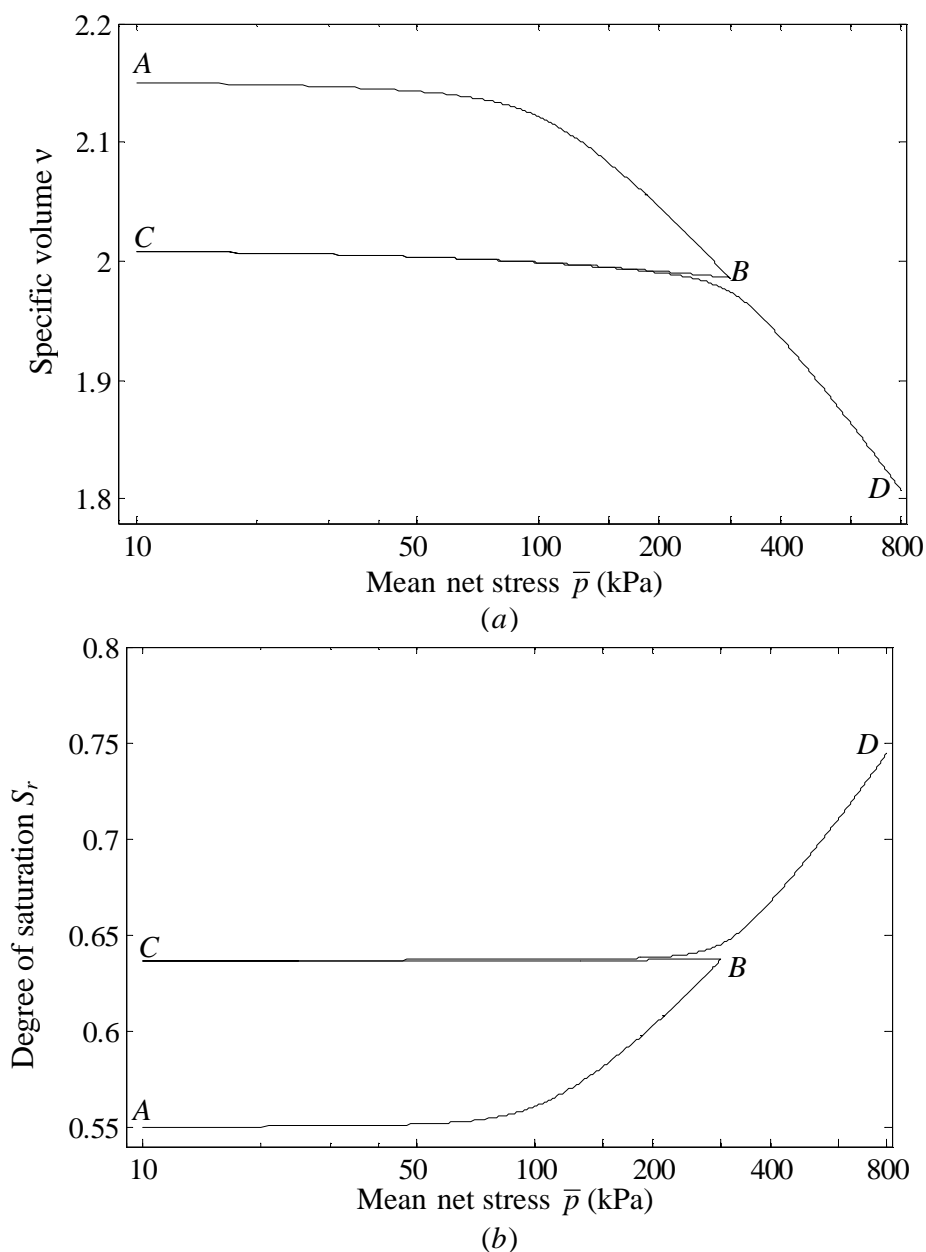


Figure 4-14 Model simulation of isotropic loading at constant suction: (a) specific volume; (b) degree of saturation

During isotropic unloading B – C the predicted variation of v is entirely elastic, because the stress point is moving away from the LC bounding curve. The corresponding variation of S_r shows extremely small plastic decrease of S_r (not visible in Figure 4-14b), because the modified suction s^* is increasing slightly (due to the elastic increase of porosity n) and hence the stress path is moving slightly towards the SI bounding curve. During re-loading C – D the predicted variations of v and S_r are qualitatively similar to the behaviour in the initial loading stage A – B.

4.4.3.b Isotropic loading after a wetting and drying cycle

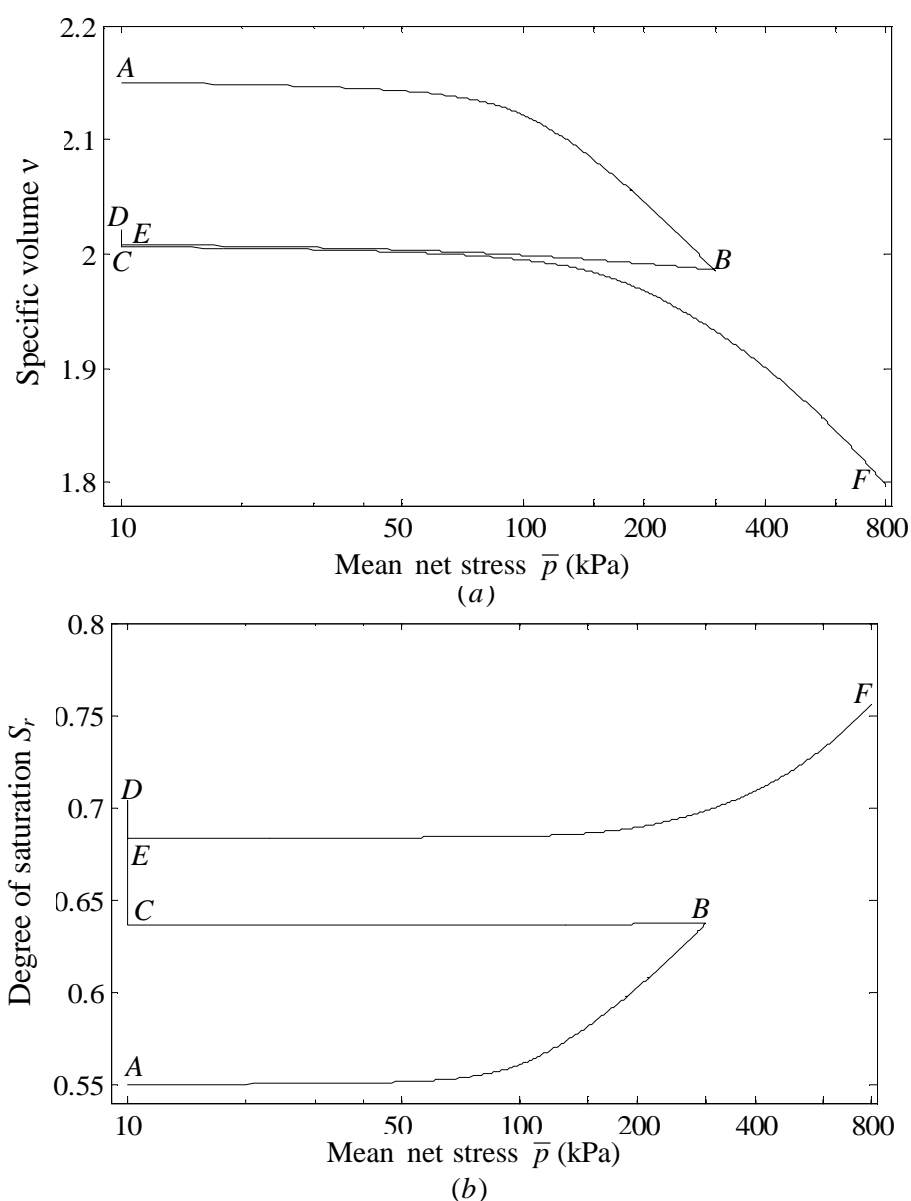


Figure 4-15 Model simulation of isotropic loading at constant suction after a wetting and drying cycle: (a) specific volume; (b) degree of saturation

This simulation, shown in Figure 4-15, was similar to the one discussed in the previous section, other than a wetting and drying cycle $C - D - E$ (to $s = 150$ kPa and then back to $s = 300$ kPa) was added between unloading and re-loading stages. During the wetting-drying cycle $C - D - E$ the predicted plastic changes of v were insignificant (see Figure 4-15a), because the stress path remained distant from the LC bounding curve throughout. In contrast, a substantial net plastic increase of degree of saturation occurred during $C - D - E$ (see Figure 4-15b), as the plastic increase of S_r during wetting $C - D$ was far larger than the plastic decrease of S_r during drying $D - E$. This net plastic increase of S_r produced a net downward movement of the SI and SD bounding curves and also a substantial coupled inward movement of the LC bounding curve. As a consequence, during the final isotropic loading stage $E - F$ the apparent “yield point”, when substantial plastic decreases of v and plastic increases of S_r commenced, occurred at a noticeably lower net stress than was the case without the wetting-drying cycle (compare Figure 4-15 with Figure 4-14). This predicted behaviour matches experimental observations by Sharma (1998) reported by Wheeler et al. (2003) (see Figure 3-3).

4.4.3.c Wetting and drying cycles

Figure 4-16 shows the predicted variations of v and S_r with suction for cycles of wetting and drying performed between $s = 300$ kPa and $s = 20$ kPa at a constant mean net stress $\bar{p} = 50$ kPa. $A - B$ represents initial isotropic loading from $\bar{p} = 10$ kPa to $\bar{p} = 50$ kPa at constant suction $s = 300$ kPa.

During the first wetting stage $B - C$, large plastic increases of S_r were predicted (see Figure 4-16b) as the stress path moved towards the SD bounding curve. This plastic increase of S_r caused a substantial coupled inward movement of the LC bounding curve. As a consequence, the stress point was getting closer to the LC bounding curve, even though the value of mean Bishop's stress p^* was reducing significantly during wetting. During the early part of wetting stage $B - C$ the stress point was still distant from the LC bounding curve and hence plastic changes of v were negligible and the predicted variation of v was dominated by elastic swelling caused by the decrease of p^* (see Figure 4-16a). However, as wetting progressed and the LC bounding curve approached the stress point, the resulting plastic decreases of v began to dominate, so

that wetting-induced swelling gradually changed to wetting-induced collapse compression (see Figure 4-16a). It is interesting to note that the sudden change from swelling to collapse compression predicted by the conventional elasto-plastic model of Wheeler et al. (2003) has been replaced by a more gradual transition in the new bounding surface version of the model.

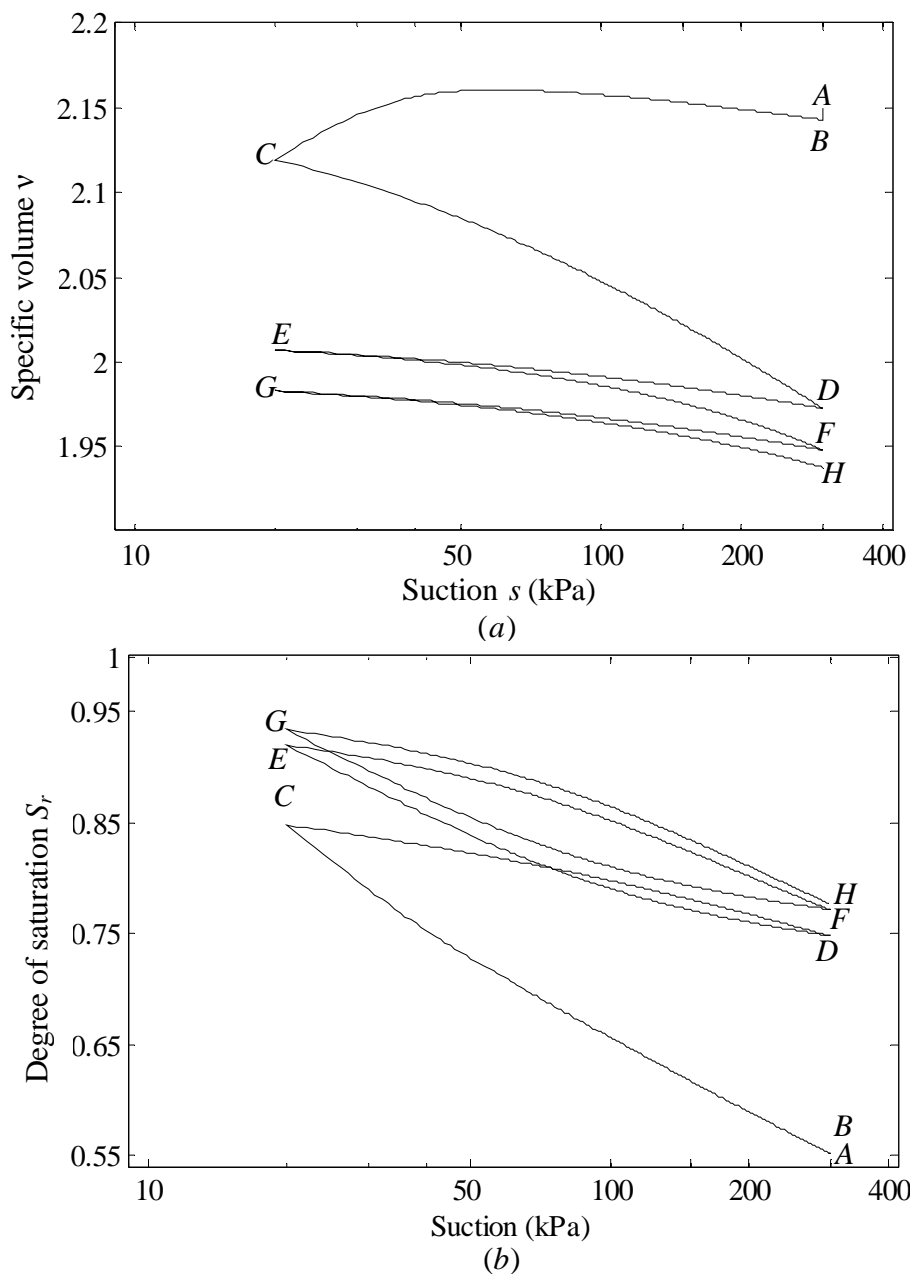


Figure 4-16 Model simulation for cycles of wetting and drying: (a) specific volume; (b) degree of saturation

During the first drying stage $C - D$, significant plastic compression was predicted from the start of the stage, because the stress point was close to the LC bounding curve and moving towards it as p^* increased. This feature of model predictions (significant plastic volumetric straining predicted from the onset of any drying stage following a wetting stage in which collapse compression occurred) is a rare qualitative aspect of the model which does not match well with experimental observations (the same applies to the conventional elasto-plastic model of Wheeler et al. (2003)). Experimental test results tend to show that plastic compression commences later in such stages (see Figure 3-4).

The predicted variation of v and S_r during subsequent wetting and drying cycles $D-E-F-G-H$ is highly realistic, with noticeable plastic compression predicted towards the end of each drying stage (Figure 4-16a) and realistic development of scanning curves in the water retention behaviour (Figure 4-16b).

4.5 SUMMARY

In this chapter, the bounding surface plasticity concept was introduced and its capabilities were examined against classical elasto-plasticity (Section 4.1 and 4.2). Later, this bounding surface plasticity concept was introduced into the water retention modelling framework proposed by Wheeler et al. (2003). It was demonstrated that more realistic prediction for water retention behaviour can be obtained even with simple bounding retention curves. By analogy, more complex forms of bounding retention curves were incorporated into the framework and then the influence of void ratio was included in the modelling framework, based on the work by Gallipoli et al. (2003a) (see Section 4.3).

A fully coupled mechanical-water retention model was then developed based on the proposals by Wheeler et al. (2003), but with bounding surface plasticity rather than classical elasto-plasticity (Section 4.4). Some model simulations were also presented to demonstrate the capability of the proposed bounding surface plasticity fully coupled mechanical-water retention model to capture some of the important features of unsaturated soil behaviour arising from the coupling of mechanical behaviour and water retention behaviour.

CHAPTER 5

EXPERIMENTAL APPARATUS AND CALIBRATION

An experimental programme was planned, in order to achieve the main objectives set out in Section 1.5, including experimental investigation of coupling between mechanical and water retention behaviour and examination of the Wheeler et al. (2003) framework and illustrative model assumptions against experimental test results. This experimental programme required suitable equipment. A previous research student, Mark Buisson, had developed two controlled-suction systems for testing unsaturated soils, one for isotropic stress path testing and the other for triaxial stress path testing, and these systems were employed in the current research project. In addition, a Bishop-Wesley type triaxial cell system for testing saturated soil samples was also used. This chapter first describes the three different isotropic or triaxial cells systems. The calibration of transducers, measuring devices and cells is then presented.

5.1 SYSTEM A – CONTROLLED-SUCTION ISOTROPIC CELL

The technique of measuring the volume change of unsaturated soil samples by monitoring the effect on the surrounding cell fluid was described in Section 2.9.1. With this technique, any volume change of the cell itself must be small and repeatable (so that it can be calibrated). Many researchers achieved this by employing a double-walled construction, as described in Section 2.9.1 (e.g. Wheeler, 1986 and Sharma, 1998). An alternative is to use a single wall of very high stiffness and made from a material with linear elastic behaviour and no creep or mechanical hysteresis (e.g. steel), as mentioned in Section 2.9.1.

Buisson (2002) developed a single-walled isotropic cell in order to test unsaturated samples of 50 mm diameter and a maximum height of 100 mm. In order to reduce the volume change of the cell with variation of cell pressure and to ensure that the wall deformed elastically in the working pressure range, a stainless steel wall of 30 mm thickness was employed.

5.1.1 Isotropic cell

In most triaxial or isotropic cells for testing unsaturated soil samples, pore water pressure is applied at the bottom of sample and pore air pressure at the top of the sample (e.g. Sivakumar, 1993). With this arrangement, the maximum length of pore water drainage is the full height of the sample. By having pore water drainage from both top and bottom of the sample, the maximum drainage length can be reduced to half the height of sample, leading to a substantial reduction of the time required for pore water pressure equalisation (e.g. Sharma, 1998). In contrast, pore air pressure can be applied from only one end of the sample, because excess pore air pressures generally dissipate much more quickly than excess pore water pressures. These two aspects have been taken into account in designing both isotropic and triaxial cells.

Figure 5-1 shows the layout of the isotropic cell. The cell base, cell wall, cell cover plate and pedestal were made out of stainless steel of significant thickness to reduce the deformation due to the variation of cell pressure. The 65 mm thick cell base accommodates all the drainage connections to the sample and the cell. The cell wall, of internal diameter 70 mm and thickness 30 mm, can be lowered onto the groove of the cell base that accommodates an O-ring to form a seal at the bottom. The cell cover of 65 mm thick also accommodates an O-ring within a groove and can be lowered on to the top surface of the cell wall. The cell cover plate has a sloping under-surface towards the centre in order to facilitate venting during filling of the cell with de-aired water. Six tie rods made out stainless steel are used to assemble the cell base, wall and cover plate in place and make a seal at the top and the bottom of the cell by pressing the top and bottom surfaces of the cell wall against the O-rings. Care should be taken to tighten each tie rod evenly to ensure proper sealing with the O-rings.

Six drainage connections can be seen passing through the cell base. Four of these are water drainage lines, two to the top of the sample and the other two to the bottom of the sample, with connection to the pore water in the sample through high air entry filters. The dual pore water drainage connections to top and bottom are to allow flushing of the entrapped air which can build up behind high air entry filters (see Section 5.1.6). The two pore water drainage lines for the top of the sample were connected through flexible tubing to the top cap as shown in Figure 5-1. The fifth drainage connection was the pore air pressure line, which was connected through a low

air entry sintered brass annulus on the pedestal (around the high air entry filter for the pore water connection). The final connection to the cell base was for applying the cell pressure.

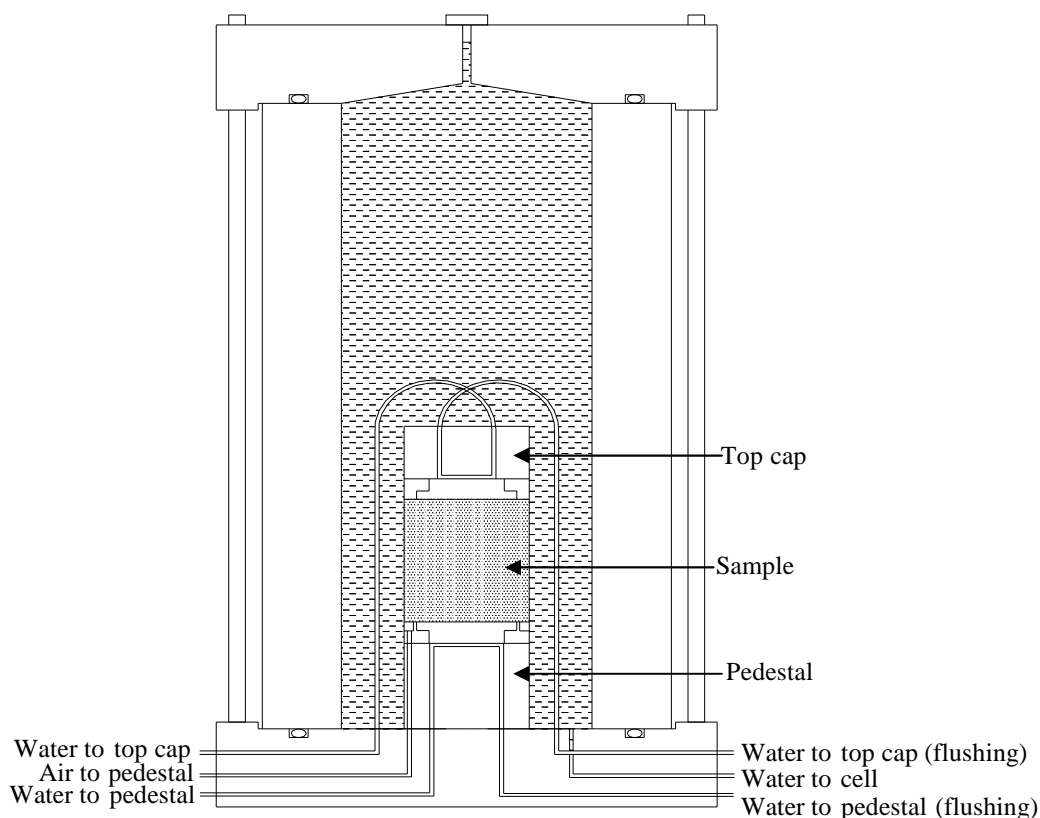


Figure 5-1 Layout of isotropic cell (after Buisson, 2002)

5.1.2 Pedestal arrangement

Figure 5-2 shows the layout of the pedestal, with the bottom filter arrangement bolted to it. A circular high air entry ceramic filter (34 mm diameter) was glued within a brass filter holder. The high air entry ceramic filter used in the experimental testings was manufactured by Soilmoisture Equipment Corporation and has an air entry value of 500 kPa. A circular sintered brass disc of 30 mm diameter was placed beneath the high air entry filter, so that the flow from the bottom of the high air entry filter took place over as large area as possible, thus minimising the head drop across the high air entry filter. A sintered brass annulus (50 mm external diameter and 40 mm internal diameter), for pore air pressure connection, was placed around the outer surface of the brass filter holder. A single 'O'-ring seal was provided at the interface between the brass filter holder and the stainless steel pedestal, in order to prevent any leakage

between the pore air and pore water drainage lines. Further ‘O’-ring seals on the three individual drainage lines (one for pore air and two for pore water) were provided at the interface between the steel pedestal and the cell base.

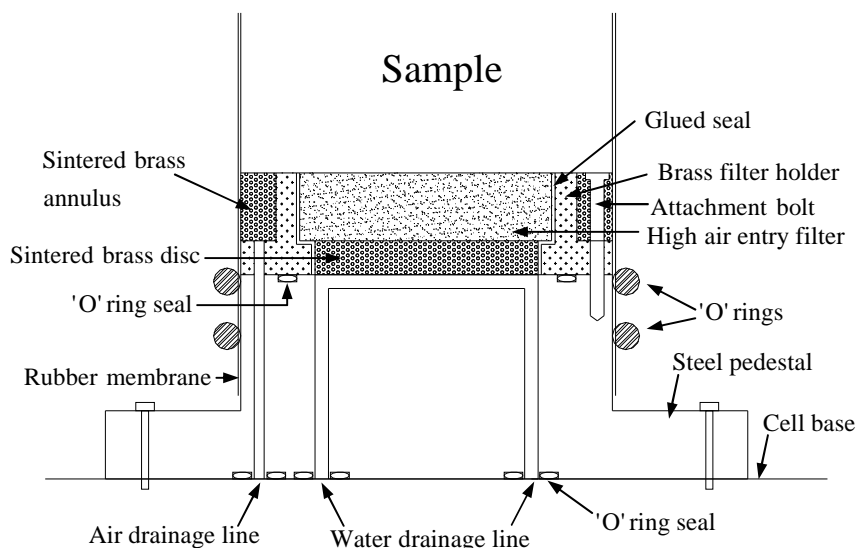


Figure 5-2 Pedestal arrangement (after Buisson, 2002)

5.1.3 Top cap arrangement

Figure 5-3 shows the layout of the acrylic top cap, with the top filter arrangement bolted to it.

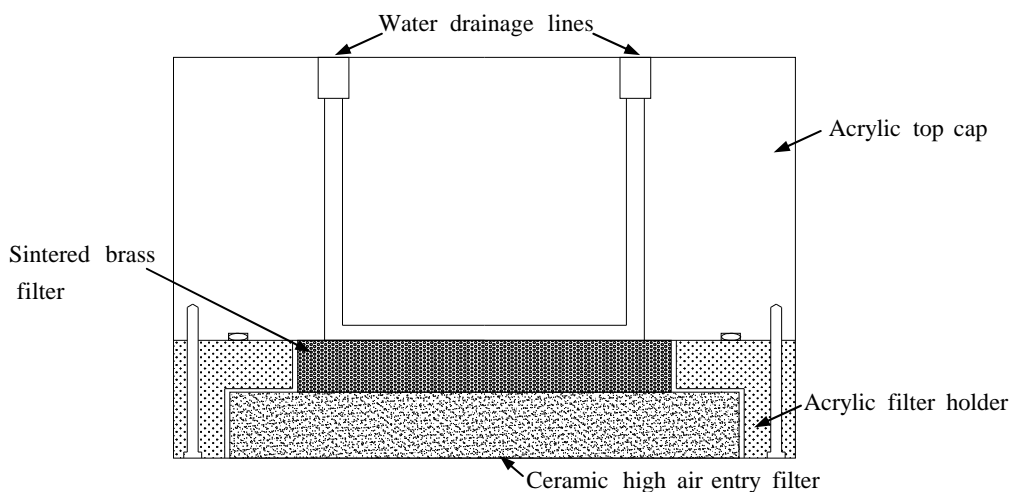


Figure 5-3 Top cap arrangement (after Buisson, 2002)

A circular high air entry ceramic filter (38 mm diameter) was glued into the acrylic filter holder, with a low air entry sintered brass filter behind, to minimize the head drop

across the high air entry filter. No pore air drainage line was provided at the top cap, as the air drainage line at the bottom of the sample was considered adequate.

5.1.4 Overall system layout

The overall setup of System A, with all the associated pressure and volume measurement/control devices and logging and control system can be seen in Figure 5-4. Here, the notations SM, PM, PT, VC, TC and AW indicate stepper motor, pressure multiplier, pressure transducer, volume change device, thermocouple and air-water interface respectively. A photograph of the same arrangement can be seen in Figure 5-5.

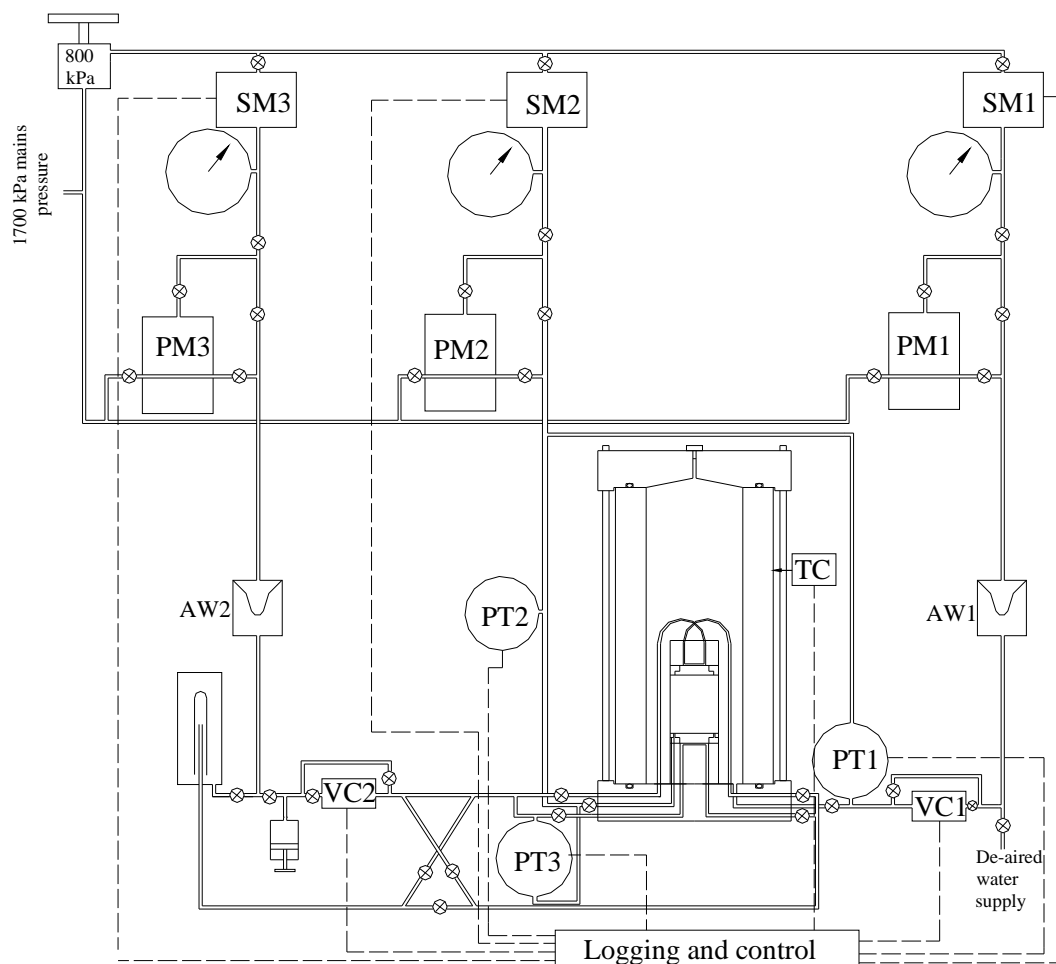


Figure 5-4 Schematic diagram of System A



Figure 5-5 Photograph of System A

Compressed air for all the testing systems was supplied by an Atlas Copco air compressor, at a line pressure of 1700 kPa. This mains pressure was then fed into a wall-mounted “off-the-shelf” pressure control system designed at Imperial College. The “off-the-shelf” system contains standard 0-800 kPa air pressure regulators operated by stepper motors.

As shown in Figure 5-4, the mains pressure of 1700 kPa was first reduced to 800 kPa by a manual regulator before feeding to the three stepper motor-controlled regulators SM1, SM2 and SM3 to control cell pressure, pore air pressure and pore water pressure respectively. A single step of each stepper motor corresponded to a pressure increment of 0.07 kPa. Each stepper-motor controlled pressure regulator had a pressure range of 0- 800 kPa. The range of pressure was further increased (if required) by employing three pressure multipliers PM1, PM2 and PM3 provided by Imperial College. In this case, the inlet valve of the required pressure multiplier was opened to the 1700 kPa mains pressure. The stepper motor controlled air pressure acts as a control pressure on the diaphragm of the pressure multiplier regulator in order to vary the outlet pressure from pressure multiplier. The ratio of the outlet pressure of the pressure multiplier to the inlet air pressure from the stepper motor regulator was 2. Two air-water interfaces AW1 and AW2 were used to convert air pressure into cell water pressure and pore water pressure.

5.1.5 Measurement devices

A differential pressure transducer PT1 with a range of 0-1000 kPa was used to measure the radial net stress and a second differential pressure transducer PT3 with a range of 0-1500 kPa was used to measure the suction s . Finally, pore air pressure u_a was measured with a standard 0-1500 kPa pressure transducer PT2. The differential pressure transducers were preferred for measuring radial net stress and suction, rather than measuring cell pressure σ_3 , pore air pressure u_a and pore water pressure u_w independently, because this improves the accuracy of measurement and control of the important stress variables of net stress and suction (the accuracy of only one transducer, rather than two, is involved in each use). This is particularly important when the value of either radial net stress ($\sigma_3 - u_a$) or suction s is relatively low, but individual values of σ_3 , u_a and u_w are much higher.

System A required two volume gauges VC1 and VC2, in order to measure the flow of water into the cell (and hence the sample volume change) and the water flow in or out of the sample respectively. Imperial College (IC) type volume gauges (shown in Figure 5-6) were used for this purpose.

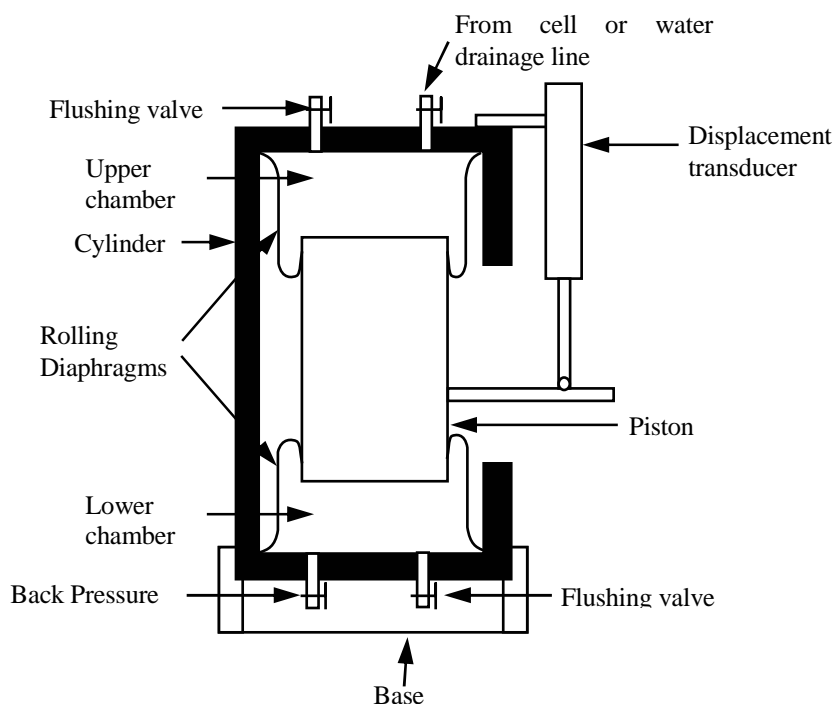


Figure 5-6 Schematic diagram of Imperial College volume change device (after Sharma, 1998)

IC volume change devices have been used by many researchers. Figure 5-6 shows a schematic diagram of such a device. If water flows in or out of the top chamber of the device through a drainage line, the piston attached to the rolling diaphragms will move vertically. This movement is detected by the displacement transducer. Hence, with a suitable calibration, the volume change can be determined. The pressure on the system is provided through a back pressure inlet to the lower chamber of the device. Both upper and lower chambers are therefore at similar pressures (the only difference being due to the weight of the piston), whereas the central portion of the device, between the two rolling diaphragms is vented to atmospheric pressure. In order to keep the two rolling diaphragms properly inflated (so that the device calibration was reliable) a minimum line pressure (acting in the upper and lower chambers) of at least 50 kPa was maintained. The portion of water enclosed within top chamber should be de-aired properly in order to get accurate measurement and a flushing valve is provided for this.

5.1.6 Diffused air flushing system

Provided that the applied suction was less than the air entry value of the high air entry ceramic filters and that the filters were properly water-saturated prior to a test, there should have been no movement of gaseous air through the high air entry ceramic filters. It was, however, still possible for dissolved air to diffuse through the ceramic filters from the soil sample to the other side (Fredlund, 1975). The diffused air then came out of solution and accumulated in the water drainage lines within the pedestal and top cap. This can cause error in the application of suction or the measurement of water volume draining from the sample (Nageswaran, 1983). Fredlund (1975) devised a setup to flush and measure the volume of this diffused air.

Figure 5-7 shows the air flushing arrangement employed in this research, consisting of a screw pump, 4-way valve system, air trapping device and air water interface. During normal operation of the experimental system, the valves $V_1, V_4, V_8, V_9, V_{10}, V_{11}$ and V_{12} were closed and the pore water pressure was applied through the air-water interface and volume change device to the top and bottom of the soil sample. During the flushing process, a screw pump was used to generate a flow through the water drainage lines, to displace the air bubbles to be collected in the air trapping device. A

4-way valve system was used to reverse the water flow direction in the drainage lines within the top cap and the pedestal.

To flush diffused air in the water drainage line within the pedestal, initially valves V_2 , V_3 , V_6 , V_8 , V_{10} and V_{11} were closed so that a water flow in the direction $V_7 - V_9$ was achieved. In order to reverse the flow direction, valves V_{10} and V_{11} were opened while the valves V_5 and V_{12} were closed. The same procedure was followed for flushing air in the water drainage lines within the top cap, by closing valves V_7 and V_9 and opening valves V_6 and V_8 . The experience from previous researchers showed that a sudden pressure pulse was sometimes necessary to displace air bubbles trapped in the water drainage line (e.g. Sharma, 1998). To achieve this, the screw pump was used to generate a pressure pulse at the start of the flushing process. The pressure pulse occurred only for a little duration so that no significant inflow water into the sample would occur, as the air water interface would ensure a rapid return to the original pore water pressure after the pressure pulse.

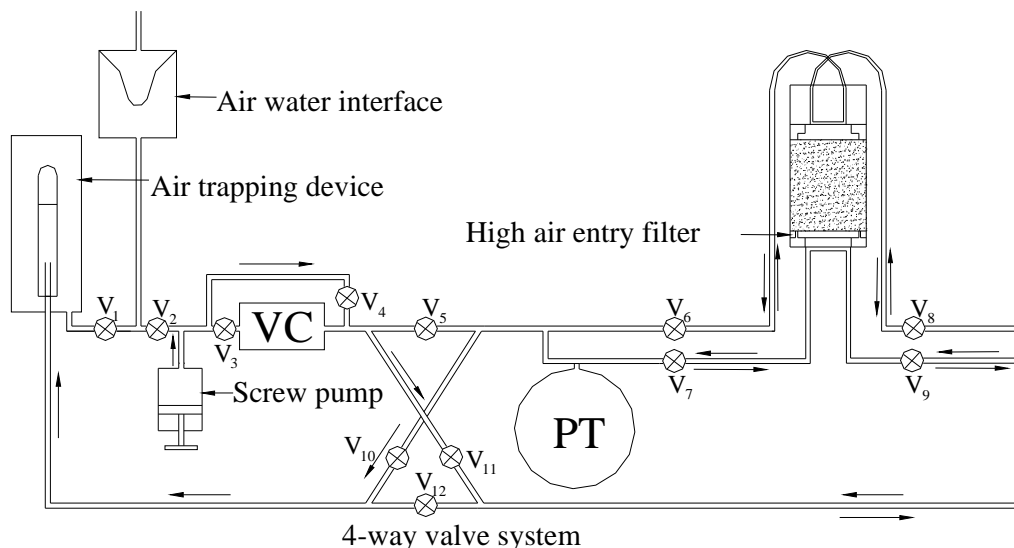


Figure 5-7 Diffused air flushing arrangement (after Buisson, 2002)

Romero (1999) reported that the rate of diffusion of dissolved air through a high air entry ceramic filter increased exponentially with suction. In addition, Buisson (2002) also observed that the rate of diffusion became unmanageable above 400 kPa suction value. It was therefore decided to limit the suction range in this research to less than

400 kPa. During the experimental programme, diffusion of dissolved air into the water line was never observed during flushing, presumably because of relatively low values of suction involved.

5.2 SYSTEM B- CONTROLLED-SUCTION TRIAXIAL CELL

5.2.1 Triaxial cell

Figure 5-8 shows the overall layout of the controlled-suction triaxial cell. The triaxial cell was able to accommodate samples of 50 mm diameter and a maximum height of 100 mm. The arrangement of stainless steel wall, cell base, pedestal and top cap was similar to that of the isotropic cell discussed in Section 5.1. However, the cell cover plate was modified in order to accommodate a loading ram and load cell for applying and measuring deviator load. As shown in Figure 5-8, two brass blocks containing ‘O’ ring sealing arrangements were inserted around the loading ram at the top and bottom sides of the cell cover plate, in order to prevent any leakage of cell water. As an additional precaution, a pressure equal to the cell pressure was applied between the two inserts, as shown in Figure 5-8. Due to this loading ram and load cell arrangement, the under-surface of the cell cover plate was machined to have a sloping surface with the highest point being off-centre in order to facilitate flushing during filling of the cell with de-aired water (see Figure 5-8).

An inverted Bishop-Wesley pressure chamber was connected to the triaxial cell, with an appropriate spacer between. The Bishop-Wesley pressure chamber was specially manufactured at Imperial College to give a maximum ram travel of 50 mm (standard travel is 25 mm). A standard 2.5 kN Imperial College submersible internal load cell was used to measure the deviator load. The electrical cable attached to the load cell was routed first through a vertical slot made at the top of the loading ram and then through an opening in the cylindrical spacer.

An axial displacement transducer (LVDT) of 50 mm travel was mounted on a cross-beam attached to the loading ram in the Bishop-Wesley pressure chamber as shown in Figure 5-8.

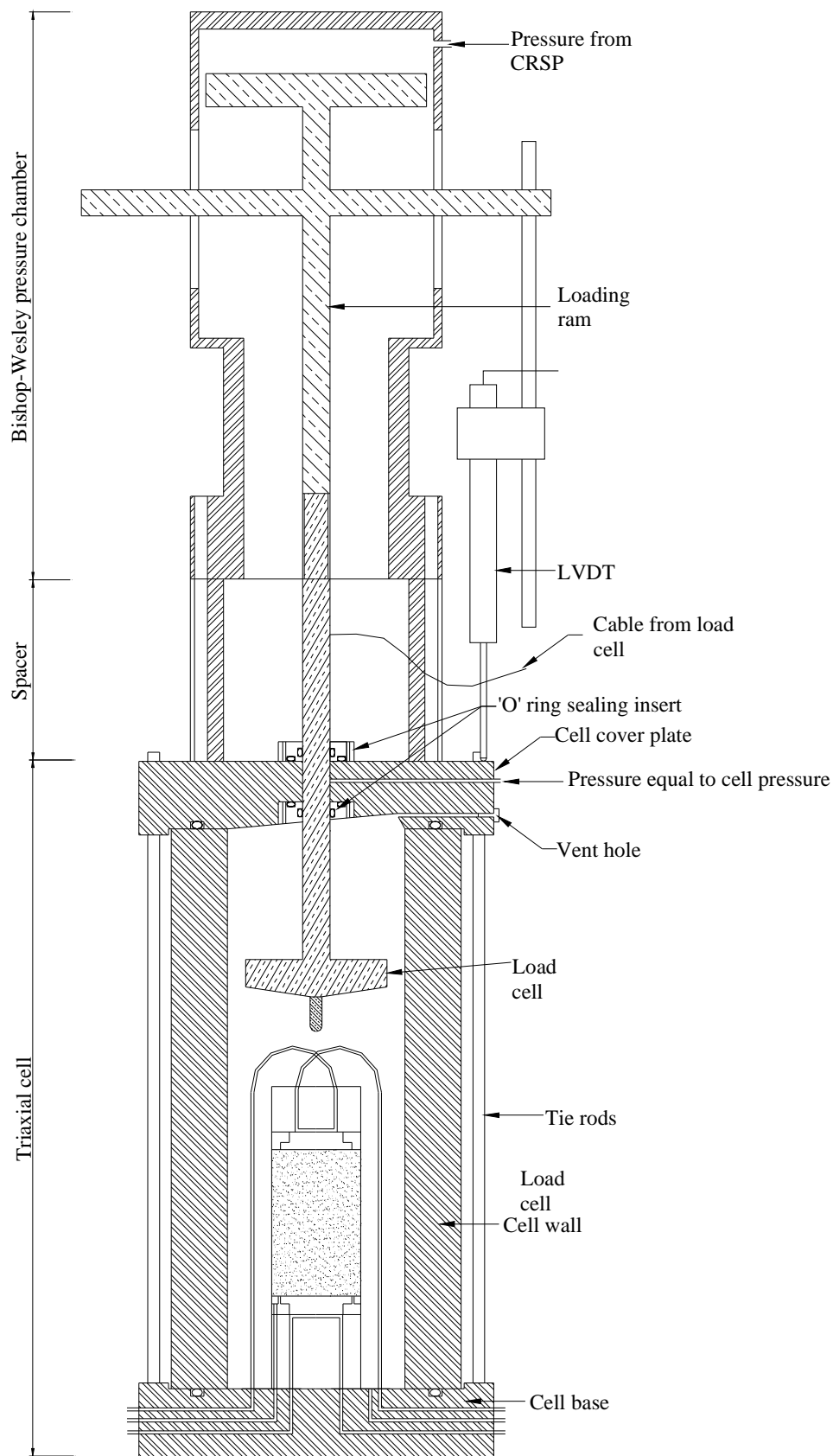


Figure 5-8 Overall layout of the controlled-suction triaxial cell (after Buisson, 2002)

5.2.2 Overall system layout

The overall layout of system B with associated equipment can be seen in Figure 5-9 and a corresponding photograph of the arrangement is shown in Figure 5-10. The overall layout of System B was similar to that of System A (see Figure 5-4). However, in order to control the deviator load, a 2 MPa Constant Rate of Strain Pump (CRSP) was employed. Each pulse generated by the CRSP corresponds to a volume of displaced fluid of 0.0001 cm^3 . By generating a water flow in or out of the upper chamber of the Bishop-Wesley cell by the CRSP (which is controlled by the Triax software), the movement of the loading ram was controlled.

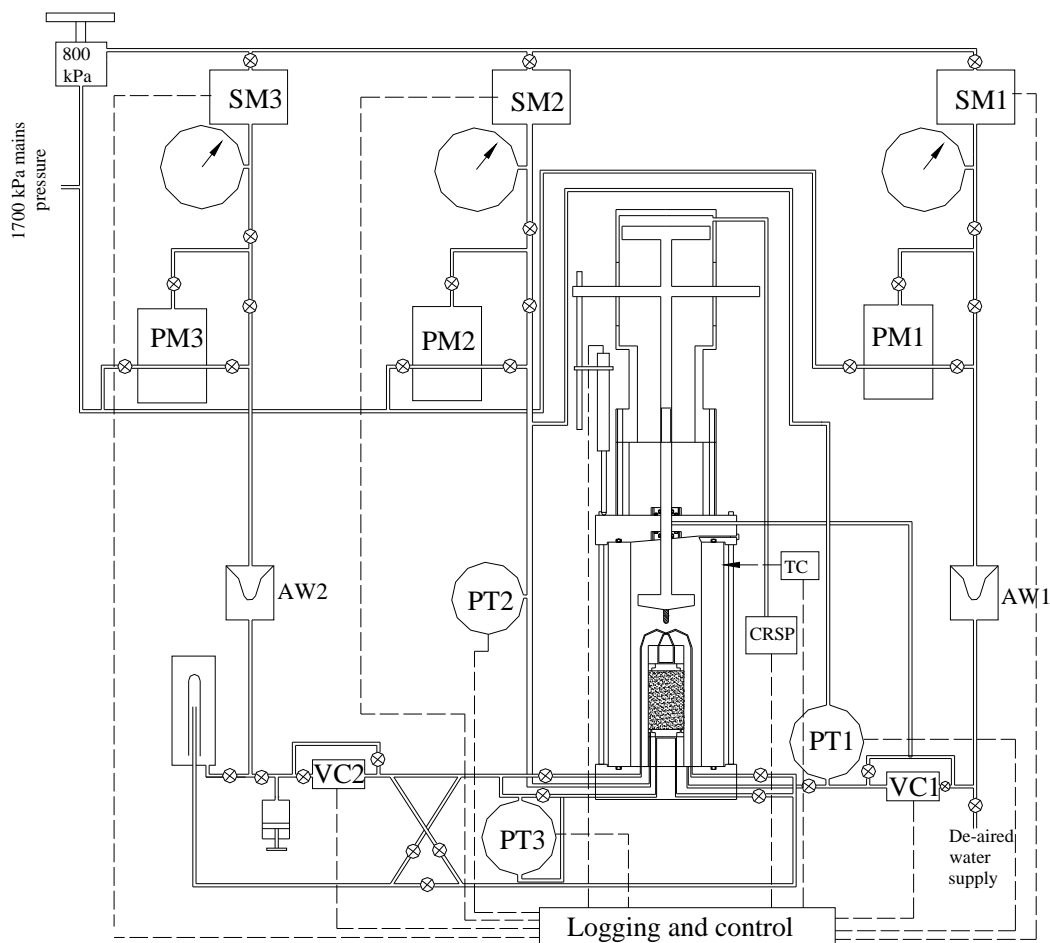


Figure 5-9 Schematic diagram of system B

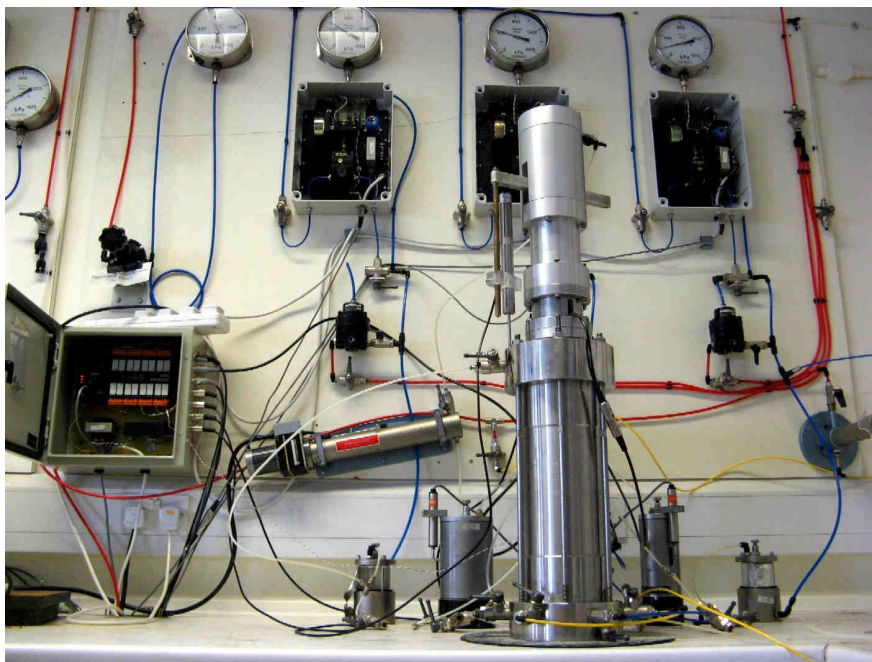


Figure 5-10 Photograph of system B

5.3 SYSTEM C- TRIAXIAL CELL FOR TESTING SATURATED SOILS

Standard Bishop-Wesley triaxial testing equipment was used to test saturated soil samples. The original pedestal was designed for testing 38 mm diameter soil samples, and this was replaced with a 50 mm diameter pedestal, so that all soil samples tested in this programme (saturated or unsaturated) were 50 mm in diameter.

Figure 5-11 shows the overall layout of the triaxial cell employed for testing saturated soil samples. The photograph of the setup of System C with associated equipment can be seen in Figure 5-12. The mains pressure of 1700 kPa was first reduced to 800 kPa by a manual regulator before feeding to two stepper motor-controlled regulators SM1 and SM2 to control cell pressure and pore water pressure respectively. Pore water pressure was applied to the bottom and top of the sample through pedestal and top cap respectively, as shown in Figure 5-11. The flow of pore water in or out of the sample was measured by an IC volume change device VC to determine the sample volume change.

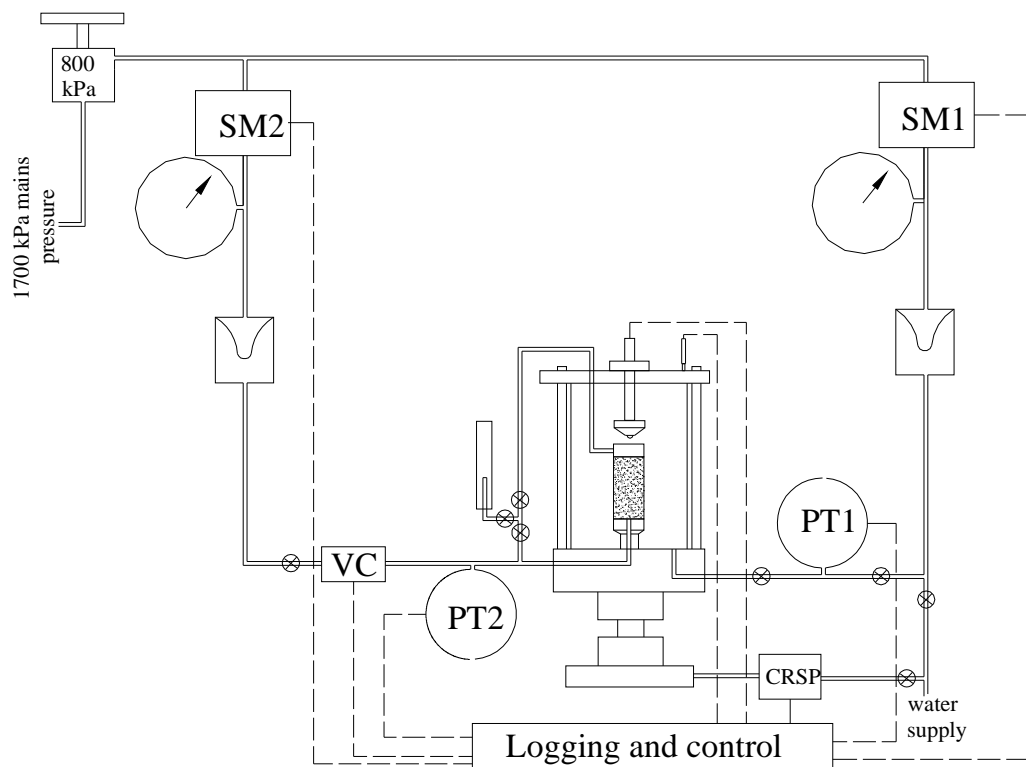


Figure 5-11 Schematic diagram of system C

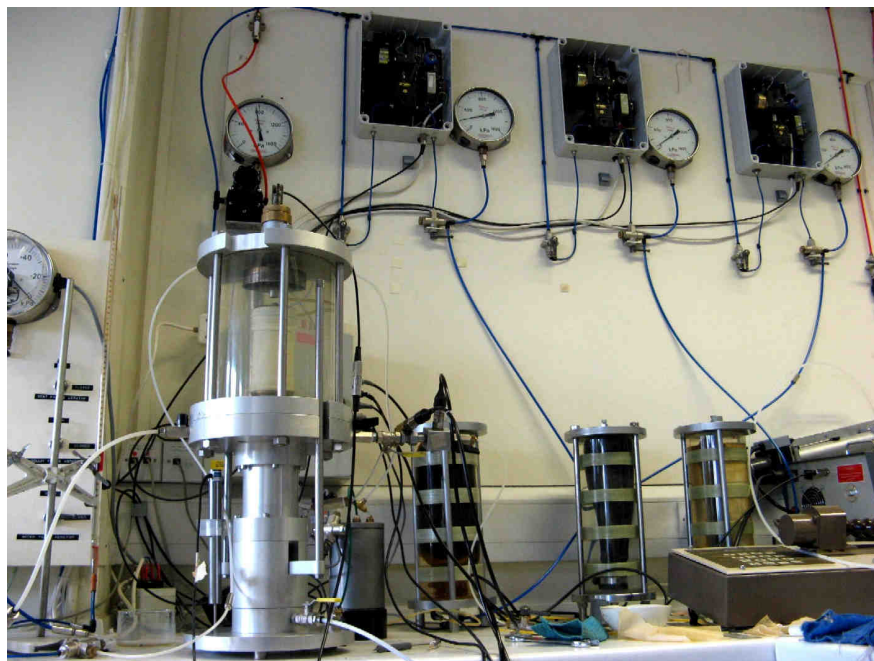


Figure 5-12 Photograph of system C

A standard submersible internal load cell of 3 kN capacity was used to measure deviator load. The movement of the load ram was controlled by a constant rate of strain pump, as shown in Figure 5-11. Axial displacement of the sample was measured by 50 mm range displacement transducer mounted on the cross-beam of the loading ram.

5.4 LOGGING AND CONTROL SYSTEM

An automatic control system was employed in the experimental research programme, because continuous variations of pressures and displacement were required, in order to identify yield points and critical state points. Moreover, some tests involved highly complex stress paths (e.g. keeping S_r constant), and thus required highly flexible control, which could not be achieved by manual control. Furthermore, due to the long durations of tests, experimental variables such as stresses and volume changes were logged using an automatic logging system.

The logging and control system for each system consisted of stepper motor controllers, an analogue to digital (A/D) converter and software called “Triax 4.3”, which was developed by Toll (2002). For System A, stepper motors for cell pressure, pore air pressure and pore water pressure needed to be controlled, whereas for System B, an additional stepper motor for the CRSP had to be controlled. For System C, stepper motors for cell pressure, pore water pressure and the CRSP were controlled. The connection between all these stepper motors and the computer was established through a digital input-output (I/O) board, which could interface with up to 12 controllers. In the Triax software, each of these controllers can be added as a device and settings for each controller can be configured appropriately. In Figure 5-13, showing the typical interface of Triax software for System B, the controllers are indicated in the window called “control” by box 1 (cell pressure), box 2 (pore air pressure), box 3 (pore water pressure) and box 4 (CRSP). Stepper motors can be controlled using Triax based on control equations defined in terms of direct transducer readings (e.g. cell pressure and LVDT reading) or user defined variables (e.g. sample volume and degree of saturation) which could involve the outputs of several transducers.

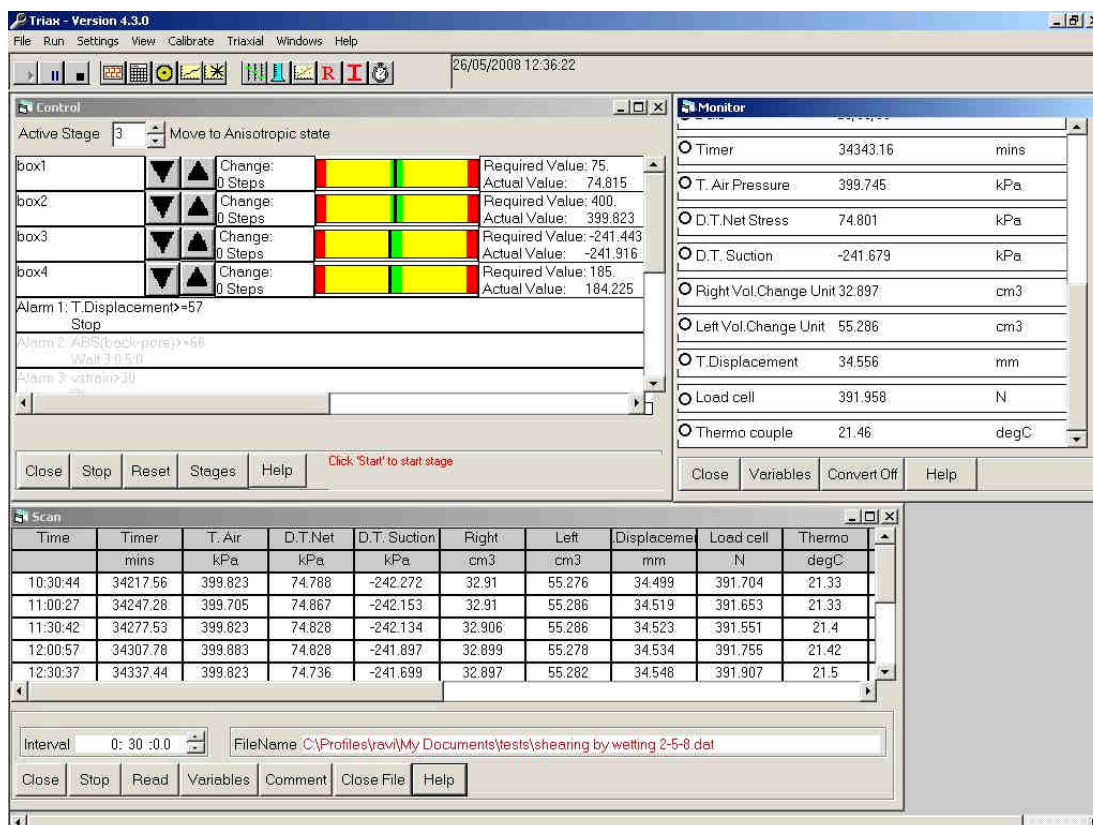


Figure 5-13 Typical interface of Triax software

The analogue signals of transducers were converted to digital signals using a Measurement System Ltd. (MSL Datascan Unit) A/D converter and transmitted to the computer through a serial port (COM1). The calibration of the various transducers was carried out using the Triax software. The calibrated readings from different transducers could be displayed (see “Monitor” window) and logged (see “Scan” window) at specified time intervals. The Triax software also allowed graphs to be plotted for different variables in real-time so that the results could be readily analysed visually. The logged data could also be transferred in spreadsheet format to other computers for post-processing using standard software such as Microsoft Excel and Matlab.

5.5 CALIBRATION OF TRANSDUCERS

In order to convert the readings of transducers from voltage to appropriate engineering units, the transducers were calibrated against appropriate references. Accurate calibration is very important for obtaining good quality experimental results. In this section, the calibration procedures for the various transducers are explained.

5.5.1 Calibration of pressure transducers

For Systems A and B, differential pressure transducers for radial net stress and suction and a standard pressure transducer for air pressure were calibrated, whereas for System C, cell pressure and pore water pressure transducers were calibrated. Each transducer was identified as a different logging channel and the raw voltage could be displayed by the Triax software. Pressure transducers were calibrated against a standard dead-weight apparatus (see Figure 5-14), in which weights acting on a vertical piston were used to apply pressure to oil contained in a sealed reservoir, which was connected to the pressure transducer through an oil-water interface by opening the valve V_1 while keeping valve V_2 closed.

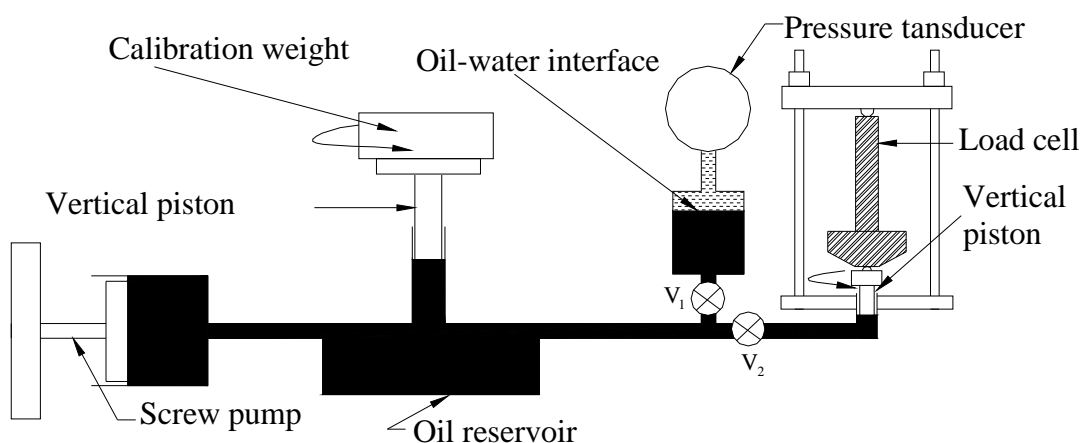


Figure 5-14 Schematic diagram of calibration system for pressure transducers and load cells

A routine incorporated in the Triax programme allowed these known pressures and the corresponding raw voltages from the transducer to be recorded and then a suitable regression (typically 1st or 2nd order polynomial) to be performed to derive the calibration equation. A linear calibration equation was found to be adequate for all pressure transducers. This can be written as:

$$y = ax + b \quad (5-1)$$

where, y is the calibrated reading in engineering units, x is the transducer output voltage and a and b are regression constants. The calibration using the dead-weight apparatus was used to determine the regression constant a (gradient). The accuracy of the calibration for the range of pressure 100- 800 kPa was found to be around ± 0.3

kPa. Regression constant b was determined by venting the transducer to atmospheric pressure. The regression constant b seemed to change slightly over time, causing a very slow drift in the transducer reading. To avoid any error from this phenomenon, transducers were always zeroed (i.e. resetting the value of constant b) against atmospheric pressure before the start of each test.

5.5.2 Calibration of volume gauges

Figure 5-15 shows the setup developed to calibrate the IC volume gauges. A glass burette with 0.01 ml precision and 5 ml capacity was connected to the upper chamber of the IC volume gauge. An acrylic cylinder surrounding the glass burette was connected to a screw pump using a flexible tube. The upper parts of both glass burette and acrylic cylinder were filled with petroleum ether, whereas the lower parts were filled with water. A back pressure of 50 kPa was maintained throughout the calibration process, by applying a pressure to the lower chamber of the volume gauge via an air-water interface. This was to ensure proper operation of the IC volume gauge (i.e. correct inflation of the rolling diaphragms).

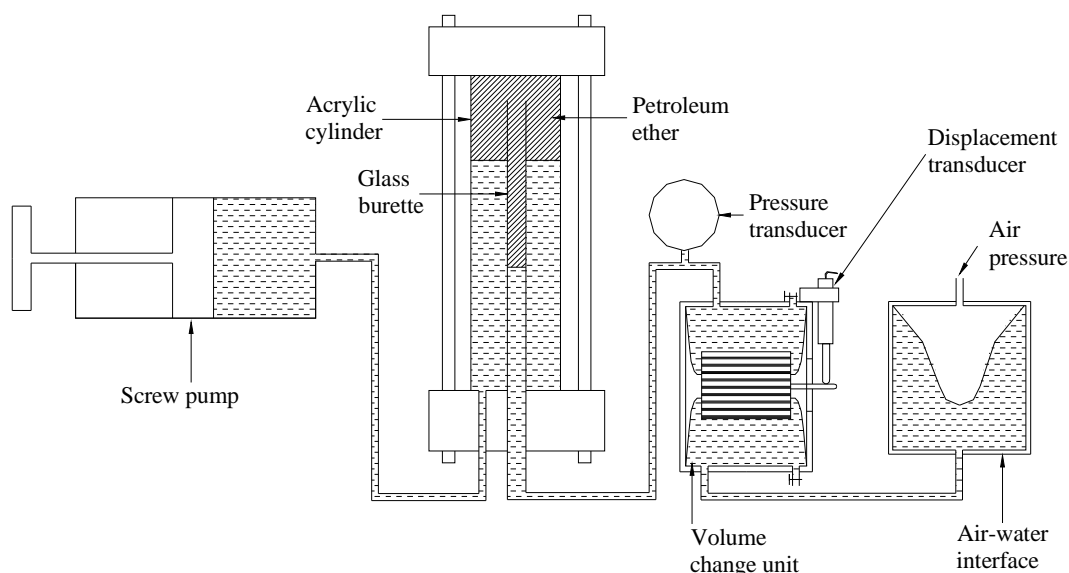


Figure 5-15 Calibration setup for Imperial College volume gauge (after Buisson, 2002)

Using the screw pump, a measured volume of water (using readings from the glass burette) was transferred to the IC volume gauge and this volume was recorded with the voltage from the displacement transducer on the volume gauge using the Triax

software in calibration mode. Calibration was carried out over almost the full range of the volume gauge: around 0-45 ml for 50 ml units and 0-95 ml for 100 ml units. A linear calibration was found to be adequate. The maximum variation of measured values from the calibration curve was about ± 0.03 ml for 50 ml units and about ± 0.08 ml for the 100 ml unit.

5.5.3 Calibration of load cells

The dead-weight system shown in Figure 5-14 was used to calibrate the load cells in Systems B and C. In this case, pressure exerted on the oil reservoir by the vertical piston (loaded with calibration weights) was transmitted to a second vertical piston (by closing valve V_1 and opening valve V_2), which then exerted a force on the load cell. The calibration was carried out for a range 200-1700 N for both Systems B and C. a linear calibration was found to be adequate and the gradient of the calibration curve was determined. In order to account for the influence of cell pressure and self weight of the load cell, the deviator force was zeroed at the start of each test. The accuracy of the linear calibration was found to be ± 1.6 N, which corresponded to an accuracy of ± 0.8 kPa on the deviator stress for a 50 mm diameter soil sample.

5.5.4 Calibration of axial displacement transducers

The calibration of axial displacement transducers of 0-50 mm range for Systems B and C was carried out using slip gauges. The LVDT was clamped to the horizontal cross-beam of the loading ram of a Bishop-Wesley cell and slip gauges of different heights were placed between the cell cover and the probe tip of the LVDT. This arrangement was chosen because any error caused by non-vertical clamping of the LVDT during the experimental testing could be eliminated. The height of the slip gauges and the corresponding voltage given by the LVDT were logged by the Triax software for the calibration. A linear calibration was obtained with an accuracy of ± 0.03 mm.

5.6 CALIBRATION OF CONTROLLED-SUCTION CELLS FOR APPARENT VOLUME CHANGE

In order to accurately measure the sample volume change in the controlled-suction isotropic cell and controlled-suction triaxial cell (Systems A and B), any flow of water

into the cell with changes of cell pressure or with time, that were not associated with change of soil sample volume, had to be calibrated. These flows of water into the cell could occur because of expansion of the cell, compression of the water within the cell, expansion or compression of flexible tubing, tube connectors or valves, and any water diffusion through the flexible tubing. In this section, the calibration for apparent volume change due to the above mentioned factors are presented.

5.6.1 Time-dependent effects

During the procedure to check for any leakage in System A, a continuous flow of water into the cell of 0.02-0.05 cm³/day was observed depending on the applied cell pressure. This was considered undesirable because experimental tests would be performed over long time periods (typically about 2 months), and given that flow of such magnitude could not be perfectly calibrated, this might have caused unacceptable errors over a full test. In order to identify the cause of these continuous water inflows, several possible causes were considered and controlled tests were carried out to identify and eliminate possible causes. These are discussed below.

5.6.1.a Creep of IC volume gauge

The IC volume gauge was de-aired by flushing with de-aired water several times in both directions under a back pressure of 100 kPa. Initially, a sudden flushing was carried out by opening the flushing valve to atmospheric pressure whilst a back pressure of 100 kPa was applied to the lower chamber. This was considered helpful in dislodging air bubbles from the internal surfaces of the volume gauge and rolling diaphragm. Shaking of the volume gauge could also help this process. Later, a gradual controlled flushing was carried out using a screw pump.

After the de-airing process, the flushing valve and the main valve from the upper chamber of the volume gauge were closed and a back pressure of 400 kPa was applied to the lower chamber. The volume change was then monitored for 1 month. The volume change was found to be around 0.003 cm³/day. This problem was considered unavoidable (without replacing the IC volume gauges with alternative devices) and the effect was considered acceptably small.

5.6.1.b Leakage from single steel walled cell

After a few weeks of monitoring a continuous small apparent flow rate into the controlled-suction isotropic cell (with cell pressure of 400 kPa applied), the valve to the cell was closed and monitoring of the volume change unit was continued for a further few weeks. The rate of change of volume was found to be unchanged, meaning that there was no creep of the cell itself or leakage directly from the cell. The continuing flow rate was therefore entirely attributable to the volume change unit and the flexible tubings, tubing connectors and valves between the volume change unit and the cell.

5.6.1.c Other possible causes

All compression tube fittings were replaced with new ones, in case of any leakage through the fittings. Care was taken to ensure that proper sealing was achieved within each compression fitting. However, no significant reduction of the flow rate was observed after replacement of the fittings.

Another possible leak could have been through the radial net stress differential pressure transducer. However, no leakage was found after some investigation.

5.6.1.d Diffusion through flexible tubings

Flexible standard nylon tube of external and internal diameters of 4 mm and 2.5 mm respectively was initially used for connecting the various components of each test system. To check for possible water diffusion through the walls of the tubing, a standard nylon tube 10 m long was pressurised to 400 kPa and the volume change was monitored for 1 week. The rate of volume change observed was 0.54 cm³/day. This clearly showed that substantial water diffusion through the tube wall was taking place. In order to reduce diffusion, all lengths of connecting tube within those parts of the system that would affect measured volume changes should be kept to a minimum and tubing constructed of a material giving lower rates of water diffusion should be used. Higher fluoride content tubing was suggested by the flexible tubing supplier (Legris Ltd.) to be less water absorbent. Hence, Polytetrafluoroethylene (PTFE) tubing (of different lengths) was tested under 400 kPa back pressure for diffusion rate as shown

in Figure 5-16. A clear reduction of diffusion rate can be observed by using PTFE tube rather than standard nylon tubing. All tubing was therefore changed to PTFE.

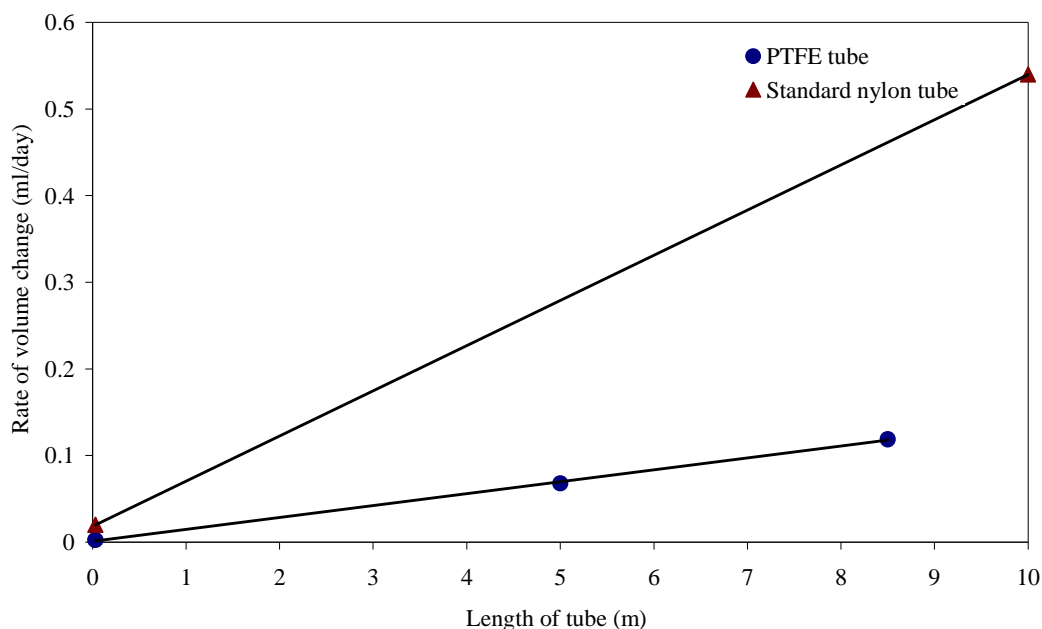


Figure 5-16 Variation of rate of water volume loss from PTFE and standard nylon tubings pressurised to 400 kPa

5.6.2 Calibration for temperature fluctuation

Errors could occur in the measurement of sample volume change due to the fluctuation of temperature within the laboratory. This is particularly important because of the large volume of cell water involved in the measurement technique. Both the steel cell and the water within the cell would expand if temperature was increased, causing two opposite effects in terms of potential water inflow to the cell. However, it was observed that the temperature-induced expansion of the water within cell was always greater than any temperature-induced expansion of the cell itself.

The temperature of the laboratory was maintained at 21⁰ C by an air conditioning unit, in order to reduce the impact of temperature fluctuation. However, variation of temperature inside the laboratory was still observed (typically a fluctuation of $\pm 0.5^0$ C). In addition, for some stress path tests which involved only small changes of sample volume (i.e. related to elastic straining), accuracy of sample volume change

measurement was extremely important. Because of these reasons, it was decided to calibrate flow of water from the cell against temperature variation.

A beaded wire type J thermocouple was installed on the outer surface of the steel-walled cell. This type of thermocouple was selected for its low cost, fast response, small size and easy installation. The inbuilt calibration for the thermocouple within the Triax software allowed logging of the temperature of the outer surface of the cell. Of course, this did not necessarily provide a perfect record of the average temperature of the entire cell and the water within it, because of the likelihood of significant temperature variation between outer surface of the cell and the cell contents.

In order to calibrate for the temperature effect on cell volume the laboratory temperature was increased twice in steps at particular time intervals using the air conditioner and thermocouple reading, and corresponding volume changes were logged using the Triax software. The average temperature reading from thermocouple measured over a period of 12 days was plotted against corresponding average cell volume changes (of each step increase of temperature) over the same period of time. Linear calibrations were found to be adequate for cells, corresponding to $0.15 \text{ cm}^3/^{\circ}\text{C}$ for isotropic cell of System A and $0.34 \text{ cm}^3/^{\circ}\text{C}$ for the triaxial cell of System B.

Figure 5-17 shows the temperature variation, the corresponding measured flow out of cell and corrected flow out of cell during a 6 day period for System B. During the first 4 days, the laboratory temperature was controlled to a specific value by the air conditioner. However, a long-time temperature fluctuation (diurnal fluctuation) of $\pm 0.5^{\circ} \text{C}$ can be observed along with small short-time fluctuations due to the automatic switch on/off of the air conditioner and sensitivity of the thermocouple. The measured outflow followed the same trend as the long-time temperature fluctuation suggesting that the temperature of the cell content was reasonably represented by the reading from the thermocouple, which was mounted on the outer surface of the cell. After about 4 days, the temperature of the laboratory was increased by about 1 degree. Point A in the plot indicates the start of the imposed step increase in temperature. Once again both the short-time and long-time temperature fluctuations can be observed.

The red line in Figure 5-17 shows the flow out of the cell after correction from the temperature effect (using the measured calibration of $0.34 \text{ cm}^3/^\circ\text{C}$). It can be seen that the temperature correction introduces small short-time period fluctuations, because of short-time period fluctuations in the temperature reading on the outer surface of the cell which are not representative of the average temperature of the water within the cell. However, the temperature correction removes the larger-time period (diurnal) temperature fluctuation and imposed temperature variation effects in the measured flow out of cell.

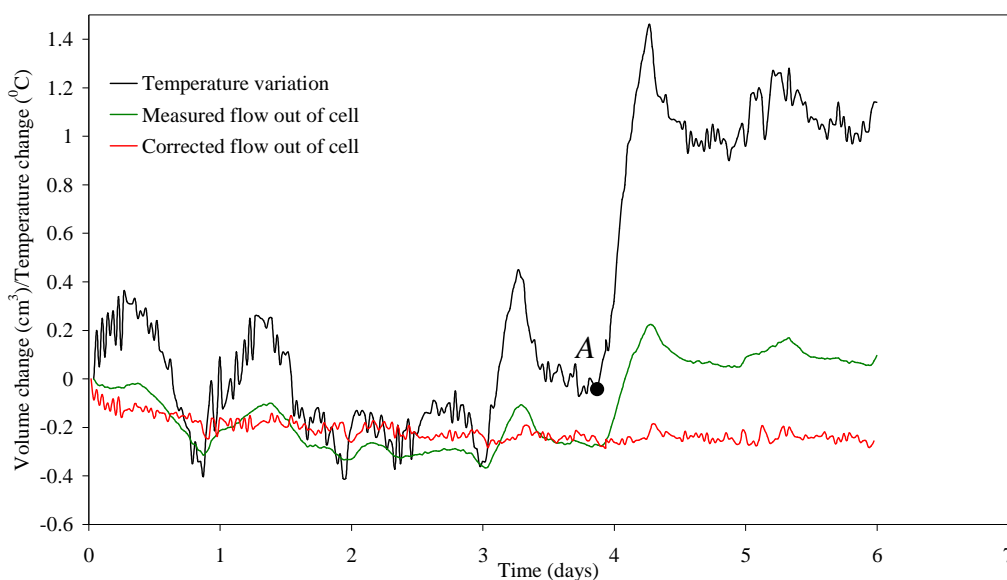


Figure 5-17 Variation of actual and corrected volume change with time (System B)

5.6.3 Calibration of apparent cell volume change with pressure

Calibration for apparent cell volume change with variation of cell pressure was performed for Systems A and B. A brass dummy sample of relevant dimensions (50 mm diameter and either 50 mm or 100 mm height) was mounted inside the cell but with the bottom filter holder on the pedestal and the top filter holder on the top cap both replaced with acrylic solid dummies of the same dimensions. All the connections and IC volume change units were flushed with de-aired water in order to remove any air bubbles. The cell was then carefully filled with de-aired water.

With zero cell pressure (i.e. cell water vented to atmosphere), the cell pressure valve at the cell base was closed. The pressure in the IC volume gauge and the cell pressure lines was raised to 50 kPa in order for proper operation of the volume gauge (i.e. to keep the rolling diaphragms properly inflated). The reading of the IC volume gauge was then set to zero (i.e. initial reading) corresponding to zero pressure on the cell but 50 kPa pressure on the IC volume gauge and the cell pressure line. Identical procedure was also followed at the start of each test on a soil sample in Systems A and B. In the experimental testing, the initial reading (with the sample initial dimensions corresponding to those measured before setting up in the cell) had to be taken at zero cell pressure (i.e. no deformation of the soil sample), but 50 kPa pressure was required in the IC volume gauge and the cell pressure lines in order to achieve proper operation of the volume gauge. By using the same procedure in the calibration process, it was possible to eliminate any error caused by expansion of the connecting tubings and rolling diaphragm of the IC volume gauge by the application of the 50 kPa pressure.

After taking the zero reading, the valve located at the cell base on the cell pressure line was opened and the cell pressure was increased to 100 kPa. Once the rate of volume change was observed to be less than $0.006 \text{ cm}^3/\text{day}$ (usually after 2-3 days) the next increment of cell pressure was applied. In this way, the cell pressure was increased in steps to 100, 200, 400 and 600 kPa and then reversed. Figure 5-18 shows the apparent cell volume change with time for System B after the correction for temperature variation.

Figure 5-19 and Figure 5-20 show the calibration of immediate cell volume change with cell pressure for Systems A and B respectively. It can be seen from these figures that different curves were followed during increase and decrease of cell pressure, particularly at low pressures. This aspect is very apparent for System B (see Figure 5-20). However, in all the experimental tests on soil samples any reduction of cell pressure was relatively small and never brought the cell pressure to less than 400 kPa. For this reason, each cell was calibrated with a second order polynomial calibration curve based on data for cell pressure increasing

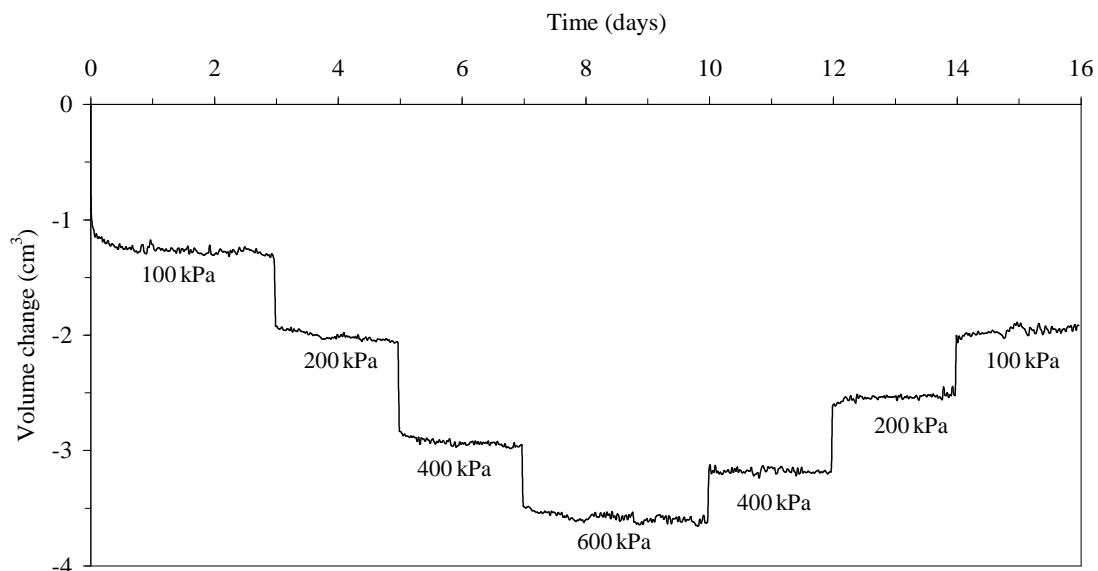


Figure 5-18 Apparent cell volume change with elapsed time (System B)

Apparent cell volume change with time due to the diffusion of water through the connecting tubes had been reduced dramatically from 0.025-0.05 cm³/day to 0.004-0.007 cm³/day after the replacement of standard nylon tube with PTFE tube. A correction of 0.006 cm³/day was used for both Systems A and B. The correction was independent of cell pressure, as the diffusion rate was found to be almost independent of pressure over the range of interest.

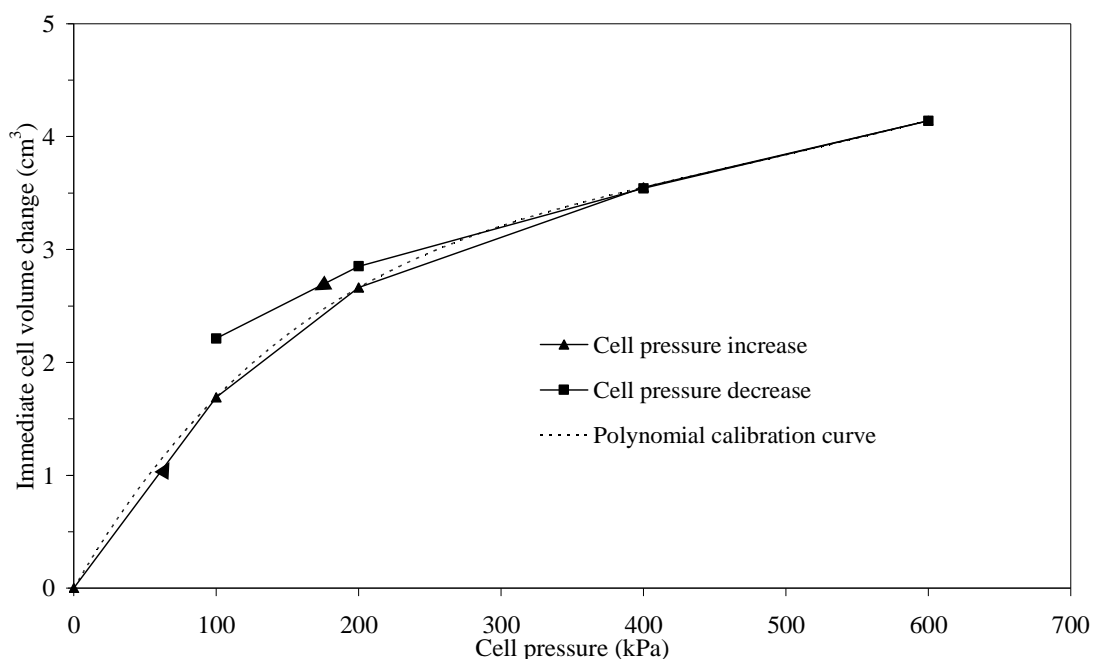


Figure 5-19 Variation of immediate cell volume change with cell pressure (System A)

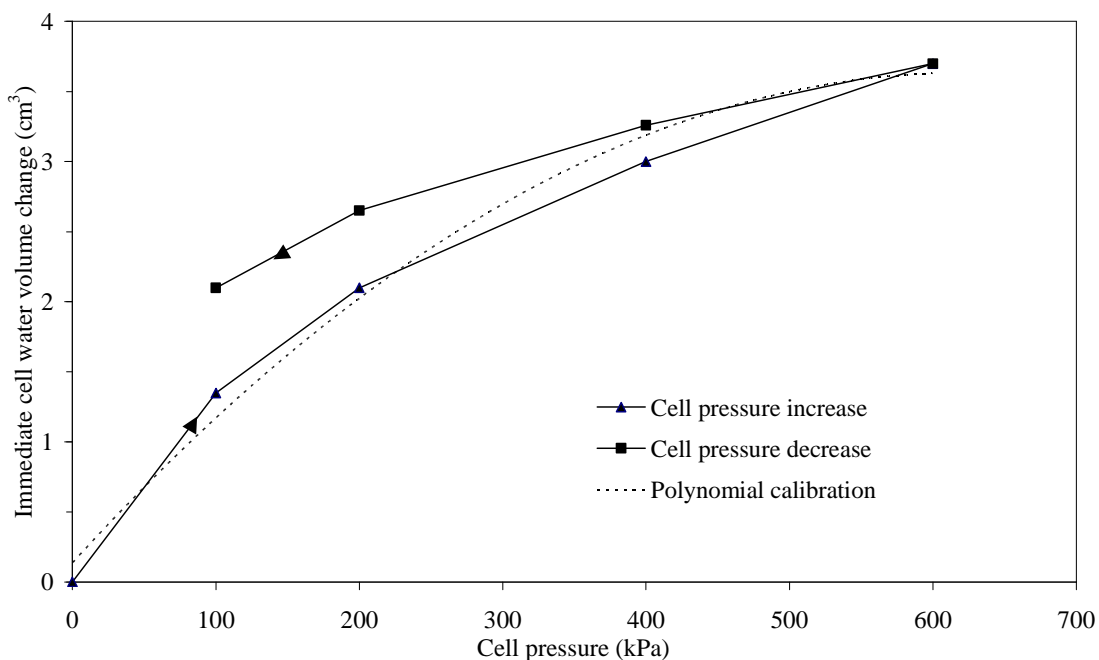


Figure 5-20 Variation of immediate cell volume change with cell pressure (System B)

For System B, an additional calibration for apparent cell volume change with movement of the loading ram was carried out. Ram displacement and corresponding water outflow from the cell were recorded and plotted, as shown in Figure 5-21. A linear calibration with accuracy of $\pm 0.0045 \text{ cm}^3$ was obtained. The effective ram area was calculated from Figure 5-21 as 2.5145 cm^2 .

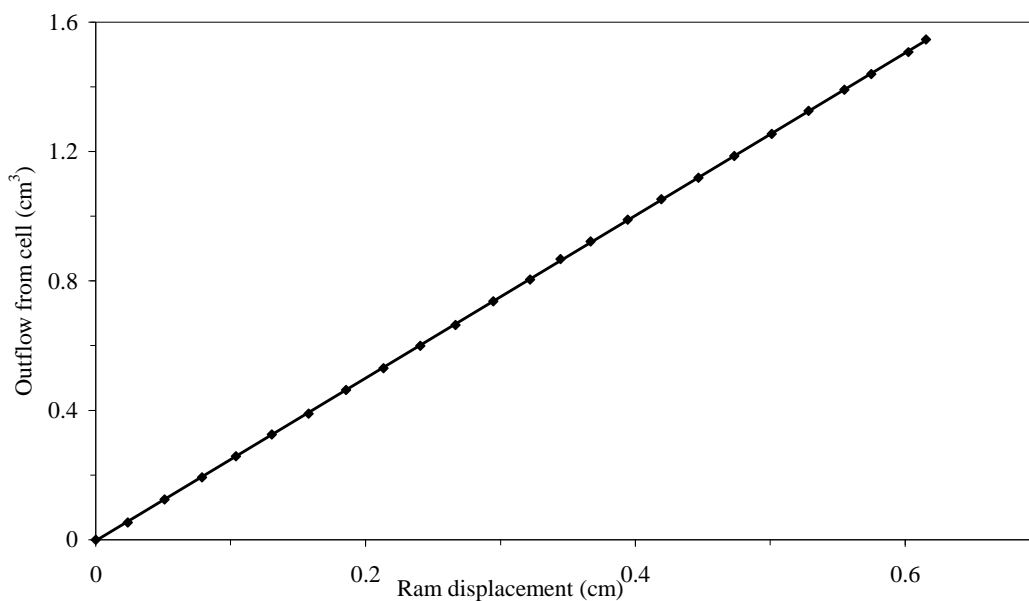


Figure 5-21 Calibration for ram displacement (System B)

5.7 CALIBRATION FOR VOLUME CHANGE OF PORE WATER LINE

The diffusion through the pore water drainage line was $0.006 \text{ cm}^3/\text{day}$ for both Systems A and B. Calibration for the temperature effect on the pore water volume change was also carried out. A thermocouple was mounted on the top surface of the relevant IC volume gauge, assuming that the temperature of the contents of the IC volume gauge and the water in the drainage line would reasonably be represented by the reading from the thermocouple. The same procedure followed in Section 5.6.2 was employed and a linear calibration was obtained, corresponding to $0.022 \text{ cm}^3/^\circ\text{C}$ for System A and $0.03 \text{ cm}^3/^\circ\text{C}$ for System B.

Calibration for the apparent pore water volume change with pressure was similar to that of cell volume change. In fact, both calibration tests were conducted simultaneously. Figure 5-22 and Figure 5-23 show the immediate volume change of the pore water drainage line with pressure, along with the second order polynomial calibration curves. Once again, different curves were observed for pressure increase and pressure decrease. However, the maximum deviation from one curve to the other was 0.05 cm^3 , which corresponded to an error of about 0.03% in the water content of a 50 mm diameter and 50 mm height sample.

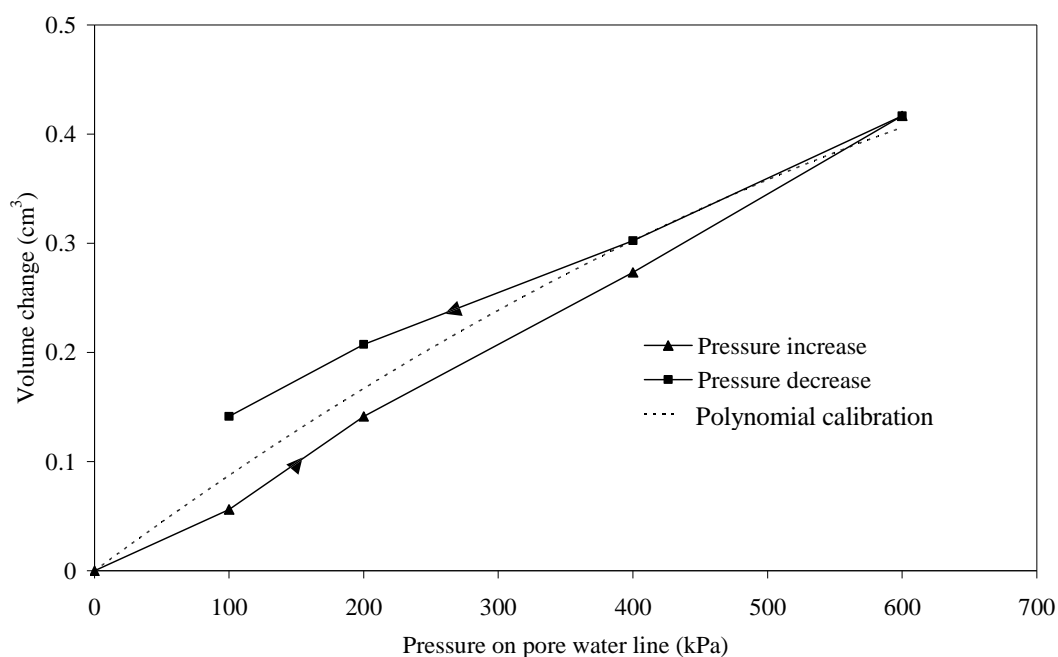


Figure 5-22 Variation of apparent immediate volume change of pore water drainage line with pressure (System A)

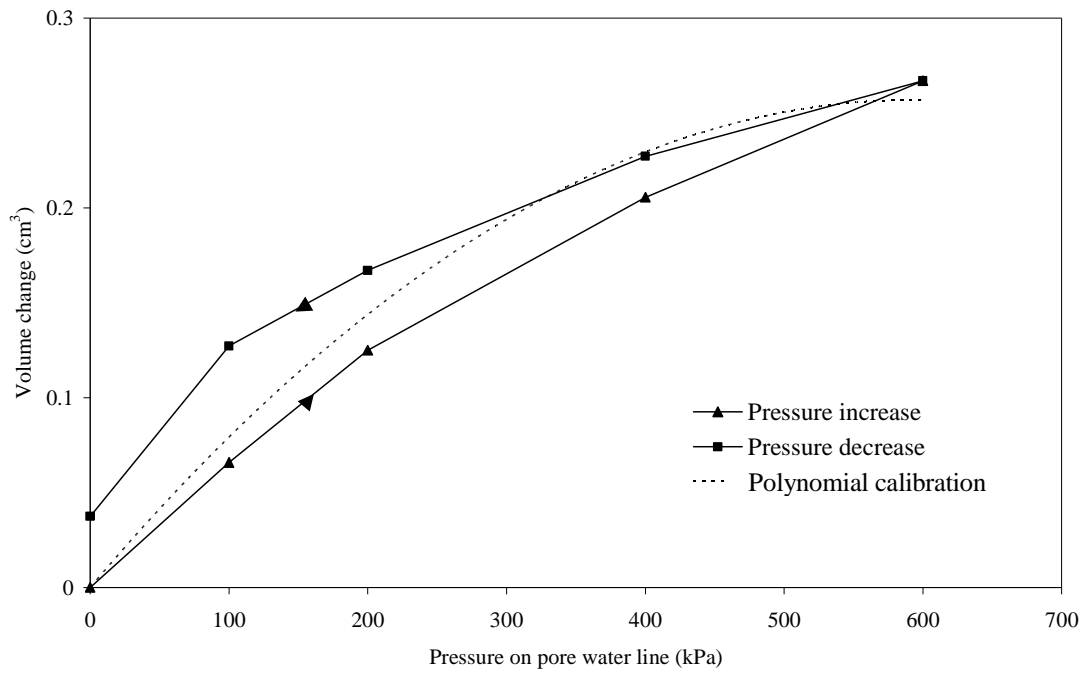


Figure 5-23 Variation of apparent immediate volume change of pore water drainage line with pressure (System B)

CHAPTER 6

SAMPLE PREPARATION AND TESTING

PROCEDURES

In the first section of this chapter, soil selection criteria and techniques involved with the sample preparation procedure are explained. In the second section, various procedures and techniques involved with setting up samples and conducting the controlled-suction stress path tests are discussed.

6.1 MATERIAL SELECTION

One of the objectives of this research was to understand the coupling of mechanical and water retention behaviour of unsaturated soils by conducting an experimental programme. Three different choices for samples are generally available for testing in a laboratory experimental programme: (1) undisturbed natural soil samples; (2) reconstituted samples and (3) compacted samples. Undisturbed natural samples are formed by complex natural processes, thus reflecting the soil behaviour at field conditions. However, the difficulty in sampling and the variability of stress history and constituents leads to non-repeatability of initial conditions, such as fabric, void ratio and water content. However, any experimental research to explore the fundamental behaviour of unsaturated soil, the repeatability of initial conditions of samples is essential. Undisturbed natural soil samples were therefore not suitable for this research. The main difference between compacted soil samples and reconstituted samples is that samples compacted dry of optimum would tend to have a bi-modal pore size distribution and reconstituted samples would have uni-modal pore size distribution. This means that the air entry value of reconstituted soil samples of clay prepared from slurry would be high (typically suctions of hundreds of kPas) as the pore sizes are predominantly associated with micro-pores between particles. Reconstituted samples were therefore considered unsuitable for this research, because the maximum suction that could be applied to the soil samples was restricted to about 400 kPa. In addition, reconstituted samples are less likely to show substantial collapse compression during

wetting, because of the absence of the macro-pores. Compacted (dry of optimum) samples were therefore used in this research, as their initial conditions are repeatable and unsaturated conditions could be maintained for the intended suction range.

Water retention behaviour was given as much importance as mechanical behaviour in this research. Wetting and drying were therefore required to be carried out with significant changes in degree of saturation. However, the suction range was limited to 0-400 kPa in this research for the reasons set out in Section 5.1.6 (i.e. the diffusion rate of dissolved air became unmanageable above a suction value of about 400 kPa). Compacted Speswhite Kaolin samples can have wide range of S_r (from around 0.60 to 1.0) within the suction range of 0-400 kPa. Hence, it was decided to use Speswhite Kaolin rather than any other fine-grained soil. Further advantages of using Speswhite Kaolin are listed below:

- Speswhite Kaolin is commercially available in 25 kg bags in uniform and homogeneous form.
- The rate of consolidation for Speswhite Kaolin is significantly faster than for most other clays, meaning that the duration of tests can be minimized. This is very important, because controlled-suction testing of unsaturated fine-grained soils is very time-consuming (because the unsaturated water permeability may be much lower than the saturated permeability).
- Several previous researchers carried out experimental research on unsaturated compacted Speswhite Kaolin samples (e.g. Sivakumar, 1993; Sharma, 1998; Tan, 2004; Sivakumar, 2005). It is useful to be able to compare experimental test results with these existing data.

6.2 SAMPLE PREPARATION

All samples used in the experimental programme were 50 mm in diameter. Samples tested in the triaxial cells of Systems B and C were 100 mm in height. The height-to-diameter ratio of 2 was selected for triaxial samples in order to avoid substantial end effects (likely with smaller height-to-diameter ratios) or significant risk of buckling (likely with larger ratios). For the isotropic cell of System A, the sample height was

reduced to 50 mm, in order to reduce the drainage path length and thus speed up the rate of testing. However, one negative effect of this reduced sample height was that the accuracy of sample volumetric strain measurement was reduced, because a given error in sample volume change measurement corresponded to a larger error in volumetric strain as the sample size was reduced.

6.2.1 Preparation of kaolin aggregates

As mentioned Section 2.1.3, the compaction water content has a big impact on the fabric and behaviour of unsaturated soils. However, the scope of this research was reduced to a single compaction water content so that any additional complexities arising from differences in compaction water content could be avoided. A compaction water content of 25 % was selected (4% dry of the optimum from Proctor compaction), in order to be consistent with previous research by Sivakumar (1993) and Sharma (1998).

In order to prepare the kaolin aggregates, 500g of air-dried kaolin was transferred to a mixing bowl. The mixing bowl was then mounted on to a domestic food mixer and 125 g of de-aired water was added gradually while mixing with a “K” beater. The mixing process was carried out for only 2-3 minutes, as further mixing was found to have no significant effect on reducing the dimensions of the aggregates that formed. The mixture was then sieved through a 1.18 mm aperture sieve. The aggregates retained on the sieve were crushed with a mortar and sieved again. In this way, the required amount of kaolin aggregates were prepared and transferred to an air-tight plastic bag, which was then placed into an air-tight container. The mixture was kept in this air tight container for 1 week, in order to achieve moisture equilibrium.

6.2.2 Preparation of sample

Sivakumar (1993) prepared samples with different compaction techniques (static loading, dynamic loading and kneading) in order to investigate the repeatability of soil samples. Static compaction was found to be more reliable than the other methods. Several other researchers successfully employed the same method for preparing samples (e.g. Zakaria, 1995 and Sharma, 1998). It was therefore decided to follow the same method as employed by Sivakumar (1993) in this research.

Multi-layered samples were prepared by placing kaolin aggregates into a compaction mould and by one-dimensionally compacting using a triaxial frame. For triaxial samples, 9 layers of aggregates were used; each with a mass of about 33 g. After placement of each additional layer, the sample was monotonically loaded at an axial displacement rate of 1.5 mm/min until the axial stress reached 400 kPa. The surface of each compacted layer was scarified before adding a new layer, in order to reduce discontinuities between layers. For samples to be tested in the isotropic cell, the numbers of layers was reduced to 5, with each layer having a mass of about 30 g.

After compaction, the sample was removed from the compaction mould. The height of the sample was measured with a height gauge having an accuracy of 0.02 mm. Four measurements were taken to get the average height of the sample. Direct measurement of the sample diameter was found to be difficult and unreliable. It was therefore decided to measure the internal diameter of the compaction mould instead (ignoring any change of diameter on removal from the mould). Finally the mass of the sample was measured using an electric balance, with a precision of 0.01 g.

6.3 SETTING-UP PROCEDURE

6.3.1 Saturation of high air entry filter

High air entry ceramic filters, with a manufacturer's specified air entry value of 500 kPa, were used for both Systems A and B. The ceramic filters were required to be properly saturated prior to use, in order to achieve the manufacturer's specified air entry value. Placing in a de-aired water bath would not guarantee full saturation of the ceramic filter. It was therefore necessary to apply water pressure in order to force any trapped air bubbles into solution and then to have a flow across the ceramic filter, in order to remove the water containing dissolved air. For System A, the controlled-suction isotropic cell was used to saturate the high air entry filters. The advantage of this arrangement was that it was not necessary to dismantle the filter arrangement, meaning that there were no uncertainties of improper sealing between the pedestal or top cap and the filter holder. However, for System B using the controlled-suction triaxial cell to saturate the high air entry filters was found to be difficult and time-consuming because of the complexity and weight of the instrument (at least two persons were necessary to set up the equipment). It was therefore decided to develop a

saturation chamber that could accommodate both top and bottom filter arrangements. A further advantage of this arrangement was that the triaxial apparatus could be used efficiently, because a new experimental test could be started immediately after the end of the previous test, using filters already saturated in the saturation chamber.

The procedures followed to saturate the high air entry filters were as listed below:

- The top and bottom high air entry filter arrangements were mounted on the top cap and pedestal respectively.
- All the drainage lines were flushed with de-aired water in order to remove air bubbles. Great care was taken with the drainage lines through the top cap and pedestal as these lines had sharp edges and small diameter.
- The cell was assembled and filled with de-aired water. A cell pressure of 700 kPa was applied and maintained for two days. During this period no water flow was allowed through the high air entry filters by closing valves on the pore water drainage lines.
- With a back pressure of 600 kPa on the pore water drainage lines the valves on these lines were opened, so that flow occurred through the high air entry filters due to the pressure difference of 100 kPa. This situation was left for 24 hours.
- The pore water drainage line pressure was then reduced gradually to 50 kPa producing an increased flow rate, due to the pressure difference of 650 kPa.
- After few hours, the valve on the cell pressure line was closed, so that the cell pressure gradually decreased to 50 kPa as water leaked out through the high air entry filter.

6.3.2 De-airing procedure

Proper de-airing of drainage lines, cell and relevant associated instruments, such as volume gauge and CRSP was important in order for accurate measurement of volume changes and proper application of stresses. A Nold de-aerator was used to de-air the tap water used to fill the cell, drainage lines and associated instruments. The de-aerator consists of a sealed container, with a capacity of approximately 8.5 litres, a rotating disc attached to a motor at the bottom of the container and a vacuum pump. The

container was first partially filled with water and a vacuum pressure of about 97 kPa was applied to the top of the container. The disc at the bottom of container was rotated to promote cavitation and hence enhance the de-aeration process.

One hour was found to be sufficient to de-air the water. The disc motor was then switched off but the vacuum pressure was kept on the container for at least 24 hours before the de-aired water was used for filling the cell for an experimental test. This procedure allowed the de-aired water temperature to reach equilibrium with the laboratory temperature before the start of a test, so that there was no unwanted volume change during the initial part of the test as the temperature of the water changed.

6.3.3 Setting up procedure for System A

Initially, all drainage valves were closed and a smear of water was maintained on the surface of the high air entry filters. Silicon grease was used to fill the large O-rings grooves in both cell base and cell cover to minimise the trapping of air within the grooves during cell assembly. If the soil sample was placed directly on the high air entry filter, there was a risk that the high air entry filter would de-saturate because of the high value of as-compacted suction in the sample. To avoid this, two curved lengths of lead solder (each about 0.5 mm in diameter and 15 mm long) were placed on the surface of the bottom high air entry filter. The intention was that the lead solder would intrude in to the relatively soft soil sample when the cell pressure was applied, and only at this point would contact be achieved between the soil sample and the high air entry filter. This technique is usually called the “fuse wire technique” and was used by several previous researchers (e.g. Sivakumar, 1993 and Sharma, 1998). Lead solder was used here because it does not corrode to damage the surface of the high air entry ceramic filter. The calibration for the penetration of lead solder into the sample was not considered in the calculation of specific volume. The error in specific volume that corresponds to the penetration of lead solder is typically 0.0005 for a 50 mm diameter 50 mm height kaolin sample.

An air-dried low air entry filter, made of sintered brass, with annular shape was placed around the high air entry filter on the base pedestal. The soil sample was then placed on the bottom filter arrangement. Two more pieces of lead solder were placed on the top surface of sample followed by the top cap with top filter arrangement attached.

Using the membrane stretcher, the rubber membrane was placed around the sample and sealed with O-rings on the top cap and pedestal. Any excess length of membrane was removed using scissors, in order to minimise any air trapped between the membrane and the pedestal or top cap surfaces.

The cell wall was lowered into place and the cell cover was fixed in position using steel tie rods. The cell was then slowly filled with de-aired water. Once the cell was filled with water, the cell valve and air vent were closed. The cell and pore water drainage lines, including the IC volume gauges, were pressurised to 50 kPa and the volume gauge readings were reset to zero.

Pressures on the cell pressure line, pore air pressure line and pore water pressure line were brought to 20 kPa, 10 kPa and 10 kPa respectively. The cell pressure and pore air pressure valves were then opened simultaneously and then both pressures were raised at a relatively fast rate, using the control system and keeping the difference between them at 10 kPa until the air pressure reached 400 kPa. Once the air pressure reached the required value, the cell pressure was then increased by a further 20 kPa for a few minutes, to give a mean net stress of 30 kPa. This procedure ensured that the pieces of lead solder were pushed into the soil sample and proper contact between the sample and the high air entry filter was achieved. The cell pressure was then adjusted to give the required value of mean net stress for the initial equalisation stage (typically 10 kPa or 20 kPa).

Significant volume change was recorded by the IC volume gauge measuring the flow into the cell during the process of elevating the cell pressure to the targeted values for initial equalisation. Even after the calibration for expansion of the cell and connections was subtracted, 3-4 cm³ of remaining volume change was observed. In almost all cases, the initial mean net stress was much less than the expected yield stress at the as-compacted suction, and it was therefore likely that the actual volume change of the sample during application of the net stress was relatively small. It was believed that the unexpected measured volume change primarily occurred because of air trapped between the membrane and the sample was compressed and then pushed into the open structure of sample. This was further confirmed as this unexpected volume change almost doubled for System B, where the soil sample was 100 mm initial height, rather

than 50 mm. It was therefore decided to assume instead that there was no sample volume change during the application of net stress and the increase of cell pressure and pore air pressure. It was therefore assumed that the sample dimensions at this point were the same as those measured prior to mounting in the cell, and this became the starting point for the measurement of sample volume change.

The pressure on the pore water drainage line was increased to the required value (to give the desired value of suction for the initial equalisation stage). The valve on the pore water drainage line was then opened, to commence the initial equalisation stage (see Section 6.5.1)

6.3.4 Setting up procedure for System B

The set-up procedure for System B was similar to that for System A. However, there were some additional procedures, because this was a triaxial cell rather than an isotropic cell. After the cell wall was lowered into place, the cell cover, with Bishop-Wesley deviator loading assembly attached, was placed in position and fixed with the tie rods. The LVDT for measuring axial displacement was then mounted to the cross-beam attached to the piston of the Bishop-Wesley deviator loading assembly. After the required pressures were attained, the internal load cell was lowered to touch the top cap until a contact stress of 5 kPa was recorded. The zero reading of the LVDT was then recorded. The load cell was then elevated back to have a safe separation from the top cap. During any subsequent test stage that involved deviator loading the load cell was lowered again to contact the top cap. The change of height of the sample up to this point was calculated by comparing the new LVDT reading with the zero reading. This procedure was preferred rather than keeping a small deviator stress on the sample until the shear stage, as some tests involved very low suction (as low as 1 kPa) for the initial equalisation. Even a small deviator loading at this suction level might have caused unwanted plastic volumetric and shear strains.

6.3.5 Setting up procedure for System C

The pore water drainage lines were flushed with de-aired water in order to remove any air bubbles. All the drainage valves were then closed. A porous sintered brass disc of 50 mm diameter was placed on the pedestal and on top of that a filter paper was located in order to avoid smearing of the soil sample into the porous disc. The same

arrangement was adopted for the top of the sample. Once the sample was properly mounted, the triaxial cell was filled with water. A cell pressure of 20 kPa was applied and a pore water pressure of 10 kPa was applied to the bottom of the sample while the top drainage line was at atmospheric pressure, in order to allow a water flow through the sample. Once air flow through the top drainage line had stopped, and it was simply water flowing from the top of the sample, the same value of pore water pressure was applied to both top and bottom of the sample. The cell pressure and pore water pressure were then raised to the required values for the initial equalisation.

6.4 CONTROL STRATEGIES

In this section, the control strategies used in the Triax software to perform stress path tests are explained.

In the Triax software, the control for a stress path test can consist of many “stages”. Each stage represented a particular part of the full stress path (e.g. equalisation, isotropic loading, wetting, shearing, etc). Table 6-1 shows the configuration for a stage, with user input values in the Triax software for shear straining by wetting the sample (with the suction gradually reduced from 300 kPa to 50 kPa) while keeping deviator stress constant at 200 kPa. The Triax software can send signals to appropriate stepper motors in order to achieve a “target” value for the specified “control variable”. This control variable can be very simple, like the value of pore air pressure or can be much more complex, such as deviator stress. Calculation of the deviator stress requires the value of deviator load (from the load cell) but also the value of the cross-sectional area of the sample. Calculation of the cross-sectional area requires the initial sample volume, the change of sample volume (which involves the measured flow into the cell and the corrections for cell pressure, time (water diffusion through the tubing) and temperature), the initial sample height and the change of sample height (from the axial displacement LVDT). Hence, calculation of the current value of deviator stress within the Triax software requires the outputs from 6 transducers (load cell, IC volume gauge for flow into cell, net stress transducer, pore air pressure transducer (these two are summed to give cell pressure), thermocouple and LVDT), together with the relevant calibration equations. If the “increment rate” is specified as zero, then the target value will have constant value that is equal to the “initial value”, otherwise the target value

will be updated continuously according to the increment rate until the “hold value” is reached (see the control of suction in Table 6-1).

A tolerance can also be specified for the target values. For example, in Table 6-1 the tolerance for the pore air pressure was specified as ± 0.5 kPa. The Triax software would therefore not send any signal to the stepper motor controlling pore air pressure if the measured air pressure was within ± 0.5 kPa of the target value. If the measured value of pore air pressure differed by more than 10 times the specified tolerance from the target value then stepper motors would be instructed to operate at maximum pulse (20 steps in this example). The step changes were reduced linearly toward zero as the difference between the measured and target values varied from 10 times the tolerance to the tolerance value. This technique allowed the stress and strain variables to achieve their target values relatively rapidly whilst avoiding any overshooting of the control variable as it approached the target value.

Several “alarms” could be set in a stage so that once a particular condition was satisfied, the Triax software could be instructed to take a predefined “action”, which, for example, could be to move to the next stage, stop the test or wait for a specified duration before stopping the test or moving to the next stage.

| Stepper motor controller | <i>1 (cell pressure)</i> | <i>2 (pore air pressure)</i> | <i>3 (pore water pressure)</i> | <i>4 (CRSP)</i> |
|--------------------------------------|--------------------------|------------------------------|--------------------------------|-----------------|
| Status | ON | ON | ON | ON |
| Control variable | Radial net stress | Pore air pressure | Suction | Deviator stress |
| Initial Value | 75 kPa | 400 kPa | 300 kPa | 200 kPa |
| Tolerance | 0.5 kPa | 0.5 kPa | 0.5 kPa | 0.7 kPa |
| Increment rate and Hold value | 0 kPa/hr | 0 kPa/hr | -0.25 kPa/hr 50 kPa | 0 kPa/hr |
| Maximum pulses | 20 | 20 | 20 | 200 |
| | Condition | | Action | |
| Alarm | Displacement > 50 mm | | Stop | |

Table 6-1 Configuration for stage in stress path test in Triax software

6.5 STRESS PATH STAGES

A typical stress path performed on an unsaturated sample in System A or B consisted of several stages. In a typical stage, one or more specified variables were varied in a predefined fashion. This section describes some of the important stages involved in the stress path tests.

6.5.1 Initial equalisation

Each experimental test was started with an equalisation stage, with particular values of mean net stress and suction imposed on the sample. During the equalisation period (varying from 3 to 10 days depending on the value of suction imposed), the sample reached equilibrium at a specified stress state. A mean net stress of 10 kPa or 20 kPa was typically applied during initial equalisation, whereas suction varied from 1 to 350 kPa in different tests. In all cases, a water flow into the sample was observed, confirming that the as-compacted suction was higher than 350 kPa. Once the rate of sample volume change and pore water volume change were observed to be less than $0.05 \text{ cm}^3/\text{day}$, corresponding to a rate of change of v or v_w of $0.0004/\text{day}$ for a typical 50 mm diameter and 50 mm height sample, equalization was assumed to be complete.

6.5.2 Equalisation stages

After each stage that involved changes in the values of stresses, an equalisation stage was performed with constant values of suction and net stresses. During this stage changes in void ratio or water content might occur if the previous stage was performed at a rate that was slightly too fast for the response of the sample to be in continuous equilibrium in terms of stresses and strains. Rates of change of stresses, such as suction and net stresses, were therefore determined to reduce the changes in void ratio and water content within the subsequent equalisation stage to allowable values while keeping the time required for a typical test manageable. Equalisation stage time was typically 24 hours.

6.5.3 Isotropic loading and unloading

Isotropic loading and unloading (at constant or varying suction) were carried out by controlling the cell pressure. A rate of 2 kPa/hr on mean net stress was found to be adequate, by considering the response of the soil sample during the subsequent

equalisation stage (i.e. to attain reasonably small changes in void ratio and degree of saturation during the subsequent equalisation stage). In most tests, isotropic loading was carried out at constant suction, however, a few tests involved simultaneous changes of both mean net stress and suction (e.g. a stress path where sample volume was kept constant)

6.5.4 Wetting and drying

A rate of change of suction of 1 kPa/hr was employed in most wetting or drying stages, as this rate could provide reasonably small changes in void ratio and degree of saturation during subsequent equalisation stages. However, in some wetting stages, it was necessary to reduce the rate to as low as 0.25 kPa/hr in order to avoid large changes in void ratio and degree of saturation in the subsequent equalisation stage. This was particularly true in wetting stages where the suction was reduced below 30 kPa and where collapse compression was also occurring.

6.5.5 Shearing

Most of the samples tested in System B were subjected to a final constant suction or varying suction shearing stage. A constant axial displacement rate of 0.072 mm/hr was employed in these cases to give a stage duration similar to other stages.

6.5.6 Constant volume wetting and drying

One stress path test in the experimental programme involved wetting and drying stages whilst keeping the sample volume constant. Pore air pressure was kept constant throughout the test. The suction was varied in this test at 1 kPa/hr by varying the pore water pressure. Instantaneous sample volume change was calculated by the Triax software using the measured flow of water into the cell, together with temperature and cell pressure along with appropriate calibration equations. Any volume change occurring due to the suction change was counteracted by modifying the mean net stress by varying the cell pressure. For example, during suction increase (drying), the sample volume tended to reduce (shrinkage). In order to counteract the shrinkage, mean net stress was reduced by the control system. In these stages, the specific volume was held constant to an accuracy of ± 0.001 .

6.5.7 Constant degree of saturation wetting and drying

In one test, wetting and drying stages were performed whilst keeping the degree of saturation constant. Similar to constant volume wetting and drying stages, suction was varied at a specified rate while mean net stress was continuously adjusted by the control system to keep S_r constant. The value of S_r was held constant to an accuracy of ± 0.002 .

6.5.8 Stress path with constant deviator stress

In a few tests, the radial net stress or suction was varied while keeping the deviator stress q constant. The axial displacement was continuously adjusted by the control system (using the CRSP) in order to keep the deviator stress constant. The value of q was held constant to an accuracy of ± 0.7 kPa.

6.6 DATA PROCESSING

The Triax software can log selected variables at specified time intervals so that data can later be accessed for detailed interpretation of test results using software such as MS Excel or MATLAB. Time, radial net stress, pore air pressure, suction, flow of water into cell, flow of water into sample, load cell reading, axial displacement and temperature were logged at 30 minutes intervals. With this raw data, the values of deviator stress q , mean net stress \bar{p} , suction s , specific volume v , degree of saturation S_r , mean Bishop's stress p^* and modified suction s^* were calculated as shown below.

$$q = \frac{F}{(V_0 - \Delta V)} (H_0 - \Delta H) - 100 \frac{\Delta H}{H_0} q_{mem} \quad (6-1)$$

$$\bar{p} = (\sigma_3 - u_a) + \frac{q}{3} \quad (6-2)$$

$$s = u_a - u_w \quad (6-3)$$

$$v = \frac{\rho_w G_s (V_0 - \Delta V)}{M_s} \quad (6-4)$$

$$S_r = \frac{\frac{1}{\rho_w}(M_0 - M_s) - \Delta V_w}{(V_0 - \Delta V) - \frac{M_s}{\rho_w G_s}} \quad (6-5)$$

$$p^* = \bar{p} + S_r s \quad (6-6)$$

$$s^* = \frac{(v-1)}{v} s \quad (6-7)$$

where F is the deviator force, V_0 is the sample volume at the start of the stage, ΔV is reduction of the sample volume since the start of the stage, H_0 is the height of the sample at the start of the stage, ΔH is the axial displacement of the sample since the start of the stage, q_{mem} is the membrane correction for 1% axial strain, ρ_w is the density of water, G_s is the specific gravity of soil particles, M_0 is the mass of the sample at the start of the test, M_s is the mass of solids within the sample (measured after oven-drying at the end of the test), and ΔV_w is the reduction of pore water volume since the start of the test.

CHAPTER 7

INITIAL TEST RESULTS AND CALIBRATION OF MODELS

This chapter has two main sections. In the first section, initial conditions of the samples are presented in order to investigate the consistency of sample preparation and testing methods. In the second section, the values of the model parameters were determined for the compacted Speswhite Kaolin for the original Wheeler et al. (2003) model, the bounding surface plasticity version of the Wheeler et al. (2003) model and the BBM. This was done by analyzing the results from a small number of tests within the experimental programme. These three sets of model parameter values are then used in Chapters 8 and 9 to simulate the full set of experimental test results.

7.1 INITIAL CONDITIONS OF SAMPLES

As described in Section 6.2.2, all samples were one-dimensionally statically compacted at the same water content and with the same compaction pressure, with the intention of achieving the same initial specific volume, degree of saturation and suction in all samples. Each test or sample is named starting with a letter representing the system in which it was carried out (i.e. A, B or C) and then a number representing the order in which tests were carried out. For example Test A6 means that it was the sixth test carried out using System A. Samples tested in the triaxial cells of Systems B and C were 100 mm in height, whereas samples tested in the isotropic cell of System A were 50 mm in height.

Table 7-1 shows the details of values of specific volume, water content and degree of saturation immediately after compaction and after initial equalization, along with the time required for the full test. The initial conditions of samples equalised at the same suction were first grouped according to chronological order. These groups were then listed in Table 7-1 in descending order based on the initial value of suction imposed during equalization.

| Test No | After compaction | | | After equalization | | | | | Full test duration (days) | Remarks |
|---------|------------------|-------|--------------------|--|---------|--------|-------|--------------------|---------------------------|---------|
| | v | w (%) | S _r (%) | p-u _a or p-u _w (kPa) * | s (kPa) | v | w (%) | S _r (%) | | |
| A2 | 2.1194 | 24.25 | 57.40 | 20 | 350 | 2.1275 | 24.95 | 58.64 | 11 | § |
| A3 | 2.1364 | 24.46 | 57.05 | 20 | 350 | 2.1380 | 25.11 | 58.47 | 36 | |
| A9 | 2.1346 | 24.50 | 57.22 | 10 | 300 | 2.1469 | 25.96 | 59.99 | 50 | |
| A11 | 2.1508 | 24.04 | 55.37 | 10 | 300 | 2.1668 | 25.66 | 58.28 | 36 | |
| B4 | 2.1461 | 24.77 | 57.28 | 10 | 300 | 2.1501 | 26.17 | 60.30 | 25 | |
| B6 | 2.1442 | 24.98 | 57.85 | 10 | 300 | 2.1587 | 26.48 | 60.56 | 68 | |
| B8 | 2.1262 | 24.17 | 56.87 | 10 | 300 | 2.1236 | 25.12 | 59.24 | 22 | |
| B10 | 2.1544 | 23.92 | 54.91 | 10 | 300 | 2.1756 | 25.93 | 58.45 | 44 | |
| B1 | 2.1190 | 23.79 | 56.34 | 50 | 200 | 2.1218 | 27.05 | 63.89 | 14 | § |
| B3 | 2.1548 | 24.70 | 56.67 | 10 | 200 | 2.2000 | 28.72 | 63.43 | 24 | |
| A1 | 2.1226 | 24.23 | 57.19 | 20 | 150 | 2.1534 | 28.30 | 65.02 | 28 | |
| A4 | 2.1455 | 23.67 | 54.75 | 20 | 150 | 2.1746 | 28.13 | 63.46 | 31 | |
| B7 | 2.1523 | 24.46 | 56.25 | 10 | 100 | 2.2291 | 30.65 | 66.09 | 37 | |
| A6 | 2.1337 | 24.44 | 57.14 | 20 | 50 | 2.1988 | 32.07 | 70.89 | 54 | |
| A7 | 2.1324 | 24.90 | 58.26 | 20 | 50 | 2.1936 | 32.21 | 71.52 | 16 | § |
| A8 | 2.1503 | 24.64 | 56.76 | 20 | 50 | 2.2090 | 32.02 | 70.19 | 60 | |
| A5 | 2.1411 | 22.91 | 53.21 | 10 | 30 | 2.2454 | 33.40 | 71.06 | 43 | |
| B2 | 2.1589 | 24.37 | 55.73 | 10 | 30 | 2.2763 | 34.98 | 72.62 | 32 | |
| B5 | 2.1472 | 24.90 | 57.52 | 10 | 30 | 2.2752 | 34.80 | 72.31 | 44 | |
| A10 | 2.1320 | 24.48 | 57.31 | 10 | 1 | 2.2368 | 42.17 | 90.36 | 87 | |
| A12 | 2.1291 | 24.04 | 56.43 | 10 | 1 | 2.2427 | 42.41 | 90.43 | 75 | |
| B9 | 2.1523 | 24.46 | 56.25 | 10 | 1 | 2.2626 | 41.26 | 86.59 | 43 | |
| C1 | 2.1540 | 24.37 | 55.96 | 10* | 0 | 2.2178 | 45.15 | - | 20 | |
| C2 | 2.1576 | 24.20 | 55.41 | 10* | 0 | 2.1890 | 43.03 | - | 27 | |
| C3 | 2.1327 | 25.00 | 58.50 | 10* | 0 | 2.2018 | 43.78 | - | 29 | |

* : p-u_w is applicable for Series C

§ : Discontinued

Table 7-1 Specific volume, water content and degree of saturation values after compaction and after equalisation

The average specific volume, degree of saturation and water content of samples immediately after compaction were 2.141 ± 0.022 , $56.5\% \pm 3.3$ and $24.4\% \pm 1.4$.

These values were slightly different from the values ($v = 2.204$ and $S_r = 53.8\%$) reported by Sivakumar (1993). This deviation can be attributed to the use of a different batch of Speswhite Kaolin, and to the fact that a different compaction system was used and a different individual performed the sample preparation.

Figure 7-1 shows the variation of specific volume after compaction for samples. It can be seen that Series A had a slightly lower average specific volume than Series B and C. This is true even if Tests A1, A2, B1, B8 and C3 are ignored (these show large deviations from the rest of the values). This difference between Series A and Series B and C can be explained by the fact that samples (of approximately 50 mm height) in Series A were prepared with 5 layers (each involving 30.3g of material), whereas samples (of approximately 100 mm height) in Series B and C were prepared with 9 layers (each involving 33.5g of material). Each layer in Series A was therefore slightly smaller in height than each layer in Series B and C, and the compaction energy per unit volume was therefore slightly greater in Series A. The numbers of layers in this research for each series were selected to be consistent with previous research (Sivakumar, 1993 and Buisson, 2002). The difference in average specific volume between Series A and Series B and C is however around 0.01, which is sufficiently small to ignore any influence on the subsequent behaviour of the samples.

Figure 7-2 and Figure 7-3 show the degree of saturation and water content immediately after compaction. It can be noted that both curves follow a similar pattern, demonstrating that any variation of degree of saturation between samples (Figure 7-2) was mainly a consequence of variation of water content (Figure 7-3), rather than the result of any variation in specific volume (see Figure 7-1, where the shape is different). Samples A4 and A5 have unusually low compaction water content, possibly because of excessive moisture loss during the preparation of the samples or the previous preparation of aggregates.

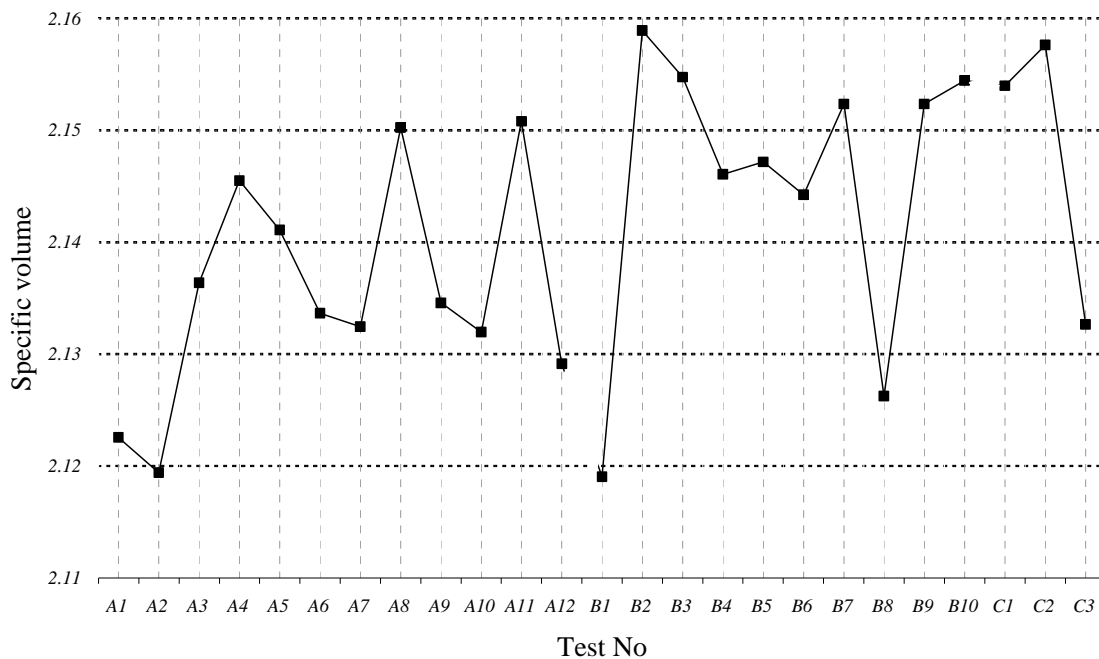


Figure 7-1 Variation of specific volume immediately after compaction

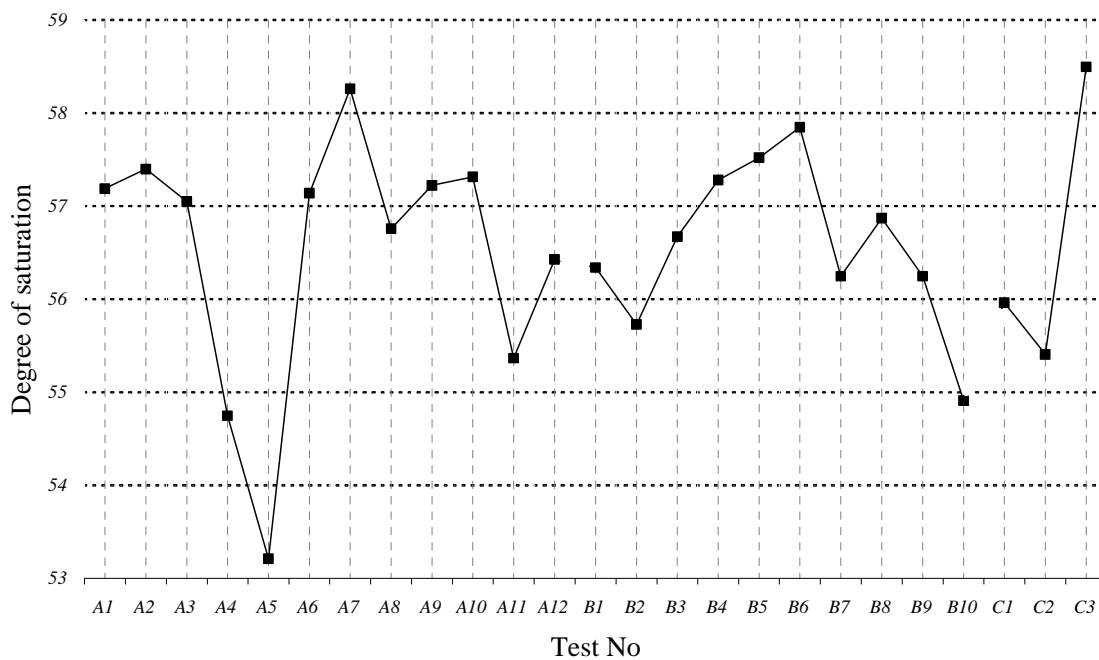


Figure 7-2 Variation of degree of saturation immediately after compaction

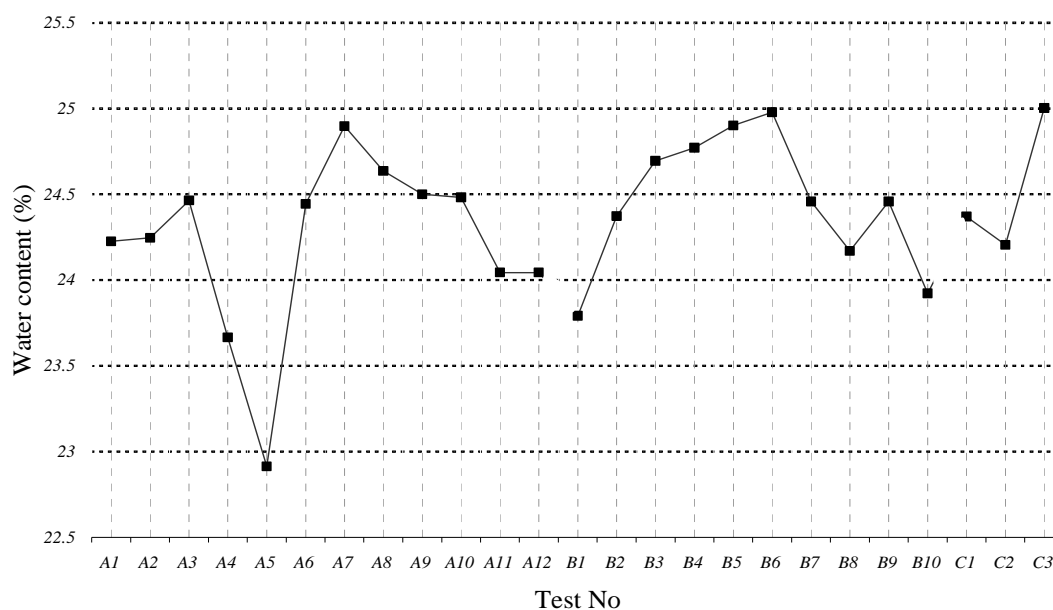


Figure 7-3 Variation of water content immediately after compaction

7.2 INITIAL EQUALISATION

During the initial equalisation, all samples showed an increase in water content (see Table 7-1), confirming that the value of suction immediately after compaction was higher than 350 kPa, which was the maximum value applied during equalisation. After equalisation, the specific volume varied from 2.127 (at $s = 350$ kPa) to 2.263 (at $s = 1$ kPa), the degree of saturation varied from 58.28 % (at $s = 300$ kPa) to 90.43% (at $s = 1$ kPa) and the water content varied from 24.95 % (at $s = 350$ kPa) to 45.15 % (at $s = 0$ kPa). It should be noted that the degree of saturation could not be measured in System C, as final sample volume was not known. However, it was assumed that samples in Series C were fully saturated, as they were flushed with water during setting-up (see Section 6.3.5).

All samples were equalised at a particular combination of mean net stress (10, 20 or 50 kPa) and suction (0, 1, 30, 50, 100, 150, 200, 300 or 350 kPa), see Table 7-1, before being subjected to subsequent stress paths. Most of the samples were equalised at a mean net stress of 10 kPa (14 tests) or 20 kPa (7 tests). Only the sample in Test B1 was equalised at a mean net stress of 50 kPa.

Figure 7-4, Figure 7-5 and Figure 7-6 show the increase in water content, degree of saturation and specific volume plotted against time during equalisation for the 7 samples tested in System A at a mean net stress of 20 kPa.

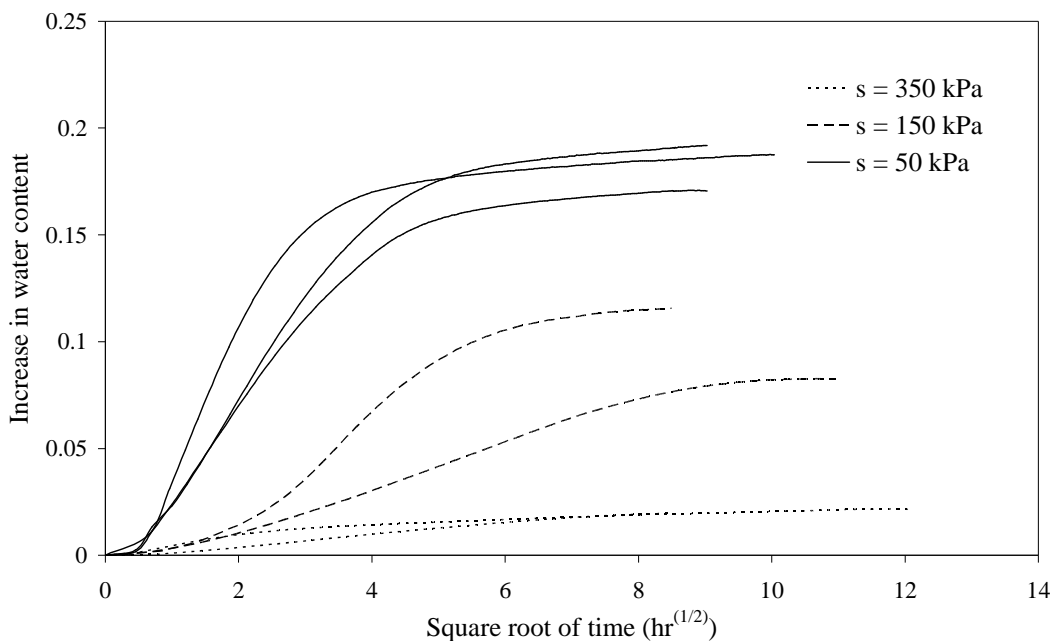


Figure 7-4 Increase in water content during equalisation at a mean net stress of 20 kPa (Series A)

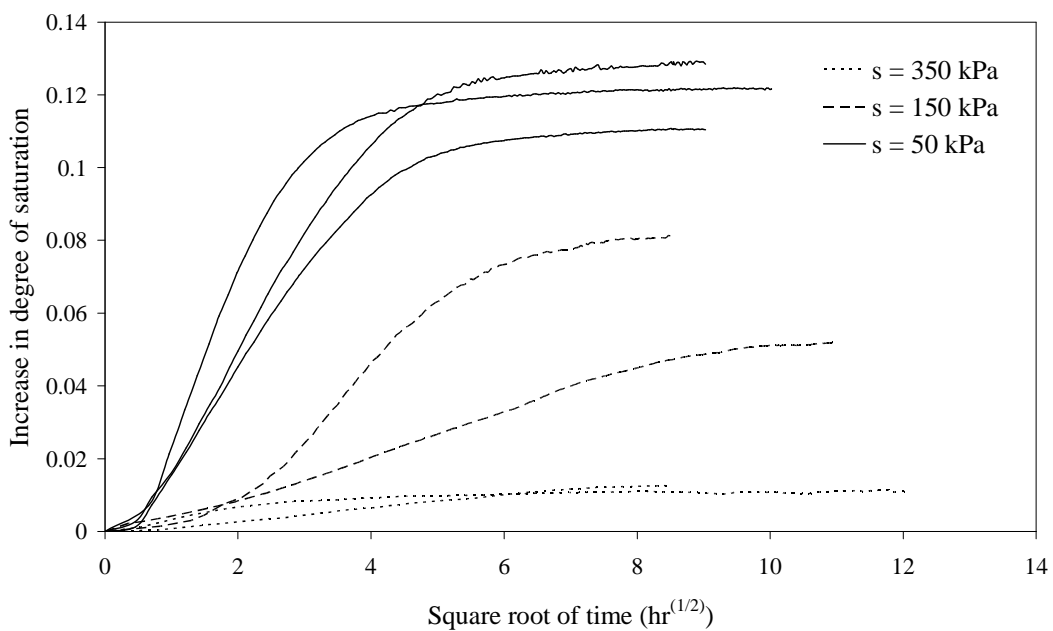


Figure 7-5 Increase in degree of saturation during equalisation at a mean net stress of 20 kPa (Series A)

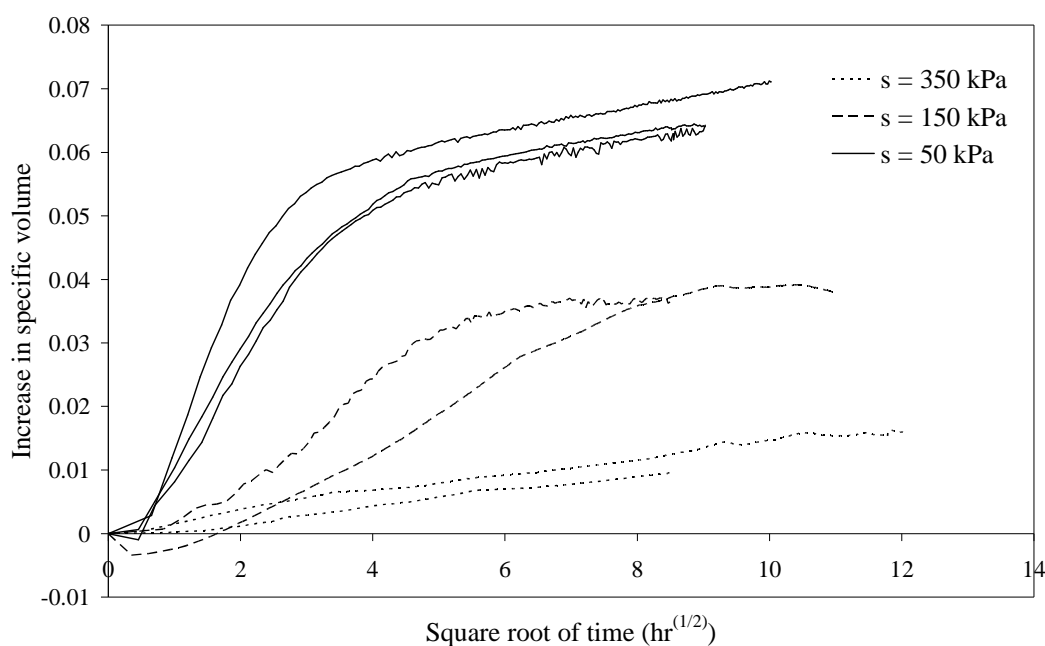


Figure 7-6 Increase in specific volume during equalisation at a mean net stress of 20 kPa (Series A)

The increases in w and S_r (see Figure 7-4 and Figure 7-5) suggest that the suction immediately after compaction was greater than 350 kPa. The two samples equalised at 150 kPa suction (Test A1 and A4) show significantly different changes in w and S_r during the equalisation (see Figure 7-4 and Figure 7-5). This is attributed to the fact that the initial values of w (23.67%) and S_r (0.5475) of Sample A4 were much lower than those of Sample A1 (24.23% and 0.5719 respectively). It can be seen from Table 7-1 that the values of w and S_r for these two samples were much more similar after equalisation than they were immediately after compaction. This observation suggests that any non-uniformity that occurred in the sample preparation was partially eliminated during subsequent equalisation.

Figure 7-7, Figure 7-8 and Figure 7-9 shows the changes in w , S_r and v plotted against time during equalisation at a mean net stress of 10 kPa. At 30 kPa suction the final changes of w and S_r of samples are slightly deviating from each other (see Figure 7-7 and Figure 7-8). This can once again be attributed to the differences in the values of w and S_r immediately after compaction (see Table 7-1).

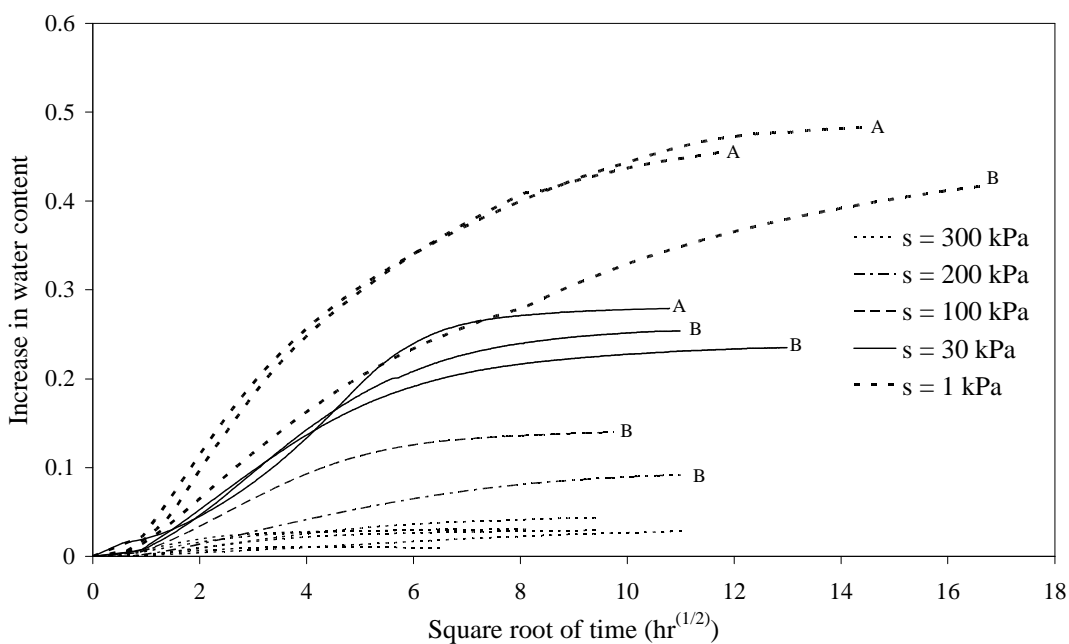


Figure 7-7 Increase in water content during equalisation at a mean net stress of 10 kPa (Series A and B)

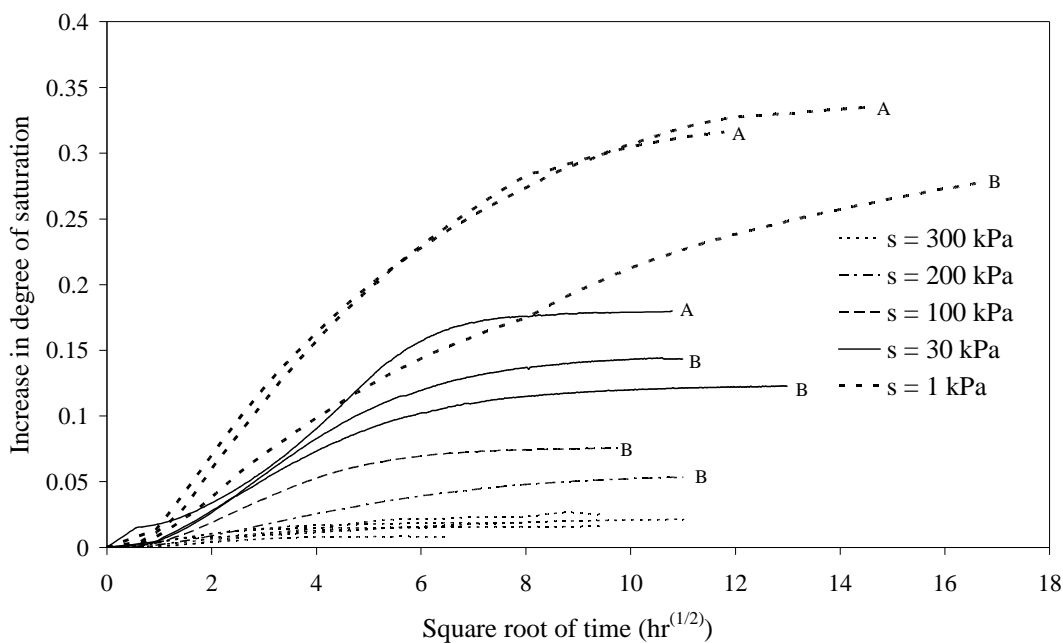


Figure 7-8 Increase in degree of saturation during equalisation at a mean net stress of 10 kPa (Series A indicated by "A" and Series B indicated by "B" where possible)

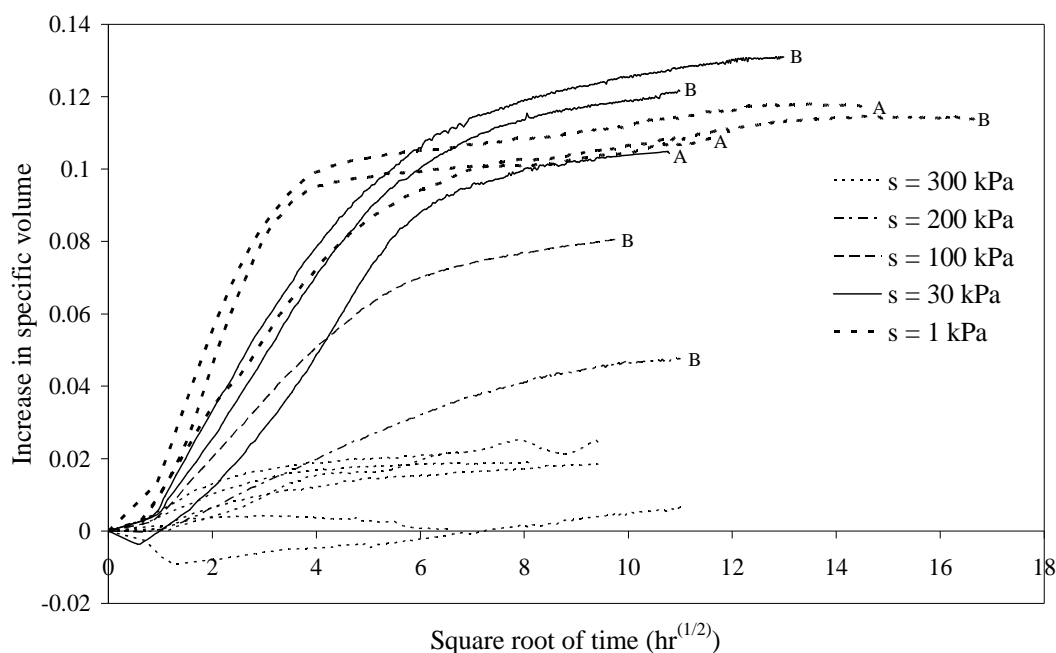


Figure 7-9 Increase in specific volume during equalisation at a mean net stress of 10 kPa (Series A indicated by “A” and Series B indicated by “B” where possible)

Three samples (A10, A12 and B9) were equalised at a suction of 1 kPa. It can be seen from Figure 7-7, Figure 7-8 and Figure 7-9 that two of these samples (A10 and A12) showed almost identical behaviour whereas Sample B9 showed smaller rates of change of w , S_r and v . This is presumably because Test B9 involved a larger sample (100 mm height) and therefore it required longer time for equalisation. It can be seen from Figure 7-8 that the degree of saturation in Test B9 might not have achieved a stable final value, and equalisation should perhaps have been continued slightly longer. It can be seen from Figure 7-9 that the final increase in specific volume for samples taken to a suction of 1 kPa was less than that for samples taken to a suction of 30 kPa. This observation suggests that in addition to elastic swelling during the equalisation, a small plastic compression (collapse compression) could have occurred for the samples equalised at 1 kPa suction.

Figure 7-10 and Figure 7-11 show the variation of water content and specific volume with suction for Series A and B after the initial equalisation. There is a suggestion that the samples equalised at a mean net stress of 20 kPa tend to have slightly lower water content and specific volume than the samples equalised at a mean net stress of 10 kPa, showing the influence of mean net stress. Inspection of Figure 7-11 also demonstrates

the wetting-induced swelling as suction is reduced from 350 kPa to 30 kPa. The slight reduction in specific volume when the suction is decreased from 30 kPa to 1 kPa suggests the possibility of a small amount of collapse compression (as discussed in the previous paragraph). It can also be observed that the scattering in the specific volume data is significantly greater than in the water content data. This is either because of difficulties in achieving accurate measurements of absolute values of specific volume or because differences in the initial values of specific volume immediately after compaction were not eradicated during equalisation as effectively as differences of water content.

No information relating to the equalisation stages in Series C was available, because a conventional triaxial apparatus was used to saturate the sample, with water inflow at the base and an unmeasured outflow of air and water from the top of the sample. During subsequent test stages, sample volume changes in System C were calculated based on the water inflow or outflow to the sample.

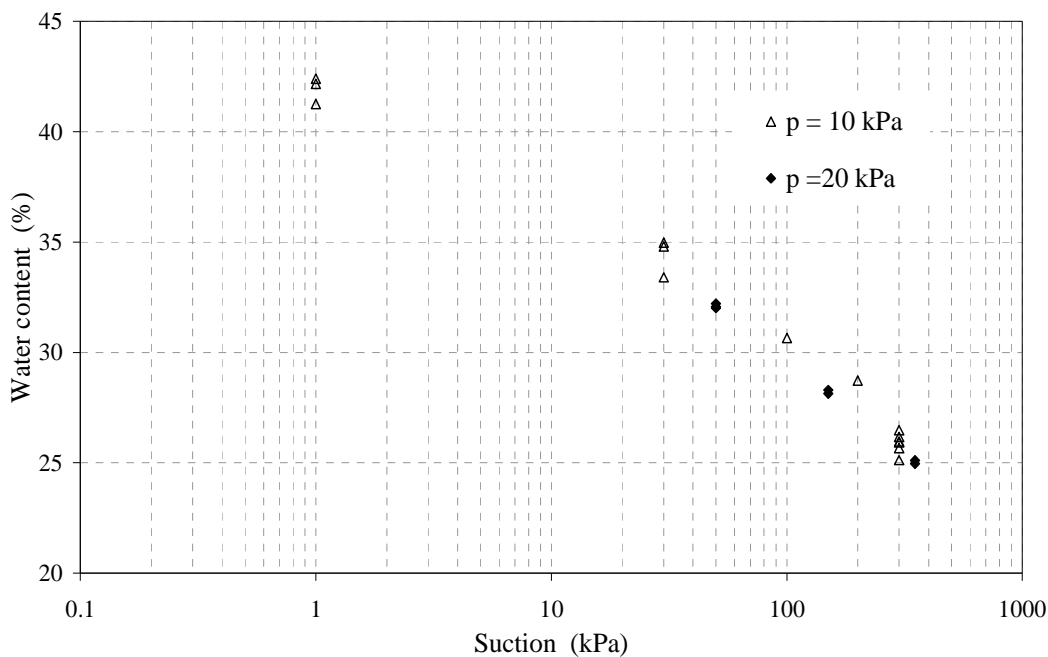


Figure 7-10 Variation of water content with suction after initial equalisation (Series A and B)

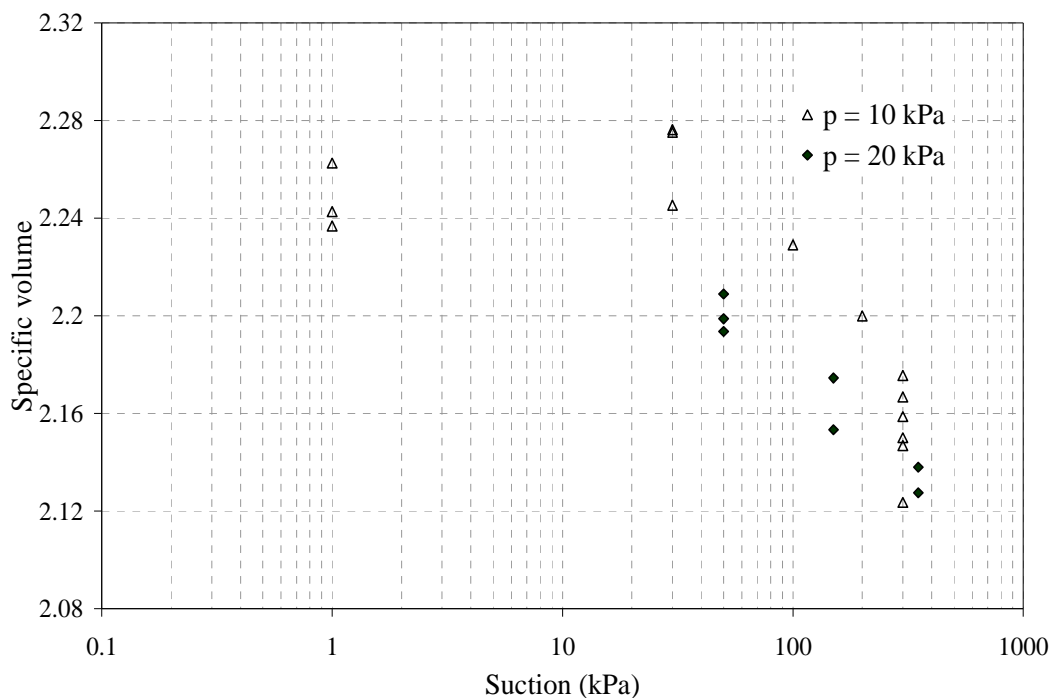


Figure 7-11 Variation of specific volume with suction after initial equalisation (Series A and B)

7.3 DETERMINATION OF BBM PARAMETER VALUES

This section describes the procedure employed to determine the BBM model parameter values, in order to subsequently perform simulations for comparison with experimental test results and Wheeler et al. (2003) model simulations. It was decided to select specific tests and results from selected stages of these tests were used to calculate the model parameter values. Tests A1, A3, A6, A11, A12, B1, C1, C2 and C3 were primarily used for this purpose. In order to calibrate the BBM and both elastoplastic and bounding surface plasticity versions of the Wheeler et al. (2003) model, some simple stress path tests were required, such as isotropic loading at different suctions (all the above tests), isotropic unloading (A1, A3 and A12), wetting and drying at constant mean net stress (A11 and A12) and shearing (C1, C2 and C3). In addition, an unusual stress path (A3) was useful in determining the value of one of the coupling parameters in the Wheeler et al. (2003) model. The above combination of tests was found to be adequate and optimum in order to determine most of the parameter values. However, determination of some parameter values, such as elastic shear modulus G and critical state parameters, required small portions of additional tests. The determination of values of critical state parameters was found to be difficult

with the author's limited experimental results on shearing to failure. It was therefore decided to also use some of the experimental results from Sivakumar (1993).

7.3.1 Parameters related to elastic behaviour of BBM model

The BBM includes three elastic parameters: elastic swelling index for changes in mean net stress, κ ; elastic swelling index for changes in suction, κ_s ; and elastic shear modulus G .

The value of κ can be calculated either from the elastic (initial) part of isotropic loading or from the elastic swelling during unloading. The former approach was found to be difficult and less reliable, because most of the experimental results showed non-linear pre-yield behaviour (when presented in a semi-logarithmic plot) during first isotropic loading, particularly at higher suction values. It was therefore difficult to identify the gradient of the elastic part of the curve. However, isotropic unloading seemed to show almost constant and consistent gradient, in the appropriate semi-logarithmic plot, in most of the tests. It was therefore decided to use all the tests involving isotropic unloading (A1, A9, A10 and A12) in order to calculate an average value for κ (see Figure 7-12). The calculated value for κ was 0.02.

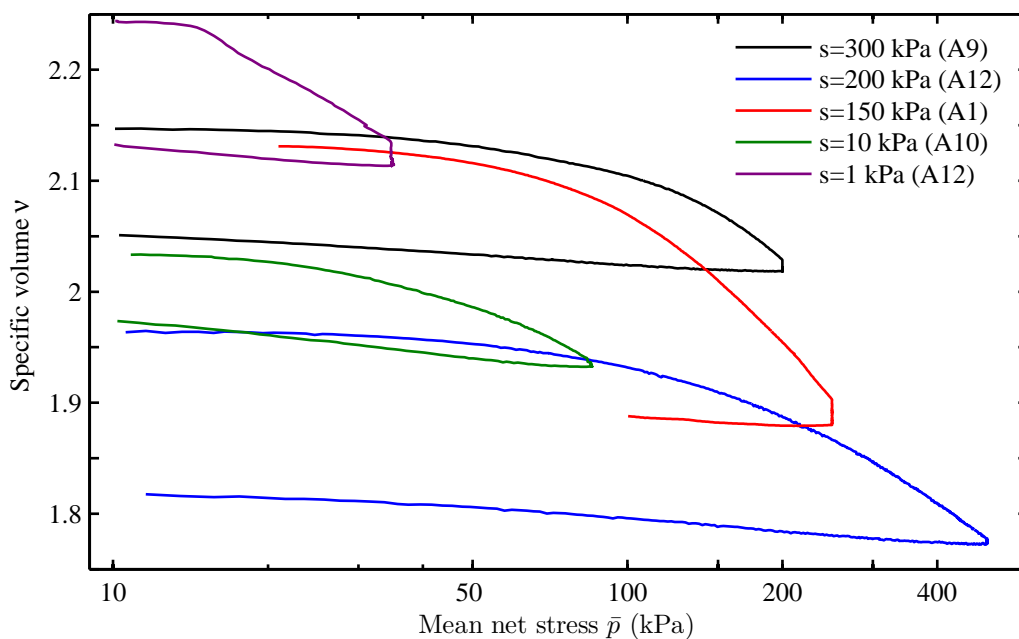


Figure 7-12 Compression curves and swell-back lines during isotropic unloading stages at different values of suctions for Tests A1, A9, A10 and A12

The value of the elastic parameter κ_s was calculated using the information from the equalisation stages of Tests A9, A10, A11, A12, B2, B3, B4, B5, B6, B8, B9 and B10 (all conducted at a mean net stress of 10 kPa). In all tests, no apparent collapse compression was observed during equalisation, meaning that the stress paths remained inside the LC yield curve. It was therefore possible to consider any swelling during equalisation as elastic behaviour. By taking the average value of v at $\bar{p}=10$ kPa and $s=300$ kPa (from initial equalisation stages of Tests A9, A11, B4, B6, B8 and B10) as a starting point and considering the wetting to a specified lower suction (200, 30 or 1 kPa) in each of the other tests it was possible to calculate a value of κ_s using Equation 2-16 for each of these equalisation stages. An average value of $\kappa_s = 0.03$ was then selected. The tests where the samples were equalised at a mean net stress of 20 kPa were not considered in the evaluation of κ_s due to concern about the reliability of the starting value of specific volume at $\bar{p}=20$ kPa and $s=300$ kPa (only two tests were available to determine this value).

All the samples tested in System B except for Sample B7 showed no apparent plastic straining prior to the first shearing stage, suggesting that for the remaining samples the stress point was inside the LC yield curve at the start of the shearing stage. From these tests, an average value for elastic shear modulus G was calculated from the initial gradients of the plots of deviator stress against shear strain (at different value of initial suction and mean net stress). An average value of $G = 3$ MPa was obtained.

7.3.2 Parameters related to isotropic normal compression lines and LC yield curve

In the BBM, a specific equation has been proposed to describe the variation with suction of the slope of isotropic normal compression lines in the $v : \bar{p}$ plane (see Equation 2-15). This equation involves the model constants $\lambda(0)$, r and β . In addition, an equation has also been derived for the shape of LC yield curve, with a critical assumption that the LC yield curve is a vertical line in the $s : \bar{p}$ plane when the isotropic yield stress at zero suction $p_o(0)$ has a value equal to a reference pressure p^c , which is a model constant (see Equation 2-17). These two equations (Equations 2-17 and 2-15) along with the value of $N(0)$ (the intercept of the normal compression

line for zero suction at $\bar{p} = p^c$) determine the forms of the normal compression lines for different values of suction. It was therefore required to determine the values of the parameters $N(0)$, $\lambda(0)$, r , β and p^c for compacted Speswhite Kaolin, in order for the model to correctly capture the positions and slopes of the normal compression lines. Gallipoli et al. (2002) discussed in detail the influence of the parameters r , β and p^c on the shape of the LC yield curve as it expands and the characteristics of the normal compression lines. It is also necessary to specify an initial value for $p_0(0)$, defining the initial position of the LC yield curve. As an alternative to a specifying a value for $N(0)$, it is possible to instead give an initial value of specific volume at specified values of mean net stress and suction.

Gallipoli et al. (2002) showed that the BBM could be used to model situations where the slope of the normal compression lines increased with increasing suction ($r > 1$), in addition to situations where the slope decreased with increasing suction ($r < 1$) as envisaged by the original authors of the BBM. For the slope of the normal compression lines to increase with increasing suction, the parameter r should be greater than 1 and the value of p^c should be significantly higher than the highest value of \bar{p} envisaged in an analysis in order to avoid unrealistic shapes of the LC yield curve. Researchers such as Sivakumar (1993) and Sivakumar (2007) often observed experimental variation of slopes of normal compression lines consistent with $r > 1$.

Figure 7-13 shows the isotropic compression curves in the $v : \bar{p}$ plane for samples which were subjected to isotropic compression at different values of suction. All the samples except A11 were isotropically loaded after the initial equalisation, while Sample A11 was first wetted from $s = 300$ to $s = 10$ kPa and then dried again to $s = 300$ kPa before being isotropically compressed. During the wetting of Sample A11, a small amount of swelling was observed, suggesting that the stress path was inside the LC yield curve according to the BBM. However, a higher reduction in specific volume occurred during the subsequent drying, leading to a net reduction in specific volume after the wetting and drying cycle (this could not be predicted by the BBM). It can be clearly seen from Figure 7-13 that each sample started to yield as the mean net stress

was increased. The isotropic yield stress increased with increasing suction, consistent with behaviour reported by previous researchers and with BBM predictions.

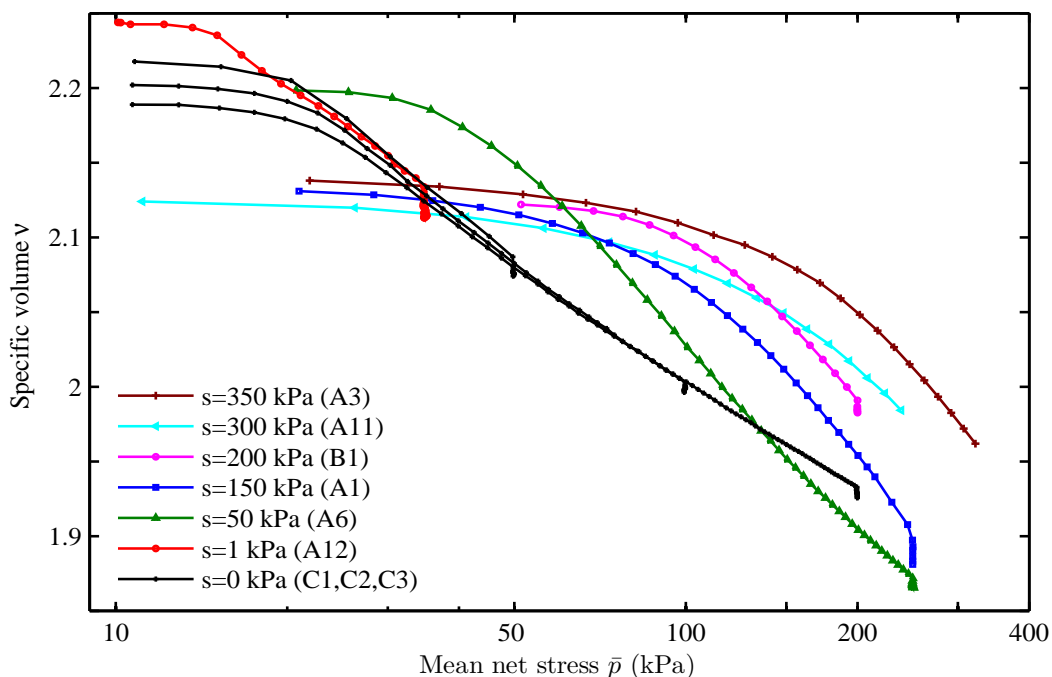


Figure 7-13 Isotropic compression curves of selected tests for the model calibration

In order to select best-fit values for the BBM model parameter values $\lambda(0)$, r , β , p^c , $N(0)$ and the initial value of $p_0(0)$, three aspects of the experimental isotropic compression curves shown in Figure 7-13 had to be considered:

- the observed variation with suction of the slope $\lambda(s)$ of the isotropic normal compression lines (this is controlled in the BBM by the values of $\lambda(0)$, r and β);
- the observed variation with suction of the isotropic yield stress \bar{p}_0 (this is controlled in the BBM by the current (i.e. initial) value of $p_0(0)$ and by the values of $\lambda(0)$, r , β and p^c);
- the observed positions of the normal compression lines for different values of suction (this is controlled in the BBM by the values of $N(0)$, $\lambda(0)$, r , β and p^c).

In the above three aspects, the positions of the experimental normal compression lines are typically not measured as reliably as the shapes (i.e. slopes and yield points) of the normal compression lines, because the absolute values of v are measured with less accuracy than changes of v . Also, the position of normal compression lines for $s = 0$ kPa was inconsistent with those of normal compression lines for other suction values, as this saturated normal compression lines crossed over the normal compression line for $s = 50$ kPa. This was possibly due to a difference between System C and Systems A and B. It was therefore decided to give more weight to the variation of the slopes of normal compression lines and the variation of yield stress with suction than to the positions of the normal compression lines, in determining values of $\lambda(0)$, r , β and p^c and the initial value of $p_0(0)$. The positions of normal compression lines were used only for selection of $N(0)$.

Figure 7-14 and Figure 7-15 shows the variation of $\lambda(s)$ and isotropic yield stress respectively (immediately after compaction) with suction for the compacted Speswhite Kaolin samples tested in the current research programme (along with the selected best fit for the BBM) and experimental results of Wheeler & Sivakumar (1995). The experimental variations of $\lambda(s)$ and isotropic yield stress from the current research shows similar trends to those from Wheeler and Sivakumar (1995), particularly the variation of yield stress, defining the LC yield curve, where the current results and those from Wheeler and Sivakumar (1995) are almost coincident. This observation suggests that the properties such as initial conditions (just after compaction) of soil samples prepared by the author and by Sivakumar (1993) were quite similar.

The experimental variation of $\lambda(s)$ with suction (see Figure 7-14) from the current research programme shows a sharp increase of $\lambda(s)$ as suction increases from zero to about 150 kPa and then a modest decrease of $\lambda(s)$ as suction is increased further (the results from Wheeler & Sivakumar (1995) showed a similar trend). This variation can not be fitted precisely with the BBM expression for the variation of $\lambda(s)$ with suction (Equation 2-15). The selection of values for $\lambda(0)$, r , β , p^c and $p_0(0)$ was therefore based upon achieving a good match to the initial shape of the LC yield curve (see Figure 7-15) while also achieving a reasonable match to the variation of $\lambda(s)$ with

suction (see Figure 7-14). The values of $\lambda(0)$, r , β , p^c and $p_0(0)$ are tabulated in Table 7-2. As a consequence of this selection procedure, the value determined for $\lambda(0)$ was slightly bigger than that obtained from the slope of the saturated normal compression line. In addition, the initial value of $p_0(0)$ was selected as the observed yield stress at a suction of 1 kPa (from Test A12), assuming that this low suction value would reasonably represent the situation at zero suction. Saturated samples were not used to determine the value of $p_0(0)$, because there was a suggestion of a small amount of collapse compression during equalisation of saturated samples. This was confirmed by comparing the yield stress at suction of 0 kPa and 1 kPa (see Figure 7-13).

The value of $N(0)$ was then selected by optimising the match of positions of normal compression lines at different suctions (largely ignoring results at $s = 0$ kPa). In Table 7-2, results are shown not as a value for $N(0)$ but instead as an initial value of v at specified values of \bar{p} and s (10 kPa and 300 kPa respectively) in order for consistency with the Wheeler et al. (2003) model (see Section 7.4).

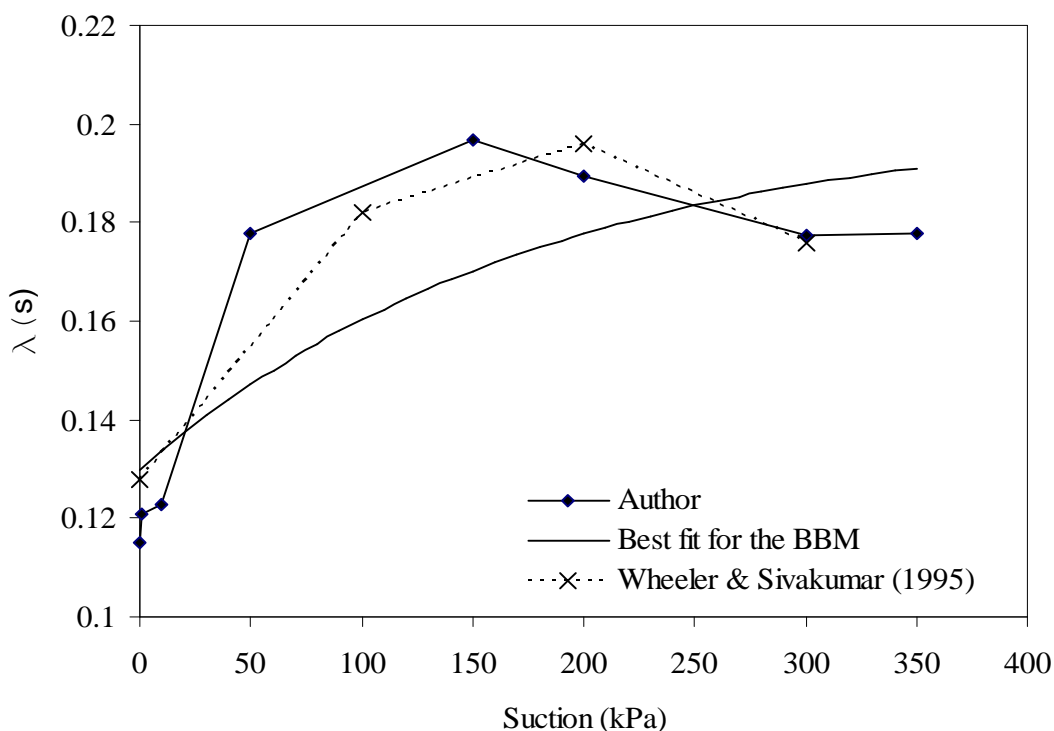


Figure 7-14 Variation of $\lambda(s)$ with suction for Speswhite Kaolin samples tested by the author, and by Wheeler & Sivakumar (1995)

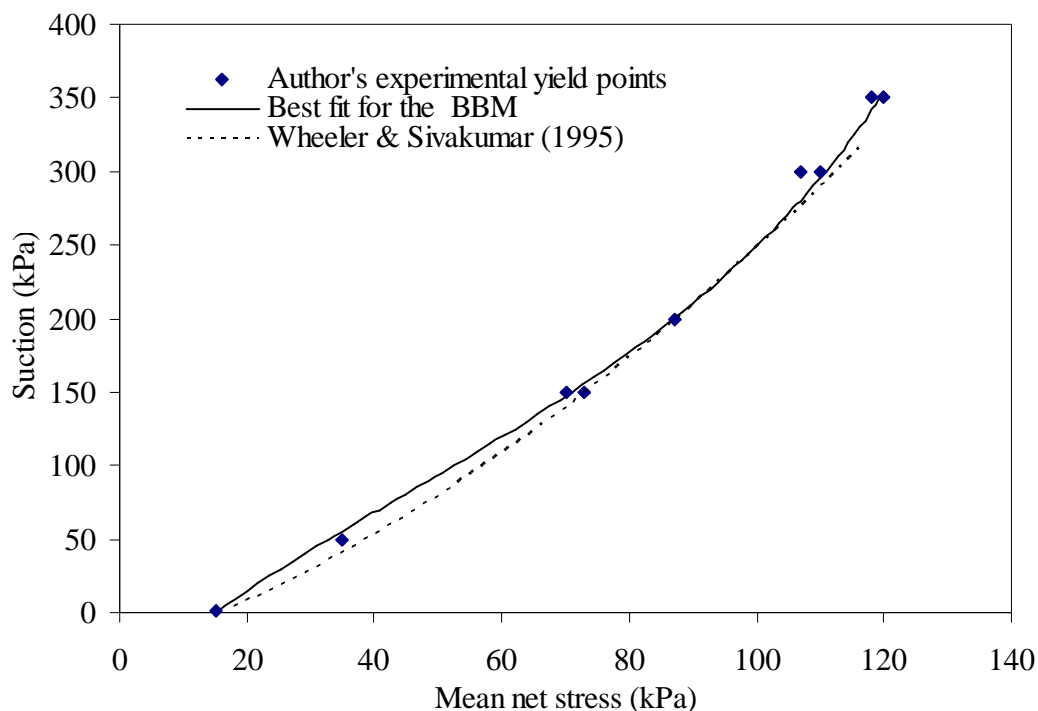


Figure 7-15 LC yield points for the samples tested by author along with best fit BBM yield curve and experimental yield curve of Wheeler & Sivakumar (1995)

| BBM model parameters | | Values (current research) | Values (Gallipoli, 2000) |
|---------------------------|---|----------------------------|---------------------------|
| <i>Soil constants</i> | G | 3000 kPa | 10000 kPa |
| | κ | 0.02 | 0.025 |
| | κ_s | 0.03 | 0.02 |
| | p^c | 5000 kPa | 2000 kPa |
| | $\lambda(0)$ | 0.13 | 0.13 |
| | r | 1.55 | 1.5 |
| | β | 0.0055 kPa ⁻¹ | 0.01 kPa ⁻¹ |
| | M | 0.889 | 0.9 |
| <i>Initial conditions</i> | $p_o(0)$ | 15 kPa | 18 kPa |
| | v at $\bar{p} = 10$ kPa and $s = 300$ kPa | 2.153 | 2.319 |

Table 7-2 Values of BBM model parameters determined from the current test programme and values proposed by Gallipoli (2000) for Sivakumar (1993) test results.

Figure 7-16 shows the experimental isotropic compression curves in the $v : \bar{p}$ plane for samples which were subjected to isotropic compression at different values of

suction along with the BBM predictions using the parameter values from Table 7-2. It can be noted that the slopes and isotropic yield stresses were predicted by the BBM with reasonable accuracy, but the positions of the normal compression curves were often poorly predicted by the BBM. This is because less importance was given to the positions of the normal compression lines than to the slopes of the lines and the initial shape of the LC yield curve in the determination of parameter values for the BBM.

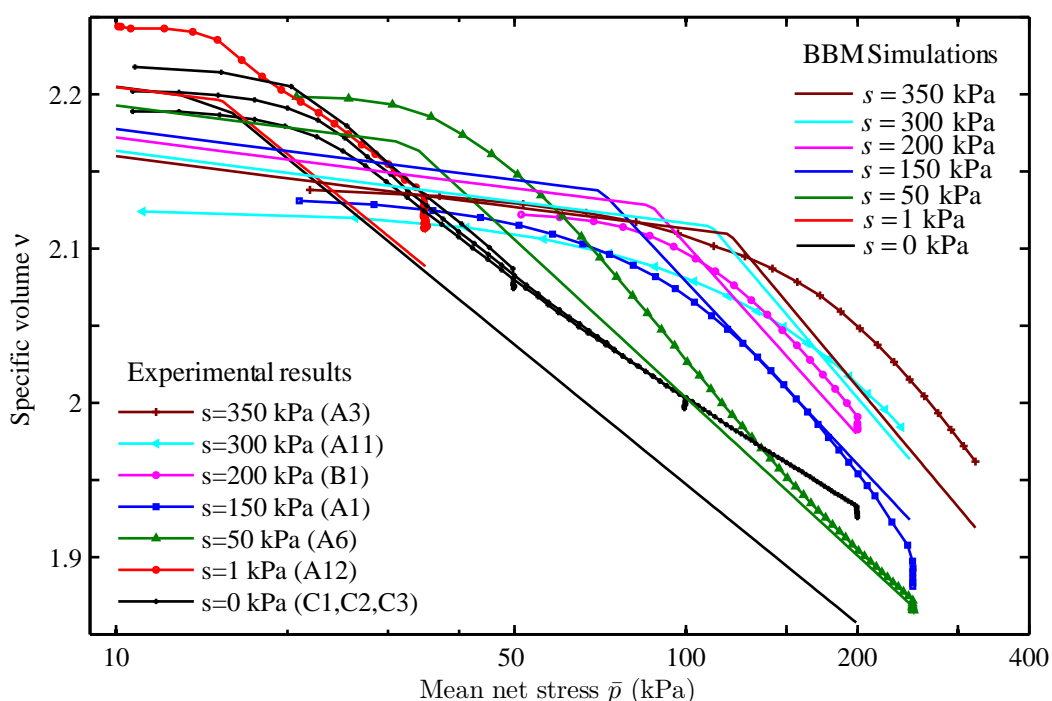


Figure 7-16 Isotropic compression curves of selected tests along with the BBM predictions

7.3.3 Parameters related to shear strength

The selection of values for the parameters M and k is discussed in this section, where M is the slope of the critical state lines for different values of suction in the $q : \bar{p}$ plot and k is the parameter controlling the variation of the cohesion intercept with suction. In the BBM model, M and k are constants, meaning that the shear strength of unsaturated soil is modelled as varying linearly with mean net stress and suction.

In this research programme, samples were sheared at suction values of 0, 200 and 300 kPa. For the $s = 200$ and 300 kPa cases, all samples were sheared at the same constant radial net stress of 75 kPa. It was therefore not possible to determine a value for the parameter M at these suction levels. However, three saturated samples were sheared at

constant radial effective stresses of 50, 100 and 200 kPa. It was therefore decided to compare the critical state data from Sivakumar (1993) with the current research data in order to determine the values for parameters M and k .

Figure 7-17 shows the critical state points for suction values of 0, 100, 200 and 300 kPa with best fit for critical state lines for Sivakumar (1993) data and current research data. Sivakumar (1993) data points are indicated by open-markers and respective best fits for the critical state lines are plotted as dashed lines while data points from the current research are shown by solid markers and the best fit line at zero suction with a solid line. The slope of the saturated critical state line was calculated as 0.889 from the current data, which is slightly larger than the saturated slope of 0.813 determined by Sivakumar (1993). Sivakumar (1993) also reported different values for M at different suction levels, varying from 0.813 to 0.959. However, with additional subsequent experimental evidence, Wheeler & Sivakumar (2000) concluded that the variation of M values for suctions between 0 and 300 kPa was insignificant and an average value of 0.863 was suggested. For the simulations in this work, it was therefore decided to use the M value for saturated soils (0.889) for all values of suction, as this value is close to the average value of M suggested by Wheeler & Sivakumar (2000).

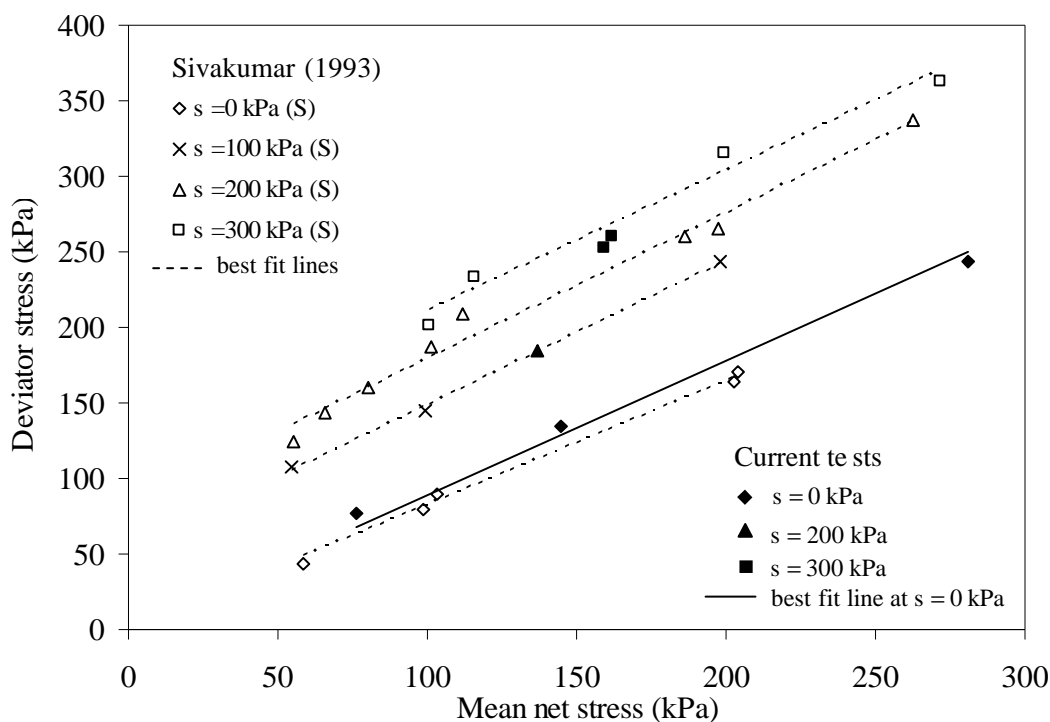


Figure 7-17 Critical state points and best fit lines for Sivakumar (1993) data and current experimental results.

The parameter k in the BBM controls the relative positions of the critical state lines for different values of suction in the $q : \bar{p}$ plane. By investigating Figure 7-17, the critical state points obtained in the current research for suction values of 0 and 300 kPa agree with the Sivakumar (1993) results. However, the two critical state points at $s = 200$ kPa (which are coincident with each other, and therefore appear as a single point in Figure 7-17) are located well below the critical state line for $s = 200$ kPa found by Sivakumar (1993). This could be partially due to the uncertainty in the failure mode observed in samples tested at 200 kPa suction (i.e. concern for a buckling failure). This issue will be discussed in detail in Section 9.2.1. Hence, it was decided to ignore the critical state points at 200 kPa suction and to use 0.5 for the value of k , which was suggested by Gallipoli (2000) for the Sivakumar (1993) test data.

The model parameter values for the BBM determined in this section for the current tests on compacted Speswhite Kaolin are tabulated in Table 7-2. Also shown in Table 7-2 are the corresponding BBM parameter values suggested by Gallipoli (2000) for the tests on compacted Speswhite Kaolin of Sivakumar (1993). Significant differences in the values of G , p^c and β can be observed when comparing the two sets of parameter. Many of these differences are attributed to differences in the interpretation as much as to differences in the experimental data.

7.4 DETERMINATION OF WHEELER ET AL. (2003) MODEL PARAMETER VALUES

This section presents the procedures and experimental test results involved with the determination of parameter values for the Wheeler et al. (2003) model. The same set of experimental test results as was used for determination of the BBM parameter values was utilized again, so that an unbiased estimation of parameters for both models could be ensured.

Table 7-3 shows the values of parameters and initial conditions determined in this exercise. The procedures for the estimation of parameter values are discussed in the subsequent sections of this chapter.

| Wheeler et al. (2003) model parameters | | Values |
|--|---|----------|
| <i>Soil constants</i> | κ | 0.02 |
| | κ_s | 0.006 |
| | λ | 0.115 |
| | λ_s | 0.055 |
| | k_1 | 0.63 |
| | k_2 | 1.05 |
| | G | 3000 kPa |
| | M^* | 0.72 |
| Initial conditions | s_D^* | 185 kPa |
| | s_I^* | 280 kPa |
| | p_0^* | 280 kPa |
| | v at $\bar{p} = 10$ kPa and $s = 300$ kPa | 2.153 |
| | S_r at $\bar{p} = 10$ kPa and $s = 300$ kPa | 0.592 |

Table 7-3 Model parameter values and initial conditions for Wheeler et al. (2003) model

7.4.1 Parameters of mechanical behaviour for isotropic stress states (κ and λ)

The value of elastic swelling index for changes in mean Bishop's stress κ was determined from the swelling lines plotted in the $v : p^*$ plane for Tests A1, A9, A10 and A12. An average value of 0.02 for the slope of the swelling lines κ was determined. The value of λ was determined using the experimental results from saturated soils. An average value of 0.115 for the parameter λ was selected based on the slopes of the normal compression lines in the $v : p'$ plane during the isotropic loading in the saturated tests C1, C2 and C3 shown in Figure 7-13. It can be noted that the value of the slope $\lambda(0)$ of the normal compression line for saturated soil determined for the BBM was 0.13 (see Section 7.3.2), which is higher than the value of λ selected for the Wheeler et al. (2003) model. In the BBM parameter determination, the selected value of $\lambda(0)$ involved a compromise to get a better representation of the variation of $\lambda(s)$ with suction (see Figure 7-14).

7.4.2 Parameters related to water retention behaviour (κ_s and λ_s)

The Wheeler et al. (2003) model involves a gradient λ_s of main wetting or drying curves in the $S_r : \ln s^*$ plane and a gradient κ_s of elastic scanning paths in the same plot (see Figure 3-10). The value of the parameter λ_s can be determined from a wetting path or a drying path, which corresponds to a stress path yielding on the SD or SI yield curve respectively (but without simultaneously yielding on the LC curve). However, in the light of the experimental results, it was often found that wetting or drying curves not only had different slopes in the $S_r : \ln s^*$ plane but also that the slopes varied dramatically with the level of degree of saturation. At higher degree of saturation (approximately $S_r > 0.85$), exceptionally low and high gradients of wetting curves and drying curves were observed respectively. During wetting at high degrees of saturation, gradients in the range of 0.01-0.02 were often found. This low apparent gradient could be associated with the occurrence of occluded air bubbles within the soil, making it difficult to increase the degree of saturation to a fully saturated state, without waiting for extremely long times (to allow diffusion of air in solution from occluded air bubbles). On the other hand, drying from very low suctions (around 1 kPa) showed significant reductions in S_r , leading to exceptionally high gradients, in the range of 0.09-0.10. This was thought to be because of emptying of macro-voids filled with water. These issues will be discussed further along with the experimental results in Chapter 8. From the above discussion, it is clear that these two cases are associated with special phenomena that can not be taken into account by the Wheeler et al. (2003) model. It was therefore decided not to consider these test results to determine the value of λ_s .

Main wetting paths were used in order to calculate the value λ_s . The values of S_r and s^* at the end of the initial equalisation stages from Tests A1, A3, A6, A11, A12 and B1 are plotted in Figure 7-18. Test A11 has two points in the figure, one during the initial equalisation at $s = 300$ kPa and another at $s = 10$ kPa after a wetting path from $s = 300$ kPa. It was assumed that all these points lie on a single main wetting line. This implies that these stress points were assumed to lie on the SD yield curve as far as the Wheeler et al. (2003) model is concerned. This assumption is supported by the

variation of S_r with suction for Test A11, as shown in Figure 7-19, in which sample was first equalised at $s=300$ kPa and $\bar{p}=10$ kPa and then wetted at constant mean net stress to $s=10$ kPa ($A-B$) before drying back to $s=300$ kPa ($B-C$). It can be seen that the wetting curve has a single gradient, suggesting that plastic changes of S_r occurred on the SD yield curve right from the beginning of wetting.

A gradient of $\lambda_s = 0.055$ was obtained from Figure 7-18 for the wetting points from different tests, which was consistent with the gradient of $\lambda_s = 0.05$ obtained from Figure 7-19 for the single wetting path. The gradients of main drying curves were often found to be less than the gradients of main wetting curves. However, according to the Wheeler et al. (2003) model, many drying paths would be expected to involve simultaneous yielding on the LC yield curve as well as the SI yield curve, and this would produce a gradient less than λ_s . Drying curves were therefore not used to determine a value of λ_s . The value of $\lambda_s = 0.055$ obtained from Figure 7-18 was used for all test simulations.

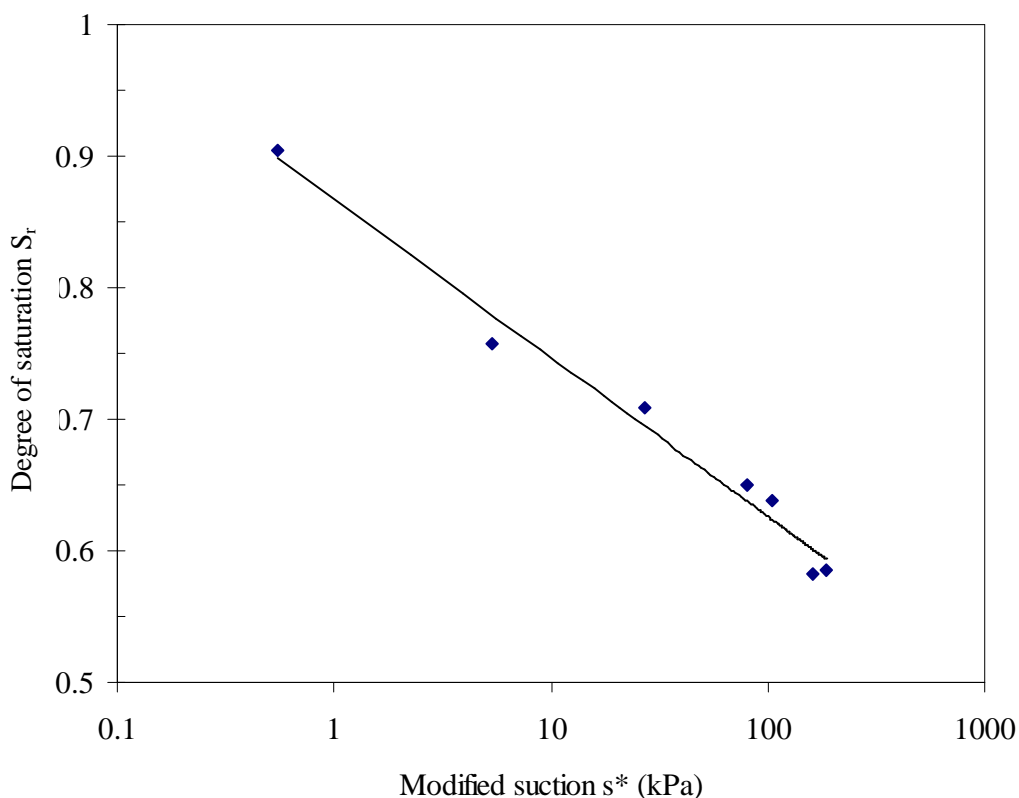


Figure 7-18 Variation of degree of saturation with modified suction for tests at different initial equalisation stress states

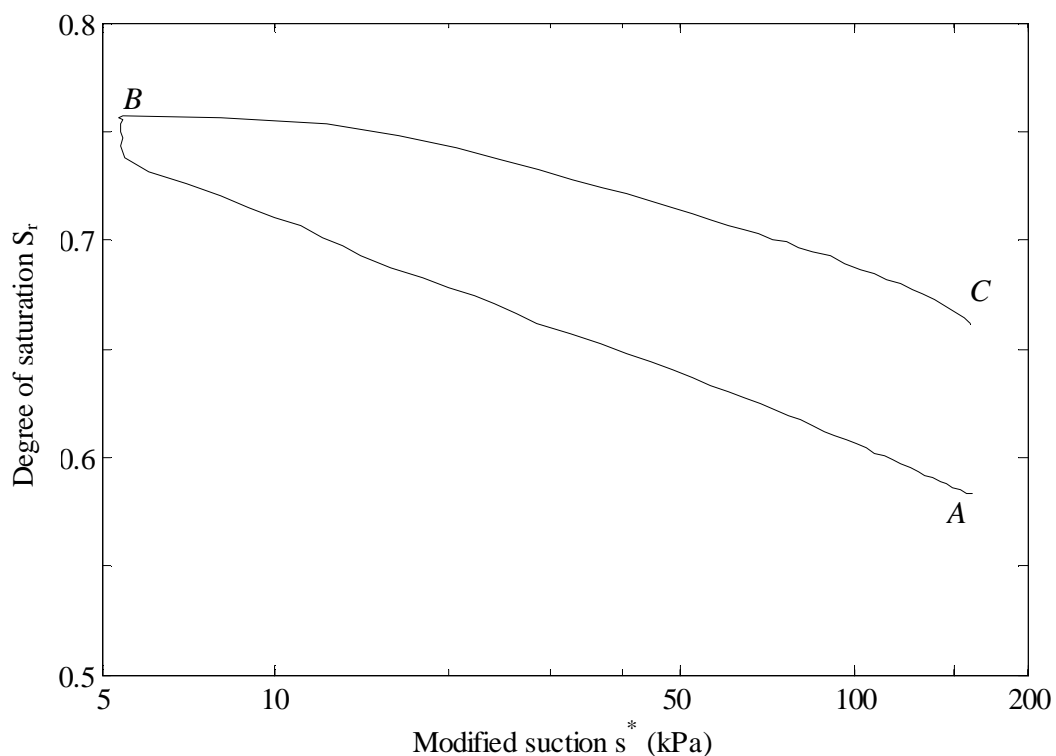


Figure 7-19 Wetting and drying path at $\bar{p} = 10$ kPa in Test A11.

The value of κ_s of 0.006 was determined from the initial slope of the drying curves in the $S_r : \ln s^*$ plane from Test A11 and A12 (e.g. see the first part of the drying curve BC in Figure 7-19).

7.4.3 Coupling parameters k_1 and k_2

In order to model the interaction between mechanical behaviour and water retention behaviour, Wheeler et al. (2003) proposed coupling equations (see Equations 3-9 and 3-6) linking the movement of the LC yield curve during yielding on the SD or SI yield curve and vice versa.

During a wetting path producing yielding on the SD yield curve only, coupling Equation 3-9 defines the path traced by the corner between the LC and SD yield curves, which is analogous to the LC yield curve proposed in the BBM. The shape of the path traced by the corner is controlled by the value of the coupling parameter k_1 i.e. parameter k_1 controls how fast the LC yield curve moves inwards during a wetting stage producing yielding on the SD yield curve only. Once the LC yield curve reaches the stress point, any additional wetting would produce collapse compression.

Considering this feature of behaviour, it was therefore decided to carry out a specific stress path test (Test A3) to determine the value of k_1 .

Figure 7-20 and Figure 7-21 show the stress path for Test A3 in the $s : \bar{p}$ plane and the $s^* : p^*$ plane respectively. The sample was isotropically loaded from $\bar{p} = 20$ kPa to $\bar{p} = 325$ kPa at $s = 350$ kPa ($A - B$), so that at the end of the stress path $A - B$ the stress point would lie at the corner between the SD and LC yield curves (see Figure 7-21). The stress path $B - C - D$ was intended to move the stress point away from both the LC and SD yield curves but without yielding on the SI yield curve. A wetting stage $D - E$ was then performed from $s = 365$ kPa to $s = 160$ kPa at $\bar{p} = 250$ kPa. Part way through the wetting process $D - E$, the onset of collapse compression was observed. This onset of collapse compression was explained within the Wheeler et al. (2003) model by yielding on the SD yield curve during wetting producing a coupled inward movement of the LC yield according to Equation 3-9, and once the LC yield curve reached the stress point, any further reduction in suction would result in plastic volumetric strain (collapse compression).

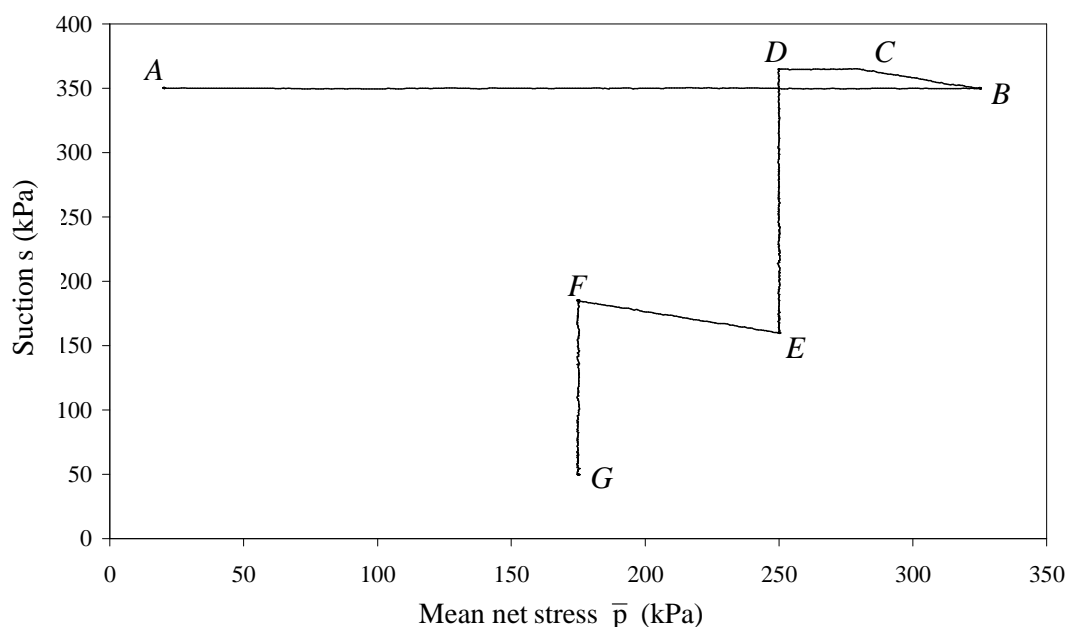


Figure 7-20 Stress path for Test A3 in the $s : \bar{p}$ plane

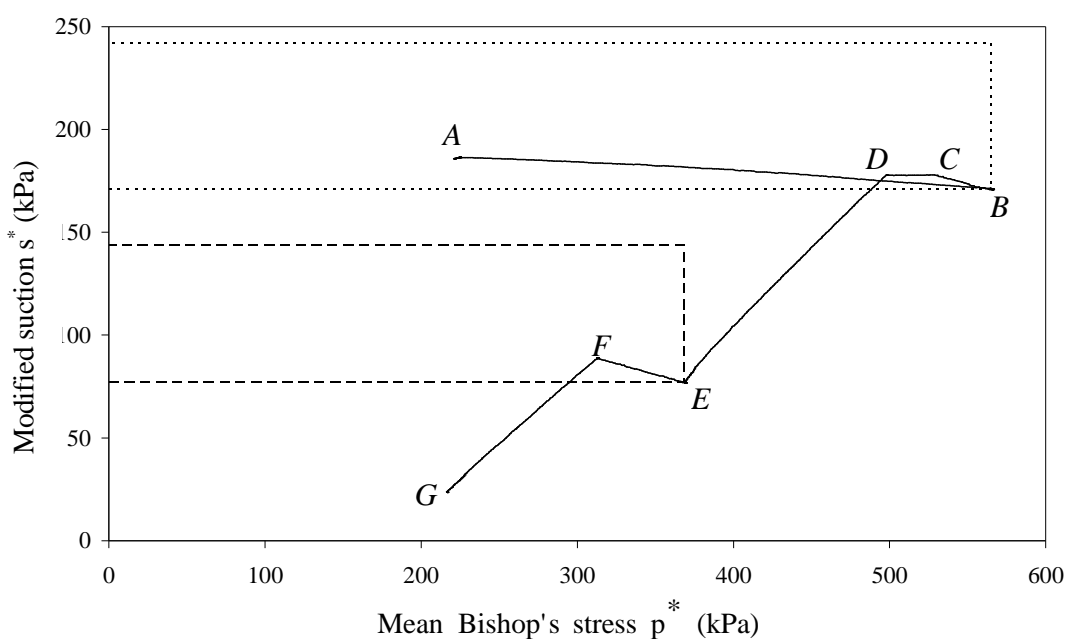


Figure 7-21 Stress path for Test A3 in the $s^* : p^*$ plane with yield curve positions indicated when the stress points is at B (dotted line) and E (dashed line)

By identifying the yield point in the $v : s$ plot during wetting, corresponding to the onset of collapse compression, it was possible to calculate the value of k_1 (by performing Wheeler et al. (2003) model simulations for stress path $B - C - D - E$) with different values of k_1 . Another value for k_1 was also determined for the subsequent similar section of stress path $E - F - G$ and an average value of $k_1 = 0.63$ was determined.

Another way of determining the value of k_1 is to use the yield points from the first isotropic loading (corresponding to yielding on the LC yield curve) for tests at different values of suction. It can be assumed that wetting to a specified value of suction during the initial equalisation stage involved yielding on the SD yield curve, and this will have produced a coupled inward movement of the LC yield curve (the magnitude of which depends on the value of k_1). For tests involving initial equalisation at different values of suction, there will have been different amounts of coupled inward movement of the LC yield curve. Consideration of Equation 3-9 shows that if the yield points from the different tests are plotted in the $\ln p^* : \ln s^*$, they should form a line with a gradient of k_1 . The yield points from the first isotropic

loading stages from Figure 7-15 have therefore been re-plotted in terms of p^* and s^* (on a log-log plot) in Figure 7-22. The gradient of the best-fit line in Figure 7-22 suggests a k_1 value of 0.53. This is slightly lower than the value of $k_1 = 0.63$ determined from Test A3. In addition, there is a suggestion that the points in Figure 7-22 do not fit a simple straight line relationship. This suggests that the coupling relationship of Equation 3-9 may require modification, and this point is discussed further in Section 10.4. For all model simulations, a value of $k_1 = 0.63$, taken from Test A3, was therefore assumed.

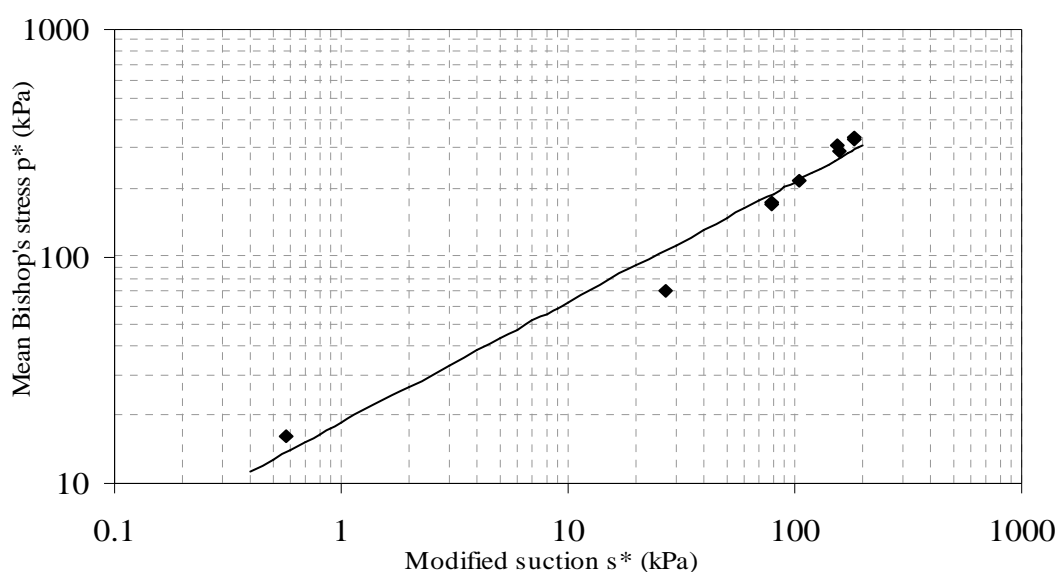


Figure 7-22 Locus of yield points from first isotropic loading in $\ln p^* : \ln s^*$ plane

The gradients of constant suction normal compression lines in the $v : \ln \bar{p}$ plane depend mainly on the values of λ, k_1 and k_2 , while the gradients of the corresponding lines in the $S_r : \ln \bar{p}$ plane depend mainly on the values of λ_s, k_1 and k_2 . Having selected values for λ, λ_s and k_1 , it was possible to select the value for k_2 by matching the gradients of normal compression lines in the $v : \ln \bar{p}$ plane and the corresponding plastic parts of the curves in the $S_r : \ln \bar{p}$ plane during isotropic loading. The selection of values for k_2 involved a small compromise as it was required to reasonably satisfy the gradients of normal compression lines in the $v : \ln \bar{p}$ plane

and plastic parts of the curves in the $S_r : \ln \bar{p}$ plane for isotropic loading paths. A value of 1.05 was selected for parameter k_2 .

7.4.4 Initial states

All the Wheeler et al. (2003) model simulations were started at an initial stress state of $\bar{p} = 10$ kPa, $s = 300$ kPa and $q = 0$ kPa. The initial positions of yield curves and specific volume and degree of saturation were therefore required at this initial stress state for the model simulations. As mentioned in the previous section, the initial equalisations stage of all the tests can be assumed as yielding on the SD yield curve only. From Tests A9, A11, B4, B6, B8 and B10 (which involved initial equalisation at $\bar{p} = 10$ kPa, $s = 300$ kPa) an average value of s^* was calculated for the initial position of SD yield curve s_D^* .

The Wheeler et al. (2003) model assumes a constant distance between the SI and SD yield curves when plotted in the $\ln s^* : p^*$ plane (i.e. the ratio s_I^*/s_D^* remains constant). In Test All, a wetting stage $A - B$ was carried out (see Figure 7-19), and at the end of this stage the stress point was assumed to be lying on the SD yield curve. During the subsequent drying stage $B - C$, there was a suggestion of yielding at a modified suction of about 10 kPa. By considering this level of modified suction as the position of the SI yield curve (after assuming that no plastic volumetric strain occurring before the onset of plastic changes of S_r during drying stage $B - C$ i.e. stress path first yielding on the SI yield curve during drying $B - C$), the ratio s_I^*/s_D^* was selected as 1.5. Using this value it was possible to estimate the initial position of the SI yield curve at an initial stress states of $\bar{p} = 10$ kPa, $s = 300$ kPa, having selected the corresponding initial position of the SD yield curve (see previous paragraph). However, the later simulations (see Chapter 8) showed that a constant value for s_I^*/s_D^* was unable to provide accurate predictions of experimental results, because this ratio changes significantly for different stress states of samples.

In the previous section, the yield points in the $\ln s^* : \ln p^*$ plane were plotted (see Figure 7-22) for first isotropic loading. The value of p^* corresponding to the yield point for isotropic loading at 300 kPa suction would therefore represent the initial

position of the LC yield curve at initial stress state $\bar{p} = 10 \text{ kPa}$, $s = 300 \text{ kPa}$. This value of p_0^* was therefore selected as the initial position of the LC yield curve.

Finally, the values of specific volume and degree of saturation at the initial state were determined by getting the average values for initial equalisation stages at $\bar{p} = 10 \text{ kPa}$, $s = 300 \text{ kPa}$ from Tests A9, A11, B4, B6, B8 and B10.

7.4.5 Parameters related to shearing G and M

The procedure for the determination of elastic shear modulus G was the same as described in Section 7.3.1. Therefore, the same value of 3 MPa was selected for G . In order to reliably estimate the slope of the critical state line M^* in the $q : p^*$ plane, ideally many experimental critical state points would be required, covering a wide range of q and p^* values. However, in the current research only limited numbers of critical state points were available, covering a narrow range of q and p^* values. Sivakumar (1993) and Wheeler & Sivakumar (2000) carried out a comprehensive range of controlled-suction triaxial tests on compacted samples of Speswhite Kaolin prepared in a similar fashion to those of the author. It was therefore decided to use their experimental data along with current test data to evaluate the value of M^* .

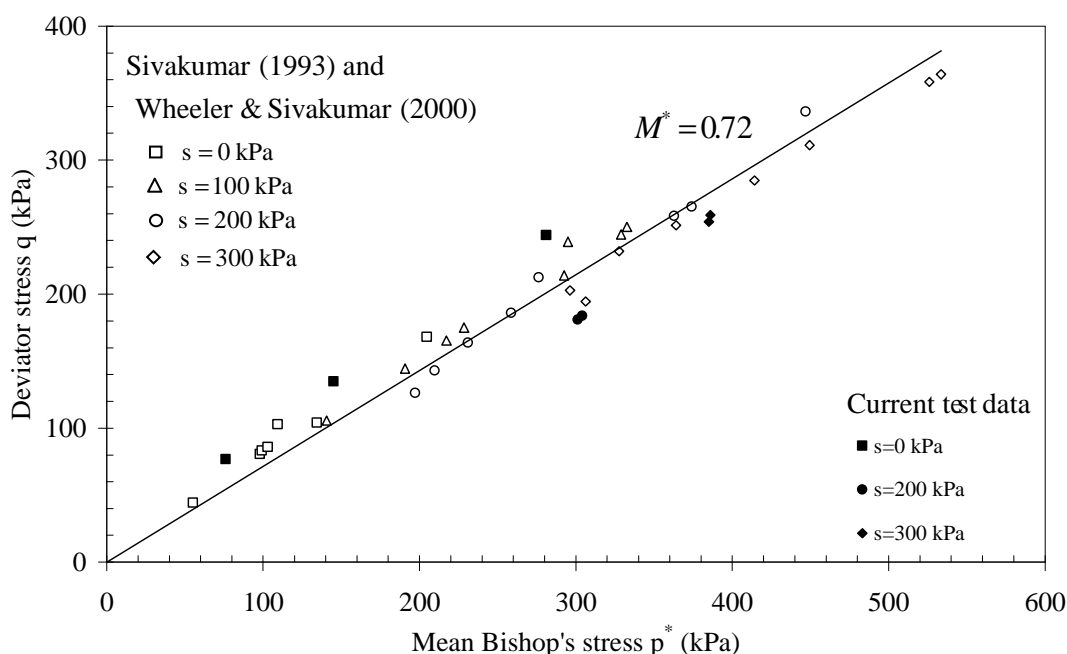


Figure 7-23 Critical state points for compacted Speswhite Kaolin samples plotted as deviator stress against mean Bishop's stress (after Gallipoli et al., 2008)

Figure 7-23 shows the critical state points for compacted Speswhite Kaolin samples plotted as deviator stress against mean Bishop's stress for the author's test data and for the data of Sivakumar (1993) and Wheeler & Sivakumar (2000). The current experimental data points are indicated by solid markers, whereas the data points from the previous research are indicated by open markers. A reasonable agreement between current experimental data and the data from the above mentioned literature can be observed. A value of 0.72 was determined as the average gradient of the critical state line using all the experimental data.

7.5 DETERMINATION OF PARAMETER VALUES FOR BOUNDING SURFACE PLASTICITY VERSION OF WHEELER ET AL. (2003) MODEL

Table 7-4 shows the values of model parameters selected for the bounding surface plasticity version of Wheeler et al. (2003) model.

| Bounding surface plasticity version of Wheeler et al. (2003) model parameters | | Values |
|---|---|---------|
| <i>Soil constants</i> | κ | 0.02 |
| | κ_s | 0.006 |
| | λ | 0.115 |
| | λ_s | 0.055 |
| | k_1 | 0.63 |
| | k_2 | 1.05 |
| | f | 10 |
| | g | 2 |
| <i>Initial conditions</i> | s_D^* | 185 kPa |
| | s_I^* | 280 kPa |
| | p_0^* | 280 kPa |
| | ν at $\bar{p} = 10$ kPa and $s = 300$ kPa | 2.153 |
| | S_r at $\bar{p} = 10$ kPa and $s = 300$ kPa | 0.592 |

Table 7-4 Model parameter values and initial conditions for bounding surface version of Wheeler et al. (2003) model.

The formulation of a bounding surface plasticity version of the fully coupled Wheeler et al. (2003) model was described in Section 4.4. As this model is simply an extension

of the Wheeler et al. (2003) model, it is logical to use the same values as determined in Section 7.4 for the parameters κ , κ_s , λ , λ_s , k_1 and k_2 and for the initial state. The values of the two additional parameters f and g , which control the prediction of the transition of mechanical behaviour and water retention behaviour from elastic to fully elasto-plastic were determined by comparing model simulations with experimental results for isotropic compression lines and for wetting and drying curves. This resulted in values of $f = 10$ and $g = 2$. The high value of the parameter f means that for mechanical behaviour the transition from elastic behaviour to fully elasto-plastic behaviour is relatively abrupt. The much lower value for the parameter g means that for water retention behaviour the transition from elastic changes of S_r to fully elasto-plastic changes of S_r (i.e. the transition from scanning curve to main drying or wetting curve) is much more gradual.

CHAPTER 8

ISOTROPIC TEST RESULTS, SIMULATIONS AND DISCUSSION

This chapter presents suction-controlled experimental test results performed under isotropic stress states in System A, along with the simulations by the BBM and the Wheeler et al. (2003) model (both original elasto-plastic and new bounding surface plasticity versions). Simulation codes for stress point simulations with the BBM, and the Wheeler et al. (2003) model (both original elasto-plastic and new bounding surface plasticity versions) were developed using Matlab. The simultaneous equations that had to be solved for increments of stress, strain and degree of saturation are presented in the Appendix for all three models. The algorithms employed in the Matlab coding in order to run a simulation for required stress paths are also presented in the Appendix.

Initial tests were primarily designed to investigate the validity of some of the main concepts of the Wheeler et al. (2003) framework and of some of the specific constitutive equations proposed in the Wheeler et al. (2003) model. Other tests were carried out to investigate further the coupling of mechanical behaviour and water retention behaviour by performing elaborate stress path tests, which involved wetting, drying, isotropic loading and unloading.

8.1 TESTS TO INVESTIGATE THE PERFORMANCE OF THE WHEELER ET AL. (2003) MODEL

One of the objectives of this research was to investigate the performance of the Wheeler et al. (2003) model in the light of experimental test results. Tests were therefore designed to investigate whether the model proposals of uncoupled elastic stress-strain behaviour, very simple yield curve shapes and particular forms of coupling relationships were consistent with experimental observations.

8.1.1 Elastic stress-strain relationships (Test A1)

Wheeler et al. (2003) proposed simple uncoupled stress-strain relationships for the development of elastic volumetric strain and elastic changes of degree of saturation, with the former dependent solely on the change of mean Bishop's stress mean p^* and the latter dependent solely on the change of modified suction s^* :

$$d\varepsilon_v^e = \frac{\kappa}{v} \frac{dp^*}{p^*} \quad (8-1)$$

$$-dS_r^e = \kappa_s \frac{ds^*}{s^*} \quad (8-2)$$

Test A1 was carried out in order to investigate the validity of these particular relationships, by performing a stress path inside the yield curves, so that the changes of degree of saturation and volumetric strain would be elastic. Table 8-1 and Figure 8-1 show the stress path.

| Stage | | | \bar{p} (kPa) | s (kPa) |
|-------|----|----------------------|-----------------|-----------|
| From | To | Description | | |
| A | A' | Initial equalisation | 20 | 150 |
| A' | B | Isotropic loading | 20 → 250 | 150 |
| B | B' | Equalisation | 250 | 150 |
| B' | C | Isotropic unloading | 250 → 100 | 150 |
| C | C' | Equalisation | 100 | 150 |
| C' | D | Drying | 100 | 150 → 250 |
| D | D' | Equalisation | 100 | 250 |
| D' | E | Isotropic loading | 100 → 200 | 250 |
| E | E' | Equalisation | 200 | 250 |
| E' | F | Wetting | 200 | 250 → 195 |

Table 8-1 Stress path for Test A1

The sample was first equalised at $\bar{p}=20$ kPa and $s=150$ kPa (stage AA'). The mean net stress was then increased at constant suction to reach $\bar{p}=250$ kPa (stage A' – B). After the equalisation stage BB', an isotropic unloading B' – C was performed to a mean net stress of 100 kPa. This was followed by a drying stage C' – D to a suction value of 250 kPa (ending with an equalisation stage DD'). The sample was then isotropically loaded (D' – E) to a mean net stress of 200 kPa (followed by

equalisation EE'). The last leg of the stress path $E' - F$ involved wetting at constant mean net stress and was planned to continue until a suction value of 150 kPa. However, the test was terminated before reaching the intended final suction value, because a pressure drop of the compressor occurred due to faulty operation of the water flushing valve of the compressor.

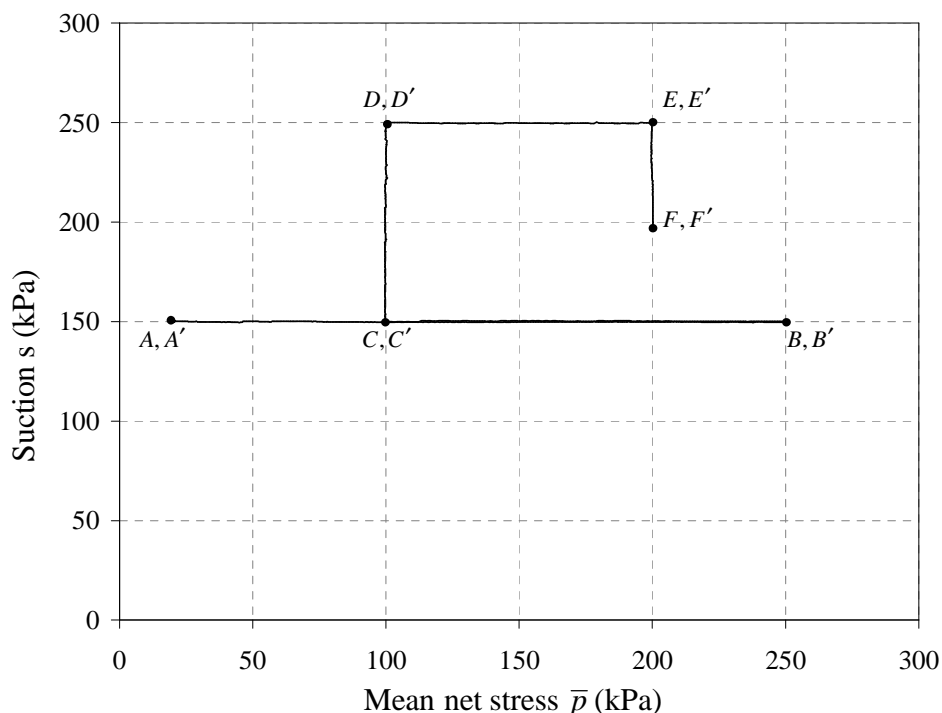


Figure 8-1 Stress path for Test A1

Figure 8-2 and Figure 8-3 show the experimental variation of ν and S_r , respectively, plotted against mean net stress \bar{p} in semi-logarithmic plots. Also shown are the simulations from the BBM, the original Wheeler et al. (2003) model (WM) and the bounding surface plasticity version of the Wheeler et al. (2003) model (WM (BS)). As \bar{p} was increased in the first isotropic loading $A' - B$, the sample showed initially a stiff response in terms of both ν and S_r (attributed to elastic behaviour), followed by transitional behaviour and then, as isotropic loading was continued further, a linear normal compression line was followed for ν and a linear post-yield line was followed for S_r (attributed to elasto-plastic behaviour).

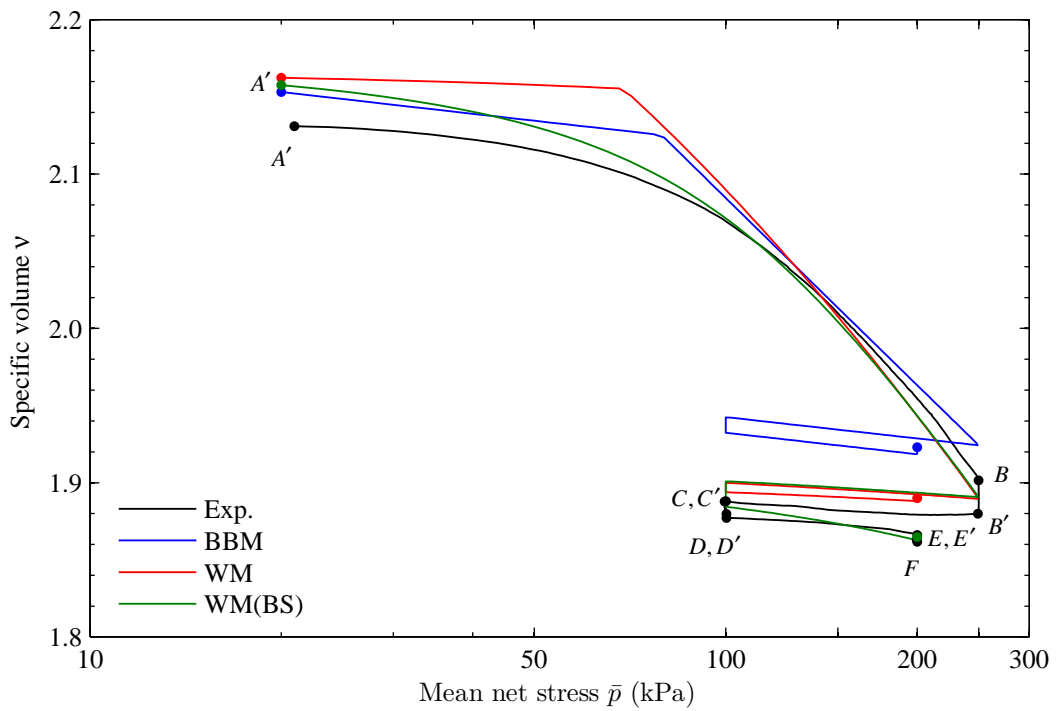


Figure 8-2 Variation of specific volume v with mean net stress \bar{p} for Test A1 along with simulations

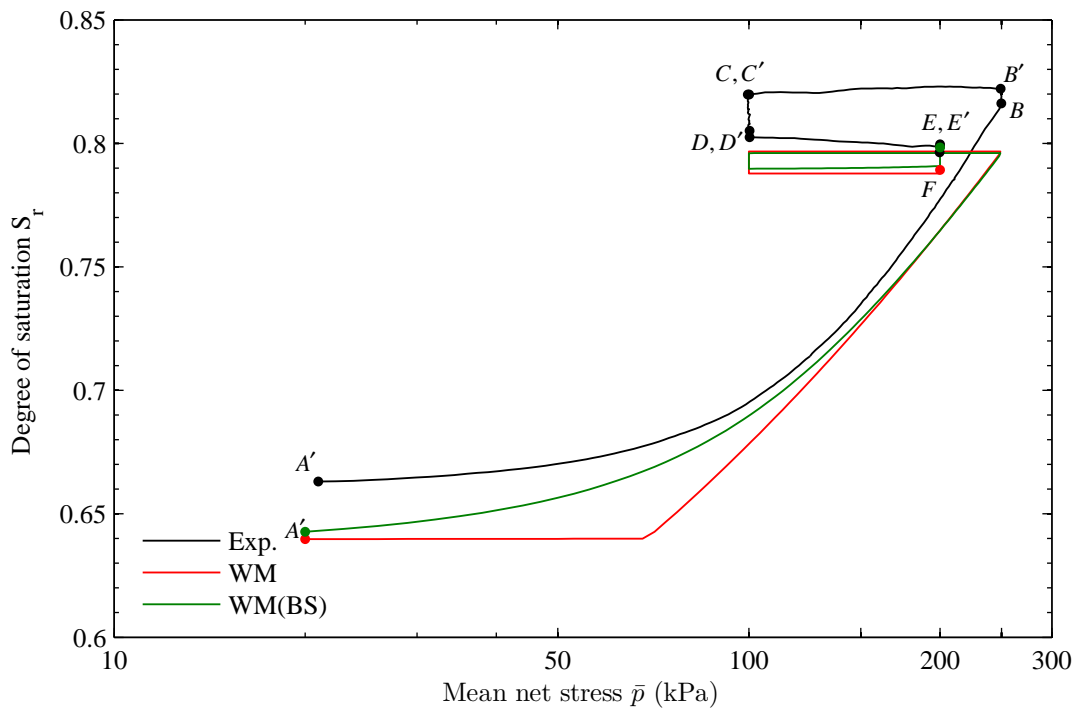


Figure 8-3 Variation of degree of saturation S_r with mean net stress \bar{p} for Test A1 along with simulations

According to the BBM, the variation of v during loading $A' - B$ is modelled by initial elastic response inside the LC yield curve (see Equation 2-16) and then as the LC yield curve is reached elasto-plastic volumetric strain is predicted (see Equation 2-14 and Figure 8-2). In the case of the WM, at the start of isotropic loading, the stress point was on the SD yield curve but inside the LC yield curve. During isotropic loading $A' - B$ the mean Bishop's stress p^* increased and elastic volumetric strain was predicted by the WM according to Equation 3-3 until the stress point reached the corner of the LC and SD yield curves. Very small elastic and plastic increases of degree of saturation were also predicted during the early part of $A' - B$ (hardly visible in the WM simulation in Figure 8-3), according to Equations 3-4 and 3-8, because of small reductions in s^* due to the occurrence of elastic volumetric strain. Once the corner of the LC and SD yield curves was reached, substantial elasto-plastic volumetric strains and increases of degree of saturation were predicted by the WM, according to Equations 3-13 and 3-14.

In the case of the WM (BS), at the start of isotropic loading the stress point was very close to the SD bounding curve and well inside the LC bounding curve. During isotropic loading $A' - B$, both plastic volumetric strain and plastic increases of degree of saturation were predicted by the WM (BS), as the stress point was moving towards the LC and SD bounding curves (see Section 4.4.2 for more information). It can be seen from Figure 8-2 and Figure 8-3 that, as the isotropic loading continues, the normal compression curve for v and post-yield curve for S_r predicted by WM and WM (BS) converged with each other.

Inspection of Figure 8-2 and Figure 8-3 shows that during the intended elastic sections of stress path ($B' - C$, $C' - D$, $D' - E$ and $E' - F$) the changes of both v and S_r were relatively small. These are now examined in more detail.

Figure 8-4 shows the variation of specific volume v re-plotted against mean Bishop's stress p^* (with p^* on a logarithmic scale). The same data is shown at larger scale in Figure 8-5, only for the intended elastic parts ($B' - C$, $C' - D$, $D' - E$ and $E' - F$) of the stress path. During unloading $B' - C$, the soil sample initially showed a very small volume reduction before swelling started to dominate the final part of stage $B' - C$.

This initial small volume reduction could be due to delayed compression from the previous isotropic loading i.e. the compression during the 48 hour equalisation stage BB' may not have entirely ceased. During drying stage $C' - D$ a reduction in volume (shrinkage) was observed, with v varying in an approximately linear fashion with $\ln p^*$. Although the maximum value of mean Bishop's stress previously achieved was exceeded during re-loading path $D' - E$, no clear yield point was observed. This can be explained by the WM if the drying stage $C' - D$ produced yielding on the SI yield curve, causing a coupled outward movement of the LC yield curve (see WM simulation in Figure 8-5).

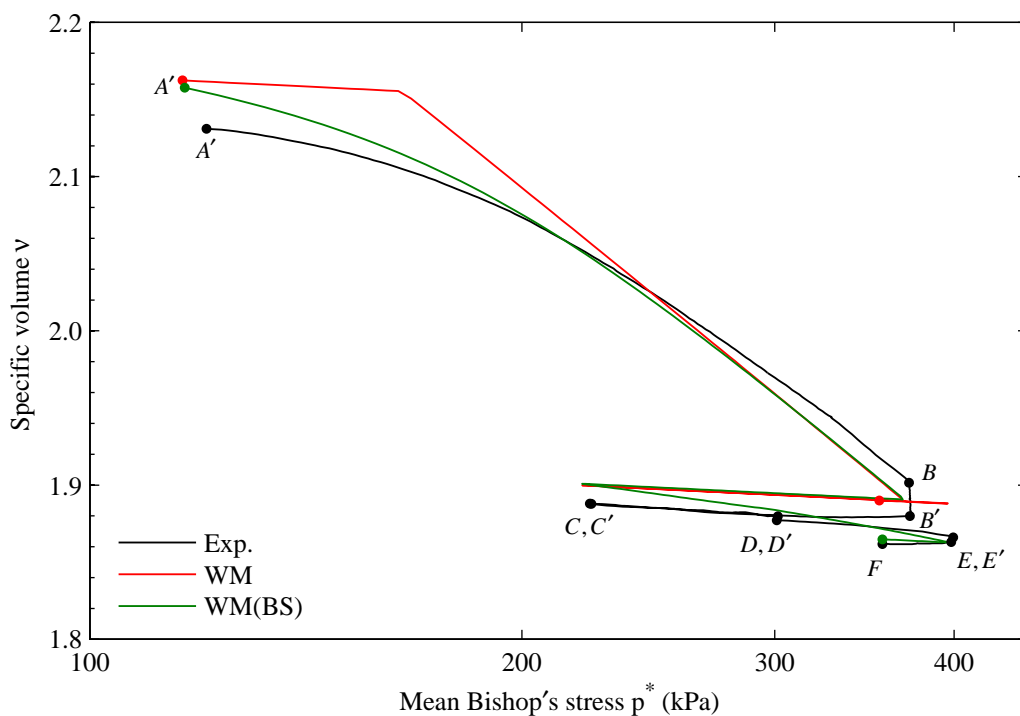


Figure 8-4 Variation of specific volume v with mean Bishop's stress p^* for Test A1 along with simulations

The observation of a very small volume reduction during wetting $E' - F$ may again have been caused by incomplete compression from the previous re-loading and equalisation stages ($D' - E$ and EE'). If, however, the very small volume reduction during wetting $E' - F$ represents collapse compression, then neither the BBM nor the WM will be able to capture this feature. It is, however, theoretically possible to model this behaviour with the bounding surface plasticity version of the Wheeler et al. (2003) model, as plastic volumetric strain can be predicted even when the stress point is well

inside the bounding curves. However, by inspecting Figure 8-5, it can be seen that, with the particular parameter values selected, WM (BS) also predicted swelling during stage $E'-F$ (elastic swelling exceeded plastic compression). It can be seen from Figure 8-5 that WM predicted elastic variation of v throughout the entire stress path $B'-CC'-DD'-EE'-F$. It can be noted that the predictions suggest that the LC yield curve was not reached until the very end of the re-loading stage $D'-E$, because the LC yield curve was pushed outward during yielding on the SI yield curve within the previous drying stage $C'-D$. On the other hand, WM (BS) predicted elastic volumetric strain during unloading and wetting stages $B'-C$ and $E'-F$, but a small elasto-plastic volumetric strain during drying and reloading stages $C'-D$ and $D'-E$ (see Figure 8-5).

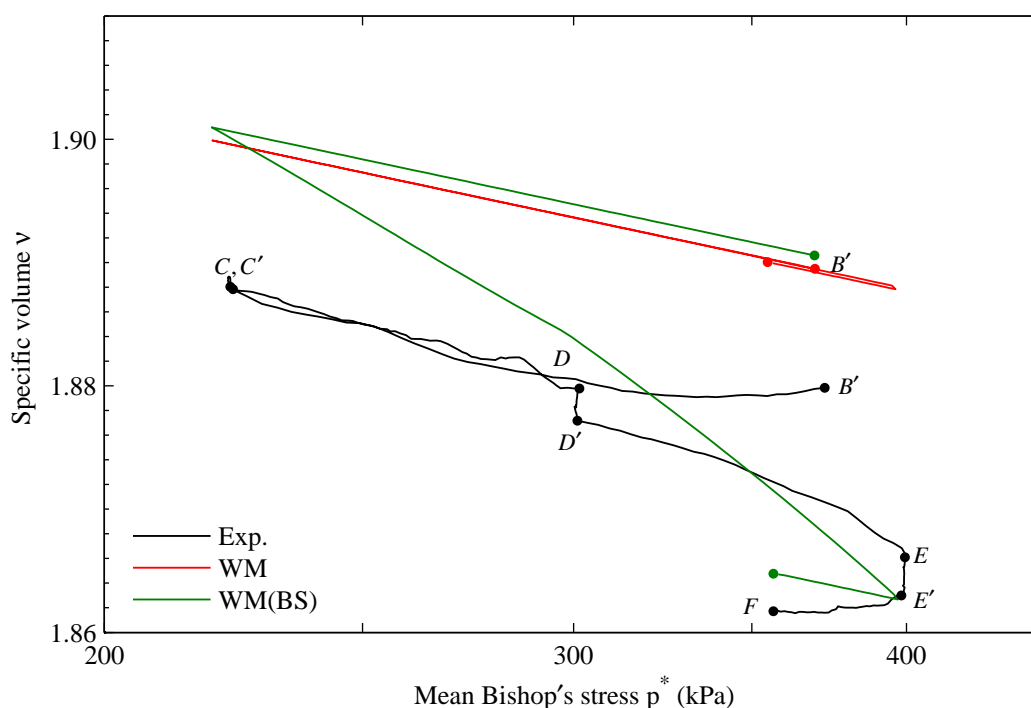


Figure 8-5 Variation of specific volume v with mean Bishop's stress p^* for intended elastic sections of stress path in Test A1 along with simulations

Figure 8-6 shows the variation of degree of saturation S_r with modified suction s^* during the intended elastic sections of the stress path $B'-C$, $C'-D$, $D'-E$ and $E'-F$. It can be clearly seen, however, that the relatively close spacing between the SI and SD yield curves selected for the WM in Chapter 7 means that, in fact, the WM simulations suggest that the stress path was not entirely elastic, but involved

yielding on the SI curve during drying $C' - D$. During unloading $B' - C$ the experimental results show that a small reduction in S_r occurred, while both WM and WM (BS) predicted extremely small decreases in S_r (too small to be visible in Figure 8-6). During drying $C' - D$, reduction of S_r was observed, and this is predicted by both WM and WM (BS), although neither model achieves a perfect prediction of the magnitude of the reduction or the shape of the curve. During re-loading $D' - E$ a further reduction of S_r was observed, whereas WM predicted an extremely small increase of S_r (too small to see in Figure 8-6) and WM (BS) predicted a small increase of S_r (observable in Figure 8-6). This discrepancy probably represents a weakness of the WM and WM (BS) models, although it is probably exaggerated by additional experimental decrease of S_r during re-loading $D' - E$ as a consequence of delayed effects from the previous drying and equalisation stages $C' - D$ and DD' . During final wetting $E' - F$ a small increase of S_r was observed. This is well matched by the WM simulation and somewhat overstated by the WM (BS) simulation.

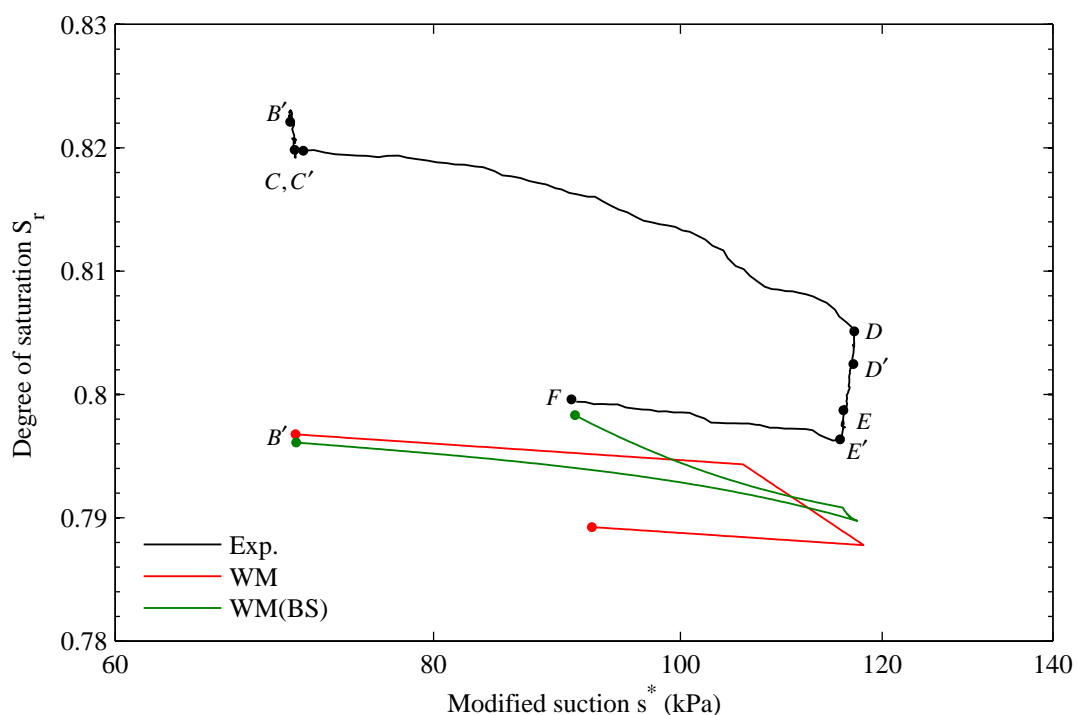


Figure 8-6 Variation of degree of saturation S_r with modified suction s^* for intended elastic sections of stress path in Test A1 along with simulations

Overall interpretation of the test results and the question of whether the results support the proposed elastic relations of Equations 8-1 and 8-2 are rather inconclusive. This is mainly because the observed changes of ν and S_r during test stages $B' - C$, $C' - D$, $D' - E$ and $E' - F$ were all relatively small and therefore susceptible to distortion by minor influence of complicating factors. If the stress path was entirely elastic, and the proposed uncoupled elastic relations of Equations 8-1 and 8-2 were correct, then the experimental results should follow a single straight line of ν against $\ln p^*$ in Figure 8-5 and a single straight line of S_r against $\ln s^*$ in Figure 8-6. Clearly this is not exactly what is seen in the experimental results. There are however two complications. Firstly, the stress path may not be entirely elastic, with significant possibilities of yielding on the SI yield curve during drying $C' - D$ (see the WM simulation in Figure 8-6) or of small components of plastic changes of ν and S_r occurring during many of the stages, if the transition from elastic to elasto-plastic behaviour is a gradual process (see the WM (BS) simulations in Figure 8-5 and Figure 8-6). Secondly, in many stages there is a distinct possibility that some changes of ν or S_r could have been due to delayed effects arising from incomplete equalisation at the end of a previous stage. Overall, therefore, the results are inconclusive as to whether Equations 8-1 and 8-2 provide a good representation of elastic changes of ν and S_r respectively.

Figure 8-7 shows the variation of specific water volume ν_w with suction in the intended elastic sections of stress path ($B' - C$, $C' - D$, $D' - E$ and $E' - F$) of Test A1. Prediction of the variation of ν_w involves prediction of the variations of both ν and S_r . It is interesting to note that the WM (BS) in particular provides reasonably successful prediction of the variation of ν_w (probably better than the individual prediction of ν and S_r).

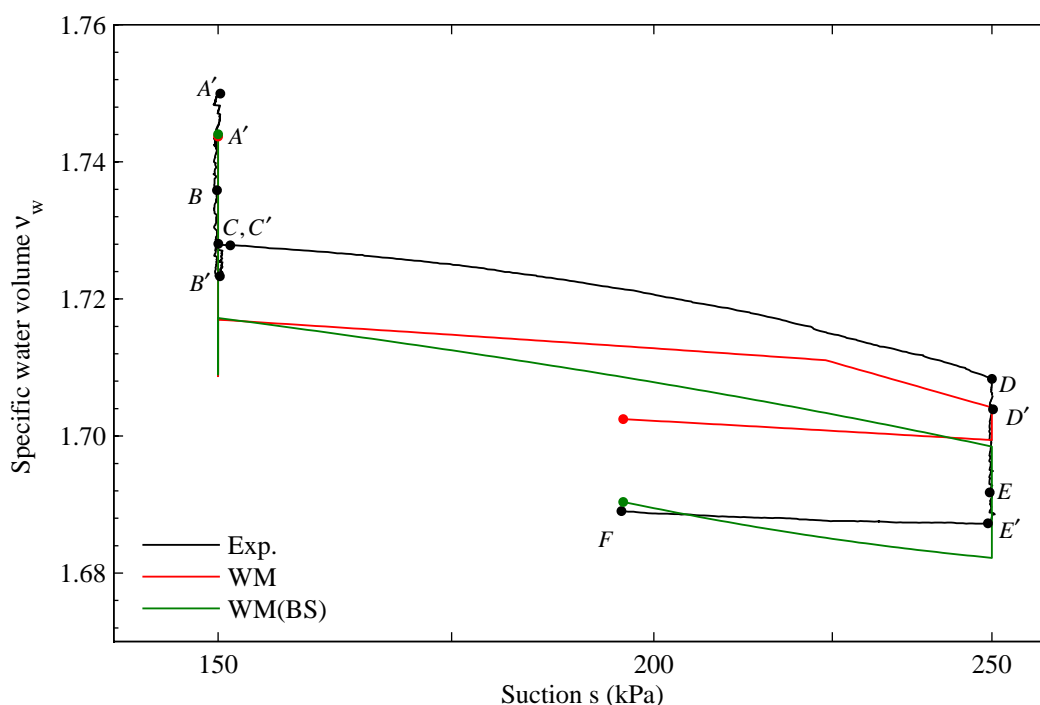


Figure 8-7 Variation of specific water volume v_w with suction s for intended elastic sections of stress path in Test A1 along with simulations

8.1.2 Relationship for coupled inward movement of LC yield curve (Test A3)

Coupled movements of the LC yield curve, caused by plastic changes of S_r , arising from yielding on the SD or SI yield curves have been proposed in the Wheeler et al. (2003) framework to incorporate the influence of water retention behaviour on mechanical behaviour. These coupled movements produced by yielding on the SD or SI yield curve alone have been assumed to follow the relationship shown below:

$$\frac{dp_0^*}{p_0^*} = k_1 \frac{ds_D^*}{s_D^*} = k_1 \frac{ds_I^*}{s_I^*} \quad (8-3)$$

To investigate the validity of this proposal, an isotropic stress path test was conducted as shown Table 8-2 and Figure 8-8. The first test (Test A2) conducted for this purpose was terminated prematurely, because of the same problem with the compressor as reported in Section 8.1.1. A second test (A3) was therefore performed. Both Tests A2 and A3 are presented, to verify the repeatability of the early part of Test A3.

In Test A2, the soil sample was first equalised at a suction of 350 kPa and mean net stress of 20 kPa (stage aa'). The sample was then isotropically compressed to a mean

net stress of 250 kPa at constant suction (stage $a' - b$). Sample A3 was equalized under the same stress conditions as Sample A2 (stage AA') and then isotropically loaded to a mean net stress of 325 kPa (stage $A' - B$). This isotropic compression was intended to ensure that the sample was yielding on both SD and LC yield curves simultaneously (i.e. producing both plastic volumetric strain and plastic increase of degree of saturation). The isotropic compression was supposed to be followed by a simultaneous unloading and drying path to a stress state well inside the yield curves to a mean net stress of 250 kPa and a suction of 375 kPa. However, the stage was terminated early at a suction of 365 kPa as shown in Figure 8-8 ($B' - C$), due to concern about a dramatic increase in the rate of diffusion of dissolved air through the high air entry filters at high suctions above about 350 kPa (Buisson, 2002). The sample was then unloaded at constant suction ($C' - D$) to a mean net stress of 250 kPa. Next a wetting stage $D' - E$ was performed to a suction of 160 kPa at a mean net stress of 250 kPa. This was intended to produce yielding on the SD yield curve and hence coupled inward movement of the LC yield curve, so that collapse compression could commence when the LC yield curve reached the current stress point. The test then continued with a second unloading and drying stage $E' - F$ and a second wetting stage $F' - G$, to try to produce the same effect again (see Table 8-2 and Figure 8-8).

| Stage | | | \bar{p} (kPa) | s (kPa) |
|-------|----|------------------------------|-----------------|-----------|
| From | To | Description | | |
| A | A' | Initial equalisation | 20 | 350 |
| A' | B | Isotropic loading | 20 → 325 | 350 |
| B | B' | Equalisation | 325 | 350 |
| B' | C | Isotropic unloading & drying | 325 → 280 | 350 → 365 |
| C | D | Isotropic unloading | 280 → 250 | 365 |
| D | D' | Equalisation | 250 | 365 |
| D' | E | Wetting | 250 | 365 → 160 |
| E | E' | Equalisation | 250 | 160 |
| E' | F | Isotropic unloading & drying | 250 → 175 | 160 → 185 |
| F | F' | Equalisation | 175 | 185 |
| F' | G | Wetting | 175 | 185 → 50 |
| G | G' | Equalisation | 175 | 50 |

Table 8-2 Stress path for Test A3

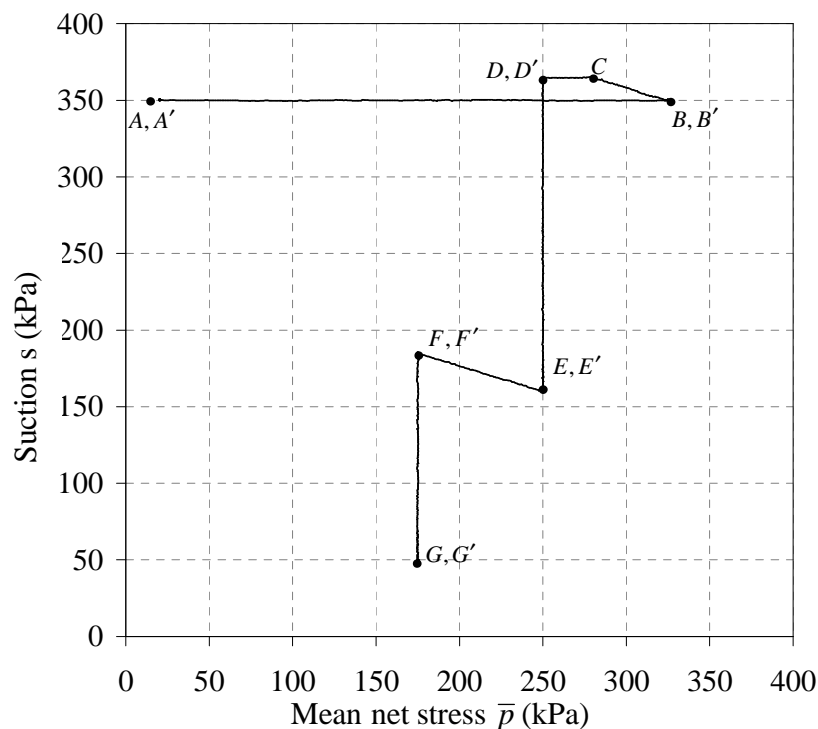


Figure 8-8 Stress path for Test A3

Figure 8-9 and Figure 8-10 show the variation of ν and S_r plotted against mean net stress \bar{p} (with \bar{p} on a logarithmic scale). The initial compression curves for a suction of 250 kPa (Figure 8-9) from Tests A2 and A3 ($a'-b$ and $A'-B$ respectively), and the corresponding variations of S_r (Figure 8-10), were in close agreement providing evidence of the repeatability of the experimental results. None of the models was able to perfectly capture the position of the normal compression line for ν and corresponding post-yield line for S_r . However, the BBM, WM and WM (BS) all predict the slope of the normal compression line with reasonable accuracy. The WM and WM(BS) appear to predict that the substantial plastic decreases of ν and increases of S_r commence too early during this isotropic loading stage.

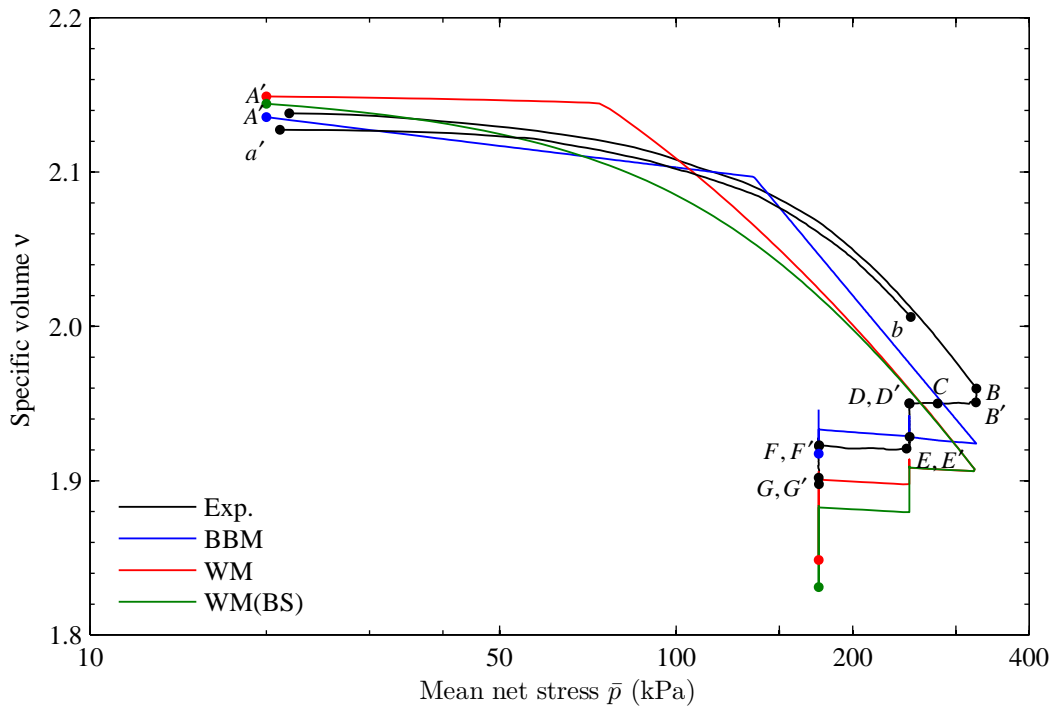


Figure 8-9 Variation of specific volume v with mean net stress \bar{p} for Tests A2 and A3 along with simulations

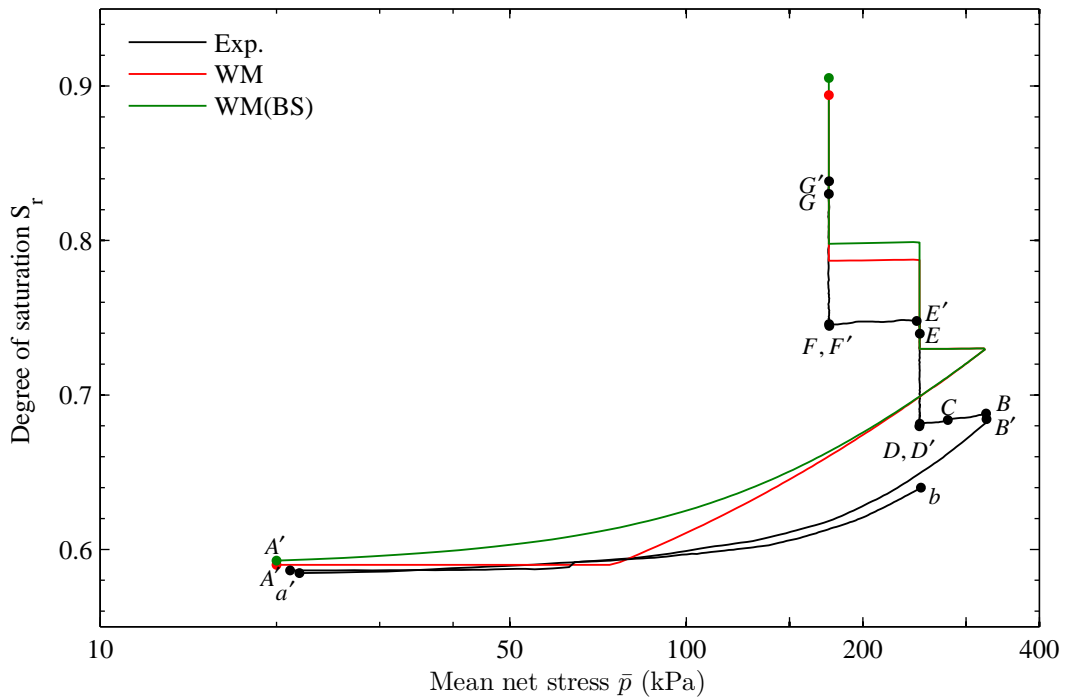


Figure 8-10 Variation of degree of saturation S_r with mean net stress \bar{p} for Tests A2 and A3 along with simulations

Figure 8-11 shows the variation of specific volume v with suction for the later stages of Test A3 ($D' - EE' - FF' - GG'$). During wetting $D' - E$, the sample showed small reductions of specific volume right from the beginning even though according to the BBM and WM, point D' was supposed to be well inside the LC yield curve. It should be noted that similar behaviour was observed in Test A1, described in Section 8.1.1. One possible explanation could be incomplete equalization during the preceding stage (DD') and hence delayed compression from the previous unloading and drying paths $B' - CC' - D$. However, the change of specific volume during the 24 hour equalization stage DD' was found to be small ($\Delta v = 0.0003$). If the small volume reduction during the early part of wetting path $D' - E$ was not attributable to delayed effects from previous stages, then the BBM or WM would not be able to capture this response. However, the bounding surface plasticity version of the WM model could theoretically predict this feature of behaviour. In fact, all 3 models predicted swelling in the initial part of wetting $D' - E$ and collapse compression in the later part (see Figure 8-11). The WM (BS) model however predicted both elastic swelling and plastic volumetric compression from the very start of wetting, with the former dominating initially and the latter gradually becoming dominant as wetting progressed.

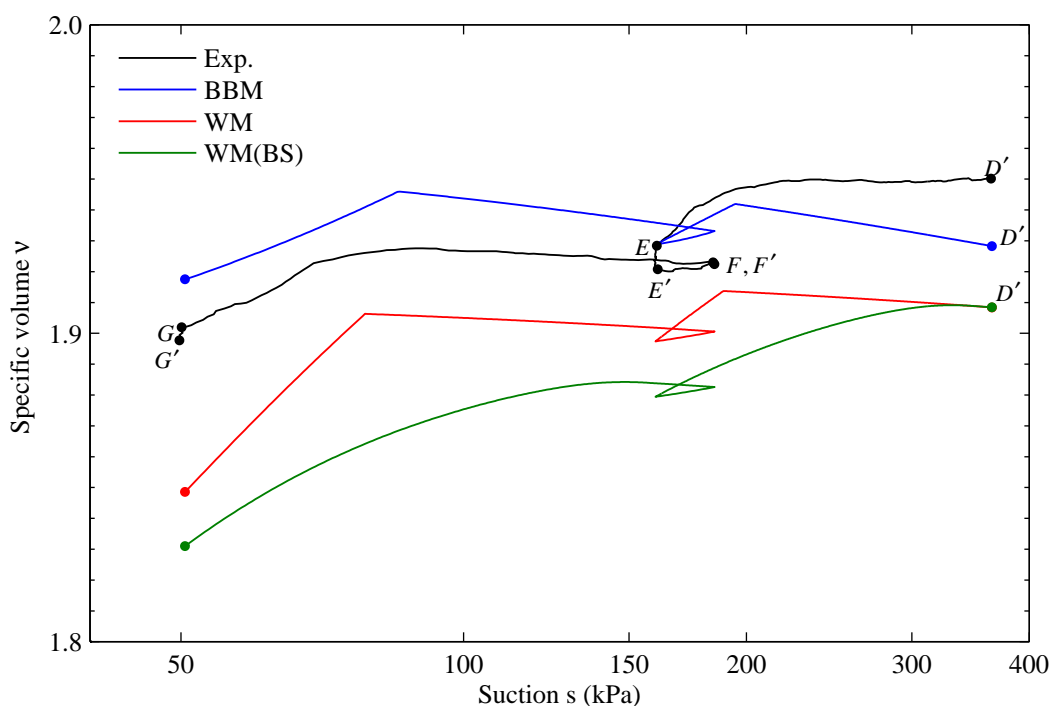


Figure 8-11 Variation of specific volume v with suction s for Test A3 along with simulations

Inspection of the experimental results in Figure 8-11 shows that the onset of significant collapse compression during wetting $D' - E$ was actually a more distinct phenomenon than predicted by WM(BS) (i.e. there is a suggestion of a yield point). The occurrence of yielding during wetting also suggests that elasto-plastic modelling (rather than bounding surface plasticity) may be sufficient to describe the mechanical behaviour of unsaturated soil (but not necessarily the water retention behaviour). Both BBM and WM were able to capture the yield points corresponding to the onset of significant collapse compression during wetting paths $D' - E$ and $F' - G$. The gradient of elastic swelling in the early part of the second wetting stage $F' - G$ was also predicted by the BBM and WM with reasonable accuracy. However, neither BBM nor WM was able to predict perfectly the gradient of elasto-plastic volumetric reduction (collapse compression) for both wetting paths $D' - E$ and $F' - G$.

In the second wetting path $F' - G$, the gradient of elasto-plastic volumetric reduction predicted by WM is higher than shown by the experimental results. By incorporating a water retention model that better represents water retention behaviour at high degrees of saturation or by modifying the coupling equation (Equation 3-9) proposed by Wheeler et al. (2003), it is possible to improve this aspect of the WM model predictions. Further experimental evidence regarding this issue will be discussed in later sections.

Figure 8-12 and Figure 8-13 show the variation of degree of saturation and specific water volume respectively with suction during the later stages of Test A3. It was predicted by the WM that during each wetting path, two yield points would be observed in Figure 8-12, the first corresponding to the stress path reaching the SD yield curve and the second when the coupled inward movement of the LC yield curve brought it to the stress point. However, there was no evidence for clear yield points in the experimental variation of S_r during either wetting stage ($D' - E$ or $F' - G$). This observation suggests that bounding surface plasticity may be helpful to describe the water retention behaviour. In addition, the absence of clear yield points in Figure 8-12 meant that it was not possible to determine the shape of the SD yield curve. WM and WM (BS) predictions showed similar variations of S_r for the stress

path $D' - EE' - FF' - GG'$. The increase in S_r observed from the experimental results was predicted by both models with reasonable accuracy.

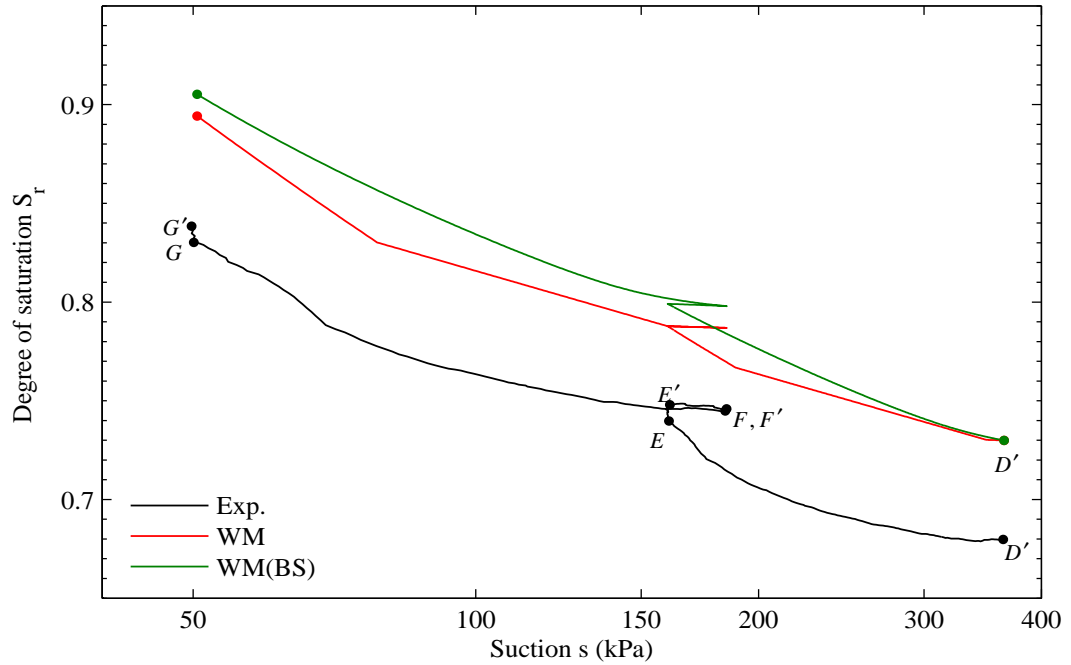


Figure 8-12 Variation of degree of saturation S_r with suction s for Test A3 along with simulations

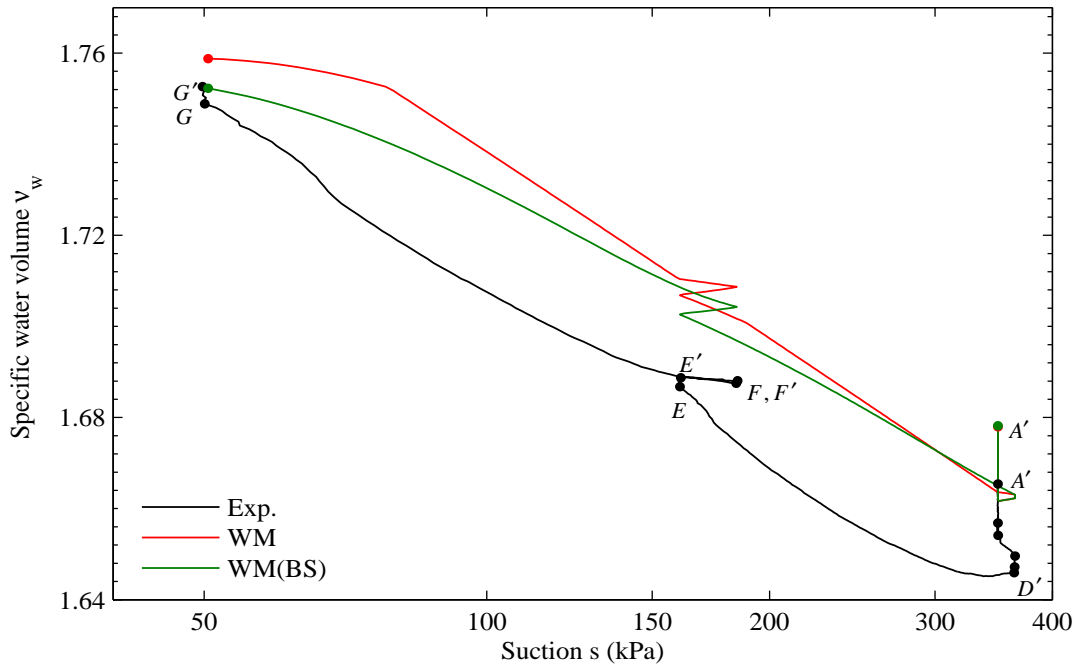


Figure 8-13 Variation of specific water volume v_w with suction s for Test A3 along with simulations

Inspection of Figure 8-13 shows that both WM and WM (BS) predict a reduction in the gradient of the curve of v_w against $\ln s$ in the later part of wetting path $F' - G$, which is not apparent in the experimental results. This was due to the fact that the amount of collapse compression (void ratio reduction) predicted by WM and WM (BS) during the later part of $F' - G$ was greater than was observed in the experimental result (see Figure 8-11), whereas the increase of degree of saturation was well represented by the models (Figure 8-12).

8.1.3 Relationship for coupled upward movement of SD yield curve (Test A4)

The Wheeler et al. (2003) model incorporates a second coupling equation to represent the influence of mechanical behaviour on water retention behaviour:

$$\frac{ds_D^*}{s_D^*} = \frac{ds_I^*}{s_I^*} = k_2 \frac{dp_0^*}{p_0^*} \quad (8-4)$$

Test A4 was devised to investigate the validity of this coupling equation and to determine the shape of the LC yield curve.

The stress path for Test A4 is shown in Table 8-3 and Figure 8-14. The soil sample was first equalized (AA') at a suction of 150 kPa and a mean net stress of 20 kPa. It was then isotropically loaded ($A' - B$) at constant suction to a mean net stress of 150 kPa, with the intention that the stress point was on both SD and LC yield curves at the end of the isotropic loading. The sample was then simultaneously unloaded and dried $B' - C$ to a mean net stress of 75 kPa and a suction of 200 kPa. This stress path was expected to be inside the yield curves, and it was followed by constant suction isotropic loading $C' - D$ to a mean net stress of 250 kPa. According to the Wheeler et al. (2003) model, during isotropic loading $C' - D$, yield should have occurred first on the LC curve and then subsequently a second yield point should have been observed when yielding also commenced on the SD curve. This isotropic loading $C' - D$ was followed with another simultaneous unloading and drying stress path $D' - E$ to a mean net stress of 150 kPa and a suction of 300 kPa. The sample was then isotropically loaded $E' - F$ to a mean net stress of 400 kPa. The final stage was a wetting $F' - G$ to a suction of 200 kPa at constant mean net stress.

| Stage | | | \bar{p} (kPa) | s (kPa) |
|-------|----|------------------------------|-----------------|-----------|
| From | To | Description | | |
| A | A' | Initial equalisation | 20 | 150 |
| A' | B | Isotropic loading | 20 → 150 | 150 |
| B | B' | Equalisation | 150 | 150 |
| B' | C | Isotropic unloading & drying | 150 → 75 | 150 → 200 |
| C | C' | Equalisation | 75 | 200 |
| C' | D | Isotropic loading | 75 → 250 | 200 |
| D | D' | Equalisation | 250 | 200 |
| D' | E | Isotropic unloading & drying | 250 → 150 | 200 → 300 |
| E | E' | Equalisation | 150 | 300 |
| E' | F | Isotropic loading | 150 → 400 | 300 |
| F | F' | Equalisation | 400 | 300 |
| F' | G | Wetting | 400 | 300 → 200 |
| G | G' | Equalisation | 400 | 200 |

Table 8-3 Stress path for Test A4

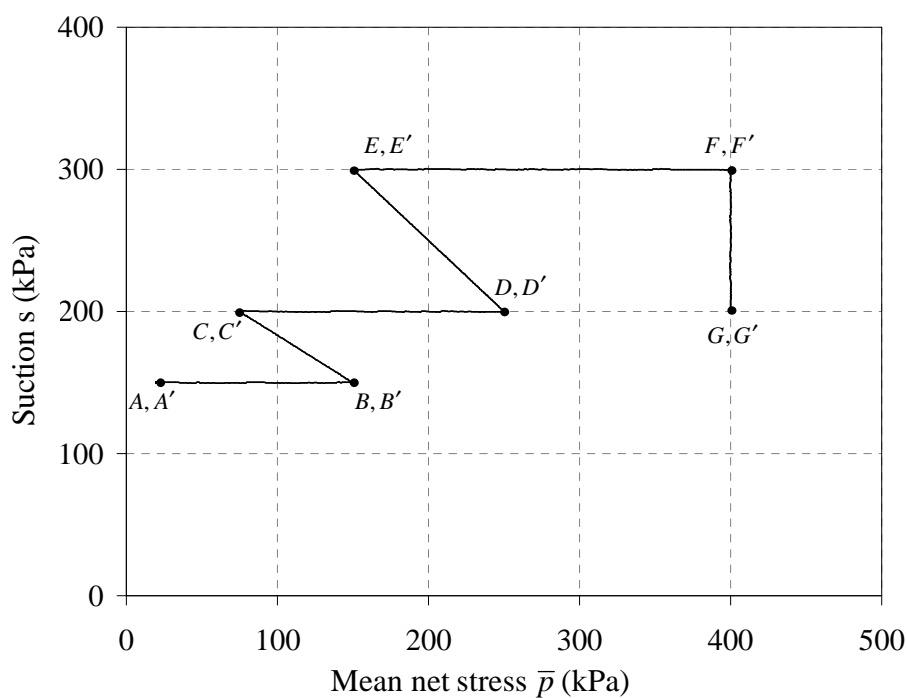


Figure 8-14 Stress path for Test A4

The stress path was designed to investigate two questions:

- was there a first yield point (on the LC curve) during isotropic loading stage $C' - D$ at a value of mean Bishop's stress equal to that previously applied at B (supporting the proposal of a vertical LC yield curve in the $s^* : p^*$ plane)?

Similarly was there a first yield point (on the LC yield curve) during isotropic loading stage $E' - F$ at a value of mean Bishop's stress equal to that previously applied at D ?

- were there second yield points (corresponding to reaching the corner of the LC and SD yield curves) during loading stages $C' - D$ and $E' - F$, and did these occur at points consistent with the predictions of the coupling relationship of Equation 8-4?

Figure 8-15 and Figure 8-16 show the variation of specific volume with mean net stress and suction respectively. It can be seen from the two figures that all three models provide reasonable predictions of the variation of v , with the WM and WM (BS) generally slightly better than the BBM (the BBM underestimates the reduction of v during isotropic loading $C' - D$, and as a consequence over-predicts the actual values of v throughout the subsequent stages of the test).

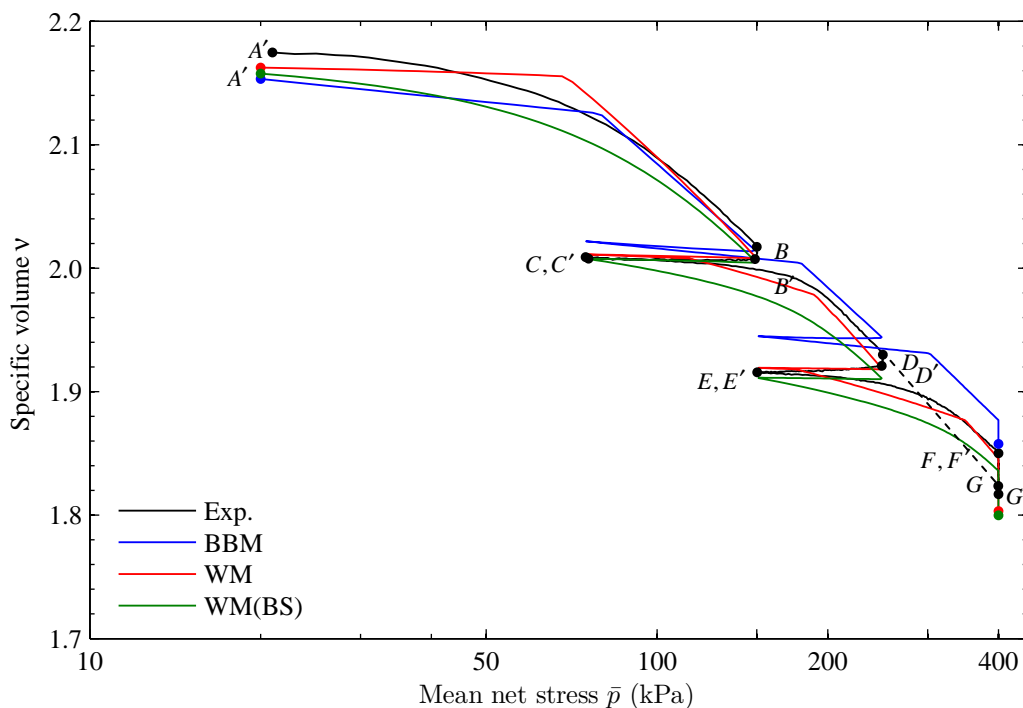


Figure 8-15 Variation of specific volume v with mean net stress \bar{p} for Test A4 along with simulations

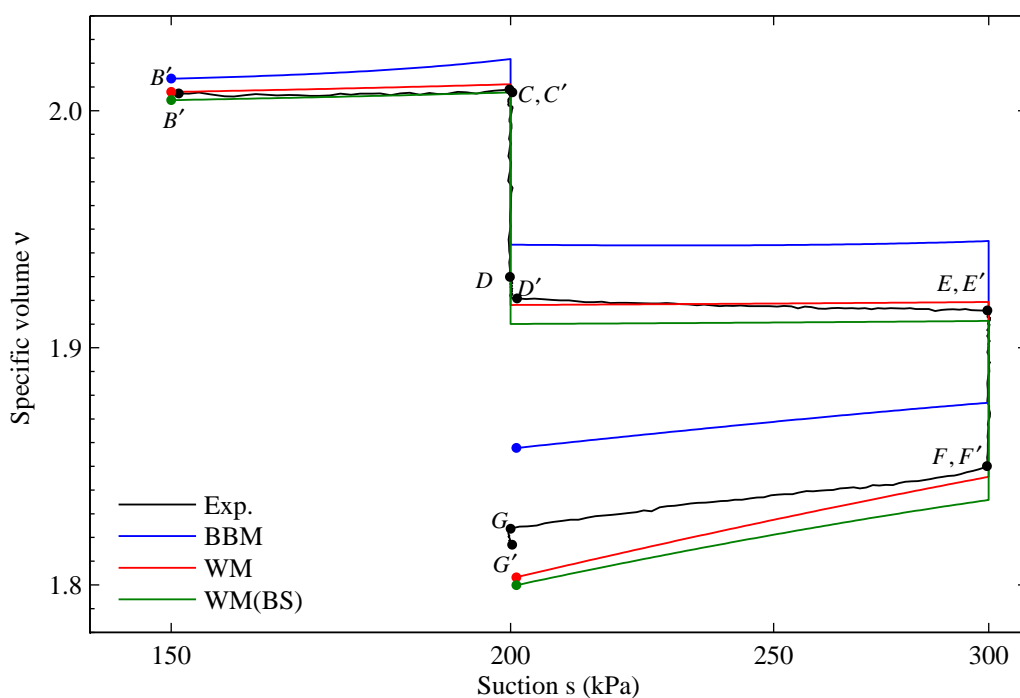


Figure 8-16 Variation of specific volume v with suction s for Test A4 along with simulations

Although both the WM and the WM (BS) provide successful overall modelling of the observed variation of v in Figure 8-15 and Figure 8-16, detailed examination of the experimental curve in Figure 8-15 shows that there is no evidence of the double yield points suggested by the WM simulations during isotropic loading stages $C' - D$ and $E' - F$. The shapes of the experimental compression curves during loading stages $C' - D$ and $E' - F$ are more consistent with either a single yield point (as suggested by the BBM) or more gradual transitions between elastic and elasto-plastic behaviour (as suggested by the WM (BS)). During the first isotropic loading stage $A' - B$, it is the gradual transition from elastic to elasto-plastic behaviour predicted by the WM (BS) which provides the best representation of the observed shape of the compression curve. The absence of two clear yield points in experimental compression curves for stages $C' - D$ and $E' - F$ in Figure 8-15 makes it impossible to investigate directly the two questions about the WM that Test A4 was designed to answer: whether the LC yield curve is a straight vertical line in the $s^* : p^*$ plane and whether the proposed coupling relationship of Equation 8-4 is correct. However, the fact that the WM and WM (BS) simulations in Figure 8-15 and Figure 8-16 provide reasonable matches to the experimental results provides indirect (but inconclusive)

evidence in support of these aspects of the modelling framework of Wheeler et al. (2003).

The dashed line in Figure 8-15 is an extension of the experimental normal compression line for 200 kPa suction from loading stage $C' - D$, and it passes through the final experimental point G (when the suction was again 200 kPa), suggesting that at the end of wetting $F' - G$, the state of the sample was once again on a unique normal compression line for 200 kPa suction. This observation is in agreement with the modelling concepts employed in either the BBM (yielding on the LC yield curve at points D and G) or the WM (yielding on the SD and LC yield curves simultaneously at points D and G).

Figure 8-17 shows the experimental variation of S_r plotted against \bar{p} , along with model simulations from WM and WM (BS). Generally, both WM and WM (BS) provide reasonable predictions of the variation of S_r throughout the test. Both models under-predict the reduction of S_r during unloading/drying stage $D' - E$, and this appears to be a weakness of the models.

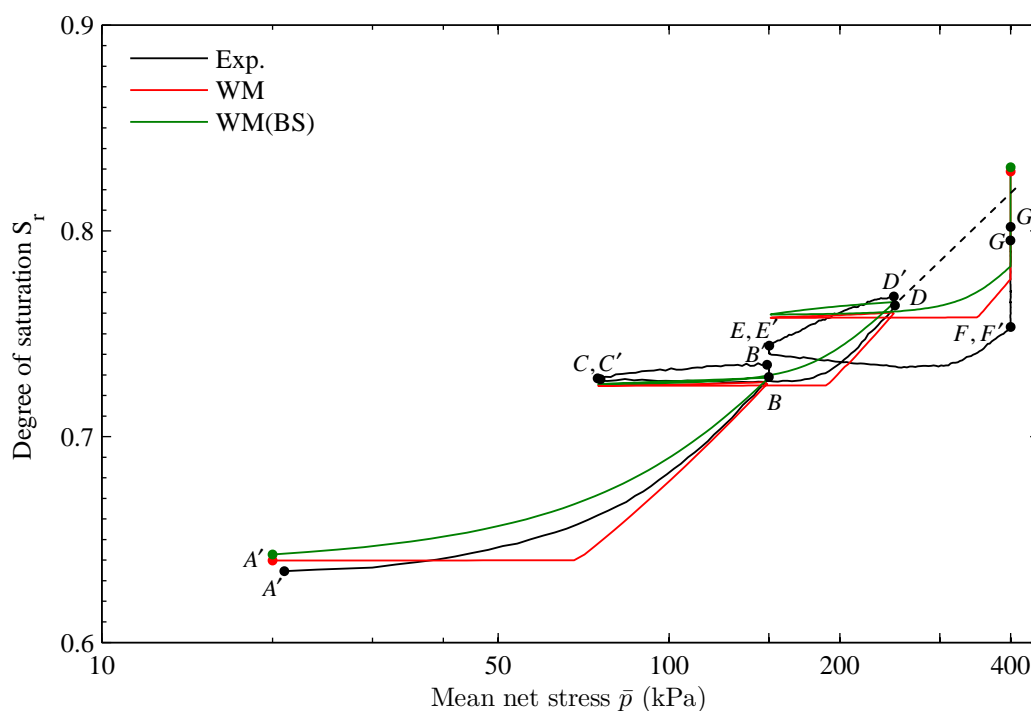


Figure 8-17 Variation of degree of saturation S_r with mean net stress \bar{p} for Test A4 along with simulations

During the initial part of isotropic loading $E' - F$, a reduction in degree of saturation can be observed from the experimental curve in Figure 8-17, whereas this is not predicted by either WM or WM (BS). It is, however, not clear whether this reduction in S_r can be attributed to delayed effects from the previous stage $D' - E$ (non-equalisation during equalisation stage EE'). It could also be perfectly possible for S_r to reduce during isotropic loading, as changes in S_r depend on both the pore water volume change and the total volume change. If the observed experimental reduction of S_r during the early part of loading stage $E' - F$ was correct, then this represents a weakness of models WM and WM (BS). However, both models correctly predict the significant increase of S_r in the final part of loading stage $E' - F$ and in the subsequent wetting stage $F' - G$. At the end of wetting stage $F' - G$ (when the suction was 200 kPa), the experimental value of S_r was less than the value given by extending the experimental curve from loading stage $C' - D$ (when the suction was also 200 kPa); see the dashed line in Figure 8-17. This observation is counter to the predictions of the WM.

Figure 8-18 and Figure 8-19 show the variation of specific volume and degree of saturation with mean Bishop's stress. Again the simulations of the WM and the WM (BS) generally provide reasonable matches of the observed behaviour, but the double yield points suggested by the WM during isotropic loading stages $C' - D$ and $E' - F$ are no more apparent in the experimental curves when plotted against p^* than in when plotted against \bar{p} (confirming that it is impossible to investigate directly the questions that Test A4 was designed to answer).

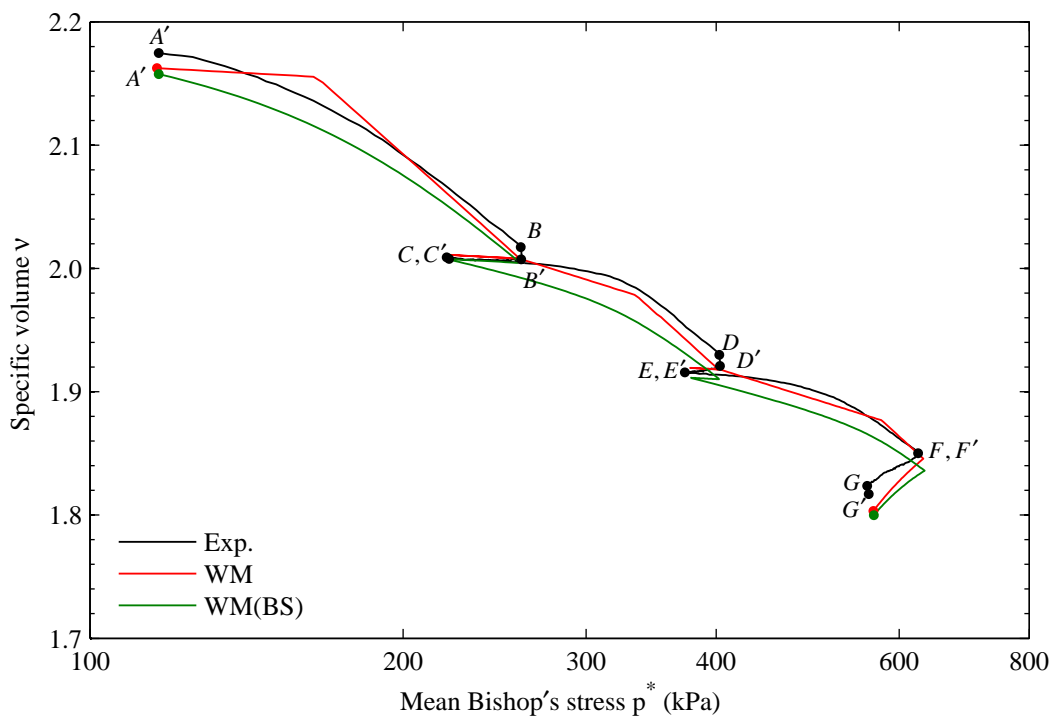


Figure 8-18 Variation of specific volume v with mean Bishop's stress p^* for Test A4 along with simulations

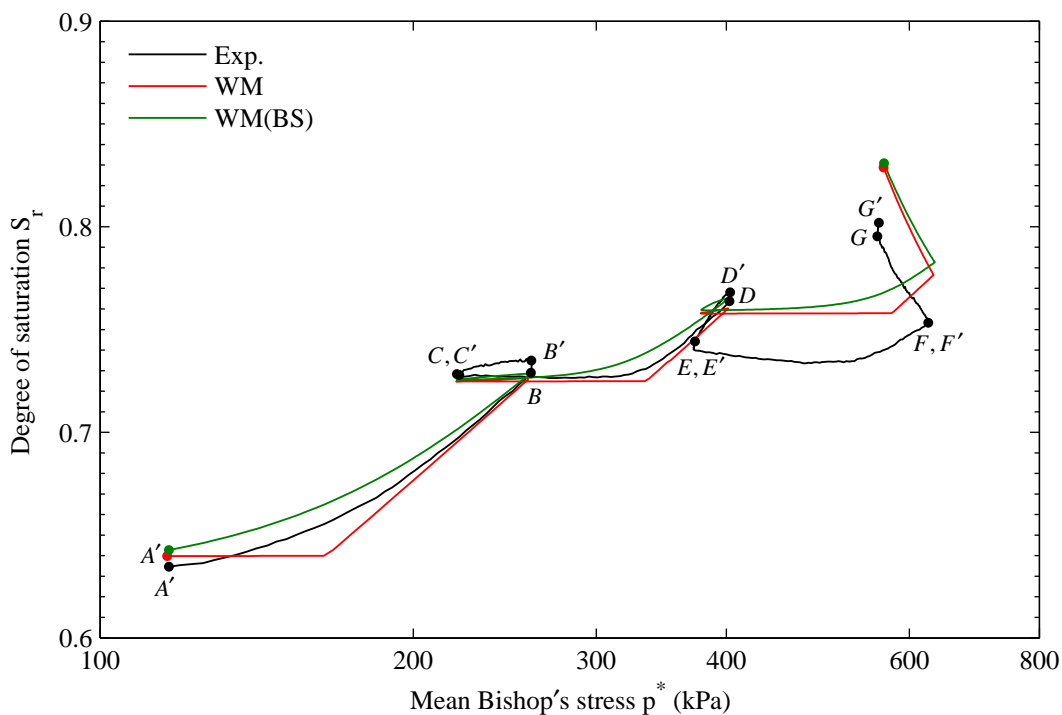


Figure 8-19 Variation of degree of saturation S_r with mean Bishop's stress p^* for Test A4 along with simulations

8.1.4 Investigation of SI and SD yield curves (Test A5)

In the Wheeler et al. (2003) framework, two yield curves (SI and SD) were proposed to represent the water retention behaviour. Test A5 involved several wetting and drying stages over a suction range from 30 to 300 kPa, with the intention of investigating the existence of these yield curves and the proposed cross-coupling between them.

In Test A5, a sample was first equalised (AA') at a mean net stress of 10 kPa and suction of 30 kPa (Table 8-4). It was then subjected to a drying-wetting cycle ($A' - B$ and $B' - C$), over a suction range of 30-300-40 kPa, performed at a constant mean net stress of 10 kPa as shown in Table 8-4 and Figure 8-20. It was then dried again ($C' - D$) to a suction of 200 kPa, before final isotropic loading ($D' - E$) at constant suction to a mean net stress of 275 kPa.

Figure 8-21 shows the variation of specific volume v plotted against suction during the drying-wetting paths of Test A5. The experimental curve shows some non-elastic behaviour, with net reduction of volume over drying-wetting cycle $A' - B' - C'$, and final drying $C' - D$ not following precisely the same path as wetting $B' - C$. None of the three models captures this behaviour well. The BBM and WM both predict entirely elastic variation of v during the drying and wetting paths, because they both predict that the stress path remains inside the LC yield curve. WM (BS) does predict non-elastic change of v , and a net reduction of v over the cycles, but the shape of the predicted curves is a poor match to the experimental results (particularly the form of irreversibility observed during stages $B' - C$ and $C' - D$).

| Stage | | | \bar{p} (kPa) | s (kPa) |
|-------|----|----------------------|-----------------|-----------|
| From | To | Description | | |
| A | A' | Initial equalisation | 10 | 30 |
| A' | B | Drying | 10 | 30 → 300 |
| B | B' | Equalisation | 10 | 300 |
| B' | C | Wetting | 10 | 300 → 40 |
| C | C' | Equalisation | 10 | 40 |
| C' | D | Drying | 10 | 40 → 200 |
| D | D' | Equalisation | 10 | 200 |
| D' | E | Isotropic unloading | 10 - 275 | 200 |

Table 8-4 Stress path for Test A5

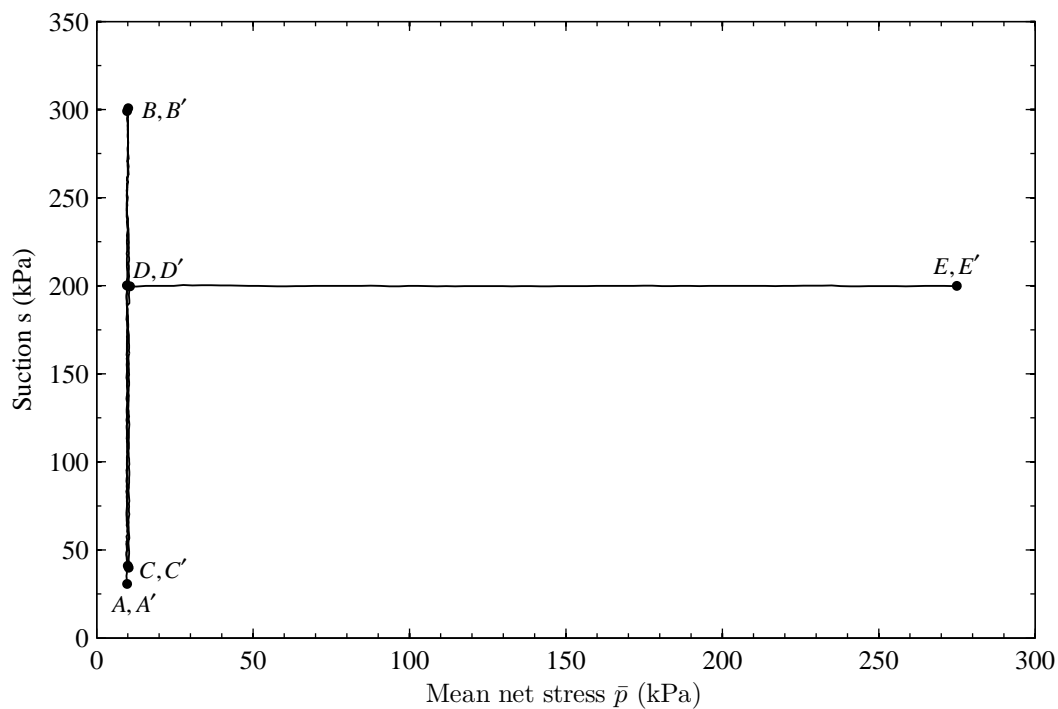


Figure 8-20 Stress path for Test A5

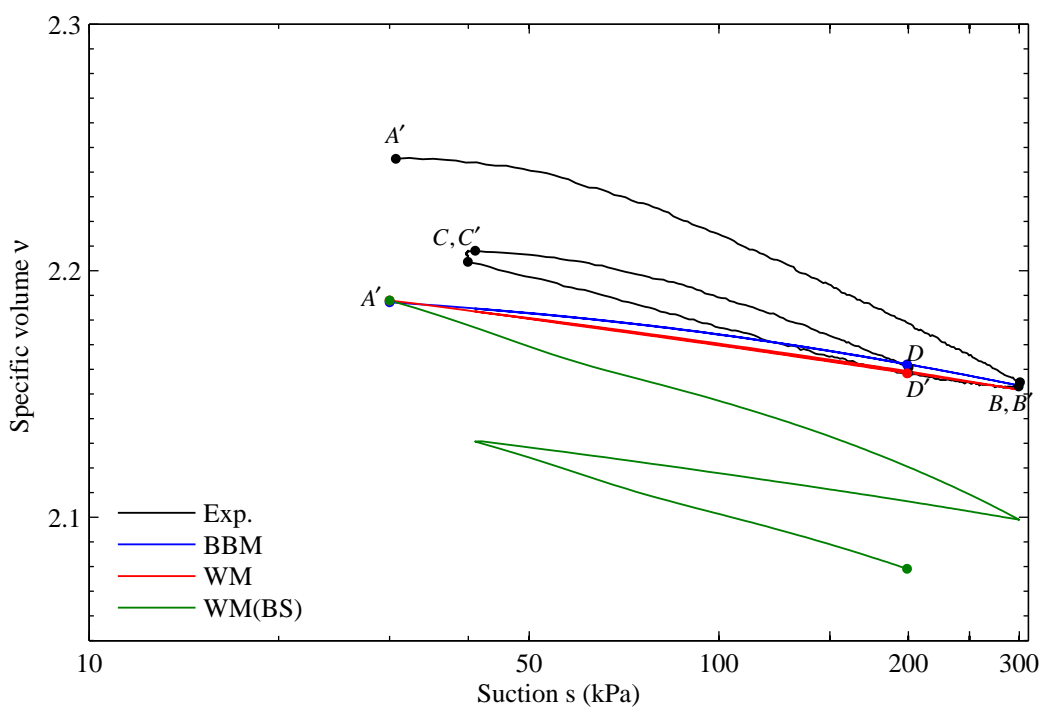


Figure 8-21 Variation of specific volume v with suction s for drying-wetting cycles of Test A5 along with simulations

Figure 8-22 and Figure 8-23 show the variation of S_r during the drying and wetting stages of Test A5 plotted against s and s^* respectively. There is very little difference

between the two plots. The experimental variation of S_r in Figure 8-22 and Figure 8-23 shows clear evidence of non-elastic behaviour, with wetting curve $B' - C$ lying below the previous drying curve $A' - B$, and final drying path $C' - D$ lying above the previous wetting path $B' - C$ and below the first drying curve $A' - B$. This pattern of behaviour is entirely consistent with the many examples of water retention behaviour reported in the literature.

Both WM and WM (BS) predict non-elastic changes of S_r during the drying and wetting paths, but neither model provides a good match to the experimental observations (see Figure 8-22 and Figure 8-23). WM predicts no plastic changes of v , and therefore the WM predictions for the variation of S_r show a simple closed elasto-plastic loop for the drying-wetting cycles. This fails to capture fully the observed irreversibility.

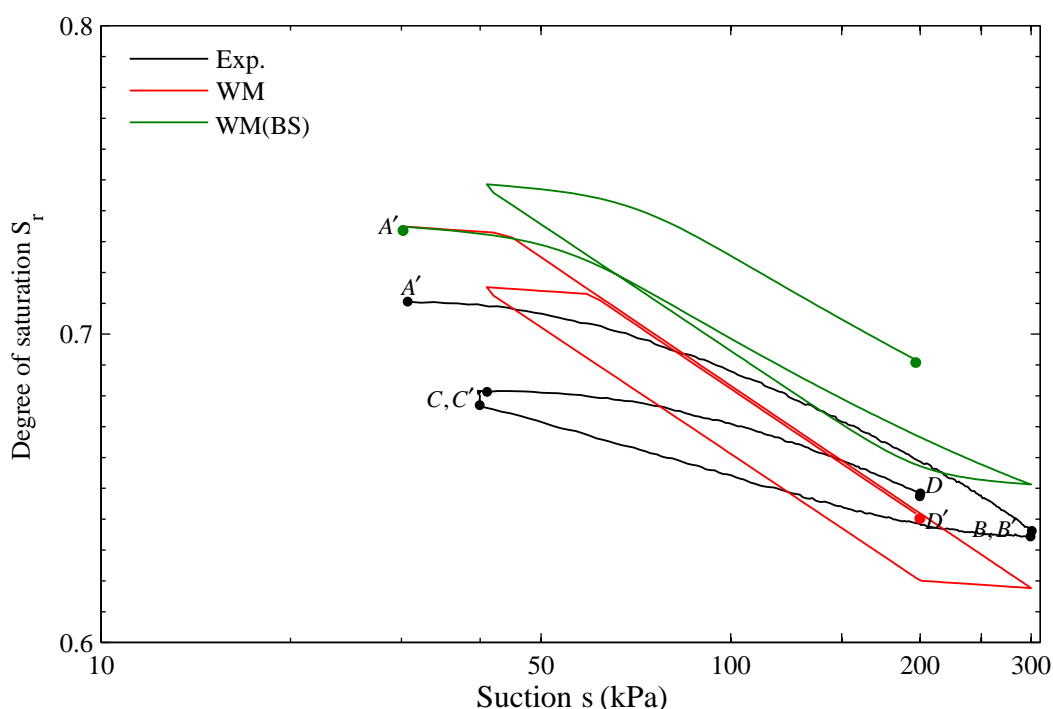


Figure 8-22 Variation of degree of saturation S_r with suction s for drying-wetting cycles of Test A5 along with simulations

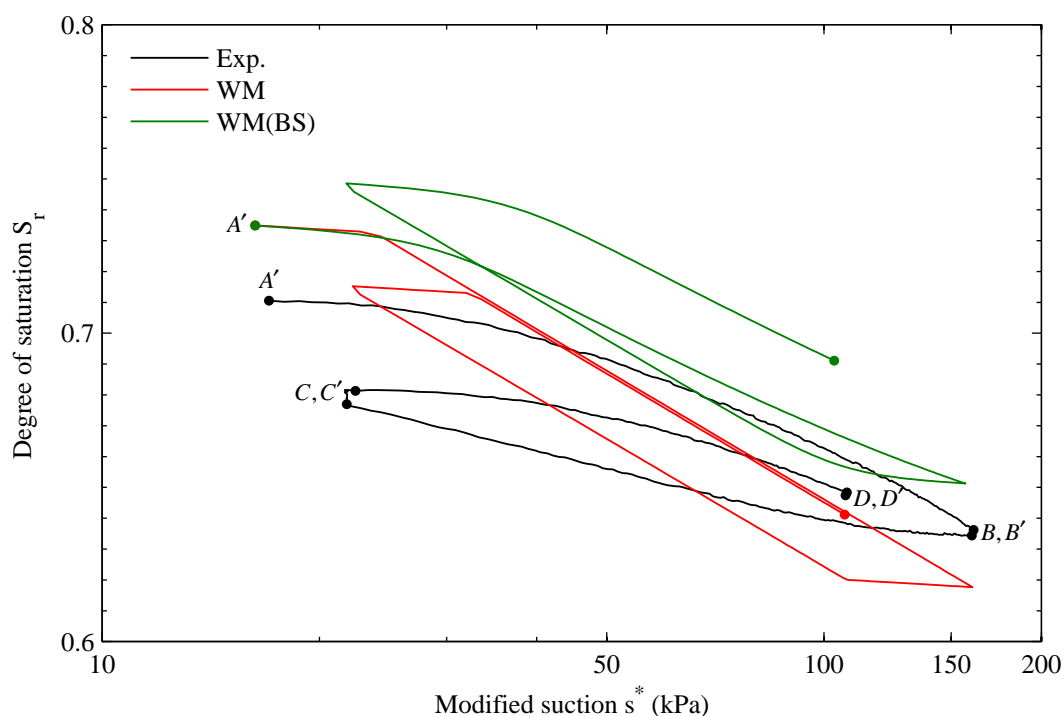


Figure 8-23 Variation of degree of saturation S_r with modified suction s^* for drying-wetting cycles of Test A5 along with simulations

The value selected for the model parameter λ_s means that, for this test, the WM simulation overestimates the final gradient of the drying curve $A' - B$ and overestimates even more severely the final gradient of the wetting curve $B' - C$. With the later part of the experimental wetting curve $B' - C$ having a gradient significantly less than that of the later part of the experimental drying curve $A' - B$, there is a suggestion from Figure 8-22 and Figure 8-23 that it is not possible to match both drying and wetting curves with a single value of λ_s in the WM. The selection of a relatively small spacing between the SI and SD yield curves for the WM simulations also seems to underestimate for this test the spacing between drying curve $A' - B$ and wetting curve $B' - C$ in Figure 8-22 and Figure 8-23.

The WM (BS) simulation presented in Figure 8-22 and Figure 8-23 shows more realistic rounded shapes of wetting and drying curves than the WM (with its sharp transitions from elastic to fully elasto-plastic behaviour). The WM (BS) also shows non-closed loops in the variation of S_r over the drying-wetting cycles. This is a consequence of the plastic volumetric strains predicted by the WM (BS) (see Figure

8-21) producing coupled upward movements of the SI and SD bounding curves in the model, and consequent shifts of the main drying and main wetting curves in the $S_r : s^*$ plane. Unfortunately, however, the irreversible changes of S_r predicted by the WM (BS) are generally not a good match to the experimental observations. The predicted plastic volumetric strains cause the main drying and wetting curves to be shifted upwards in the $S_r : s^*$ plane, so that generally net increases of S_r are predicted by the WM(BS) over the drying-wetting cycles (see Figure 8-22 and Figure 8-23). This contrast with the experimental observations, which tend to show a net reduction of S_r over the cycles.

Figure 8-24 shows the variation of specific water volume v_w with suction during the drying and wetting paths of Test A5. Again the WM and WM (BS) simulations are not particularly good match to the observed behaviour. The model predictions for the variation of v_w are calculated from the predicted variations of v and S_r . It is, however, interesting to note that, whereas the WM and WM (BS) produce distinctly different predictions for the variations of v and S_r (see Figure 8-21 and Figure 8-22), the two models produce very similar predictions for the variation of v_w (see Figure 8-24).

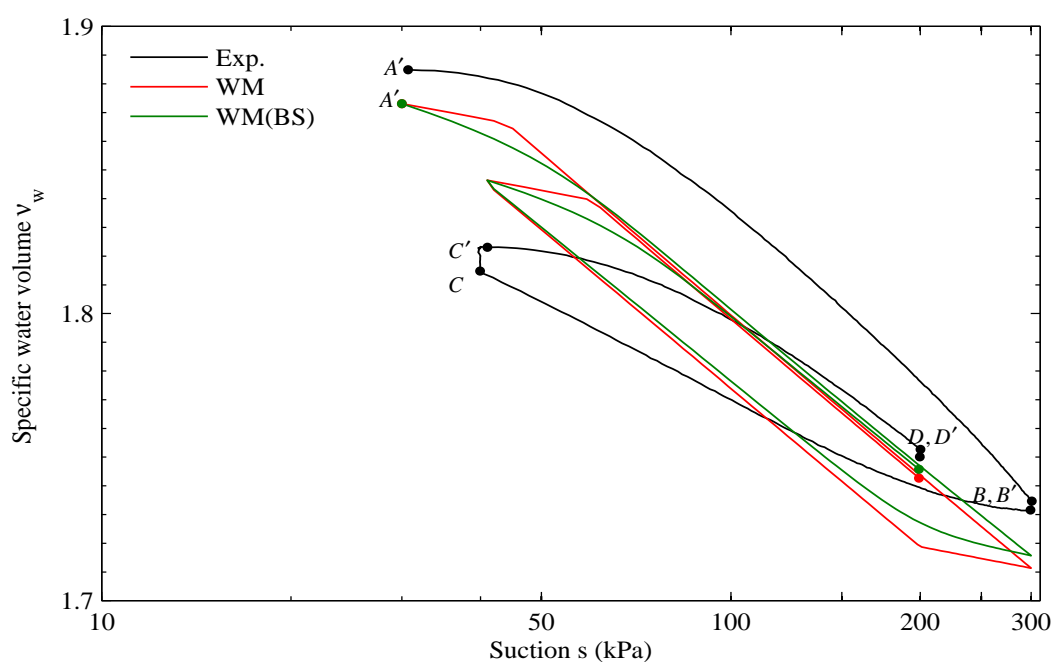


Figure 8-24 Variation of specific water volume v_w with suction s for drying-wetting cycles of Test A5 along with simulations

Figure 8-25 and Figure 8-26 show the variation of specific volume and degree of saturation against mean net stress for the final isotropic loading stage $D' - E$ of Test A5. All three models provide a good prediction of the final value of v (see Figure 8-25), even though the starting value of v is under-predicted by the WM (BS) because of the poor prediction of v at the end of the previous drying-wetting cycles (see Figure 8-21). Detailed inspection of Figure 8-25 shows that the WM and WM (BS) provide a slightly better match than the BBM to the final gradient of the normal compression line. Figure 8-26 shows that both the WM and WM (BS) provide a good prediction of the final value of S_r at the end of isotropic loading stage $D' - E$. This is despite the fact that the WM (BS) overestimates the value of S_r at the start of stage $D' - E$, because of problems in correctly predicting the value of S_r at the end of the previous drying-wetting cycles (see Figure 8-22)

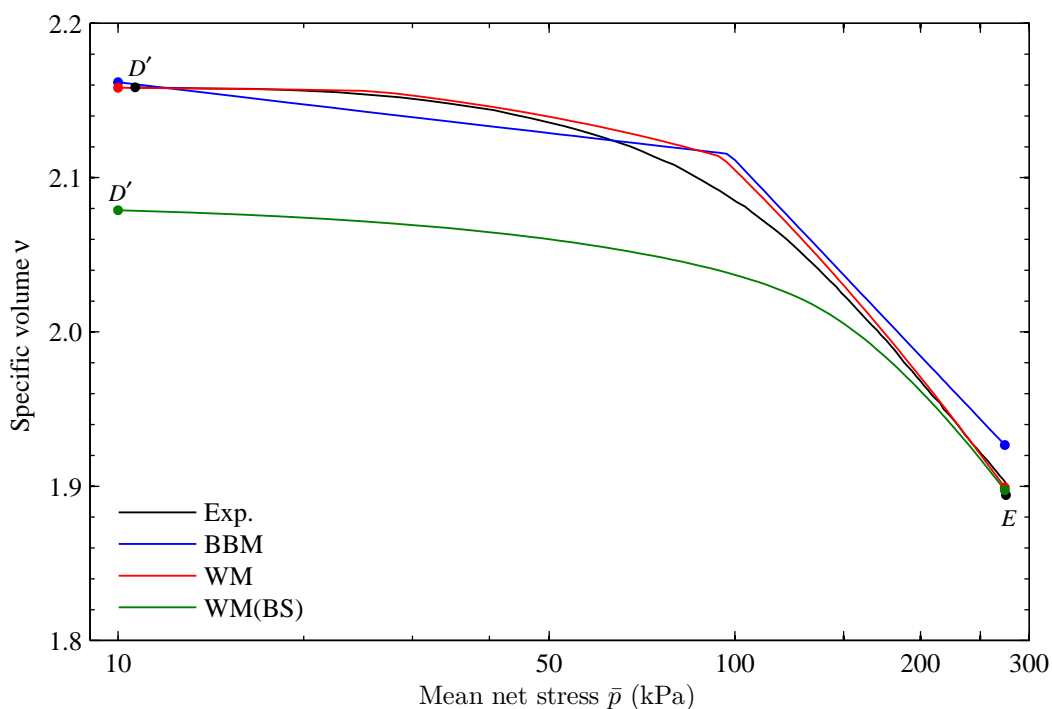


Figure 8-25 Variation of specific volume v with mean net stress \bar{p} for final loading stage of Test A5 along with simulations

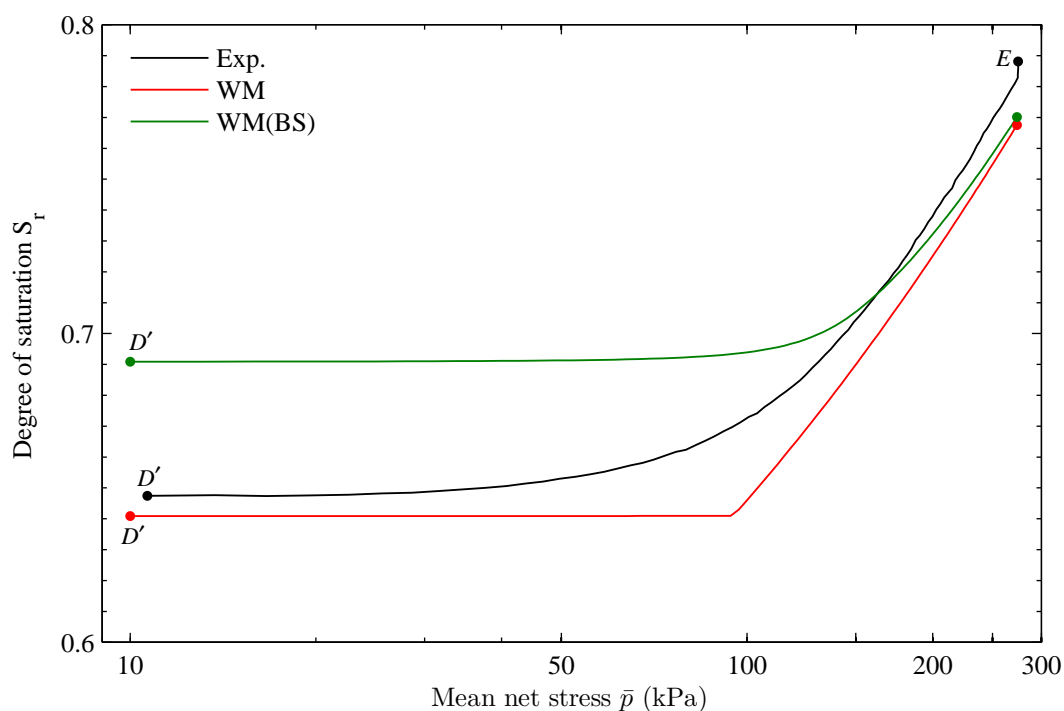


Figure 8-26 Variation of degree of saturation S_r with mean net stress \bar{p} for final loading stage of Test A5 along with simulations

8.1.5 Suction cycles under constant volume condition (Test A6)

The Wheeler et al. (2003) framework has been proposed in terms of mean Bishop's stress mean p^* and modified suction s^* and specific constitutive equations are proposed for predicting the changes in specific volume and degree of saturation. By performing a test in which either specific volume or degree of saturation is held constant, it may be possible to gain some insight into the soil behaviour and to investigate the validity of aspects of the model, such as the links between stress and strain variables, the shapes of the yield curves or the forms of coupling equations. Test A6 was therefore performed by incorporating several constant volume stages in which \bar{p} and s were varied. To keep the sample volume constant, one of the stress variables was varied at a constant rate and the other stress variable was then adjusted in such a way as to maintain constant volume. It was decided to vary suction at constant rate and then to adjust the mean net stress to keep the sample volume constant, because the response time of a sample to suction changes is generally very large. Changes of mean net stress, however, generally produce sample volume change in reasonably short periods of time.

Table 8-5 and Figure 8-27 show the stress path for Test A6. The soil sample was initially equalised (AA') at a mean net stress of 20 kPa and a suction of 50 kPa. An isotropic loading stage $A'-B$ was then performed at constant suction to a mean net stress of 250 kPa. During subsequent stage $B'-C$ the suction was increased at a constant rate of 1 kPa/hr to a value of 338 kPa while adjusting the mean net stress to keep specific volume at approximately 1.865. The stage was terminated when the mean net stress reduced to a value of 10 kPa. Suction was then decreased during subsequent stage $C'-D$ at a constant rate of 1 kPa/hr to 25 kPa while keeping the sample volume constant by varying the mean net stress (which reached 155 kPa at the end of stage $C'-D$). A final constant volume stage $D'-E$ was then performed by increasing the suction again at a constant rate of 1 kPa/hr to a final value of 200 kPa, while varying the mean net stress to a final value of 28 kPa. During the equalisation stages CC' , DD' and EE' after the constant volume stages $B'-C$, $C'-D$ and $D'-E$ respectively, suction and mean net stress were held constant, and no attempt was made to keep specific volume constant by varying mean net stress as this might have led to substantial fluctuation of mean net stress. Any changes of v during these equalisation stages were very small. The final stage $E'-F$ involved isotropic loading at a constant suction of 200 kPa, but unfortunately it had to be terminated earlier than intended at a mean net stress of 430 kPa due to a power cut for electrical repairs.

| Stage | | | \bar{p} (kPa) | s (kPa) | v |
|-------|----|--------------------------------|-----------------|-----------|-------------|
| From | To | Description | | | |
| A | A' | Initial equalisation | 20 | 50 | 2.128-2.199 |
| A' | B | Isotropic loading | 20 → 250 | 50 | 2.199-1.873 |
| B | B' | Equalisation | 250 | 50 | 1.873-1.865 |
| B' | C | Suction increase at const vol. | 250 → 10 | 50 → 338 | 1.865 |
| C | C' | Equalisation | 10 | 338 | 1.865 |
| C' | D | Suction decrease at const vol. | 10 → 155 | 338 → 25 | 1.865 |
| D | D' | Equalisation | 155 | 25 | 1.865 |
| D' | E | Suction increase at const vol. | 155 → 28 | 25 → 200 | 1.865 |
| E | E' | Equalisation | 28 | 200 | 1.865 |
| E' | F | Isotropic loading | 28 → 430 | 200 | 1.865-1.805 |

Table 8-5 Stress path for Test A6

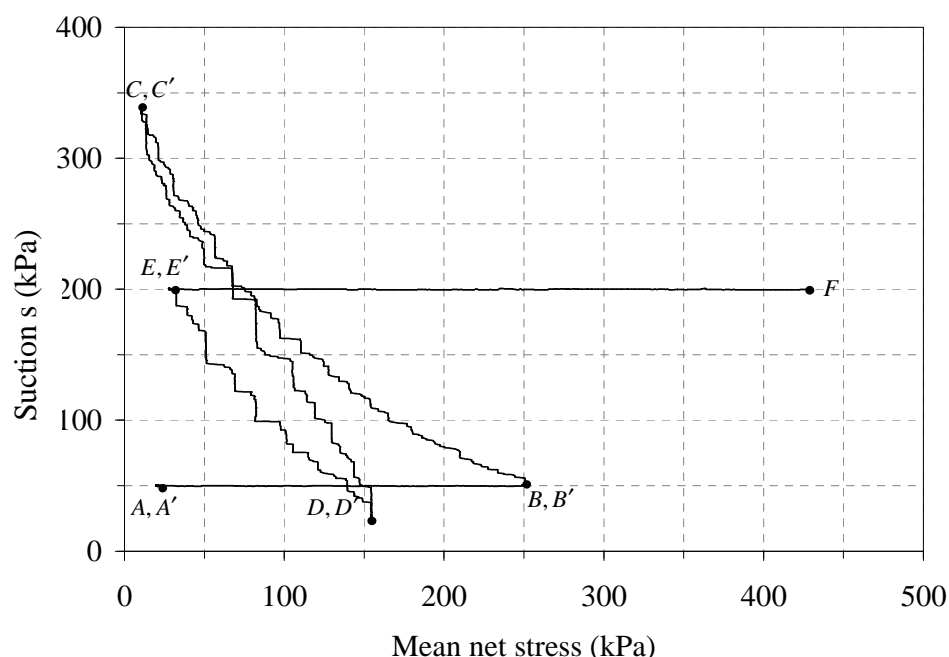


Figure 8-27 Stress path for Test A6

Figure 8-28 shows the experimental variation of v plotted against \bar{p} , along with model simulations from all three models. WM and WM (BS) simulations for the final constant suction isotropic loading stage $E' - F$ are not shown, because these two models predicted impossible stress states (negative values of \bar{p}) before the end of the previous drying stage $D' - E$.

Inspection of Figure 8-28 shows that, during the initial constant suction isotropic loading stage $A' - B$, the BBM provides a significantly better match to the experimental compression curve than either the WM or WM (BS). This is because the WM and WM (BS) struggle to predict correctly the gradient of constant suction isotropic normal compression lines over the full experimental range of suction values, and, with the selected parameter values, the predicted gradient is particularly poor at a suction of 50 kPa. This issue is addressed in Section 10.4. This failure by the WM and WM (BS) to predict accurately the compression curve during stage $A' - B$ means that the simulations of these models for the subsequent constant volume drying and wetting stages are actually performed at an incorrect value of v (see Figure 8-28).

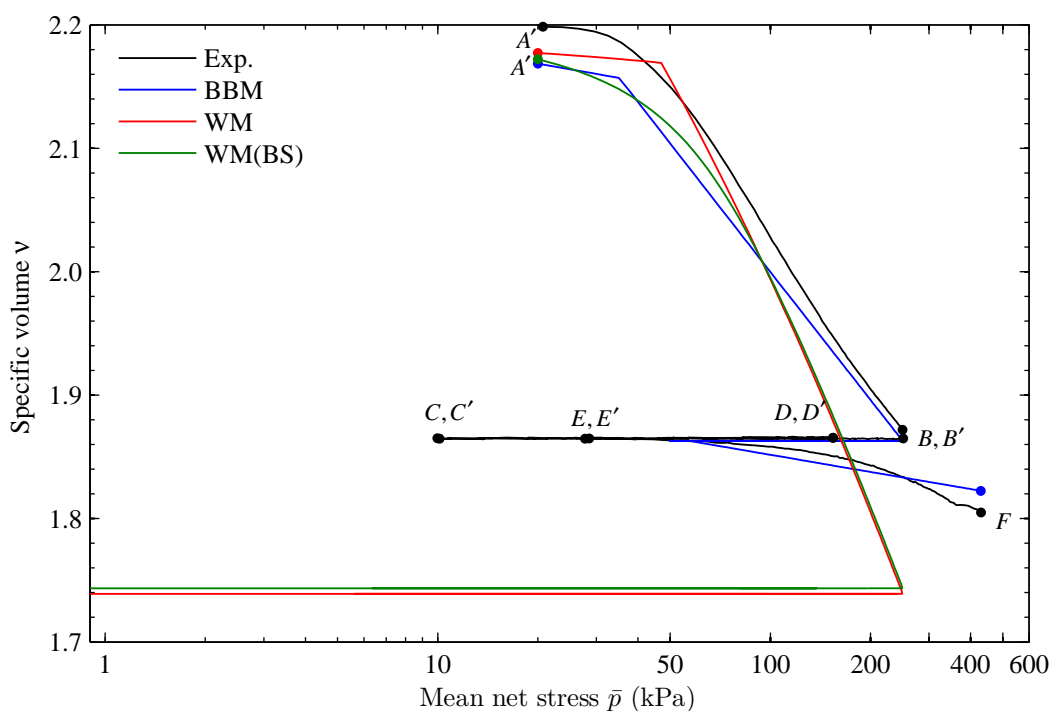


Figure 8-28 Variation of specific volume v with mean net stress \bar{p} for Test A6

Figure 8-29 illustrates the stress path during constant volume drying and wetting stages $B' - C$, $C' - D$ and $D' - E$ in terms of s and \bar{p} , obtained from the experimental results and from the predictions from all three models. Figure 8-30 shows equivalent results in terms of s^* and p^* (here the model simulations have to be restricted to WM and WM (BS)). Inspection of the experimental curve in Figure 8-29 reveals that mean net stress was adjusted mostly in a non-smooth manner to keep the sample volume constant, with maximum step changes of about 25 kPa. As a consequence of these step changes in \bar{p} , p^* also shows significant fluctuation throughout stages $B' - C$, $C' - D$ and $D' - E$ (see Figure 8-30). This kind of stress path was unavoidable, mainly due to the delayed response of the soil sample to changes of mean net stress.

Inspection of Figure 8-29 shows that the BBM does not provide a good match to all aspects of the experimental stress path. The BBM predicts elastic behaviour during drying stage $B' - C$, with mean net stress reduced in order to induce elastic swelling to counteract the elastic shrinkage caused by the suction increase. This is a reasonable match to the observed behaviour, although the reduction of \bar{p} is underestimated by the

model. During the subsequent wetting stage $C' - D$ the BBM initially predicts elastic behaviour, with a corresponding increase of \bar{p} required in order to maintain constant volume. However, when the suction is reduced below 50 kPa, in the later part of wetting stage $C' - D$, the BBM predicts the onset of wetting-induced collapse compression, due to yielding on the LC yield curve. The model therefore predicts a sudden change of stress path direction within wetting stage $C' - D$, with mean net stress now reducing (see Figure 8-29), so as to produce additional elastic swelling (in order to offset the effects of plastic collapse compression). Although the experimental results show irreversible behaviour during these drying and wetting stages $B' - C$ and $C' - D$, and a net reduction of \bar{p} over the two stages, there is no evidence of the predicted reversal of stress path direction during wetting stage $C' - D$. During the final drying stage $D' - E$, the BBM once more predicts elastic behaviour, and the predicted decrease of mean net stress provides a reasonable match to the observed behaviour (see Figure 8-29).

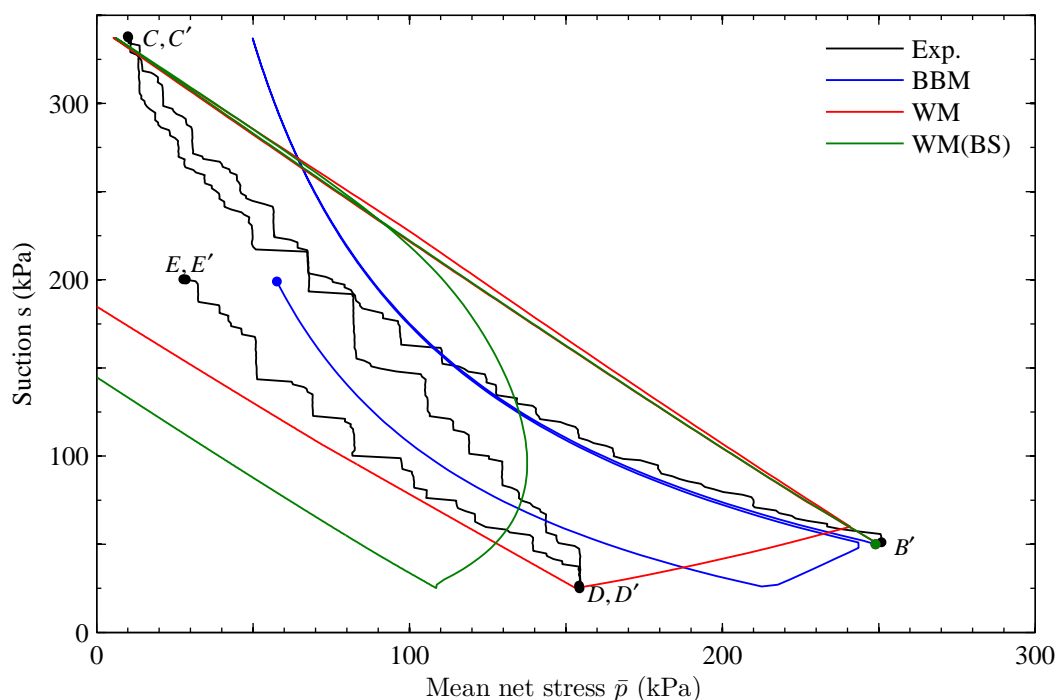


Figure 8-29 Stress path for constant ν condition of Test A6 in terms of suction s and mean net stress \bar{p}

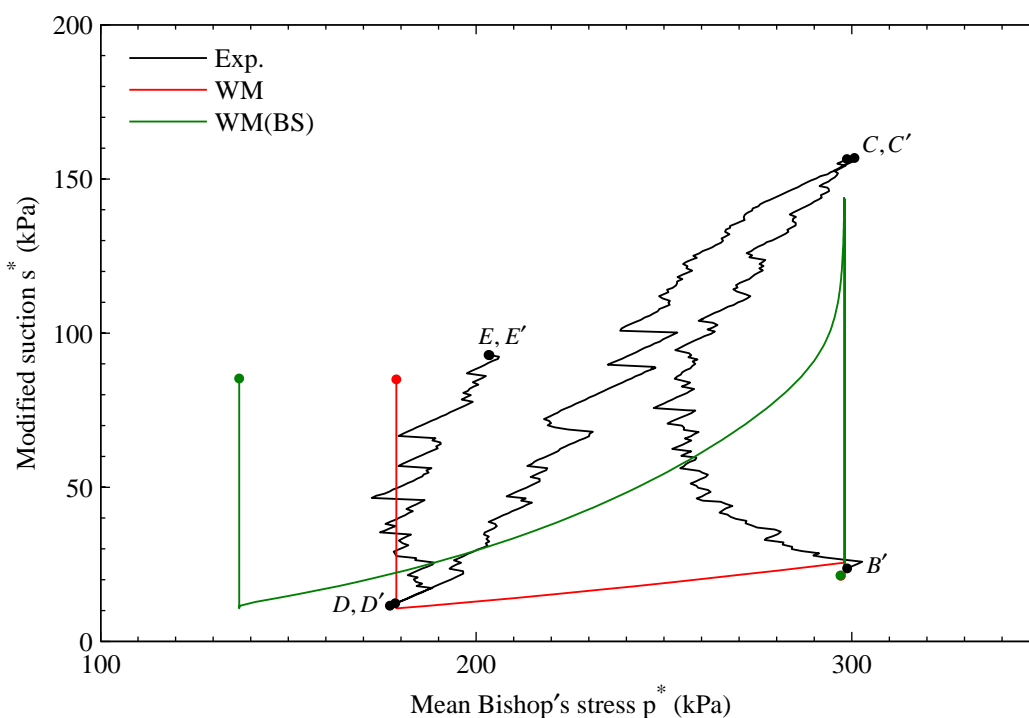


Figure 8-30 Stress path for constant v condition of Test A6 in terms of modified suction s^* and mean Bishop's stress p^*

Inspection of Figure 8-29 indicates that the WM and WM (BS) provide worse matches to the observed stress path than the BBM. During constant volume drying stage $B' - C$ the WM predicts elastic behaviour at constant mean Bishop's stress p^* (Figure 8-30), so that there is no elastic change of v . In order to maintain p^* constant, a decrease of \bar{p} is predicted during the drying stage (offsetting the predicted increase of $S_r s$ (note $p^* = \bar{p} + S_r s$)). This predicted decrease of \bar{p} during drying stage $B' - C$ is a reasonable match to the observed stress path (see Figure 8-29), although the curvature in the observed stress path is not captured. During subsequent constant volume wetting stage $C' - D$, the WM initially predicts elastic wetting behaviour at constant p^* (and increasing \bar{p}) (see Figure 8-30 and Figure 8-29). However, during drying stage $B' - C$ and wetting stage $C' - D$ plastic changes of S_r occurred due to yielding on the SI and SD yield curves, and this caused coupled movements of the LC yield curve. As a consequence, the LC yield curve was predicted to reach the stress point when the s and s^* were reduced to the values at stress state of B' during wetting stage $C' - D$ (but not accurately predicted by the WM because of small numerical errors in the

simulation). Further reduction of suction produced prediction of plastic compression (wetting-induced collapse compression) during the remainder of wetting stage $C' - D$. To offset this effect, the WM predicts a reduction of mean Bishop's stress p^* during the later part of wetting stage $C' - D$, to produce elastic swelling to counteract the predicted plastic compression. This results in a sudden change of stress path direction during $C' - D$ in both the $s^* : p^*$ plot (Figure 8-30) and the $s : \bar{p}$ plane (Figure 8-29), which is not a good match to the observed behaviour. During final constant volume drying stage $D' - E$ the WM predicts elastic behaviour at constant p^* (Figure 8-30) and decreasing \bar{p} (Figure 8-29) which is a good match to the experimental behaviour as far as the shapes of the curves are concerned. However, part way through stage $D' - E$ the predicted values of mean net stress go negative (see Figure 8-29). This is, of course, not possible. The WM (BS) predictions in Figure 8-29 and Figure 8-30 are similar to the WM predictions, except that a gradual onset of plastic volumetric strain is predicted during constant volume wetting stage $C' - D$, as the LC bounding curve approaches the stress point, and this produces a gradual change of stress path direction in both plots.

Figure 8-31 shows the experimental variation of S_r plotted against \bar{p} for Test A6, along with model simulations from WM and WM (BS). Although both models provide a reasonably good match for initial constant suction isotropic loading stage $A' - B$, the predictions for the subsequent constant volume drying and wetting stages ($B' - C, C' - D, D' - E$) are generally not a good match with the experimental observations. In particular, during the later part of wetting stage $C' - D$, both WM and WM (BS) predict a significant increase in degree of saturation to reach a saturated state, with a small decrease in mean net stress. These predictions were not supported by the experimental results even at a qualitative level (see Figure 8-31).

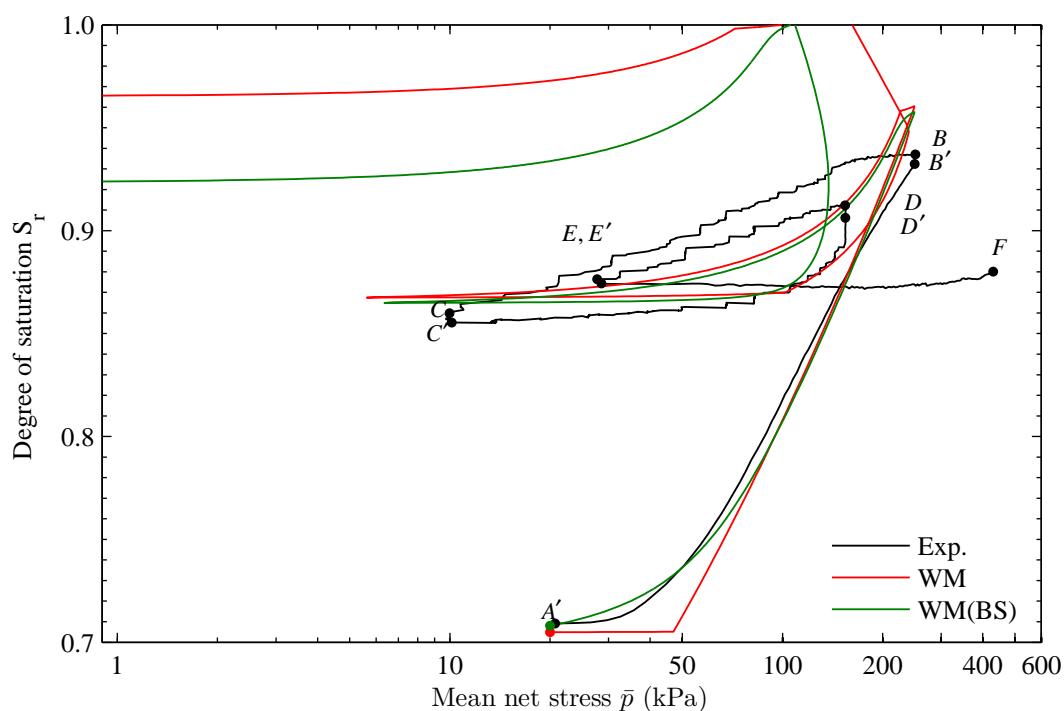


Figure 8-31 Variation of degree of saturation S_r with mean net stress \bar{p} for Test A6

8.1.6 Suction cycles under constant S_r condition (Tests A7 and A8)

Test A8 involved several stress path stages at constant S_r . Test A7, was originally intended for the same purpose, but unfortunately had to be terminated prematurely, due to a bug in the complex control equation employed in the Triax software to keep S_r constant. However, this incomplete test is presented here with the completed Test A8, in order to demonstrate the repeatability of the initial part of the tests.

Table 8-6, Table 8-7 and Figure 8-32 show the stress paths for Tests A7 and A8. Samples A7 and A8 were first equalised (aa' and AA') at a mean net stress of 20 kPa and a suction of 50 kPa. Suction was then increased to 325 kPa in Test A7 and to 300 kPa in Test A8 at a constant rate of 1 kPa/hr and mean net stress was varied in order to keep S_r constant, reaching a final value of 224 kPa in Test A7 and 170 kPa in Test A8 (see $a'-b$ and $A'-B$ respectively in Figure 8-32). Even though there was a slight difference in the stress paths $a'-b$ and $A'-B$, the overall trend seems to be similar, demonstrating reasonable repeatability (see Figure 8-32).

In Test A8, the suction was then decreased (stage $B' - C$) at a constant rate of 1 kPa/hr to 111 kPa. In the meantime, mean net stress was varied to keep S_r constant, decreasing to a final value of 5 kPa. Another suction increase stage at constant S_r ($C' - D$) was then performed to a suction value of 200 kPa with mean net stress increasing to 94 kPa. Sample A8 was then isotropically loaded ($D' - E$) at a constant suction of 200 kPa to a mean net stress of 250 kPa. A drying stage $E' - F$ to 300 kPa suction was then carried out, followed by a wetting stage $F' - G$ to 100 kPa suction and finally a drying stage $G' - H$ to 253 kPa suction. Stages $E' - F$, $F' - G$ and $G' - H$ were all performed at a constant mean net stress of 250 kPa (see Figure 8-32).

| Stage | | | \bar{p} (kPa) | s (kPa) | S_r |
|-------|------|------------------------------------|-----------------|-----------|-------------|
| From | To | Description | | | |
| a | a' | Initial equalisation | 20 | 50 | 0.605-0.715 |
| a' | b | Suction increase at constant S_r | 20 → 224 | 50 → 325 | 0.715-0.719 |
| b | b' | Equalisation | 224 | 325 | 0.719 |

Table 8-6 Stress path for Test A7

| Stage | | | \bar{p} (kPa) | s (kPa) | S_r |
|-------|------|------------------------------------|-----------------|-----------|-------------|
| From | To | Description | | | |
| A | A' | Initial equalisation | 20 | 50 | 0.572-0.702 |
| A' | B | Suction increase at constant S_r | 20 → 170 | 50 → 300 | 0.702-0.697 |
| B | B' | Equalisation | 170 | 300 | 0.697-0.695 |
| B' | C | Suction decrease at constant S_r | 170 → 5 | 300 → 111 | 0.695-0.698 |
| C | C' | Equalisation | 5 | 111 | 0.698-0.697 |
| C' | D | Suction increase at constant S_r | 5 → 94 | 111 → 200 | 0.697 |
| D | D' | Equalisation | 94 | 200 | 0.697 |
| D' | E | Isotropic loading | 94 → 250 | 200 | 0.697-0.755 |
| E | E' | Equalisation | 250 | 200 | 0.755-0.759 |
| E' | F | Drying | 250 | 200 → 300 | 0.759-0.738 |
| F | F' | Equalisation | 250 | 300 | 0.738-0.737 |
| F' | G | Wetting | 250 | 300 → 100 | 0.737-0.808 |
| G | G' | Equalisation | 250 | 100 | 0.808-0.817 |
| G' | H | Drying | 250 | 100 → 253 | 0.817-0.791 |

Table 8-7 Stress path for Test A8

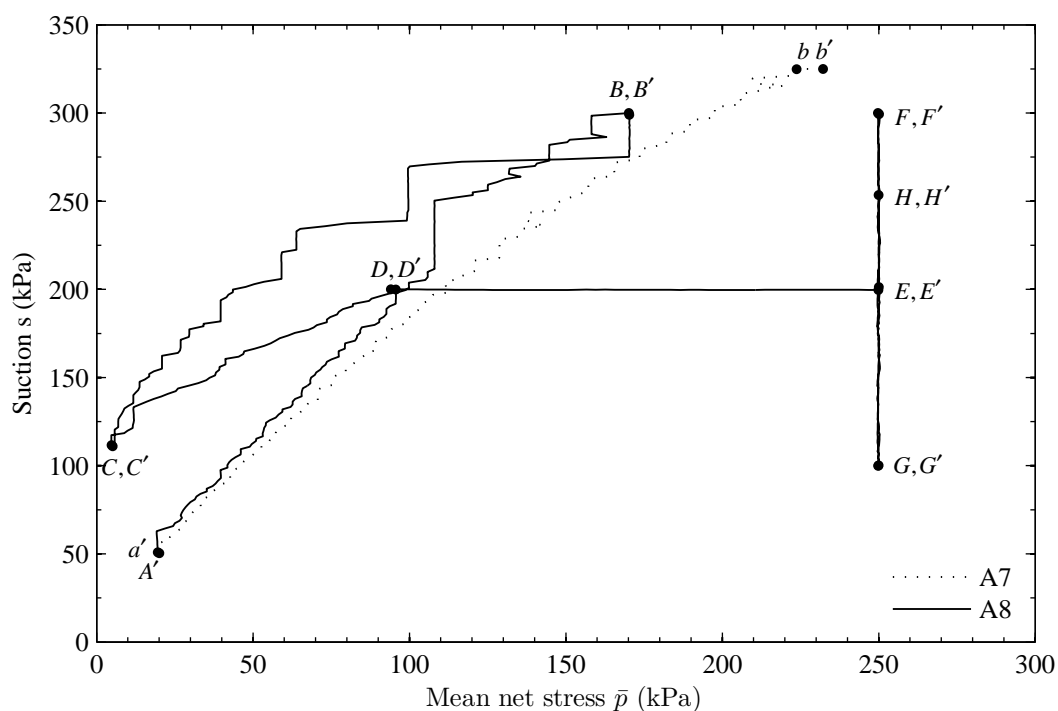


Figure 8-32 Stress paths for Tests A7 and A8

Inspection of the experimental stress path for the constant S_r stages of Test A8, viewed in the $s : \bar{p}$ plane (Figure 8-33) and in the $s^* : p^*$ plane (Figure 8-34) reveals that a smooth variation of mean net stress was not achieved, particularly for the stage which involved reduction in mean net stress ($B' - C$). In Test A8, the fluctuation in S_r during constant S_r stress path $AA' - BB' - CC' - DD'$ was about ± 0.003 , which is reasonably small given that no attempt was made to control S_r during equalisation stages BB' , CC' and DD' . It can be clearly seen from Figure 8-33 and Figure 8-34 that in order to keep S_r constant, both \bar{p} and p^* had to be increased in the stages where s (or s^*) was increased ($A' - B$ and $C' - D$), whereas both \bar{p} and p^* had to be decreased in order to keep S_r constant in the stage when s (or s^*) was decreased ($B' - C$). It is interesting to note that, for the constant S_r stress cycles of Test A8, the experimental stress path in the $s^* : p^*$ plane (Figure 8-34) suggests almost reversible behaviour, whereas when the experimental stress path is presented in the $s : \bar{p}$ plane (Figure 8-33) there is a stronger suggestion of irreversible behaviour.

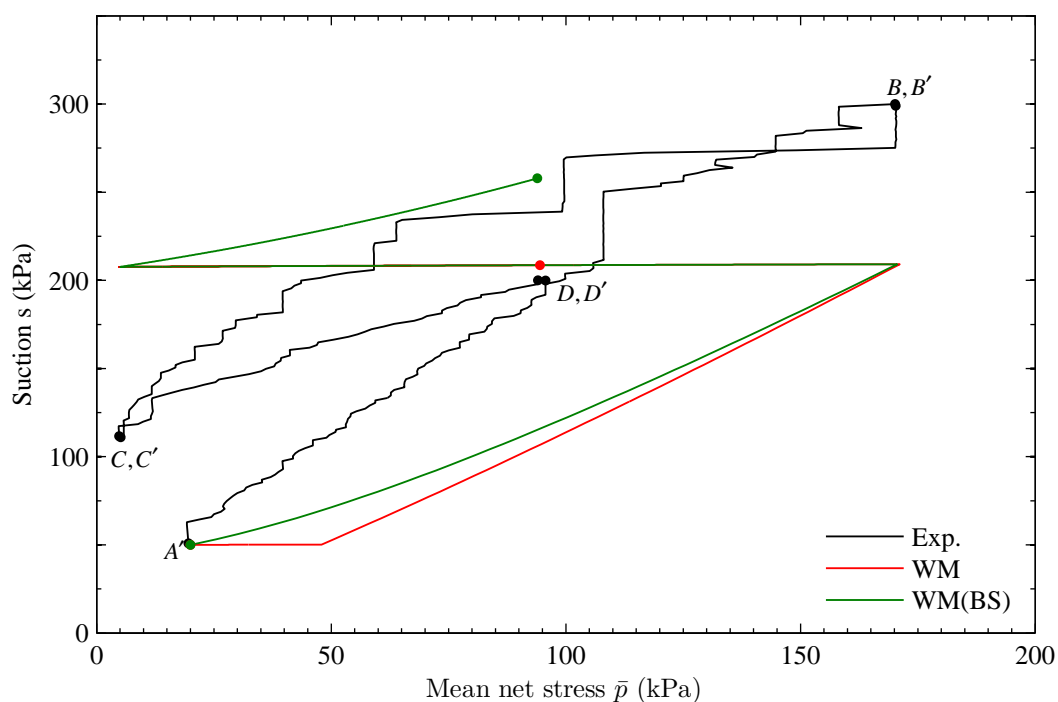


Figure 8-33 Stress path for constant S_r stages of Test A8 in terms of suction s and mean net stress \bar{p}

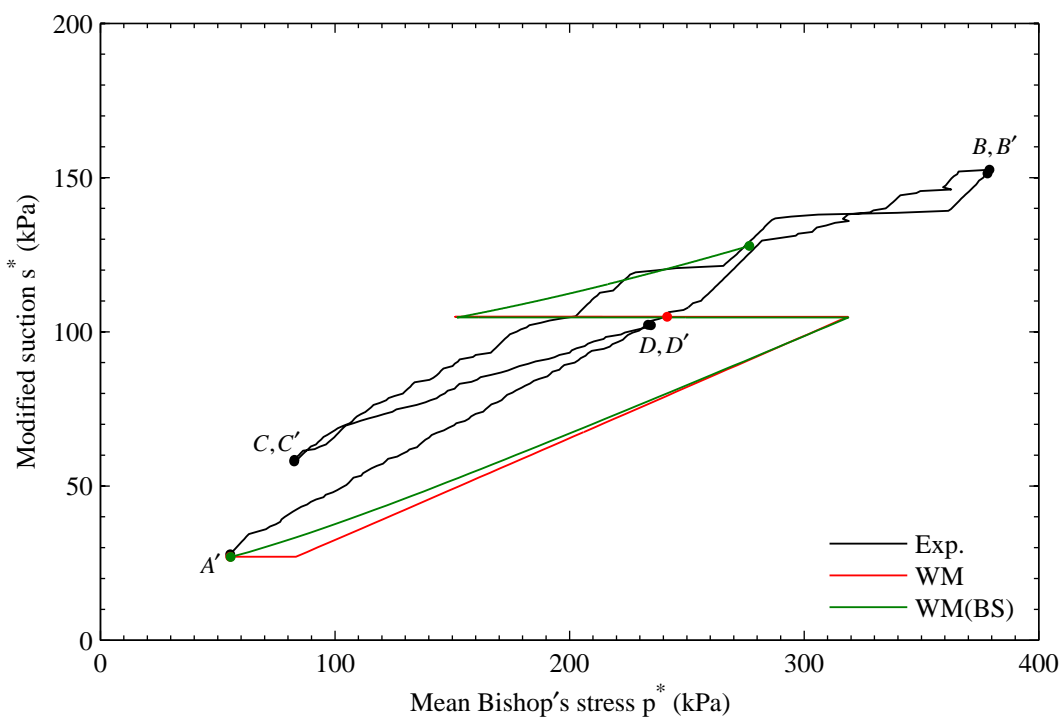


Figure 8-34 Stress path for constant S_r stages of Test A8 in terms of modified suction s^* and mean Bishop's stress p^*

Simulations from the WM and WM (BS) are also shown in Figure 8-33 and Figure 8-34. The WM and WM (BS) simulations shown in Figure 8-33 and Figure 8-34 for each constant S_r stage $A' - B$, $B' - C$ or $C' - D$ were performed by varying mean net stress \bar{p} over the same range as employed in the corresponding stage of the experimental test, and then calculating the variation of suction s required by the model in order to maintain S_r constant. This was the reverse of the procedure employed in the experiment (where s was varied at a constant rate and then \bar{p} was adjusted in order to maintain S_r constant). However, this was a more stable and realistic way of performing the simulations, because the model simulations suggested that for some of the test stages very small suction changes would correspond to substantial changes of \bar{p} (i.e. the model predictions suggest almost constant suction for some of the constant S_r stages). BBM simulations were, of course, not possible for the constant S_r stages $A' - B$, $B' - C$ or $C' - D$ (without the additional assumption of an independent water retention model).

At the end of equalisation stage AA' , according to the WM, the stress point was on the SD yield curve and inside the LC yield curve. During constant S_r loading stage $A' - B$ the simulation involved increase of mean net stress, with suction then varied in order to maintain S_r constant. The WM prediction shows the first part of this stage as elastic, and therefore at constant s^* , so that there was no elastic change of S_r predicted (see Equation 8-2). This first section of the predicted stress path is therefore traversing along the SD yield curve in the $s^* : p^*$ plane, but without any yielding on the SD yield curve (see Figure 8-34). As the increase of p^* produces elastic volumetric strain (see Equation 8-1), and hence a reduction of porosity n , the predicted suction s increases slightly in order to maintain s^* constant. This small increase of suction in the first part of the WM prediction for stage $A' - B$ is too small to see in the stress path in the $s : \bar{p}$ plane shown in Figure 8-33. This WM simulation for the first part of stage $A' - B$ is not a good match to the experimental stress path (see Figure 8-33 and Figure 8-34).

Part way through stage $A' - B$, the WM simulation shows the stress path reaching the LC yield curve (at the corner between SD and LC yield curves). Yielding on the LC

yield curve now produces plastic volumetric strain and coupled upward movement of the SD yield curve. As a consequence, simultaneous yielding on the LC and SD yield curves is predicted for the remainder of stage $A' - B$. Yielding on the SD curve produces plastic increases of S_r , which must be counterbalanced by elastic decreases of S_r , so that overall value of S_r remains constant. This implies an increase of s^* (see Figure 8-34) in order to produce the elastic decrease of S_r . The WM prediction for this later part of stage $A' - B$ therefore involves increases of both p^* and s^* (see Figure 8-34). It also involves increases of both \bar{p} and s (see Figure 8-33). This is a reasonable match to the experimentally observed behaviour.

During constant S_r unloading stage $B' - C$ the WM simulation involved decrease of \bar{p} , with suction then varied in order to keep S_r constant. The WM simulation for this stage shows elastic behaviour, at constant s^* and decreasing p^* , with the stress path traversing along the SD yield curve (see Figure 8-34). In terms of s and \bar{p} , the stress path involves a large reduction of \bar{p} and a very small reduction of s (too small to see in Figure 8-33). Similar elastic behaviour is predicted by the WM for the constant S_r re-loading stage $C' - D$. The predicted stress paths for stages $B' - C$ and $C' - D$ are a poor match to the experimental behaviour, which showed significant variation of s and s^* in these stages (see Figure 8-33 and Figure 8-34).

The prediction of the WM(BS) for the constant S_r loading stage $A' - B$ is similar to that of the WM, but with s^* increasing from the start of the stage, due to the predicted gradual onset of plastic volumetric strains and plastic increases of S_r (see Figure 8-34). During constant S_r unloading stage $B' - C$ the WM(BS) shows elastic behaviour at constant s^* (the same as the WM prediction), which is not a good match to the experimental behaviour. However, plastic volumetric strains and plastic increases of S_r are again predicted by the WM(BS) throughout the constant S_r re-loading stage $C' - D$, and as a consequence an increase of s^* is predicted (in order to produce elastic decreases of S_r to counterbalance the plastic increases). This WM(BS) prediction for stage $C' - D$ is a reasonable match to the experimental behaviour.

Figure 8-35 shows the variation of v against \bar{p} for constant S_r stages $A' - B$, $B' - C$ and $C' - D$ and subsequent isotropic loading stage $D' - E$. The experimental curve in Figure 8-35 shows a yield point early in the constant S_r loading stage $A' - B$, and then the rest of the stage defines a constant S_r normal compression line. Experimental curves for the constant S_r unloading and re-loading stages $B' - C$ and $C' - D$ show approximately elastic behaviour but with a significant hysteresis loop. In Figure 8-35 the experimental curve for the final constant suction loading stage $D' - E$ (at a suction of 200 kPa), appears to have almost the same initial gradient as the final gradient from the previous constant S_r loading stage $C' - D$, so that the changeover between the two curves is almost imperceptible. There is then a yield point during stage $C' - D$, with the remainder of the experimental curve defining a constant s normal compression line.

Inspection of Figure 8-35 shows that both the WM and the WM(BS), particularly the latter, provide reasonable predictions of the variation of v during constant S_r loading stage $A' - B$. Both models predict only very small elastic increases of v during constant S_r unloading stage $B' - C$, which under-predict the experimental increase of v . The WM prediction also shows small elastic decreases of v during constant S_r re-loading stage $C' - D$, whereas the WM(BS) predicts the gradual onset of plastic decreases of v during stage $C' - D$. Both WM and WM(BS) predict that the change-over from constant S_r loading stage $C' - D$ to constant s loading stage $D' - E$ is imperceptible in Figure 8-35 (like the experimental results). The WM predicts elastic behaviour during the first part of stage $D' - E$, and then after a yield point the later part of the WM simulation curve defines a constant s normal compression line. The WM(BS) predicts a gradual build up of plastic volumetric strain during stage $D' - E$. It is important to note that, whereas the experimental value of suction at the end of constant S_r loading stage $C' - D$ was 200 kPa, the corresponding values of suction from the WM and WM(BS) simulations were 208 kPa and 258 kPa respectively. This means that, whereas the final constant s loading stage $D' - E$ was actually conducted at a suction of 200 kPa, in the WM and WM(BS) simulations this stage was performed at a different suction of 208 kPa or 258 kPa.

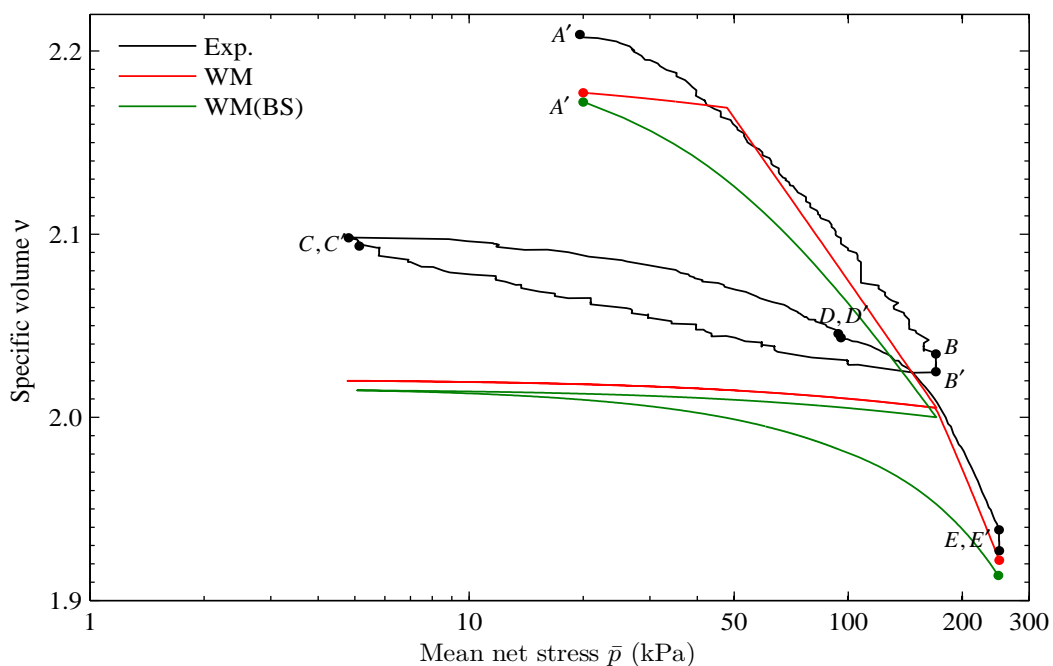


Figure 8-35 Variation of specific volume v against mean net stress \bar{p} for constant S_r stages and constant s stage of Test A8 along with simulations.

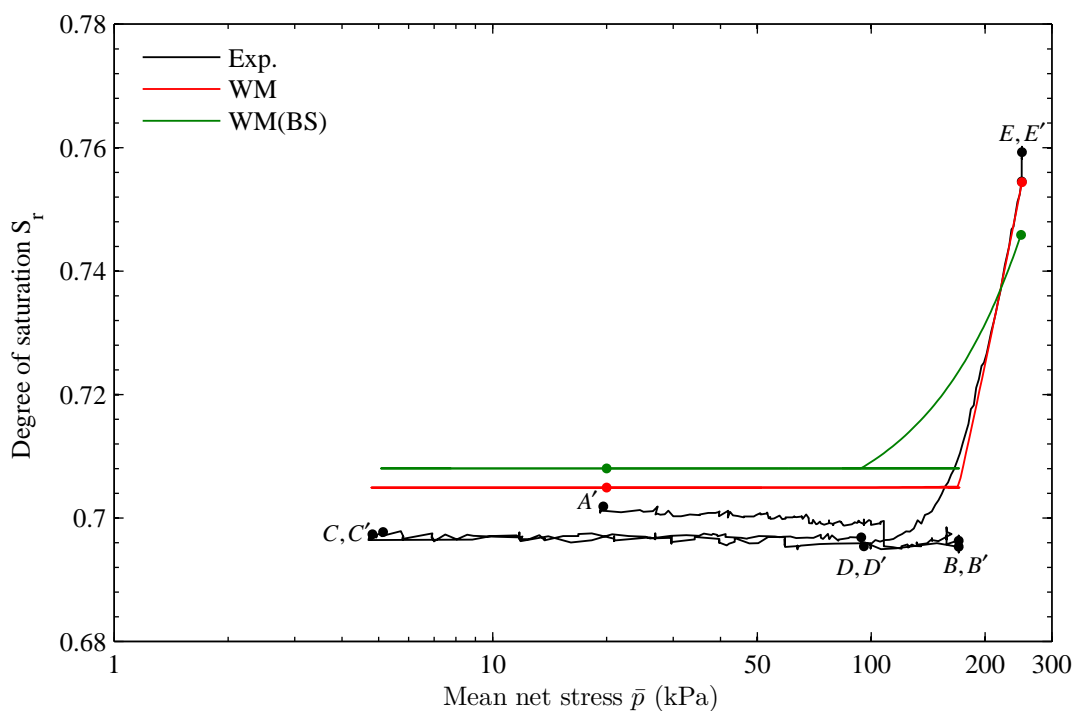


Figure 8-36 Variation of degree of saturation S_r against mean net stress \bar{p} for constant S_r stages and constant s stage of Test A8 along with simulations.

Figure 8-36 shows the variation of S_r against \bar{p} during Test A8, together with the WM and WM(BS) simulations. Inspection of the experimental curve in Figure 8-36 demonstrates S_r was kept constant during stages $A' - B$, $B' - C$ and $C' - D$ with a minimal fluctuation of ± 0.003 . It can be seen from Figure 8-36 that the WM and WM (BS) provide a reasonable match to the increase of S_r during the final isotropic loading stage $D' - E$.

Figure 8-37 shows the variation of v against suction for drying and wetting cycles $E' - F$, $F' - G$ and $G' - H$, all performed at constant \bar{p} of 250 kPa. Over the cycles of drying and wetting ($E' - FF' - GG' - HH'$) significant reduction of v occurred. During stages $E' - F$ and $G' - H$ each show a reduction of volume (shrinkage), and the gradients of the $v : \ln s$ curves during these two drying stages are almost the same. Although the reduction in v during drying stage $E' - F$ is small, it seems to be associated with an elasto-plastic process, because it is not reversed during the initial part of the subsequent wetting stage $F' - G$. During wetting stage $F' - G$ there was initially a very small reduction of v (too small to be observed in Figure 8-37), and this was then followed by a yield point and more substantial collapse compression from a suction of about 150 kPa.

The WM and WM(BS) simulations for the drying-wetting cycles commence at a suction of 208 kPa or 258 kPa, rather than the correct suction of 200 kPa. Figure 8-37 shows that both the WM and the WM(BS) provide a reasonable qualitative match to the observed variation of v during the drying-wetting-drying stages $E' - F$, $F' - G$ and $G' - H$, although the reduction of v during wetting stage $F' - G$ is over-predicted, and hence the predicted values of v are too low throughout the final drying stage $G' - H$. Both models are able to predict that the shrinkage during drying stage $E' - F$ is not reversible. This is a consequence of the prediction of yielding on the LC yield curve from the start of drying stage $E' - F$, and the same is predicted by the WM during the early part of the final drying stage $G' - H$. The BBM would, in contrast, predict entirely elastic shrinkage during drying stages $E' - F$ and $G' - H$. In addition, the WM is correctly able to predict that the yield point marking the start of collapse compression during wetting stage $F' - G$ occurs at a suction lower than the

value at the start of the drying-wetting cycles at E' . Again the BBM could not predict this.

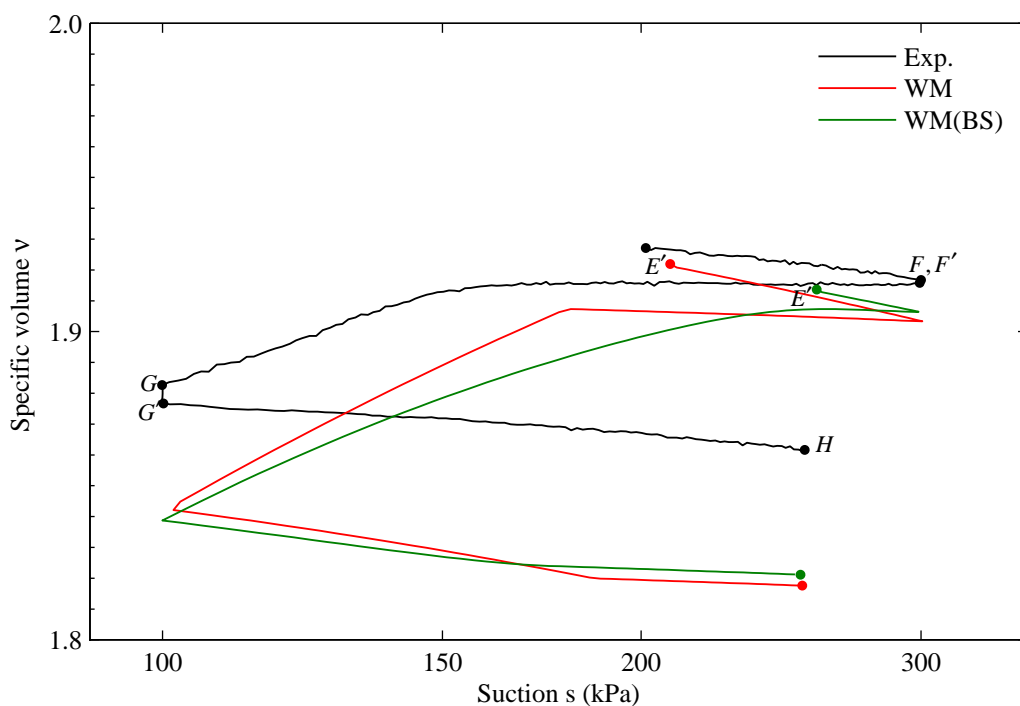


Figure 8-37 Variation of specific volume v against suction s for final drying-wetting cycles of Test A8 along with simulations.

Figure 8-38 shows the variation of degree of saturation S_r with suction s for stages $E' - F$, $F' - G$ and $G' - H$. During the drying-wetting-drying cycles ($E' - F$, $F' - G$ and $G' - H$), clear hydraulic hysteresis can be identified, with the first part of wetting curve $F' - G$ lying below the previous drying curve $E' - F$, and the final drying curve $G' - H$ lying above both previous wetting path $F' - G$ and the previous drying path $E' - F$. It is interesting to note that during wetting stage $F' - G$ a change in gradient occurred at suction of about 150 kPa, which is associated with the onset of collapse compression (see Figure 8-37).

Inspection of Figure 8-38 shows that the WM and WM(BS) do not predict well the variation of S_r during the initial drying stage $E' - F$. However, both models then provide reasonable predictions of the variation of S_r during the subsequent wetting stage $F' - G$ and drying stage $G' - H$ (although the increase of S_r during wetting stage $F' - G$ is over-predicted)

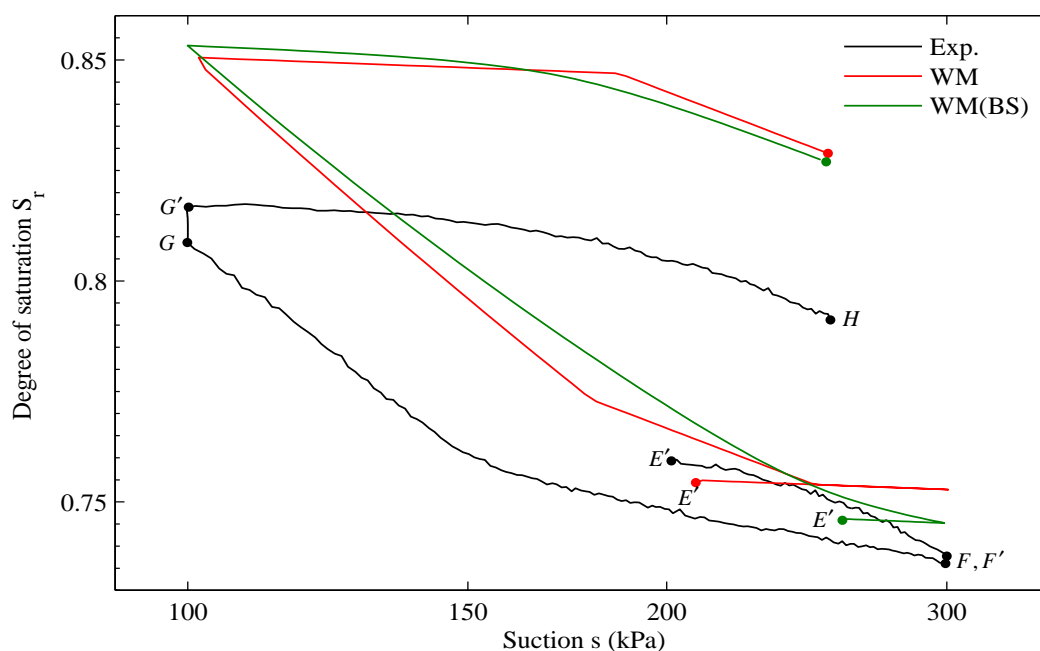


Figure 8-38 Variation of degree of saturation S_r against suction s for final drying-wetting cycles of Test A8 along with simulations.

8.2 OTHER TESTS INVESTIGATING THE COUPLING OF MECHANICAL BEHAVIOUR AND WATER RETENTION BEHAVIOUR

Tests A9 A10, A11 and A12 were performed with several wetting, drying, loading, unloading and re-loading stages, primarily in order to explore inter-dependency of mechanical behaviour and water retention behaviour.

8.2.1 Test A9

Test A9 was carried out in order to examine the influence of a wetting and drying cycle on subsequent behaviour during isotropic loading. Table 8-8 and Figure 8-39 show the stress path followed in Test A9. Initial equalisation was performed at a mean net stress of 10 kPa and a suction of 300 kPa. Sample A9 was then subjected to isotropic loading $A' - B$ to a mean net stress of 200 kPa, followed by an unloading stage $B' - C$ to a mean net stress of 10 kPa. After this cycle of loading and unloading, the sample was wetted to a suction of 10 kPa at constant mean net stress (stage $C' - D$), followed by a drying stage $D' - E$ to a suction of 300 kPa. Finally, an

isotropic loading stage was performed to a mean net stress of 375 kPa at a constant suction of 300 kPa.

| Stage | | | \bar{p} (kPa) | s (kPa) |
|-------|----|----------------------|-----------------|-----------|
| From | To | Description | | |
| A | A' | Initial equalisation | 10 | 300 |
| A' | B | Isotropic loading | 10 → 200 | 300 |
| B | B' | Equalisation | 200 | 300 |
| B' | C | Isotropic unloading | 200 → 10 | 300 |
| C | C' | Equalisation | 10 | 300 |
| C' | D | Wetting | 10 | 300 → 10 |
| D | D' | Equalisation | 10 | 10 |
| D' | E | Drying | 10 | 10 → 300 |
| E | E' | Equalisation | 10 | 300 |
| E' | F | Isotropic loading | 10 → 375 | 300 |
| F | F' | Equalisation | 375 | 300 |

Table 8-8 Stress path for Test A9

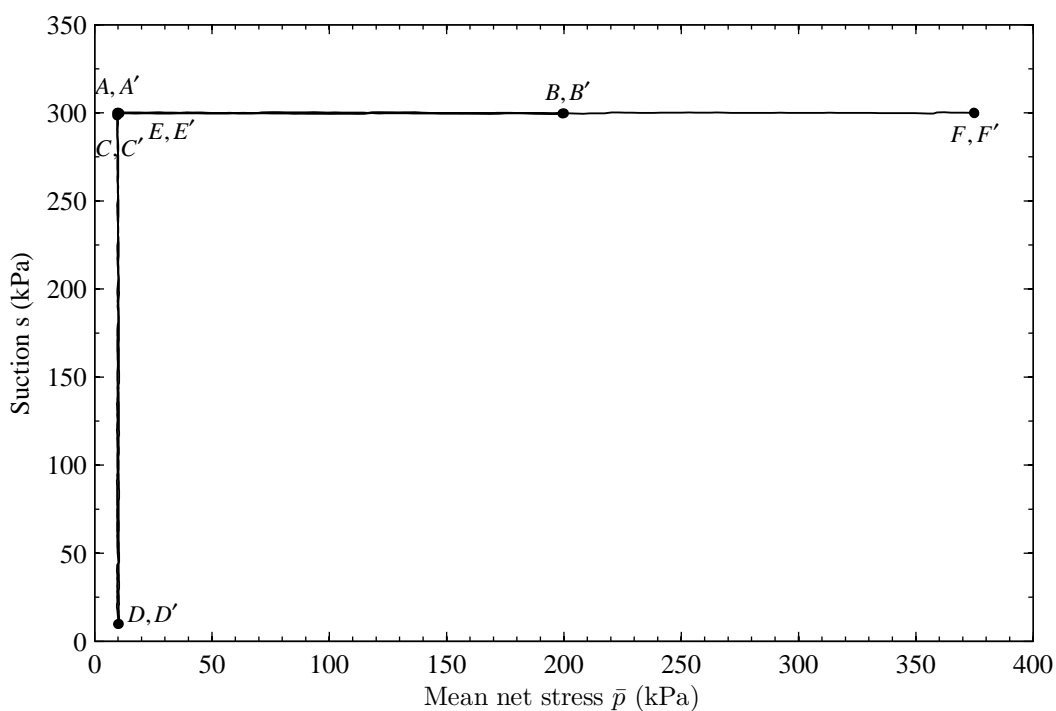


Figure 8-39 Stress path for Test A9

Figure 8-40 and Figure 8-41 show the variation of specific volume and degree of saturation respectively plotted against mean net stress for Test A9.

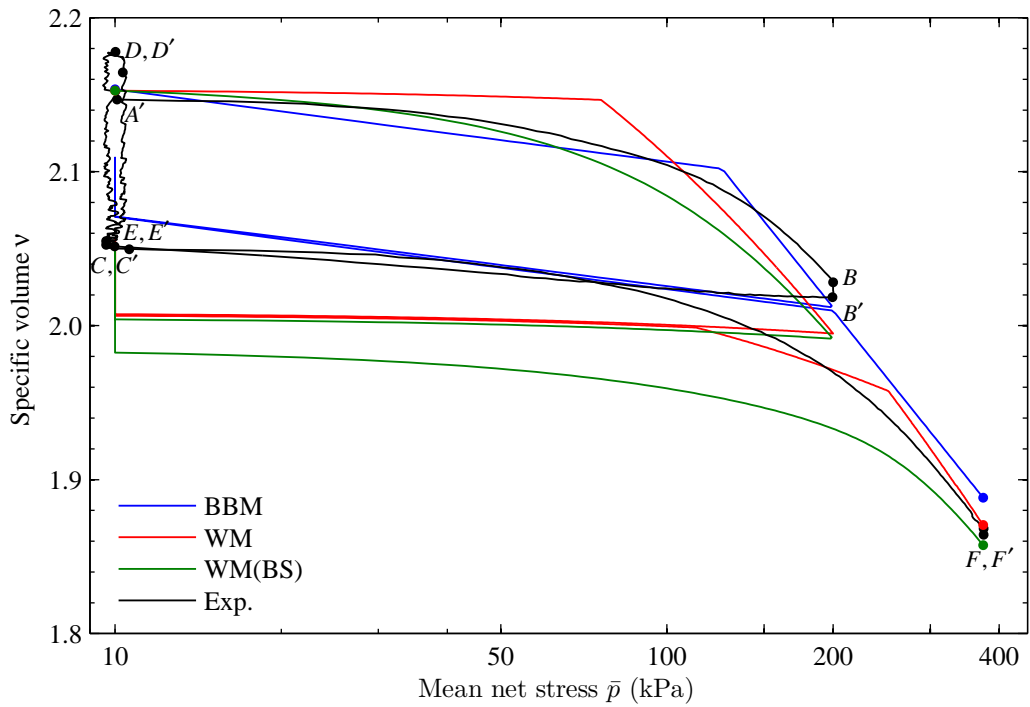


Figure 8-40 Variation of specific volume v against mean net stress \bar{p} for Test A9 along with simulations.

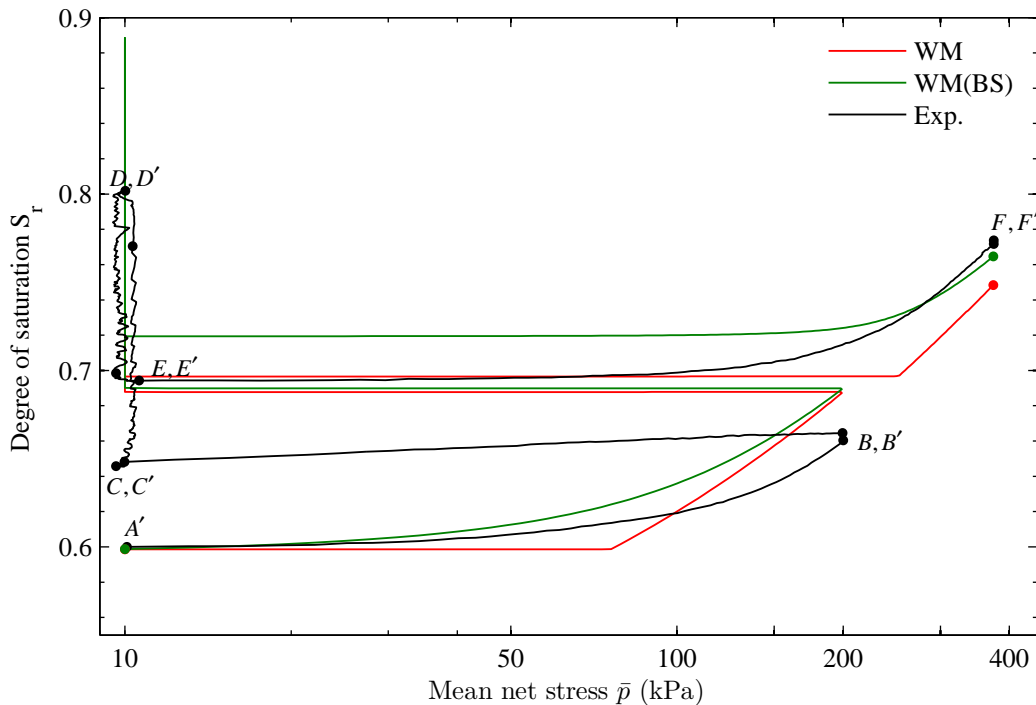


Figure 8-41 Variation of degree of saturation S_r against mean net stress \bar{p} for Test A9 along with simulations.

During the first isotropic loading stage $A' - B$ the sample showed a gradual yielding in terms of the variation of v with \bar{p} (and also the variation of S_r with \bar{p}), and swelling behaviour during the subsequent unloading stage $B' - C$. The wetting-drying cycle $C' - DD' - E$ performed after the unloading ($B' - C$) did not produce any net change in v (see Figure 8-40), whereas a significant net increase of S_r (around 0.05) over the cycle can be observed (Figure 8-41). The influence of this increase in the degree of saturation (reduction of the number of meniscus water rings, and hence reduced stability of inter-particle contacts) on the subsequent isotropic loading stage $E' - F$ can be clearly observed from Figure 8-40, where the sample showed a tendency to yield at a value of \bar{p} that was lower than the maximum value previously experienced by the sample (200 kPa). This experimental observation is consistent with the finding of Sharma (1998) (see Figure 3-3).

All three models provide a good prediction for the final value of v (Figure 8-40), even though the value of v at the start of the final loading stage $E' - F$ is under-predicted by both WM and WM (BS) because of the poor prediction of v at the end first isotropic loading $A' - B$ (WM (BS) also incorrectly predicts a net reduction of v over the wetting-drying cycle $C' - DD' - E$). The BBM, however, generally provides a good match to the experimental observations for the variation of v against \bar{p} (see Figure 8-40), although the ‘early yielding’ behaviour observed during re-loading stage $E' - F$ was not captured by the BBM. This feature of behaviour was explained by Wheeler et al. (2003) by considering the influence of S_r in addition to suction on the yielding behaviour (see Section 3.2.1). Both WM and WM (BS) captures this “early yielding” behaviour observed in Figure 8-40. However, there was no suggestion of two yield points, as predicted by the WM during the re-loading stage $E' - F$.

Inspection of Figure 8-41 shows that both WM and WM (BS) over-predict the increase of S_r during the first loading-unloading cycle $A' - BB' - C$ and under-predict the net increase of S_r over the subsequent wetting-drying cycle $C' - DD' - E$. However, both models predict the final value of S_r with reasonable accuracy. Overall, the WM (BS) simulations in Figure 8-40 and Figure 8-41 show more realistic rounded shapes for compression curves and the variation of S_r than the WM.

Figure 8-42 , Figure 8-43 and Figure 8-44 show the variation of v , S_r and v_w respectively against suction for wetting-drying cycle $C' - DD' - E$. Inspection of Figure 8-42 shows that there was no net change of v during wetting-drying cycle $C' - DD' - E$, even though there was a suggestion of a yield point during drying stage $D' - E$ but not during the previous wetting stage $C' - D$. None of the three models is able to provide a good match to the experimentally observed behaviour. Both BBM and WM predict elastic changes of v during the wetting-drying cycle while the WM (BS) predicts a small plastic reduction of v during drying stage $D' - E$.

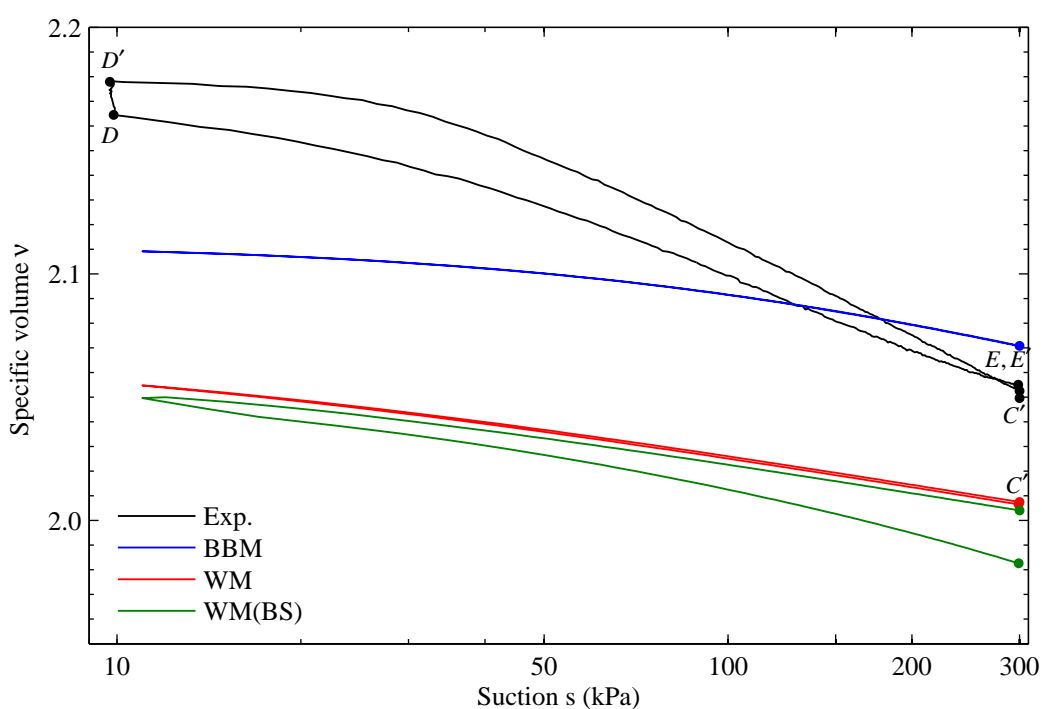


Figure 8-42 Variation of specific volume v against suction s for wetting-drying cycle of Test A9 along with simulations.

The experimental variation of S_r against suction shown in Figure 8-43 shows clear evidence of elasto-plastic behaviour, with drying curve $D' - E$ lying above the previous wetting curve $C' - D$. However, no clear yield point can be observed during either wetting or drying stages. Both WM and WM (BS) poorly predict the observed experimental behaviour (see Figure 8-43).

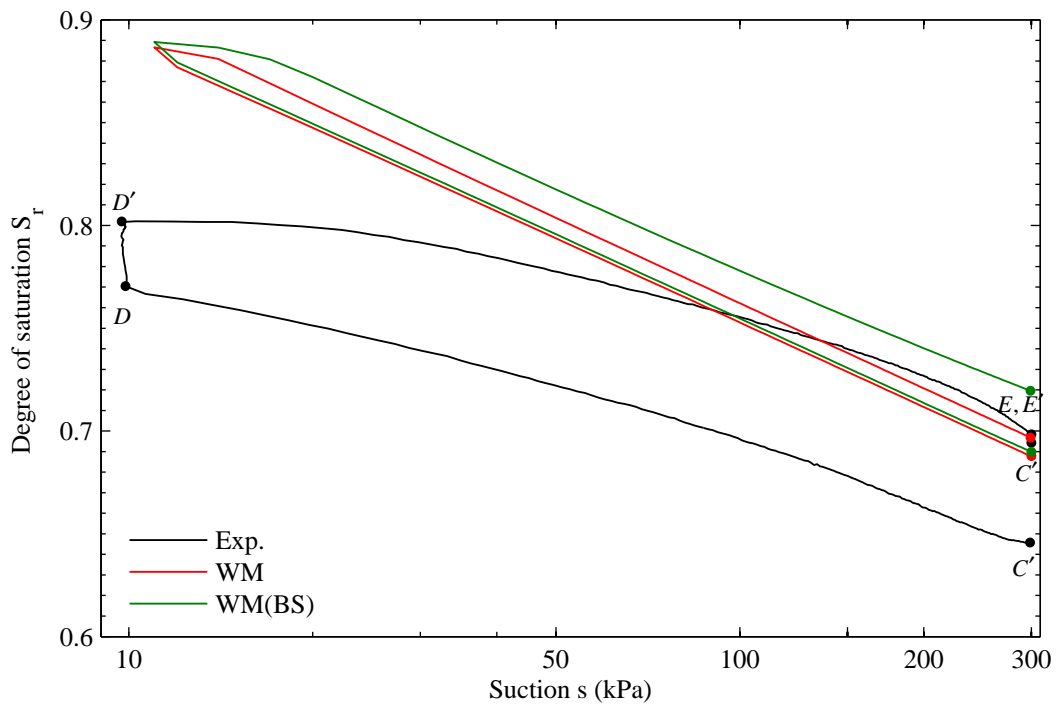


Figure 8-43 Variation of degree of saturation S_r against suction s for wetting-drying cycle of Test A9 along with simulations.

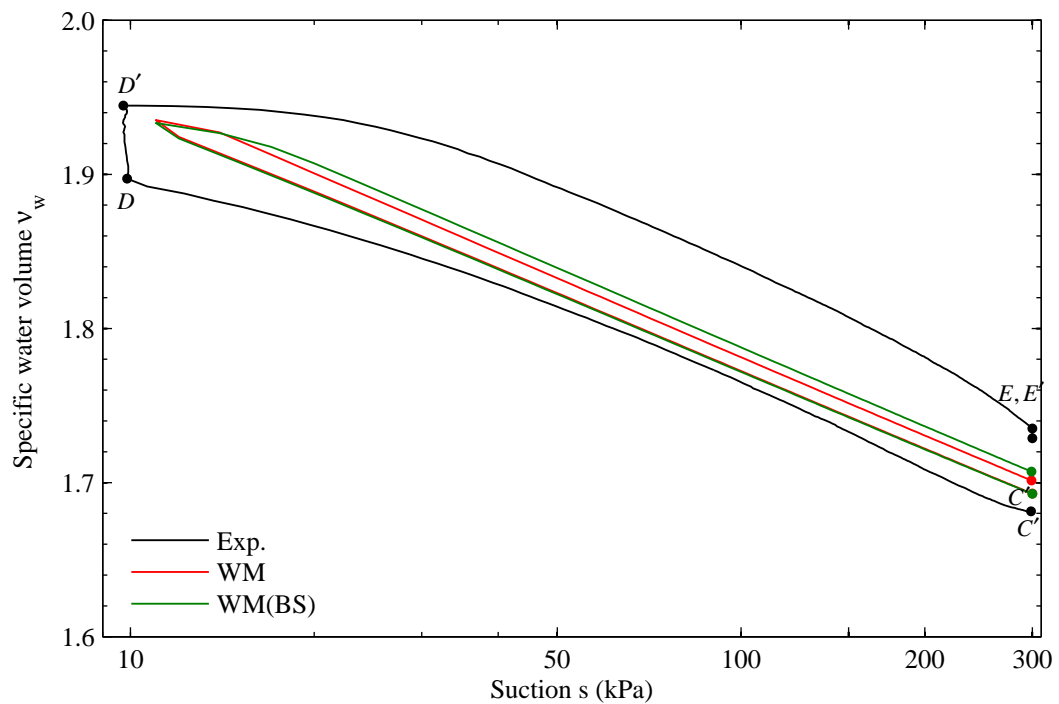


Figure 8-44 Variation of specific water volume v_w against suction s for wetting-drying cycle of Test A9 along with simulations.

The experimental variation of v_w against suction plotted in Figure 8-44 shows a similar trend to the variation of S_r , because the influence of the variation of v on the variation S_r is negligible. Both WM and WM (BS) predict the gradient of the water retention curve plotted in terms of v_w against suction (see Figure 8-44) with reasonable accuracy. It can, however, be noted that the spacing between the wetting and drying curves is underestimated by both WM and WM (BS) (see Figure 8-43 and Figure 8-44).

8.2.2 Test A10

The influence of a wetting-drying cycle on subsequent isotropic loading was explored with experimental results from Test A9 in the previous section. In Test A10, the influence of a drying-wetting cycle on the response of soil sample during subsequent isotropic loading and the influence of loading-unloading on the behaviour of soil during a subsequent drying-wetting path were investigated.

Table 8-9 and Figure 8-45 show the stress path followed in Test A10.

| Stage | | | \bar{p} (kPa) | s (kPa) |
|-------|----|----------------------|-----------------|-----------|
| From | To | Description | | |
| A | A' | Initial equalisation | 10 | 1 |
| A' | B | Drying | 10 | 1 → 350 |
| B | B' | Equalisation | 10 | 350 |
| B' | C | Wetting | 10 | 350 → 10 |
| C | C' | Equalisation | 10 | 10 |
| C' | D | Isotropic loading | 10 → 60 | 10 |
| D | D' | Equalisation | 60 | 10 |
| D' | E | Isotropic unloading | 60 → 10 | 10 |
| E | E' | Equalisation | 10 | 10 |
| E' | F | Drying | 10 | 10 → 300 |
| F | F' | Equalisation | 10 | 300 |
| F' | G | Wetting | 10 | 300 → 10 |
| G | G' | Equalisation | 10 | 10 |
| G' | H | Isotropic loading | 10 → 85 | 10 |
| H | H' | Equalisation | 85 | 10 |
| H' | I | Isotropic unloading | 85 → 10 | 10 |
| I | I' | Equalisation | 10 | 10 |
| I' | J | Drying | 10 | 10 → 325 |
| J | J' | Equalisation | 10 | 325 |

Table 8-9 Stress path for Test A10

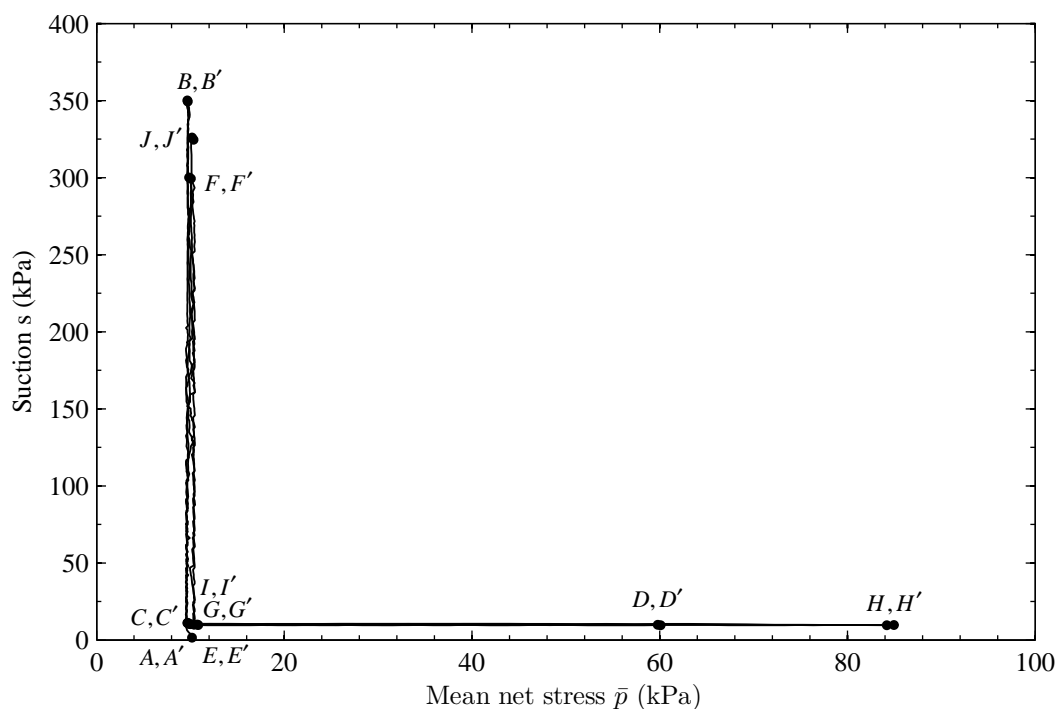


Figure 8-45 Stress path for Test A10

Sample A10 was first equalised at a suction of 1 kPa and a mean net stress of 10 kPa. It was then subjected to a drying and wetting cycle $A' - BB' - C$, over a suction range of 1-350-10 kPa. Isotropic loading $C' - D$ to a mean net stress of 60 kPa was then performed, followed with an unloading stage $D' - E$ to a mean net stress of 10 kPa. A second drying- wetting cycle $E' - FF' - G$, this time over a suction range of 10-300-10 kPa, was then carried out. After this drying -wetting cycle, the sample was subjected to a loading and unloading cycle $G' - HH' - I$ over a mean net stress range of 10-85-10 kPa. Finally, a drying stage $I' - J$ was performed to a suction of 325 kPa.

Figure 8-46 illustrates the variation of v with suction during Test A10. During the first and second drying-wetting cycles $A' - BB' - C$ and $E' - FF' - G$, the experimental curves show non-elastic behaviour, with net reduction of volume over each of the two cycles. Close inspection of Figure 8-46 reveals that the net reduction of v during the first drying-wetting cycle is larger than that observed in the second drying-wetting cycle. In addition, the first drying curve $A' - B$ exhibits a clear yield point at a suction of about 10 kPa, but the yield points during the second ($E' - F$) and final ($I' - J$) drying stages are not clear (see Figure 8-46). A significant net reduction of v can also

be observed over each of the loading-unloading cycles $C' - DD' - E$ and $G' - HH' - I$.

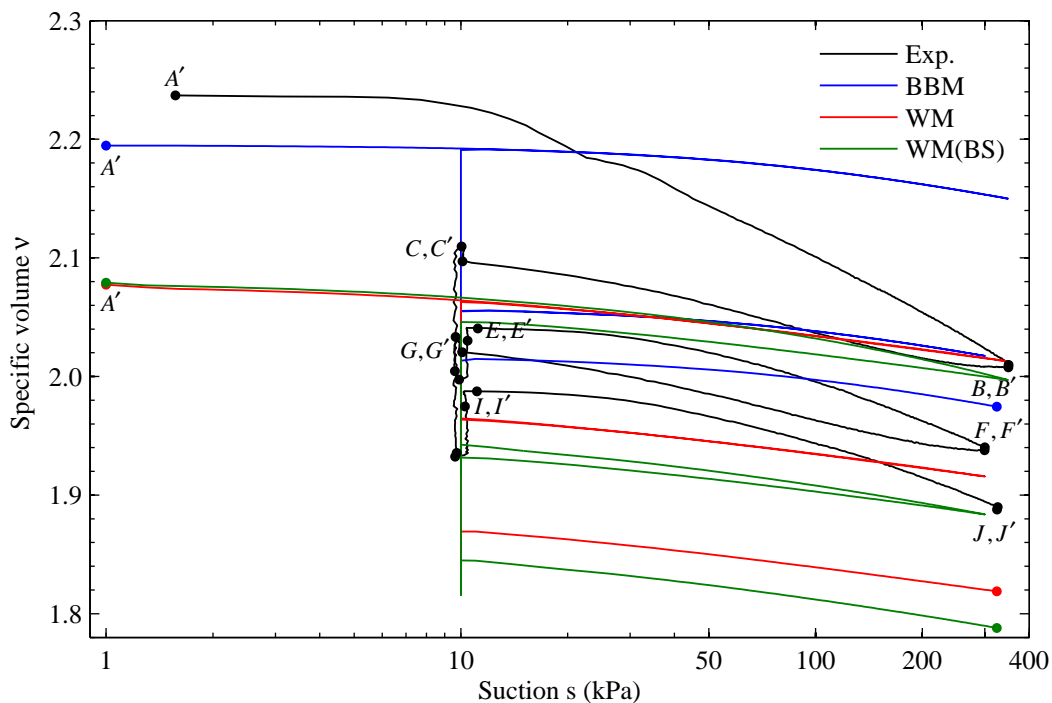


Figure 8-46 Variation of specific volume v against suction s for Test A10 along with simulations.

None of the three models provides a good match to the experimentally observed behaviour in Figure 8-46. The BBM predicts elastic behaviour during both drying-wetting cycles ($A' - BB' - C$ and $E' - FF' - G$) and final drying stage $I' - J$, which is not a good match to the observed behaviour. BBM also predicts net reduction of v during both loading-unloading cycles ($C' - DD' - E$ and $G' - HH' - I$), due to yielding on the LC yield curve, and this is qualitatively consistent with the observed behaviour. Both WM and WM (BS) underestimate the starting value of v at point A' , because they both predict collapse compression during the initial equalisation stage AA' (not observed in the experimental results). WM then predicts elastic changes of v during all wetting and drying stages which is not a good match to the experimental observations, and net reduction of v during both loading-unloading cycles (i.e. qualitatively similar to the BBM predictions). The WM could, in theory, predict plastic reduction of v during drying paths (which would provide a better match to the experimental results) by yielding on the LC curve during drying, however, the selected

values of model parameters resulted in only elastic variation of ν predicted during drying paths. The WM (BS) predictions for drying-wetting stages show some elasto-plastic behaviour. However, the predicted shapes of the drying-wetting curves are a poor match to the experimentally observed shapes of the curves (see Figure 8-46).

Figure 8-47 shows the variation of S_r against suction for Test A10. During both drying-wetting cycles $A' - BB' - C$ and $E' - FF' - G$ strong evidence of hydraulic hysteresis can be observed, with a net reduction of S_r over each of the two drying-wetting cycles. Also, there are significant net increases of S_r over each of the two loading-unloading cycles $C' - DD' - E$ and $G' - HH' - I$.

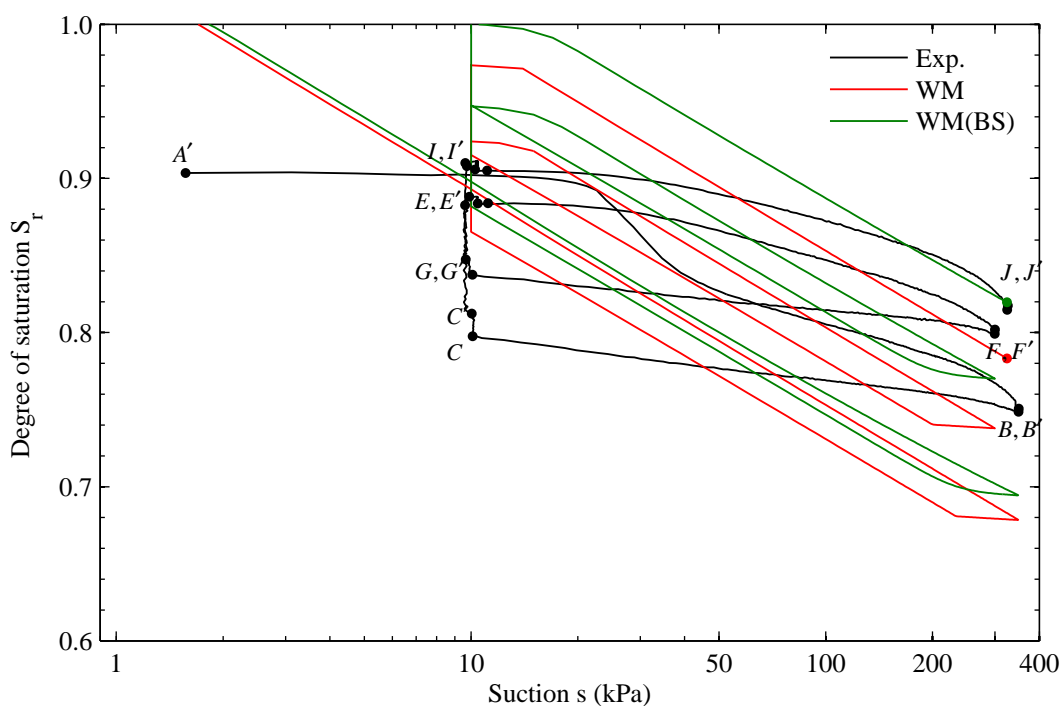


Figure 8-47 Variation of degree of saturation S_r against suction s for Test A10 along with simulations.

Close inspection of Figure 8-47 reveals some interesting features of the water retention behaviour. During the first drying stage $A' - B$, a clear yield point can be seen at a suction of about 25 kPa. This occurs at a higher suction than the yield point observed for the variation of ν (see Figure 8-46). This shows the dominant effect of water outflow rather than sample volume change on the variation of degree of saturation. There is then a flattening of the drying retention curve $A' - B$ at a suction of about 40

kPa, and a slight suggestion of a second steepening towards the very end of stage $A' - B$ (though not conclusive). If there is really a double steepening of the retention curve during the first drying stage it may be explained by the double porosity nature of the soil i.e. the first steepening corresponds to draining of macro-voids whereas the second steepening corresponds to draining of micro-voids (see Section 2.1.3). This feature cannot be captured by either WM or WM (BS).

The second and third drying curves $E' - F$ and $I' - J$ show more rounded shapes, without any suggestion for clear steepenings or yield points. One possible explanation for the absence of clear yield points at low suction in these second and third drying stages is that the suction decrease during the previous wetting stages $B' - C$ and $F' - G$ might not have been enough to flood the macro-voids with water. It is also possible that these macro-voids could have been compressed during the drying stages ($E' - F$ and $I' - J$) and the isotropic loading stage $C' - D$.

Both the wetting curves $B' - C$ and $F' - G$ exhibit almost linear behaviour in the semi-logarithmic plot of Figure 8-47, with a gradient significantly lower than that observed for the drying curves. There is no suggestion of any steepening of the wetting curve during the later part of stage $B' - C$ or $F' - G$, as would be predicted as the scanning wetting curve re-joined the main wetting curve. This behaviour may be linked to trapping of air within the sample (in the form of occluded bubbles) at relatively high degree of saturation (which could then only be removed by the very slow process of diffusion of dissolved air).

The WM assumes that the main wetting and main drying curves are both linear in the $S_r : \ln s^*$ plot and that they have the same gradient. Inspection of Figure 8-47 indicates that this does not provide a good match to the experimental behaviour. Neither does the WM(BS) provide a good match. The match of both models might be slightly improved by selecting alternative model parameter values, with a lower gradient of λ_s and a wider spacing s_I^*/s_D^* , but this would not really address the main problems of the mis-matches in Figure 8-47. However, the poor model predictions in Figure 8-47 are probably exaggerated by the possible limitation of experimental technique associated with trapping of air within sample during wetting stages at higher values of S_r .

Although both models capture the progressive upward movement of the hysteresis loops with the accumulation of plastic volumetric strain they overestimate the magnitude of shifting of the hysteresis loop.

Figure 8-48 and Figure 8-49 show the variation of specific volume and degree of saturation with mean net stress respectively. During both isotropic loading –unloading cycles $C' - DD' - E$ and $G' - HH' - I$, significant net reductions of v and increases of S_r were observed, and the experimental curves showing the variations of v and S_r have rounded shapes, hence making it difficult to identify yield points.

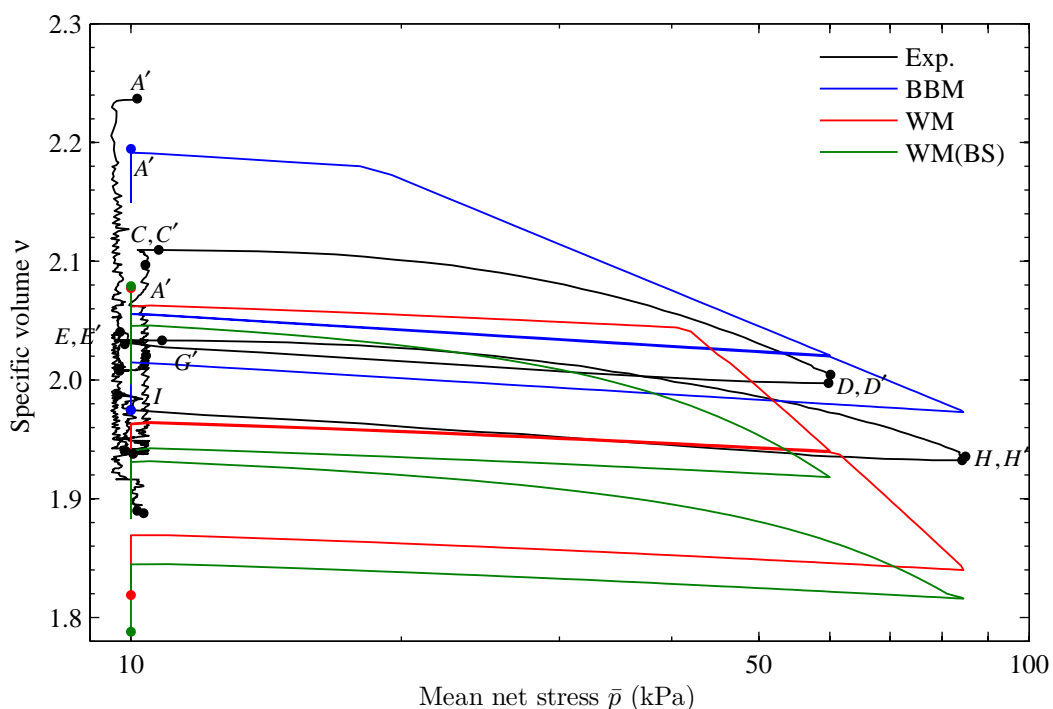


Figure 8-48 Variation of specific volume v against mean net stress \bar{p} for Test A10 along with simulations.

Close inspection of Figure 8-49 and Figure 8-48 shows that the drying-wetting cycle $E' - FF' - G$ produced significant net reduction of S_r while there was negligible net reduction of v . According to the Wheeler et al. (2003) framework, this reduction of S_r would mean an increase in the stability of inter-particle contacts because of the increase in number of meniscus water rings. This would mean that, during subsequent isotropic loading stage $G' - H$, the sample would start to yield at a mean Bishop's stress (and mean net stress) higher than the maximum value applied during the

previous isotropic loading stage $C' - D$. However, this argument was not supported by the experimental results, which suggest that plastic straining builds up gradually during isotropic loading $G' - H$ and commences at a stress less than the maximum value previously applied (see Figure 8-48 and Figure 8-49). No reason could be put forward to explain this feature of behaviour. Overall, Test A10 demonstrates the complexity of the challenge of modelling unsaturated soil behaviour.

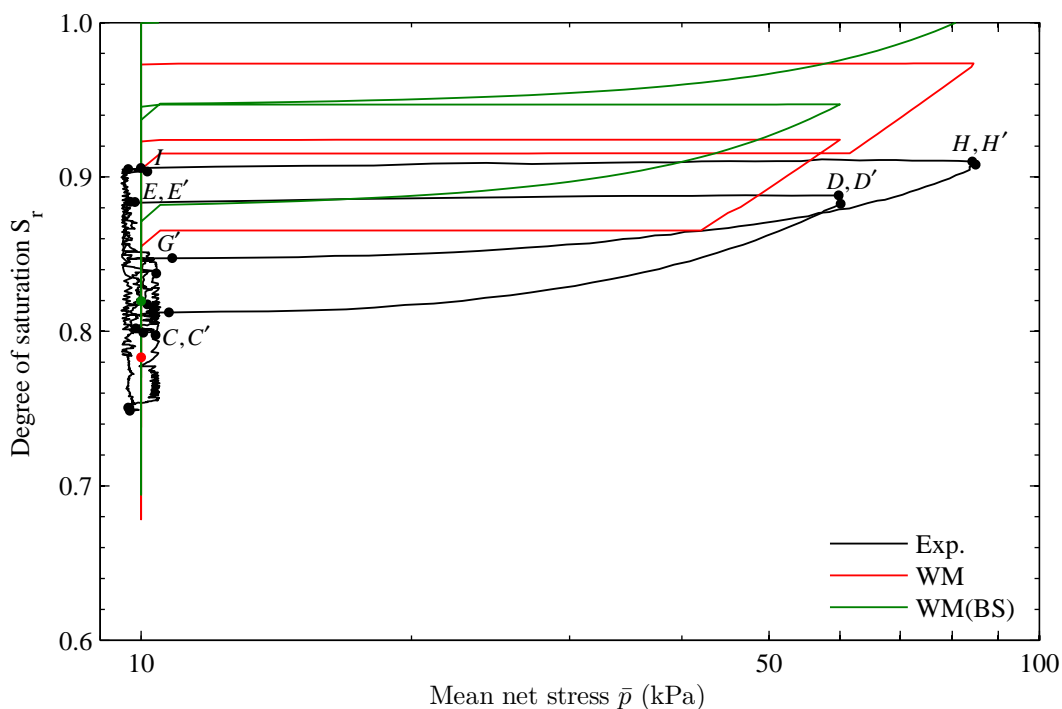


Figure 8-49 Variation of degree of saturation S_r against mean net stress \bar{p} for Test A10 along with simulations.

All three models provide imperfect matches to the observed experimental behaviour shown in Figure 8-48. The BBM tends to over-predict the values of v , whereas both WM and WM (BS) underestimate the values of v . However, closer inspection shows that the BBM captures the gradient of normal compression lines and the yield stress during first isotropic loading $C' - D$ with reasonable accuracy, whereas this is done less well by the WM (see Figure 8-48). As discussed in the previous paragraph, the WM predicts a yield value of \bar{p} during the second isotropic loading $G' - H$ that is slightly higher than the maximum value previously applied, because of the net decrease in S_r over the previous drying-wetting cycle $E' - FF' - G$. It can also be

noted that WM (BS) predicts rounded shapes for the compression curves, very similar to that observed from the experimental results (see Figure 8-48).

Both WM and WM (BS) overestimate the values of S_r in Figure 8-49. Close inspection of Figure 8-49 reveals that WM (BS) predictions for the shapes of the curves of S_r plotted against \bar{p} are a better representation of the experimental behaviour than the WM predictions, although the absolute values of S_r predicted by WM (BS) typically show worse over-prediction than WM.

8.2.3 Test A11

In Test A9, a wetting and drying cycle was performed after an isotropic loading and unloading cycle (see Section 8.2.1). In Test A11, a similar wetting and drying cycle was carried out, but without any previous isotropic loading and unloading cycle. By comparing both tests, it is possible to investigate the influence of a loading and unloading cycle on both mechanical and water retention behaviour during the subsequent wetting and drying cycle.

Figure 8-50 and Table 8-10 show the stress path followed in Test A11. The sample was first equalised (AA') at a mean net stress of 10 kPa and a suction of 300 kPa. A wetting and drying cycle ($A' - BB' - C$) over a suction range of 10 to 300 kPa was then carried out. Finally, an isotropic loading stage ($C' - D$) was performed to a mean net stress of 250 kPa at a suction of 300 kPa.

| Stage | | | \bar{p} (kPa) | s (kPa) |
|-------|----|----------------------|-----------------|-----------|
| From | To | Description | | |
| A | A' | Initial equalisation | 10 | 300 |
| A' | B | Wetting | 10 | 300 → 10 |
| B | B' | Equalisation | 10 | 10 |
| B' | C | Drying | 10 | 10 → 300 |
| C | C' | Equalisation | 10 | 300 |
| C' | D | Isotropic loading | 10 → 250 | 300 |
| D | D' | Equalisation | 250 | 300 |

Table 8-10 Stress path for Test A11

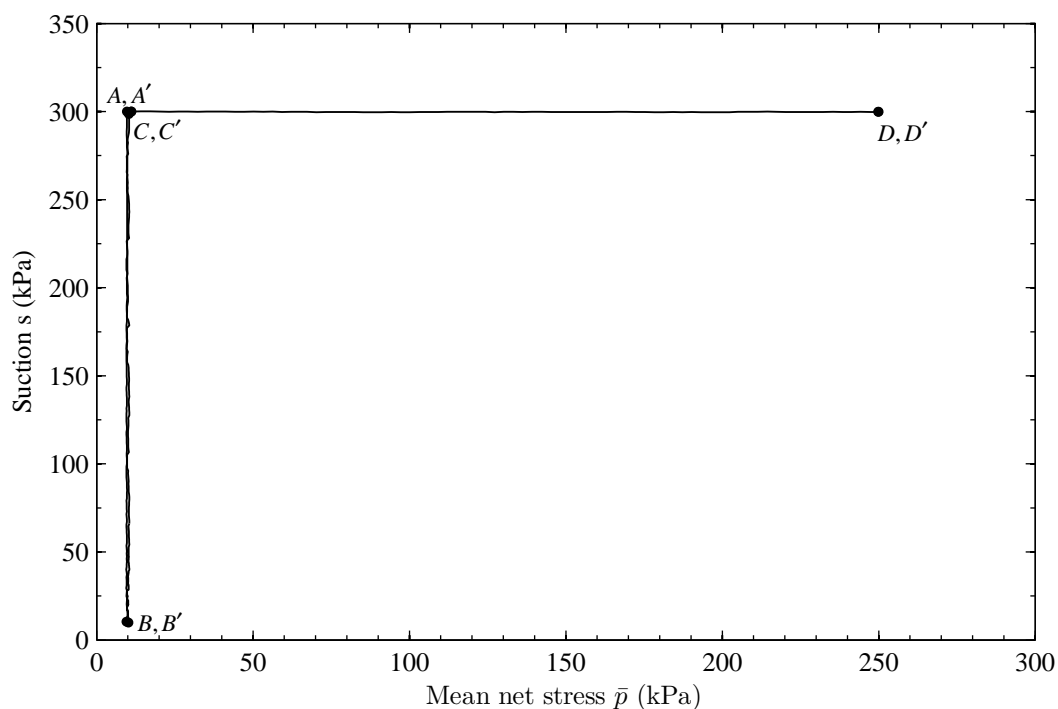


Figure 8-50 Stress path for Test A11

Figure 8-51 and Figure 8-52 show the variation of specific volume and degree of saturation against suction respectively. Significant net decrease of ν and increase of S_r occurred over the wetting-drying cycle $A' - BB' - C$, suggesting elasto-plastic behaviour for both mechanical and water retention behaviour. Close inspection of Figure 8-51 suggests a yield point in the variation of ν at a suction of about 25 kPa during drying $B' - C$, with no yield point visible during the previous wetting stage $A' - B$, suggesting that plastic volumetric strains occurred during the drying stage. However, Figure 8-52 does not show any clear yield point during either wetting ($A' - B$) or drying ($B' - C$) stages.

None of the models provides a good match to the experimentally observed behaviour in Figure 8-51. As expected, the BBM predicts both wetting ($A' - B$) and drying ($B' - C$) as elastic processes, because the stress point remains inside the LC yield curve. Although, the WM can theoretically predict plastic volumetric strain during drying (by yielding on the LC curve), the selected parameter values and the initial positions of the yield curves means that during drying stage ($B' - C$) the LC curve was not reached in the simulation, and thus no plastic volumetric strain was predicted. Although, the WM (BS) is able to capture the overall shape of the curves of ν against

suction (see Figure 8-51), with plastic volumetric strain predicted during drying stage $B' - C$, it under-predicts the absolute values of v , mainly because of underestimation of the value of v at the end of the initial equalisation stage AA' .

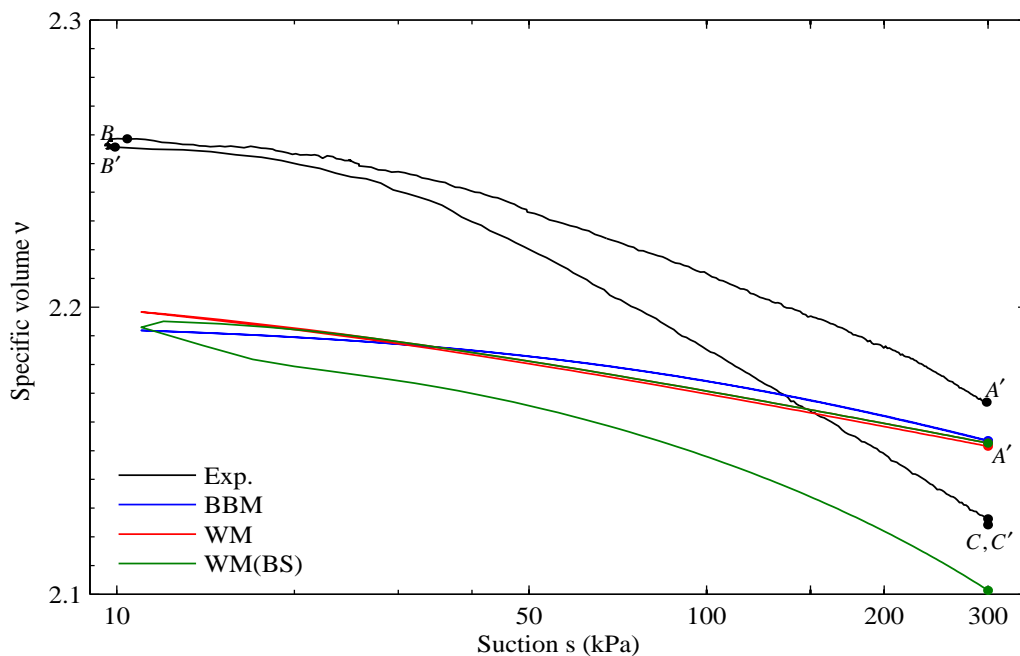


Figure 8-51 Variation of specific volume v against suction s for wetting-drying cycle of Test A11 along with simulations.

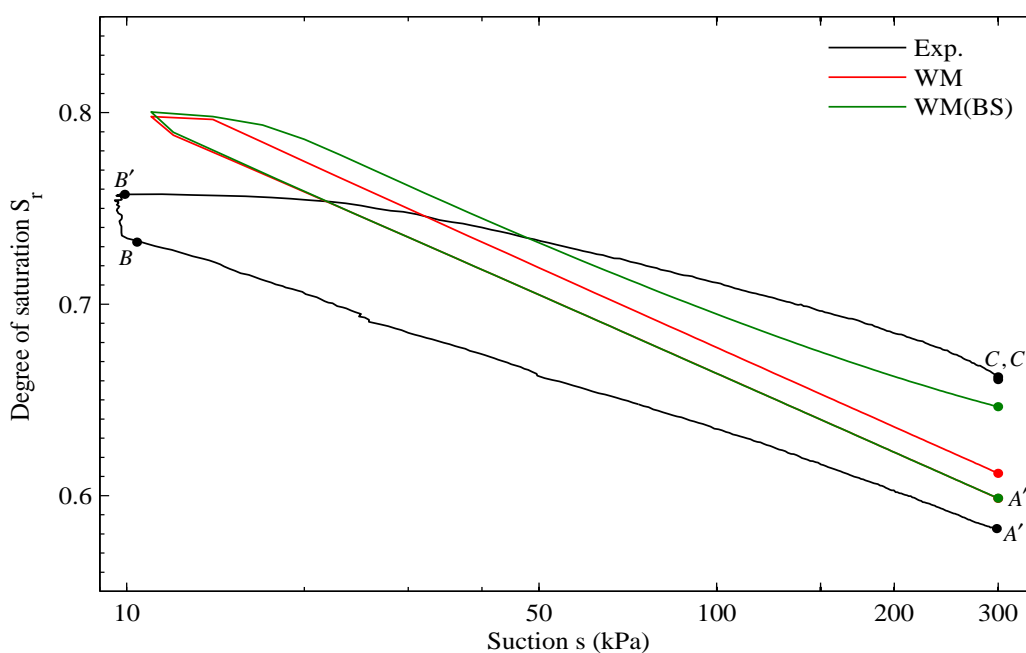


Figure 8-52 Variation of degree of saturation S_r against suction s for wetting-drying cycle of Test A11 along with simulations.

Both WM and WM (BS) provide imperfect predictions for the experimental variation of S_r with suction (see Figure 8-52) for the wetting-drying cycle $A' - BB' - C$. Although, the two models do capture the hydraulic hysteresis observed in the experimental result, the values of model parameters selected (particularly λ_s and the spacing s_I^*/s_D^* between the SI and SD bounding curves) provide a poor match to the observed behaviour in this test. During drying stage $B' - C$, the WM (BS) simulation traces a drying water retention curve which is progressively shifted to higher suction range (see Figure 8-52) due to the prediction of plastic volumetric strain during drying (see Figure 8-51).

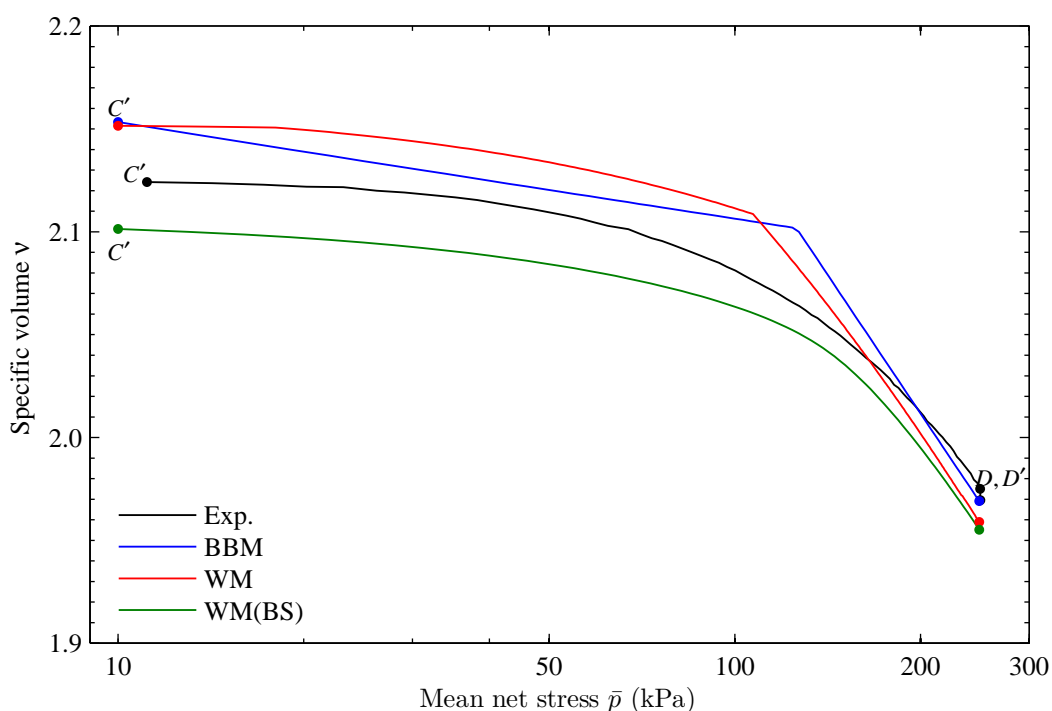


Figure 8-53 Variation of specific volume v against mean net stress \bar{p} for isotropic loading stage of Test A11 along with simulations.

The variation of specific volume and degree of saturation against mean net stress for isotropic loading stage $C' - D$ are shown in Figure 8-53 and Figure 8-54 respectively. All three models provide reasonably good predictions for the variation of v (see Figure 8-53), particularly the final value of v and the final slope of the normal compression curve, despite the fact that the initial value of v for isotropic loading $C' - D$ is either under-predicted (WM (BS)) or over-predicted (BBM and WM). For

the variation of S_r with \bar{p} (see Figure 8-54), both WM and WM(BS) provide a good match to the final value of S_r and the final gradient of the curve, even though the initial value of S_r at the start of this stage is significantly under-predicted by the WM simulation.

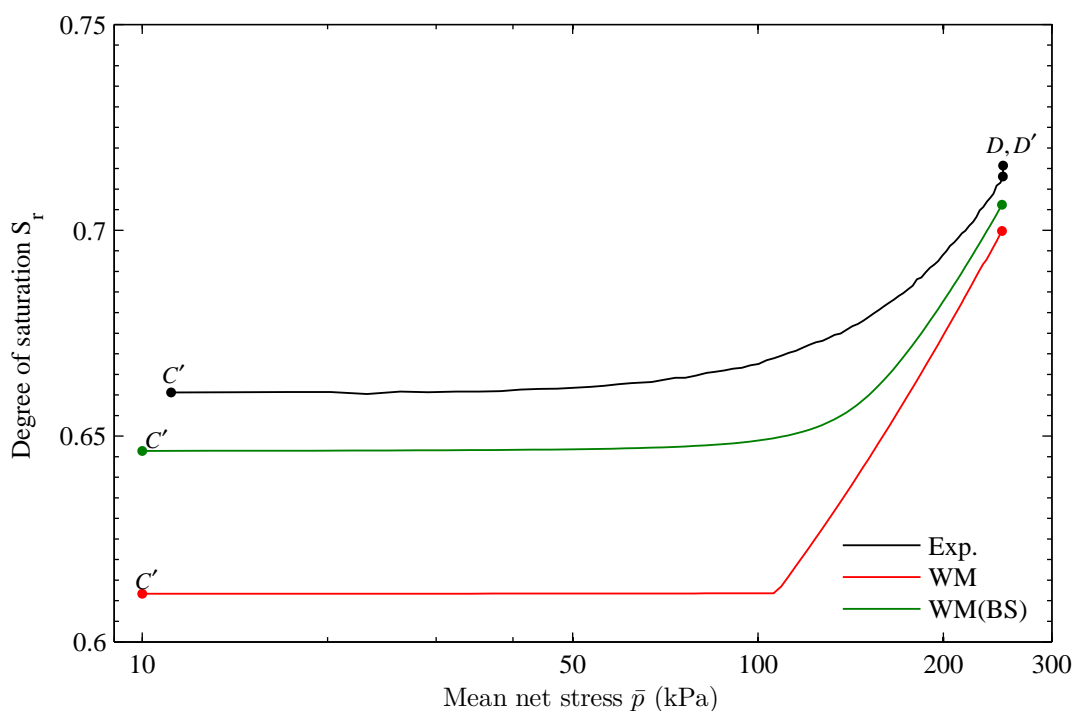


Figure 8-54 Variation of degree of saturation S_r against mean net stress \bar{p} for isotropic loading stage of Test A11 along with simulations.

Figure 8-55, Figure 8-56 and Figure 8-57 compare the experimental variations of specific volume, degree of saturation and specific water volume during the wetting - drying cycle of Tests A9 and A11. These figures demonstrate the impact of the preceding loading-unloading cycle in Test A9 (which was absent in Test A11). Inspection of Figure 8-55 reveals that the specific volume at the start of the wetting-drying cycle was lower in Test A9 than in Test A11, because of the plastic compression during the preceding loading-unloading cycle in Test A9. In addition, however, Sample A9 showed no net change of v over the wetting-drying cycle, whereas Sample A11 showed some non-elastic behaviour, with a net reduction of v over the cycle. One possible reason for this difference is that the isotropic loading-unloading cycle performed prior to the wetting-drying cycle in Test A9 induced hardening of the soil and thus the subsequent wetting-drying cycle was fully elastic.

This feature of behaviour can not be predicted by models like BBM. However, the conceptual idea of the WM and WM (BS) is consistent with the experimental observation and these models can predict this feature of behaviour, with plastic volumetric strain occurring during drying associated with yielding on the same LC yield curve that is responsible for any plastic volumetric strain during loading or wetting.

The influence of void ratio on the water retention behaviour is clearly demonstrated in Figure 8-56, where both wetting and drying curves are shifted upwards in Test A9 when compared with Test A11. This feature is once again consistent with the modelling ideas of the Wheeler et al. (2003) framework. It is interesting to note that the shapes of the water retention curves (in the $S_r : \ln s$ plane) of Tests A9 and A11 are quite similar. However, close inspection of Figure 8-56 shows that the net increase in degree of saturation over the wetting-drying cycle is higher in Test A11 than in Test A9 (so that the disparity in S_r values between the two samples is reduced by the wetting-drying cycle).

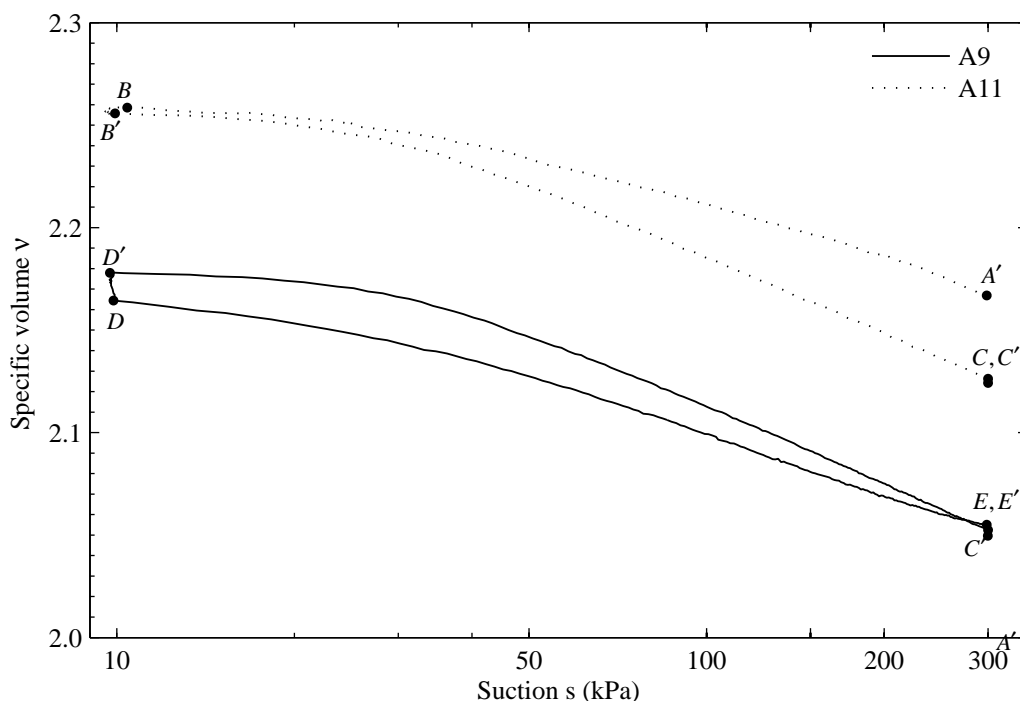


Figure 8-55 Experimental variation of specific volume v against suction s for wetting-drying cycles of Tests A9 and A11.

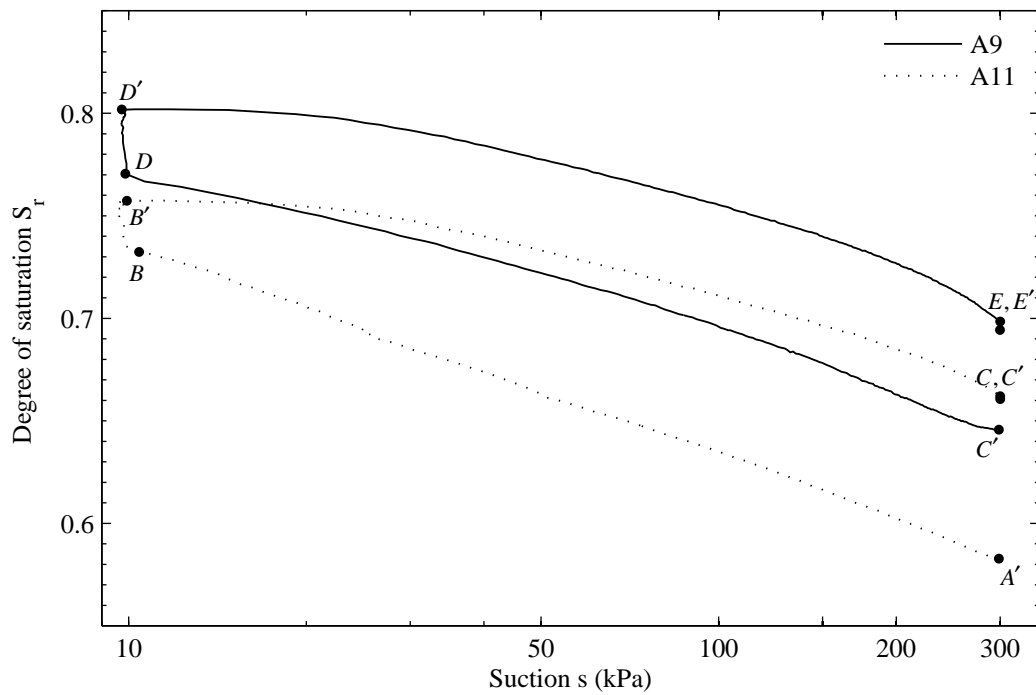


Figure 8-56 Experimental variation of degree of saturation S_r against suction s for wetting-drying cycles of Tests A9 and A11.

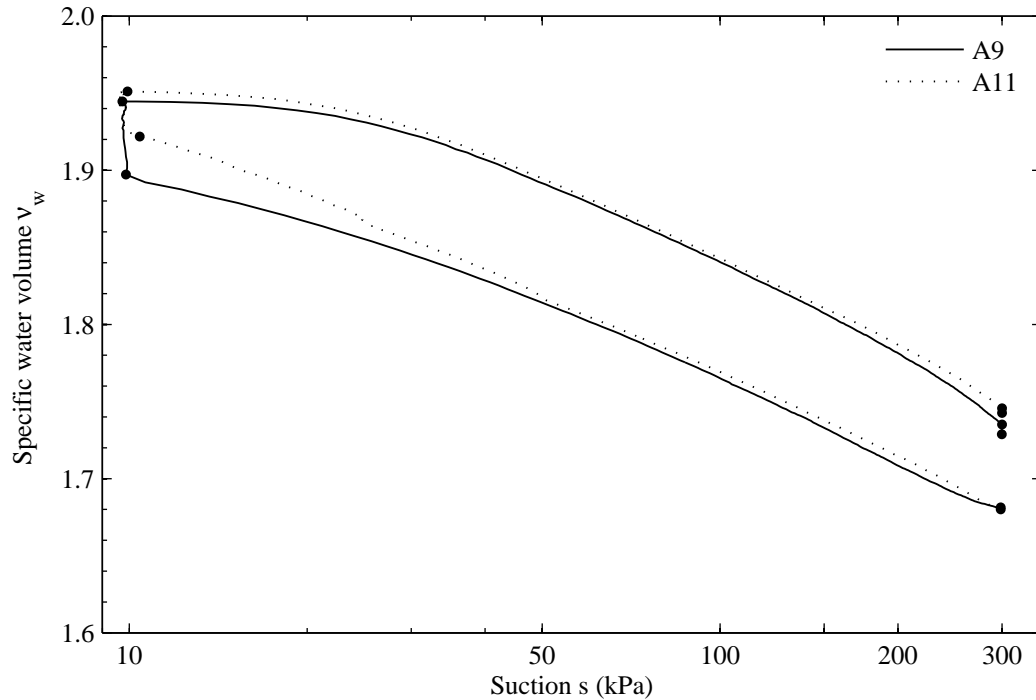


Figure 8-57 Experimental variation of specific water volume v_w against suction s for wetting-drying cycles of Tests A9 and A11.

The water retention behaviour is plotted in terms specific water volume against suction in Figure 8-57. Interestingly, the experimental results from Test A9 and Test A11 almost coincide with each other when plotted in terms of v_w . This means that the influence of void ratio on the variation of specific water volume may not be as significant as on the variation of degree of saturation. This experimental observation suggests that the water retention behaviour expressed in terms of v_w may be considered uncoupled from the mechanical behaviour to a certain extent.

8.2.4 Test A12

Sample A10 was first subjected to a drying-wetting cycle (1kPa \rightarrow 300kPa \rightarrow 10kPa) as discussed in Section 8.2.2. It was decided to investigate the influence of a previous isotropic loading-unloading cycle on the behaviour of the soil during this type of drying- wetting cycle, by performing a comparator test (A12).

Figure 8-58 and Table 8-11 show the stress path followed in Test A12.

| Stage | | | \bar{p} (kPa) | s (kPa) |
|-------|----|----------------------|----------------------|---------------------|
| From | To | Description | | |
| A | A' | Initial equalisation | 10 | 1 |
| A' | B | Isotropic loading | 10 \rightarrow 35 | 1 |
| B | B' | Equalisation | 35 | 1 |
| B' | C | Isotropic unloading | 35 \rightarrow 10 | 1 |
| C | C' | Equalisation | 10 | 1 |
| C' | D | Drying | 10 | 1 \rightarrow 300 |
| D | D' | Equalisation | 10 | 300 |
| D' | E | Wetting | 10 | 300 \rightarrow 1 |
| E | E' | Equalisation | 10 | 1 |
| E' | F | Drying | 10 | 1 \rightarrow 200 |
| F | F' | Equalisation | 10 | 200 |
| F' | G | Isotropic loading | 10 \rightarrow 500 | 200 |
| G | G' | Equalisation | 500 | 200 |
| G' | H | Isotropic unloading | 500 \rightarrow 10 | 200 |
| H | H' | Equalisation | 10 | 200 |

Table 8-11 Stress path for Test A12

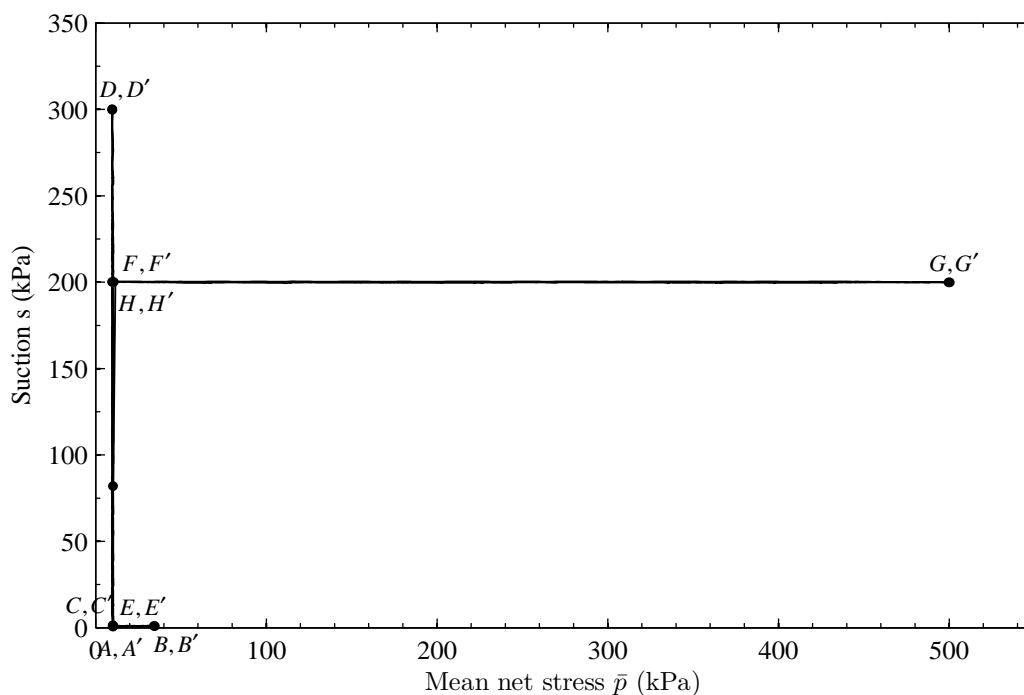


Figure 8-58 Stress path for Test A12

After an initial equalisation stage (AA') at a mean net stress of 10 kPa and a suction of 1 kPa, an isotropic loading-unloading cycle $A' - BB' - C$ was carried out over a range of \bar{p} from 10 to 35 kPa. The sample was then subjected to a drying-wetting cycle $C' - DD' - E$ over a suction range of 1 to 300 kPa. The suction was then increased to 200 kPa at constant a mean net stress of 10 kPa ($E' - F$). Finally, an isotropic loading ($F' - G$) and unloading ($G' - H$) cycle was conducted between 10 and 500 kPa of mean net stress.

Figure 8-59 and Figure 8-60 show the variation of specific volume and degree of saturation with mean net stress respectively. During the first isotropic loading $A' - B$ at a suction of 1 kPa, a clear yield point can be identified for both v and S_r variation at a mean net stress of about 15 kPa. The subsequent drying and wetting stages ($C' - D, D' - E, E' - F$), produced irreversible volumetric strains (see Figure 8-59) and a net decrease of S_r (see Figure 8-60). During the final isotropic loading $F' - G$ at a suction of 200 kPa there is a suggestion of a yield point at a \bar{p} value of 150 to 200 kPa.

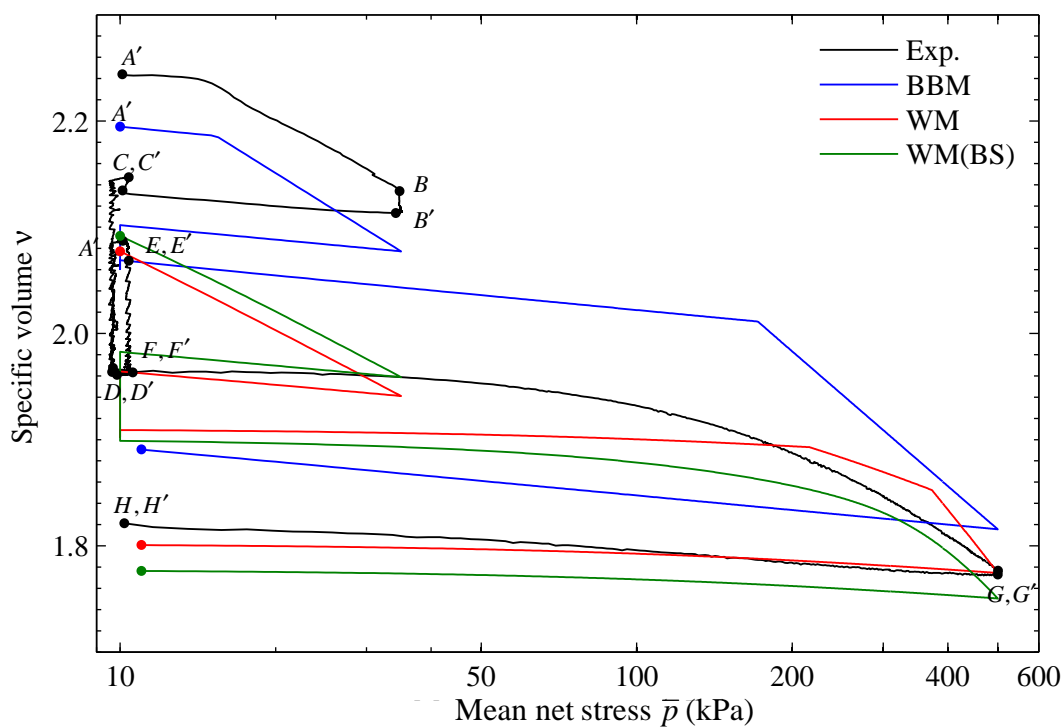


Figure 8-59 Variation of specific volume v against mean net stress \bar{p} for Test A12 along with simulations.

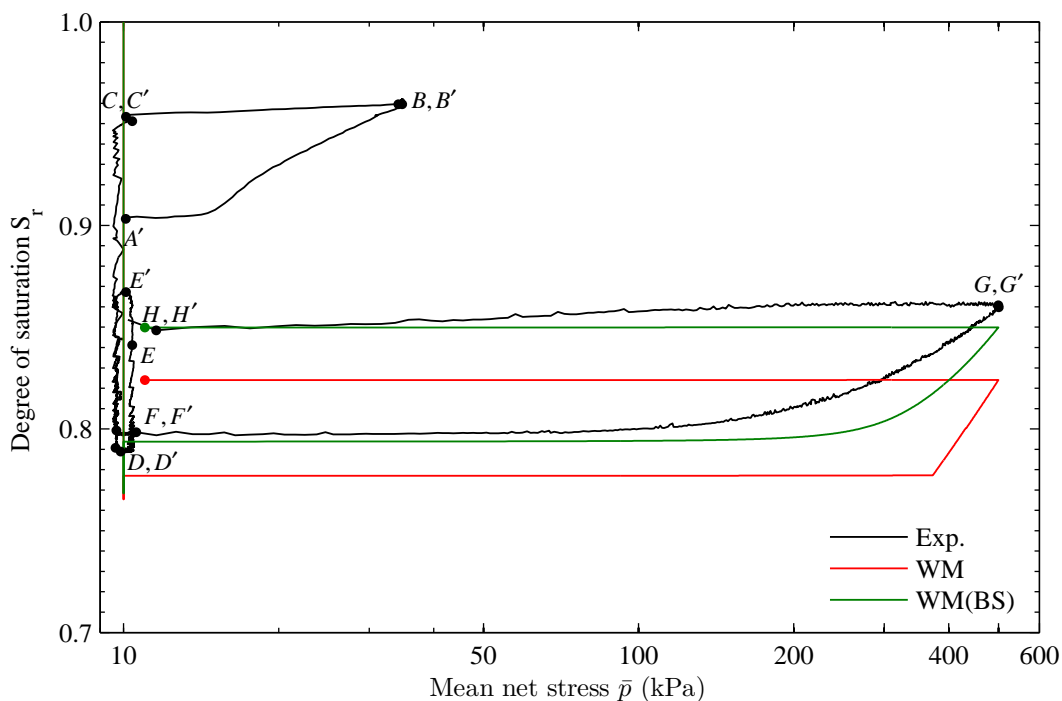


Figure 8-60 Variation of degree of saturation S_r against mean net stress \bar{p} for Test A12 along with simulations.

Inspection of Figure 8-59 reveals that none of the models provides an overall good match to the experimental behaviour for the variation of ν against \bar{p} . The BBM, however, captures the yield points for both isotropic loading stages ($A' - B$ and $F' - G$) with a reasonable accuracy. Both the WM and the WM (BS) provide poor predictions for the first isotropic compression curve $A' - B$, because they predict plastic behaviour from the start of the stage and they mis-predict the position of the normal compression line. The WM and WM (BS) do, however, provide a slightly better match than the BBM for the second isotropic compression curve $F' - G$ (see Figure 8-59). Once again, the double yield points predicted by the WM during stage $F' - G$ are not evident in the experimental results.

The overall predictions of the WM and WM (BS) for the variation of S_r against \bar{p} (see Figure 8-60) are generally unsatisfactory. Both models predict saturated conditions ($S_r = 1$) throughout the first isotropic loading-unloading cycle $A' - BB' - C$, in contrast to the experimental observations, which show unsaturated conditions and a net increase of S_r over the loading-unloading cycle. However, the WM (BS) provides a good match to the observed experimental behaviour during the second isotropic loading-unloading cycle $F' - GG' - H$ (see Figure 8-60), while the WM underestimates S_r throughout cycle $F' - GG' - H$.

Figure 8-61 shows the variation of specific volume against suction for Test A12. The experimental curves show some non-elastic behaviour, with net reduction of ν over drying-wetting cycle $C' - DD' - E$, and final drying $E' - F$ not following precisely the same path as wetting $D' - E$. None of the models captures this behaviour well. The BBM and the WM predict entirely elastic behaviour during the drying-wetting-drying stages $C' - DD' - EE' - F$. Although the WM (BS) predicts a small plastic reduction of ν during drying stages $C' - D$ and $E' - F$, the predicted shape is a poor match to the observed behaviour (see Figure 8-61)

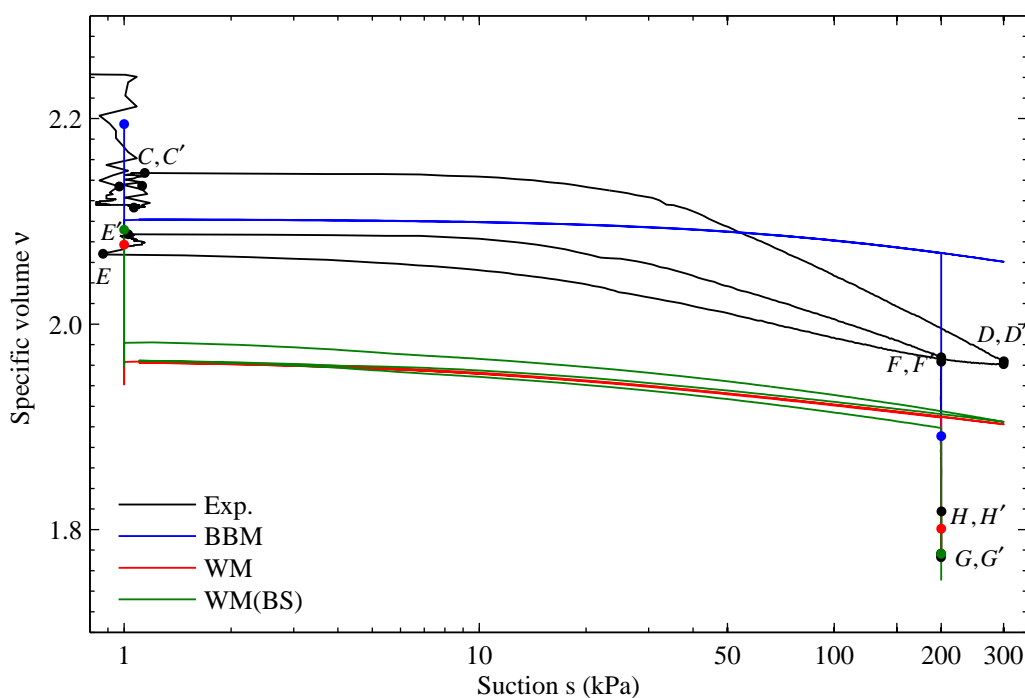


Figure 8-61 Variation of specific volume v against suction s for Test A12 along with simulations.

Figure 8-62 and Figure 8-63 show the variation of S_r and v_w against suction for Test A12. The experimental drying curves ($C' - D$ and $E' - F$) expressed in terms of both S_r and v_w show a steep gradient just after the yield suction of about 25 kPa and the gradient then gradually decreased as the suction increased further. Similar to the observed behaviour in Figure 8-47 in Section 8.2.2, there is some suggestion of a second steepening of the water retention curve at a suction of about 300 kPa (although not conclusive) during the first drying stage $C' - D$. Also, the wetting curve $D' - E$ shown in both Figure 8-62 and Figure 8-63 exhibits low gradient compared to drying curves $C' - D$ and $E' - F$, with no suggestion of a yield point. It can be seen from both figures that neither the WM nor the WM (BS) provide a good match to the observed experimental features of behaviour, particularly the slope and position of drying and wetting curves and the spacing between the drying and wetting curves.

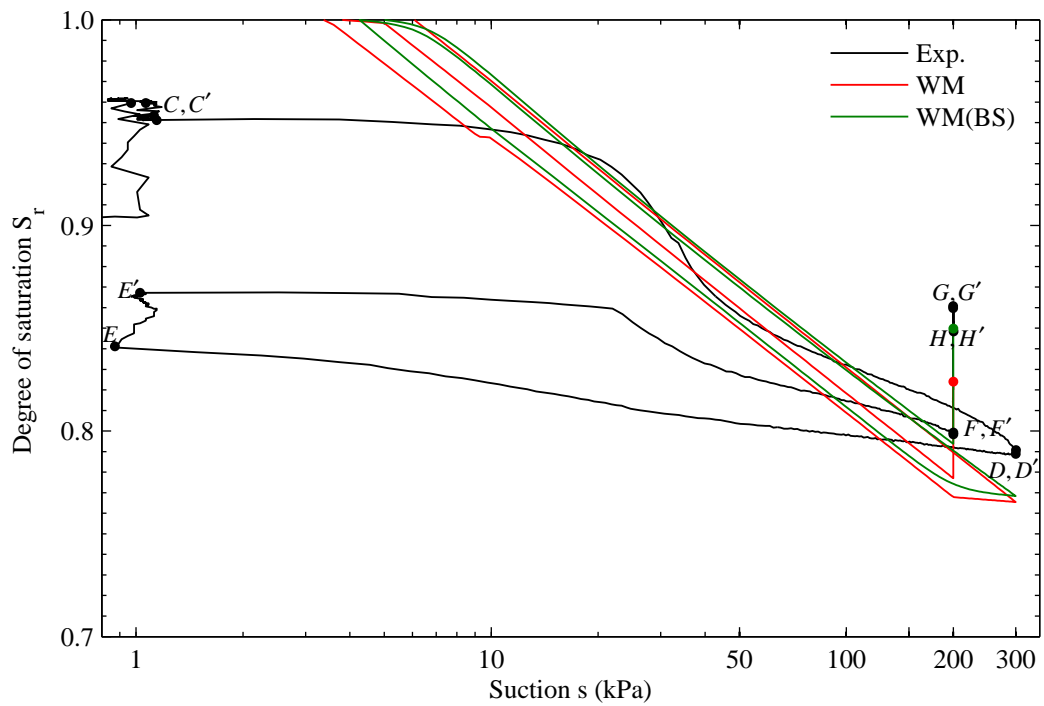


Figure 8-62 Variation of degree of saturation S_r against suction s for Test A12 along with simulations.

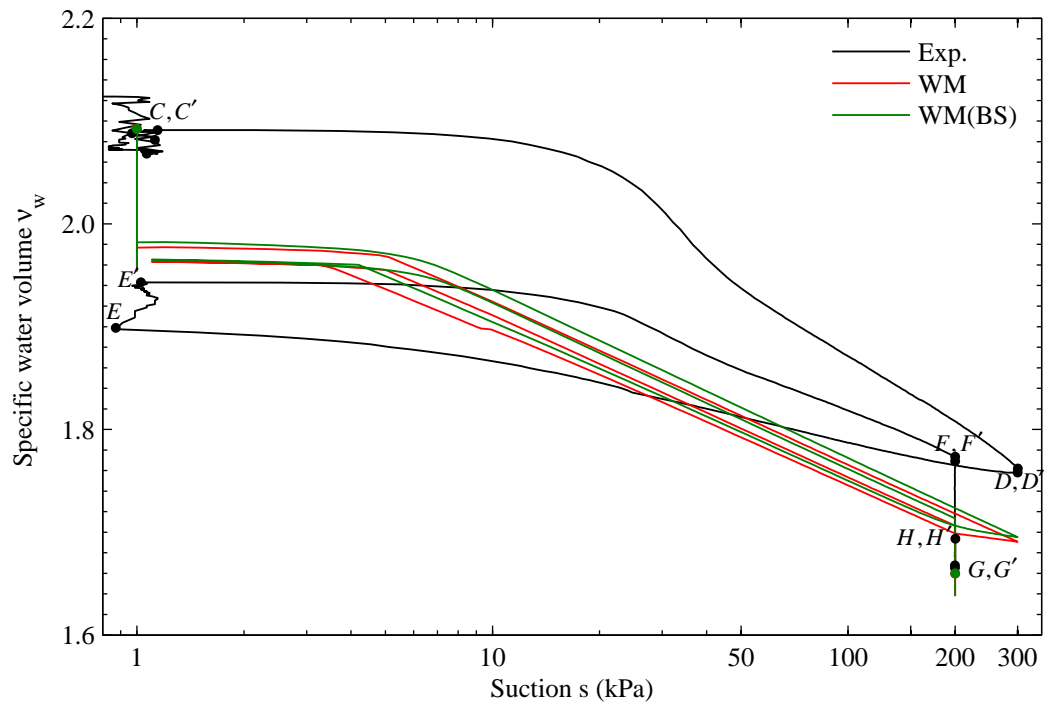


Figure 8-63 Experimental variation of specific water volume v_w against suction s for Test A12 along with simulations.

Figure 8-64, Figure 8-65 and Figure 8-66 show the experimental variations of specific volume, degree of saturation and specific water volume with suction for the first drying-wetting cycle of Tests A10 and A12. Inspection of Figure 8-64 reveals that the previous isotropic loading-unloading cycle carried out in Test A12 provided a reduction in the value of v at the start of the drying-wetting cycle. As a consequence, the yield value of suction observed in the drying stage was increased to around 30 kPa, compared to Test A10 where the sample started to yield at a suction of about 15 kPa. However, no significant difference between the two tests can be observed for the yield stress taken from the variation of S_r or v_w with suction during drying (see Figure 8-65 and Figure 8-66). Inspection of Figure 8-65 reveals that the drying and wetting retention curves of Test A12 plotted in terms of S_r were shifted to higher suctions than in Test A10, because of the influence of the reduced void ratio in Test A12. However, this influence of isotropic loading and unloading and the consequent reduction in void ratio is not apparent when the same data is plotted in terms of v_w against suction (see Figure 8-66).

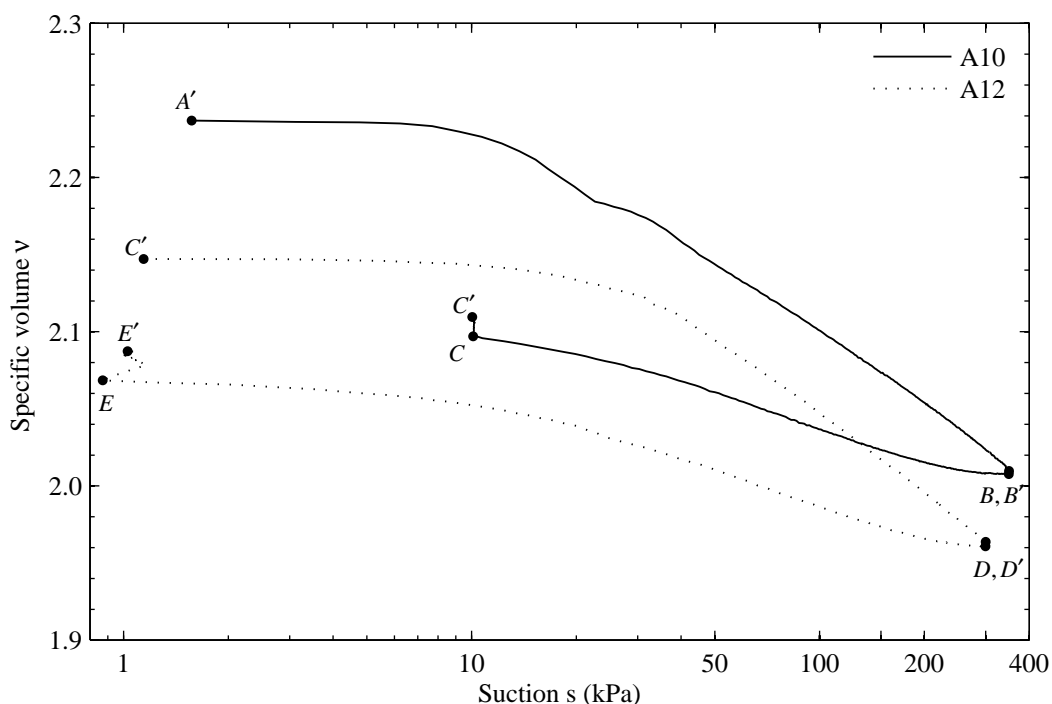


Figure 8-64 Experimental variation of specific volume v against suction s for drying-wetting cycles of Tests A10 and A12.

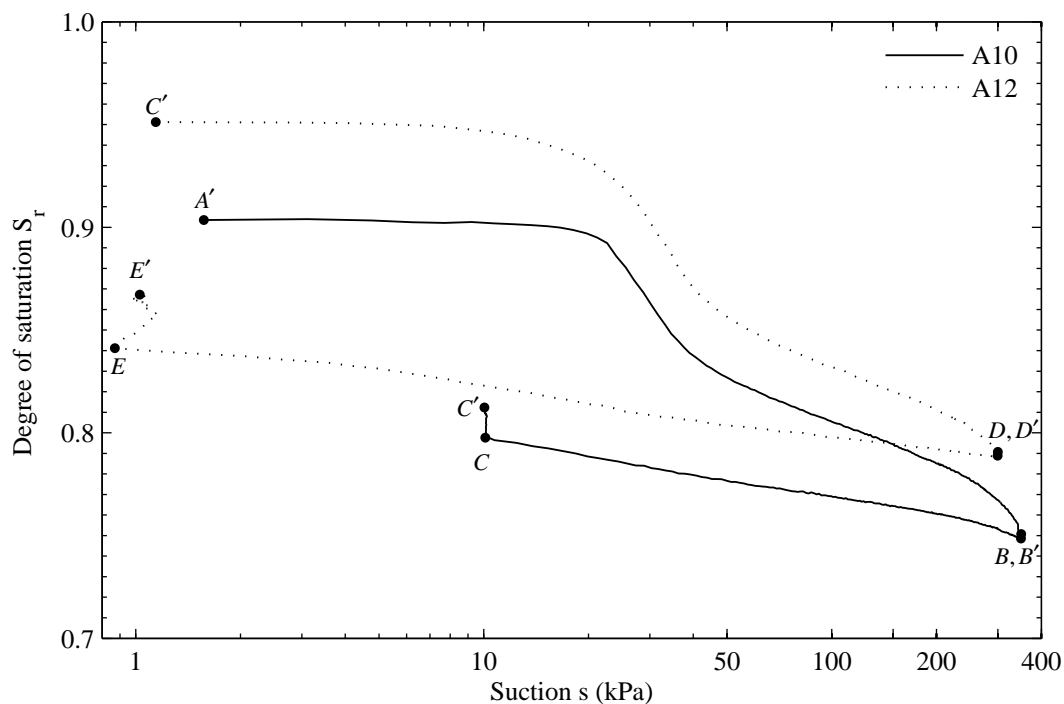


Figure 8-65 Experimental variation of degree of saturation S_r against suction s for drying-wetting cycles of Tests A10 and A12.

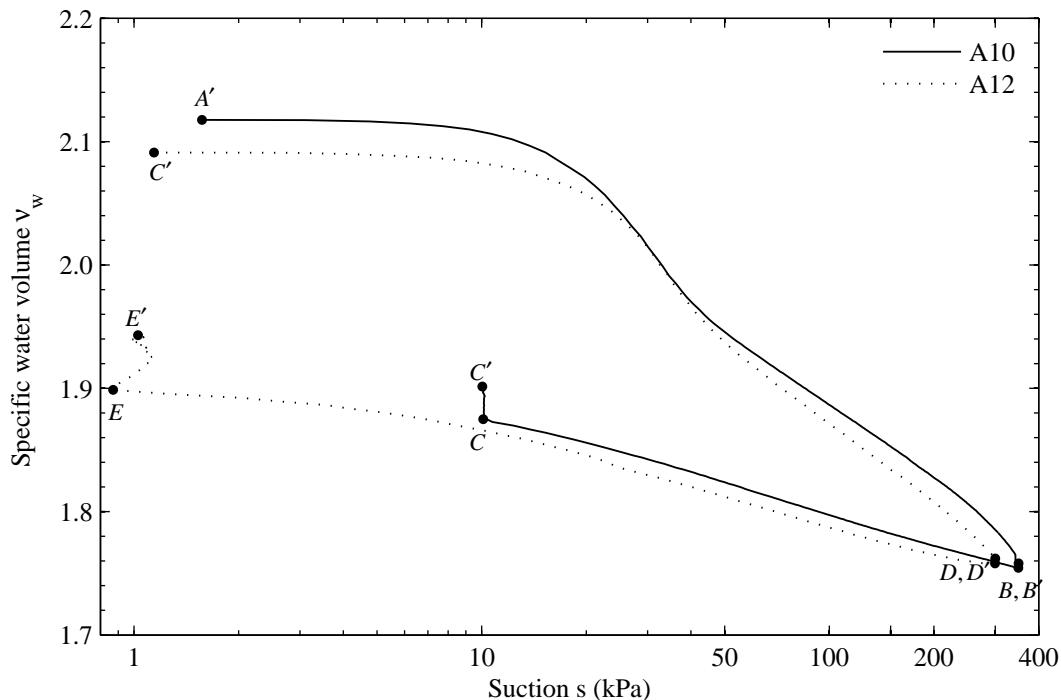


Figure 8-66 Experimental variation of specific water volume v_w against suction s for drying-wetting cycles of Tests A10 and A12.

CHAPTER 9

TRIAXIAL TEST RESULTS, SIMULATIONS AND DISCUSSION

This chapter presents experimental test results obtained from suction-controlled triaxial tests carried out using Systems B and C. Simulations from the BBM and the triaxial version of the Wheeler et al. (2003) model, proposed in Section 3.6.3, are also compared with the experimental results in order to investigate the performance of the models. Many of the stress path tests carried out in the suction-controlled apparatus of System B were designed so that the influence of wetting and drying on the subsequent shearing behaviour could be explored. Other tests in System B were conducted to investigate particular features of behaviour of unsaturated soil subjected to specific stress paths. In the conventional Bishop-Wesley triaxial cell of System C, three fully drained tests on saturated soil samples were carried out, in which the samples were isotropically consolidated and then sheared under different radial effective stresses. The tests carried out using System C were primarily intended for determining the values for the slope of the saturated normal compression line λ and the slope of the saturated critical state line M .

For BBM simulations, a non-associated flow rule, suggested by Alonso et al. (1990), was employed on the elliptical yield surface in the $q : \bar{p}$ plane. In order for an unbiased comparison of predictions with the BBM, a similar non-associated flow rule was adopted for the LC yield curve in the $q : p^*$ plane for the WM simulations (see Equation 3-21).

9.1 PRELIMINARY TEST (TEST B1)

In order to verify the proper operation of System B, a preliminary test (Test B1) without shearing was carried out. Table 9-1 shows the stress path for Test B1. The sample was first equalised ($A_1 A_1'$) at a mean net stress of 20 kPa and a suction of 200 kPa. The sample was then isotropically loaded ($A_1' - B_1$) at constant suction of 200 kPa

to a mean net stress of 200 kPa, and then an isotropic unloading stage $B'_1 - C_1$ was performed to a mean net stress of 100 kPa.

| Stage | | | q (kPa) | \bar{p} (kPa) | s (kPa) |
|--------|--------|----------------------|-----------|-----------------------|-----------|
| From | To | Description | | | |
| A_1 | A'_1 | Initial equalisation | 0 | 20 | 200 |
| A'_1 | B_1 | Isotropic loading | 0 | 20 \rightarrow 200 | 200 |
| B_1 | B'_1 | Equalisation | 0 | 200 | 200 |
| B'_1 | C_1 | Isotropic unloading | 0 | 200 \rightarrow 100 | 200 |
| C_1 | C'_1 | Equalisation | 0 | 100 | 200 |

Table 9-1 Stress path for Test B1

Figure 9-1 and Figure 9-2 show the variation of specific volume and degree of saturation respectively with mean net stress for Test B1 and for the isotropic loading stages conducted at a suction of 200 kPa in Tests A4, A5, A8 and A12 (the starting points for these tests in System A all vary, because the isotropic loading at a suction of 200 kPa was preceded by a variety of different stress paths). It can be clearly seen that the results from Test B1 are consistent with the results from the tests performed in System A, thus confirming the proper operation of System B.

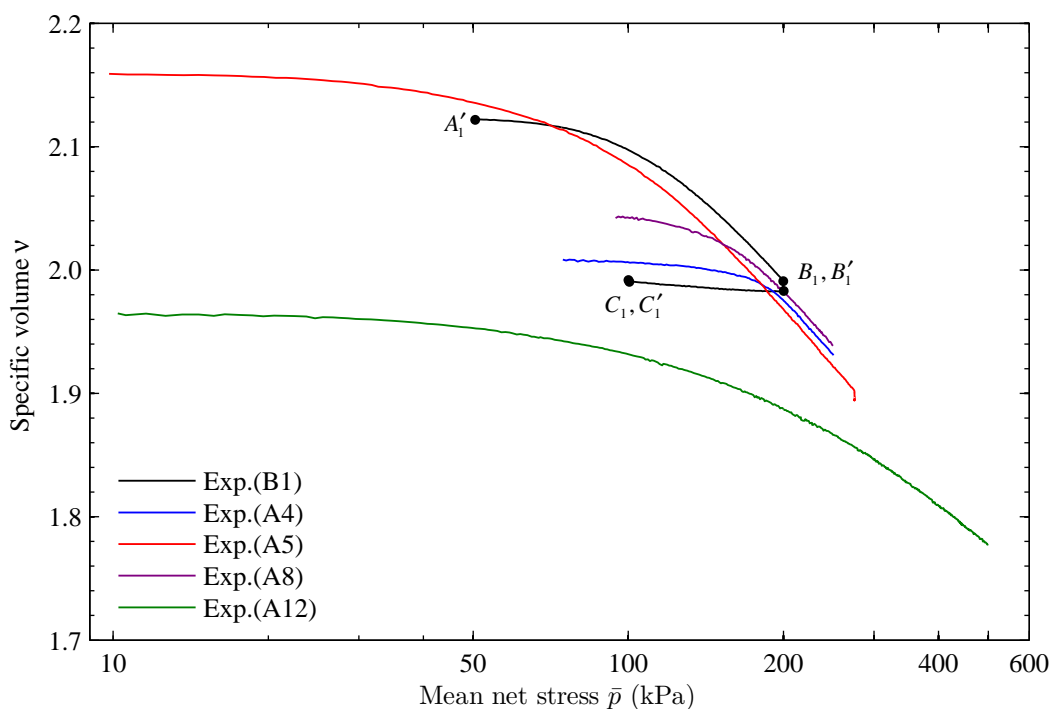


Figure 9-1 Variation of specific volume with mean net stress for Test B1 along with results for Tests A4, A5, A8 and A12 for isotropic loading at suction of 200 kPa

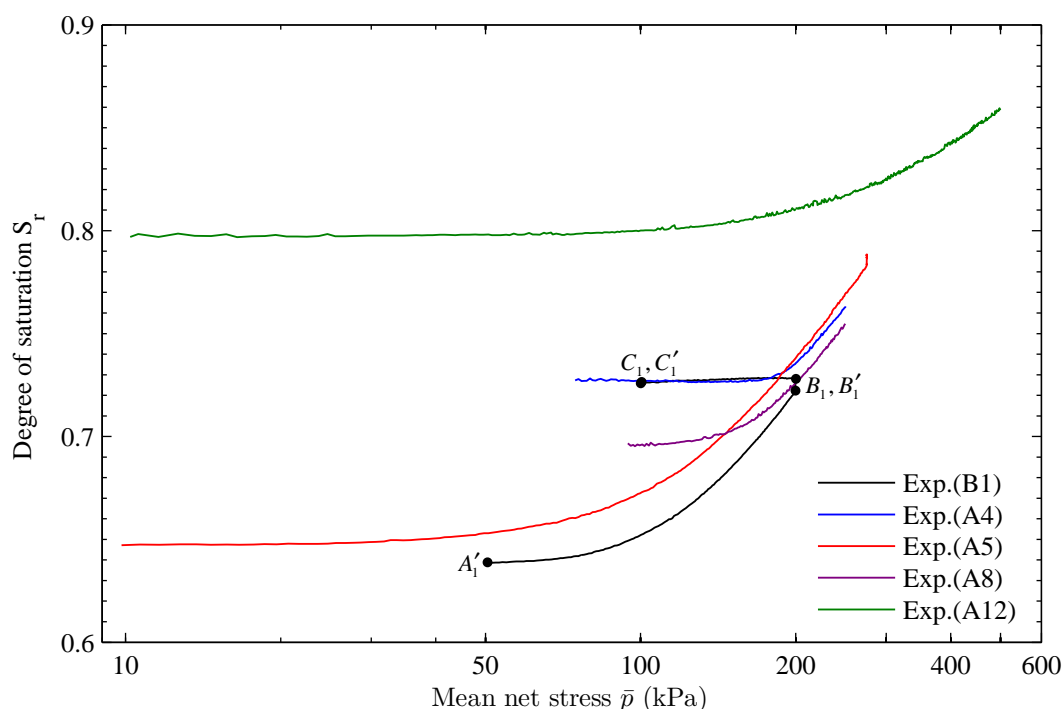


Figure 9-2 Variation of degree of saturation with mean net stress for Test B1 along with results for Tests A4, A5, A8 and A12 for isotropic loading at suction of 200 kPa

9.2 INFLUENCE OF A WETTING AND DRYING CYCLE ON THE SHEAR BEHAVIOUR OF UNSATURATED SOIL

In Section 8.2.1, the influence of a wetting and drying cycle on the behaviour during subsequent isotropic loading was investigated. In this section, tests performed in order to investigate the influence of a wetting and drying cycle on the soil behaviour during a subsequent shearing stage are presented, along with model predictions from the BBM and WM.

9.2.1 Shearing at 200 kPa suction (Tests B2 and B3)

Table 9-2 and Table 9-3 show the stress paths followed in Tests B2 and B3 respectively, and the stress paths are also illustrated in Figure 9-3. In Test B2, the sample was first equalised ($A_2A'_2$) at a mean net stress of 10 kPa and a suction of 30 kPa. The suction was then increased to 200 kPa at constant mean net stress (stage $A'_2 - B_2$). The sample was then subjected to an isotropic loading stage $B'_2 - C'_2$ to a mean net stress of 75 kPa. Finally, shearing stage $C'_2 - D_2$ was carried out to failure at a constant radial net stress of 75 kPa and a constant suction of 200 kPa. In

Test B3, the sample was equalised ($B_3B'_3$) at a suction of 200 kPa and a mean net stress of 10 kPa and a mean net stress of 10 kPa. It was then isotropically loaded to 75 kPa mean net stress (stage $B'_3 - C_3$) and finally sheared ($C'_3 - D_3$) under constant radial net stress of 75 kPa and constant suction of 200 kPa. Test B3 did not therefore include the initial wetting to a simulation of 30 kPa that occurred in Test B2.

| Stage | | | q (kPa) | \bar{p} (kPa) | s (kPa) |
|--------|--------|----------------------|---------------------|----------------------|----------------------|
| From | To | Description | | | |
| A_2 | A'_2 | Initial equalisation | 0 | 10 | 30 |
| A'_2 | B_2 | Drying | 0 | 10 | 30 \rightarrow 200 |
| B_2 | B'_2 | Equalisation | 0 | 10 | 200 |
| B'_2 | C_2 | Isotropic loading | 0 | 10 \rightarrow 75 | 200 |
| C_2 | C'_2 | Equalisation | 0 | 75 | 200 |
| C'_2 | D_2 | Shearing | 0 \rightarrow 185 | 75 \rightarrow 137 | 200 |

Table 9-2 Stress path for Test B2

| Stage | | | q (kPa) | \bar{p} (kPa) | s (kPa) |
|--------|--------|-------------------|---------------------|----------------------|-----------|
| From | To | Description | | | |
| B_3 | B'_3 | Equalisation | 0 | 10 | 200 |
| B'_3 | C_3 | Isotropic loading | 0 | 10 \rightarrow 75 | 200 |
| C_3 | C'_3 | Equalisation | 0 | 75 | 200 |
| C'_3 | D_3 | Shearing | 0 \rightarrow 186 | 75 \rightarrow 137 | 200 |

Table 9-3 Stress path for Test B3

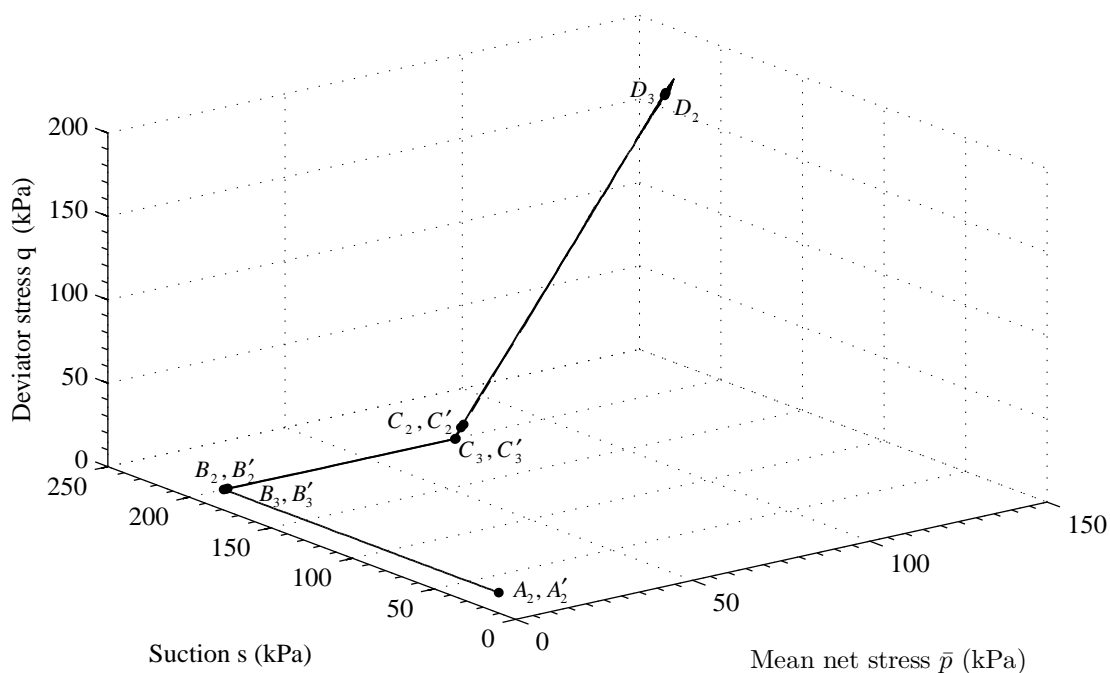


Figure 9-3 Stress path for Tests B2 and B3

Figure 9-4 and Figure 9-5 show the experimental variation of deviator stress q and volumetric strain ε_v , respectively against true shear strain ε_s for the shearing stages of Test B2 and Test B3, along with the BBM and WM predictions. The experimental curves in the $q:\varepsilon_s$ plane for Test B2 and B3 look similar (see Figure 9-4). In particular, the magnitude of deviator stress approached at the end of the test is almost identical. However, close inspection of Figure 9-4 reveals that during the initial part of the shearing stage Sample B2 showed lower shear stiffness than Sample B3, because of the previous wetting and drying cycle ($A_2A'_2$, $A'_2 - B_2$) experienced by Sample B2.

As mentioned in Section 7.3.3 the shear strength obtained from Tests B2 and B3 for 200 kPa suction is considerably less than the value suggested by Sivakumar (1995) (see Figure 7-17). Figure 9-6 shows the shape of Samples B2, B3, B4 and B5 at the end of testing. Samples B2 and B3 clearly show buckling, suggesting that failure might have been attained by buckling rather than shearing. This could be a possible reason for the significant reduction in the shear strength.

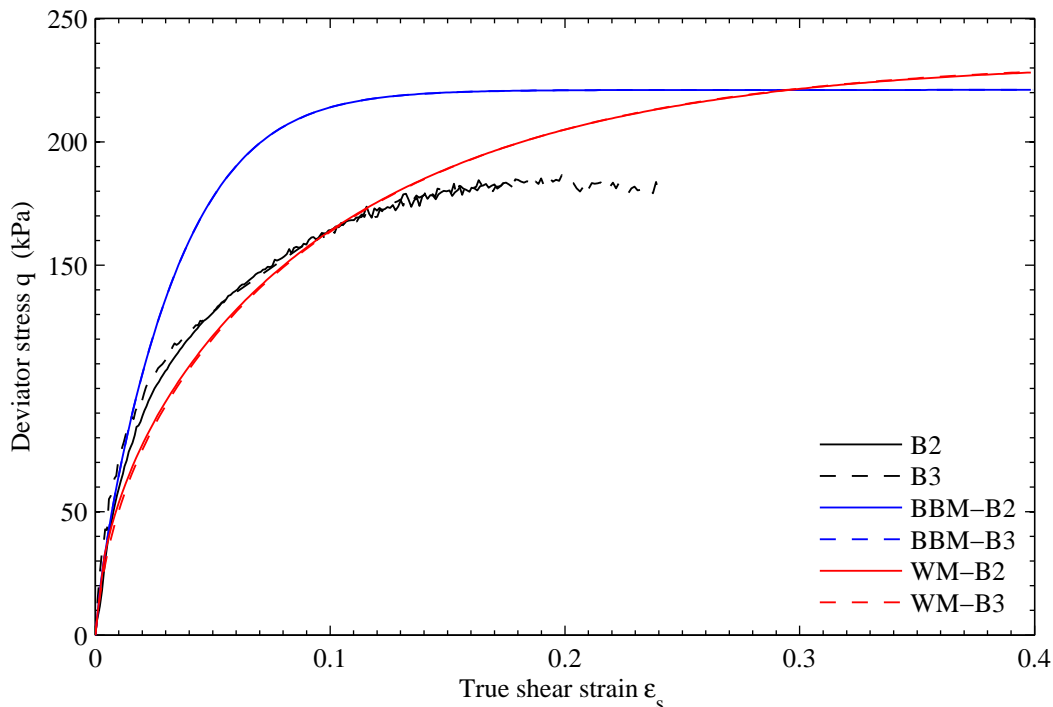


Figure 9-4 Variation of deviator stress q against true shear strain ε_s in Tests B2 and B3 along with BBM and WM predictions

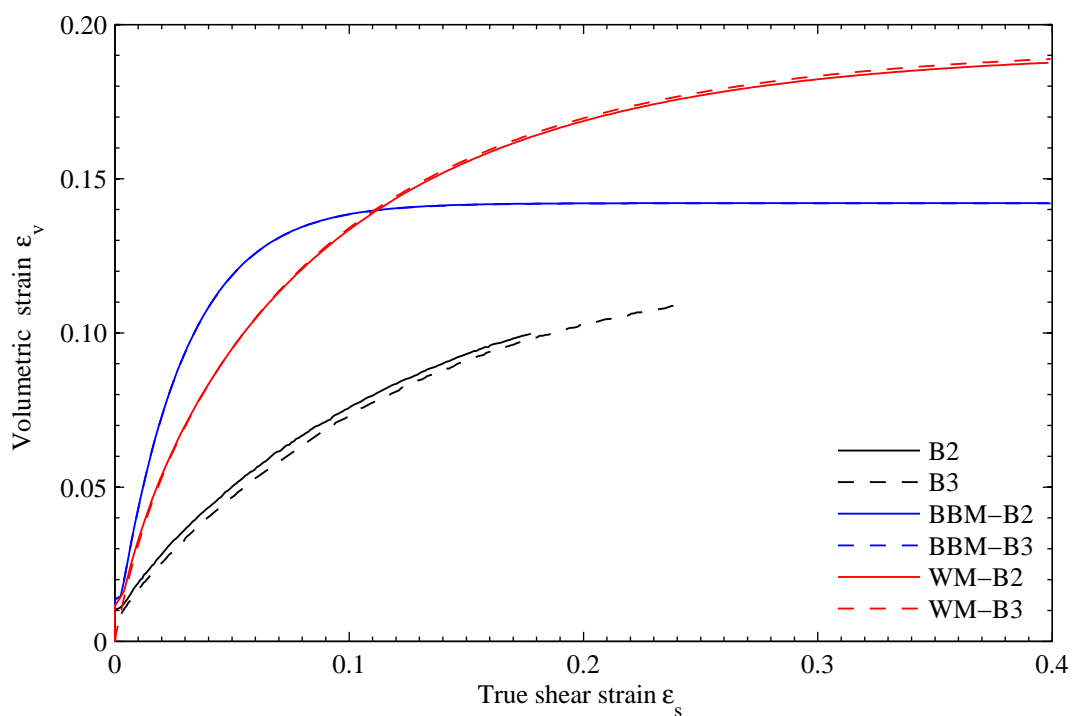


Figure 9-5 Variation of volumetric strain ϵ_v against true shear strain ϵ_s in Tests B2 and B3 along with BBM and WM predictions

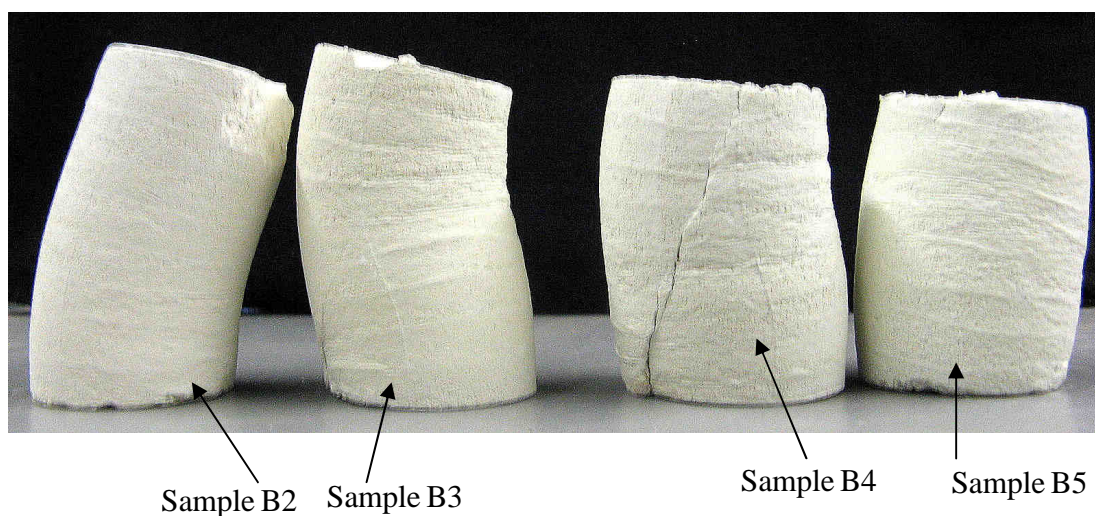


Figure 9-6 Deformed shapes of Samples B2, B3, B4 and B5 at the end of tests

The experimental variations of volumetric strain with shear strain for Samples B2 and B3 are almost identical (see Figure 9-5), suggesting that the influence of the wetting-drying cycle on the volumetric behaviour of Sample B2 during subsequent shearing was not significant. The experimental results presented in Figure 9-5 show that for both samples the specific volume was still changing at the end of shearing (a true

critical state was not reached), even though the deviator stress had stabilized (Figure 9-4).

Inspection of Figure 9-4 shows that both BBM and WM do not provide a good match to the observed behaviour. The BBM predicts the same results in the shearing stages of Test B2 and B3, whereas the WM predicts slightly different behaviour during the shearing stages of the two tests. The BBM always overestimates the values of q , including the critical state deviator stress, whereas the WM initially under-predicts and then over-predicts the values of q , including over-prediction of the critical state deviator stress (see Figure 9-4). These over-predictions of critical state deviator stress by both the BBM and the WM may be partly because of the occurrence of buckling failure, as discussed earlier. It can be seen from Figure 9-4 that according to the WM prediction the deviator stress is still increasing at a shear strain of 0.4, and this is not in agreement with the experimental observation. Inspection of Figure 9-5 reveals that both the BBM and WM significantly over-predict the amount of volumetric strain throughout the shearing stage.

Figure 9-7, Figure 9-8 and Figure 9-9 show the variation of specific volume, degree of saturation and specific water volume respectively against mean net stress for both Test B2 and Test B3. Inspection of Figure 9-7 and Figure 9-8 shows that at the end of the wetting-drying cycle ($A_2A'_2$, $A'_2 - B_2$) performed in Test B2 the value of v was identical to the value of v at the end of initial equalisation ($B_3B'_3$) of Test B3, but the value of S_r was, as intended, higher in Test B2 than in Test B3. During the subsequent isotropic loading stage ($B' - C$) and shear stage $C' - D$ of Tests B2 and B3, almost identical variation of v against mean net stress can be observed in the two tests (see Figure 9-7). This experimental observation once again confirms that the influence of the wetting-drying cycle on the subsequent variation of v for Test B2 is negligible. It can be seen from Figure 9-7 that both BBM and WM tend to underestimate the value of v throughout the isotropic loading ($B' - C$) and shearing ($C' - D$). The BBM does not predict any influence of the wetting-drying cycle ($A_2A'_2$, $A'_2 - B_2$) in Test B2 on the subsequent stages, as the wetting and drying stages were predicted to be inside the LC yield curve. In contrast, the WM predicts slightly different behaviour in the two

tests, with a yield point early in isotropic loading stage $B'_2 - C'_2$ of Test B2, corresponding to yielding on the LC curve only, because the LC yield curve was dragged inwards during the previous wetting-drying cycle ($A_2 A'_2$, $A'_2 - B_2$). This prediction of the WM, that the behaviour of samples B2 and B3 during isotropic loading $B' - C$ should be different, is not supported by the experimental observation (see Figure 9-7).

Inspection of Figure 9-8 and Figure 9-9 shows that the values of S_r and v_w at the start of isotropic loading were significantly higher in Test B2 than in Test B3, as a consequence of the previous wetting-drying cycle in Test B2. These differences in S_r and v_w between Test B2 and Test B3 were maintained throughout the isotropic loading stage $B' - C$, but then gradually reduced during the shearing stage $C' - D$ to reach almost identical values of S_r and similar values of v_w by the end of shearing (see Figure 9-8 and Figure 9-9). This suggests that any changes produced by the wetting - drying cycle in Test B2 were wholly or partially removed by the occurrence of plastic processes during the shearing stage.

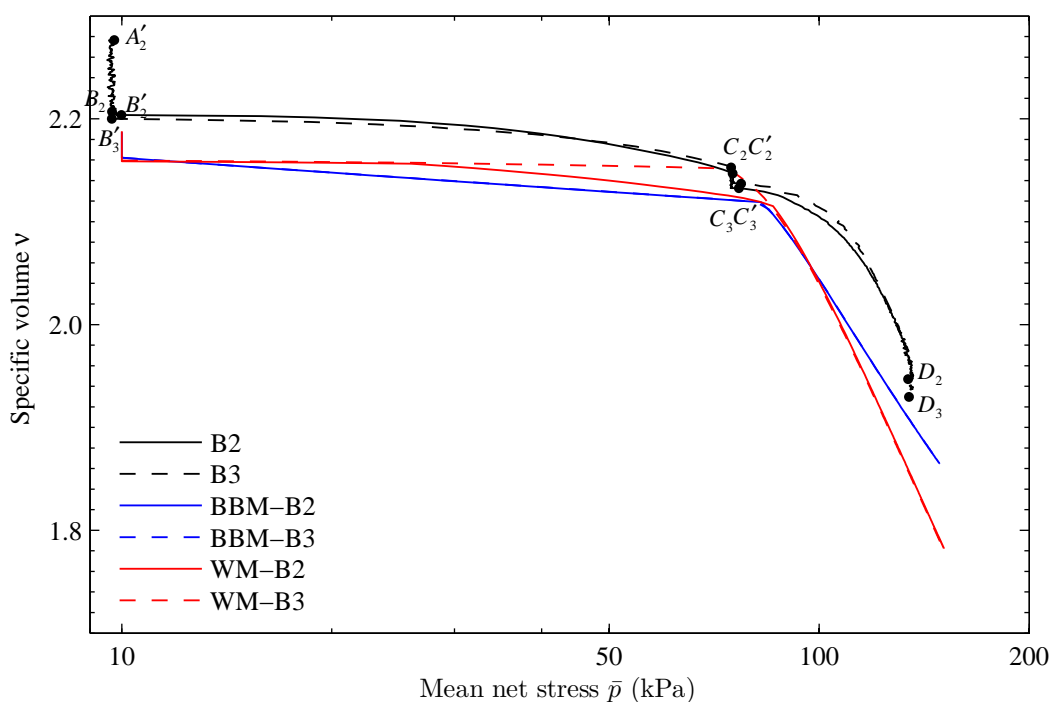


Figure 9-7 Variation of specific volume v against mean net stress \bar{p} in Tests B2 and B3 along with BBM and WM predictions

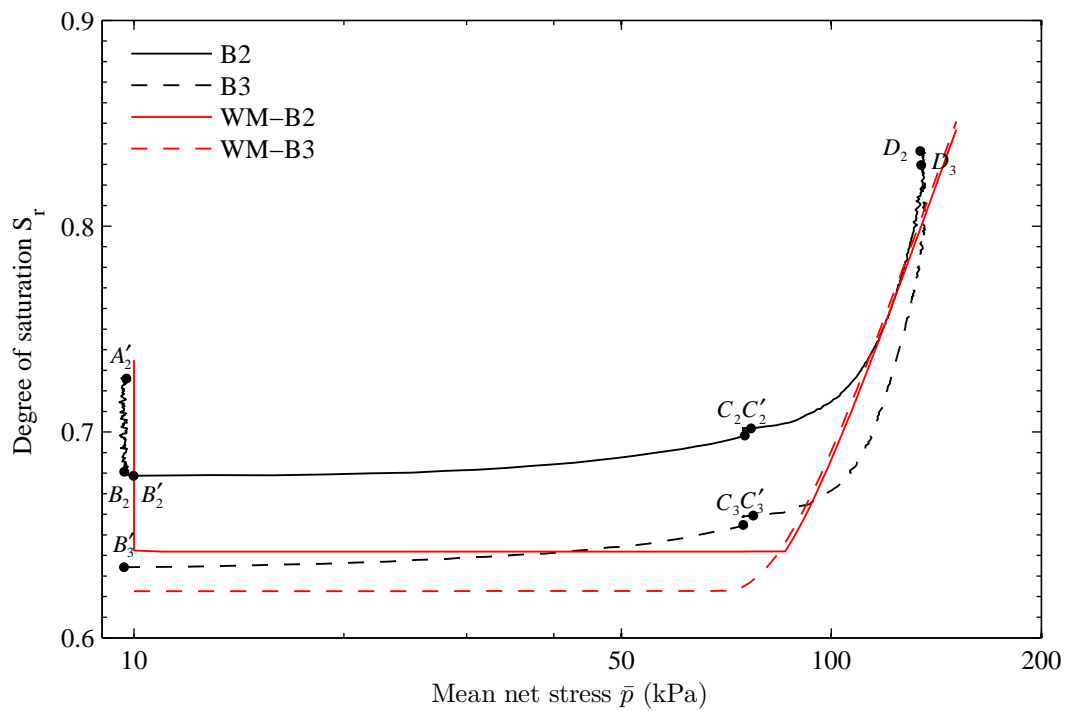


Figure 9-8 Variation of degree of saturation S_r against mean net stress \bar{p} in Tests B2 and B3 along with BBM and WM predictions

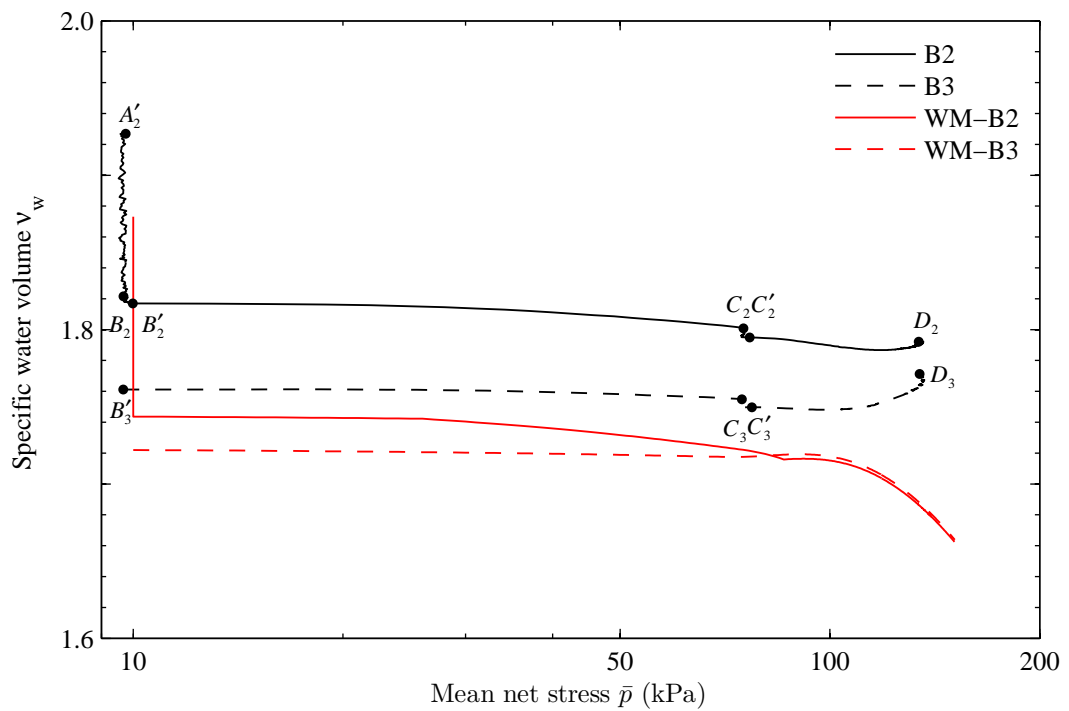


Figure 9-9 Variation of specific water volume v_w against mean net stress \bar{p} in Tests B2 and B3 along with BBM and WM predictions

It can be seen from Figure 9-8 that the WM correctly predicts a higher value of S_r at the start of isotropic loading in Test B2 (which involved a wetting-drying cycle) than in Test B3, although the model under-predicts the values of S_r . The predictions for the variation of S_r during the isotropic loading and subsequent shearing stages of both Test B2 and B3 are a good qualitative match to the experimental behaviour, although the model predicts a rapid convergence of the values of S_r from the two tests once shearing commences, whereas the experimental results show a more gradual convergence. For a better modelling of this feature of behaviour, a bounding surface plasticity model is required. The gradient of the post-yield curve and the value of the yield stress during shearing $C' - D$ are both slightly under-predicted by the WM (see Figure 9-8).

Inspection of Figure 9-9 shows that the WM once again correctly captures the qualitative influence of the wetting-drying cycle in Test B2, with a higher value of v_w at the start of the isotropic loading stage in Test B2 than in Test B3. During the isotropic loading stage $B' - C$ the WM provides a good match to the variation of v_w , with a very small decrease in v_w , although the model under-predicts the values of v_w . The prediction is, however, less good during shearing stage $C' - D$, where the WM predicts a decrease in v_w during shearing whereas an increase in v_w was observed in the experimental results (see Figure 9-9).

9.2.2 Shearing at 300 kPa suction (Tests B4, B5, B8 and B9)

In Section 9.2.1, the influence of a wetting-drying cycle on subsequent behaviour during shearing was investigated. Although there was a suggestion that a wetting-drying cycle affects the subsequent shearing behaviour, particularly the variation of S_r and v_w , it was not conclusive whether the wetting-drying cycle influences critical states (see Figure 9-8 and Figure 9-9). Further experimental tests were therefore carried out to investigate this further, with the intention of producing more substantial differences in the values of S_r at the start of shearing by performing a previous wetting-drying cycle over an increased range of suction.

Table 9-4, Table 9-5, Table 9-6 and Table 9-7 show the stress paths for Tests B4, B8, B5 and B9 respectively, and Figure 9-10 illustrates the stress paths of all the tests.

| Stage | | | q (kPa) | \bar{p} (kPa) | s (kPa) |
|--------|--------|----------------------|---------------------|----------------------|-----------|
| From | To | Description | | | |
| B_4 | B'_4 | Initial equalisation | 0 | 10 | 300 |
| B'_4 | C_4 | Isotropic loading | 0 | 10 \rightarrow 75 | 300 |
| C_4 | C'_4 | Equalisation | 0 | 10 | 300 |
| C'_4 | D_4 | Shearing | 0 \rightarrow 260 | 75 \rightarrow 162 | 300 |

Table 9-4 Stress path for Test B4

| Stage | | | q (kPa) | \bar{p} (kPa) | s (kPa) |
|--------|--------|----------------------|---------------------|----------------------|-----------|
| From | To | Description | | | |
| B_8 | B'_8 | Initial equalisation | 0 | 10 | 300 |
| B'_8 | C_8 | Isotropic loading | 0 | 10 \rightarrow 75 | 300 |
| C_8 | C'_8 | Equalisation | 0 | 10 | 300 |
| C'_8 | D_8 | Shearing | 0 \rightarrow 255 | 75 \rightarrow 160 | 300 |

Table 9-5 Stress path for Test B8

| Stage | | | q (kPa) | \bar{p} (kPa) | s (kPa) |
|--------|--------|----------------------|---------------------|----------------------|----------------------|
| From | To | Description | | | |
| A_5 | A'_5 | Initial equalisation | 0 | 10 | 30 |
| A'_5 | B_5 | Drying | 0 | 10 | 30 \rightarrow 300 |
| B_5 | B'_5 | Equalisation | 0 | 10 | 300 |
| B'_5 | C_5 | Isotropic loading | 0 | 10 \rightarrow 75 | 300 |
| C_5 | C'_5 | Equalisation | 0 | 75 | 300 |
| C'_5 | D_5 | Shearing | 0 \rightarrow 278 | 75 \rightarrow 168 | 300 |

Table 9-6 Stress path for Test B5

| Stage | | | q (kPa) | \bar{p} (kPa) | s (kPa) |
|--------|--------|----------------------|----------------------|-----------------------|---------------------|
| From | To | Description | | | |
| A_9 | A'_9 | Initial equalisation | 0 | 10 | 1 |
| A'_9 | B_9 | Drying | 0 | 10 | 1 \rightarrow 300 |
| B_9 | B'_9 | Equalisation | 0 | 10 | 300 |
| B'_9 | C_9 | Shearing | 0 \rightarrow 85 | 10 \rightarrow 38 | 300 |
| C_9 | C'_9 | Equalisation | 85 | 38 | 300 |
| C'_9 | D_9 | Isotropic loading | 85 | 38 \rightarrow 103 | 300 |
| D_9 | D'_9 | Equalisation | 85 | 103 | 300 |
| D'_9 | E_9 | Shearing | 85 \rightarrow 288 | 103 \rightarrow 171 | 300 |

Table 9-7 Stress path for Test B9

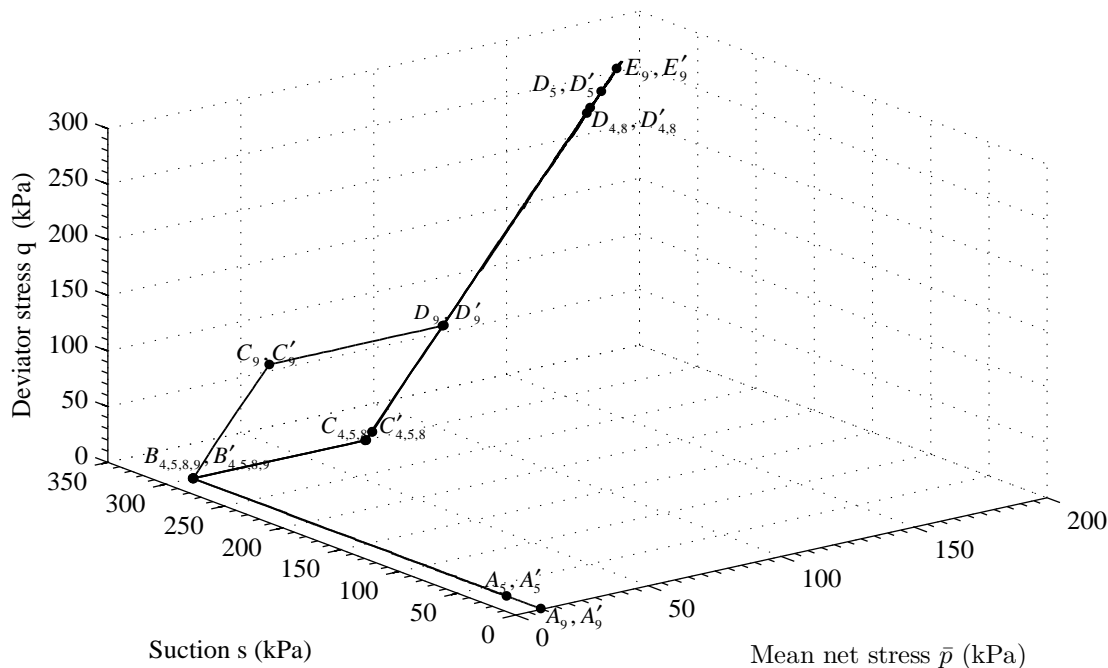


Figure 9-10 Stress paths for Tests B4, B5, B8 and B9

In Test B4, the sample was initially equalised ($B_4B'_4$) at a mean net stress of 10 kPa and a suction of 300 kPa. It was then isotropically compressed to a mean net stress of 75 kPa at constant suction (stage $B'_4 - C_4$). Finally, a shearing stage $C'_4 - D_4$ was carried out at constant suction and radial net stress until the sample reached failure. Test B8 was just a repetition of Test B4 (see Table 9-5), which was carried out in order to verify the repeatability of experimental testing. The stress path for Test B5 was similar to that of Test B4 and B8, except an additional wetting-drying cycle was involved. The sample was initially equalised ($A_5A'_5$) at a mean net stress of 10 kPa and a suction of 30 kPa. The sample was then subjected to a drying stage ($A'_5 - B_5$) to a suction of 300 kPa followed with an isotropic loading stage $B'_5 - C_5$ to a mean net stress of 75 kPa. Finally the sample was sheared ($C'_5 - D_5$) at constant suction of 300 kPa with constant net radial stress of 75 kPa.

In Test B9 the sample was first equalised ($A_9A'_9$) at a suction of 1 kPa and a mean net stress of 10 kPa. A drying stage ($A'_9 - B_9$) was then performed to a suction of 300 kPa. The next stage was originally intended to be an isotropic loading stage to a mean net stress of 75 kPa. Unfortunately, a shearing stage $B'_9 - C_9$ at a constant radial net

stress of 10 kPa was started by mistake and then terminated at a deviator stress of 85 kPa. The radial net stress was then increased to 75 kPa with the deviator stress held at 85 kPa (stage $C'_9 - D_9$). Finally, a shearing stage $D'_9 - E_9$ was performed at a constant suction of 300 kPa and a constant radial net stress of 75 kPa until the sample was brought to failure.

Figure 9-11 shows the experimental variation of deviator stress with true shear strain for the shearing stages of Tests B4, B5, B8 and B9. The experimental test results from Test B4 and B8 almost coincided with each other, providing confidence about the repeatability of experimental technique and sample preparation. The verification of the quality of experimental results was very important in this test series, as the differences in the experimental results between Tests B4 and B8 and Tests B5 and B9 (which involved a previous wetting-drying cycle) were relatively small.

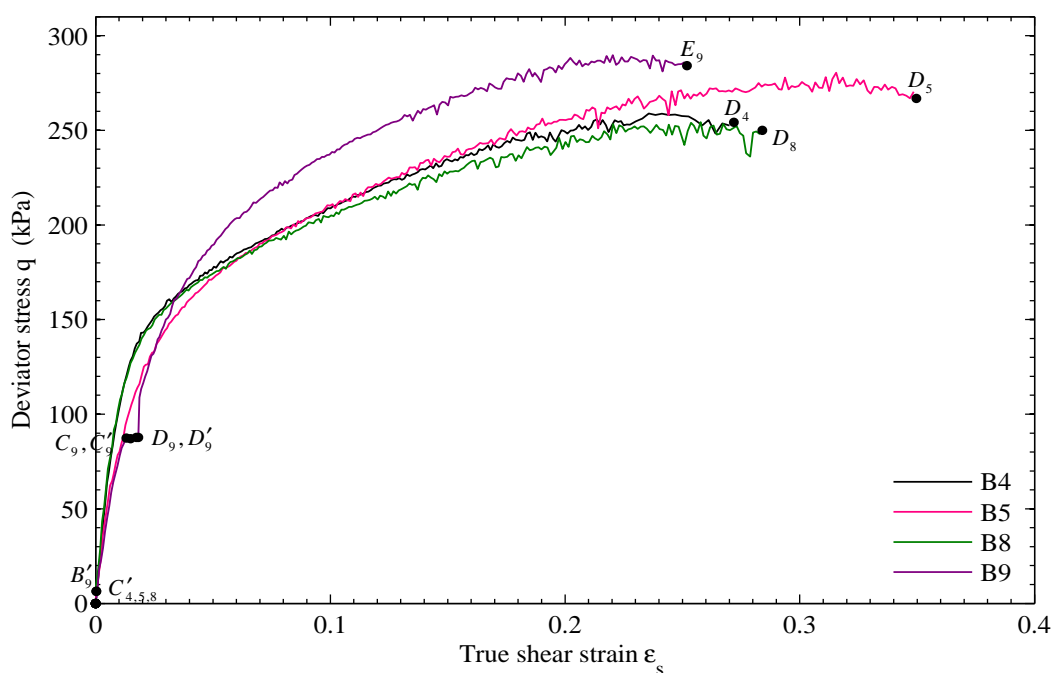


Figure 9-11 Variation of deviator stress q against true shear strain ϵ_s for Tests B4, B5, B8 and B9

From Figure 9-11, it can be seen that in the later part of the shearing stages of all tests, there were small fluctuations in the values of deviator stress. Although a constant rate of strain pump (CRSP) was used to achieve a constant displacement rate (0.072 mm/hr) for the shear stage, the shearing was not, in fact, a continuous process because

the operation of the CRSP was controlled by the Triax software. According to the control strategy of the Triax software, no signal is sent to the constant rate of strain pump (CRSP) if the actual axial displacement of the sample is within the tolerance range (± 0.01 mm) of the current target value. Once the tolerance was exceeded, the Triax would instruct the CRSP to advance, leading to increase in the deviator stress. Once the actual sample displacement fell into the tolerance range the movement of the CRSP would be stopped. However, during this inactive period of the CRSP, a significant additional axial deformation of the sample would occur due to drainage to or from the sample. This leads to a relaxation of the deviator stress, with a negative gradient of the $q : \varepsilon_s$ curve that is controlled by the (non-infinite) stiffness of the loading system (the CRSP, the Bishop-Wesley cylinder on the triaxial cell and the connecting tubing). The relaxation of the deviator stress is not evident in the early part of the shearing stage, probably because of the stiff response of the sample (i.e. additional axial deformations due to drainage are small). This process therefore leads to fluctuations in the deviator stress in the later part of the shearing stage. However, these fluctuations do not influence the overall shape of the curves (see Figure 9-11), and the maximum fluctuation of the deviator stress was only about $\pm 2\%$ of the critical state value of deviator stress.

It can be clearly seen from Figure 9-11 that Samples B5 and B9 exhibit slightly higher values of critical state deviator stress than Samples B4 and B8, presumably because of the previous wetting-drying cycles performed in Tests B5 and B9. This issue will be discussed now, considering the influence of v and S_r on critical state deviator stress.

Figure 9-12 shows the experimental variation of deviator stress against shear strain for Tests B4, B5, B8 and B9 and corresponding predictions by both BBM and WM. Figure 9-13, Figure 9-14 and Figure 9-15 show the variation of specific volume, degree of saturation and specific water volume against mean net stress.

Inspection of Figure 9-12 shows that the previous wetting-drying cycles performed in Tests B5 and B9 decreased the initial shear stiffness of the soil samples when compared with results from Tests B4 and B8. This decrease in initial shear stiffness is consistent with the observation made in Section 9.2.1. In addition, an increase in

critical state deviator stress of about 20 kPa for Test B5 and about 30 kPa for Test B9 can be observed from Figure 9-12 compared with the results from Tests B4 and B8.

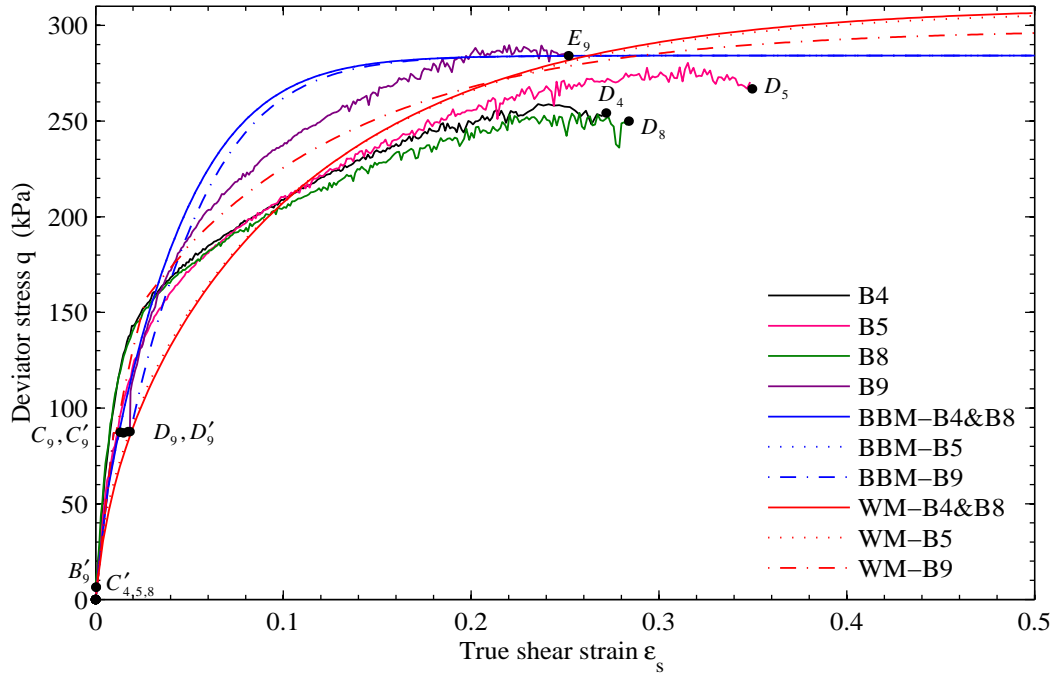


Figure 9-12 Variation of deviator stress q against true shear strain ϵ_s along with BBM and WM predictions

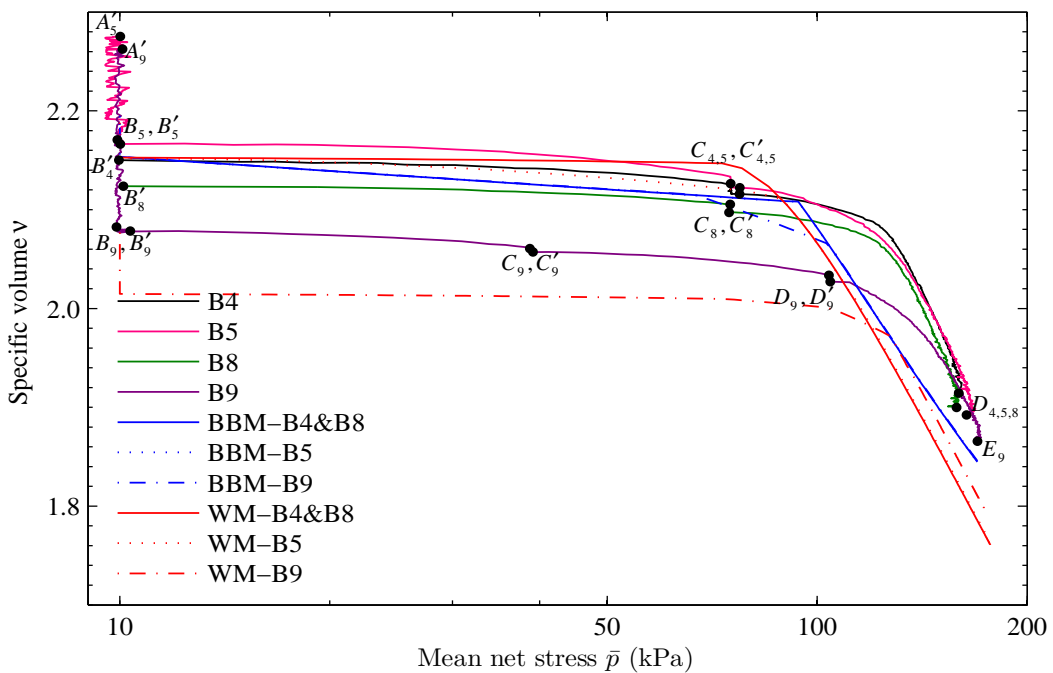


Figure 9-13 Variation of specific volume v against mean net stress \bar{p} along with BBM and WM predictions

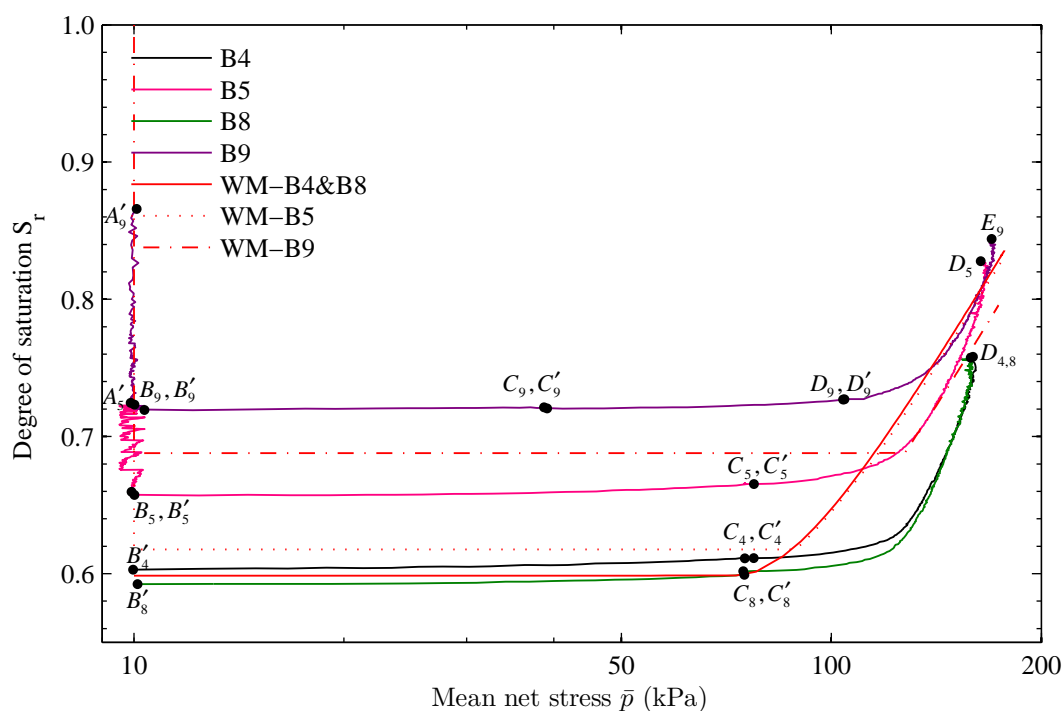


Figure 9-14 Variation of degree of saturation S_r against mean net stress \bar{p} along with BBM and WM predictions

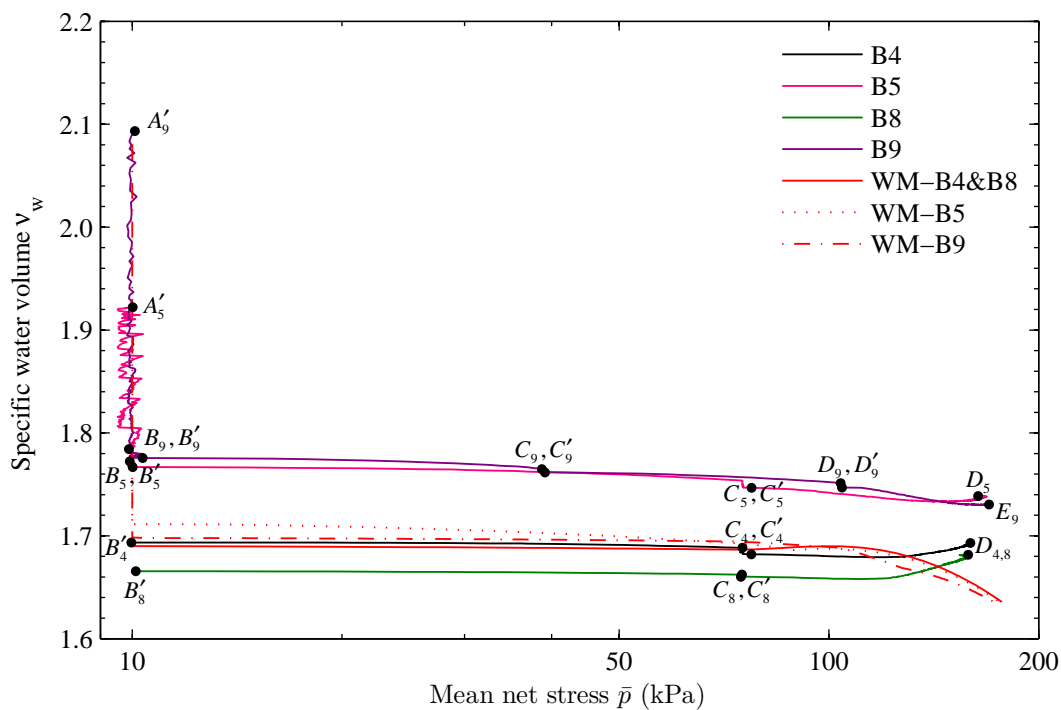


Figure 9-15 Variation of specific water volume v_w against mean net stress \bar{p} along with BBM and WM predictions

Inspection of Figure 9-13 shows that the value of v at the end of the wetting-drying cycle in Test B5 is similar to that at the end of equalisation in Tests B4 and B8, whereas the value of v at the end of the larger wetting-drying cycle in Test B9 is significantly smaller than that at the end of equalisation in Tests B4 and B8. However, in all tests the differences in v at the end of shearing stages were observed to be very small (see Figure 9-13), suggesting that the critical state value of v was hardly affected by the wetting-drying cycles performed in Tests B5 and B9.

Inspection of Figure 9-14 and Figure 9-15 shows that the values of S_r and v_w at the end of the wetting-drying cycles performed in Tests B5 and B9 were significantly higher than those at the end of initial equalisations stages in Tests B4 and B8. In addition, the value of S_r at the end of the wetting-drying cycle in the case of Test B9 is higher than that observed in Test B5, because Sample B9 went through a larger wetting-drying cycle than Sample B5 (down to a suction of 1 kPa instead of 30 kPa). Interestingly, no significant difference in the values of v_w at the end of the wetting-drying cycles was observed between Tests B5 and B9 (see Figure 9-15).

Samples B5 and B9 showed significantly higher values of S_r and v_w at the end of shearing stages $C'_5 - D_5$ and $D'_9 - E_9$ than the corresponding values for Samples B4 and B8 at the end of shearing (see Figure 9-14 and Figure 9-15). The differences in the critical state deviator stress observed in Figure 9-12 could then have been linked to differences in the degree of saturation at the end of shearing. This clearly indicates the influence of degree of saturation on the shear strength of the soil, in addition to suction and mean net stress.

The BBM is not able to capture the apparent dependency of critical state shear strength on S_r and therefore predicts unique shear strength regardless of whether a wetting-drying cycle was performed before shearing (see Figure 9-12). However, the extended Wheeler et al. (2003) model (i.e. extended to triaxial states) can incorporate this feature of behaviour (in theory) as the shear strength of unsaturated soil is uniquely related to the mean Bishop's stress, which depends on degree of saturation in addition to suction as given below:

$$q = M^* p^* = M^* (\bar{p} + S_r s) \quad (9-1)$$

However, in the WM simulation, the influence of the previous wetting-drying cycle was erased during the shearing stage, long before the critical state was reached (because of the parameter values and initial positions of the yield surfaces selected in the simulation), leading to no difference in the predicted critical state values of deviator stress for Tests B4, B8 and B5. The WM simulations show a lower value of critical state deviator stress for Test B9 than for the other 3 tests (see Figure 9-12). However, the reason for difference is that in the WM simulation for Test B9 the sample reached fully saturated conditions while wetting to a suction of 1 kPa and the occurrence of plastic volumetric strains during subsequent suction increase (at saturated state) caused a different critical state for a particular suction value. This inconsistency of the WM model will be discussed in detail in Section 10.5. Generally, the WM under-predicts the values of q during the initial part of the shearing stage and over-predicts during the later part of shearing (see Figure 9-12), with the WM prediction showing q still increasing slightly at shear strain of 0.5.

Inspection of Figure 9-13 reveals that both the BBM and the WM under-predict the yield stress and the values of v during the shearing stage. Although, the WM predicts slightly different behaviour during isotropic loading of Test B5 with an earlier yield point than in Tests B4 and B8, this prediction is difficult to compare with the experimental results because of the very small experimental and predicted variations of v during isotropic loading in Tests B4, B5, B8 and B9. The BBM provides slightly better prediction than the WM for the critical state value for v . Once again, the WM prediction for the variation of v of Test B9 produced a different compression curve during shearing stage $D'_9 - E_9$ because of the inconsistency of the model discussed in Section 10.5. However, given that the error caused by the inconsistency of the WM during the wetting-drying cycle in Test B9 is very small, the WM correctly captures the observed lower value of v at point B'_9 in Test B9 than the values at points B'_4 , B'_5 and B'_8 (see Figure 9-13).

Inspection of Figure 9-14 shows that the WM qualitatively captures the influence of the wetting-drying cycles in Tests B5 and B9, with the prediction of higher values of

S_r than in Tests B4 and B8 both at the start of isotropic loading and at the start of shearing (although the magnitudes of the differences of S_r are not accurately predicted). The model predicts a unique critical state value for S_r , except for Test B9 (and this was a consequence of the problem with the model discussed in Section 10.5). In contrast, the experimental results show higher critical state values of S_r in Tests B5 and B9 than in Tests B4 and B8. This could (in theory) be predicted by the WM with alternative selections for model parameter values, in particular a wider spacing between the SI and SD yield surfaces.

Inspection of Figure 9-15 shows that the WM captures the higher values of v_w at the end of wetting-drying cycles in Tests B5 and B9 when compared with the corresponding values at the end of the equalisation stages in Tests B4 and B8. However, the predicted values of v_w at the end of the wetting-drying cycles in Tests B5 and B9 are significantly less than experimental values. The WM provide a good match to the observed variation of v_w during the isotropic loading stages of Test B4, B5 and B8. During the shearing stage, Samples B4 and B8 showed increase in specific water volume, whereas, in Test B5 and B9, the specific water volume first decreased and then in the later part of the shearing stage a slight increase in the specific water volume was observed. However, the WM predicted a decrease in specific water volume during shearing for all four tests.

9.3 OTHER TESTS

9.3.1 Test B6

The influence of degree of saturation on the shear behaviour of unsaturated soil was investigated in Sections 9.2.1 and 9.2.2 by performing tests with a wetting-drying cycle under isotropic stress states before shearing was commenced. In Test B6, it was intended to investigate the influence of a wetting-drying cycle performed under a non-isotropic stress state on the subsequent shear behaviour. Table 9-8 and Figure 9-16 show the stress path followed in Test B6. The sample was first equalised (A'_6) at a suction of 300 kPa and a mean net stress of 10 kPa. It was then isotropically loaded at constant suction (stage $A'_6 - B_6$) to a mean net stress of 75 kPa. A shearing stage

$B'_6 - C_6$ was then followed to a deviator stress of 78 kPa at constant suction and radial net stress. Two cycles of wetting and drying ($C'_6 - D_6, D'_6 - E_6$ and $E'_6 - F_6, F'_6 - G_6$) were performed over a range of suction from 300 to 100 kPa while keeping deviator stress and mean net stress constant. Finally, the sample was sheared to failure at constant suction of 300 kPa and constant radial net stress of 75 kPa (stage $G'_6 - H_6$).

| Stage | | | q (kPa) | \bar{p} (kPa) | s (kPa) |
|--------|--------|----------------------|----------------------|-----------------------|-----------------------|
| From | To | Description | | | |
| A_6 | A'_6 | Initial equalisation | 0 | 10 | 300 |
| A'_6 | B_6 | Isotropic loading | 0 | 10 \rightarrow 75 | 300 |
| B_6 | B'_6 | Equalisation | 0 | 75 | 300 |
| B'_6 | C_6 | Shearing | 0 \rightarrow 78 | 75 \rightarrow 101 | 300 |
| C_6 | C'_6 | Equalisation | 78 | 101 | 300 |
| C'_6 | D_6 | Wetting | 78 | 101 | 300 \rightarrow 100 |
| D_6 | D'_6 | Equalisation | 78 | 101 | 100 |
| D'_6 | E_6 | Drying | 78 | 101 | 100 \rightarrow 300 |
| E_6 | E'_6 | Equalisation | 78 | 101 | 300 |
| E'_6 | F_6 | Wetting | 78 | 101 | 300 \rightarrow 100 |
| F_6 | F'_6 | Equalisation | 78 | 101 | 100 |
| F'_6 | G_6 | Drying | 78 | 101 | 100 \rightarrow 300 |
| G_6 | G'_6 | Equalisation | 78 | 101 | 300 |
| G'_6 | H_6 | Shearing | 78 \rightarrow 280 | 101 \rightarrow 168 | 300 |

Table 9-8 Stress path for Test B6

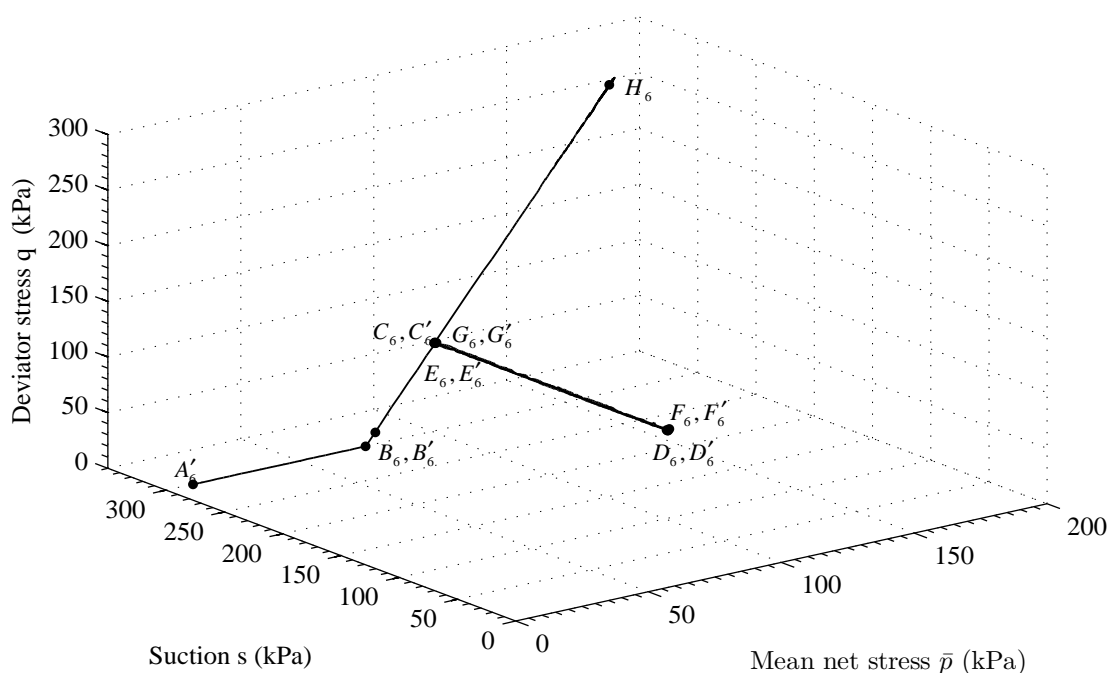


Figure 9-16 Stress path for Test B6

Figure 9-17 and Figure 9-18 show the variation of specific volume and degree of saturation respectively against mean net stress for Tests B6 and B4. Experimental results from Test B4 are presented alongside those from Test B6 to show the influence of wetting-drying cycles on the subsequent shear behaviour. In Test B6 a significant reduction in v and significant increase in S_r occurred over the wetting-drying cycles $C'_6 - G_6$. These changes in v and S_r were associated with plastic processes and will be discussed in detail later in this section. Because of these plastic changes of v and S_r an increase in yield stress can be observed compared to the results from Test B4 during shearing stage $G'_6 - H_6$ (see Figure 9-17 and Figure 9-18). Inspection of Figure 9-17 and Figure 9-18 also shows that the critical state values of v and S_r at the end of shearing stage $G'_6 - H_6$ of Test B6 are significantly different from the values obtained in Test B4. These differences can be attributed to the influence of the additional wetting-drying cycles $C'_6 - G_6$ performed in Test B6.

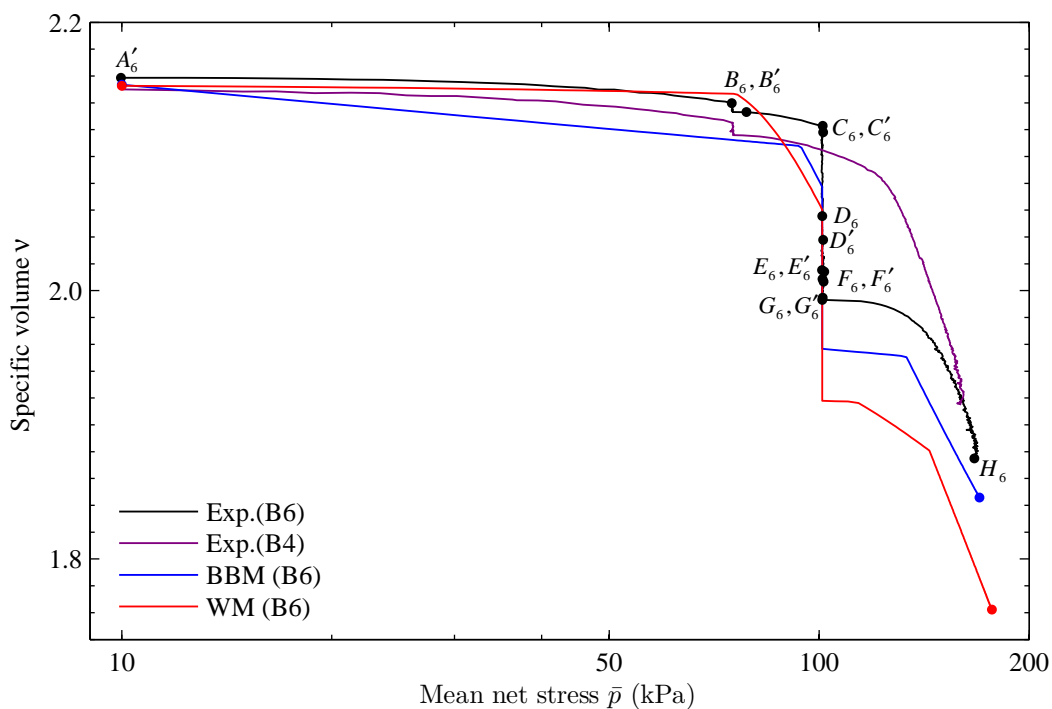


Figure 9-17 Variation of specific volume v against mean net stress \bar{p} for Tests B6 and B4 along with BBM and WM predictions for Test B6

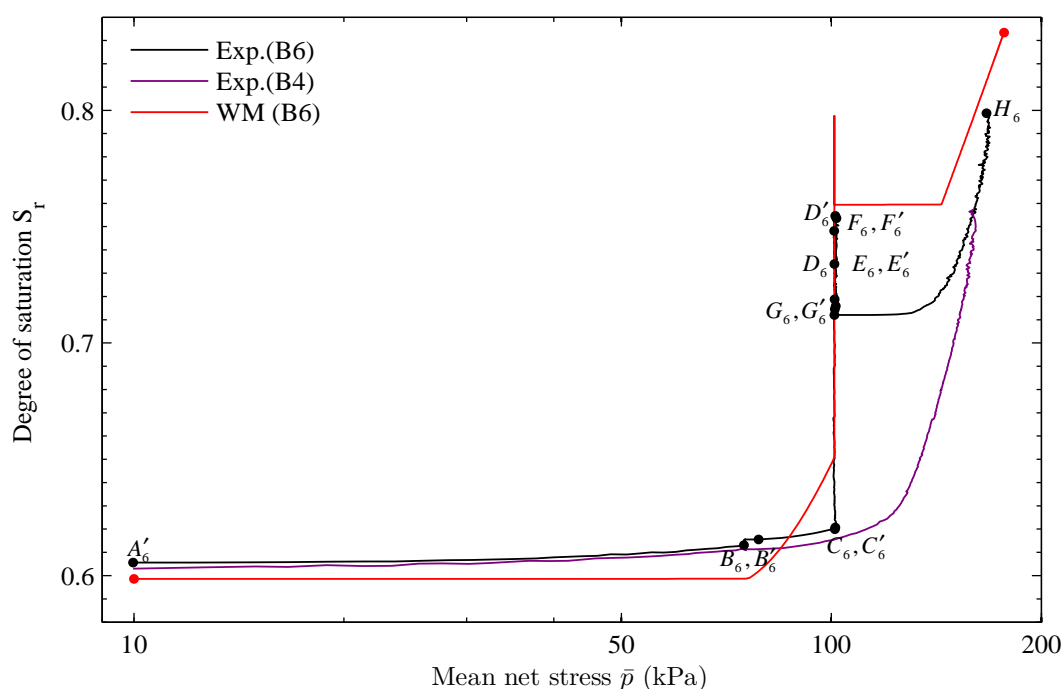


Figure 9-18 Variation of degree of saturation S_r against mean net stress \bar{p} for Tests B6 and B4 along with BBM and WM predictions for Test B6

Inspection of Figure 9-17 shows that neither the BBM nor the WM provides a perfect match to the overall experimental variation of ν against \bar{p} of Test B6, with both models mostly underestimating the values of ν throughout the test. However, the BBM provides slightly better prediction than the WM, particularly capturing the value of yield stress during shearing stage $G'_6 - H_6$ with reasonable accuracy. The double yield points (yielding first on LC curve then on LC and SD curves simultaneously) predicted by the WM during shearing stage $G'_6 - H_6$ is not supported by the experimental observation (see Figure 9-17). Inspection of Figure 9-18 shows that the WM captures the overall shape of the curve of S_r against \bar{p} , although it over-predicts the values of S_r in most stages of the test, with slight over-prediction of the yield stress during shearing stage $G'_6 - H_6$.

Figure 9-19 shows the variation of specific volume with suction for Test B6. Significant irreversible reduction of ν occurred over the wetting-drying cycles ($C'_6 - G_6$). Close inspection of Figure 9-19 reveals that the reduction of ν largely occurred during the first wetting stage $C'_6 - D_6$, associated with a collapse compression

with no suggestion of a clear yield point as the volumetric compression was very gradual. During the subsequent drying ($D'_6 - E_6$), wetting ($E'_6 - F_6$) and drying ($F'_6 - G_6$) stages, a small net reduction in v occurred (see Figure 9-19). Both BBM and WM under-predict the values of v throughout the wetting and drying stages $C'_6 - G_6$. Although the BBM predicts the overall shape of the curves for the first cycle of wetting and drying ($C'_6 - D_6$ and $D'_6 - E_6$) with reasonable accuracy, it fails to capture the additional irreversible volumetric compression that occurred during the subsequent wetting-drying cycle ($E'_6 - F_6, F'_6 - G_6$). The WM captures the shape of the curves for variation of v for both wetting-drying cycles, including the irreversible behaviour observed in the second wetting-drying cycle.

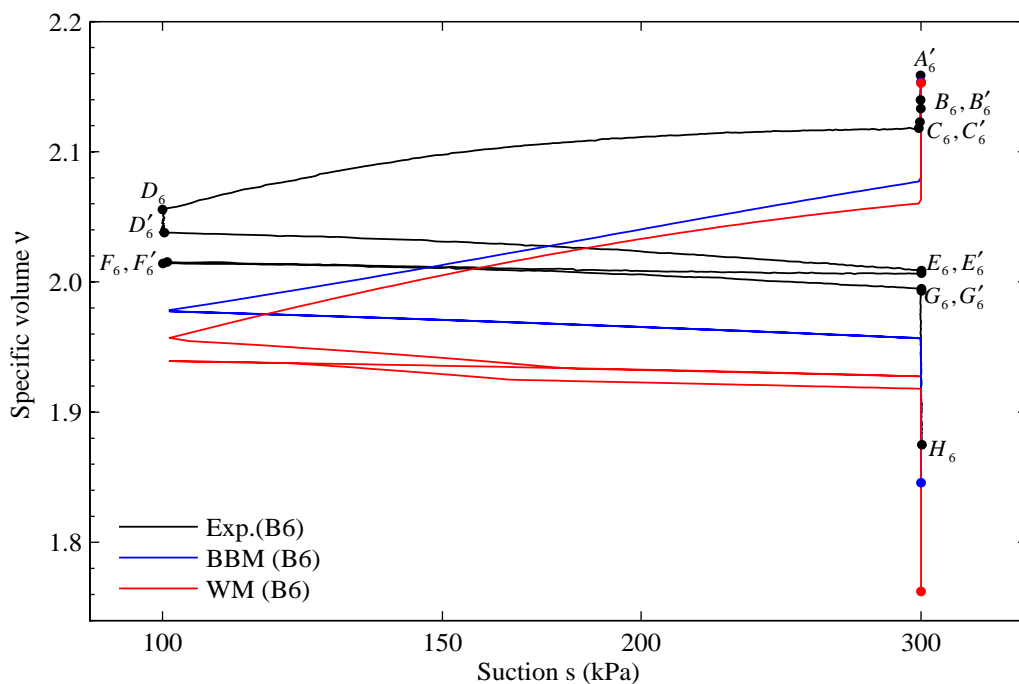


Figure 9-19 Variation of specific volume v against suction s for Test B6 along with BBM and WM predictions

Figure 9-20 shows the variation of degree of saturation against suction for Test B6. During the first wetting stage $C'_6 - D_6$ a significant increase in S_r occurred, once again with no suggestion of a clear yield point. During the subsequent drying-wetting-drying stages ($D'_6 - E_6, E'_6 - F_6, F'_6 - G_6$) a closed loop of water retention curves in the $S_r : \ln s$ plane can be observed. It can be seen from Figure 9-20 that the WM

captures the overall shapes of water retention curve with reasonable accuracy. However, the model tends to over-predict the values of S_r throughout the cycles of wetting and drying.

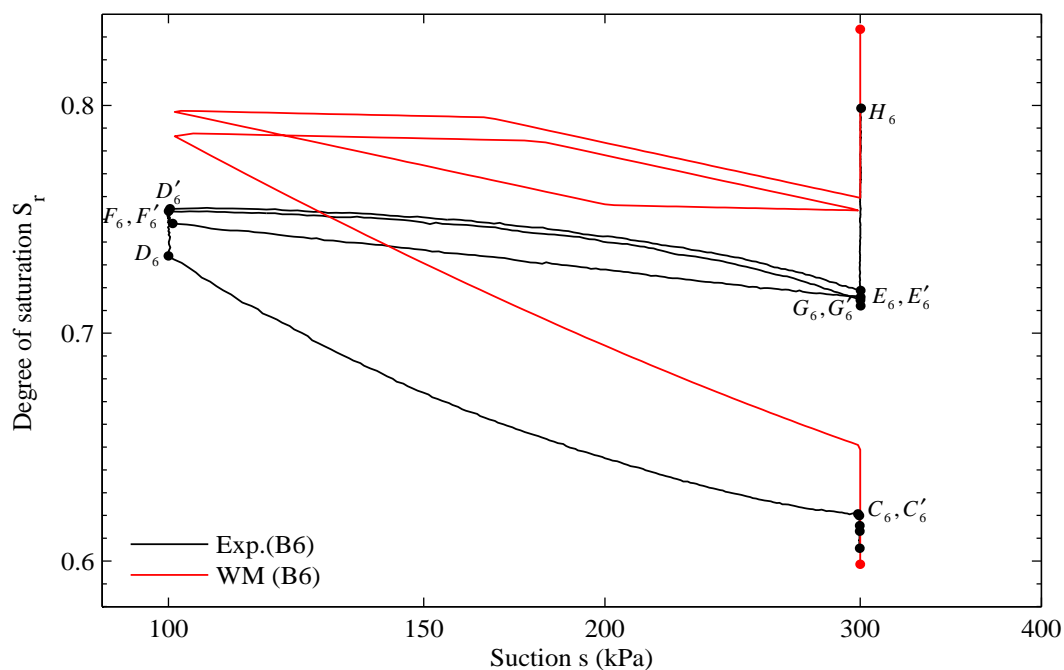


Figure 9-20 Variation of degree of saturation S_r against suction s for Test B6 along with BBM and WM predictions

Figure 9-21 shows the variation of shear strain against suction for Test B6. During the first wetting stage $C'_6 - D_6$ significant irreversible increase in shear strains occurred, with very small changes (almost reversible) of shear strain during the subsequent drying-wetting-drying stages ($D'_6 - E_6$, $E'_6 - F_6$, $F'_6 - G_6$). Inspection of Figure 9-21 reveals that both BBM and WM provide good prediction for the observed variation of ϵ_s during the two wetting-drying cycles ($C'_6 - G_6$).

Figure 9-22 shows the experimental variation of deviator stress with shear strain for Tests B6 and B4 along with the BBM and the WM predictions for Test B6. The critical state deviator stress in Test B6 was about 20 kPa higher than that in Test B4, because of the influence of the wetting and drying cycles $C'_6 - G_6$.

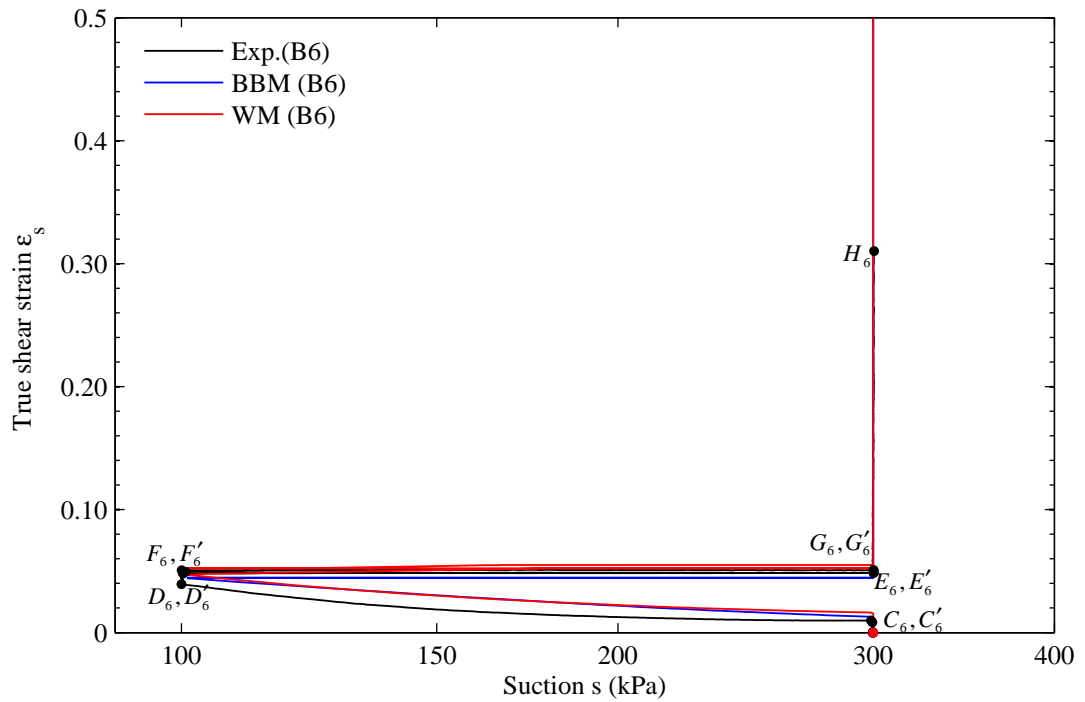


Figure 9-21 Variation of true shear strain ϵ_s against suction s for Test B6 along with BBM and WM predictions

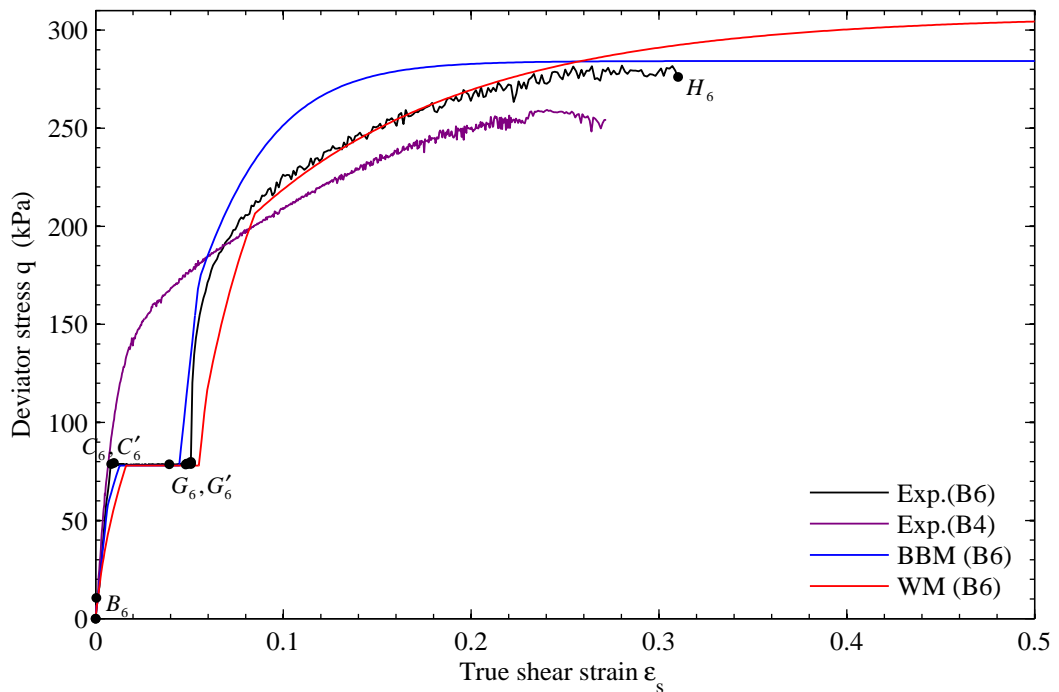


Figure 9-22 Variation of deviator stress q against true shear strain ϵ_s for Tests B6 and B4 along with the BBM and the WM predictions for Test B6

The prediction of the BBM for the overall variation of the deviator stress, including at the critical state, is a good match to the observed behaviour (see Figure 9-22). The WM does provide a very good match to the experimental behaviour during the initial part of shearing $G'_6 - H_6$, although it slightly overestimates the critical state value of deviator stress. However, both models predict the same value of critical state deviator stress in Test B6 and B4 (see Figure 9-22 and Figure 9-12), failing to capture the experimental results of higher critical state deviator stress in Test B6 than in Test B4.

9.3.2 Test B7

Test B7 was performed in order to investigate the behaviour of unsaturated soil during drying stages at constant mean net stress and deviator stress, and shearing stages at different suction values. Table 9-9 and Figure 9-23 demonstrate the stress path for Test B7.

| Stage | | | q (kPa) | \bar{p} (kPa) | s (kPa) |
|--------|--------|----------------------|-----------|-----------------|-----------|
| From | To | Description | | | |
| A_7 | A'_7 | Initial equalisation | 0 | 10 | 100 |
| A'_7 | B_7 | Isotropic loading | 0 | 10 → 75 | 100 |
| B_7 | B'_7 | Equalisation | 0 | 75 | 100 |
| B'_7 | C_7 | Shearing | 0 → 75 | 75 → 100 | 100 |
| C_7 | C'_7 | Equalisation | 75 | 100 | 100 |
| C'_7 | D_7 | Drying | 75 | 100 | 100 → 200 |
| D_7 | D'_7 | Equalisation | 75 | 100 | 200 |
| D'_7 | E_7 | Shearing | 75 → 175 | 100 → 133 | 200 |
| E_7 | E'_7 | Equalisation | 175 | 133 | 200 |
| E'_7 | F_7 | Drying | 175 | 133 | 200 → 300 |
| F_7 | F'_7 | Equalisation | 175 | 133 | 300 |
| F'_7 | G_7 | Shearing | 175 → 260 | 133 → 162 | 300 |

Table 9-9 Stress path for Test B7

The sample was first equalised ($A_7A'_7$) at a suction of 100 kPa and a mean net stress of 10 kPa. The sample was then isotropically loaded to a mean net stress of 75 kPa (stage $A'_7 - B_7$). A shearing stage $B'_7 - C_7$ at constant radial net stress was then followed at constant suction to a deviator stress of 75 kPa. The next stage was a drying stage $C'_7 - D_7$ at constant deviator stress and constant mean net stress to a suction of 200 kPa. This drying stage was then followed by a shearing stage $D'_7 - E_7$ at constant suction and constant radial net stress to a deviator stress of 175 kPa. Another constant q and constant \bar{p} drying stage $E'_7 - F_7$ was then performed to a suction of 300 kPa.

Finally, a shearing stage to failure $F'_7 - G_7$ was carried out at constant suction of 300 kPa and constant radial net stress of 75 kPa.

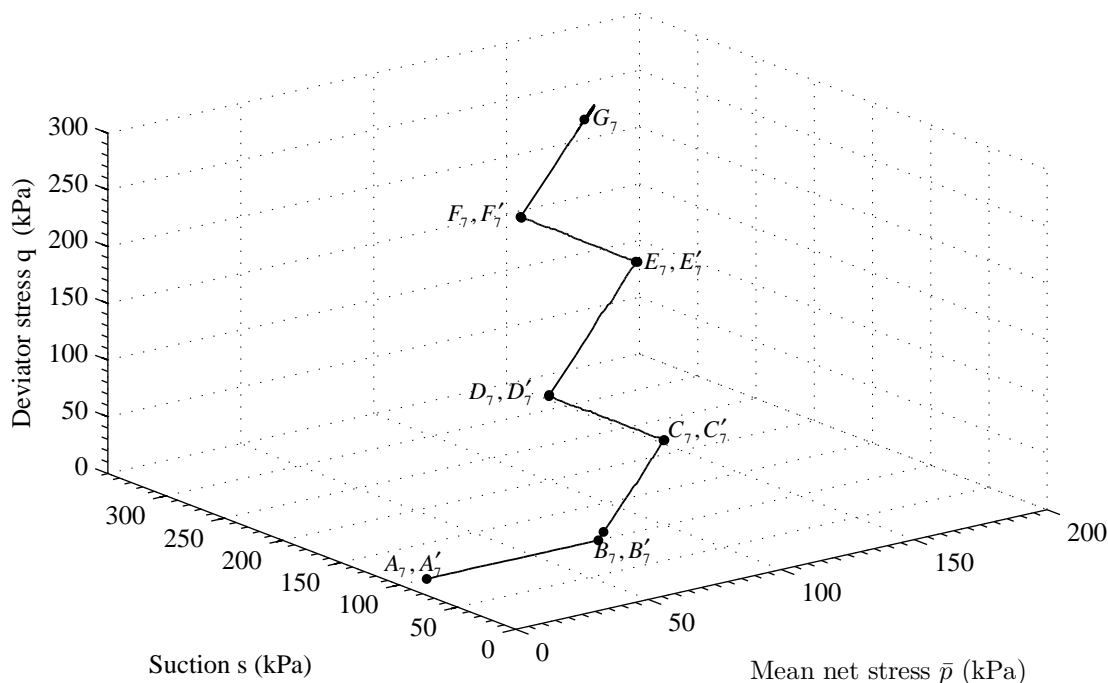


Figure 9-23 Stress path for Test B7

Figure 9-24 and Figure 9-25 show the experimental variation of specific volume and degree of saturation respectively against mean net stress for Tests B7 and B4 along with the BBM and the WM predictions for Test B7. During the isotropic loading $A'_7 - B_7$ a considerable reduction of ν and increase in S_r can be observed, with a non-linear (possibly elasto-plastic) behaviour during the later part of stage $A'_7 - B_7$. Subsequent shearing stage $B'_7 - C_7$ at suction of 100 kPa produced a large reduction of ν and a large increase of S_r without any clear indication of a yield point. The second ($D'_7 - E_7$) and final ($F'_7 - G_7$) shearing stages at suction of 200 kPa and 300 kPa, however, produced clear yield points. During the drying stages $C'_7 - D_7$ and $E'_7 - F_7$ there were considerable changes of ν and S_r and these will be discussed in detail later in this section. It is interesting note that the combination of drying and shearing stages performed in Test B7 prior to the final shearing stage $F'_7 - G_7$ produced significantly different values for ν and S_r at critical state compared to the values obtained for Test B4.

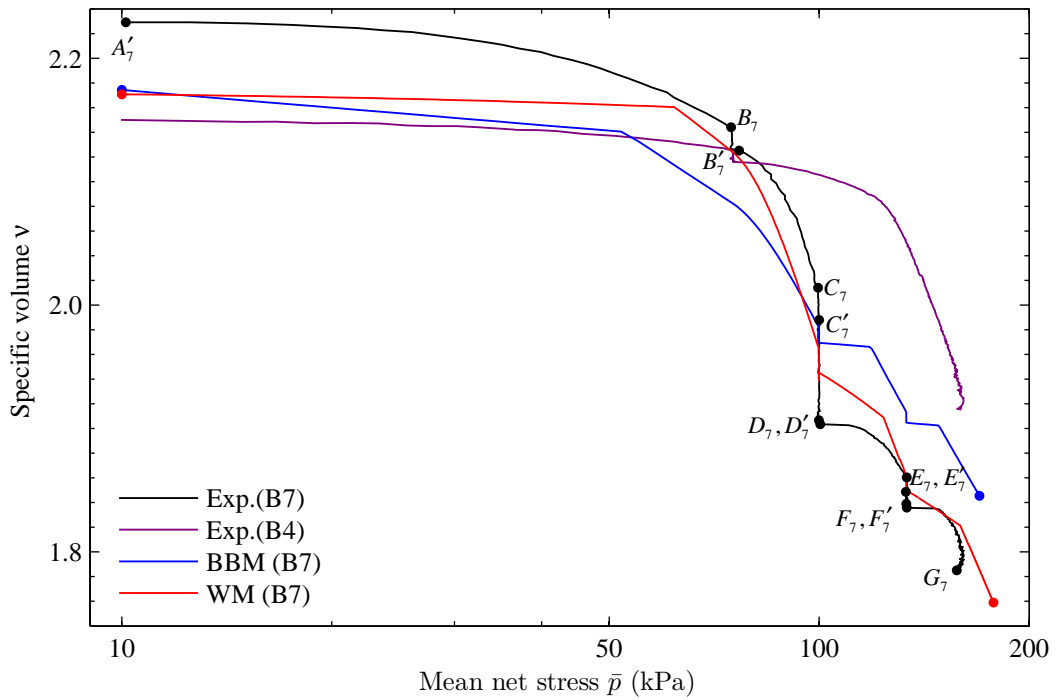


Figure 9-24 Variation of specific volume v against mean net stress \bar{p} for Tests B7 and B4 along with the BBM and the WM predictions for Test B7

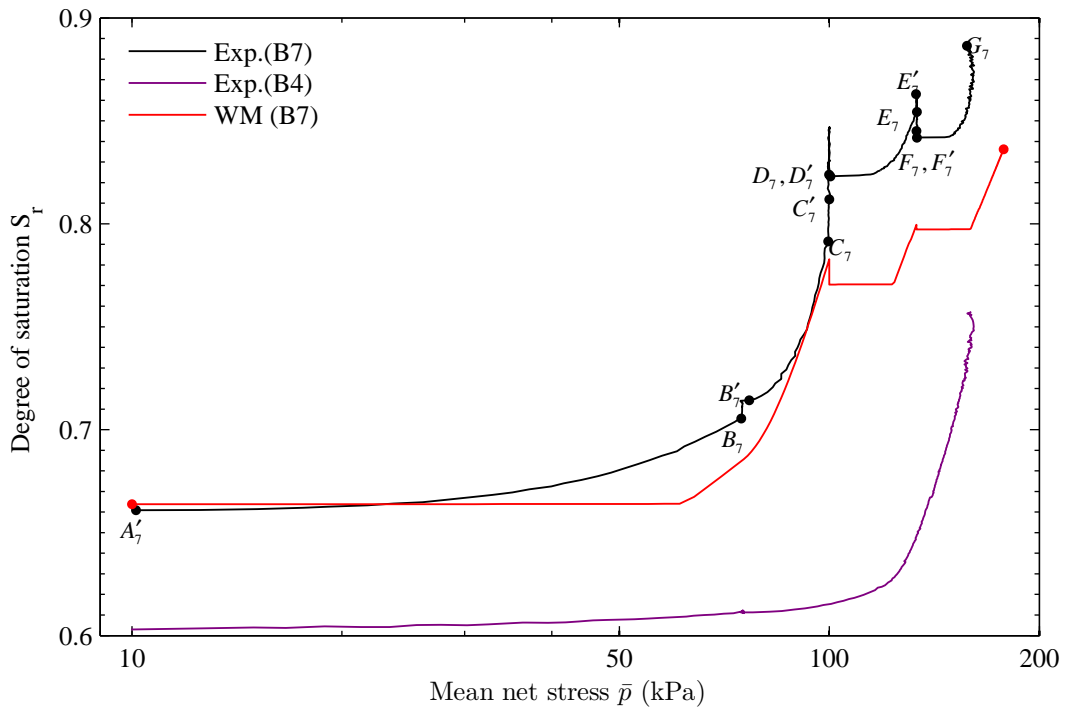


Figure 9-25 Variation of degree of saturation S_r against mean net stress \bar{p} for Tests B7 and B4 along with the WM predictions for Test B7

The BBM prediction for the overall shape of the curve in the $v : \ln \bar{p}$ plane (shown in Figure 9-24), including the yield points during shearing stages $D'_7 - E_7$ and $F'_7 - G_7$, is a reasonably good match to the observed behaviour of Sample B7. However, the predictions of the BBM for the actual values of v are not a good match to the observed behaviour, particularly due to the underestimation of the reduction of v during drying stage $C'_7 - D_7$. Although the WM provides a slightly better match to the experimental values of v than the BBM, the predicted shape of the curve is not such a good match to the experimental results, particularly during the second and final shearing stages, with plastic volumetric strains predicted from the beginning of these shearing stages, corresponding to yielding on the LC yield surface, whereas the experimental results show a stiff (elastic) response during the initial parts of these second and final shearing stages.

Inspection of Figure 9-25 shows that the WM generally underestimates the values of S_r , particularly after the first shearing stage $B'_7 - C_7$. However, the model predicts the overall shape of the experimental curve in the $S_r : \ln \bar{p}$ plane with reasonable accuracy, including the yield points during shearing stages $D'_7 - E_7$ and $F'_7 - G_7$.

Figure 9-26, Figure 9-27 and Figure 9-28 show the variation of specific volume, specific water volume and degree of saturation respectively against suction for Test B7. During the initial section of the first drying stage $C'_7 - D_7$ a dramatic reduction of v (shrinkage) occurred, with the slope of curve reducing in the later part of the stage, whereas a relatively small reduction of v can be seen with a constant gradient of curve during the second drying stage $E'_7 - F_7$ (see Figure 9-26). A similar trend of behaviour can also be seen in Figure 9-27 for the variation of v_w , with a clear yield point at a suction of about 120 kPa during the first drying stage $C'_7 - D_7$ and a relatively constant gradient of curve during the second drying stage $E'_7 - F_7$.

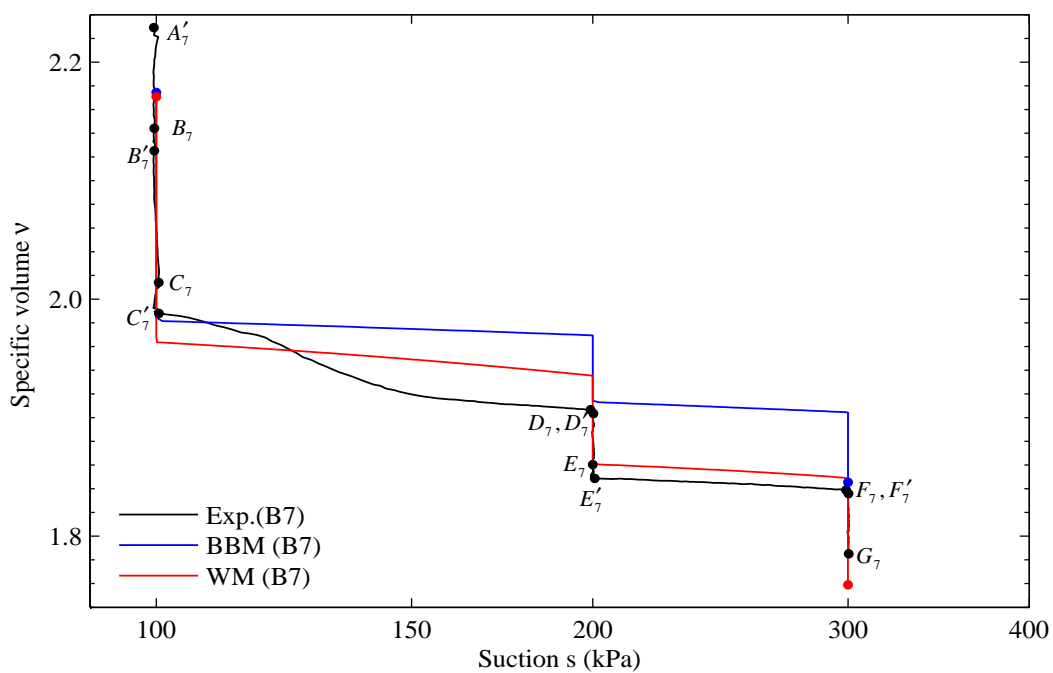


Figure 9-26 Variation of specific volume v against suction s for Test B7 along with the BBM and the WM predictions

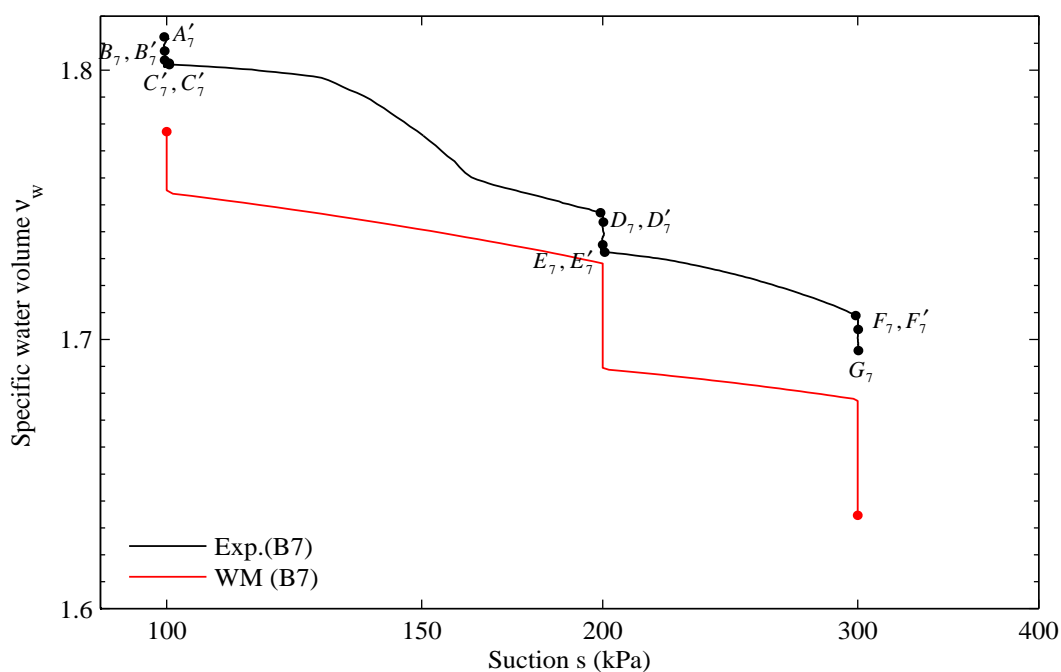


Figure 9-27 Variation of specific water volume v_w against suction s for Test B7 along with WM prediction

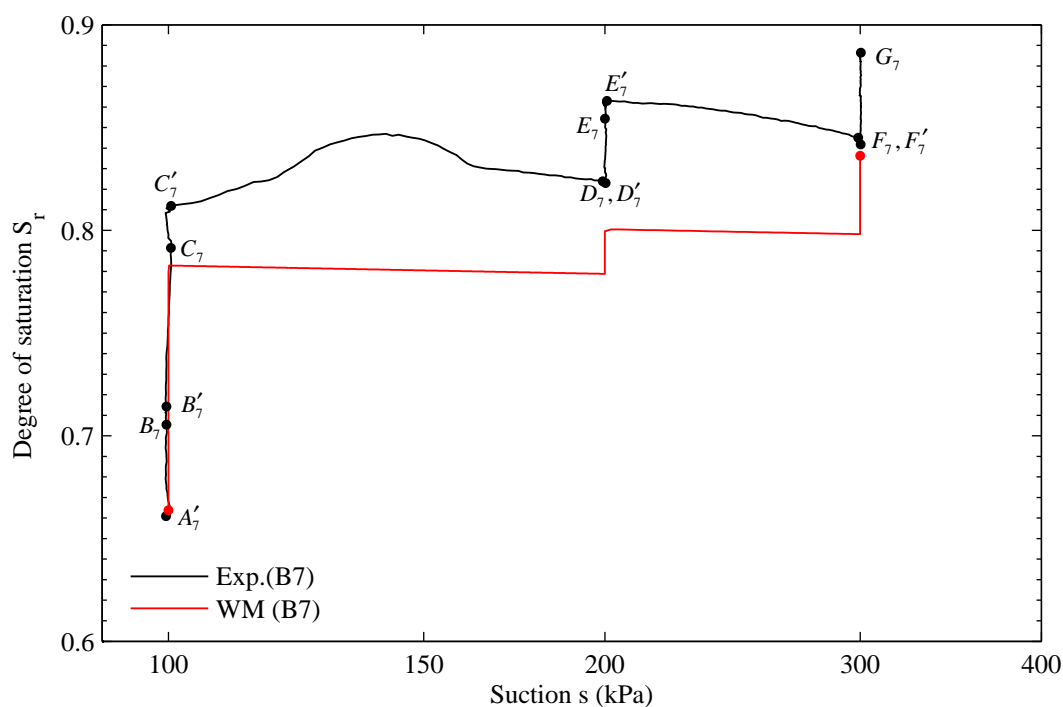


Figure 9-28 Variation of degree of saturation S_r against suction s for Test B7 along with the WM prediction

The experimental variation of S_r in Figure 9-28, derived from the variation of v and v_w (from Figure 9-26 and Figure 9-27), shows some interesting behaviour during the first drying stage $C'_7 - D_7$, where the value of S_r initially increased and then decreased. This initial increase in the value of S_r demonstrates the dominant influence of sample volume change over the pore water outflow during the initial part of the first drying stage. During the second drying stage $E'_7 - F_7$ a gradual reduction of S_r can be seen with no suggestion of a yield point.

Inspection of Figure 9-26 shows that the WM provides a slightly better match than the BBM to the experimental behaviour during drying stages $C'_7 - D_7$ and $E'_7 - F_7$. During the first drying stage $C'_7 - D_7$, the BBM predicts elastic volumetric strains, whereas the WM predicts elasto-plastic volumetric strains. However, both the models could not capture the observed substantial reduction of v during the initial section of first drying ($C'_7 - D_7$). The WM, in theory, could predict the initial steep curve followed by a reduction in the gradient, by yielding initially on the LC curve only and then subsequently yielding on both LC and SI curves simultaneously. However, for

the selected parameter values, this does not occur in the WM simulation. During the second drying stage $E'_7 - F_7$ both models capture the shape of the curve with reasonable accuracy. However, the WM provides a better prediction than the BBM in matching the experimental values of v .

Inspection of Figure 9-27 and Figure 9-28 reveals that the WM captures the shape of the curves for the variations of v_w and S_r , except during the initial section of the first drying stage $C'_7 - D_7$, with reasonable accuracy. However, the model tends to underestimate the values of v_w and S_r throughout the test.

Figure 9-29 shows the experimental variation of deviator stress with shear strain for Tests B7 and B4 along with the BBM and the WM predictions for Test B7. The value of deviator stress at the end of the first shearing stage $B'_7 - C_7$ was 75 kPa, which is about 40% of the critical state value of deviator stress at that suction level (100 kPa) and radial net stress (75 kPa), as computed from the strength parameters for compacted Speswhite Kaolin suggested by Wheeler and Sivakumar (1995). No evidence for any yield point can be seen during this shearing stage $B'_7 - C_7$, suggesting that the stress point is on the LC yield curve from the beginning of the first shearing stage (the gradient is more consistent with elasto-plastic behaviour than with elastic behaviour).

It is interesting to see from the experimental curve in Figure 9-29 that negative shear strains occurred during the first drying stage $C'_7 - D_7$, even though the soil was subjected to a positive value of deviator stress. In order to investigate this feature, the variation of both radial and axial strains should be considered, as the experimental shear strain is calculated from the following equation:

$$d\epsilon_s = \frac{2}{3}(d\epsilon_a - d\epsilon_r) = d\epsilon_a - \frac{1}{3}d\epsilon_v \quad (9-2)$$

where $d\epsilon_a$, $d\epsilon_r$ and $d\epsilon_v$ are the increments of axial strain, radial strain and volumetric strain respectively. From the above equation, it is clear that the radial strain was higher than the axial strain during the drying stage $C'_7 - D_7$ in order for a negative shear strain to occur. One possible reason for the negative shear strain is that anisotropy

produced during the sample preparation and the previous shearing stage $B'_7 - C_7$ might influence the behaviour of the soil sample during the drying stage $C'_7 - D_7$.

During the second shearing stage ($D'_7 - E_7$), there is a suggestion of a yield point in the $q : \epsilon_s$ plane (see Figure 9-29). At the end of the second shearing stage, a deviator stress of 175 kPa was reached (75% of the critical state deviator stress at a suction of 200 kPa and a radial net stress of 75 kPa, according to the strength parameters suggested by Wheeler and Sivakumar (1995)). It can be seen from Figure 9-29 that positive shear strains occurred during the subsequent drying stage $E'_7 - F_7$, possibly because the applied deviator stress was now a high percentage of the corresponding critical state value, and the effect of this was sufficient to outweigh any impact of soil anisotropy.

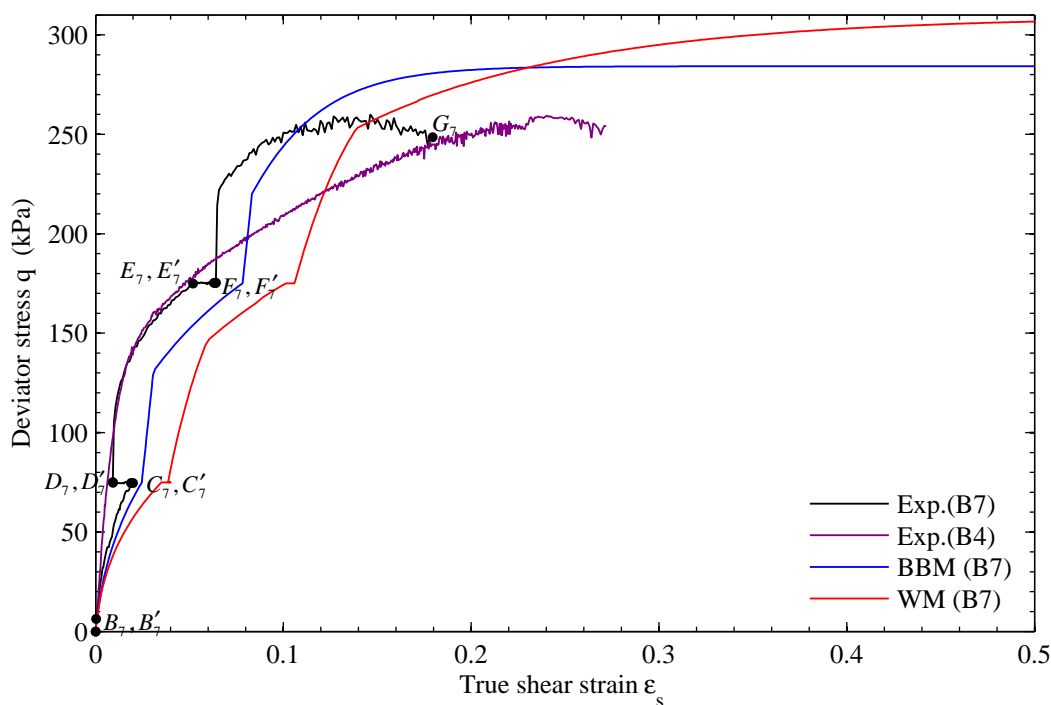


Figure 9-29 Variation of deviator stress q against true shear strain ϵ_s for Tests B7 and B4 along with BBM and WM predictions for Test B7

The final shearing stage ($F'_7 - G_7$) at a suction of 300 kPa resulted in failure of the sample at a deviator stress of 260 kPa, which was equal to that of Test B4. However, it can be noted that the degree of saturation at the failure state for Test B7 was much

higher than that of Test B4 (see Figure 9-25) and the value of ν was significantly lower than that of Test B4 (see Figure 9-24). According to the argument put forward in Section 9.2.2, one would expect a higher shear strength in Test B7 than in Test B4, because of the higher final value of S_r in Test B7. One possible explanation for this unexpected behaviour could be that during the second shearing stage $D'_7 - E_7$ the sample could have almost reached a critical state. The increase in the suction in the subsequent drying stage might not have provided the full expected contribution to increase of critical state strength. The final failure of the sample at a value of shear strain less than that observed in Test B4 further supports this argument.

Inspection of Figure 9-29 shows that both the BBM and the WM overestimate the values of shear strain throughout most of the test, but then over-predict the final observed critical state deviator stress. The BBM does not predict any shear strain (elastic or plastic) during drying stages $C'_7 - D_7$ and $E'_7 - F_7$ as there was no change in deviator stress (hence no predicted elastic shear strains) and no predicted yielding (hence no predicted plastic shear strains). The WM predicts (plastic) positive shear strains in both drying stages by yielding on the LC surface. This matches the observed positive shear strains during the second drying stage $E'_7 - F_7$, but not the observed negative shear strains during the first drying stage $C'_7 - D_7$.

The BBM probably provides a better match to the yield points in the second and final shearing stages $D'_7 - E_7$ and $F'_7 - G_7$ than the WM (see Figure 9-29). Also it can be noted that during the initial section of the second and final shearing stages the sample showed a very stiff response, attributed to elastic behaviour. This was well captured by the BBM as the stress point moves inside the LC yield surface during each of the drying stages. However, according to the WM, at the end of each drying stage in this particular simulation, the stress point was on the LC yield surface, meaning that during the subsequent shearing stage plastic volumetric strain and plastic shear strain would occur from the beginning (see Figure 9-29).

9.3.3 Test B10

In Test B10, the behaviour of unsaturated soil during a wetting-induced shearing stage was explored and the abilities of the BBM and the WM to model this type of behaviour

were investigated. Table 9-10 and Figure 9-30 show the stress path followed in Test B10. The sample was first equalised ($A_{10}A'_{10}$) at a mean net stress of 10 kPa and a suction of 300 kPa. It was then isotropically loaded to a mean net stress of 75 kPa (stage $A'_{10} - B_{10}$). This was followed with a shearing stage $B'_{10} - C_{10}$ at constant suction of 300 kPa and a constant radial net stress of 75 kPa to a deviator stress of 185 kPa. Finally, a wetting stage $C'_{10} - D_{10}$ was performed with deviator stress and mean net stress held constant, with the intention of reaching shear failure by wetting. During the final wetting stage, the suction was reduced to 125 kPa at a slower rate of 0.25 kPa/hr than the typical rate of 1 kPa/hr, in order to minimize any non-equalisation of suction within the sample during wetting-induced shear straining.

| Stage | | | q (kPa) | \bar{p} (kPa) | s (kPa) |
|-----------|-----------|----------------------|---------------------|----------------------|-----------------------|
| From | To | Description | | | |
| A_{10} | A'_{10} | Initial equalisation | 0 | 10 | 300 |
| A'_{10} | B_{10} | Isotropic loading | 0 | 10 \rightarrow 75 | 300 |
| B_{10} | B'_{10} | Equalisation | 0 | 75 | 300 |
| B'_{10} | C_{10} | Shearing | 0 \rightarrow 185 | 75 \rightarrow 137 | 300 |
| C_{10} | C'_{10} | Equalisation | 185 | 137 | 300 |
| C'_{10} | D_{10} | Wetting | 185 | 137 | 300 \rightarrow 125 |

Table 9-10 Stress path for Test B10

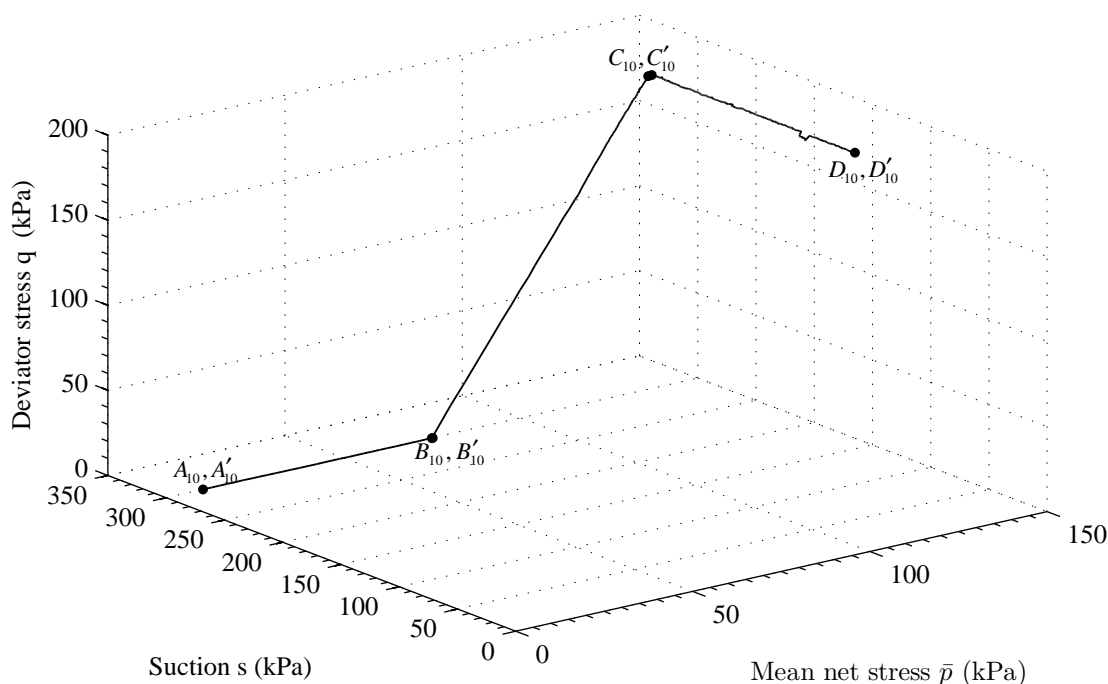


Figure 9-30 Stress path for Test B10

Figure 9-31 and Figure 9-32 show the variation of deviator stress and volumetric strain against shear strain. It can be seen from Figure 9-31 that in the later part of the shearing stage $B'_{10} - C_{10}$ there was slightly non-linear behaviour, suggesting some elasto-plastic straining. Both the BBM and the WM overestimate the development of shear strain during the early part of shearing stage $B'_{10} - C_{10}$, but they predict the value of shear strain at the end of shearing $B'_{10} - C_{10}$ with reasonable accuracy.

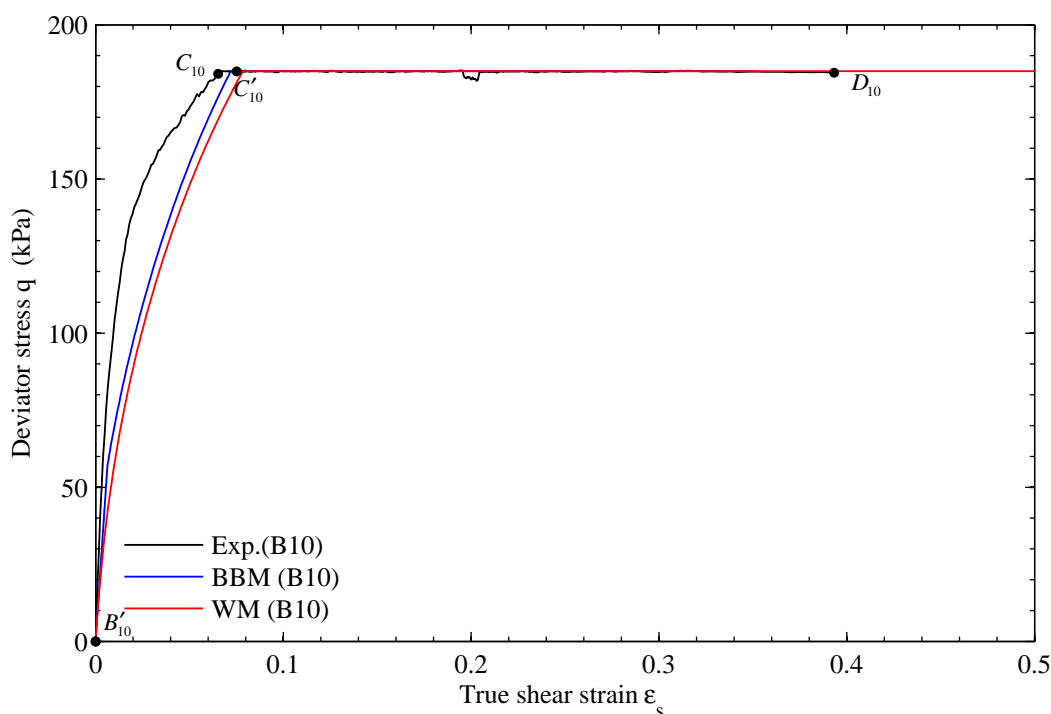


Figure 9-31 Variation of deviator stress q against true shear strain ϵ_s for Test B10 along with BBM and WM predictions

Inspection of Figure 9-32 reveals that during the wetting stage $C'_{10} - D_{10}$ the value of volumetric strain was approaching a limiting value, corresponding to a critical state. According to the values suggested by Wheeler and Sivakumar (1995) for the critical state strength parameters for compacted Speswhite Kaolin prepared in a same way as followed in the current tests, the sample would fail at a suction just above 100 kPa. Although the value of shear strain at the end of the wetting stage was very high compared to other tests, it is not clear whether a true critical state was reached, as small volumetric strains were still occurring at the end of the stage. It is interesting to note that even though Figure 9-32 shows the variation of volumetric strain for the shearing

stage $B'_{10} - C_{10}$ and the subsequent wetting stage $C'_{10} - D_{10}$, there was no visible discontinuity in the curve for this abrupt change in stress path direction. This observation supports the suggestion (present in both the BBM and the WM) of representing plastic behaviour during both shearing and wetting as yielding on the same yield surface (i.e. the LC yield surface). Both the BBM and the WM overestimate the values of ε_v throughout stages $B'_{10} - C_{10}$ and $C'_{10} - D_{10}$. However, the BBM prediction for the critical state value of ε_v is a reasonable match to the observed value, whereas the WM significantly over-predicts the critical state value for ε_v (see Figure 9-32).

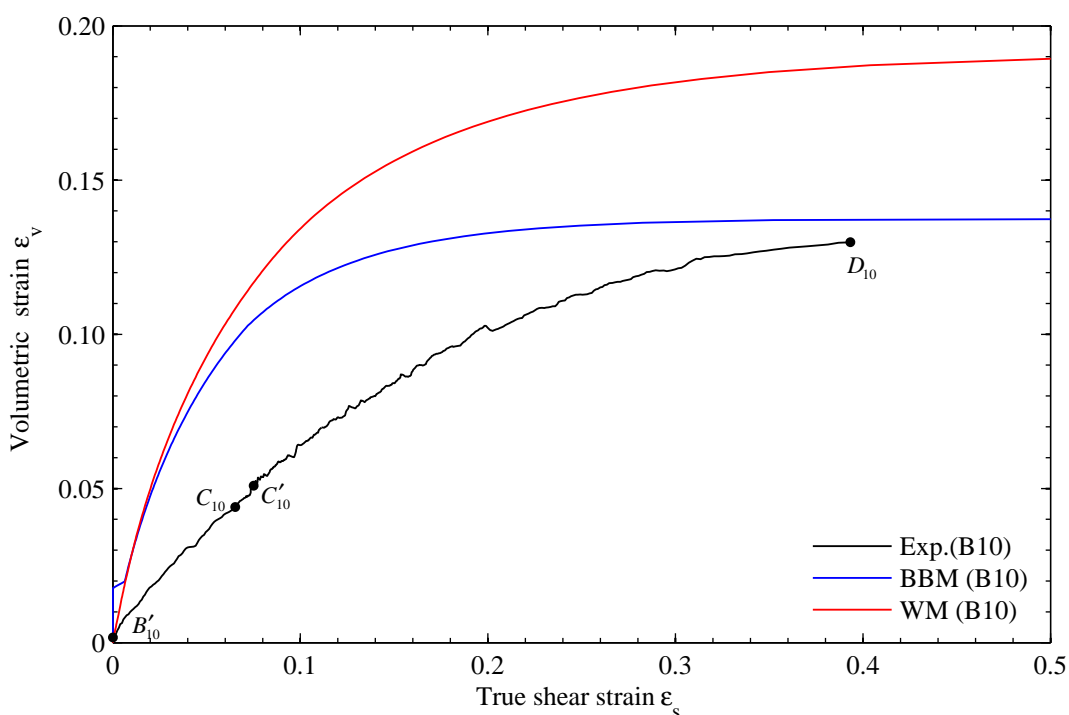


Figure 9-32 Variation of volumetric strain ε_v against true shear strain ε_s for Test B10 along with BBM and WM predictions

Figure 9-33, Figure 9-34 and Figure 9-35 show the variation of specific volume, degree of saturation and specific water volume with suction. Inspection of Figure 9-33 shows that plastic volumetric strain occurred during the wetting stage $C'_{10} - D_{10}$ right from the beginning of the stage (see Figure 9-33). Although both models captured the occurrence of plastic volumetric strains by yielding on the LC yield surface from the beginning of the wetting stage, they under-predicted the values of v throughout this

wetting stage. The BBM predicts the final value of v at the end of the wetting stage with reasonable accuracy, but fails to capture the gradient of the curve during stage $C'_{10} - D_{10}$. A completely opposite observation can be made for the prediction by the WM, where the WM predicts the gradient of the curve accurately but not the final value of v (see Figure 9-33).

From the experimental variation of S_r with suction during wetting stage $C'_{10} - D_{10}$, there is a slight suggestion of a yield point at a suction of about 290 kPa (see Figure 9-34). This is not captured by the WM, as it predicts elasto-plastic changes of S_r from the beginning of the wetting stage by yielding on the SD surface. Inspection of Figure 9-34 also reveals that the WM predicts the value of S_r at the end of wetting stage with reasonable accuracy, but the prediction for the gradient of the $S_r : \ln s$ curve during stage $C'_{10} - D_{10}$ is not a good match to the observed behaviour.

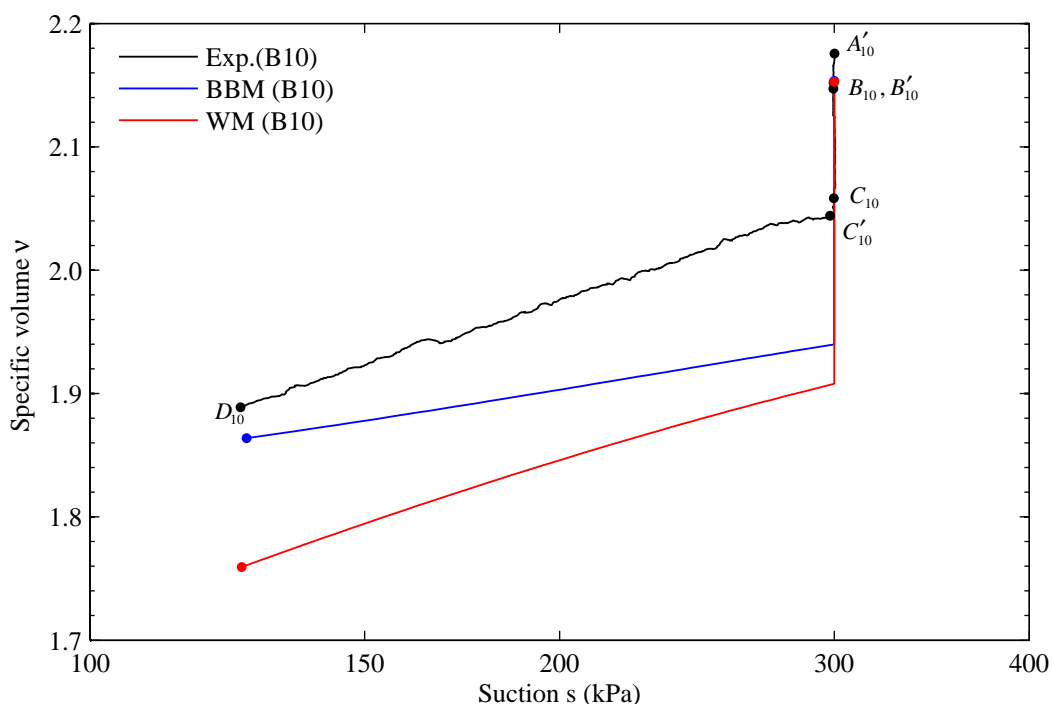


Figure 9-33 Variation of specific volume v against suction s for Test B10 with the BBM and WM predictions

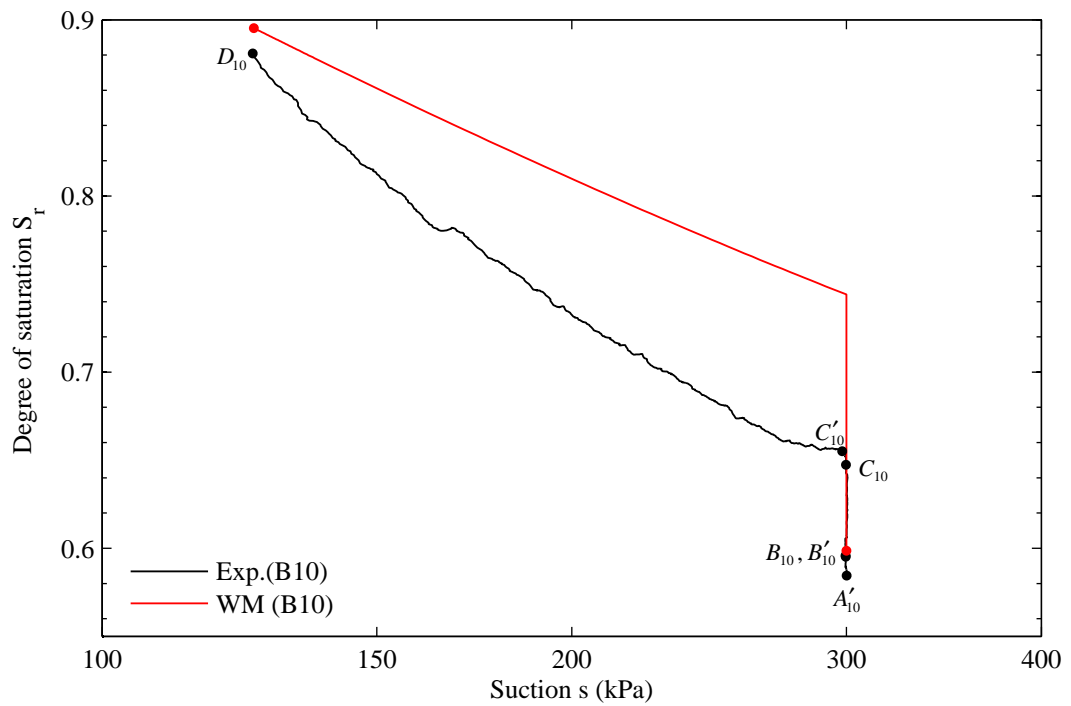


Figure 9-34 Variation of degree of saturation S_r against suction s for Test B10 with the WM predictions

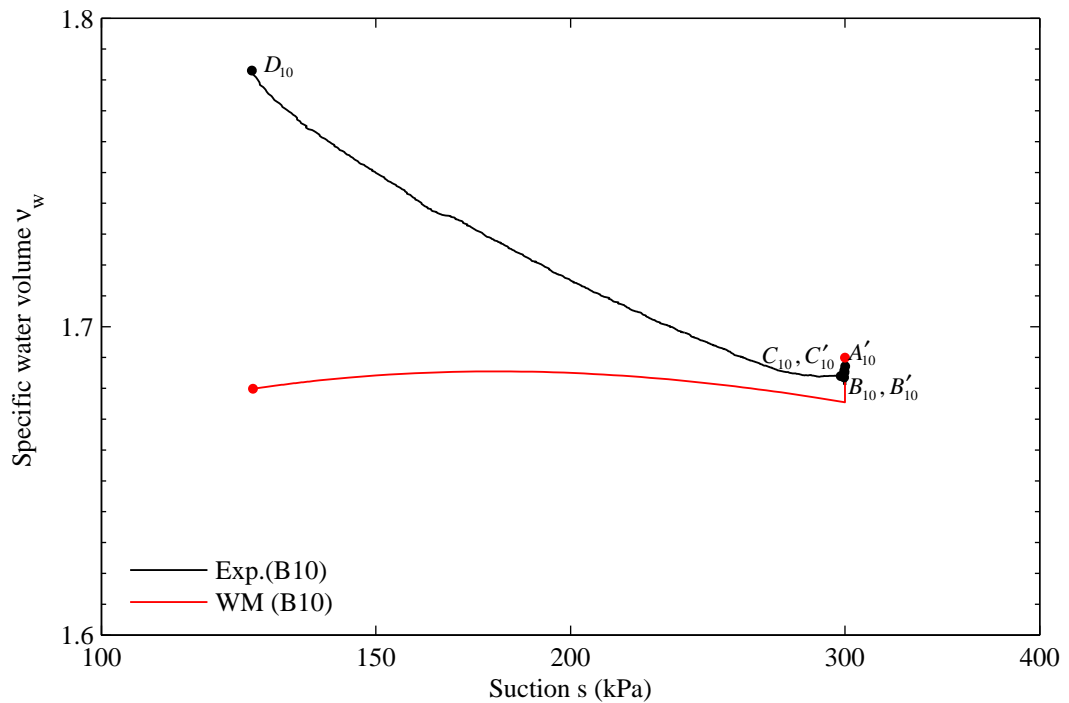


Figure 9-35 Variation of specific water volume v_w against suction s for Test B10 with the WM predictions

Inspection of Figure 9-35 shows a significant increase in the values of v_w during the wetting stage $C'_{10} - D_{10}$, with a suggestion for a yield point at a suction of about 290 kPa. However, it should be noted that the initial flat response for the variation of S_r and v_w during wetting stage $C'_{10} - D_{10}$ may also be attributable to the delayed response of the sample to the suction decrease. The WM prediction for the variation of v_w is not a good match to the experimental behaviour even at a qualitative level, because, the WM predicts a small increase of v_w during the initial part of the wetting stage followed by a small reduction of v_w predicted in the later part of the stage, leading to a very small net increase in v_w predicted over the entire stage $C'_{10} - D_{10}$, whereas the experimental results show a significant monotonic increase in v_w .

9.3.4 Tests C1, C2 and C3

Test Series C on saturated samples was carried out using the conventional Bishop-Wesley triaxial cell of System C (see Section 5.3). Samples were first saturated according to the procedure detailed in Section 6.3.5. They were then isotropically loaded to different radial effective stress (50, 100 and 200 kPa for Tests C1, C2 and C3 respectively). Finally, the samples were sheared at a constant displacement rate of 0.072 mm/hr under fully drained conditions and constant radial effective stress until shear failure occurred.

Figure 9-36 and Figure 9-37 show the experimental variations of deviator stress and volumetric strain against shear strain for Tests C1, C2 and C3 along with the predictions by the BBM and the WM. Inspection of Figure 9-36 shows that the BBM predicts the critical state deviator stress with reasonable accuracy for all three tests, whereas the WM underestimates the critical state values of deviator stress. It should be noted that the WM over-predicted the critical state values of deviator stress for unsaturated samples at suctions of 200 kPa and 300 kPa. These observations clearly show that the single critical state line in the $q : p^*$ plane given by Equation 9-1 cannot uniquely represent the experimental results (see Figure 7-23). Instead, as mentioned in Section 3.6.3, the critical state points for saturated samples consistently lie at the top of the range whereas the results for unsaturated samples at highest values of suction consistently lie at the bottom of the range. Inspection of Figure 9-37 shows that both

the BBM and the WM significantly over-predicted the volumetric strain throughout the shearing stage, including the critical state value of ϵ_v .

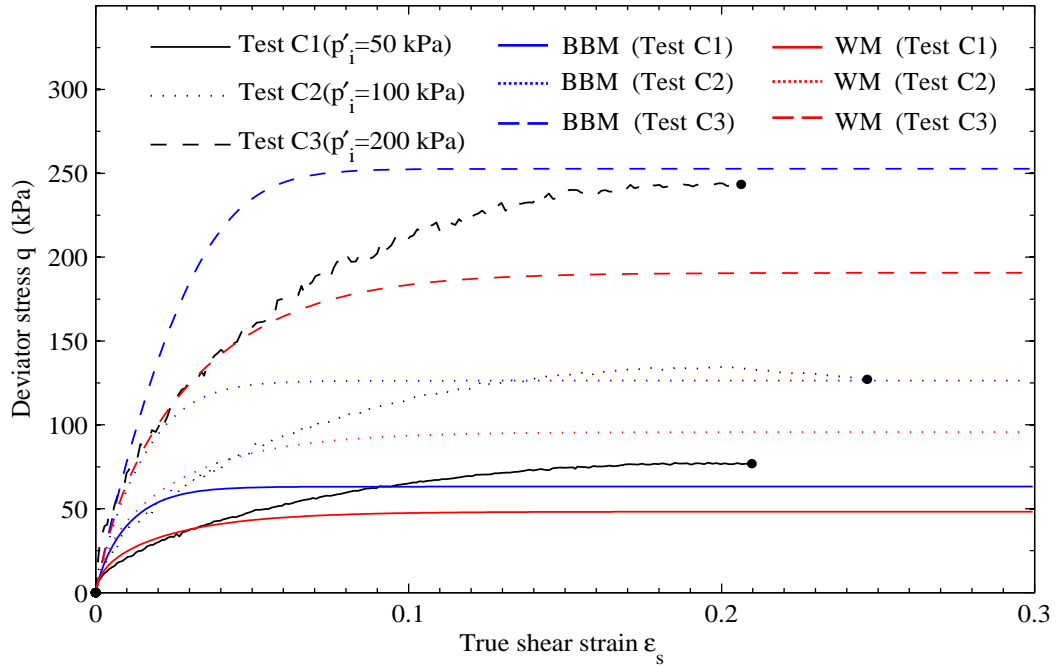


Figure 9-36 Variation of deviator stress q against true shear strain ϵ_s for Tests C1, C2 and C3 with the BBM and WM predictions

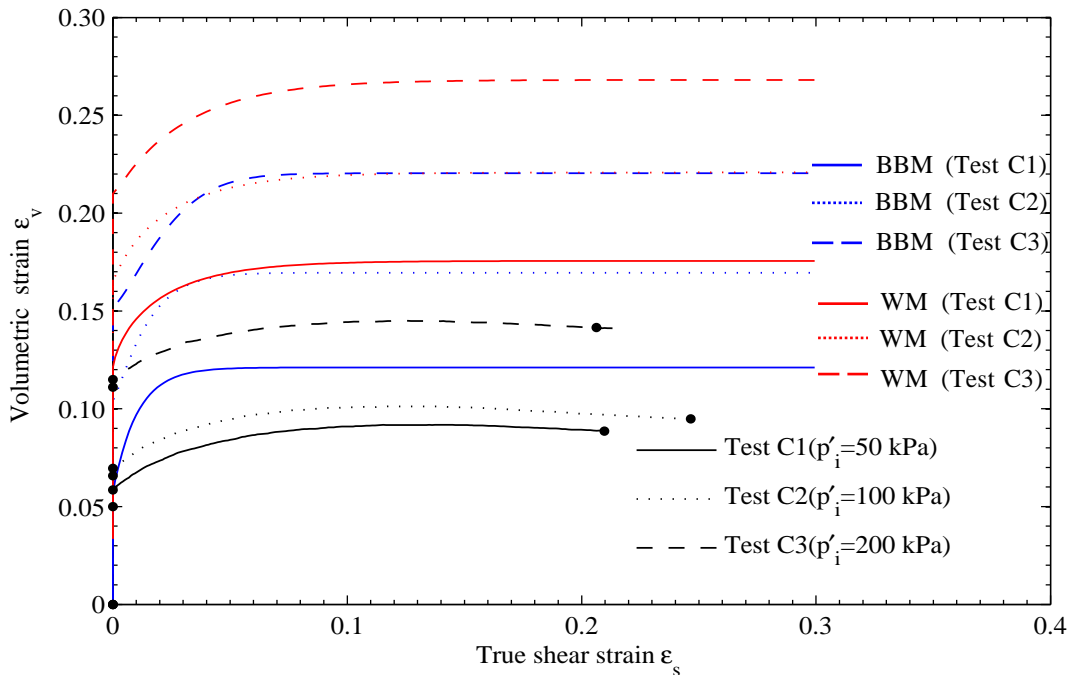


Figure 9-37 Variation of volumetric strain ϵ_v against true shear strain ϵ_s for Tests C1, C2 and C3 with the BBM and WM predictions

Figure 9-38 shows the variation of specific volume against mean effective stress. Interestingly, the normal compression line for 1 kPa suction (from Test A12) almost coincided with the saturated normal compression lines, from Test Series C given that test series A and C were carried out in different systems with different measurement techniques to determine the sample volume change. The yield stress observed for Test A12 is slightly less than that of Tests C1, C2 and C3. This could be due to a small collapse compression during the saturation of sample for test series C as the initial specific volume observed in test series C is slightly lower than that of Test A12. Even though the BBM and the WM predicted the slope of the saturated normal compression line accurately, the BBM provides a better prediction of the position of the saturated normal compression line than the WM.

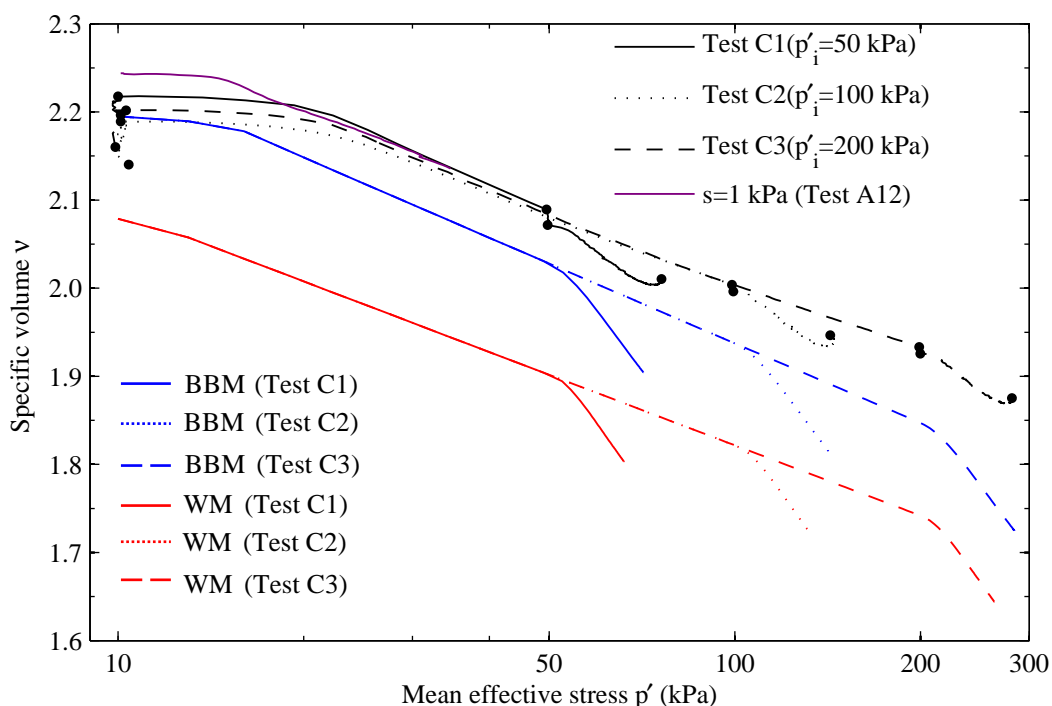


Figure 9-38 Variation of specific volume v against suction s for Tests C1, C2, C3 and A12 with the BBM and WM predictions

CHAPTER 10

DISCUSSION OF WHEELER ET AL. (2003) MODEL

The model simulations and the experimental test results presented in Chapters 8 and 9 show that the WM provides reasonably good predictions in some cases, particularly during isotropic loading and unloading, and a poor match to experimental behaviour in some other cases, particularly during wetting and drying paths. In this section, the strengths and weaknesses of the Wheeler et al. (2003) model will be discussed in the light of the experimental test results.

10.1 STRESS STATE VARIABLES

The Wheeler et al. (2003) framework was proposed in terms of Bishop's stress tensor σ_{ij}^* and modified suction s^* . For the simplified stress states of the triaxial test this reduces to mean Bishop's stress p^* , deviator stress q and modified suction s^* .

The use of p^* as a stress state variable involves a major assumption that the air-filled voids and water-filled voids can be considered together, by using a weighted average of the two pore pressures (weighted by the degree of saturation). With this assumption, three key aspects of the model were proposed to be controlled by p^* and they are:

- (a) elastic variation of specific volume (see Equation 3-3);
- (b) mechanical yielding behaviour (a vertical LC yield curve in the $s^* : p^*$ plane) with additional influence by the plastic changes of S_r (dS_r^p);
- (c) shear strength (see Equation 3-24).

The validity of the formulation for elastic volumetric strain was investigated in Test A1 (see Section 8.1.1). Isotropic loading, unloading, wetting and drying paths were followed, with the intention that these stress paths were inside the LC, SD and SI yield curves. Although inspection of the variation of v against p^* (see Figure 8-4) showed the possibility of unique relation between elastic volumetric strains and changes in p^* ,

no firm conclusion could be reached, because the small measured changes of specific volume were highly susceptible to any measurement errors or problems of experimental technique and because there were doubts about whether the stress paths were truly fully elastic.

In the Wheeler et al. (2003) model, the mechanical yielding characteristics were proposed to be independent of modified suction, but predominantly controlled by the value of p^* (with additional influence from the plastic changes of S_r) by having a straight vertical LC yield curve in the $s^* : p^*$ plane. Investigation of this aspect of behaviour will be discussed in detail in the next section.

In the WM extended to triaxial stress states, the shear strength was proposed to be uniquely related to p^* . However, close inspection of the critical state data from Sivakumar (1993), Wheeler and Sivakumar (2000) and the author plotted in the $q : p^*$ plane shows that there is a small but consistent trend with variation of suction, with the saturated critical state data points lying at the top of the range and the highest suction data points lying at the bottom of the range (see Figure 7-23). This observation suggests that the assumption of a unique critical state line in the $q : p^*$ plane may not be true for the whole range of suction values.

Wheeler et al. (2003) proposed modified suction s^* as a second stress state variable, in addition to the Bishop's stress tensor σ_{ij}^* . This proposal of using s^* in combination with σ_{ij}^* was merely based on the equation derived by Houlsby (1997) for the increment of work input per unit volume of unsaturated soil. In almost all cases, it was found that plotting water retention curves either in the $S_r : \ln s$ plane or in the $S_r : \ln s^*$ plane did not show any significant differences in the shapes of curves (see for example Figure 8-22 and Figure 8-23), suggesting that there is no particular practical advantage of using the complex stress state variable s^* over the simple and widely used variable s . The Wheeler et al. (2003) model involves two key proposals in the role of the stress state variable s^* :

(a) elastic changes of S_r are related solely to changes of s^* (see Equation 3-4);

(b) water retention yielding behaviour is assumed to be dependent on the value of s^* (horizontal SD and SI yield curves in the $s^* : p^*$ plane) with additional influence from the plastic volumetric strains ($d\varepsilon_v^p$).

In the illustrative Wheeler et al. (2003) model, elastic changes of degree of saturation were expressed exclusively in terms of changes of modified suction (see Equation 3-4). Test A1 was used to investigate this proposal (see Section 8.1.1). However, the results of the test did not provide conclusive evidence supporting the form of this equation, because of similar practical difficulties to those discussed earlier in connection with the proposed link between elastic volumetric strain and changes of p^* (susceptibility to small measurement errors and problems of experimental technique, and uncertainty whether the stress path was truly elastic). However, it is important to note that elastic changes in degree of saturation and elastic volumetric strains are in reality be very small. It may therefore be acceptable to express the elastic changes in v and S_r uniquely in terms of changes of p^* and changes of s^* respectively, in order to preserve the simplicity of the Wheeler et al. (2003) model.

The Wheeler et al. (2003) model also assumes that yielding characteristics associated with water retention behaviour are controlled predominantly by the value of s^* , by employing horizontal SD and SI yield curves in the $s^* : p^*$ plane, with additional influence of the plastic volumetric strains $d\varepsilon_v^p$. This issue will be discussed in detail in Section 10.3.

10.2 SHAPE OF LC YIELD CURVE AND FLOW RULE

Wheeler et al. (2003) proposed that the LC yield curve associated with inter-particle slippage could be represented by a straight vertical line in the $s^* : p^*$ plane. The proposal was theoretically supported by analysing the influence of suction within the meniscus water rings around spherical particles in contact (see Section 2.3), which led to the argument that plastic changes of S_r (i.e. changes in the number of meniscus

water rings) rather than changes of s or s^* play a key role in determining the yielding characteristics as far as mechanical behaviour is concerned. In order to investigate this proposal, Test A4 was carried out (see Section 8.1.3). In Test A4 the sample was first isotropically loaded (stage $A' - B$) at constant suction of 150 kPa to a mean net stress of 150 kPa, with the intention of reaching the corner of LC and SD curves at the end of this stage. The mean net stress was then decreased to 75 kPa with a simultaneous increase in suction to 200 kPa (stage $B' - C$), with the intention of moving away from both SD and LC yield curves (but not yielding on the SI yield curve). During the subsequent isotropic loading $C' - D$ at constant suction of 200 kPa the experimental result plotted in the $v : \ln p^*$ plane (see Figure 8-18) clearly shows a yield point at a value of p^* higher than the maximum value previously experienced by the sample, even though no significant plastic reduction of degree of saturation occurred during the previous stress path $B' - C$ (i.e. no yielding on the SI yield curve). This experimental observation indicated that the LC yield curve may not be a straight vertical line in the $s^* : p^*$ plane, as assumed for isotropic stress states, suggesting that the influence of suction within the meniscus water rings significantly affects the stability of inter-particle contacts, and this aspect may need to be incorporated in the framework (by an inclined LC yield curve).

The Wheeler et al. (2003) model predicts plastic volumetric strains but no plastic changes of S_r during yielding on the LC yield curve, because of the assumption of an associated flow rule on the LC yield curve. However, experimental isotropic compression curves in the $v : \ln \bar{p}$ plane and the corresponding variation of S_r plotted in the $S_r : \ln \bar{p}$ plane show a yield point in the $S_r : \ln \bar{p}$ plane at the same stress as the yield point in the $v : \ln \bar{p}$ plane in almost all cases (see for example Figure 8-16 and Figure 8-17), i.e. there is a clear suggestion that plastic changes of S_r occur during yielding on the LC yield curve. This means that a non-associated flow rule may be required for yielding on the LC yield curve if the LC yield curve is assumed to be vertical in the $s^* : p^*$ plane. It is also possible to have an associated flow rule to predict both $d\varepsilon_v^p$ and dS_r^p during yielding on the LC yield curve if the LC yield curve is inclined, as described in the previous paragraph.

10.3 SD AND SI YIELD CURVES

It can be seen from Sections 8.1, 8.2, 9.2 and 9.3 that the water retention behaviour, presented as variation of degree of saturation or specific water volume against suction, was poorly predicted by both WM and WM (BS). It is obvious that the water retention behaviour during wetting and drying (variation of s) is more complex than during isotropic loading and unloading (variation of \bar{p}). Even though, in the experimental results, yield points corresponding to the onset of plastic changes of S_r , could be identified during most drying stages, there was rarely the suggestion of an equivalent yield point during wetting paths, especially at high degrees of saturation (e.g. Figure 8-47, Figure 8-52 and Figure 8-62). At high degree of saturation, a wetting stage often provided an approximately straight line relationship in the $S_r : \ln s$ plane, with low gradient compared to a drying stage (see Figure 8-65). This is probably because of trapped air within the soil sample in the form of occluded bubbles, where the air can move to the boundary of the sample only by diffusing in solution through the surrounding water voids. As a consequence, extremely long test durations would have been required to reach true equilibrium conditions during wetting at high degrees of saturation, and the experimental results during such stages may not be fully reliable. The non-existence of yield points during most of wetting stages makes it almost impossible to identify the position of the SD yield curve. The absence of clear yield points in most of the wetting curves in the $S_r : \ln s$ plane also suggests that bounding surface plasticity is more suitable to describe water retention behaviour than classical elasto-plasticity.

In the Wheeler et al. (2003) framework the SD and SI yield curves were proposed to be straight horizontal lines in the $s^* : p^*$ plane. One of the objectives of Test A3 was to investigate this proposal of a horizontal SD yield curve. Unfortunately, the attempt to determine the shape of the SD yield curve in Test A3, with stress paths $B' - CC' - DD' - E$ and $E' - FF' - G$ (see Figure 8-8), was unsuccessful, because it was difficult to find yield points during the wetting processes corresponding to yielding on the SD yield curve only. It was therefore almost impossible to verify the shape of the SD yield curve. No specific test was performed to determine the shape of the SI yield curve.

In the Wheeler et al. (2003) model, the spacing between the SI and SD yield curves was assumed to be constant when plotted in terms of $\ln s^*$. It was intended to investigate this arbitrary assumption in the light of the experimental test results. However, the complex nature of the water retention behaviour, together with the absence of yield points in the $S_r : \ln s^*$ plot during wetting stages meant that this assumption could not be directly investigated. However, the spacing between the SI and SD yield curves can be inferred from the spacing between the wetting and drying curves in the $S_r : \ln s^*$ plot (if the form of elastic variation of S_r is known or can be assumed). Unfortunately, the experimental results showed that the spacing between the wetting and drying curves in the $S_r : \ln s^*$ plane can not be taken as constant, as it varied continuously from one test to another, primarily depending on the level of suction and degree of saturation. A value of 1.5 for the ratio s_I^*/s_D^* was selected for the simulations (see Section 7.4.4). However, many of the subsequent comparisons between model simulations and experimental results suggest that selection of a significantly higher value for the ratio s_I^*/s_D^* would have given a better match to the experimental water retention behaviour (see, for example, Figure 8-43, Figure 8-47, Figure 8-52 and Figure 8-62). It is therefore recommended that a higher value for s_I^*/s_D^* is appropriate for the compacted Speswhite Kaolin in order to obtain better predictions of water retention behaviour in the $S_r : \ln s$ plane or in the $v_w : \ln s$ plane.

According to the WM, during a drying stage it is possible for yielding to occur either first on the LC curve (plastic volumetric strains predicted) or first on the SI curve (plastic decrease of S_r predicted), depending on the positions of these yield curves in relation the current stress point. However, during most of the drying stages the yield points observed in the $S_r : \ln s$ plane appear to coincide with the yield points observed in the $v : \ln s$ plane (see for example Figure 8-21 and Figure 8-22). The only exception is the drying stage $A' - B$ in Test A10, where the yield value of suction observed in the $v : \ln s$ plot is significantly less than that observed in the $S_r : \ln s$ plot (see Figure 8-64 and Figure 8-65). The experimental observation, during a typical drying stage, of similar yield values of suction in the $v : \ln s$ and $S_r : \ln s$ plots can be better represented by the WM (BS), because a typical drying stage simulation produces both

$d\varepsilon_v^p$ and dS_r^p simultaneously from the beginning and if either $d\varepsilon_v^p$ or dS_r^p increases dramatically in the simulation this tends to produce an associated increase of the other.

In many tests, the gradient of water retention curves in the $S_r : \ln s$ plane during drying seems to be higher than that during wetting, suggesting that, in the WM, different values of λ_s should be used for yielding on the SD and SI yield curves. This is more pronounced at higher degrees of saturation (see Section 8.2.2 and 8.2.4). In the simulations, a value of 0.055 was selected for the value of λ_s . However, comparison of model simulations with experimental results showed that in many cases the selected value of λ_s overestimated the gradient of wetting and drying curves in the $S_r : \ln s$ plane, suggesting that a smaller value should have been selected for λ_s . However, it should be acknowledged here that the value of λ_s also has a strong influence on the gradient of curves in the $S_r : \ln \bar{p}$ plot associated with yielding on the SD curve during isotropic loading, and therefore a compromise should be made in the choice of values for λ_s . In fact, the very basic water retention model (see Figure 3-10) proposed in the Wheeler et al. (2003) model should be replaced with a more realistic water retention model in order to better represent the water retention behaviour.

10.4 PREDICTION OF BEHAVIOUR DURING ISOTROPIC LOADING

Figure 10-1 shows the as-compacted LC yield points for the samples tested by the author along with the BBM yield curve and the yield points predicted by the WM. The yield points predicted by the WM correspond to the onset of yielding on the LC curve, as outward movement of the stress point and coupled inward movement of the LC curve (caused by yielding on the SD curve) bring the current stress point and the LC curve together. It can be clearly seen that the WM cannot predict the variation of yield stress accurately with suction. The prediction of the variation of yield stress by the WM is predominantly determined by the coupling equation given by:

$$\frac{dp_0^*}{p_0^*} = k_1 \frac{ds_D^*}{s_D^*} \quad (10-1)$$

The above equation represents a straight line yield locus in the $\ln s^* : \ln p^*$ plane, whereas the experimental yield locus for as-compacted samples was found to be non-linear as already mentioned in Section 7.4.3 (see Figure 7-22). It may therefore be necessary to modify the form of the coupling equation, in order to get better prediction for the variation of yield stress with suction in the $s : \bar{p}$ plane.

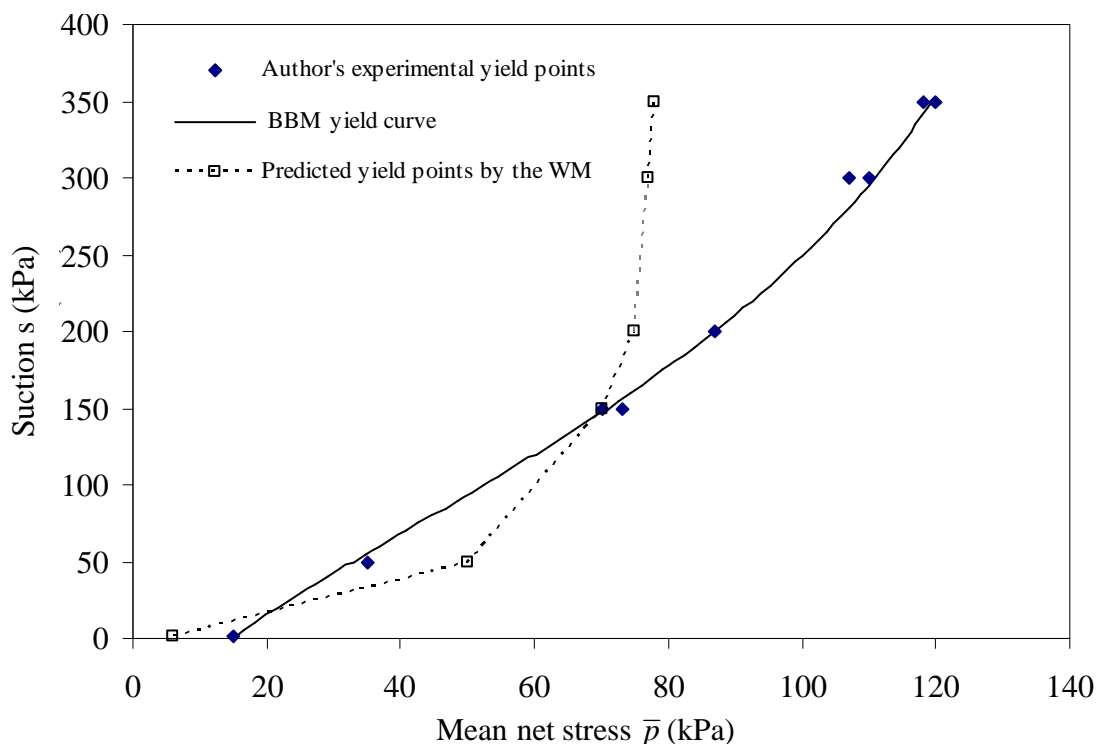


Figure 10-1 As-compacted LC yield points for the samples tested by author along with BBM yield curve and predicted yield points from the WM

The WM also could not provide a perfect prediction for the variation of the gradient of constant suction normal compression lines in the $v : \ln \bar{p}$ plot for a wide range of suction. Although the model provides a good match to the experimentally observed gradient of normal compression lines for high suction values (at suctions of 150, 200 and 300 kPa), it overestimates the gradient at low suction values (at suctions of 10 and 50 kPa). The WM predicts that the gradients of these constant suction normal compression lines hardly vary with suction (being substantially greater than λ for all values of s greater than zero provided that the soil is still unsaturated, see next section), whereas the experimental results show a more gradual variation of gradient with suction. The gradients of constant suction normal compression lines predicted by the WM (during yielding on LC and SD curves simultaneously) are predominantly

controlled by the parameters λ , k_1 and k_2 . One possible solution to this problem is to modify the forms of the two coupling equations proposed by Wheeler et al. (2003) in order to better predict the gradual variation of gradient of constant suction normal compression lines for a wide range of suction values.

10.5 A PROBLEM OF INCONSISTENCY IDENTIFIED IN THE ILLUSTRATIVE MODEL OF WHEELER ET AL. (2003)

In this current research a problem was identified in the Wheeler et al. (2003) illustrative model, associated with inconsistency of the model if plastic volumetric strains occur while the soil is in a saturated condition. This issue is discussed in this section.

Figure 10-2(a) shows the compression curves predicted by the WM for constant suction isotropic loading stages performed at different suction values. Parameter values and initial conditions used in these simulations are those listed in Table 7-3. It can be seen from Figure 10-2 (a) that after the initial elastic behaviour different constant suction normal compression curves are predicted for different values of suction and all of these initially have a gradient greater than λ , as a consequence of simultaneous yielding on the LC and SD curves (additional yielding on the LC yield curve is required, in order to offset the coupled inward movement of the LC curve caused by yielding on the SD curve). During these constant suction isotropic loading stages the predicted degree of saturation increases (see Figure 10-2(b)), and in each case a point is reached where fully saturated conditions are predicted. The subsequent predicted compression curve then follows a saturated normal compression line with a gradient of λ (see Figure 10-2(a)). The inconsistency identified in the Wheeler et al. (2003) model is, however, that the saturated normal compression lines predicted for different values of suction are not unique; rather the saturated normal compression line is shifted down with increasing suction. This non-uniqueness in the positions of saturated normal compression lines was also observed when plotted in the $v : \ln p^*$ plane. The reason for this non-unique saturated normal compression line is now discussed.

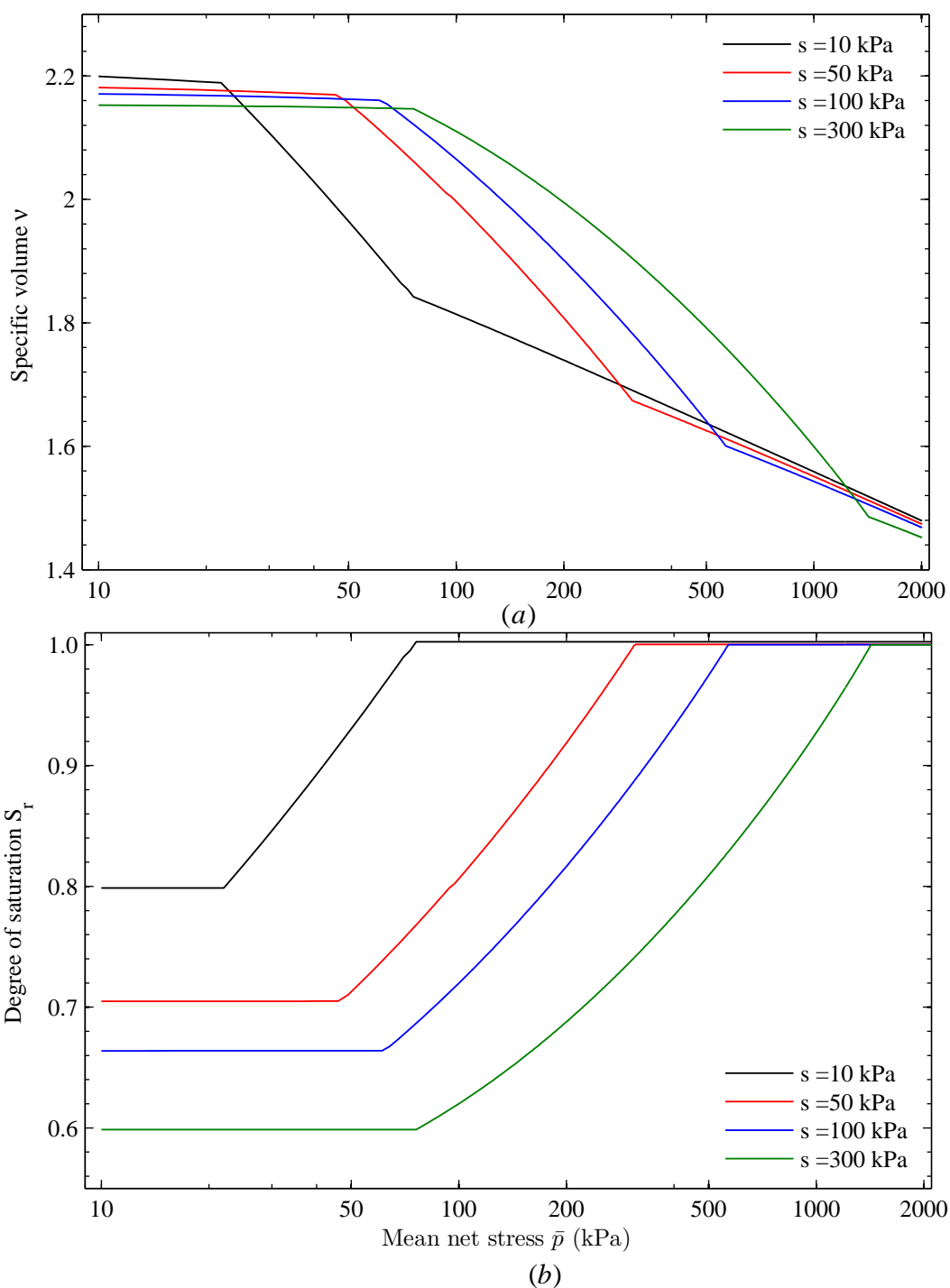


Figure 10-2 Behaviour predicted by the WM in the (a) $v : \bar{p}$ plane and (b) $S_r : \bar{p}$ plane during constant suction isotropic loading at different values of suction

The prediction of a non-unique saturated normal compression line in Figure 10-2(a) is an indication of a problem with the Wheeler et al. (2003) model, which arises if plastic volumetric strains occur while the degree of saturation is 1 (or zero). This is because the model assumes that both plastic and elastic components of change of degree of

saturation cease while S_r remains at 1 (or zero), as shown in Figure 10-3. If plastic volumetric strains occur (due to yielding on the LC curve) while $S_r = 1$ this produces a shift in the air-entry value of the soil (due to coupled movements of the SI and SD curves) and hence a change in the value of s^* at which elastic changes of S_r recommence during drying. This can lead to irreversibility of elastic changes of S_r , which is fundamentally unacceptable.

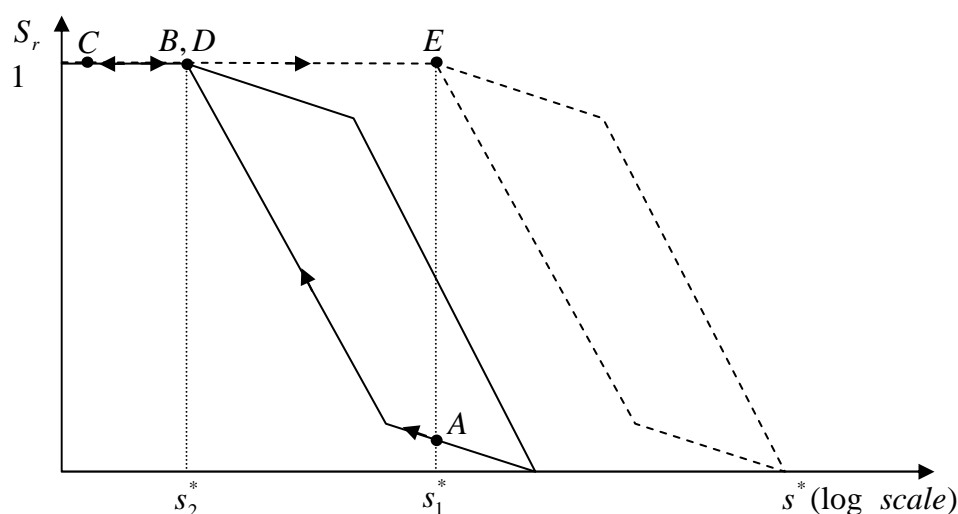


Figure 10-3 Variation of S_r against s^* during a specified stress path

Figure 10-3 shows the variation of S_r against s^* for a specified stress path of interest. The initial positions of main wetting and drying curves are shown by the continuous lines. During a wetting stage $A - B - C$ starting at $s^* = s_1^*$, with no plastic volumetric strains occurring, the Wheeler et al. (2003) model predicts initially elastic increases of S_r and then elasto-plastic increases of S_r (corresponding to yielding on the SD yield curve only) to reach a saturated state at $s^* = s_2^*$ (point B). During stage $C - D - E$ a drying stress path is followed, with increase of modified suction. However, if substantial plastic volumetric strains happen to occur (as a consequence of yielding on the LC curve) while the soil is fully saturated during path $B - C - D - E$, the main wetting and drying curves are shifted to higher suctions, as indicated by the dashed lines. Hence, desaturation only occurs at point E . Consider a range of modified suction s_1^* to s_2^* . On wetting (between A and B), there is an elastic component of change of S_r given by Equation 3-4. However, on drying over the same s^* range (from D

to E), there is no elastic change of S_r . This predicted irreversibility of elastic water retention behaviour introduces inconsistency into the model (by incorporating a permanent memory of past history associated with plastic volumetric straining at saturated state) as demonstrated in Figure 10-2.

The inconsistency of the model can be further illustrated by considering constant S_r lines in the $v : \ln p^*$ plot corresponding to simultaneous yielding on SD and LC curves. By adding elastic and plastic volumetric strain increments given by Equations 3-3 and 3-13 respectively, the increment of specific volume during simultaneous yielding on SD and LC yield curves is given by:

$$-dv = \frac{\kappa dp^*}{p^*} + \frac{(\lambda - \kappa)}{(1 - k_1 k_2)} \left(\frac{dp_0^*}{p_0^*} - k_1 \frac{ds_D^*}{s_D^*} \right) \quad (10-2)$$

Similarly by combining Equations 3-4 and 3-14, the change of S_r during simultaneous yielding on SD and LC yield curves is given by:

$$-dS_r = \kappa_s \frac{ds^*}{s^*} + \frac{(\lambda_s - \kappa_s)}{(1 - k_1 k_2)} \left(\frac{ds_D^*}{s_D^*} - k_2 \frac{dp_0^*}{p_0^*} \right) \quad (10-3)$$

Because the stress point remains at the corner of LC and SD curves the following equations are applicable:

$$\frac{ds^*}{s^*} = \frac{ds_D^*}{s_D^*} \quad (10-4)$$

$$\frac{dp^*}{p^*} = \frac{dp_0^*}{p_0^*} \quad (10-5)$$

The variation of specific volume with mean Bishop's stress for constant degree of saturation lines can be derived by making $dS_r = 0$ in Equation 10-3 and then solving Equations 10-2 and 10-3 simultaneously (after inserting Equations 10-4 and 10-5) to eliminate ds^*/s^* :

$$-dv = \left(\frac{\lambda\lambda_s - k_1k_2\kappa\kappa_s}{\lambda_s - k_1k_2\kappa_s} \right) \frac{dp^*}{p^*} = \lambda^* \frac{dp^*}{p^*} \quad (10-6)$$

where

$$\lambda^* = \frac{\lambda\lambda_s - k_1k_2\kappa\kappa_s}{\lambda_s - k_1k_2\kappa_s} \quad (10-7)$$

Equation 10-6 represents straight parallel lines with a constant gradient λ^* (greater than λ) in the $v : \ln p^*$ plot for different values of degree of saturation as shown by the thin continuous lines in Figure 10-4. The dashed line is the corresponding locus of states at which full saturation occurs during simultaneously yielding on the LC and SD yield curves for different stress paths. This also takes the form of a straight line of gradient λ^* .

In order to explain the prediction of non-unique saturated normal compression lines, two stress path tests (Tests 1 and 2) are considered, in both of which the stress point remains at the corner of SD and LC yield curves throughout. In Test 1, a stress path $A_1 - B_1$ was followed until full saturation was achieved, and then loading was continued $B_1 - C_1$ in a fully saturated condition. During this fully saturated loading $B_1 - C_1$ the predicted response follows a saturated normal compression line of gradient λ (Equation 10-6 no longer applies, because elastic and plastic changes of S_r have been switched off). In the second test a different stress path was followed (but still involving simultaneous yielding on SD and LC curves), so that full saturation is reached at B_2 . As consequence, during subsequent saturated loading $B_2 - C_2$ the saturated normal compression line, of gradient λ , that is followed is in a different location to the corresponding line from Test 1. In addition, if the soil is subsequently de-saturated (e.g. stage $C_2 - D_2$ in Test 2) after undergoing plastic volumetric strain while fully saturated, it will be found that there will have been a shift in the predicted positions of the unsaturated constant S_r lines corresponding to simultaneous yielding on LC and SD curves (i.e. the thin continuous lines of gradient λ^* in Figure 10-4 will have shifted).

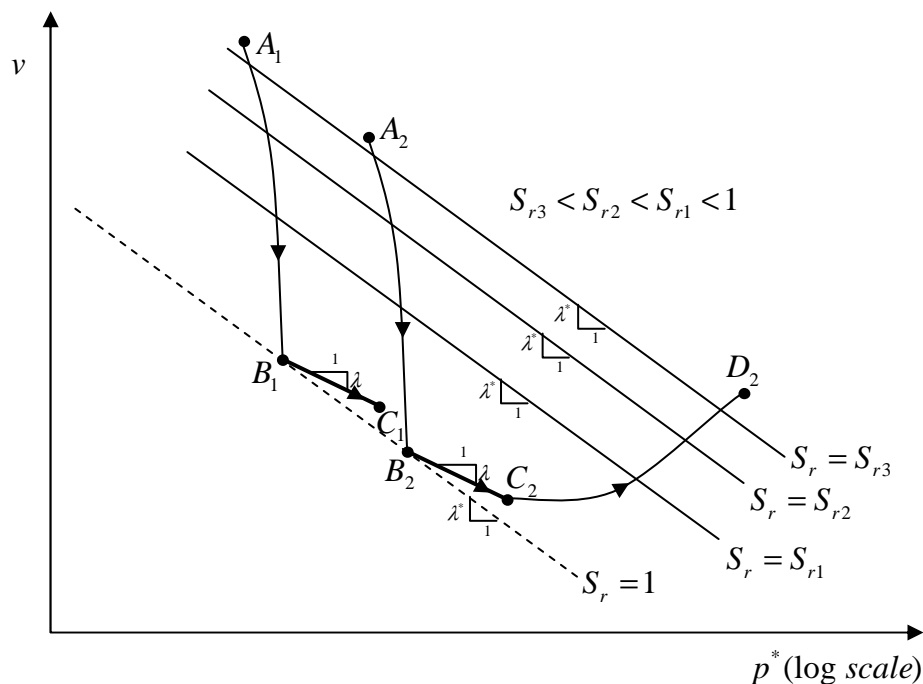


Figure 10-4 Predicted constant degree of saturation lines in the $v : p^*$ plane during simultaneous yielding on SD and LC curves

The original developers of the Wheeler et al. (2003) model intended that a feature of the model would be that, for two samples of the same soil with different stress histories, the specific volume v and degree of saturation S_r would be identical if the stress states (in terms of p^* , q and s^*) were the same for the two samples and if the yield surfaces were in the same locations for the two samples. This has the effect that the mechanical and water retention behaviour of the soil can be affected by the recent stress history (e.g. a wetting-drying cycle), but this memory of the stress history is then gradually erased by subsequent plastic behaviour. This is a physically sensible feature to include in a model, and the formulation of the Wheeler et al. (2003) model ensures that it holds true while the soil remains unsaturated. However, the inconsistency of the model identified and described in this section means that this desirable feature of the model is lost if plastic volumetric strains occur while the soil is fully saturated (more strictly, if $S_r = 1$ or $S_r = 0$).

The problem identified in this section occurs because of irreversibility of elastic changes of S_r if plastic volumetric strains occur while $S_r = 1$ or $S_r = 0$. One simple way of solving this problem is to put $\kappa_s = 0$, so that elastic changes of S_r are always

zero. As an illustration, inspection of Equation 10-7 shows that $\lambda^* = \lambda$ if $\kappa_s = 0$, so that all the constant S_r lines shown in Figure 10-4 now became parallel to a unique saturated normal compression line. Putting $\kappa_s = 0$ would, however, results in highly unrealistic modelling of water retention behaviour in the original classical elasto-plastic version of the Wheeler et al. (2003) model (WM). Making the assumption $\kappa_s = 0$ is less of a problem in the bounding surface plasticity version of the model (WM(BS)), because plastic changes of S_r are predicted for all wetting and drying paths in the bounding surface plasticity model. Alternative adjustments to the models (rather than setting $\kappa_s = 0$) may also provide solutions to the problem identified here, but an initial investigation indicates that this is not easy without introducing new problems into the model, and further research is required.

10.6 OVERALL COMPARISON OF PERFORMANCE OF THE WM AND WM (BS) AGAINST THAT OF THE BBM

In this section the performance of both the WM and the WM (BS) against experimental results is compared with that of the BBM, in order to determine whether the Wheeler et al. (2003) framework represents a real advance on models such as BBM. Important advantages and disadvantages or problems of the WM and WM (BS) over the BBM are therefore presented here. Firstly, important advantages of the WM and WM (BS) over the BBM are listed below.

- The WM can predict both the mechanical behaviour and the water retention behaviour, together with coupling between them, whereas the BBM can predict only the mechanical behaviour. For the BBM a separate retention model will be required for the solution of coupled hydro-mechanical problems, and there is no scope to include the influence of water retention behaviour on mechanical behaviour.
- 8 model parameters are required for the WM (triaxial version) compared to 9 parameters for the BBM (and further model parameters would be required for an accompanying water retention model with the BBM).

- The WM(BS) model would require 10 model parameters if extended to triaxial stress states (two additional parameters compared to the WM) but it can provide some improved predictions, particularly for water retention behaviour.
- The WM can capture the experimentally observed influence of S_r on the mechanical behaviour at a qualitative level.
- The WM can predict the occurrence of plastic volumetric strains and plastic shear strains during drying stages as often observed in experimental results, through yielding on the LC yield surface.
- In theory, the WM can incorporate dependency of critical states on S_r in addition to suction and mean net stress.

Some problems or disadvantages of the WM and WM (BS) are listed below:

- The double yield points predicted by the WM for many stress paths corresponding to yielding first on the LC curve and then on the SD curve as well, are not evident from the experimental results. The experimental results normally suggest the existence of a single yield point, as predicted by the BBM.
- The BBM provides better predictions than the WM of the variation with suction of the slope of constant suction normal compression lines. The BBM also provides better match than the WM to the shape of the initial yield locus observed from constant suction isotropic loading tests performed at different values of suction.
- Although the WM can predict the observed plastic volumetric strain during a drying stage, by yielding on the LC surface, it cannot predict the observed initial elastic response of soil sample during a subsequent isotropic loading or shearing stage, because the WM would predict elasto-plastic volumetric strains from the beginning of this isotropic loading or shearing stage by yielding on LC yield surface.
- Inconsistencies are introduced into the WM or WM (BS) if plastic volumetric strains occur while $S_r = 1$ or $S_r = 0$.

- Critical state values of deviator stress over wide range of suction are better predicted by the BBM than by the WM.

From the above lists it can be clearly seen that although the WM and WM(BS) have some disadvantages over the BBM in providing worse predictions of some conventional aspects of the mechanical behaviour of unsaturated soils, such as the variation with suction of the slope of normal compression lines and the values of isotropic yield stress, they show some advantages in predicting features associated with coupling of mechanical behaviour and water retention behaviour, such as plastic shrinkage on drying and the influence of S_r on mechanical behaviour. One of the major problems identified in the WM is the inconsistency discussed in Section 10.5. Further investigation into this issue is necessary to incorporate realistic water retention modelling without sacrificing the consistency of the model. Some modifications may be required both at a framework level (e.g. the shape of the yield curves and the use of non-associated flow rules) and at a specific model level (i.e. the precise mathematical forms of specific constitutive equations such as coupling equations). From the above discussion, it can be concluded that both the WM and WM (BS) have considerable potential to better represent the real behaviour of unsaturated soil, and to be a significant advance over more conventional models such as the BBM, but further modifications are essential in order to improve the model predictions.

CHAPTER 11

CONCLUSIONS AND RECOMMENDATIONS

Many researchers, such as Wheeler et al. (2003) and Gallipoli et al. (2003b), demonstrated through experimental observations the importance of the coupling of mechanical behaviour and water retention behaviour (see Chapter 3). Several features of behaviour, such as drying-induced plastic volumetric compression or a reduction in the yield stress observed during isotropic loading as consequence of a previous wetting-drying cycle, can not be explained by models like the Barcelona Basic model (BBM). Several modelling proposals to incorporate the coupling of mechanical and water retention behaviour have been put forward, including the framework proposed by Wheeler et al. (2003).

In this research, an experimental programme was carried out in order to investigate the coupling of mechanical and water retention behaviour using three experimental systems. On the constitutive modelling front, extensions were proposed to improve the capabilities of the Wheeler et al. (2003) model and the model performance was investigated by comparing model simulations with corresponding experimental results. This chapter covers the main conclusions arising from the research described in the thesis (Sections 11.1 to 11.5). In addition, some recommendations for future work are also suggested (Section 11.6).

11.1 CONSTITUTIVE MODEL DEVELOPMENT

- The original Wheeler et al. (2003) model was extended to triaxial stress states, to include the influence of deviator stress q (see Section 3.6.3)
- A new bounding surface plasticity model was proposed for the water retention behaviour, to provide realistic modelling of scanning curve development and, if desired also the influence of void ratio on water retention behaviour (see Sections 4.3.2 and 4.3.3). This bounding surface plasticity

water retention model is suitable for use in combination with conventional mechanical models for unsaturated soils, such as the BBM.

- A bounding surface plasticity version of the fully coupled mechanical and water retention model of Wheeler et al. (2003) was developed (see Section 4.4).
- Simulation codes using Matlab software were developed for stress point simulations with the original elasto-plastic version of the Wheeler et al. (2003) model (WM), the new bounding surface plasticity version of the model (WM(BS)) and the conventional BBM (see Appendix).

11.2 EXPERIMENTAL EQUIPMENT AND PROCEDURES

11.2.1 Suction-controlled isotropic and triaxial cells

- The single steel-walled cell design used for suction-controlled isotropic and triaxial cells (Systems A and B) avoided the problem of water absorption which occurs with a double acrylic-walled cell. However, use of the steel-walled cells did mean that air bubbles trapped within cell during filling and any problem with sample set-up (e.g. whether the sample remained vertical) could not be observed.
- The dependency of apparent cell volume changes on cell pressure changes was slightly difficult to calibrate, because of hysteresis in the apparent cell volume variation during cell pressure increases and decreases (see Section 5.6.3).
- Both Systems A and B provided good quality experimental results, with reasonable repeatability (see Sections 8.1.2, 8.1.6 and 9.2.2).
- The experimental results from Systems A and B are comparable to each other (see Section 9.1).

11.2.2 Sample preparation technique

- 50 mm diameter samples of compacted Speswhite Kaolin were prepared by static compaction, as described in Section 6.2. The samples used for isotropic testing in System A were 50 mm in height, whereas the samples used for

triaxial testing in Systems B and C were 100 mm in height. The 100 mm height samples were compacted in 9 layers, whereas the 50 mm height samples were compacted in 5 layers. The 100 mm samples consistently showed slightly higher initial specific volume than 50 mm height samples (see Figure 7-1).

- The variation in the specific volume and the water content was ± 0.022 and $\pm 1.4\%$ respectively (see Section 7.1). Given that two different sets of samples were prepared, the repeatability of sample preparation technique was reasonable.

11.2.3 Experimental techniques

- A continuous loss of pressurised water from both the cell pressure line and the pore water pressure line was observed, due to diffusion of water through the nylon tubing. The nylon tubes were then replaced with Polytetrafluoroethylene (PTFE) tubes, which reduced the diffusion by about 80% (see Section 5.6.1).
- In order to determine the sample height at the start of the shearing in the triaxial cell the following procedure was followed. Immediately after setting up of a sample (of known height), the loading ram was lowered to just touch the top cap and the reading from the LVDT was recorded. The loading ram was then withdrawn to sufficient level to avoid any contact with the sample during the subsequent isotropic stages. For the shearing stage, the loading ram was lowered again to just touch the top cap and the reading from the LVDT was recorded. The difference in the two readings gave the change of sample height between setting up and start of shearing (see Section 6.3.4).

11.3 EXPERIMENTAL RESULTS (BASIC BEHAVIOUR)

11.3.1 Equalisation

- During initial equalisation, water flowed into the sample in all cases, meaning that the as-compacted suction was higher than 350 kPa, which was the maximum suction value applied during initial equalization (see Table 7-1).

- At a mean net stress of 10 kPa the values of specific volume at the end of initial equalisation at a saturated state or at 1 kPa suction were slightly lower than after equalisation at a suction of 30 kPa, suggesting that a small collapse compression might have occurred as suction was decreased below 30 kPa (see Table 7-1).
- The variability in specific volume, degree of saturation and specific water volume immediately after compaction was reduced by the equalisation process, particularly for degree of saturation and specific water volume (see Table 7-1).

11.3.2 Isotropic loading and unloading

- The yield stress observed during isotropic loading increased with increasing suction. Clear yield points were identified at low suction levels (e.g. Section 8.2.4), but at higher suction levels yielding was more gradual and post-yield curves (normal compression curves) were slightly non-linear (e.g. Section 8.1.2).
- The locus of initial yield stresses in the $s : \bar{p}$ plane closely matched the one determined for compacted Speswhite Kaolin samples by Wheeler and Sivakumar (1995) (see Figure 7-15), meaning that the sample preparation procedures used in this research produced very similar samples to those produced by Wheeler and Sivakumar (1995).
- The slope of constant suction normal compression lines $\lambda(s)$ increased with increasing suction. However, there was a suggestion that the value of $\lambda(s)$ levelled off or even decreased for suctions more than about 150 kPa. The variation of $\lambda(s)$ with suction was similar to that observed by Wheeler and Sivakumar (1995) (see Figure 7-14). However, the positions of the constant suction normal compression lines for different values of suction in the $v : \ln \bar{p}$ plane were slightly below those reported by Wheeler and Sivakumar (1995).

11.3.3 Wetting and drying

- For wetting and drying, a rate of suction increase/decrease of 1 kPa/hr was typically employed in the experimental programme. This rate was adequate

for all cases except during a wetting process involving collapse compression or wetting below 30 kPa suction.

- Wetting-drying cycles (e.g. Section 8.2.1) or drying-wetting cycles (e.g. Section 8.2.4) led to a net change in degree of saturation called hydraulic hysteresis.
- Drying from very low suction (as low as 1 kPa) showed some interesting features of water retention behaviour in the $S_r : \ln s$ plot (e.g. Section 8.2.4). A steepening of the curve at suctions between 20 kPa and 50 kPa was observed, followed by a gradual reduction in the slope. There was also a suggestion of another steepening at a suction of about 300 kPa. The large reduction in S_r between suctions of 20 kPa and 50 kPa could be associated with emptying of macro-voids, which were filled with water during a previous wetting stage. In order to re-fill these macro-voids with water, it seemed to be necessary to reduce the suction to less than 10 kPa. This observation is consistent with conclusions made by Sivakumar (2005).
- Wetting at a high degree of saturation (more than 0.85) generally produced a small change in degree of saturation compared to a drying stage over the same suction range. These relatively small increases in S_r during wetting at high values of S_r were probably due to the trapping of air within the samples in the form of occluded bubbles (e.g. Section 8.2.4).

11.3.4 Shearing

- During shearing at 0 and 200 kPa suction and radial net stress of 75 kPa, there was no visible evidence for a yield point in the $q : \epsilon_s$ plot, suggesting that the stress state of the samples might be on the LC yield surface at the start of shearing (see Figure 9-4 and Figure 9-36). However, pre-yield behaviour can be observed during the initial stage of shearing at constant suction of 300 kPa and radial net stress of 75 kPa (see Figure 9-11).

11.3.5 Calibration of models

- With the BBM it was impossible to select a single set of model parameter values to match the observed slopes and positions of the normal compression

lines for all suction values and the observed initial shape of the LC yield curve. Priority was given to matching the yield points rather than the positions of the normal compression lines (see Section 7.3.2).

- To determine the slope of the critical state line M^* in the $q : p^*$ plane for the WM, critical state points for both saturated and unsaturated samples were used, so that the average value of M^* could be obtained (see Section 7.4.5).

11.4 COUPLING OF MECHANICAL BEHAVIOUR AND WATER RETENTION BEHAVIOUR: EXPERIMENTAL RESULTS AND MODEL PREDICTIONS

In addition to standard stress paths, such as isotropic loading, unloading, wetting, drying and shearing, many non-standard stress path tests were also performed. These non-standard stress path tests produced a unique data set, providing evidence of aspects of behaviour never previously studied.

11.4.1 Influence of wetting and drying on isotropic loading

- A wetting-drying cycle produced a net increase of the degree of saturation and led to early yielding behaviour during subsequent isotropic loading. This feature of behaviour was consistent with the observation of Sharma (1998) and was captured by the WM (see Section 8.2.1).
- A drying-wetting cycle produced net reduction in degree of saturation and also led to early yielding during subsequent isotropic loading. The WM could not predict this feature of behaviour (see Section 8.2.2).

11.4.2 Wetting and drying

- The position of water retention curves in the $S_r : \ln s$ plane was influenced by changes of void ratio. An isotropic loading-unloading cycle which involved plastic volumetric strain shifted the water retention curve to higher suctions. However, there was typically no visible change in the overall shape of the water retention curve during this shift (see Figure 8-56 and Figure 8-65). There was a suggestion that water retention curves plotted in the

$v_w : \ln s$ plane were less affected by changes of void ratio (see Figure 8-57 and Figure 8-66).

- Irrecoverable volumetric strains occurred during most drying stages (although sometimes very small). However, volumetric strains during a drying stage were generally recoverable if the drying stage was preceded by a loading-unloading cycle involving plastic volumetric strain (see Section 8.2.3). This feature can be captured by the WM, as plastic volumetric strains occurring during drying and during isotropic loading are represented by yielding on a single LC yield curve.
- Irrecoverable volumetric strain and no indication of a yield point (suggesting plastic behaviour from the outset) occurred during a drying stage performed immediately after a wetting stage that involved collapse compression (see Section 9.3.1). This experimental observation is consistent with the WM predictions.
- Collapse compression occurred from the start of any a wetting stage preceded by an isotropic loading stage involving plastic volumetric strain, (see Section 9.3.1). This observation is consistent with both BBM and WM predictions.
- If irrecoverable volumetric strains occurred during a drying stage, this significantly reduced the suction at which collapse compression would commence during a subsequent wetting stage (see Section 8.1.6). This feature can be predicted by the WM.

11.4.3 Shearing

- In shearing stages performed at suctions of 200 or 300 kPa the initial shear stiffness was reduced by the occurrence of a previous wetting-drying cycle which produced a net increase of S_r (hydraulic hysteresis) but no net change of v . The occurrence of a previous wetting-drying cycle did not produce any significant change in the yield stress observed during shearing in the $v : \ln \bar{p}$ and $S_r : \ln \bar{p}$ plots but a slight increase was observed in the yield stress in the $q : \varepsilon_s$ plane (see Sections 9.2.1 and 9.2.2).

- A previous wetting-drying cycle (under isotropic stress states) had a significant influence on the critical state values of S_r and q . With an increase in the critical state value of degree of saturation there was an increase in the critical state value of deviator stress, suggesting that degree of saturation influences the shear strength in addition to suction and radial net stress. However, there was a suggestion that the critical state value of specific volume was uniquely dependent on suction and radial net stress i.e. independent of degree of saturation (see Section 9.2.2). With the model parameter values selected, the WM predicted unique critical state values of S_r , v and q for particular values of suction and radial net stress. However, the WM could in theory predict different values of S_r (and hence q) at critical states, by employing different parameter values, particularly a higher s_I^*/s_D^* ratio.
- Wetting and drying stages performed under anisotropic stress states seemed to produce complex effects on subsequent shearing stages and critical states. For a constant suction and constant radial net stress the values of deviator stress, specific volume and degree of saturation at critical states are significantly influenced by the previous wetting and drying stages under triaxial stress states (see Sections 9.3.1 and 9.3.2).

11.5 OVERALL PERFORMANCE OF WM AND WM(BS)

11.5.1 Elastic behaviour

- No firm conclusion could be reached on the validity of the elastic relationships proposed within the WM, which associate elastic volumetric strains exclusively with changes in p^* and elastic changes of S_r exclusively with changes of s^* . This was because of the susceptibility of the small measured changes of v and S_r to measurement errors or problems of experimental technique and because of the difficulty of ensuring that the stress path was entirely elastic (see Section 8.1.1).

11.5.2 Yield curves and flow rules

- There was some experimental evidence that the LC yield is inclined in the $s^* : p^*$ plane (see Section 10.2), rather than vertical, as assumed in the WM.
- The occurrence of a simultaneous yield point in the $S_r : \ln \bar{p}$ plane whenever a yield point was observed in the $v : \ln \bar{p}$ plane (e.g. See Section 8.1.3), suggested that yielding on the LC yield curve produced plastic changes of S_r as well as plastic volumetric strains. This suggests a non-associated flow rule on the LC yield curve if the LC yield curve is assumed to be a vertical line in the $s^* : p^*$ plane.
- The absence of yield points in most of the wetting curves in the $S_r : \ln s$ plane during wetting paths meant that it was not possible to investigate the shape of the SD yield curve. It was unclear whether this absence of yield points in the $S_r : \ln s$ plots during wetting stages represented a real weakness of the WM framework, or whether it was due to experimental difficulties associated with trapping of occluded air within samples during wetting at relatively high values of S_r .
- No particular test was performed in order to investigate the shape of the SI yield curve.
- The simultaneous occurrence of yield points in the $v : \ln s$ plane and in the $S_r : \ln s$ plane at the same value of s , during a typical drying stage suggests that the WM(BS) may better predict the mechanical and water retention behaviour than the WM during a typical drying stage.

11.5.3 Revised choice of some model parameter values

- Comparison of the WM predictions for water retention behaviour with the experimental results suggests that, in hindsight, a higher value for the ratio s_I^*/s_D^* than that used in the simulations would have resulted in better predictions (e.g. see Figure 8-43 and Figure 8-53).

- The value of λ_s selected for the WM simulations led to over-prediction of the experimental values of gradient in the $S_r : \ln s$ plane in most cases (e.g. see Figure 8-43 and Figure 8-53), and better predictions would probably have been achieved with a lower value of λ_s .

11.5.4 Inconsistency in the WM model

- A theoretical inconsistency of the WM and WM(BS) was identified. This inconsistency occurs if plastic volumetric strains are predicted at $S_r = 1$ or $S_r = 0$ (see Section 10.5).
- This theoretical inconsistency in the WM and WM(BS) can be avoided by putting $\kappa_s = 0$. Although this solution would provide unrealistic predictions in the WM (because of the absence of elastic changes of S_r), the assumption $\kappa_s = 0$ is less of a problem in the WM(BS), because plastic changes of S_r are predicted for all wetting and drying paths in the bounding surface plasticity version of the model.

11.6 RECOMMENDATIONS FOR FUTURE WORK

The experimental programme in this research has helped to provide a better understanding of unsaturated soil behaviour, particularly the coupling of mechanical behaviour and water retention behaviour. In addition, several proposals were made for new constitutive models or modifications of existing models. However, many issues regarding experimental technique, experimental results and constitutive models are yet to be addressed. In the following sections, some of the issues that were identified to be addressed in future research are set out.

11.6.1 Experimental technique

- During the calibration procedure, apparent changes in cell volume with cell pressure showed strong hysteresis during pressure increase and decrease (see Figure 5-20). This could be largely due to air trapped in the cell during the filling procedure. However, it was not possible to confirm this, as visual inspection inside cell was impossible because of the steel cell wall. Applying

a vacuum during filling of the cell might reduce the amount of any air trapped within the cell.

- There was a suggestion that occluded air was trapped within the soil samples during wetting at high degree of saturation. This would mean that proper equilibrium conditions were not achieved after that point i.e. the pore air pressure within the trapped air would not necessarily be equal to the pore air pressure applied at the sample boundary. To ensure full equilibration of pore air pressure once the pore air was discontinuous, extremely long test durations would be required, to allow equalisation by diffusion of dissolved air. The way in which the pore air pressure and pore water pressure were applied (pore water pressure applied through high air entry ceramic discs at both top and bottom of the sample whereas pore air pressure was applied only from the bottom of the sample through a sintered brass annulus) may have exacerbated the problem of trapped air during wetting. With water entering the sample from both top and bottom it is possible for large volumes of occluded air to be trapped in the central part of the sample by zones of high S_r above and below. This issue of large volume of trapped air might be reduced by reverting to a conventional system which uses single water drainage (from the bottom) and single air drainage (from the top), because the water front would then be advancing from a single end with air free to leave the sample from the other end. Controlled experiments should be performed using single and double pore water drainage systems to verify this issue.

11.6.2 Experimental results

- Drying from very low suction values produced a significant steepening of the $S_r : \ln s$ curve at a suction of about 20 kPa. There was a suggestion for another steepening at about 300 kPa suction, suggesting the presence of double porosity (see Figure 8-62). However, more experimental data covering a wider range of suction values is required to confirm the presence of the double steepening.
- A drying-wetting cycle resulted in a net decrease in the degree of saturation and led to early yielding during subsequent isotropic loading (see Section

8.2.2). This experimental evidence is against the physical explanation put forward by Wheeler et al. (2003) for early yielding after a wetting-drying cycle. Further experimental data is necessary to fully investigate this phenomenon.

11.6.3 Constitutive modelling

The Wheeler et al. (2003) model provided a good match to experimental results during some stress paths, particularly during isotropic loading and unloading (including the effects of previous wetting and drying) and a poorer match to experimental behaviour in some other cases, particularly during wetting and drying paths. Some of the predictions by the WM could be improved by modifying the specific mathematical forms of some of the equations in the model, giving more flexibility to the model. However, in order to incorporate some experimentally observed features of behaviour, modification at the framework level would be necessary. The following lists the features of behaviour that needs to be incorporated in a constitutive model and suggestions for the modifications.

- The experimental wetting curves in the $S_r : \ln s$ plane at high degree of saturation showed significantly lower gradient than the wetting curves predicted by the WM, and there was no suggestion of a yield point in the experimental $S_r : \ln s$ curves during wetting (see Figure 8-62). There may, however, have been experimental problems in achieving true equilibrium values of S_r during wetting at high degrees of saturation, because of the occurrence of trapped air (which could escape from the sample only by extremely slow diffusion of dissolved air). This issue should be explored experimentally by conducting a single wetting test at an extremely slow rate. The problem of trapped air could also be reduced by reverting to a system of water drainage from only one end of the sample. These issues should be fully explored experimentally before attempting to modify the constitutive model to better match the $S_r : \ln s$ wetting curves observed in the current experimental programme.
- If possible, the impact of the double porosity on the water retention curve should be incorporated within the water retention model proposed in the WM.

- After a drying-induced plastic volumetric strain, an elastic response was always observed during the initial part of subsequent isotropic loading or shearing. This is in contrast to WM predictions, which suggest that elasto-plastic volumetric strains occurring during drying correspond to yielding on the LC surface and yielding on this LC surface should continue immediately from the start of any subsequent isotropic loading or shearing. Three possible physical processes may explain this initial stiff elastic response of the sample during isotropic loading or shearing after the occurrence of drying-induced plastic volumetric strains.
 - a. The rate of changes of stresses imposed on samples may have been too high, so that the sample was not able to respond fully to the stress changes during the initial part of the isotropic loading or shearing. This problem could be solved by performing a test at adequately slow rate.
 - b. Saturated soil behaviour always shows temporary high stiffness after a significant change of stress path direction in the $q : p'$ plane (see Atkinson et al. 1990). It is therefore likely that the same phenomenon takes place in unsaturated soils if there is a significant change of stress path direction in $q : \bar{p} : s$ space.
 - c. Possible creep strains and ageing may harden the soil sample during the previous equalization stage, leading to apparent over-consolidation and therefore an initial stiff response during a subsequent isotropic loading or shearing stage.

The possible occurrence of these physical processes should be investigated and if necessary incorporated into the model.

- There were experimental indications that the LC yield curve should not be a vertical line in the $s^* : p^*$ plane, but a curve with positive gradient. There was no clear evidence for the shapes of SD and SI yield curves in the $s^* : p^*$ plane. More experimental evidence is necessary to explore this issue and modifications to the model might then be made.

- The non-associated flow employed on the LC yield surface of the WM for triaxial stress states did not provide a good prediction of shear strains. It is therefore desirable to replace it with an improved flow rule.
- The inconsistency in the WM and WM(BS) identified and discussed in Section 10.5 should be investigated further, to see whether this inconsistency can be removed by modifying the models in a more satisfactory manner than simply putting $\kappa_s = 0$.
- The Wheeler et al. (2003) model was proposed in terms of stress variables p^*, s^* and q , rather than in terms of \bar{p} , s and q , because of the following possible advantages: (1) simple uncoupled elastic behaviour for both mechanical and water retention behaviour; (2) simple yield curve shapes in the $s^* : p^*$ plane; (3) simple flow rules; (4) simple critical state relationship; (5) the ability to model coupling between mechanical and water retention behaviour. In this research, no firm conclusion could be made on whether all the above assumptions are valid. The experimental results do cast some doubts on each of the first 4 of these points. During future investigation of the model against experimental data, if it turns out that most of the 5 assumptions are not reasonably realistic, then it will probably be advisable develop a new framework in terms of \bar{p} , s and q rather than the more complex stress variables p^*, s^* and q .

REFERENCES

- Adams, B. A., Wulfsohn, D., and Fredlund, D. G. (1996). Air volume change measurement in unsaturated soil testing using a digital pressure-volume controller. *ASTM Geotechnical Testing Journal*, Vol.19 (1), pp. 12-21.
- Agus, S.S. and Schanz, T. (2005). An investigation into hydro-mechanical behaviour of an expansive soil using axis-translation and vapor equilibrium techniques. International symposium on Advanced Experimental Unsaturated Soil Mechanics-EXPERUS, pp. 53-60
- Aitchison, G.D. (ed.) (1965). Moisture equilibria and moisture changes in soils beneath covered areas. A symposium in print. Butterworths, Sydney, Australia.
- Al-Mukhtar, M., Beck, K., Van, T.T. and Vanapalli, S.K. (2006) Water Retention Characteristics of Two Limestones, Unsaturated Soils, *Proc. 4th Int. Conf. Unsaturated Soils*, Arizona Vol.2, pp. 1833-1844
- Alonso, E. E. (1998). Modeling expansive soil behavior. *Proc. 2nd Int. Conf. on Unsaturated Soils*, Beijing, Vol.2, 37–70.
- Alonso, E. E., Gens, A. and Gehling, W.Y.Yuk. (1994). Elastoplastic model for unsaturated expansive soils. *Numerical Methods in Geotechnical Engineering*, Smith (ed.), pp. 11-18
- Alonso, E. E., Gens, A. and Hight, D. W. (1987). Special problem soils. *General Rep. Proc., 9th European Conf. Soil Mechanics and Foundation Engineering*, Dublin, Vol. 3, pp.1087–1146.
- Alonso, E.E., Gens, A., Josa, A. (1990). A constitutive model for partially saturated soils. *Géotechnique*, Vol.40 (3), pp. 405-430.
- Alonso, E.E., Lloret, A., Gens, A. and Yang, D.Q., (1995). Experimental behaviour of highly expansive double-structure clay. *Proc. 1st Int. Conf. on Unsaturated Soils*, Paris, Vol. 1, pp. 11–16.

- Alonso, E.E., Vaunat, J. and Gens, A. (1999). Modelling the Mechanical Behaviour of Expansive Clays. *Engineering Geology*, Vol. 54, pp. 173-183.
- Al-Tabbaa, A. (1987). Permeability and stress–strain response of speswhite kaolin. *PhD thesis*, University of Cambridge, United Kingdom.
- Al-Tabbaa, A., and Muir Wood, D. (1989). An experimentally based ‘bubble’ model for clay. In *Numerical Models in Geomechanics: NUMOG III* (eds. S. Pietruszczak and G. N. Pande), London: Elsevier Applied Science, pp. 91–99.
- Atkinson, J.H., Richardson, D. and Stallebrass, S.E. (1990). Effect of recent stress history on the stiffness of overconsolidated soil. *Géotechnique*, Vol. 40(4), pp. 531-541.
- Atkinson, J. H. and Sallfors G. (1991). Experimental determination of soil properties. General Report to Session 1, *Proc. 10th ECSMFE*, Florence, Vol. 3, pp. 915–956.
- Atkinson, J.H. and Stallebrass, S.E. (1991). A model for recent stress history and non-linearity in the stress–strain behavior of overconsolidated soil, *Proc. of the Seventh IACMAG*, Cairns, pp. 555–560
- Barden, L. and Sides, G. R. (1970). Engineering behaviour and structure of compacted clay. *J. Soil Mech. Found. Engng ASCE* 96, Vol. SM4, pp. 1171–1201.
- Bardet, J. P. (1986). Bounding surface plasticity model for sands. *J. of Engineering Mechanics*, Vol. 112 (11), pp. 1198 - 1217.
- Barrera M. (2002). Estudio experimental del comportamiento hidro-mecánico de suelos colapsables. *Thesis doctoral*, Universitat Politecnica de Catalunya, Spain.
- Bishop, A. W. (1959). The principle of effective stress. *Teknisk Ukeblad*, Vol. 39, pp. 859–863.

- Bishop, A.W., Alpan, I., Blight, G.E. and Donald, I.B. (1960). Factors Controlling the Strength of Partly Saturated Cohesive Soils, *Proc. ASCE Research Conf. on Shear Strength of Cohesive Soils*, Boulder, pp. 503-532.
- Bishop, A. W. and Blight, G. E. (1963). Some aspects of effective stress in saturated and unsaturated soils. *Geotechnique*, Vol. 13, pp. 177–197.
- Bishop, A.W. and Donald, I.B. (1961). The experimental study of partly saturated soil in the triaxial apparatus. *Proceedings of the 5th International Conference on Soil Mechanics and Foundation Engineering*, Paris, Vol. 1, pp. 13–21.
- Bishop, A.W. and Henkel, D.J. (1962). The measurement of soil properties in triaxial test. (2nd ed.), Edward Arnold Limited, London.
- Bolzon, G., Schrefler, B. A. and Zienkiewicz, O. C. (1996). Elasto-plastic soil constitutive laws generalized to partially saturated states. *Geotechnique* Vol.46 (2), pp. 279–289.
- Borja, R.I. and Amies, A.P. (1994). Multiaxial cyclic plasticity model for clays. *J. Geotech Eng* Vol. 120(6), pp.1051–1070
- Brooks, R.H. and Corey, A.T. (1964). Hydraulic properties of porous media. *Hydrology Paper No.3*, Colorado State Univ., Fort Collins, CO.
- Brutsaert, W. (1966). Probability laws for pore size distribution. *Soil Science*, Vol.101, pp. 85-92.
- Buckingham, E. (1907). Studies on the movement of soil moisture. USDA, Bureau of Soils Bulletin No. 38
- Buisson, M. S. R (2002). Mechanical behaviour of unsaturated compacted clays during stress path involving wetting and drying cycles. *Internal Report*, University of Glasgow.
- Buisson, M. S. R. & Wheeler, S. J. (2000). Inclusion of hydraulic hysteresis in a new elasto-plastic framework for unsaturated soils. *Experimental evidence and*

- theoretical approaches in unsaturated soils* (eds. A. Tarantino and C. Mancuso), Rotterdam: Balkema, pp. 109– 119.
- Burland, J. B. (1965). Some aspects of the mechanical behaviour of partly saturated soils. *Moisture Equilibria and Moisture Changes in the Soils Beneath Covered Areas*, G. D. Aitchison, ed., Butterworth, Sydney, Australia, pp. 270–278.
- Burland, J.B. (1989). Ninth Lauritz Bjerrum Memorial Lecture: "Small is beautiful" - the stiffness of soils at small strains. *Canadian Geotechnical Journal*, Vol. 26, pp. 499-516.
- Chu, T. Y. and Mou, C. H. (1973). Volume change characteristic of expansive soils determined by controlled suction tests. *Proc. 3rd Int. Conf. on Expansive Soils*, Haifa, pp. 177–185.
- Clayton, C. R. I. and Heymann, G. (2001). Stiffness of geomaterials at very small strains. *Geotechnique*, Vol. 51(3), pp. 245-255
- Collins, IF, Boulbibane, M. (2000). Geomechanical analysis of unbound pavements based on shakedown theory. *Journal of Geotechnical and Geoenvironmental Engineering*. Vol. 126(1), pp. 50–59.
- Croney, D. (1952). The movement and distribution of water in soils. *Geotechnique*, Vol. 3(1), pp. 1–16.
- Croney, D. and Coleman, J.D. (1961). Pore pressure and suction in soils. *Proceedings, Conference on Pore Pressure and Suction in Soils*. Butterworths, London, pp. 31-37.
- Cui, Y.J. (1993). Etude du comportement d'un limon compacté non saturé et de sa modélisation dans un cadre élastoplastique. *PhD thesis*, Ecole Nationale des Ponts et Chaussées, Paris.
- Cui, Y.J. and Delage, P. (1996). Yielding and plastic behaviour of unsaturated compacted silt. *Géotechnique*, Vol. 46 (2), pp. 291-311.

- Dafalias, YF. (1975). On cyclic and anisotropic plasticity. *PhD thesis*, University of California, Berkeley.
- Dafalias, Y.F. and Herrmann, L.R. (1982). Bounding Surface Formulation of Soil Plasticity, *Soil Mechanics – Transient and Cyclic Loads*, G. Pande and O.C. Zienkiewicz, eds., John Wiley and Sons, Inc., London, pp. 253-282
- Dane, J.H. and Wierenga, P.J. (1975). Effect of hysteresis on the prediction of infiltration, redistribution and drainage of water in layered soil. *Journal of Hydrology*, Vol. 25, pp. 229–242.
- Dangla, P., Malinsky, L. and Coussy, O. (1997). Plasticity and imbibition-drainage curves for unsaturated soils: a unified approach. *Proc. 6th Int. Symp. Numer. Models Geomech. (NUMOG VI)*, Montreal, pp. 141–146.
- Datcheva, M. and Schanz, T. (2003). Anisotropic bounding surface plasticity with rotational hardening for unsaturated frictional materials, *Journal de Physique IV*, Vol.105, pp. 305-312.
- Delage, P. and Cui, Y.J. (2008). An evaluation of the osmotic method of controlling suction. *Geomechanics and Geoengineering: An International Journal* Vol.3 (1), pp. 1-11.
- Delage, P., Howat, M. and Cui, Y.J. (1998). The relationship between suction and swelling properties in a heavily compacted unsaturated clay. *Eng. Geology*, Vol. 50 (1-2), pp. 31-48.
- Delage, P., Suraj De Silva, G.P.R. and Vicol, T. (1992). Suction controlled testing of non saturated soils with an osmotic consolidometer. *7th Int. Conf. Expansive Soils*, Dallas, pp. 206-211.
- Diamond, S. (1970). Pore size distribution in clays. *Clays and Clay Minerals*, Vol.18, pp. 7-23.
- Dineen, K. and Burland, J.B. (1995). A new approach to osmotically controlled oedometer testing. *Proc. 1st Conf on Unsaturated Soils Unsat'95*, Paris, Balkema, Vol. 2, pp. 459-465.

- Dunlap, W.H. and Weber, J.A., (1971). Compaction of an unsaturated soil under a general state of stress. *Trans. ASAE*, Vol.14 (4), pp. 601–607
- Escario, V. (1980). Suction controlled penetration and shear tests. *Proc. 4th Int. Conf. on Expansive Soils*, Denver, Vol. 2, pp. 781–797.
- Escario, V. and Juca, J.F.T. (1989). Strength and Deformation of Partly Saturated Soils, *Proc. 12th Int. Conf. on Soil Mechanics and Foundation Engineering*, Rio de Janeiro, Vol. 1, pp. 43-46.
- Escario, V. and Saez, J. (1986). The Shear Strength of Partly Saturated Soils, *Géotechnique*, Vol. 36(3), pp. 453-456.
- Estabragh, A. R. and Javadi, A. A. (2008). Critical state for overconsolidated unsaturated silty soil, *Can. Geotech. J.* Vol. 45(3), pp. 408-420.
- Feng, M. and Fredlund, D.G. (1999). Hysteretic influence associated with thermal conductivity sensor measurements. *Proceedings from Theory to the Practice of Unsaturated Soil Mechanics in Association with the 52nd Canadian Geotechnical Conference and the Unsaturated Soil Group*, Regina, Sask., pp. 14:2:14–14:2:20.
- Fisher, R. A. (1926). On the capillary forces in an ideal soil: correction of formulae given by W. B. Haines. *J. Agric. Sc.* Vol. 16(3), pp. 492–505.
- Fredlund, D.G. (1975). A diffused air indicator for unsaturated soils, *Canadian Geotechnical Journal*. Vol. 12, pp. 533-539.
- Fredlund, D.G. (1979). Appropriate concepts and technology for unsaturated soils. *Canadian Geotechnical Journal*, Vol. 16(1), pp. 121–139.
- Fredlund, D.G. and Morgenstern, N.R. (1976). Constitutive relations for volume change in unsaturated soils. *Canadian Geotechnical Journal*, Vol.13 (3), pp. 261–276.
- Fredlund, D.G. and Morgenstern, N.R. (1977). Stress state variables for unsaturated soils. *ASCE Journal of Geotechnical Engineering*. Vol. 103(5), pp. 447-466.

- Fredlund, D.G., Morgenstern, N.R. and Widger, R.A. (1978). The shear strength of unsaturated soils. *Canadian Geotechnical Journal*, Vol.15, pp. 316-321.
- Fredlund, D.G., and Rahardjo, H. (1987). Soil mechanics principles for highway engineering in arid regions. *Transportation Research Board, Transport Research Record*, No. 1137, pp. 1-11.
- Fredlund, D.G. and Rahardjo, H. (1993). An Overview of Unsaturated Soil Behaviour, *Proceedings of ASCE Specialty Series on Unsaturated Soil Properties*, Dallas, TX, pp. 1-31.
- Fredlund, D.G., Vanapalli, S.K., Xing, A. and Pufahl, D.E. (1995). Predicting the Shear Strength Function for Unsaturated Soils Using the Soil-Water Characteristic curve, *Proc. First Int. Conf. on Unsaturated soils (I)*, Paris, International Academic Publishers, pp. 63-69
- Fredlund D.G and Xing, A.Q. (1994). Equations for the soil–water characteristic curve. *Canadian Geotech. Journal*, Vol. 31(4), pp. 521–532.
- Fredlund, D.G., Xing, A. and Huang, S. (1994). Predicting the permeability function for unsaturated soil using the soil–water characteristic curve. *Canadian Geotechnical Journal*. Vol.31, pp. 533–546.
- Gachet, P., Geiser, F., Laloui, L. and Vulliet, L. (2007) Automated Digital Image Processing for Volume Change Measurement in Triaxial Cells. *Geotechnical Testing Journal*, Vol. 30(2), pp. 98-103.
- Gallipoli, D. (2000). Constitutive and numerical modelling of unsaturated soils. *PhD thesis*, University of Glasgow, UK.
- Gallipoli, D., Gens, A., Chen, G. and D'Onza, F. (2008). Modelling unsaturated soil behaviour during normal consolidation and at critical state, *Computers and Geotechnics*, Vol. 35 (6), pp.825-834.
- Gallipoli, D., Gens, A., Sharma, R. S. and Vaunat, J. (2003b). An elasto-plastic model for unsaturated soil incorporating the effect of suction and degree of saturation on mechanical behaviour. *Geotechnique*, Vol. 53(1), pp. 123-135.

- Gallipoli, D., Wheeler, S. J. and Karstunen, M. (2003a). Modelling the variation of degree of saturation in a deformable unsaturated soil. *Geotechnique*, Vol. 53(1), pp. 105–112.
- Gan, J.K.M., and Fredlund, D.G. (1988). Multistage direct shear testing of unsaturated soils. *Geotechnical Testing Journal*, Vol. 11(2), pp. 132-138.
- Gardner, W. (1956). Mathematics of Isothermal Water Condition in Unsaturated Soils. Highway Research Board Special Report 40, *International Symposium on Physico-Chemical Phenomenon in Soils*. Washington D.C., pp.78-87.
- Geiser, F., Laloui, L., and Vulliet, L. (2000). On the volume measurement in unsaturated triaxial test. *Unsaturated soils for Asia*. Eds. H. Rahardjo, D.G. Toll, and E.C. Leong. A.A. Balkema, Rotterdam, The Netherlands, pp. 669–674.
- Gens, A. (1995). Constitutive laws. *Modern issues in non-saturated soils*, Wien: Springer-Verlag, pp. 129–158.
- Gens, A. and Alonso, E. E. (1992). A framework for the behaviour of unsaturated expansive clays. *Can. Geotech. J.* Vol. 29, pp. 1013–1032.
- Gens, A., Vaunat, J. and Ledesma, A. (1995). Analysis of hydration of an engineered barrier in a radioactive waste repository scheme using an elasto-plastic model. *Proc. 1st Int. Conf. Unsaturated Soils*, Paris, pp. 1065–1073.
- Haines, W.B. (1930). Studies in the physical properties of soil – V: The hysteresis effect in capillary properties and the modes of water distribution associated therewith. *Journal of Agricultural Science*, Vol. 20, pp. 97–116.
- Hanks, R.J., Klute, A. and Bresler, E. (1969). A numerical method for estimating infiltration redistribution, drainage, and evaporation of water from soil. *Water Resources Research*, Vol. (13), pp. 992–998.
- Harvey, E.N., Barnes, D.K., McElroy, W.D., Whiteley, A.H., Pease, D.C. and Cooper, K.W. (1944). Bubble formations in animal, 1-Physical Factor, *J. Cellular and Comparative Physiology*, 24(1), 1-22.

- Hashiguchi, K. (1985). Two- and three-surface models of plasticity. *Proc. 5th Int. Conf. on Numerical Methods in Geomechanics*, Nagoya, pp. 125-134.
- Hayashida, Y., Kohgo, Y., and Asano, I. (2003). A hysteresis model with continuity of tangential slopes of soil–water retention curves. *Proceedings of the 2nd Asian Conference on Unsaturated Soils*, Osaka, Japan, Edited by D. Karube, A. Iizuka, S. Kato, K. Kawai, and K. Tateyama. pp. 325–333.
- Hilf, J.W. (1956). An investigation of pore-water pressure in compacted cohesive soils. *Tech. Memo. 654*. U.S. Bureau of reclamation, Design and construction Div. Denver, USA.
- Hoffmann, C., Romero, E. and Alonso, E.E. (2005). Combining different suction controlled techniques to study the volume change response of expansive clays. *International symposium on Advanced Experimental Unsaturated Soil Mechanics-EXPERUS 2005*, pp. 61-67
- Houlsby, G. T. (1997). The work input to an unsaturated granular material. *Geotechnique* Vol. 47(1), pp. 193–196.
- Hueckel, T. and Nova, R. (1979). Some hysteresis effects of the behaviour of geological media, *Int. J. Solids Struct.* Vol. (15), pp. 625-642.
- Iwata, S., Tabuchi, T. and Warkentin, B.P. (1995). Soil-water interactions: mechanisms and applications. Marcial Dekker, NY., pp. 286–291.
- Jardine, R.J. (1985). Investigations of Pile-Soil Behaviour with Special Reference to the Foundations of Offshore Structures. *Ph.D. Thesis*, University of London, London
- Jardine, R.J. (1992). Some Observations on the Kinematic Nature of Soil Stiffness. *Soils and Foundations*, pp. 111-124
- Jardine, R.J., Lehane, B.M., Smith, P.R. and Gileda, P.A. (1995), Vertical loading experiments on rigid pad foundations at Bothkennar, *Geotechnique*, Vol. 45 (4), pp. 573-597.

- Jardine, R.J., Potts, D.M., Fourie, A. and Burland, J.B. (1986). Studies of the Influence of Non-Linear Stress-Strain Characteristics in Soil-Structure Interaction. *Geotechnique*, Vol. 36 (3), pp. 377-396
- Jardine, R.J., Potts, D.M., St. John, H.D., Hight, D.W. (1991). Some practical applications of a non-linear ground model. *Proc. X ECSMFE*, Florence, Vol.1, pp. 223-228
- Jennings, J. E. B. and Burland, J. B. (1962). Limitations to the use of effective stresses in unsaturated soils. *Geotechnique*, Vol.12, pp. 125–144.
- Jommi, C. (2000). Remarks on the constitutive modelling of unsaturated soils. *Proceedings of the international workshop on unsaturated soils*, Trento, pp. 139–153.
- Jommi, C. and Di Prisco, C. (1994). Un semplice approccio teorico per la modellazione del comportamento meccanico dei terreni granulari parzialmente saturi (in Italian). *In Atti Convegno sul Tema: Il Ruolo dei Fluidi nei Problemi di Ingegneria Geotecnica*, Mondovì, pp. 167–188.
- Juang, C.H. and Holtz, R.D. (1986). A probabilistic permeability model and the pore size density function. *International Journal of Numerical and Analytical Methods in Geomechanics*, Vol.10, pp. 543-553.
- Kassiff G. and Ben Shalom A. (1971). Experimental relationship between swell pressure and suction. *Géotechnique* Vol. 21, pp. 245-255.
- Kawai, K., Karube, D., and Kato, S. (2000). The model of water retention curve considering effects of void ratio. *Proceedings of Asian Conference on Unsaturated Soils*, Singapore. Edited by H. Rahardjo, D.G. Toll, and E.C Leong. A.A. Balkema, Rotterdam, The Netherlands. pp. 329–334.
- Khalili, N., Habte, M. and Valliappan S. (2005). A bonding surface plasticity model for cyclic analysis of sands, *Int. J. Num. Meth. Engng*, Vol. 63(14), pp. 1939-1960,

- Khalili, N. and Khabbaz, M. H. (1998). A unique relationship for χ for the determination of shear strength of unsaturated soils. *Geotechnique*, Vol. 48 (5), pp. 681–688.
- Klausner, Y. (1991). Fundamentals of continuum mechanics of soils. Springer-Verlag, New York.
- Kohgo, Y., Nakano, M. and Miyazaki, T. (1993a), Theoretical Aspects of Constitutive Modelling for Unsaturated Soils, *Soils and Foundations*, Vol. 33(4), pp. 49-63.
- Kohgo, Y., Nakano, M. and Miyazaki, T. (1993b) Verification of the Generalized Elastoplastic Model for Unsaturated Soils, *Soils and Foundations*, Vol. 33 (4), pp. 64-73.
- Kosugi, K. (1994). The parameter lognormal distribution model for soil water retention. *Water Resource Research*, Vol. 30, pp. 891-901.
- Lagerwerff, J.V., Ogata, G. and Eagle, H.E. (1961). Control of osmotic pressure of culture solutions with polyethylene glycol. *Science*, Vol.133, pp. 1486-1487.
- Leong, E. C. and Rahardjo, H. (1997a). Permeability functions for unsaturated soils. *J. Geotech. Geoenviron. Engng.* Vol. 123 (12), pp. 1118–1126.
- Leong, E. C. and Rahardjo, H. (1997b). Review of soil water characteristic curve equations, *Journal of Geotechnical and Geoenvironmental Engineering*. Vol. 123(12), pp. 1106-1117.
- Li, X.S. (2005). Modelling of hysteresis response for arbitrary wetting/drying paths. *Computers and Geotechnics*; Vol. 32 (2), pp. 133–137.
- Li, X. S. (2007a). Thermodynamics-based constitutive framework for unsaturated soils. 1: Theory. *Geotechnique*, Vol. 57 (5), pp. 423-436.
- Li, X. S. (2007b). Thermodynamics-based constitutive framework for unsaturated soils. 2: A basic triaxial model. *Geotechnique*, Vol. 57 (5), pp. 411-22.

- Liu, C. and Muraleetharan, K. (2006). Description of soil water characteristic curves using the bounding surface plasticity theory. *Unsaturated soils, Proc. 4th Int. Conf. Unsaturated Soils*, Arizona Vol. 2, 2432-2440.
- Lloret, A., and Alonso, E. (1985). State surface for partially saturated soils. *Proceedings of the 11th International Conference on Soil Mechanics and Foundation Engineering*, San Francisco, Calif., Vol. 2, pp. 557–562.
- Loret, B. and Khalili, N. (2000). A three phase model for unsaturated soils. *Int. J. Numer. Analyt. Meth. Geomech.*, Vol. 24(11), pp. 893–927.
- Luckner, L., Van Genuchten M. Th. and Nielsen, D. R. (1989). A consistent set of parameteric models for the flow of water and air as immiscible fluids in the subsurface. *Water Resource Res.* Vol. 25, pp. 2187-2189
- Maatouk, A., Leroueil, S. and La Rochelle, P. (1995). Yielding and critical state of a collapsible unsaturated silty soil. *Géotechnique*, Vol. 45, pp. 465-477.
- Macari, E.J., Parker, J.K. and Costes, N.C. (1997). Measurement of volume changes in triaxial tests using digital imaging techniques. *Geotechnical Testing Journal*, Vol. 20(1), pp. 103–109.
- Matyas, E. L. and Radhakrishna, H. S. (1968). Volume change characteristics of partially saturated soils. *Geotechnique*, Vol. 18, pp. 432–448.
- McKee, C. and Bumb, A. (1987). Flow-testing coalbed methane production wells in the presence of water and gas. *SPE Formation Evaluation*, pp. 599-608.
- Modaressi, A. and Abou-Bekr, N. (1994). A unified approach to model the behaviour of saturated and unsaturated soils. ed. Siriwardane, *Proc., 8th Int. Conf. on Computer Methods and Advances in Geomechanics*, Morgantown, Balkema, Rotterdam, pp. 1507–1513.
- Monroy, R., Ridley, A., Dineen K. and Zdrakovic L. (2007). The suitability of osmotic technique for the long term testing of partly saturated soils. *Geotechnical Testing Journal*, Vol. 30 (3), pp. 220-226.

- Mroz, Z., Norris, V. A. and Zienkiewicz, O. C. (1978). An anisotropic hardening model for soils and its application to cyclic loading. *Int. J. Numer. Anal. Meth. Geomech.*, Vol. 2, pp. 203 - 221.
- Mroz, Z., Norris, V. A. and Zienkiewicz, O. C. (1979). Application of an anisotropic hardening model in the analysis of elasto-plastic deformation of soils. *Géotechnique*, Vol. 29, pp. 1 - 34.
- Mualem, Y. (1974). A conceptual model of hysteresis. *Water Resources Research*, Vol. 10, pp. 514–520.
- Nageswaran, S. (1983). Effect of gas bubbles on the sea-bed behavior. *Ph.D. thesis*, Oxford University, Oxford, England.
- Néel, L. (1942). Théorie des lois d'aimantation de Lord Rayleigh, 1. *Cahiers de Physique*, Vol. 12, pp. 1–20.
- Néel, L. (1943). Théorie des lois d'aimantation de Lord Rayleigh, 2. *Cahiers de Physique*, Vol. 13, pp. 18–30.
- Ng, C.W. W., Zhan, L. T. and Cui, Y J. (2002). A New Simple System for Measuring Volume Changes in Unsaturated Soils. *Canadian Geotechnical Journal*, Vol. 39, pp. 757-764.
- Nuth, M. and Laloui, L. (2007). Implications of a generalized effective stress on the constitutive modelling of unsaturated soils. *Mechanics of unsaturated soils*, Weimar, Springer Proceedings in Physics, pp. 75-82.
- Pakzad, M. (1995). Modélisation du comportement hydro-mécanique des argiles gonflantes a faible porosité, Thèse de Doctorat, Université d'Orleans
- Pastor, M., Zienkiewicz, O.C. and Chan, A.H.C. (1990). Generalized plasticity and the modeling of soil behavior. *International Journal for Numerical and Analytical Methods in Geomechanics*, Vol. 14(3), pp. 151-190.
- Philip, J.R. (1964). Similarity hypothesis for capillary hysteresis in porous materials. *Journal of Geophysical Research*, Vol. 69, pp. 1553–1562.

- Poulovassilis, A. (1962). Hysteresis of pore water – an application of the concept of independent domains. *Journal of Soil Science*, Vol. 92, pp. 405–412.
- Prapaharan, S., White, D.M. and Altschaeffl, A.G. (1991). Fabric of field and laboratory compacted clay. *J. Geotech. Engrg.*, ASCE, Vol.117(12), pp. 1934-1940.
- Prevost, J. H. (1977). Mathematical modeling of monotonic and cyclic undrained clay behavior. *International Journal of Numerical Analysis Methods in Geomechanics*, Vol.1, pp. 195-216.
- Prevost, J. H. (1978). Plasticity theory for soil stress-strain behaviour. *Proc. ASCE, J. Engng Mech. Div.* Vol. 104, No. EM5, pp. 1177-1194.
- Proctor, R. R. (1933). Fundamental principles of soil compaction. Description of field and laboratory methods. *Engineering News Record*, Vol. 111, pp. 286-289.
- Puzrin, A.M. and Burland J.B. (1998). Nonlinear model of small strain behaviour of soils, *Geotechnique*, Vol. 48(2), pp. 217-233.
- Richards, B.G. (1965). Measurement of the free energy of soil moisture by the psychrometric technique using thermistors. *In Moisture equilibria and moisture changes in soils beneath covered areas. Edited by G.D. Aitchison.* Butterworth & Co. Ltd., Sydney, Australia, pp. 39-46.
- Ridley, A.M. and Burland, J.B. (1993). A new instrument for the measurement of soil moisture suction. *Géotechnique*, Vol. 43(2), pp. 321-324.
- Ridley, A. M. and Burland, J. B. (1999). Discussion: ‘Use of the tensile strength of water for the direct measurement of high soil suction’ by Guan & Fredlund. *Can. Geotech. J.* Vol. 36, pp. 178–180.
- Ridley, A.M. and Wray, W.K. (1995). Suction measurement: A review of current theory and practices. E.E. Alonso & P. Delage (Eds), *Unsaturated Soils, Proc. 1st Int. Conf. Unsaturated Soils*, Paris, Vol. 3, pp. 1293-1322.

- Romero, E. (1999). Characterisation and thermo-hydromechanical behavior of unsaturated Boom clay: an experimental study. *Ph.D. thesis*, Universitat Politècnica de Catalunya.
- Romero, E., Lloret, F., Gen, J.A., and Alonso, E.E. (1997). A new suction and temperature controlled triaxial apparatus. *Proceedings of the 14th International Conference on Soil Mechanics and Foundation Engineering*, Hamburg, Vol. 1, pp. 185–188.
- Romero, E. and Vaunat, J. (2000). Retention curves of deformable clays. *Experimental evidence and theoretical approaches in unsaturated soils* (eds. A. Tarantino and C. Mancuso), Rotterdam: Balkema, pp. 91–106.
- Russell, A.R. and Khalili, N. (2004). A bounding surface plasticity model for the behaviour of sands exhibiting particle crushing. *Canadian Geotechnical Journal*, Vol. 41, pp. 1179-1192.
- Russell, A.R. and Khalili, N. (2006). A unified bounding surface plasticity model for unsaturated soils. *International Journal of Numerical and Analytical Methods in Geomechanics*, Vol. 30(3), pp. 181-212.
- Sharma, R. S. (1998). Mechanical behaviour of unsaturated highly expansive clays. *PhD thesis*, University of Oxford, UK.
- Sharma, R. S. and Wheeler, S. J. (2000). Behaviour of an unsaturated highly expansive clay during cycles of wetting and drying. *Proceedings Asian conference on unsaturated soils*, Singapore, pp. 721–726.
- Sillers, W. S. (1997). The mathematical representation of the soil-water characteristic curve. *MSc. Thesis*, University of Saskatchewan.
- Sillers, W. S., Fredlund, D. G., and Zakerzadeh, N. (2001). Mathematical attributes of some soil-water characteristic curve models. *Geotechnical and Geological Engineering*, Vol. 19, pp. 243–283.

- Sills, G.C., and Nageswaran, S. (1984). Compressibility of gassy soils. *Proceedings of Oceanology International, Society for Underwater Technology*, Brighton, England, pp. OI 2.6/1–18.
- Sills, G.C., Wheeler, S.J., Thomas, S.D. and Gardner, T.N. (1991). The Behaviour of Offshore Soils containing Gas Bubbles. *Geotechnique*, Volume 41(2), pp. 227-241
- Sivakumar, R. (2005). Effects of anisotropy on the behaviour of unsaturated compacted clay. *Ph.D. thesis*, Queen's University, Belfast, U.K.
- Sivakumar, V. (1993). A critical state framework for unsaturated soil. *PhD thesis*, University of Sheffield, UK.
- Sivakumar, V. and Wheeler, S. J. (2000). Influence of compaction procedure on the mechanical behaviour of an unsaturated compacted clay. Part 1: Wetting and isotropic compression. *Geotechnique* Vol. 50(4), pp. 359–368.
- Slatter E.E., Allman A.A. and Smith D.W. (2000). Suction controlled testing of unsaturated soils with an osmotic oedometer. *Proc. Int. Conf. Geo-Eng*, Melbourne, Australia.
- Stallebrass, S. E. and Taylor, R. N. (1997). Prediction of ground movements in overconsolidated clay. *Géotechnique* Vol. 47(2), pp. 235–253.
- Stropeit, K., Wheeler, S.J. and Cui, Y.J. (2008). An anisotropic elasto-plastic model for unsaturated soils, Unsaturated soils: *Advances in Geo-Engineering, Proc. 1st European conf. for unsaturated soils*, Durham, pp. 625-631.
- Sun, D., Sheng, D.C., Cui, H.B. and J., Li. (2006). Effect of density on the soil-water-retention behaviour of compacted soil. Unsaturated soils. *Proc. 4th Int. Conf. Unsaturated Soils*, Arizona Vol. 2, pp. 1338-1347.
- Sun, D., and Xiang, L. (2007). An Elastoplastic Hydro-mechanical Model for Unsaturated Soils. *International Conference on Computational Science*, Vol.3, pp. 1138-1145

- Tabor, D. (1979). Gases, liquids and solids, 2nd ed. Cambridge University Press.
- Tamagnini, R. (2004). An extended Cam-Clay model for unsaturated soils with hydraulic hysteresis. *Géotechnique* Vol. 54(3), pp. 223–228.
- Tan, E. (2004). Analysis of Temperature and Soil Suction for the Purpose of Optimizing Road Bans in Saskatchewan. *Ph.D. thesis*. University of Saskatchewan, Canada.
- Tang, G.H., Graham, J., Blatz, J. Gray M. and Rajapakse, R.K.N.D. (2002). Suction, stresses and strengths in unsaturated sand-bentonite, *Engineering Geology*, Vol.64, pp. 147–156.
- Tarantino, A. (2007). A possible critical state framework for unsaturated compacted soils. Technical Note, *Géotechnique*, Vol. 57(4), pp. 385-389.
- Tarantino, A. and Mongiovi, L. (2000). Experimental investigations on the stress variables governing unsaturated soil behaviour at medium to high degrees of saturation. *Experimental Evidence and Theoretical Approaches in Unsaturated Soils, Proc. of an International Workshop*, Trento, Italy. Rotterdam: A. A. Balkema, pp. 3-20.
- Tarantino, A. and Tombolato, S. (2005). Coupling of hydraulic and mechanical behaviour in unsaturated compacted clay. *Géotechnique*, Vol. 55(4), pp. 307–317
- Terzaghi, K. (1936). The shearing resistance of saturated soils and the angle between the planes of shear. *Proc. 1st Int. Conf. Soil Mech. Found. Engng*, Cambridge, MA 1, 54–56.
- Thom, R., Sivakumar, R. and Sivakumar, V. (2006). Effects of Pressure on the Destruction of Bi-Modal Pore Size Distribution in Unsaturated Kaolin. *Proceedings of the Fourth International Conference on Unsaturated Soils*, Arizona, Vol. 2, pp. 1461-1472
- Toll, D.G., (1990). A framework for unsaturated soil behavior. *Géotechnique* Vol. 40(1), pp. 31–44.

- Toll, D.G. (2002). "Triax 4.3" user manual. *Geotechnical System Research*.
- Vachaud, G., Thony, J.L. (1971). Hysteresis during infiltration and redistribution in a soil column at different initial water contents. *Water Resour. Res.* Vol. 7, pp. 111-127.
- Van Genuchten, M. T. (1980). A closed-form equation for predicting the hydraulic conductivity of unsaturated soil. *Soil Sci. Soc. Am. J.* Vol. 44, pp. 892–898.
- Van Genuchten, M.Th., Leij, F.J. and Yates, S.R. (1991). The RETC code for quantifying the hydraulic functions of unsaturated soils. Rep. EPA/600/2–91/065. R.S. Kerr Environmental Research Laboratory, USEPA, Ada, OK.
- Van't Hoff, J. H. (1887). Die Rolle des osmotischen Druckes in der Analogie zwischen Lösungen und Gasen. *Zeitschr. physikal. Chem.* Vol.1, pp. 481-508.
- Vanapalli, S.K., Fredlund, D.G., Pufahl, D.E., and Clifton, A.W. (1996). Model for the prediction of shear strength with respect to soil suction. *Canadian Geotechnical Journal*, Vol. 33, pp. 379–392.
- Vanapalli, S.K., Pufahl, D.E. and Fredlund, D.G. (1999). The influence of soil structure and stress history on the soil-water characteristic of a compacted till. *Geotechnique*, Vol. 49(2), pp.143-159.
- Vanoudheusden, E., Sultan, N. and Cochonat, P. (2003). Hydro-mechanical behaviour of gassy soils. *Submarine mass movements and their consequences: 1st international symposium*, Kluwer academic publishers, Netherlands, pp. 145-153.
- Vaunat, J., Romero, E. and Jommi, C. (2000). An elasto-plastic hydro mechanical model for unsaturated soils. *In Experimental evidence and theoretical approaches in unsaturated soils* (eds. A. Tarantino and C. Mancuso), Rotterdam: Balkema, pp. 121–138.
- Waldron, L.J. and Manbeian, T. (1970). Soil moisture characteristics by osmosis with polyethylene glycol: a simple system with osmotic pressure data and some results. *Soil Science* Vol. 110 (6), pp. 401-404.

- Wan, A.W.L., Gray, M.N. and Graham, J., (1995). On the relations of suction, moisture content and soil structure in compacted clays. Editors: Alonso, E.E. and Delage, P., *Proc. 1st Int. Conf. on Unsaturated Soils*, Balkema/Presses des Ponts et Chaussées, Paris, Vol. 1, pp. 215–222.
- Wheeler, S.J. (1986). The stress-strain behavior of soils containing gas bubbles. *Ph.D. thesis*, Oxford University, Oxford, U.K.
- Wheeler, S.J. (1988a). A conceptual model for soils containing large gas bubbles. *Géotechnique*, Vol. 38(3), pp. 389–397.
- Wheeler, S.J. (1988b). The undrained shear strength of soils containing large gas bubbles. *Géotechnique*, Vol. 38 (3), pp. 399–413.
- Wheeler, S. J., Gallipoli, D. and Karstunen, M. (2002). Comments on use of the Barcelona basic model for unsaturated soils. *International journal for numerical and analytical methods in Geomechanics* Vol. 26(15), pp. 1561-1571.
- Wheeler, S. J. and Karube, D. (1995). Constitutive modelling. *Proc. 1st Int. Conf. Unsaturated Soils*, Paris Vol. 3, pp. 1323–1356.
- Wheeler, S.J., Näätänen, A., Karstunen, M. and Lojander, M. (2003). An anisotropic elasto-plastic model for natural soft clays. *Canadian Geotechnical Journal*, Vol. 40(2), pp. 403-418.
- Wheeler, S. J., Sharma, R. S. and Buisson, M. S. R. (2003). Coupling of hydraulic hysteresis and stress–strain behaviour in unsaturated soils. *Geotechnique*, Vol. 53(1), pp. 41-54
- Wheeler, S. J. and Sivakumar, V. (1995). An elasto-plastic critical state framework for unsaturated soil. *Geotechnique* Vol. 45(1), pp. 35–53.
- Wheeler, S. J. and Sivakumar, V. (2000). Influence of compaction procedure on the mechanical behaviour of an unsaturated compacted clay. Part 2: Shearing and constitutive modelling. *Geotechnique* Vol. 50(4), pp. 369–376.

- Whittle, A.J. (1993). Evaluation of a constitutive model for overconsolidated clays. *Géotechnique*, Vol. 43 (2), pp. 289-313.
- Yang, C., Cui, Y.J., Pereira, J.M. and Huang, M.S. (2008). A constitutive model for unsaturated cemented soils under cyclic loading. *Computers and Geotechnics*, Vol. 35, pp. 853-859.
- Zakaria, I. (1995). Yielding of unsaturated soil. *PhD thesis*, University of Sheffield, UK.
- Zienkiewicz, O.C. and Mroz Z. (1984), Generalized plasticity formulation and application to geomechanics. *Mechanics of Engineering Materials*, C.S. Desai and R.H. Gallagher, Eds, John Wiley and Sons, pp. 655-680.
- Zur B. (1966). Osmotic control the matrix soil water potential. *Soil Science*, Vol. 102, pp. 394-398.

APPENDIX

PROCEDURES FOR SIMULATIONS WITH THE MODELS

In this research many elaborate isotropic and triaxial stress path tests were performed using Systems A and B respectively. The experimental results from these tests were required to be compared against three constitutive models (WM, WM(BS) and BBM) in order to investigate their strengths and weaknesses. Because of the complex nature of stress paths and number of constitutive models involved, it was necessary to develop a comprehensive program using Matlab in order to perform simulations efficiently. In this Appendix the equations for calculation of incremental quantities are first presented for all three models (Section A.1), followed with a section (Section A.2) explaining the procedures employed for the simulations with all three models.

A.1 CALCULATION OF INCREMENTAL QUANTITIES FOR THE SIMULATIONS

In this section simultaneous equations (which contain incremental quantities) relevant to each model for specified conditions (e.g. yielding on the LC surface) are presented. The unknown incremental quantities were determined by solving these equations by specifying the required number of known incremental quantities. For example, a particular model can be described by m simultaneous equations for a specified condition. The number of unknown incremental quantities is $n(> m)$. It is therefore possible to solve the m simultaneous equations for m unknown incremental quantities if the values of $n - m$ incremental quantities are specified.

A.1.1 The WM

The general equations for the WM are given below.

$$d\mathbf{p}^* = d\bar{p} + S_r ds + s dS_r \quad (\text{A. 1})$$

$$ds^* = \frac{(v-1)}{v} ds - \frac{s}{v} d\varepsilon_v \quad (\text{A. 2})$$

$$d\varepsilon_v^e = \frac{\kappa}{v} \frac{dp^*}{p^*} \quad (\text{A. 3})$$

$$d\varepsilon_v^p = \frac{(\lambda - \kappa)}{v(1 - k_1 k_2)} \left(\frac{dp_0^*}{p_0^*} - k_1 \frac{ds_{I/D}^*}{s_{I/D}^*} \right) \quad (\text{A. 4})$$

$$d\varepsilon_v = d\varepsilon_v^e + d\varepsilon_v^p \quad (\text{A. 5})$$

$$-dS_r^e = \frac{\kappa_s ds^*}{s^*} \quad (\text{A. 6})$$

$$-dS_r^p = \frac{(\lambda_s - \kappa_s)}{(1 - k_1 k_2)} \left(\frac{ds_{I/D}^*}{s_{I/D}^*} - k_2 \frac{dp_0^*}{p_0^*} \right) \quad (\text{A. 7})$$

$$-dS_r = -dS_r^e - dS_r^p \quad (\text{A. 8})$$

$$d\varepsilon_s^e = \frac{dq}{3G} \quad (\text{A. 9})$$

$$d\varepsilon_s^p = \frac{2q\alpha}{M^{*2}(2p^* - p_0^*)} d\varepsilon_v^p \quad (\text{A. 10})$$

$$d\varepsilon_s = d\varepsilon_s^e + d\varepsilon_s^p \quad (\text{A. 11})$$

In the above 11 equations, 16 incremental quantities can be found. If any three incremental quantities (e.g. $d\bar{p}$, ds and dq) are specified, this leaves 13 unknown incremental quantities (shown with bold font), and therefore two further equations are required, in addition to Equations A.1 –A.11. The nature of these two further equations depends upon whether yielding is occurring, and if so on which yield surfaces. The two additional equations are selected from:

$$d\varepsilon_v^p = 0 \quad (\text{A. 12})$$

$$dS_r^p = 0 \quad (\text{A. 13})$$

$$dp_0^* = \frac{(2q/M^{*2})dq + (2p^* - p_0^*)dp^*}{p^*} \quad (\text{A. 14})$$

$$\frac{ds_{I/D}^*}{s_{I/D}^*} = \frac{ds^*}{s^*} \quad (\text{A. 15})$$

For elastic behaviour, the two additional equations are Equations A.12 and A.13. For yielding on the LC yield surface alone, Equations A.13 and A.14 are selected, whereas for yielding on the SI or SD surface alone, Equations A.12 and A.15 are selected. Finally for yielding simultaneously on the LC surface and on the SI or SD surface, Equations A.14 and A.15 are selected.

While the soil is in a saturated state both elastic and plastic increments of degree of saturation are set to zero. Equation A.13 therefore applies and Equation A.6 is replaced by:

$$dS_r^e = 0 \quad (\text{A. 16})$$

The final equation when the soil is saturated is either Equation A.12 (if the behaviour is elastic) or Equation A.14 (if yielding is occurring on the LC yield surface). As the soil first arrives at a saturated state it will often be on the SD yield surface. However, while it remains saturated Equation A.15 no longer applies. While the soil is saturated the value of s^* may be less than the value of s_D^* i.e. the stress state can lie below the SD yield curve in the $s^* : p^*$ plane. The saturated version of the equations should be used if $S_r = 1$ and if either $ds^* < 0$ or $s^* < s_D^*$ (or both). If s^* subsequently becomes equal to or greater than s_D^* , an increase of s^* will lead to the soil becoming unsaturated again, with the set of equations reverting to the standard form.

A.1.2 The WM (BS)

The general equations for the WM(BS), for isotropic stress states, are given below.

$$dp^* = d\bar{p} + S_r ds + s dS_r \quad (\text{A. 17})$$

$$ds^* = \frac{(v-1)}{v} ds - \frac{s}{v} d\varepsilon_v \quad (\text{A. 18})$$

$$d\varepsilon_v^e = \frac{\kappa}{v} \frac{dp^*}{p^*} \quad (\text{A. 19})$$

$$d\varepsilon_v^p = \frac{R_p(\lambda - \kappa)}{v} \left(\frac{dp^*}{p^*} - \frac{k_1}{(\lambda_s - \kappa_s)} (-dS_r^p) \right) \quad (\text{A. 20})$$

$$d\varepsilon_v = d\varepsilon_v^e + d\varepsilon_v^p \quad (\text{A. 21})$$

$$-dS_r^e = \frac{\kappa_s ds^*}{s^*} \quad (\text{A. 22})$$

$$-dS_r^p = R_s(\lambda_s - \kappa_s) \left(\frac{ds^*}{s^*} - \frac{k_2 v}{(\lambda - \kappa)} d\varepsilon_v^p \right) \quad (\text{A. 23})$$

$$-dS_r = -dS_r^e - dS_r^p \quad (\text{A. 24})$$

$$\frac{dp_0^*}{p_0^*} = \frac{v}{\lambda - \kappa} d\varepsilon_v^p + \frac{k_1}{\lambda_s - \kappa_s} (-dS_r^p) \quad (\text{A. 25})$$

$$\frac{ds_{I/D}^*}{s_{I/D}^*} = \frac{-dS_r^p}{\lambda_s - \kappa_s} + \frac{k_2 v}{\lambda - \kappa} d\varepsilon_v^p \quad (\text{A. 26})$$

The scaling functions R_p and R_s are defined by:

$$R_p = \left(\frac{p^*}{p_0^*} \right)^f \quad \text{for} \quad \frac{dp^*}{p^*} > \frac{k_1}{(\lambda_s - \kappa_s)} (-dS_r^p) \quad (\text{A. 27})$$

$$R_p = 0 \quad \text{for} \quad \frac{dp^*}{p^*} < \frac{k_1}{(\lambda_s - \kappa_s)} (-dS_r^p) \quad (\text{A. 28})$$

$$R_s = \left(\frac{s^*}{s_I} \right)^g \quad \text{for} \quad \frac{ds^*}{s^*} > \frac{k_2 v}{(\lambda - \kappa)} d\varepsilon_v^p \quad (\text{A. 29})$$

$$R_s = \left(\frac{s_D^*}{s^*} \right)^g \quad \text{for} \quad \frac{ds^*}{s^*} < \frac{k_2 v}{(\lambda - \kappa)} d\varepsilon_v^p \quad (\text{A. 30})$$

In the above 10 equations (Equations A.17- A.26), 12 incremental quantities can be found. It is therefore possible to solve these equations for 10 unknown incremental quantities (typically those shown in bold font) if any two incremental quantities are specified (typically $d\bar{p}$ and ds).

While the soil is saturated, Equations A.22 and A.23 are replaced by:

$$dS_r^e = 0 \quad (\text{A. 31})$$

$$dS_r^p = 0 \quad (\text{A. 32})$$

Again, while the soil is saturated the stress state may lie below the SD bounding curve in the $s^* : p^*$ plane ($s^* < s_D^*$). The saturated version of the equations should be used if $S_r = 1$ and if either $ds^* < 0$ or $s^* < s_D^*$ (or both). If s^* subsequently becomes equal to or greater than s_D^* , an increase of s^* will lead to the soil becoming unsaturated again, with the set of equations reverting to the standard form.

A.1.3 The BBM

General constitutive equations for the BBM are given below.

$$d\varepsilon_v^e = \frac{\kappa}{v} \frac{d\bar{p}}{\bar{p}} + \kappa_s \frac{ds}{(s + p_{atm})} \quad (\text{A. 33})$$

$$d\varepsilon_v^p = (\lambda(0) - \kappa) \frac{dp_0(0)}{vp_0(0)} \quad (\text{A. 34})$$

$$d\varepsilon_v = d\varepsilon_v^e + d\varepsilon_v^p \quad (\text{A. 35})$$

$$d\boldsymbol{\varepsilon}_s^e = \frac{dq}{3G} \quad (\text{A. 36})$$

$$d\boldsymbol{\varepsilon}_s^p = \frac{2q\alpha}{M^2(2\bar{p} + ks - \bar{p}_0)} d\boldsymbol{\varepsilon}_v^p \quad (\text{A. 37})$$

$$d\boldsymbol{\varepsilon}_s = d\boldsymbol{\varepsilon}_s^e + d\boldsymbol{\varepsilon}_s^p \quad (\text{A. 38})$$

$$d\lambda(s) = -\lambda(0)\beta(1-r)e^{(-\beta s)} ds \quad (\text{A. 39})$$

$$\ln\left(\frac{\bar{p}_0}{p^c}\right) d\lambda(s) = (\lambda(0)-\kappa) \frac{dp_0(0)}{p_0(0)} - (\lambda(s)-\kappa) \frac{d\bar{p}_0}{\bar{p}_0} \quad (\text{A. 40})$$

In the above 8 equations (Equations A.33-A.40) 12 incremental quantities can be found. If any three incremental quantities (e.g. $d\bar{p}$, ds and dq) are specified, this leaves 9 unknown incremental quantities (shown with bold font), and therefore one more equation is required, in addition to Equations A.33-A.40, to solve for the unknown incremental quantities. The nature of this additional equation depends upon whether behaviour is elastic or yielding on LC surface is occurring.

For elastic behaviour the additional equation is given by:

$$d\boldsymbol{\varepsilon}_v^p = 0 \quad (\text{A. 41})$$

For yielding on the LC yield surface the additional equation is given by:

$$d\bar{p}_0 = \frac{(2q/M^2)dq + (2\bar{p} + ks - \bar{p}_0)d\bar{p} - (\bar{p}_0 - \bar{p})kds}{(\bar{p} + ks)} \quad (\text{A. 42})$$

A.2 CALCULATION PROCEDURES

A.2.1 The WM

Figure A.1 shows the flow chart for the WM simulations performed using Matlab. Firstly, the values of model parameters and initial conditions are obtained from a data file. The type of stage (e.g. wetting) is then selected and corresponding values of three

known incremental quantities are specified for the first increment. In the next step, the unknown incremental quantities are calculated using the simultaneous equations provided in Section A.1.1 for all 8 different cases i.e. (1) elastic behaviour, (2) yielding on LC yield surface only, etc. The next step involves checking, for each of the 8 different cases, whether the values calculated for the various incremental quantities are consistent with this particular case. This involves checking 8 different conditions, which are described in detail later in this section. If the checks show that one and only one of the conditions is satisfied, then this defines unambiguously which one of the 8 possible cases applies. However, because of the finite size of increments it is possible that more than one condition is satisfied. For example, at the end of an increment it is possible that conditions for “yielding on the LC surface only” and “yielding on SI and LC surfaces simultaneously” are both satisfied. If this happens then the increment sizes are reduced (see Figure A.1) and the procedure is repeated until only one condition is satisfied. Once only one of the 8 conditions is satisfied then incremental quantities are added to the respective values of variables. The program then moves on to the next increment. This procedure is repeated until the required stress path simulation is completed.

When assuming “elastic behaviour”, with soil unsaturated, Equations A.1 to A.13 are used and Condition 1 that must be checked has the following 3 parts:

$$\frac{(q + dq)^2}{M^2(p^* + dp^*)} + (p^* + dp^*) \leq p_0^* \quad \& \quad (s^* + ds^*) \geq s_D^* \quad \& \quad (s^* + ds^*) \leq s_I^*$$

These 3 parts of Condition 1 must all be satisfied, and each one involves checking that the final stress point (at the end of the increment) does not lie outside one of the yield surfaces (with the yield surface in the position it was in at the start of the increment).

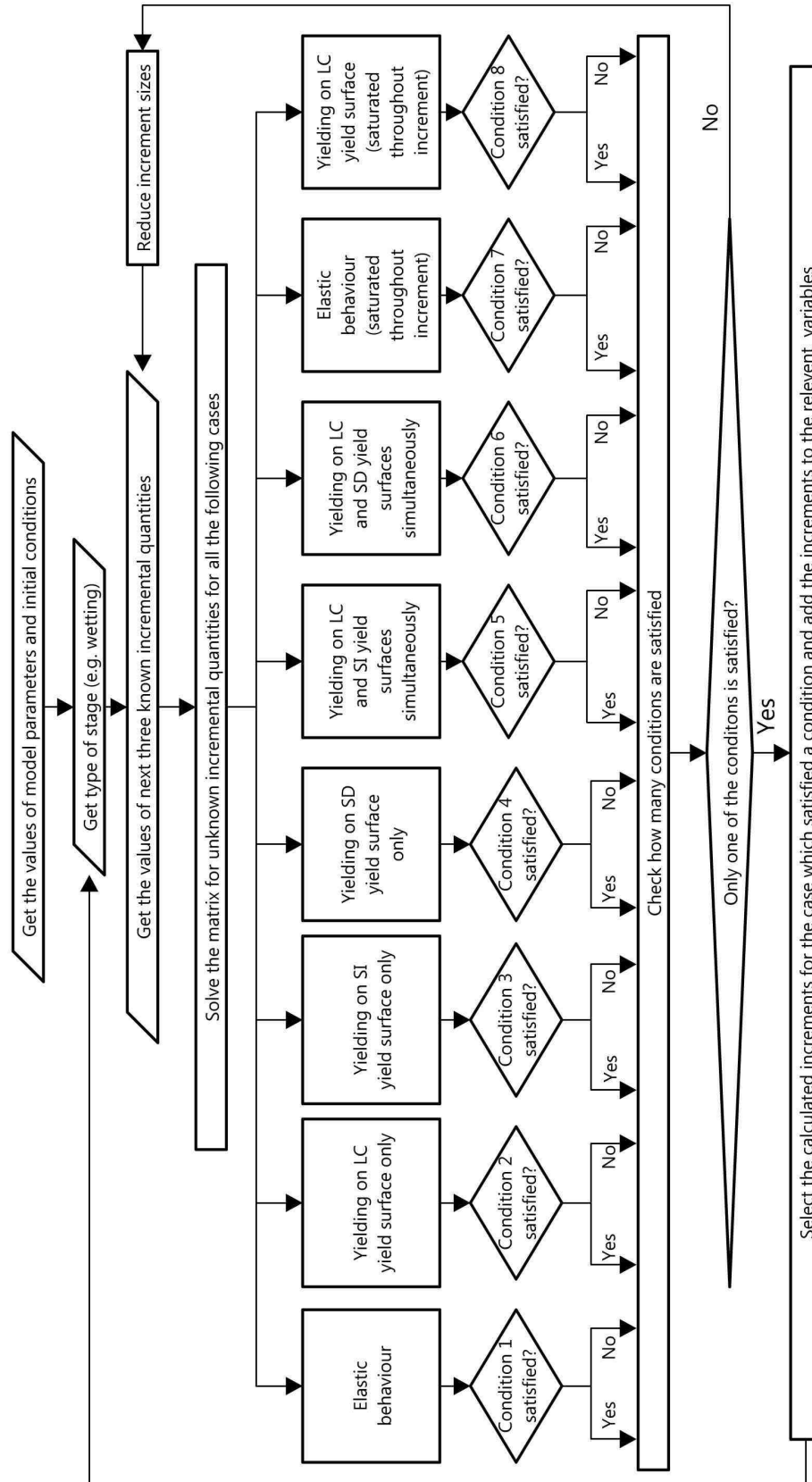


Figure A.1 Flowchart for the WM simulations

When assuming “yielding on LC yield surface only”, with soil unsaturated, Equations A.1 to A.11, A.13 and A.14 are used and Condition 2 that must be checked has the following 3 parts:

$$\frac{(q + dq)^2}{M^{*2}(p^* + dp^*)} + (p^* + dp^*) > p_0^* \quad \& \quad (s^* + ds^*) \geq s_D^* + k_2 \frac{vd\varepsilon_v^p}{\lambda - \kappa} s_D^*$$

$$\& \quad (s^* + ds^*) \leq s_I^* + k_2 \frac{vd\varepsilon_v^p}{\lambda - \kappa} s_I^*$$

These 3 parts of Condition 2 must all be satisfied. The first part of equations checks whether the final stress point (at the end of the increment) lies outside the LC yield surface (with the LC yield surface in the position it was in at the start of increment). The second part of the condition checks (assuming yielding occurring only on the LC yield surface) that the final stress point is inside the SD yield surface after adding the coupled movement of the SD yield surface (due to yielding on the LC surface). Similarly, the final part of the condition checks whether the final stress point is inside the SI yield surface after adding the coupled movement of the SI yield surface.

When assuming “yielding on SI yield surface only” Equations A.1 to A.11, A.12 and A.15 are used and Condition 3 that must be checked has the following two parts to be satisfied:

$$(s^* + ds^*) > s_I^* \quad \& \quad \frac{(q + dq)^2}{M^{*2}(p^* + dp^*)} + (p^* + dp^*) \leq p_0^* + k_1 \left(\frac{-dS_r^p}{\lambda_s - \kappa_s} \right) p_0^*$$

The first part of the condition checks whether the final stress point lies outside the position of the SI yield surface at the start of increment. The second part of the condition checks whether the final stress point lies inside the LC yield surface after adding the coupled component of movement of the LC yield surface (due to yielding on the SI yield surface).

When assuming “yielding on SD yield surface only” Equations A.1 to A.11, A.12 and A.15 are used and Condition 4 that must be checked has the following three parts to be satisfied:

$$S_r < 1 \ \& \ (s^* + ds^*) < s_D^* \ \& \ \frac{(q + dq)^2}{M^{*2}(p^* + dp^*)} + (p^* + dp^*) \leq p_0^* + k_1 \left(\frac{-dS_r^p}{\lambda_s - \kappa_s} \right) p_0^*$$

The first part of the condition checks whether soil is unsaturated. The second part of the condition checks whether the final stress point lies outside the position of the SD yield surface at the start of increment. The final part of the condition checks whether the final stress point lie inside the LC yield surface after adding the coupled component of movement of the LC yield surface (due to yielding on the SD yield surface).

When assuming “yielding on SI and LC yield surfaces simultaneously” Equations A.1 to A.11, A.14 and A.15 are used and Condition 5 that must be checked has the following two parts to be satisfied:

$$\frac{(q + dq)^2}{M^{*2}(p^* + dp^*)} + (p^* + dp^*) > p_0^* + \frac{k_1}{(\lambda_s - \kappa_s)} (-dS_r^p) p_0^*$$

$$\& \ (s^* + ds^*) > s_I^* + \frac{k_2 v}{(\lambda - \kappa)} d\varepsilon_v^p s_I^*$$

The first part of the condition checks whether the final stress point lies outside the position of the LC yield surface after adding the coupled component of movement of the LC yield surface (due to yielding on the SI yield surface). The second part of the condition checks whether the final stress point lies outside the SI yield surface after adding the coupled component of movement of the SI yield surface (due to yielding on the LC yield surface).

When assuming “yielding on SD and LC yield surfaces simultaneously” Equations A.1 to A.11, A.14 and A.15 are used and Condition 6 that must be checked has the following three parts to be satisfied:

$$S_r < 1 \ \& \ \frac{(q + dq)^2}{M^{*2}(p^* + dp^*)} + (p^* + dp^*) > p_0^* + \frac{k_1}{\lambda_s - \kappa_s} (-dS_r^p) p_0^*$$

$$\& \ (s^* + ds^*) < s_D^* + \frac{k_2 v}{\lambda_s - \kappa_s} d\varepsilon_v^p s_D^*$$

The first part of the condition checks whether soil is unsaturated. The second part of the condition checks whether the final stress point lies outside the position of the LC yield surface after adding the coupled component of movement of the LC yield surface (due to yielding on the SD yield surface). The final part of the condition checks whether the final stress point lies outside the SD yield surface after adding the coupled component of movement of the SD yield surface (due to yielding on the LC yield surface).

When assuming “elastic behaviour with soil saturated”, Equations A.1- A.5, A.7 –A.13 and A.16 are used and Condition 7 that must be checked has the following 3 parts to be satisfied:

$$S_r \geq 1 \ \& \ (ds^* < 0 \ \text{or} \ (s^* + ds^*) \leq s_D^*) \ \& \ \frac{(q + dq)^2}{M^{*2}(p^* + dp^*)} + (p^* + dp^*) \leq p_0^*$$

The first part of the condition checks whether the soil is saturated. The second part of the condition checks whether the soil remains saturated (either because $ds^* < 0$ or because the final stress point lies outside the position of the SD yield surface at the start of increment). The final part of the condition checks whether the final stress point lies inside the LC yield surface at the start of increment.

When assuming “Yielding on LC surface with soil saturated”, Equations A.1- A.5, A.7 –A.11, A.13, A.14 and A.16 are used and Condition 8 that must be checked has the following 3 parts to be satisfied:

$$. \ S_r \geq 1 \ \& \ (ds^* < 0 \ \text{or} \ (s^* + ds^*) \leq s_D^*) \ \& \ \frac{(q + dq)^2}{M^{*2}(p^* + dp^*)} + (p^* + dp^*) > p_0^*$$

The first part of the condition checks whether the soil is saturated. The second part of the condition checks whether the soil remains saturated (either because $ds^* < 0$ or because the final stress point lies outside the position of the SD yield surface at the start of increment). The final part of the condition checks whether the final stress point lies outside the LC yield surface at the start of increment.

A.2.2 The WM(BS)

Figure A.2 shows the flow chart for the WM(BS) simulations performed using Matlab. Firstly, the values of model parameters and initial conditions are obtained from a data file. The type of stage (e.g. wetting) is then specified and corresponding values of two unknown incremental quantities are specified for the first increment. In the next step, the unknown incremental quantities are calculated using the simultaneous equations provided in Section A.1.2 for 6 different cases. Next, for each of these 6 different cases, the relevant condition is checked (these conditions are described in detail later in this section). If more than one condition is satisfied then the increment sizes are reduced (see Figure A.2) and the procedure is repeated until only 1 condition is satisfied. Once only one of the 6 conditions is satisfied then incremental quantities are added to the respective values of variables at the start of increment. The program then moves on to the next increment. This cycle goes on until the required stress path simulation is completed.

When assuming “stress point moving away from LC bounding curve and towards SI bounding curve” Equations A.17 to A.26 are used, with R_p and R_s given by Equations A.28 and A.29 respectively, and Condition 1 that must be checked has the following two parts to be satisfied:

$$\frac{dp^*}{p^*} < k_1 \left(\frac{-dS_r^p}{\lambda_s - \kappa_s} \right) \quad \& \quad \frac{ds^*}{s^*} > k_2 \left(\frac{vd\varepsilon_v^p}{\lambda - \kappa} \right)$$

The first part of the condition checks whether the stress point is moving away from the LC bounding curve. The second part of the condition checks whether the stress point is moving towards the SI bounding curve.

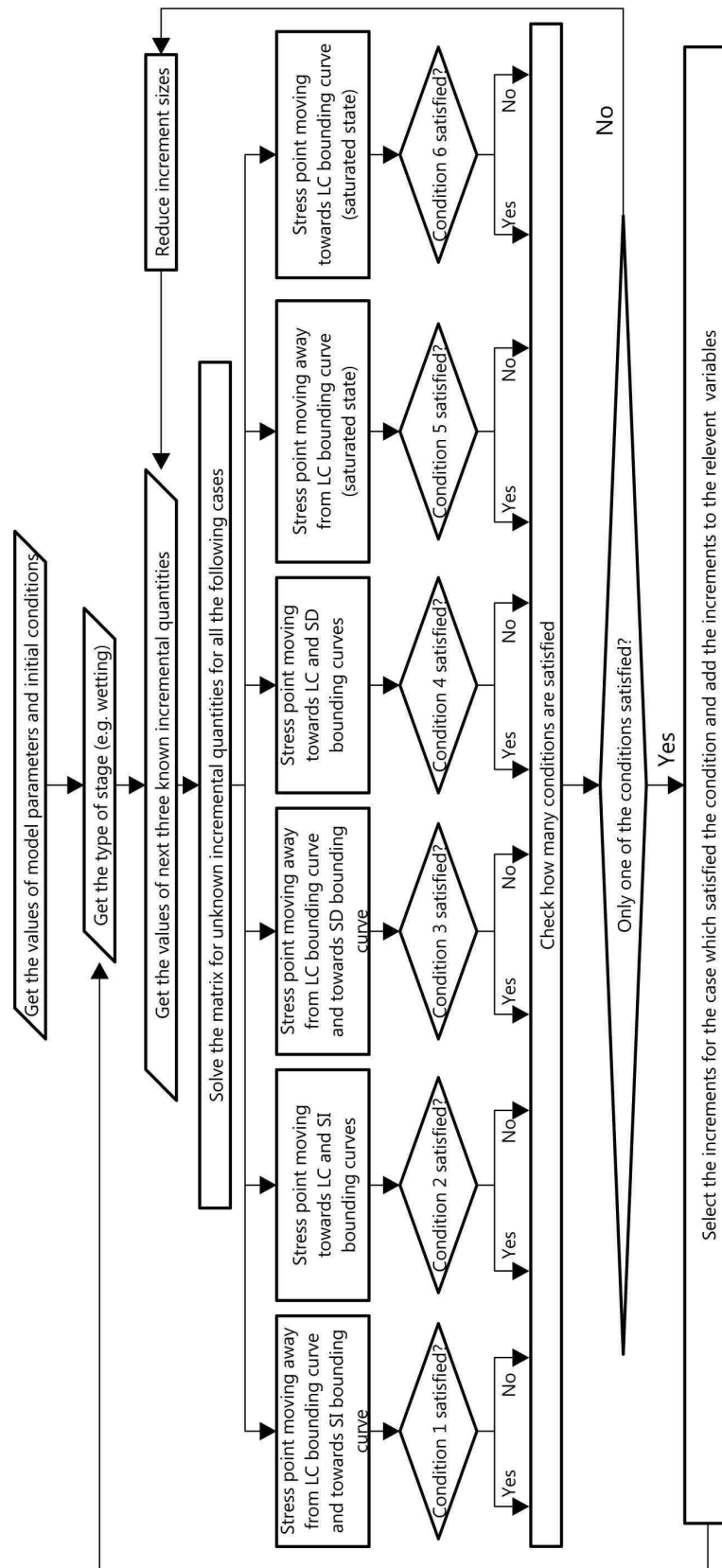


Figure A.2 Flowchart for the WM(BS) simulations

When assuming “stress point moving towards LC and SI bounding curves” Equations A.17 to A.26 are used, with R_p and R_s given by Equations A.27 and A.29 respectively, and Condition 2 that must be checked has the following two parts to be satisfied:

$$\frac{dp^*}{p^*} > k_1 \left(\frac{-dS_r^p}{\lambda_s - \kappa_s} \right) \ \& \ \frac{ds^*}{s^*} > k_2 \left(\frac{vd\epsilon_v^p}{\lambda - \kappa} \right)$$

The first part of the condition checks whether the stress point is moving towards the LC bounding curve. The second part of the condition checks whether the stress point is moving towards the SI bounding curve.

When assuming “stress point moving away from LC bounding curve and towards SD bounding curve” Equations A.17 to A.26 are used, with R_p and R_s given by Equation A.28 and A.30 respectively, and Condition 3 that must be checked has the following two parts to be satisfied:

$$\frac{dp^*}{p^*} < k_1 \left(\frac{-dS_r^p}{\lambda_s - \kappa_s} \right) \ \& \ \frac{ds^*}{s^*} < k_2 \left(\frac{vd\epsilon_v^p}{\lambda - \kappa} \right)$$

The first part of the condition checks whether the stress point is moving away from the LC bounding curve. The second part of the condition checks whether the stress point is moving towards the SD bounding curve.

When assuming “stress point moving towards LC and SD bounding curves” Equations A.17 to A.26 are used, with R_p and R_s given by Equations A.27 and A.30 respectively, and Condition 4 that must be checked has the following two parts to be satisfied:

$$\frac{dp^*}{p^*} > k_1 \left(\frac{-dS_r^p}{\lambda_s - \kappa_s} \right) \ \& \ \frac{ds^*}{s^*} < k_2 \left(\frac{vd\epsilon_v^p}{\lambda - \kappa} \right)$$

The first part of the condition checks whether the stress point is moving towards the LC bounding curve. The second part of the condition checks whether the stress point is moving towards the SD bounding curve.

When assuming “stress point moving away from LC bounding curve with soil saturated”, Equations A.17-A.21, A.24-A.26, A.31 and A.32 are used, with R_p given by Equation A.28, and Condition 5 that must be checked has the following 3 parts to be satisfied:

$$S_r \geq 1 \ \& \ (ds^* < 0 \ \text{or} \ (s^* + ds^*) \leq s_D^*) \ \& \ dp^* \leq 0$$

The first part of the condition checks whether the soil is saturated. The second part of the condition checks whether the soil remains saturated (either because $ds^* < 0$ or because final stress point lies outside the position of the SD bounding curve at the start of increment). The final part of the condition checks whether the stress point is moving away from the LC bounding curve.

When assuming “stress point moving towards LC bounding curve with soil saturated”, Equations A.17-A.21, A.24-A.26, A.31 and A.32 are used and Condition 6 that must be checked has the following 3 parts to be satisfied:

$$S_r \geq 1 \ \& \ (ds^* < 0 \ \text{or} \ (s^* + ds^*) \leq s_D^*) \ \& \ dp^* > 0$$

The first part of the condition checks whether the soil is saturated. The second part of the condition checks whether the soil remains saturated (either because $ds^* < 0$ or because final stress point lies outside the position of the SD bounding curve at the start of increment). The final part of the condition checks whether the stress point is moving towards the LC bounding curve.

A.2.3 The BBM

Figure A.3 shows the flow chart for the BBM simulations performed using Matlab. Firstly the values of model parameters and initial conditions are obtained from a data file. The type of stage (e.g. wetting) is then selected and corresponding values of three unknown incremental quantities are specified for the first increment. In the next step,

the unknown incremental quantities are calculated using the simultaneous equations provided in Section A.1.3 for two different cases. Next, for each of these 2 cases the relevant condition is checked (these conditions are described in detail later in this section). If more than one condition is satisfied, the increment size is reduced. Once only one condition is satisfied the incremental quantities are added to the respective values of variables at the start of increment. The program then moves on to the next increment. This cycle continues until the required stress path simulation is completed.

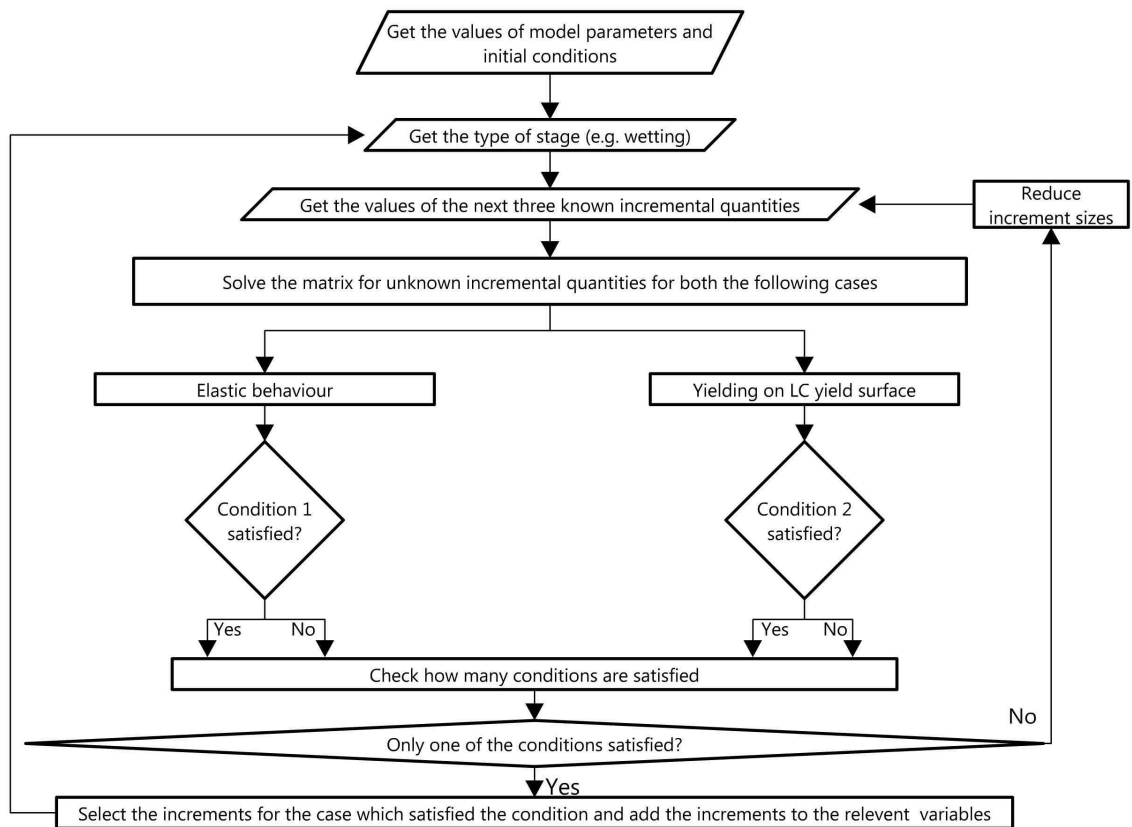


Figure A.3 Flowchart for the BBM simulations

When assuming “elastic behaviour” Equations A.33 to A.41 are used and Condition 1 must be checked:

$$\frac{(q + dq)^2}{M^2((\bar{p} + d\bar{p}) + k(s + ds))} + (\bar{p} + d\bar{p}) \leq p_0$$

This condition involves checking that the final stress point (at the end of the increment) does not lie outside the LC yield surface (with the yield surface in the position it was in at the start of the increment).

When assuming “yielding on the LC yield surface” Equations A.33 to A.40 and A.42 are used and Condition 2 must be checked:

$$\frac{(q + dq)^2}{M^2((\bar{p} + d\bar{p}) + k(s + ds))} + (\bar{p} + d\bar{p}) > p_0$$